NASA/CP–2019-219039

International VLBI Service for Geodesy and Astrometry 2018 General Meeting Proceedings

"Global Geodesy and the Role of VGOS – Fundamental to Sustainable Development"

Kyla L. Armstrong, Karen D. Baver, and Dirk Behrend

August 2019

NASA STI Program ... in Profile

Since its founding, NASA has been dedicated to the advancement of aeronautics and space science. The NASA scientific and technical information (STI) program plays a key part in helping NASA maintain this important role.

The NASA STI program operates under the auspices of the Agency Chief Information Officer. It collects, organizes, provides for archiving, and disseminates NASA's STI. The NASA STI program provides access to the NTRS Registered and its public interface, the NASA Technical Reports Server, thus providing one of the largest collections of aeronautical and space science STI in the world. Results are published in both non-NASA channels and by NASA in the NASA STI Report Series, which includes the following report types:

- TECHNICAL PUBLICATION. Reports of completed research or a major significant phase of research that present the results of NASA Programs and include extensive data or theoretical analysis. Includes compilations of significant scientific and technical data and information deemed to be of continuing reference value. NASA counterpart of peer-reviewed formal professional papers but has less stringent limitations on manuscript length and extent of graphic presentations.

- TECHNICAL MEMORANDUM. Scientific and technical findings that are preliminary or of specialized interest, e.g., quick release reports, working papers, and bibliographies that contain minimal annotation. Does not contain extensive analysis.

- CONTRACTOR REPORT. Scientific and technical findings by NASA-sponsored contractors and grantees.

- CONFERENCE PUBLICATION. Collected papers from scientific and technical conferences, symposia, seminars, or other meetings sponsored or co-sponsored by NASA.

- SPECIAL PUBLICATION. Scientific, technical, or historical information from NASA programs, projects, and missions, often concerned with subjects having substantial public interest.

- TECHNICAL TRANSLATION. English-language translations of foreign scientific and technical material pertinent to NASA's mission.

Specialized services also include organizing and publishing research results, distributing specialized research announcements and feeds, providing information desk and personal search support, and enabling data exchange services.

For more information about the NASA STI program, see the following:

- Access the NASA STI program home page at http://www.sti.nasa.gov

- E-mail your question to help@sti.nasa.gov

- Phone the NASA STI Information Desk at 757-864-9658

- Write to:
  NASA STI Information Desk
  Mail Stop 148
  NASA Langley Research Center
  Hampton, VA 23681-2199

NASA/CP–2019-219039

International VLBI Service for Geodesy and Astrometry 2018 General Meeting Proceedings

"Global Geodesy and the Role of VGOS – Fundamental to Sustainable Development"

Kyla L. Armstrong (ed.)
NVI, Inc., Greenbelt, MD

Karen D. Baver (ed.)
NVI, Inc., Greenbelt, MD

Dirk Behrend (ed.)
NVI, Inc., Greenbelt, MD

Proceedings of the 10th General Meeting of the International VLBI Service for Geodesy and Astrometry
Hosted by the Norwegian Mapping Authority (Kartverket),
Longyearbyen, Svalbard, Norway
June 3-8, 2018

National Aeronautics and
Space Administration

Goddard Space Flight Center
Greenbelt, MD 20771

August 2019

Level of Review: This material has been technically reviewed by technical management.

Available from

NASA STI Program
Mail Stop 148
NASA's Langley Research Center
Hampton, VA 23681-2199

National Technical Information Service
5285 Port Royal Road
Springfield, VA 22161
703-605-6000

Available in electronic form at https://www.sti.nasa.gov and https://ntrs.nasa.gov

Preface

This volume is the proceedings of the tenth General Meeting (GM2018) of the International VLBI Service for Geodesy and Astrometry (IVS), held in Longyearbyen, Svalbard, Norway, June 3–8, 2018.

Fig. 1 Banner of the tenth IVS General Meeting.

The keynote of the tenth IVS General Meeting was the contribution of the VLBI Global Observing System (VGOS) to the Global Geodetic Observing System (GGOS) in its endeavor to render sustainable development possible under the theme "Global Geodesy and the Role of VGOS – Fundamental to Sustainable Development." The United Nations recognized the importance of geospatial information to address global challenges with creating a UN-GGIM Subcommittee on Geodesy and following through with a roadmap to implement a Global Geodetic Reference Frame (GGRF). The space-geodetic techniques of VLBI, GPS, SLR, and DORIS will be fundamental for an accurate, accessible and sustainable GGRF to support science and society.

The tenth General Meeting was held at the culture house ("Kulturhuset") in Longyearbyen, Svalbard, Norway and was hosted by the Norwegian Mapping Authority (NMA). The goal of the meeting was to provide an interesting and informative program for a wide cross-section of IVS members, including station operators, program managers, and analysts. The Opening included a 30-minute video by a Norwegian documentary filmmaker about the importance of global geodesy for the world as well as a keynote speech about the UN-GGIM initiative on the Global Geodetic Reference Frame by IAG Vice-President Zuheir Altamimi.

This volume contains the following:

- **The papers presented at the meeting.** There are five major sections of this volume, each corresponding to a meeting session. Poster and oral papers are mixed. The five sessions cover the following topics:

  1. Building the VGOS Network
  2. VGOS Technique and Observation
  3. Legacy S/X and Mixed Legacy/VGOS Operations
  4. VLBI Core Products and Their Improvements
  5. Extending the Scope of VLBI Usage/Applications

  This volume includes 59 papers. All papers of this volume were edited by the editors for usage of the English language, form, and minor content-related issues.
- **An author index.**

The contents of this volume also appear on the IVS Web site at

`https://ivscc.gsfc.nasa.gov/publications/gm2018`

Slightly more than 100 registered participants from around the world attended the meeting. In the five sessions of the meeting, the participants gave 96 presentations; 62 of these were talks, and 34 were poster pre-

Fig. 2 Participants of the tenth IVS General Meeting at the bust of Roald Amundsen in the center of Ny-Ålesund.

sentations. The overall quality of the presentations was very high—a clear testament to the usefulness of the General Meeting as a knowledge exchange for all matters VLBI. While the attendance level was not as high as with the previous few GMs, the turnout can nonetheless be considered excellent given the remoteness of the location and the associated relatively high travel costs.

The August 2018 issue of the IVS Newsletter has a feature article about the meeting. The Newsletter is available at

`https://ivscc.gsfc.nasa.gov/newsletter/issue51.pdf`

The GM included the inauguration event of the new Earth Observatory in Ny-Ålesund. This necessitated a five-hour boat ride from Longyearbyen to Ny-Ålesund and then back. The two sailings through the Arctic scenery were mostly smooth and enjoyable—clearly something many participants will remember for a long time. Special treats were a walrus colony stopover and a helicopter rescue training exercise.

The meeting was a huge success, showcasing outstanding research, productive interactions, and diverse social activities, all in a very friendly atmosphere and unique venue. The organization was flawless, and for that, the LOC cannot be thanked enough.

Fig. 3 IVS Chair Axel Nothnagel during the opening session.

The editors would like to thank the contributors to this volume.

Kyla Armstrong, Karen Baver, and *Dirk Behrend*
GM2018 Proceedings editors
Greenbelt, MD · March 2019

Fig. 4 Per Erik Opseth (right) introduces the members of the LOC to the meeting participants.

Fig. 7 The twin telescopes at Ny-Ålesund during the inauguration event of Kartverket's new Earth Observatory.

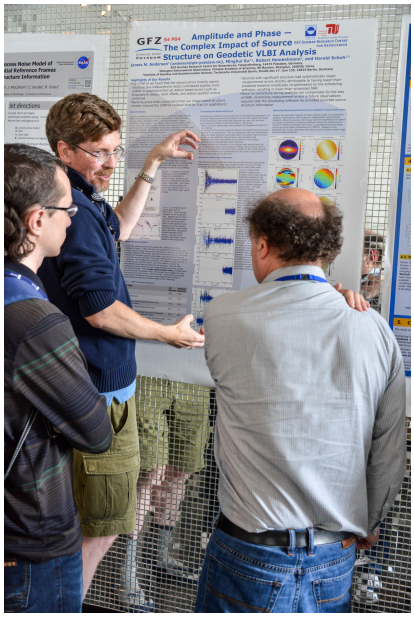

Fig. 5 James Anderson (center) discussing source structure impacts with Alexander Plavin (left) and Patrick Charlot (right) during the poster session.

Fig. 8 A helicopter rescue training excercise during the crossing from Longyearbyen to Ny-Ålesund.

Fig. 6 The walrus colony at Poolepynten.

Fig. 9 Experiencing the midnight sun on the sailing back to Longyearbyen.

Table of Contents

Session 1

Building the VGOS Network

The Status of RAEGE

P. de Vicente [1], J. González [1], J.A. López-Pérez [1], R. Bolaño [1], S. García Espada [1], P. García [1], F. Beltrán [1], M. Patino [1], O. García [1], J.M. Serna [1], B. Vaquero [1], I. Malo [1], O. García-Pérez [1], J.A. López Fernández [1]

Abstract We describe the status of the RAEGE network reviewing each of the stations that compose it. The Observatory of Yebes station is equipped with a broadband receiver and it has been taking part in VGOS observations since mid 2016. Works to improve and minimize the impact of RFI are presented. Santa Maria station is currently running a tri-band receiver, whereas the first works to construct a 13.2-m telescope at Gran Canaria were initiated. We also review the activities of the Observatory of Yebes as a Technological Development Center for the IVS. These are mainly related to the construction of broadband receivers, a cable calibration system, RFI measurements, and a harwdare solution for converting linear to circular polarizaton in a broadband regime.

Keywords RAEGE, VGOS, broadband receivers, RFI, polarization

1 Introduction

RAEGE stands for Red Atlantica de Estaciones Geoespaciales and it is an array composed of four 13.2-m diameter VGOS radiotelescopes located in Spain and Portugal. There are already two telescopes built and in operation at the Observatory of Yebes (Spain) and on Santa Maria (Azores Islands, Portugal). Two more telescopes are foreseen for Gran Canaria (Canary Islands, Spain) by 2020 and for Flores (Azores Islands, Portugal) beyond 2021. The baseline distances range between 800 km and 2,300 km, with the longest one being East-West, very appropiate for UT1 studies.

RAEGE will be part of the global VGOS network since all its telescopes are fast moving, 12 degrees per second in azimuth and six degrees per second in elevation, and equipped with broadband cryogenic receivers.

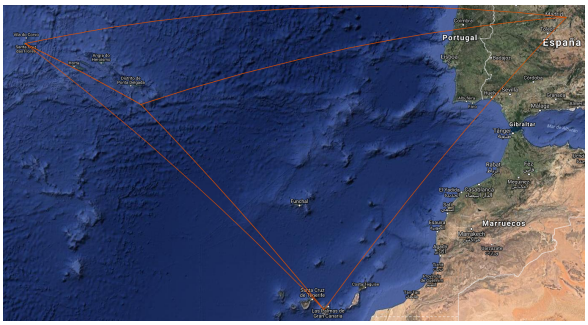

Fig. 1 RAEGE antennas and baselines depicted on a physical map. Already built and running telescopes: Yebes and Santa Maria. Its baseline is around 2,000 km long.

2 The Yebes 13.2-m RT

Currently the Yebes 13.2-m telescope is part of the CORE VGOS network and takes part in most of the tests performed since 2016. In 2016 the telescope was using two DBBC2s and a Mark6 as VLBI backends and recorder, respectively, and took part in 11 short observations. In 2017, the telescope started using four RDBE-Gs and took part in 24 24-hour observations. In 2018, the number of observations decreased due to a mechanical error at the telescope. VGOS observations have served to debug, correct, and optimize observa-

1. Observatorio de Yebes, Instituto Geográfico Nacional

tional procedures. Measures were taken to ensure the reliability of the operations avoiding the repetition of past errors.

The broadband receiver currently delivers an average system temperature of 50 K at 65 degrees elevation. Frequencies below 4 GHz are plagged with Radio Frequency Interference (RFI) causing an important increase of the system temperature, up to 100 K at some ranges (see Figure 2).

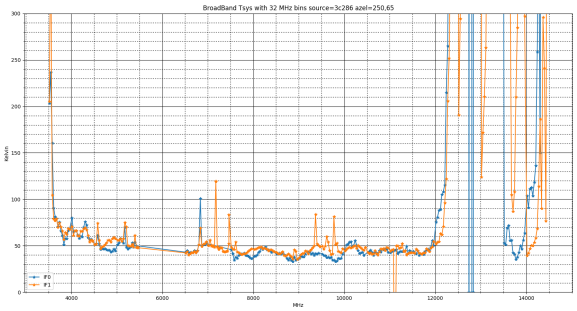

Fig. 2 System temperature for both polarizations at 250 degrees azimuth and 65 degrees elevation. It was obtained using a noise diode and while observing 3C286 under good weather conditions. The determination was done using a low band pass filter with a cut frequency of 12 GHz.

The frontend delivers two linear polarizations that are injected into an optical fiber module which transports the signals (1–14 GHz) to the backends room. Each polarized signal is then sent to a distribution module that amplifies and splits the input into four identical outputs that go into the up-down converter. The up-down converters follow the overall design by A. Rogers (2010) [6] and were developed and built at the Observatory of Yebes. Each up-down converter can be remotely commanded, allows to select the frequency input interval, and delivers the correct IF signal (0–500 MHz) to the RDBE-Gs. The digitized and packetized signal is directed towards the Mark6 after using a CX4-Optical-Fiber converter.

RFI is a severe problem at the Observatory of Yebes (OY), especially at lower frequency bands. Broadband receivers are specially vulnerable since the LNAs can saturate and cause non linear effects across the whole band. Fortunately this was not the case for the 13.2 m at Yebes, but there are issues with the optical fiber amplifiers that can break above 12 dBm. We have studied the environment of the OY with the broadband receiver and plotted the total power detected in the 2–12 GHz range across the sky. Figure 3 shows the distribution of power in a color diagram. Most of RFI happens at elevations below ten degrees and above 70 degrees. There are also some azimuths at which RFI is almost present at all elevations. The high power due to RFI led us to remove the amplifiers at ambient temperature after the cryostat and before the optical transceiver module to protect the latter but causing an increase in system temperature.

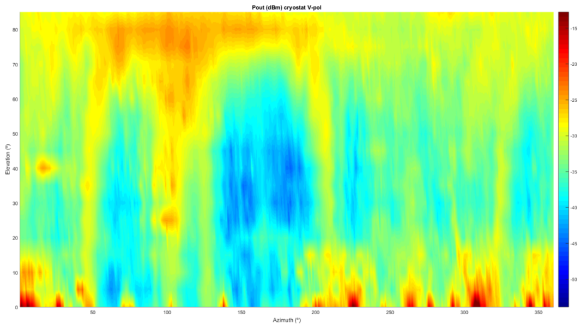

Fig. 3 Power in dBm from vertical polarization across the whole sky using the broadband receiver without filtering the data. The data are integrated between 2 and 12 GHz.

In order to decrease the system temperature and to keep at low level the RFI pollution, the output band from the amplifiers was split in two, above and below 4 GHz, and the amplifiers were reinstalled. In the band below 4 GHz a bandpass filter between 2 GHz and 2.35 GHz was installed and the signals from both bands were combined again before being injected into the optical fiber transceiver. The result of such combination is depicted in Figure 4 which shows a dramatic improvement resulting in strong RFI only below five degrees elevation and towards some selected azimuths. The average system temperature decreased from 70 K to below 50 K across the whole band. These results are part of a study on the RFI environment and mitigation by P. García (2018) [2].

A final iteration was used and the final setup consists in one amplifier per polarization after the cryogenic stage, a high pass band filter above 3 GHz, and a pin diode that limits the delivered output towards the optical fiber transceiver, keeping the linearity up to 6 dBm but limiting its maximum value to 10 dBm to protect all elements after. Figure 5 shows the final setup for the IF of the receiver.

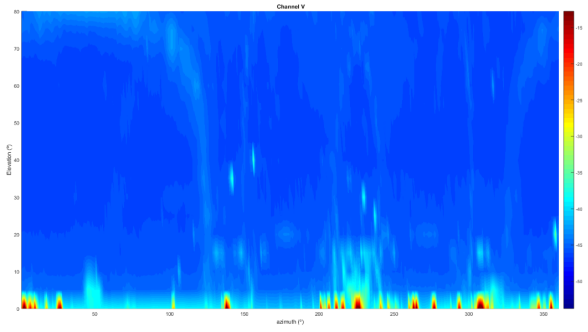

Fig. 4 Power in dBm from vertical polarization across the whole sky using the broadband receiver after filtering the data (see text for further details). The data are integrated between 4 and 12 GHz.

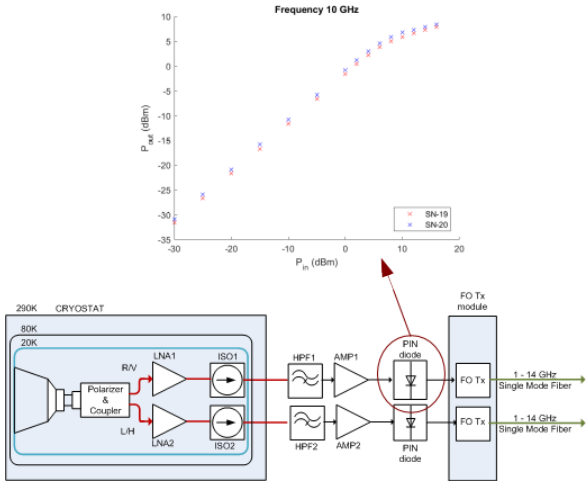

Fig. 5 Broadband receiver final setup. The high pass band filter has a cut frequency of 3 GHz. To avoid damaging the optical module, a diode pin that limits the current was installed. The curve with the response of the diode pin at 10 GHz is shown above.

3 The Santa Maria 13.2-m RT

The Santa Maria radiotelescope is currently equipped with a tri-band receiver. The first single dish successful observations were in July 2017 at S-, X-, and Ka-band. VLBI fringes were obtained at S- and X-band between Sm and Ys. The correlation was done at JIVE and repeated later at Yebes using a DiFX software correlator.

Current operations were paused for three months due to a hardware problem at the receiver, but observations have resumed in late August 2018 with legacy IVS observations and devoted observations at 2 and 8 GHz between Wettzell and Santa Maria to determine UT1. See Böhm et al. (2018) [1] in this same volume.

4 Gran Canaria and Flores Radio Telescopes

The 13.2-m radio telescope will be definitively installed at Gran Canaria island instead of being at Tenerife island, a location considered during the past years a potential site. The definitive location is at 1,100 meters above sea level in an enviromental protected area. Gran Canaria is an older and more stable island than Tenerife and thus probably a better fit for geodetic VLBI observations. Both of them are on the African plate.

Administrative work has started and it is foreseen that civil works will begin within the next months. Construction work is not allowed between March and September for enviromental reasons; therefore, the radio telescope will probably not be finished before 2020. The antenna is stored in a warehouse in Gran Canaria island, ready to be deployed when the site is ready. To ensure remote operations the IGN has signed an agreement with the technical University of Gran Canaria. The EVGA 2019 will take place in Gran Canaria in March 2019, on the premises of the University.

The status at Flores has not changed and there is no definitive site decided yet. Funds have not been secured by the Regional Government of Azores yet and there is still some preparation work to be performed first.

5 Technological Developments

The Observatory of Yebes is a Technological Development Center of the IVS and this section describes some of the activities performed during the last two years.

Within BRAND, a Radionet work package for developing a low frequency (1.5–15 GHz) broadband receiver, two of our engineers have measured the RFI environment at three EVN stations using portable equipment. Measurements were obtained between 1 and 18 GHz sweeping the whole horizon at different elevations. Spectra of RFI at each location were produced and they can be easily compared. This work has also interest for geodetic stations.

We have developed four cable and phase calibration systems composed of an antenna unit that generates pulses every 5 MHz and a ground unit which measures cable length variations with time. The design is based in the legacy design by A. Rogers [5] and it was implemented using printed circuit boards. Five more units will be built in the next year. Some of them will be delivered to BKG (Germany), FGI (Finland), and NMA (Norway). Improvements to the design using an ADC and some digital operations and filtering are already being considered and will be implemented in the next months. A prototype is being used at the Yebes 13.2-m radio telescope.

The Observatory of Yebes has installed and succesully tested a tri-band receiver at the two new NMA VGOS antennas in Ny-Ålesund. We installed the control system for the telescopes and performed the first single dish observations at both antennas remotely from Yebes. Three broadband receivers, two for NMA and one for FGI, are being built at our laboratories and it is foreseen to have them ready by 2019.

We have designed and are ready to develop a distribution module compatible with VLBI R2DBE and DBBC3 backends. The system creates four identical prefiltered outputs (4 GHz) per polarization prepared for a DBBC3 and six base bands at 2 GHz bandwidth following B. Petrachenko's proposal [4] prepared for the R2DBEs.

There has also been an important activity developing a hardware solution for the conversion between linear and circular polarization. It is well known that broadband receivers yield linear polarization. VGOS can work with linear polarizations at the correlator if both are present, but it requires a careful treatment of the data. A conversion to circular polarization at each station would ease the operations at the correlator. We have developed a solution for BRAND that has a direct application for VGOS. This solution requires the usage of hybrids and balanced Low Noise Amplifiers (LNAs). The hybrids were measured between 2 and 14 GHz and they deliver very good characteristics: low cross polarization ($<$ 25 dB) and low phase errors ($<$ 4 degs). These excellent results strongly depend on the control of the relative lengths of the cables, which is feasible using special connectors whose electrical length is tunable. If this solution worked operationally, it could lead to broadband receivers which could be used for legacy observations. A report by García-Pérez (2018) [3] was delivered to the VGOS Technical Committee.

References

1. J. Böhm, R. Bolaño, S. García Espada, J. González, G. Kronschnabl, A. Neidhardt, A. Phogat, C. Plötz, T. Schüler, P. de Vicente. European Intensive sessions for the estimation of Universal Time. In D. Behrend and K. Baver, editors, *International VLBI Service for Geodesy and Astrometry 2018 General Meeting Proceedings*, this volume.
2. P. García et al. RFI measurements in the Observatory of Yebes and mitigation measures. *In preparation 2018.*
3. O. García-Pérez, F. Tercero, I. Malo, J.A. López Pérez. Linear to circular polarization using microwave hybrids for VGOS (2-14 GHz). *CDT Technical Report 2018-13, 2018.*
4. B. Petrachenko. Continuous Frequency Coverage Using the R2DBE. *Private communication. 2017*
5. A.E.E. Rogers. Phase and group delay calibration of a very long baseline interferometer by East Coast VLBI Group. *NASA Goddard Space Flight Center Radio Interferometry; p. 255–261, 1980.*
6. A.E.E. Rogers. Performance characteristics and operation of Updown converter. *Haystack Observatory Memo 57. 2010.*

Technical Progress of the Chinese VLBI Network

Weimin Zheng [1,2], Juan Zhang [1], Guangli Wang [1,2], Renjie Zhu [1], Li Tong [1], Fengxian Tong [1], Fengchun Shu [1,2], Lei Liu [1], Zhengxiong Sun [1]

Abstract In recent years, the Chinese VLBI network has been greatly promoted by Chinas Lunar Exploration Project (CLEP) and the VLBI Global Observation System (VGOS). The new VGOS station will be put into trial observation in 2018. Both the new VGOS wideband VLBI terminal and the integrative data acquisition and transmission VLBI terminal for deep-space tracking have been installed. The correlator has been successfully applied to lunar probes and GEO satellites for phase reference precision positioning experiments. In combination with geodetic observations, precision comparisons have been performed with the DiFX and K5 correlators, and the CVN correlator is planned to be used for IVS data processing. According to the plan, a new VGOS station is under construction and it will join the CVN at the end of 2018. Besides, the first multi-purpose Earth-Moon baseline space VLBI experiment will be carried out, extending the CVN baseline length to 300,000 km.

Keywords VGOS, Chang'E lunar probes, VLBI terminal, software correlator, Earth-Moon space VLBI

1 Introduction

The Chinese VLBI Network (CVN) includes five antennas and one data-processing center now. The new Shanghai VGOS station is located in the Tianma 65-m telescope park. The Shanghai Astronomical Observatory (SHAO) has carried out development work on VLBI digital baseband converters and software correlator for many years. The new CDAS2 terminals data rate is up to 16 Gbps with VDIF output data format and it has the ability of 1–16 bits quantization. A general purpose software VLBI correlator for space probe tracking, geodesy, and astrophysics is under development. Aside from Chinas Lunar Exploration Project (CLEP), it was applied to Chinas Chang'E-3 (CE-3) lunar lander phase referenced VLBI positioning experiment. It will be used in Chang'E-5 (CE-5) dual objects same beam VLBI tracking as well as routine IVS data processing. According to comparison results from geodesy observations, the results of the Shanghai software correlator (SCORR) are highly consistent with the DiFX and K5 correlator results.

1. Shanghai Astronomical Observatory, CAS
2. Key Laboratory of Radio Astronomy, CAS.

2 TmVGOS Station

Fig. 1 The TmVGOS antenna (left), VLBI terminals (middle), and observation room (right).

A new VGOS station is under construction near the Tianma 65-m radio telescope. The antenna is manufactured by CETC-54 institute. The system consists of UDC, CDAS2, Mark 6, and DBBC3; a hydrogen maser

imported from Russia is already running. The station will install a real-time reference point monitoring system. The first fringe test was completed in September using an ambient temperature test receiver. Experimental observations with a cooled receiver are expected for the end of 2018.

3 Digital Terminal

Due to the requirements of CLEP and VGOS, a new VGOS wideband VLBI terminal and an integrated data acquisition and transmission VLBI terminal for deep-space tracking were installed. Table 1 shows a comparison of these terminals.

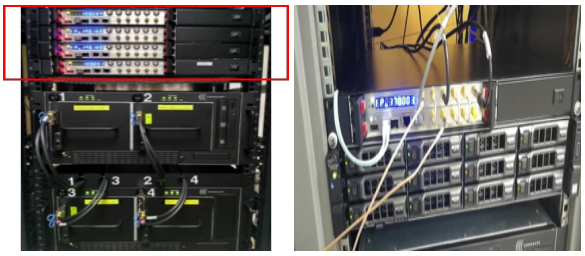

Fig. 2 VGOS Wideband VLBI terminal (left). Integrated data acquisition and transmission VLBI terminal for deep-space tracking (right).

The Chinese VLBI Data Acquisition System (CDAS) is the first generation digital BBC installed at CVN stations for astronomy, geodesy, and deep space observations. It has four Intermediate Frequency (IF) channels and the maximum data rate is 2,048 Mbps with 2-bit quantization capabilities. Due to the different requirements of astronomy, geodesy, and deep-space observations, the second generation VLBI backend CDAS2 was designed. For quasar observations, CDAS2 can work in the wide bandwidth with 1 or 2-bit quantization, while in deep-space probe observations, it can work in the narrow bandwidth with multi-bit quantization.

The VGOS wideband VLBI terminal and the integrated data acquisition/transmission VLBI terminal for deep-space tracking are both based on the CDAS2 platform installed in a 1U chassis.

The VGOS wideband VLBI terminal CDAS2-PFB needs four CDAS2 modules which are implemented with PFB algorithm, shown in Figure 2 (left). Each CDAS2-PFB can process a dual-polarized intermediate frequency signal with 512-MHz bandwidth. Each 512-MHz bandwidth has been divided into 16 sub-channels by the PFB algorithm. The data sent from a single 10 GE SPF+ port on each module are up to 4,096 Mbps. The VGOS wideband VLBI terminal is composed of four CDAS2-PFB modules and has the capability to process four dual-polarized IF signals and to send the data to a Mark 6 through four SFP+ ports. The total data rate is up to 16,384 Mbps.

The integrated data acquisition and transmission VLBI terminal for deep-space tracking only needs one CDAS2 module implemented with DDC algorithm, called CDAS2-DDC, shown in Figure 2 (right). It is suitable for S/X dual-band system. There are also two IF channels, one for S-band and the other for X-band. The functionionality of the CDAS2-DDC is the same as CDAS [1].

Considering briefly the developing cycle, a general purpose and low-cost VLBI terminal based on ROACH2 platform, in collaboration with the Xinjiang Astronomical Observatory (XAO), is under development. This is a general purpose terminal for VLBI and pulsar observations by upload different softwares.

Table 1 Comparison of the various terminals.

	CDAS	CDAS2-PFB	CDAS2-DDC	Roach2
Algorithm	DDC	PFB	DDC	PFB
Total Bandwidth(MHz)	4IF × 512	2IF × 512 × 4	2IF ×512	2IF × 512
Max Data Rate(Gbps)	2	16	2	2
Data Format	/	VDIF	MK5B	MK5B
Interface	VSI	SFP+× 4	SFP+× 1	SFP+× 1
Sample Bits	1/2	1/2	1/2/4/8/16	1/2
Subbandwidth(MHz)	1/2/4/8/16/32	32	0.5/1/2/4/8/16/32	32
Max Channels	16	120	16	15
Key Processer	Xilinx XC 4VLX160	Xilinx XC 7K355T	Xilinx XC 7K480T	Xilinx XC 6VSX475
Recorder	Mark5B+	Mark6	Commercial server	GPU server
Target	IVS, Lunar project	VGOS	Lunar and Deep space mission	VLBI, Pulsar(XAO +SHAO)

By the end of 2018, the CDAS3 platform will be finished. The maximum data rate is up to 32 Gbps. Fur-

thermore, an RF sampling solution has been put on the schedule. It will cover up to 14-GHz bandwidth.

4 Software Correlator

SCORR was originally developed for Chinas Lunar Exploration Project (CLEP), including CE-1, 2, 3, CE5T1, and CE-4 experiments. In these missions, it has played an important role in orbital determination of the spacecraft. The software correlator is written in C and uses MPI and pthread for parallelization. At present, the correlator supports multiple types of raw data formats, including Mark 5A, Mark 5B, and VDIF. As a correlator, which is mainly used in China's space missions in its early stage, it features real-time data processing for high reliability. Besides this, it supports real-time satellite signal fringe search, which means it is able to construct delay models by searching delay and delay rate from raw data. This function is especially useful during orbital maneuver when no fringe is available with predicted models.

CE-4 Queqiao relay satellite was launched on May 21, 2018. The CE-4 lander and rover will land on the lunar far-side surface at the end of 2018. We used VLBI technology in CE-4 successfully.

4.1 Specification of SCORR

SCORR consists of several modules such as Data Preprocess, Phase Calibration Signal (PCAL) extractor, Fringe searcher, Spacecraft Delay Model Reconstruction, and Correlation, among others.

Table 2 The specifications of SCORR.

Frequency Channel	16–16,384
Output Format	CVN, FIT-IDI, Mk4
Developing Language and Library	C, C++, CUDA, IPP, MPI, PThread, OpenMP
Computing Platform	Cluster+GPU+Storage Server
Data Recorded Format	MK5B,VDIF
Application	Deep Space, Geodesy, Astronomy, Spacecraft phase-reference VLBI experiments, and others

We hope to upgrade SCORR to a general purpose software correlator and support astronomy, geodesy, and deep-space observations. Table 2 lists the specifications of SCORR.

In the Rendezvous and Docking (RvD) phase of CE-5 Orbiter and Ascender, we plan to track the orbiter and the ascender in some special same beam VLBI cases. New dual objects algorithm are developed. We also developed a new fringe searcher algorithm for reducing the computation. For a real-time system, the calculation speed should be increased two times. GPU and IPP libraries are used to increase the computational capabilities.

4.2 Comparison with Other Popular Correlators

To verify the precision of SCORR, we have carried out detailed comparisons with other popular correlators, including DiFX [3, 4] and K5 developed by NICT, Japan. The comparison data is from IVS observing session K14349, which lasted for one hour and included four stations: Ny, Sh, Ts, and Wz.

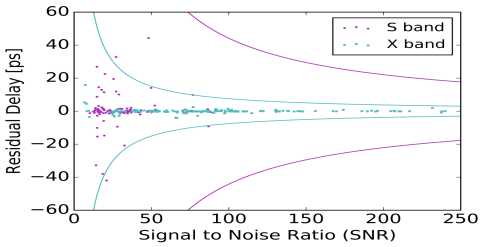

Fig. 3 Discrepancy of residual delay as a function of SNR. The blue and magenta curves correspond to theoretical uncertainties in S- and X-band, respectively.

In the comparison with DiFX, we did the correlation using the same delay model for both correlators. For this reason, the DiFX delay models were replaced with the SCORR models. Figure 3 shows the discrepancy of residual delay. The two correlator results fit quite well. The weighted root mean square is 9 ps in S- and 3 ps in X-band. The discrepancy of delay rate is within 0.1 ps/s. The SNR difference is within 0.5%.

The delay models of K5 are calculated for a reference station instead of the geocenter in SCORR and

DiFX; we had to make corrections to the K5 results. Figure 4 shows the comparison result. The discrepancies of the multi-band delay in X- and S-band are around 13 ps and 80 ps, respectively. Besides that, there is a constant offset for each baseline, which is due to the different usages of PCAL signals.

The constant offset will be removed in the post-processing. Discrepancies of the delay rate are within 0.5 ps/s and 1 ps/s for X- and S-band, respectively. The comparison test results show a good agreement of SCORR with the DiFX and K5 correlators. SCORR is accurate enough to process IVS observations.

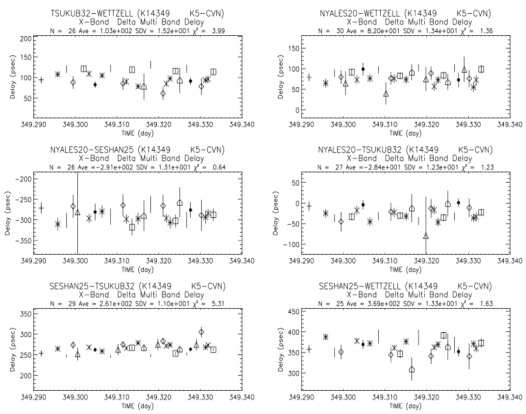

Fig. 4 Comparison of the multi-band delay in X-band for the K5 and CVN software correlators.

5 Satellite Observation Experiments

To assess the ability of satellite positioning using the CVN, several satellite observation experiments were carried out. The results show that the CVN is very effective, and its angular accuracy can reach tens of mas (milli-arcsecond) or even better.

Two Chinese VLBI antennas (Seshan & Urumqi) were used to test GPS observations of GPS-PRN28. Figure 5 shows the clear fringe of GPS-PRN28. That means Chinese VLBI antennas can observe near-earth satellites.

Figure 6 shows VLBI imaging results of a GEO satellite when using five Chinese VLBI antennas (Seshan, Kuming, Urumqi, Kashi, Jiamus). The ∼10 m (∼50 mas) positioning accuracy was achieved which met well the current meter-level GEO satellite positioning accuracy.

Phase referenced VLBI was also used to determine the CE-3 lander position. Two sessions were carried out. The positioning results discrepancy between these two sessions was ∼12 mas (∼10.5 mas in right ascension, ∼5.9 mas in Declination), which equals to ∼2 4m positioning discrepancy.

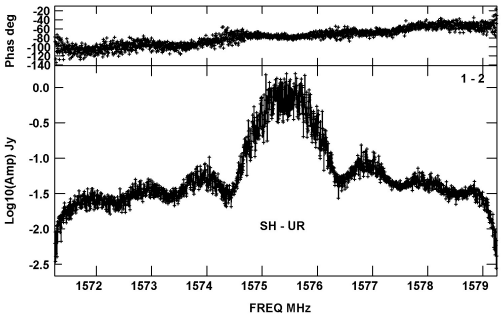

Fig. 5 Cross-spectrum of GPS-PRN28 on the baseline Sh–Ur.

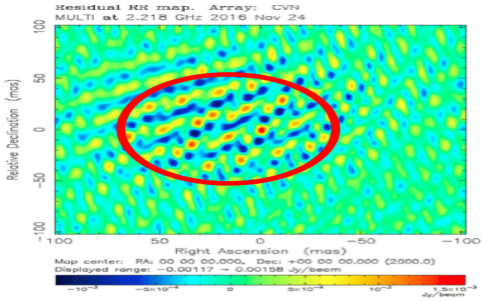

Fig. 6 GEO satellite phase referenced VLBI observation result.

6 VLBI Application in CE-4

ChangE-4 (CE-4) is the fourth Chinese lunar mission. It is the first time to land on and explore the far side of the moon. Queqiao relay satellite, which will establish the communication between the Earth and the CE-4 prober landing on the far side of the Moon, was launched on May 21, 2018. Now, it is orbiting around the Earth-Moon L2 point. The CE-4 probe will be launched at the end of 2018. As with previous missions, VLBI observations were used in the orbit determination of the relay satellite.

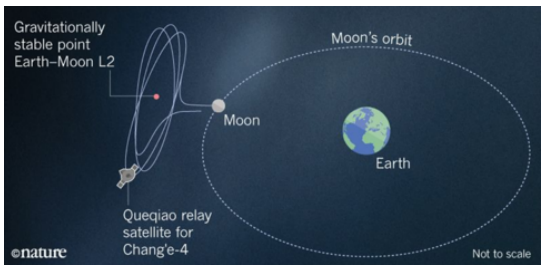

Fig. 7 Queqiao relay satellite tracks the Moon from a gravitationally stable point Earth-Moon L2 [5].

In the Queqiao mission, the CVN made use of S-band Delta-DOR in real time orbit measurement and CDAS2-DDC was successfully used for the first time. The whole CVN system performed much better than expected. More than 80% of the delays are better than 0.2 ns and the orbit determination errors were generally at the hundred meter level.

7 Earth-Moon Space VLBI

In the next mission of CLEP, there will be another relay satellite in lunar orbit. VLBI payloads such as the receiver, the H-maser, and VLBI terminal will be mounted on the relay satellite. Because of the longest baseline up to 400 km, cooperated with the ground based big antennas, the first Earth-Moon baseline space VLBI experiments of deep space probe tracking, astrometry, and astrophysics experiments will be carried out.

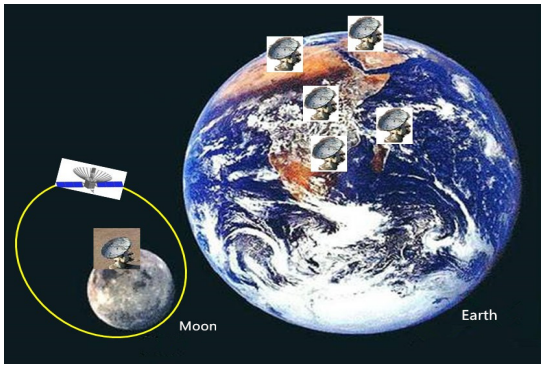

Fig. 8 The first Earth-Moon space VLBI experiment will be carried in the next lunar mission.

8 Conclusion

The CVN has made numerous technical advances. There will be more antennas to join the CVN in the future. We plan to carry out research on ultra-broadband receivers, 14-GHz bandwidth direct RF sampling terminals, GPU-based software correlators, and space VLBI technology.

Acknowledgements

This work is sponsored by the Natural Science Foundation of China General Program (11573057), the Ten thousand plan, Shanghai Key Laboratory of Space Navigation and Positioning Techniques, the CAS Key Technology Talent Program, and the Program of Shanghai Subject Chief Scientist (14XD1404300). We would like to thank Dr. Tetsuro Kondo for K5 correlator comparison, Dr. Lucia McCallum and Dr. Jamie McCallum for GPS observation data, and the observations of Australian antennas (Ceduna 30-m & Hobart 26-m), Russian antennas, New Zealand antennas, South African antennas, and the CVN.

References

1. Zhu Renjie, Zhang Xiuzhong, Wei Wenren, Xiang Ying and Li Bin. The Progress of Modern Chinese Data Acquisition System, Progress in Astronomy, Vol. 29, pp. 207–217, May 2011.
2. Lei Liu, Weimin Zheng et al. Precision Analysis of Chinese VLBI Network Software Correlator for Geodetic Applications. Accepted in Acta Geodaetica et Cartographica Sinica, 2017.
3. A.T. Deller, S.J. Tingay, M. Bailes, C. West. DiFX: A Software Correlator for Very Long Bsedline Interferometry Using MultiProcessor Computing Environments. Publications of the Astronomical Society of the Pacific, 119:318–336, March 2007.
4. A.T. Deller, W.F. Brisken, C.J. Phillips, J. Morgan et al. DiFX-2: A More Flexible, Efficient, Robust and Powerful Software Correlatior. Publications of the Astronomical Society of the Pacific, 123:275–287, March 2011.
5. D. Castelvecchi. Chinese satellite launch kicks off ambitious mission to Moon's far side. Nature, 557(7706):478–479, May 2018. doi: 10.1038/d41586-018-05231-9.

Extending of "Quasar" VLBI-Network: VGOS-compatible Radio Telescope in Svetloe

Evgeny Nosov, Dmitry Ivanov, Alexander Ipatov, Vyacheslav Mardyshkin, Dmitry Marshalov, Andrey Mikhailov, Ismail Rakhimov, Alexander Salnikov, Alexander Vytnov

Abstract IAA RAS has finished the construction of a new radio telescope in Svetloe, and the first fringes will be received in September of 2018. The new 13.2-m antenna will extend the facilities of the "Quasar" VLBI-network to six radio telescopes, and it will be the first one fully compatible with other VGOS stations worldwide. This paper is focused on equipment that makes it possible. The equipment of the Badary and Zelenchukskaya stations will also be upgraded soon to allow all three observatories of "Quasar" to join the international VGOS network.

Keywords Quasar-network, Svetloe, Tri-band receiver, Ultra-wideband receiver, MDBE, digital backend

1 Introduction

The Russian VLBI-network "Quasar" currently consists of three observatories: Zelenchukskaya, Badary, and Svetloe [1]. The 32-meter radio telescopes (RT-32) located at each of the observatories are part of international VLBI-networks (IVS and EVN), and they participate in many international and domestic observations. Since 2015 in Zelenchukskaya and Badary, there have been fast 13-meter radio telescopes (RT-13) operating in S/X/Ka wideband mode, mostly for domestic programs [2]. The antennas of RT-13 are VGOS-compatible, but they are equipped with Tri-band receivers and the Broadband Acquisition System that do not fully correspond to VGOS requirements. In 2018, the Svetloe observatory also got a new RT-13 radio telescope. The equipment of the new antenna is mostly ready, and the first fringes are going to be received in September 2018. The important point is that the new antenna is equipped with two types of receivers: both Tri-band and Ultra-wideband (UWB). The last one is VGOS-compatible and in conjunction with the new Multifunctional Digital BackEnd (MDBE), making it possible for the new radio telescope to join the international VGOS network. This paper is focused on the equipment of the new antenna that allows this.

Institute of Applied Astronomy of the Russian Academy of Sciences (IAA RAS)

2 Receiving System

The new antenna at Svetloe can be equipped with either a Tri-band (Figure 1) or a UWB (Figure 2) receiver. All parts are designed to allow easy and fast interchange of the receivers that takes just around six hours. It makes switching between the existing networks observing in S/X/Ka bands and the VGOS network possible.

The Tri-band receiver is similar to the ones used on RT-13 in Badary and Zelenchukskaya [3]. It simultaneously receives signals in S, X, and Ka bands in both circular polarizations. Both feed and low noise amplifiers (LNAs) are cryogenically cooled to keep the noise temperature low. Noise and phase calibration signals are injected into the signal chain before the LNAs.

Up-down converters (UDC) move the signals' required radio frequency range to intermediate frequencies (IF) used by the digital backend (from 1 to 2 GHz). In each polarization there are three UDCs for X-band, one UDC for S-band, and three UDCs for Ka-band. In total this gives 14 IF signals. By using a commutator,

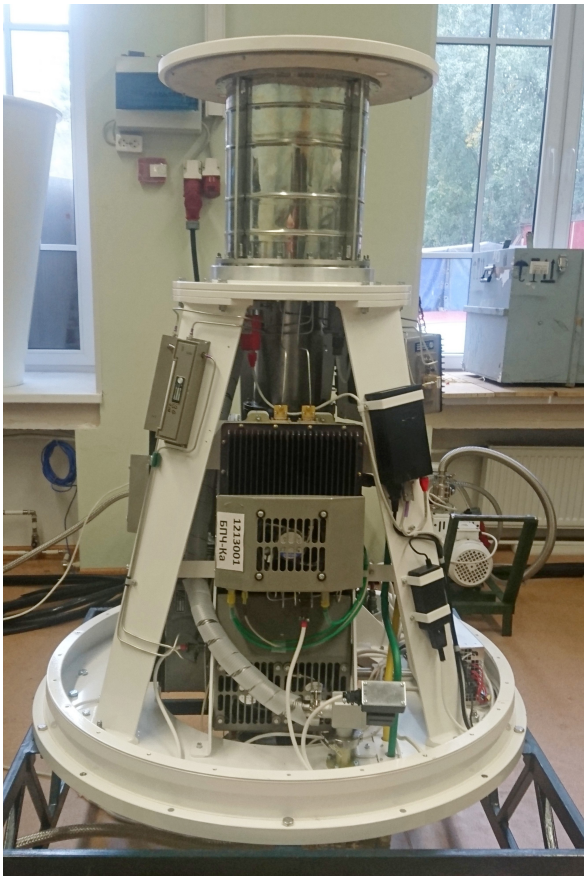

Fig. 1 The Tri-band receiving system.

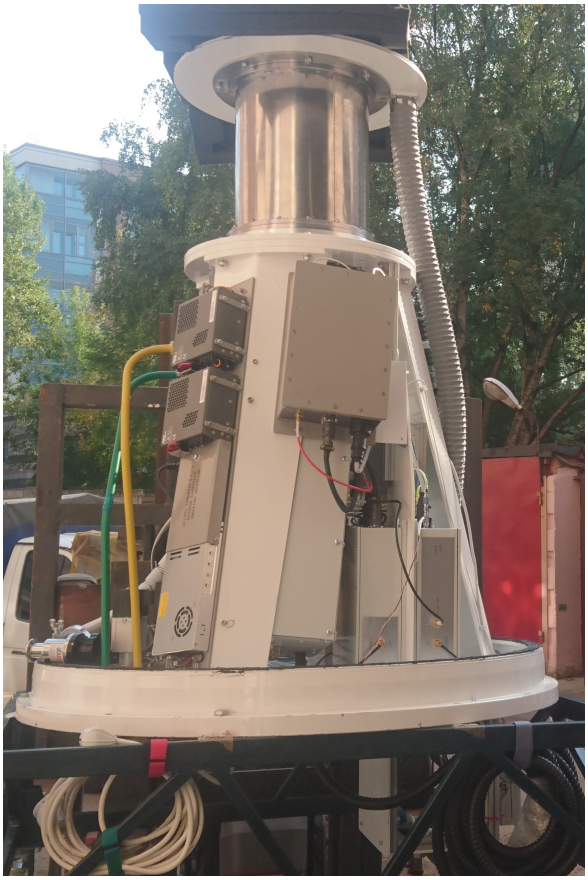

Fig. 2 The ultra-wideband receiving system.

eight of them are available outside of the receiver and transmitted to the digital backend.

Unlike the Tri-band receiver, the UWB receiver has a continuous frequency range from 3 to 16 GHz [4]. It uses a cryogenically cooled feed of QRFH type. Noise and phase calibration signals also can be used and injected into the signal chain before the LNAs. There are four UDCs in the receiver for each of the linear polarizations. The output signals of the UDCs lie in the frequency range of 1 to 2 GHz and are directly connected with the digital backend. Key parameters of the Tri-band and UWB receivers are summarized in Table 1.

Table 1 Key parameters of the Tri-band and UWB receiving systems.

Parameter	Tri-band	UWB
Input frequency range	2.2-2.6 GHz (S-band) 7.0-9.5 GHz (X-band) 28-34 GHz (Ka-band)	3-16 GHz
Polarizations	Dual circular	Dual linear
Noise temperature	$<$ 35 K (S-band) $<$ 33 K (X-band) $<$ 80 K (Ka-band)	$<$50 K
Step of local oscillators	0.1 MHz in S-band 0.4 MHz in X/Ka-bands	0.4 MHz
Output IF range	1-2 GHz	1-2 GHz
Output channels	(1 S + 3 X) x 2 pol. (8 total) (1 X + 3 Ka) x 2 pol. (8 total) (1 S + 2 X + 1 Ka) x 2 pol. (8 total)	4 x 2 pol.

3 Digital Backend

Currently, the RT-13 at Svetloe is equipped with the Broadband Acquisition System (BRAS) that is the

same as at the Zelenchukskaya and Badary observatories [5]. This system digitizes up to eight input signals in the frequency range between 1 and 1.5 GHz. Each signal is quantized to 2-bit samples with the root mean square value as a threshold. The data is then packed into VDIF frames without any sub-channelization and comes to the recording system over fiber link through a 10 G Ethernet interface. BRAS is a simple and low cost system, but it supports only 512 MHz bandwidth per channel and the only mode of operation. Because of these limitations it does not completely meet VGOS requirements, although it has been successfully used since 2015 for domestic observation programs.

In 2019, BRAS will be replaced with the new Multifunctional Digital BackEnd (MDBE) that is free of the listed limitations. The MDBE contains up to 12 DSP units (Figure 3 and Figure 4) that can digitize either one signal of 2 GHz bandwidth or two signals of 1 GHz bandwidth. Each DSP unit is based on a powerful FPGA that can perform quite advanced signal processing compared with the DSP units of BRAS. In conjunction with the remote firmware reconfiguration, it allows implementation of any required operational mode, including digital downconverter mode, to maintain compatibility with other astronomical backends. It also supports single dish modes for radiometric and spectrometric observations.

Besides its main purpose, the MDBE performs some signal analysis features like full input power measurement and PCAL extracting. Monitoring PCAL tones in time gives useful information about equipment stability and overall signal chain health. These features are very convenient for the equipment debugging and early detection of faults and performance degradation. To help hardware debugging, the MDBE can also perform FFT of input signals and can capture raw data from ADCs.

As timing issues are very important for VLBI applications, the MDBE has a number of tools to control it. The system clock is synchronized with the clock of the radio telescope by using a 1 PPS signal. The MDBE constantly monitors the delay between internal and external clocks to detect any jumps. It also can monitor the difference with the GNSS receiver clock. To take into account the fine effects of instrumental delay variations, the MDBE provides calibration loops to measure variations in the sampling clock synthesizer and clock distribution network. The key parameters of the MDBE are summarized in Table 2. In general, the MDBE will expand functionality of the radio telescopes and will unify backend equipment over the "Quasar" VLBI-network. It also will help to achieve compatibility with other VLBI radio telescopes worldwide.

Table 2 Key parameters of the MDBE.

Input bandwidth of DSP unit	Up to 2 GHz
Number of DSP units	Up to 12
Data rate	Up to 96 Gbps (2-bit quantization)
Data outputs	VDIF, 10GbE/40GbE, Fiber link
Remote reconfiguration	yes
Operational modes	VLBI: wideband channels, DDCs, PFB
	Single-dish: spectrometer, radiometer
Auxiliary features	PCAL extraction and analysis
	Internal delay instability measurement
	Embedded CDMS
	Signal capturing and FFT

4 Recording System

The data recording system for the new antenna is similar to that used for the other RT-13s [6], [7]. It is based on commercial, off-the-shelf hardware and provides recording of eight channels from the MDBE or BRAS with a total data rate up to 32 Gbps. The recording system supports transferring data to the Correlation Center of IAA RAS simultaneously with data recording. It helps to achieve low latency of VLBI results. The capacity of the storage is up to 200 TB, allowing data to record for a full day of observation programs.

5 Time and Frequency Transfer System

The time and frequency transfer system (TFTS) transmits required clock signals from the H-maser to equipment inside the focal cabin of the antenna. The MDBE, local oscillators of the receiving system, and PCAL generator use a 100 MHz signal as a reference clock. It comes to the focal cabin through the fiber line and is distributed to consumers through short and phase stable coaxial cables.

The TFTS includes a loopback to implement a cable delay measurement system (CDMS). It uses the same fiber to send back a received clock signal on

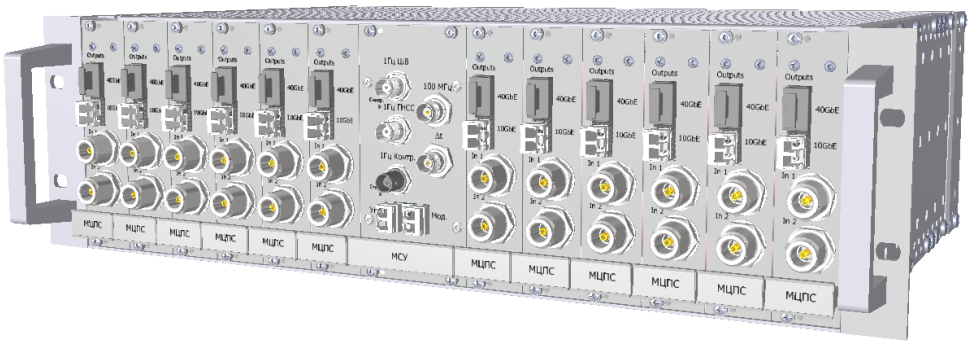

Fig. 3 A 3D model of the MDBE.

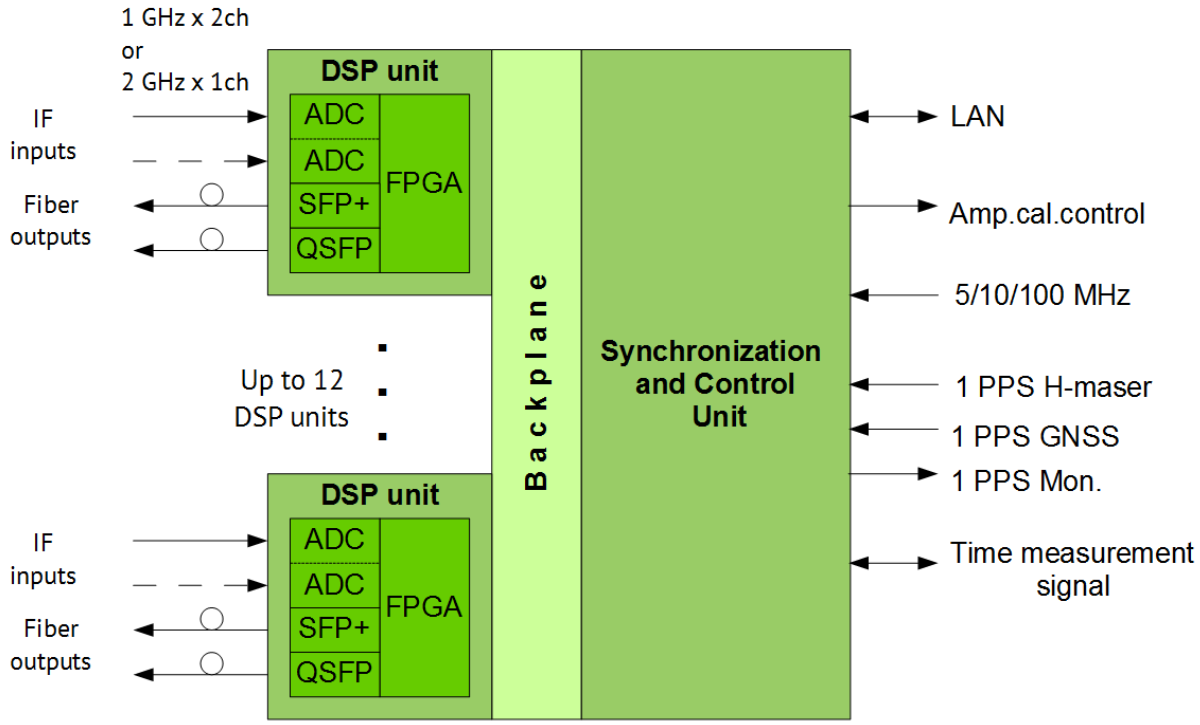

Fig. 4 An MDBE structure.

another optical wavelength. The CDMS allows measurement of cable delay variations at the 1 ps level. 1 PPS signals are also transferred to the focal cabin over fibers.

6 Conclusions

The construction of the new radio telescope RT-13 in Svetloe is finished. The first fringes are expected in September 2018. The newly created RT-13 is equipped with a Tri-band receiving system to provide regular observations with the other RT-13 antennas of

the “Quasar” VLBI-network. A new ultra-wideband receiving system is also ready for testing to allow joint observations with VGOS stations. The new Multifunctional Digital BackEnd will help to achieve full compatibility with other known backends used for VLBI.

References

1. Finkelstein A., Ipatov A., Smolentsev S. “The Network ‘Quasar’: 2008-2011”. *Measuring the Future: Proceedings of the Fifth IVS General Meeting*, A. Finkelstein, D. Behrend (Eds), pp. 39–46, 2008.
2. Ipatov A. “A new-generation interferometer for fundamental and applied research”. *Physics-Uspekh*, V. 56, No 7, pp. 729–737, 2013.
3. Chernov V., et al. “The S/X/Ka Receiving System for Radio Telescope RT-13 of the ‘Quasar’ VLBI Network”, *Proc. of IAA RAS*, No 41, pp. 79–84, 2017.
4. Evstigneev A., et al. “The Ultra-Wideband Receiver System for RT-13 Radio Telescope IAA RAS ‘Quasar’ Network”, *Proc. of IAA RAS*, No 41, pp. 49–51, 2017.
5. Nosov E., Marshalov D., Melnikov A. “Operating Experience of Broadband Acquisition System on RT-13 Radio Telescopes”, *IVS 2016 General Meeting Proceedings: ‘New Horizons with VGOS’*, Dirk Behrend, Karen D. Baver, and Kyla L. Armstrong (Eds), NASA/CP-2016-219016, pp. 53–57, 2016.
6. Bezrukov I., Salnikov A., Vylegzhanin A. “Russian Data Recording System of New Generation”, *IVS 2014 General Meeting Proceedings: “VGOS: The New VLBI Network”*, Dirk Behrend, Karen D. Baver, and Kyla L. Armstrong (Eds), ISBN 978-7-03-042974-2, pp. 130–133, 2014.
7. Bezrukov I., et al. “A Data Buffering and Transmission System: A Study of the Performance of a Disk Subsystem”, *Instruments and Experimental Techniques*, Volume 61, Issue 4, pp. 467–472, 2018.

Status of the Onsala Twin Telescopes – One Year After the Inauguration

Rüdiger Haas, Simon Casey, Gunnar Elgered, Roger Hammargren, Leif Helldner, Thomas Hobiger, Karl-Åke Johansson, Mikael Lerner, Lars Pettersson, Miroslav Pantaleev, Lars Wennerbäck

Abstract We briefly describe the status of the Onsala twin telescopes and the experience gained since the official inauguration in May 2017.

Keywords VGOS, OTT, broadband observations

1 Introduction

The Onsala twin telescopes [1] are two identical VGOS-type telescopes which are named ONSA13NE and ONSA13SW in IVS terminology. They are designed by MT Mechatronics and are equipped with 13.2-m diameter main reflectors and ring-focus subreflectors. The telescopes were built during 2015–2017 [2] and inaugurated in connection with the 23rd Working Meeting of the European VLBI group for Geodesy and Astrometry (EVGA) in May 2017, see Figure 1.

The telescopes are located at a distance of 70 m. There are two slightly different receiver systems installed on the telescopes. ONSA13NE hosts a receiver with a QRFH-feed covering 3–18 GHz, while ONSA13SW is equipped with an Eleven-feed covering 2.2–14 GHz [3]. Both feeds are dual-linear polarized. The two receiver systems are cryogenically cooled [4] and are connected to one phase and cable delay measurement system (CDMS) each. The two CDMS were purchased from the MIT Haystack Observatory. The H-maser for the time and frequency distribution is located in the maser room at about a 1 km cable distance from the telescopes. Each system has a digital backend of type DBBC3 with eight Core3H boards, which are located in the backend room within about a 15 m distance from the observatory maser room. The signal chain for both the CDMS systems and the received signals from the telescopes to the backend room uses optical fibers that are insulated against temperature variations. The two DBBC3s are connected to a FlexBuff recorder that currently has a capacity of 360 TB and is connected with a 10 Gbps connection to the Swedish fiber backbone. Both telescope towers, as well as the elevation and azimuth cabins, are equipped with numerous temperature and humidity sensors to monitor environmental changes.

Fig. 1 Picture taken during the inauguration of the Onsala twin telescopes in May 2017, with ONSA13SW on the left and ONSA13NE on the right side. (Photo Onsala Space Observatory)

Chalmers University of Technology, Department of Space, Earth and Environment, Onsala Space Observatory

2 VGOS Test Observations

We began participating in VGOS test experiments with the two telescopes in the autumn of 2017. These were primarily performed with the current "Haystack VGOS setup", i.e. eight frequency bands of 32 MHz bandwidth each for four RF-bands and two polarizations, e.g. 64 frequency bands in total. First fringes in some of the frequency bands were found with ONSA13NE for session VT7268 on 25/26 September 2017. A couple of days later, first fringes in some RF-bands for ONSA13SW were found in session MC7278 on 5/6 October 2017. Based on the experience gained, the systems were improved, and for VT7317 on 13/14 November 2017, fringes in all bands and all polarizations were found for ONSA13NE. A comparable performance was achieved for ONSA13SW in VT8039, observed 8/9 February 2018.

The ambitious plan to participate also in the CONT17-VGOS sessions could unfortunately not be realized because it had not been proven before CONT17 that the necessary system performance could be achieved.

Figure 2 gives an example of a fringe plot for an observation on the baseline GGAO12M to ONSA13NE. This fringe plot was kindly provided by Mike Titus from the MIT Haystack Observatory, who is correlating the VGOS test sessions. It becomes clear that fringes were found in all frequency channels and both polarizations, but at that time the ONSA13NE system had some variations in the amplitude of the four IF-bands.

Because the DBBC3 backends can be configured flexibly in various different modes, we also started to carry out test observations together with the Kashima 34-m telescope using the "Kashima VGOS setup", i.e. observing and recording complete 1-GHz windows. The first session, OK8051, was performed on 20 February 2018 using one 1 GHz wide band in two polarizations, and fringes were found.

Table 1 gives an overview of all VGOS test sessions that one or both OTT participated in until June 2018.

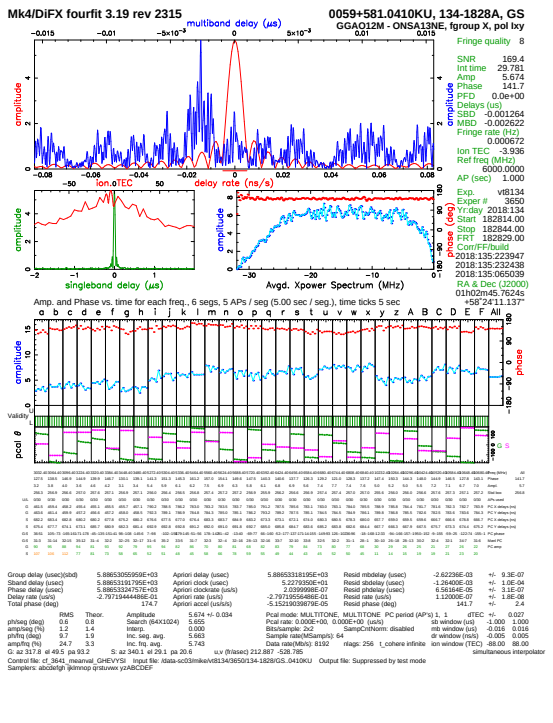

Fig. 2 Fringe plot of a scan observed during VT8134 on baseline GGAO12M-ONSA13NE. (Kindly provided by Mike Titus from the MIT Haystack Observatory.)

Table 1 Overview of the VGOS test sessions in which ONSA13NE (Oe) and ONSA13SW (Ow) participated between September 2017 and June 2018. Both VGOS flavors, i.e. the "Haystack VGOS setup" (VT- and MC-sessions) and the "Kashima VGOS setup" (OK-sessions) were observed.

Session	date	duration	systems	
VT7268	2017-Sep-25	24 h	Oe	–
MC7277	2017-Oct-04	24 h	Oe	Ow
MC7278	2017-Oct-05	24 h	Oe	Ow
VT7303	2017-Oct-30	24 h	Oe	Ow
VT7317	2017-Nov-13	24 h	Oe	Ow
VT7331	2017-Nov-27	24 h	–	Ow
VT8039	2018-Feb-08	24 h	–	Ow
VT8060	2018-Mar-01	24 h	Oe	–
VT8067	2018-Mar-08	24 h	Oe	–
VT8078	2018-Mar-19	24 h	Oe	–
VT8095	2018-Apr-05	24 h	Oe	–
VT8109	2018-Apr-19	24 h	Oe	–
VT8123	2018-May-03	24 h	Oe	–
VT8134	2018-May-14	24 h	Oe	–
VT8149	2018-May-29	24 h	Oe	–
OK051	2018-02-20	1 h	Oe	–
OK065	2018-03-06	1 h	Oe	–
OK074	2018-03-15	1 h	Oe	–
OK086	2018-03-27	20 h	Oe	–
OK136	2018-05-16	1 h	Oe	–
OK141	2018-05-21	20 h	Oe	–

3 Conclusions and Outlook

Since September 2017 we have participated in VGOS test sessions with one or both of the Onsala twin telescopes. We experienced a steep learning curve concerning, for example, the input RF-levels, the level of phase calibration signals (PCAL), interaction between the VLBI Field System (FS) and the DBBC3 backends, and operations as such. In general we achieved a steady improvement of the performance. Nevertheless, there are still aspects to improve, such as improved FS-DBBC3 communication, routine and simple determination and monitoring of system temperature (Tsys) and system equivalent flux density (SEFD), and fine-tuning of the CDMS system.

During the coming months we will thus continue the fine-tuning of the VGOS systems in order to improve the performance. We aim at participating in all possible VGOS sessions using all possible VGOS configurations. Our goal for 2018 is to gradually improve the system performance, as well as reliability, in order to become fully operational in 2019 with both ONSA13NE and ONSA13SW.

Acknowledgements

We acknowledge the support provided by the Knut and Alice Wallenberg foundation and Chalmers University of Technology.

References

1. Haas R (2013) The Onsala Twin Telescope Project. In: N. Zubko and M. Poutanen (eds.) *Proc. 21st EVGA Working Meeting*, 61–65.
2. Elgered G., Haas R, Conway J, Hammargren R, Helldner L, Hobiger T, Pantaleev M, Wennerbäck L (2017) The Onsala Twin Telescopes: the Status at the Time for the Inauguration. In: R. Haas and G. Elgered (eds.), *Proc. 23rd EVGA Working Meeting*, 136–139.
3. Flygare J, Pantaleev M, Billade B, Dahlgren M, Helldner L, Haas R (2017) Sensitivity and antenna noise temperature analysis of the feed system for the Onsala twin telescopes. In: R. Haas and G. Elgered (eds.), *Proc. 23rd EVGA Working Meeting*, 10–14.
4. Pantaleev M, Helldner L, Haas R, Johansson K-Å, Petterson L, Dahlström J, Dahlgren M, Kylenfall U, Billade B, Flygare J (2017) Design, implementation and tests of the signal chain for the twin telescopes at Onsala Space Observatory. In: R. Haas and G. Elgered (eds.), *Proc. 23rd EVGA Working Meeting*, 15–19.

Progress and Current Status of the VGOS Project at the Metsähovi Geodetic Research Station

Nataliya Zubko [1], Jyri Näränen [1], Guifré Molera Calvés [1], Markku Poutanen [1]

Abstract We report on the progress of the VGOS radio telescope system construction project in Finland. The new telescope was installed at the Metsähovi Geodetic Research Station during summer 2018. The construction of the signal chain components is moving forward. The installation and integration of the signal chain components is scheduled for spring 2019. It is expected to have first observational tests in the second half of 2019.

Keywords VGOS, radio telescope

1 Introduction

The new radio telescope dedicated to the VLBI Global Observing System (VGOS) was installed at the Metsähovi Geodetic Research Station. Metsähovi is a key infrastructure of the Finnish Geospatial Research Institute (FGI) and one of the core sites of the Global Geodetic Observing System (GGOS). It is located in southern Finland (60.2°N, 24.4°E). Metsähovi is one of the few geodetic stations that has all major geodetic observing instruments co-located. These include satellite laser ranging (SLR), very long baseline interferometry (VLBI), global navigation satellite systems (GNSS), superconducting and absolute gravimeters, and a DORIS beacon. The Ministry of Agriculture and Forestry has allocated a special funding for the renewal of the Metsähovi instruments and infrastructure during 2012–2018.

1. Finnish Geospatial Research Institute

The VGOS project in Finland started at the beginning of 2016. It is funded by the National Land Survey of Finland together with the Finnish Ministry of Forestry and Agriculture. FGI procured the radio telescope system in 2016. It was manufactured and installed by MT Mechatronics. The signal chain components were procured from various manufacturers and will be integrated into the system by FGI.

2 Metsähovi VGOS Radio Telescope Construction

Fig. 1 Foundation construction and installation of the anchor ring.

The preparation for the telescope installation at Metsähovi started in spring 2017. The selected site of the telescope is situated about 150 m away from the main building and SLR observatory. The area was

Fig. 2 Assembly of the steel pedestal.

Fig. 3 Assembly of the radio telescope.

cleared of trees and the upper layer of soil was removed; and after that it was covered with gravel.

The concrete foundation for the radio telescope was built on bedrock, where the steel anchor ring was installed (Figure 1). The anchor ring is part of the steel pedestal design that was developed by the telescope manufacturer.

The manufacturing of the radio telescope started in April 2017. The main technical characteristics of the telescope system are described in Table 1. The manufacturing of the complete system was finished at the beginning of 2018.

Table 1 Telescope technical characteristics.

Title	Description
Antenna mount	Standard azimuth-elevation type
Reflector optics	Cassegrain, ring focus
Diameter of the main reflector	13.2 m
Surf. accuracy of the main refl.	< 0.3 mm rms
Surf. accuracy of the subrefl.	< 0.1 mm rms
Antenna motion	
Velocity in azimuth	12 deg/s
Velocity in elevation	6 deg/s
Acceleration in azimuth	2.5 deg/s^2
Acceleration in elevation	2.5 deg/s^2

The telescope was delivered to Finland in June 2018 and the installation of the telescope at the Metsähovi site started immediately. First, the steel pedestal was mounted and attached to the anchor ring (Figure 2). The assembly and installation of the telescope electronic cabinets, motors, and electrical cabling work in the azimuth and elevation cabins was performed simultaneously with the telescope mechanical construction. The telescope assembling work at different stages can be seen in Figure 3.

The installation of the telescope progressed according to plan and was completed in twelve weeks. Figure 4 shows the new VGOS telescope built at Metsähovi. The telescope commissioning is planned for October 2018 and the final acceptance test is scheduled for December 2018.

3 Signal Chain

Metsähovi selected the Yebes Astronomical Center (CAY/IGN) as the manufacturer of their VGOS-compatible broadband receiver. It is planned to have the front end finished by March 2019. The receiver will use a Quadridge Feed Horn (QRFH) and operate in the frequency range between 2.1 and 14.1 GHz. The

Fig. 4 The VGOS radio telescope installed at Metsähovi.

observed RF signal will be then separated between low and high frequencies and send via optic fiber from the elevation cabin to the server room. The distance from the radio telescope to the main building is about 100 meters. The installation of the digital base band converter (DBBC3-H) capable of full VGOS operations and a data-storage facility, like a Flexbuff, is scheduled for fall 2018.

4 Conclusions

The VGOS project on building a new telescope system at Metsähovi will continue in 2019. It is planned to integrate signal chain components into the system and then start with first observational tests.

Building the New VGOS Radio Telescope at Hartebeesthoek as Part of Our New Geodetic Infrastructure

Philip Mey, Roelf Botha

Abstract The Geodesy Programme at Hartebeesthoek has been expanding since its first geodetic VLBI session with the 26-m radio telescope during 1986. Various equipment types were added on site as well as at several remote locations. The latest additions and expansions include a Site Tie, a data management system, and a VGOS dish. The VGOS dish project plan for implementation is a long-term undertaking which started during 2014. Mechanical commissioning has concluded during June 2018; the next stage will be sourcing and equipping it with the necessary receiver and backend instruments.

Keywords VGOS, Geodesy, Hartebeesthoek

1 Introduction

The Hartebeesthoek site, previously known as the Hartebeesthoek Radio Astronomy Observatory, now forms part of the larger South African Radio Astronomy Observatory (SARAO). Geodesy is one of the main activities on this site, which are aligned to support the Global Geodetic Observing System (GGOS) goals. Monitoring the global sea level change is one of the most demanding applications which drives the continued improvement and expansion of instruments and instrumentation networks [1]. The Hartebeesthoek site plays an important role in the international networks and is expanding to meet the new requirements of fiducial sites.

South African Radio Astronomy Observatory: Hartebeesthoek site

2 Geodesy Program and Equipment

The geodetic activities at the Hartebeesthoek site took off during 1986 with the first IVS-linked geodetic VLBI and later with the installation of the GNSS reference station *HRAO* during 1996. Since then the site has been expanding its geodetic activities and instrumentation by participation in geodetic VLBI using the 26-m radio dish, installation of a DORIS beacon, addition of GNSS reference stations, conversion of a 15-m radio dish for geodetic use, installation of a seismometer and accelerometer, and the establishment of two Satellite Laser Rangers. The Hartebeesthoek site is considered a fiducial site due to the co-location of all these techniques. Recently we have secured funding for and obtained, a total station for use in an automated site tie and a 13.2-m VGOS-type radio dish. These new additions to the site helps to ensure our continued participation in, and support of, global geodetic networks and experiments. We also have a distributed geodetic sensor network in and around Southern Africa with stations from Antarctica to Ghana, each consisting of at least a GNSS reference system. All these instruments and techniques produce large volumes of data and products; therefore, a new Geodetic Research Data Management System (GRDMS) is also being implemented piecewise.

2.1 Automated Site Tie

The Site Tie system at the Hartebeesthoek site will be used to determine mm-level inter-instrumentation offsets on a regular basis. This data will be used in-house and available to the community for accurate site defor-

mation studies in the drive to support the GGOS goal of mm-level positional accuracy [1]. The instrumentation hardware (Figure 1) and software was installed and initial tests, measurements, and calibrations are in process. Once an experimental method delivering consistent and accurate results is developed, this process will be automated.

Fig. 1 The Leica MS50 Total Station of the Site Tie.

2.2 Distributed Sensor Network

The distributed sensor network is currently being expanded by 10+ stations combining at least GNSS, meteorological, and seismic equipment. Of particular interest is the derived products that can be obtained from the co-location. These stations are placed throughout Southern Africa and even at locations such as the Ghana Radio Astronomy Observatory at Kutunse, Marion and the Gough Islands.

2.3 Geodetic Research Data Management System

Through the years the data management systems were developed on an *ad hoc* and per-technique basis, resulting in fragmented systems. These also do not cater for the large data volumes resulting from modern techniques and the increased number of instruments. This necessitated the design of a new and unified GRDMS [2, 3] which is currently being implemented.

3 Overview of the VGOS-SA Project

During 2014 we received funding to build a new Very Long Baseline Interferometry (VLBI) Global Observing System (VGOS) antenna. Such antennas are required for achieving GGOS goals by having faster slew rates, observing at higher frequencies and higher data rates. Our VGOS project was divided into four phases: planning, civil works, antenna construction, and commissioning.

3.1 Planning – June 2014 to March 2016

Activities during this stage included visiting other observatories with VGOS antennas and attending conferences to become knowledgeable about improvements and the implementation of VGOS related technologies.

- Detailing the specifications of the VGOS antenna towards tender documentation.
- Performing an Environmental Impact Assessment to ensure compliance with environmental regulations and best practices.
- Analyzing the Radio Frequency Interference experienced on our site.
- Using Direct Current Resistivity measurements to ascertain the ground conditions with subsequent verification of the depth to bedrock through core drilling.

3.2 Civil works – April 2016 to February 2017

During November 2015, the tender for the VGOS antenna was awarded and the design and infrastructure requirements was finalized. The antenna design incorporates a concrete base upon which the moving parts are mounted. This base structure contains steel reinforcement throughout with the concrete being poured in five stages: first the foundations measuring 9 m by 9 m with a depth of around 2 m; thereafter the ground

floor, walls, top floor, and finally the tapered walls. Figure 2 is a photo of the finished base prior to assembly of the radio dish.

Fig. 2 The finished concrete base.

3.3 Assembling the Dish – April 2017 to June 2017

Assembly started with installing the control, power, and drive cabinets inside the base. It was easier to preassemble the azimuth and elevation cabins on ground level, before installing it on top of the concrete base. Most of the work was therefore completed before the backup structure, quadrupod, and subreflector were assembled (Figure 3). Assembly of the azimuth cabin

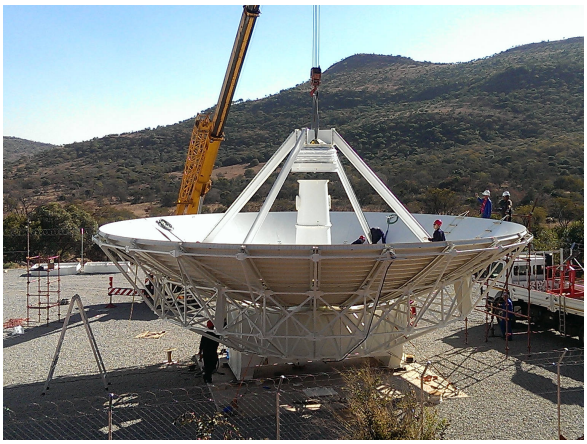

Fig. 3 Assembly of the main reflector.

with the counterweights and the main reflector was completed by mounting these parts, in sequence, onto the concrete base. To finish off the process, the exposed bolts were painted, cables were routed and connected, and the panel alignment was verified through photogrammetry.

3.4 Commissioning – September 2017 to June 2018

Commissioning of the VGOS dish involved the checking and verification of all electrical connections, calibration of sensors, and following all of the Site Acceptance Tests (SAT). Typically this process takes around three months, but due to unforeseen circumstances our process had to be interrupted and was finalized during 2018. The VGOS antenna eventually passed all SATs during June 2018 (Figure 4). Our 13.2-m VGOS dish can sustain slew rates of 12°/s in azimuth, 6°/s in elevation, and has a surface accuracy of 189.4 µm *RMS*. Although it is mechanically fully functional a lot remains to be done before it can participate in international VLBI experiments.

Fig. 4 The VGOS radio dish, far left, at Hartebeesthoek.

4 Next Steps in our VGOS Project

Work is in progress to monitor and control the VGOS dish remotely from a Linux-based system. The ideal would be to have the same software interface to all our radio telescopes albeit with different limitations as imposed by the equipment. During the next few months the plan is to install an ambient temperature 12-GHz

receiver (Figure 5), with a radiometer as backend, to start defining a pointing map. Many decisions have to be made before we can participate in VGOS observations:

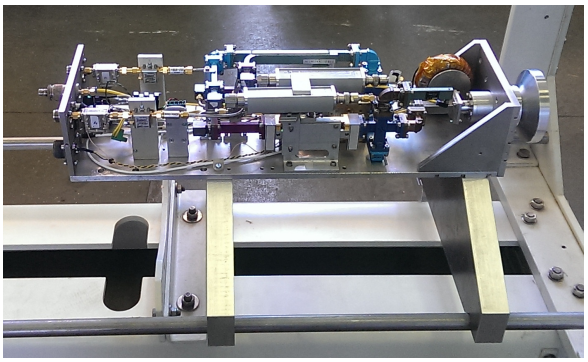

Fig. 5 A 12-GHz ambient temperature receiver that was built in-house.

- **Recorder**: Taking into consideration the vast amounts of data that will be acquired during VGOS observations and the significant investment in network infrastructure required at the correlators, a Mark 6 recorder was procured. This allows more flexibility with regards to e-shipping data or physically storing and shipping disk packs.
- **Backend**: During 2012, tests were performed to investigate and compare the available digital backends with a focus on the growing VGOS network [4]. Currently the DBBC-3, R2DBE, ADS-3000+, and CDAS implementations are still undergoing development and engineering changes to address challenges identified from VGOS test observations.
- **Receiver**: Two broadband feed types are of interest: the Quadridge Feed Horn and the Eleven Feed. A clear case comparing the advantages and disadvantages of these feeds has yet to be concluded since there is no consensus about which feed to use within the global community.

Ideally the VGOS network should have identical equipment at all observatories—this is impossible to achieve in such a diverse society. It is, however, possible to have antennas with comparable specifications delivering data formats that are compatible—therefore the networks' datasets can still be correlated. There are advantages in having a larger user base of a specific technology and while research and development continues, our VGOS dish will be used for other experiments to test its operational capabilities until such time that an informed decision can be made about our signal chain specifics.

5 Conclusions

The addition of a Site Tie instrument as well as a VGOS dish are important steps in achieving the alignment with GGOS goals, while the implementation of a unified and modern data management system forms part of the supporting infrastructure. Work on all these and supporting systems are ongoing but contribution to the international networks should start during 2019.

Acknowledgements

We express our gratitude to South Africa's Department of Science and Technology for their grant, which enables expansion and upgrading of the capabilities of the geodesy program with a modern VGOS dish. This work is based on the research supported by the National Research Foundation of South Africa (National Equipment Programme Grant 86041 and Strategic Research Infrastructure Allocations).

References

1. Plag, H.-P. and Pearlman, M. (eds) (2009) *Global Geodetic Observing System.* Berlin, Heidelberg: Springer Berlin Heidelberg.
2. Coetzer, G., Botha, R.C., Combrinck, W.L. and Fourie, C.J.S. *A New Geodetic Research Data Management System at the Hartebeesthoek Radio Astronomy Observatory.* In Proceedings of the Library and Information Services in Astronomy VII: Open Science at the Frontiers of Librarianship. ASP Conference Series, Vol. 492:22–30.
3. Coetzer, G., Botha, R. and Jacobs, L. *Progress with implementing the new research data management system at HartRAO.* In Proceedings of the Library and Information Services in Astronomy VIII: Astronomy Librarianship in the era of Big Data and Open Science. EPJ Web of Conferences, 186, article 12002.
4. Whitney, A. *Report on 2012 Digital Backend Intercomparison Testing.* In Proceedings of the 21st Meeting of the European VLBI Group for Geodesy and Astronomy, p. 1–2.

Extension and Optimization of the Local Geodetic Network at the Onsala Space Observatory

Cornelia Eschelbach [1], Michael Lösler [1], Rüdiger Haas [2], Henrik Fath [3]

Abstract Since May 2017, the Onsala Space Observatory (OSO) has hosted the Onsala twin telescopes (OTT), two identical telescopes fulfilling the VGOS-specifications. The local geodetic ground network has to be extended to the area around the OTT to provide local tie vectors for combining different geodetic space techniques at the observatory. Furthermore, this network is essential for monitoring the temporal and spatial stability of the new radio telescopes. Both network configuration and measurement uncertainties of the terrestrial observations have a strong impact on the obtainable accuracy of the reference points. Network optimization procedures help to avoid misconfigurations and provide suitable network configurations. For OSO, an extended ground network and an optimal observation schedule are derived that fulfill the accuracy requirements for monitoring processes. The observation schedule, derived by a second order design optimization, focuses on a practical experience when using modern geodetic instruments.

Keywords Second Order Design, Criterion Matrix, Integer Least-Squares, Network Optimization, Local Ties

1. Frankfurt University of Applied Sciences, Laboratory for Industrial Metrology
2. Chalmers University of Technology, Onsala Space Observatory
3. Freistaat Bayern, Körperschaft des öffentlichen Rechts, Amt für Ländliche Entwicklung Unterfranken

1 Introduction

In May 2017, the Onsala Space Observatory (OSO) inaugurated the Onsala twin telescopes (OTT). Both VLBI radio telescopes are identical in design and construction and fulfill the VGOS-specifications. For combining VLBI results of the OTT with other geodetic space techniques, i.e. for deriving the local tie vectors, as well as for monitoring the temporal and spatial stability of the new radio telescopes, the local geodetic ground network at OSO must be extended. The obtainable accuracies for, e.g. the reference points depend on the network configuration and the measurement uncertainties of the observations. The natural environment and especially the rough terrain limit the selection of locations for markers or pillars and their metrological connections. Network optimization procedures help to avoid misconfigurations and provide suitable network configurations. The optimal selection of locations and the optimization of the required observation weights are known as first order design (FOD) and second order design (SOD), respectively. Whereas — in most cases — the FOD cannot be optimized by analytical or numerical methods, the required weights of the SOD are estimable. For OSO, an extended ground network and an optimal observation schedule are derived that fulfill the accuracy requirements for monitoring processes. The observation schedule focuses on practical experience when using modern geodetic instruments.

2 Optimization of Geodetic Networks

A geodetic network is designed to observe topographic properties of the landscape or geometrical phenomena,

e.g. deformations on buildings. The configuration depends on the purpose of the network. Usually, four design states are distinguished. The definition of an ideal datum of the network is called zero-order design (ZOD). The optimization of the network configuration and the observation schedule are called first-order design (FOD), where the uncertainties of the observations are known. ZOD and FOD mainly depend on the topography and the realizable metrological connections. In most cases, ZOD and FOD cannot be optimized completely by numerical methods. The second-order design (SOD) is characterized to optimize the uncertainties of the observations, while the network configuration is kept unchanged. The evaluation of the improvement of further points and observations, which are introduced to an existing network, is summarized as third-order design (TOD). Thus, TOD combines the optimization techniques used by FOD and SOD.

The optimization of a single stage cannot be done independently of the prior states, e.g. the optimization of the uncertainties of the observations (SOD) requires a meaningful configuration (FOD) and a proper datum (ZOD) of the network. Table 1 summarizes the parameters which are assumed to be known and the parameters to be optimized during the optimization process. Here, the network configuration is given by the design matrix $\mathbf{A}$, the positive-definite dispersion matrix of the observations $\mathbf{l}$ is denoted by $\mathbf{P}^{-1}$, and $\mathbf{Q} = \left(\mathbf{A}^{\mathrm{T}}\mathbf{P}\mathbf{A}\right)^{-}$ is the dispersion matrix of the unknown parameters $\mathbf{x}$, e.g. the coordinates of the points. The generalized inverse is denoted by $(\,)^{-}$ and depends on the nullity of $\mathbf{A}$, i.e. the definition of the geodetic datum. Due to the natural

Table 1 Characterization of the parameters that will be optimized during the optimization process w.r.t. the parameters that are assumed to be known (e.g. [12]).

Design	Known parameters	Optimizable parameters
ZOD	**A**, **P**	**x**, **Q**
FOD	**P**, **Q**	**A**
SOD	**A**, **Q**	**P**
TOD	**Q**	**A**, **P**

environment and the local terrain there is only a limited number of suitable locations for survey pillars and ground markers, which determines ZOD and FOD of the network. In most cases, the optimizations are carried out without numerical efforts. For SOD, several approaches are known for deriving optimal uncertainties of the observations w.r.t. the required and idealized dispersion matrix $\mathbf{K}$ (e.g. [4, 10, 16]).

2.1 Procedure of second order design

The goal of the SOD is to find reliable weights $\mathbf{P}$, so that

$$\left(\mathbf{A}^{\mathrm{T}}\mathbf{P}\mathbf{A}\right)^{-} = \mathbf{Q} \doteq \mathbf{K}. \tag{1}$$

The matrix $\mathbf{K}$ is often called *criterion matrix*. Such a criterion matrix contains a homogeneous-isotropic structure of the point uncertainties and their dependencies and can be expressed by a so-called Taylor-Karman matrix (cf. [6])

$$\tilde{\mathbf{K}} = \sigma_0^2 \left(\phi_t(s)\,\mathbf{E} + \frac{\phi_t(s) - \phi_l(s)}{s^2}\mathbf{D} \right). \tag{2}$$

Here, the transversal and longitudinal correlation functions are given by $\phi_t(s)$ and $\phi_l(s)$, respectively; σ_0^2 is the variance of unit weight, and $s = \sqrt{\Delta x^2 + \Delta y^2 + \Delta z^2}$ is the distance between the points in the network. The identity matrix is denoted by $\mathbf{E}$ and the symmetric matrix $\mathbf{D}$ reads

$$\mathbf{D} = \begin{pmatrix} \Delta x^2 & \Delta x\Delta y & \Delta x\Delta z \\ \Delta y\Delta x & \Delta y^2 & \Delta y\Delta z \\ \Delta z\Delta x & \Delta z\Delta y & \Delta z^2 \end{pmatrix}. \tag{3}$$

Using the modified Bessel function of the second kind, the longitudinal and transversal correlation functions are given by

$$\phi_l(s) = \frac{4d^2}{s^2} - 2K_0\left(\frac{s}{d}\right) - \frac{4d}{s}K_1\left(\frac{s}{d}\right), \tag{4}$$

$$\phi_t(s) = \frac{2s}{d}K_1\left(\frac{s}{d}\right) - \phi_l(s) \tag{5}$$

where K_0 and K_1 are the modified Bessel function of zero and first order, and d is the so-called characteristic distance. There are several approaches for defining a suitable characteristic distance d (e.g. [11, 14]). According to Yazji [15], the characteristic distance is set to

$$d = \sqrt{2}\min s. \tag{6}$$

The derived criterion matrix $\tilde{\mathbf{K}}$ is unrelated to the specified ZOD datum. Hence, $\tilde{\mathbf{K}}$ is transformed to the de-

fined datum via an S-transformation, i.e.

$$\mathbf{K} = \mathbf{S}\tilde{\mathbf{K}}\mathbf{S}^{\mathrm{T}} \tag{7}$$

where $\mathbf{S}$ is the specific transformation matrix (cf. [1]).

In this distribution, a modified approach of the direct approximation of the inverse criterion matrix is applied (e.g. [7]). The inverse representation of Equation 1 is given by

$$\mathbf{A}^{\mathrm{T}}\mathbf{P}\mathbf{A} = \mathbf{Q}^{-} \doteq \mathbf{K}^{-}. \tag{8}$$

The corresponding normal equation system reads

$$\left(\mathbf{M}^{\mathrm{T}}\mathbf{M}\right)\mathbf{p} = \mathbf{M}^{\mathrm{T}}\mathbf{k}, \tag{9}$$

where

$$\mathbf{M} = \left(\mathbf{A}^{\mathrm{T}} \odot \mathbf{A}^{\mathrm{T}}\right). \tag{10}$$

Here, $\odot$ denotes the Khatri-Rao product, $\mathbf{p} = \operatorname{diag}\mathbf{P}$, and $\mathbf{k} = \operatorname{vec}\mathbf{K}^{-}$ (e.g. [12])[1,2]. To avoid negative weights during the estimation process, convex optimization with inequality constraints are recommended (e.g. [10]). The estimated weights $\mathbf{p}$ are optimal in the least-squares sense for $\mathbf{K}^{-}$ but not necessarily for $\mathbf{K}$. According to Illner and Müller [7] a correction factor

$$\lambda_u = \frac{\operatorname{tr}(\mathbf{QQ})}{\operatorname{tr}(\mathbf{QK})} \tag{11}$$

is introduced and the final weights are given by

$$\mathbf{P}_u = \lambda_u \mathbf{P}. \tag{12}$$

The estimated weights $\mathbf{P}_u$ of the SOD optimization are unrelated to instruments used during the field work, and the necessary number of repetitions of the observations are simply derived w.r.t. the a-priori uncertainty of a single measurement (e.g. [10, 13]). Practical experiences when using modern instrumentation are not included in the optimization process. For example, modern automated total stations register slope distances, directions, and zenith angles in parallel. A single element of a polar measurement triple cannot be observed without further ado. Moreover, a repetition of a full set of a standpoint can be carried out automatically by the total station. To limit the effort of the measurement procedure, the number of observed target points in a set should be kept unchanged. To take these practical aspects into account an adapted approach is needed.

[1] Function diag extracts the main diagonal of a matrix.

[2] Function vec vectorizes a matrix by stacking its columns.

2.2 Adapted Approach of SOD

The a-priori uncertainties of a single polar measurement triple can be evaluated by metrological experience and knowledge about the measurement instrument. It is the deterministic part of the weights $\mathbf{P}_{\mathrm{det}}$. The unknown part is the number of necessary repetitions $\mathbf{P}_{\mathrm{rep}}$ of the grouped observations. Groupings are applied to force full polar triples and to force the repetition of a full set of target points of a standpoint using specific grouping matrices $\mathbf{G}_{\mathrm{trip}}$ and $\mathbf{G}_{\mathrm{set}}$, respectively. A grouping matrix (e.g. [13])

$$\mathbf{G} = \left[\, \mathbf{g}_1 \ \ldots \ \mathbf{g}_i \ \ldots \ \mathbf{g}_g \,\right] \tag{13}$$

is setup by g group vectors $\mathbf{g}_i^{\mathrm{T}} = \left(0 \ldots 0\ 1 \ldots 1\ 0 \ldots 0\right)$, where ones indicate observations of the i-th group. Equation 10 is extended by the deterministic part of the weights $\mathbf{P}_{\mathrm{det}}$ and the specific grouping matrix $\mathbf{G}$, i.e.

$$\mathbf{M}_{\mathrm{rep}} = \mathbf{M}\mathbf{P}_{\mathrm{det}}\mathbf{G}. \tag{14}$$

Substituting Equation 14 into Equation 9 provides the repetition part $\mathbf{p}_{\mathrm{rep}} = \operatorname{diag}\mathbf{P}_{\mathrm{rep}}$ via

$$\left(\mathbf{M}_{\mathrm{rep}}^{\mathrm{T}}\mathbf{M}_{\mathrm{rep}}\right)\mathbf{p}_{\mathrm{rep}} = \mathbf{M}_{\mathrm{rep}}^{\mathrm{T}}\mathbf{k}, \tag{15}$$

and the weights of the observations, which are scaled by Equation 11, are given by

$$\mathbf{P}_u = \lambda_u \mathbf{P}_{\mathrm{det}}\mathbf{P}_{\mathrm{rep}}. \tag{16}$$

Whereas the estimated repetition part results in real numbers, only integer numbers are useful for practical application. As demonstrated in [9], the solution of an integer least-squares problem and the rounded solution of the corresponding real least-squares solution differ. For example, letting

$$\mathbf{M} = \begin{pmatrix} 1 & 4 \\ 2 & 5 \\ 3 & 6 \end{pmatrix}, \ \mathbf{k} = \begin{pmatrix} 1 \\ 1 \\ 1 \end{pmatrix},$$

the real solution is

$$\mathbf{p}^{\mathrm{T}} = \left(-\tfrac{1}{3} \;\; \tfrac{1}{3} \right).$$

Rounding the entries of $\mathbf{p}$ to their nearest integer value yields

$$\lceil \mathbf{p}^{\mathrm{T}} \rfloor = \left(0 \; 0 \right),$$

whereas the optimal integer least-squares solution reads (cf. [9])

$$\mathrm{p}^{\mathrm{T}} = \left(-2 \; 1 \right).$$

In geodesy, integer least-squares are used, for example, to estimate the GNSS double-difference integer ambiguity. The algorithm to solve integer least-squares problems is based on a tree search (cf. [2]). Therefore, the numerical effort and the runtime are larger than for the ordinary real least-squares algorithm. According to Chang et al. [3], a real least-squares solution can be transformed to its optimal integer solution. To get a useful solution of the SOD, finally, integer least-squares techniques are applied to transform $\mathbf{P}_{\mathrm{rep}}$ to its optimal integer representation.

3 Results and Conclusion

Two different network configurations were simulated mainly differing in the number of pillars near the OTT and in the number of connecting standpoints. Whereas the pillars surround the new telescopes and are predestined for reference point determinations, the standpoints are necessary to combine the network around the 20-m telescope with the newly designed network of the OTT. The first configuration forms the network of six pillars and 23 further standpoints, and the second configuration uses eight pillars and 24 standpoints. A detailed description is given in [5]. The results of both configurations are quite similar; therefore, we restrict the discussion to the eight pillar configuration.

The uncertainties of the terrestrial instrument are derived by an absolute uncertainty term σ_{c} and a distance-dependent uncertainty term σ_{v}. The combined uncertainty of a slope distance σ_{SD}, a horizontal direction σ_{HD}, and a vertical angle σ_{VA} measurement, respectively, are (cf. [8])

$$\sigma_{\mathrm{SD}} = \sqrt{\sigma_{\mathrm{c,s}}^2 + (s \cdot \sigma_{\mathrm{v,s}})^2}, \tag{17}$$

$$\sigma_{\mathrm{HD/VA}} = \sqrt{\sigma_{\mathrm{c,a}}^2 + (\rho \cdot \frac{\sigma_{\mathrm{v,a}}}{s})^2}, \tag{18}$$

where s denotes the distance and ρ is the conversion factor between radian and gon. Using Equations 17 and 18 and the values given in Table 2, the deterministic part of the weights $\mathbf{P}_{\mathrm{det}}$, cf. Equation 16, is defined.

Table 2 A-priori uncertainties of the polar measurement elements used for defining the stochastic model of the SOD. The constant uncertainties σ_{c} as well as the distance-dependent uncertainties σ_{v} are presented for polar observations.

Uncertainty	Distance	Direction	Vertical angle
σ_{c}	1.0 mm	0.3 mgon	0.3 mgon
σ_{v}	2.5 ppm	0.75 mm	1.0 mm

The criterion matrix is set up by Equation 2, using a target uncertainty $\sigma_0 = 0.5$ mm of a coordinate component, and S-transformed by Equation 7 to the geodetic datum of the ZOD process. Here, the geodetic datum is defined by marked points, i.e. ground markers and pillars.

The SOD process is carried out sequentially. In the first step, $\mathbf{G}_{\mathrm{trip}}$ is introduced in Equation 14 to identify the necessary polar observation triples that form the network with the specified point uncertainties. Using the remaining observation triples of the first analysis step and the extended grouping matrix $\left(\mathbf{G}_{\mathrm{trip}}\mathbf{G}_{\mathrm{set}}\right)$, which ties a full set of target points of a standpoint for repetition, the optimal number of repetition in real number representation is derived by solving Equation 15. Finally, using integer least-squares techniques the real least-squares result is transformed to the optimal integer solution, to get a useful solution. The final solution contains 22 standpoints and requires 137 grouped polar observation triples, cf. Figure 1. The repetition numbers are one, two and one-time nine. The large repetition number of nine is derived for a close range distance of about $s = 5.2$ m, which results in large angle uncertainties, cf. Equation 18.

In comparison to the spatial confidence intervals of the points derived by $\mathbf{K}$, the corresponding intervals derived by $\mathbf{C}$ are always smaller, cf. Figure 1. Thus, the solution derived by $\mathbf{P}_{\mathrm{rep}}$ reaches the specified target uncertainty of the points.

Summarizing, the optimization of geodetic networks allows for an evaluation of expected point

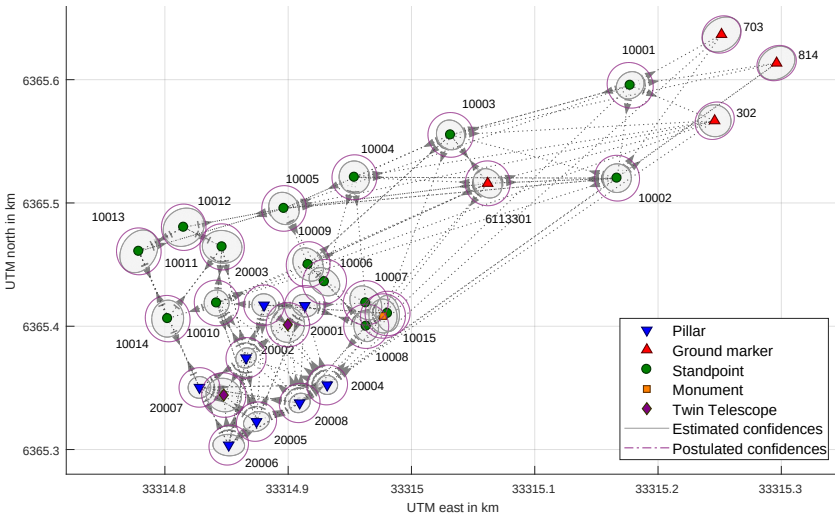

Fig. 1 Resulting network configuration and postulated and estimated confidences, as well as the SOD optimization observation plan.

uncertainties before markers are installed or measurements are carried out. For optimizing the second order design (SOD) numerical methods are well-known.

In this distribution, an extended network at the OSO was derived, which surrounds the new OTT. During the SOD optimization, the deviation between a Taylor-Karman based criterion matrix and the derived dispersion matrix was minimized. By grouping observations during the optimization process, practical experiences when using modern geodetic instruments are considered. Finally, integer least-squares techniques are applied to get a practically usable solution of the SOD.

References

1. W. Baarda: S-transformations and criterion matrices. *Netherlands Geodetic Commission*, Publications on Geodesy, 5(1), Delft, 2nd edn.
2. M.A. Borno, X.-W. Chang, X.H. Xie: On decorrelation in solving integer least-squares problems for ambiguity determination. *Surv. Rev.*, 46(334), 37–49, 2014.
3. X.-W. Chang, X. Yang, T. Zhou: MLAMBDA: A modified LAMBDA method for integer least-squares estimation. *J. Geod.*, 79(9), 552–565, 1997.
4. P.A. Cross: Numerical methods in network design. In: Grafarend W, Sansõ F (eds.): *Optimization and Design of Geodetic Networks*, Springer, Berlin, 132–168, 1985.
5. H. Fath: Planning of the monitoring network of the VGOS twin telescopes at the Onsala Space Observatory in Sweden (in German). *Master Thesis*, Frankfurt University of Applied Sciences, Chalmers University of Technology, unpublished, 2017.
6. E. Grafarend, B. Schaffrin: Kriterion-Matrizen I - zweidimensionale homogene und isotrope geodätische Netze. *zfv*, 104(4), 133–149, 1979.
7. M. Illner, H. Müller: Gewichtsoptimierung geodätischer Netze – Zur Anpassung von Kriteriumsmatrizen bei der Gewichtsoptimierung. *avn*, 91(7), 253–269, 1984.
8. M. Lösler, R. Haas, C. Eschelbach: Automated and continual determination of radio telescope reference points with sub-mm accuracy – Results from a campaign at the Onsala Space Observatory. *J. Geod.*, 87(8), 791–804, 2013.
9. S. Qiao: Integer least squares: Sphere decoding and the LLL algorithm. In: *Proceedings of the 2008 Canadian Conference on Computer Science and Software Engineering (C3S2E) conference*, 23–28, 2008.
10. L. Roese-Koerner, W.-D. Schuh: Convex optimization under inequality constraints in rank-deficient systems. *J. Geod.*, 88(5), 415–426, 2014.
11. G. Schmitt: Second order design of a free distance network, considering different types of criterion matrices. *Bull. Geodesique*, 54(4), 531–543, 1980.
12. G. Schmitt: Review of Network Designs: Criteria, Risk, Functions, Design Ordering. In: W. Grafarend, F. Sansõ (eds.): *Optimization and Design of Geodetic Networks*, Springer, Berlin, 6–10, 1985.
13. G. Schmitt: Second order design. In: W. Grafarend, F. Sansõ (eds.): *Optimization and Design of Geodetic Networks*, Springer, Berlin, 74–120, 1985.
14. H. Wimmer: Ein Beitrag zur Gewichtsoptimierung geodätischer Netze. *Dissertation*, DGK-C 269, Munich.
15. S. Yazji: The Effect of the Characteristic Distance of the Correlation Function on the Optimal Design of Geodetic Networks. *Acta Geod. Geoph. Hung*, 33(2-4), 215–234, 1998.
16. M. Yetkin, C. Inal, C.O. Yigit: Use of the particle swarm optimization algorithm for second order design of levelling networks. *J. Appl. Geod.*, 3(6), 171–178, 2009.

VGOS Wideband Reception and Emerging Competitor Occupations of the VLBI Spectrum

Vincenza Tornatore [1], Hayo Hase [2], Benjamin Winkel [3], Pietro Bolli [4]

Abstract The VGOS wideband receivers cover a spectrum from 2 to 14 GHz. In this range, many frequencies are allocated to other services. VGOS provides up to four 1 GHz wide sub-bands, which can be tuned to frequencies where detrimental radio frequency interference is absent. The increasing demand of commercial users of radio spectrum and related on-going telecommunication projects are threatening the VGOS observation plans. The examples of a compatibility study for 5G concerning the German Wettzell site and the global availability of Starlink/OneWeb illustrate the impact on VGOS and the need of regulation by spectrum authorities. This article contains a brief introduction how spectrum management is organized and what needs to be done on the national level to achieve protection for VGOS sites.

Keywords VGOS, wideband, spectrum management, RFI, 5G, Starlink, OneWeb, ITU, CRAF, CORF, RAFCAP, WRC

1 Introduction

New technologies making use of large bandwidths at frequencies above 2 GHz are introduced into the mass market. For example, the mobile Internet is rapidly spreading both in developed and developing countries. It is expected that the number of mobile Internet users will outperform the users of fixed access in the coming years. Mobile phone services based on Internet technology are expanding in the demand for a more electromagnetic spectrum in terms of global coverage. Undisturbed parts in the radio spectrum are becoming fewer and fewer, and radio-quiet remote rural regions are becoming less. Satellite and airborne radio transmission services are another threat to radio astronomy observatories, since they overcome the shielding by the local terrain. Many of these services have plans to emit broadband signals in a range that overlaps in several parts of the range of the spectrum where old legacy VLBI antennas (2.20−2.35 GHz, 8.1−8.9 GHz) and new VGOS[1] radio telescopes (2−14 GHz) intend to receive signals from weak natural radio sources.

We will briefly present in this paper two of the upcoming active services: 5G mobile telephone (3.3−4.2 GHz, 4.4−4.9 GHz, 5.9−7.1 GHz) and the satellite-based communication infrastructure (10.7−12.7 GHz), which are using parts of the spectrum now for tests. These frequencies are also targeted to be used by the new VGOS broadband receivers.

There have been numerous cases in the past where a satellite system was responsible for strong emissions into radio astronomical bands, effectively blinding the radio antennas in parts of the sky or for some time [Jessner 2013].

Spectrum allocations to radio services are established by international conventions in a complex process, considering not only the technical feasibility, but also driven by economic and historical aspects. It is

1. Politecnico di Milano, Italy
2. Bundesamt für Kartographie und Geodäsie, Germany
3. Max-Planck-Institut für Radioastronomie, Germany
4. Arcetri Astrophysical Observatory, Italy

[1] VGOS: *VLBI Global Observing System* is the contribution of the International VLBI Service to the Global Geodetic Observing System (GGOS). It comprises a modernized version of geodetic and astrometric VLBI to achieve globally 1 mm accuracy in positioning. The global network will extend to more than 15 new VGOS radio telescopes.

very difficult to increase the allocations to scientific services, or to adapt their protection to modern developments in the current climate of the high commercial exploitation of the radio spectrum.

At the same time, as the emerging competitors are asking for more spectrum, the geodetic and geoscience community also reached high-level recognition and was given tasks, which are in practice related to Earth monitoring by VLBI:

- [UN-Resolution 69/266] of the General Assembly on February 26th, 2015;
- [Directive 2007/2/EC] of the European Parliament and of the Council on establishing an Infrastructure for Spatial Information in the European Community (INSPIRE), March 14, 2007;
- [ITU-R TF.460] Standard-frequency and time-signal emissions, determination of UT1 by VLBI provided by the IERS.

This legal frame demonstrates an administrative interest to get information from VLBI observations. One important requirement to conduct VLBI observations is the absence of harmful radio interference. The expansion of wireless communication is a threat to exercise the VLBI task properly.

In this paper we will give an overview of the bodies involved at national, regional and global level for spectrum management (Section 2). We will demonstrate two cases of emerging spectrum competitors to VGOS: 5G (Section 3.1) and Broadband communication satellites for global internet and mobile telephone (Section 3.2). Action strategies against the threat of losing spectrum is discussed in our conclusions.

2 Spectrum Management

The use of the electromagnetic spectrum is managed by national, regional, and global regulatory frameworks. Spectrum management aims at coordinating the frequency allocation for different telecommunication systems. The finite resource of radio spectrum is oversubscribed and does not satisfy the demand of the wireless technologies without compromising existing services.

The International Telecommunication Union (ITU) is the authority responsible to regulate globally information and communication technologies. The treaty organization that deals with radio waves is the Radiocommunication Sector of the ITU (ITU-R). It divides the world into three administrative regions. The interests of the European radio astronomers in ITU-R1, are represented by the Committee on Radio Astronomy Frequencies (CRAF), an Expert Committee of the European Science Foundation. Similar organizations to protect radio astronomy interests exist both for the Americas (CORF) in ITU-R2 and for the Asian-Pacific areas in ITU-R3 (RAFCAP).

ITU activity is organized in about four-year cycles, which culminate in the World Radio Conference (WRC), a major event assembling all national spectrum agencies and sector members with an interest in the radio frequency spectrum.

Common interests of a particular region are discussed within regional international groups. Member states within a region may, and often do, have bilateral or multilateral agreements. It is worth noting that each national administration has the sovereign right to administer spectrum use within its borders, as long as they do not violate ITU-R radio regulations.

At the European level, the European Conference of Postal and Telecommunications Administrations (CEPT) is the official body dealing with spectrum management issues. Some of the other regional administration bodies in the world are the Inter-American Telecommunications Commission (CITEL), the African Telecommunications Union (ATU), the Asia-Pacific Telecommunity (APT), and the Arab Spectrum Management Group (ASMG). Structures of spectrum management differ among the nations. Some nations have internal structures to provide input both to national regulation and to the WRC.

Regulations established at international levels are implemented in each country through the national frequency allocation tables. In addition to the regulatory work, there is a great deal of technical and policy expertise and consultative infrastructure around the ITU-R, primarily centered on the so-called Study Groups. The Study Groups are broken down into Working Parties and ad-hoc Task Groups, where the adopted questions and assigned WRC agenda items are studied and considered. Study Group 7 addresses issues for the scientific services, WP7D is concerned with radio astronomy.

The Radio Astronomy Service (RAS) was recognized as a service at the 1959 World Administrative Radio Conference. Radio astronomy is very sensitive to the protection of its bands being a passive service

(only reception) and receiving extremely faint signals. For radio astronomy, threshold levels of detrimental interference for both single-dish and VLBI mode are provided in the recommendation [ITU-R RA.769-2].

3 Examples of Potential Interferers

3.1 5G Earth Base and Mobile Stations

Broadband mobile radio systems are based on the ITU International Mobile Telecommunications (IMT) standard, for example IMT-2000 for the 3G system and IMT-Advanced for 4G. [ITU IMT-2020] is the standard platform on which to build the next generation (5G) of broadband connection. 5G performance targets include high data rate, reduced latency, energy saving, cost reduction, higher system capacity, and massive device connectivity.

WRC-15 has harmonized the existing spectrum and identified new bands for IMT. The focus is now on feasibility studies for the identification and allocation of frequency bands for IMT-2020 (5G) operations (WRC-19 agenda item 1.13). The cooperation of all nations within the regional groups is of vital importance in order to achieve the optimal use of the spectrum resources. Different countries have proposed and are working on different frequency bands that range from 600 MHz to 71 GHz. There is a lower band and a higher band in each country and region. In Europe, for example, there is a focus on mid-band (3.4−3.8 GHz) and 26 GHz (24.25−27.50 GHz).

5G will likely be available in pre-standard form by late 2018 and early 2019. However, the technology is not to be prevalent until the 2020s. 5G networks will enable more Internet-of-things (IoT) capabilities as well as connected cars and smart city applications. 5G networks consist of base stations (BS) and user equipment (UE), although alternatives such as mesh-network based topologies seem also viable. The targeted densities and antenna heights are not fully defined yet [Draft ECC Report 281].

The 5G operations represent a potential detriment to observations at radio telescopes. Compatibility studies have to be performed to determine the expected level of radio frequency interference at an RAS-site due to an active service. For this, the Python package `pycraf` was used [Winkel, Jessner 2018][2]. It implements algorithms recommended by ITU-R, e.g., [ITU-Rec. P.452-16], that can be used to calculate the path attenuation between a transmitter and the radio telescope, accounting for various effects such as diffraction at elevated terrain features.

For the upcoming use of the 3.4−3.8 GHz band, technical parameters are still under discussion. One major uncertainty is the final deployment density of 5G equipment. Therefore, only the so-called single-interferer case, where the compatibility of VGOS observations vs. a single base station is analyzed, is discussed here. It is likely, that in this frequency band, 5G BS will utilize antenna arrays to improve the effective gain of the links (to the cell phones) with the help of beam forming. Since the beams will point quasi-randomly to any direction in the forward sector, the single-element antenna pattern can be used on average to sufficiently predict the typical effective gain towards the RAS station. The acceptable emitted power levels (EIRP) are still under debate, which is why the calculations have been done for 30, 40, 50, and 60 dBm/MHz. Terrain height profiles have been queried from SRTM Space Shuttle Mission data [Farr et al. 2007]. For VGOS operations, the VLBI thresholds in [ITU-R RA.769-2] were interpolated, giving a value of -203 dB W/m^2/Hz that must not be exceeded. It is foreseeable that 5G base stations will usually be installed in locations where substantial clutter attenuation provides additional shielding. However, the worst-case of zero clutter loss here is assumed to obtain the size of a coordination zone, within which one should carefully assess potential installation locations.

Given path attenuation and considering the transmitted power and the power level acceptable for the radio telescope, coordination zones were calculated. Figure 1 shows the results of simulations for the German VGOS station Wettzell. The blue lines mark the coordination zone for base stations with 30 dBm/MHz at 3.4 GHz. If the base stations had more power, the coordination zones would need to be larger. With 40 dBm/MHz even the city of Munich falls into the coordination zone, as well as parts of the Czech Republic. The results presented here are only valid under the assumptions made. Especially the true

[2] The open source software `pycraf` can be retrieved from https://pypi.org/project/pycraf/

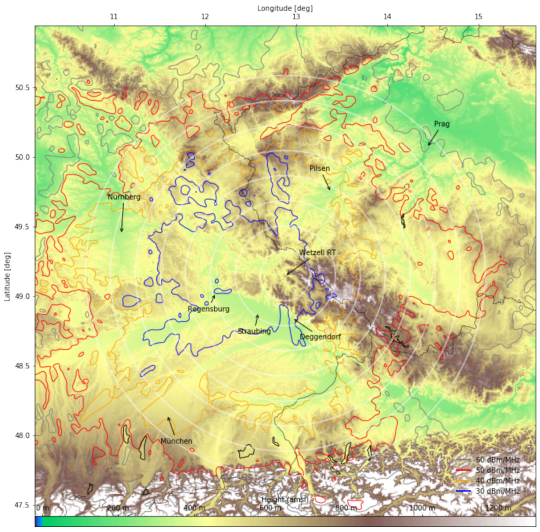

Fig. 1 Compatibility study for Wettzell site: coordination zone for 5G at 3.4 GHz (blue 30dBm/MHz, red 50dBm/MHz). White circles mark distances to the RAS station in steps of 20 km.

effective antenna gain and possible clutter attenuation can make a big difference. Also, a 5G operator could choose to provide additional mitigation measures (i.e., lower output power, decreased effective gain to RAS station by antenna pointing/beam forming, and utilizing clutter attenuation), which would allow to use equipment within the coordination zone without doing any harm.

These results are important for the national authorities as they have to implement the coordination zone. In the case of Germany, the Wettzell observatory is protected by national law [BGeoRG], which entrusts BKG to contribute to the global reference frame activities.

3.2 Satellite Missions at Ku Band

Several companies are working on projects to supply global Internet access via satellites. More advanced are SpaceX and OneWeb. The non-geostationary orbit (NGSO) satellite systems are operating in 10.70−12.75 GHz (space-to-Earth), in 12.75−13.25 GHz, and 14.0−14.5 GHz (Earth-to-space) bands in Fixed Satellite Service (FSS) allocations (for fixed and moving platforms). The new services will contain hundreds or even thousands of small satellites that can provide high-capacity and low-latency multimedia services and may generate harmful interference, especially for a passive service as VGOS. Figure 2 shows the future number of visible active satellites vs. latitude.

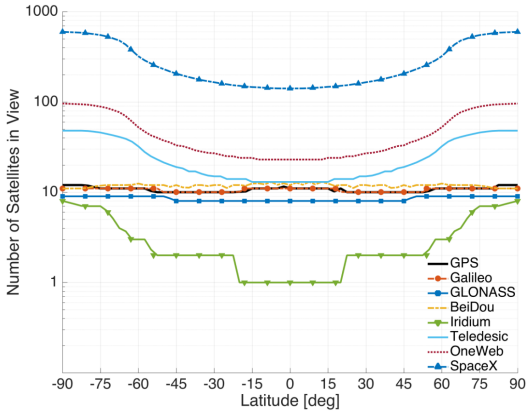

Fig. 2 Number of satellites in view vs. latitude (graphic from: https://pdfs.semanticscholar.org/487e/24483f22b43d57da78772dac9d20a948ec23.pdf.)

The SpaceX company wants to create a giant constellation named Starlink of nearly 12,000 satellites by mid-2020. One set of 4,425 satellites will be placed at an altitude of approximately 1,100 km, while 7,518 satellites will sit about 300 km up. Such a massive satellite fleet will be constantly in motion around the planet and will supposedly be able to provide coverage to basically any spot on Earth at all times. The first two prototype satellites, called Tintin A and Tintin B, were already launched on 22 February 2018.

The OneWeb satellite constellation is supposed to be made up of approximately 882 satellites to become operational in 2019−2020. The 882 communication satellites will operate in circular low Earth orbit, at approximately 1,200 km altitude, transmitting and receiving in the Ku band. Most of the capacity of the initial 648 satellites has been sold, and OneWeb is considering nearly quadrupling the size of the satellite constellation by adding 1,972 additional satellites.

4 Conclusions

The modernization of the global VLBI observation infrastructure, called VGOS, demands for wider observation spectra in the range of 2−14 GHz in order

to achieve the goals of the establishment of a Global Geodetic Observing System (GGOS). The societal need for precise global reference frames calls for extended VGOS observation programs.

This effort is contrasted by projects to improve the global communication abilities. Projects like 5G and satellite-based Internet may have a strong impact on the conduction of VGOS observations. We showed by the examples of the compatibility study to 5G for the VGOS site Wettzell and the scenario of Starlink/OneWeb that a severe impact on the VGOS operation must be expected. The upcoming WRC-19 will be an important forum at which VGOS will need many voices from the national and regional authorities.

Considering the increasing demand for spectrum in the radio window of the atmosphere targeted by VGOS observations, a strategic plan needs to be addressed by the IVS community. We propose to the VLBI sites:

1. Strengthen the link to the authorities responsible for the radio spectrum.
    a. Sharpen the awareness of national authorities about VLBI requirements. Today VGOS sites can plead the UN resolution, the EC directive and the ITU document cited in Section 1.
    b. Request compatibility studies from national spectrum authorities considering VGOS sites.
    c. Register your VGOS site through your national authority at ITU-R [Hase et al. 2016].
2. Perform compatibility studies to compare to the results of the national authority or other services.
3. Cooperate with RAS groups CRAF, CORF, and RAFCAP. Share information and documents on actions and achievements at your national or regional level with CRAF, CORF, or RAFCAP members.

Besides the regulation on spectral use, the IVS community should also address technical radio frequency interference (RFI) mitigation strategies at their radio telescope sites:

1. Investigate mitigation of RFI in the signal chain: providing a high-dynamic range with switchable filter banks and using 14-bit analog-digital converter to channelize 32 MHz without clipping.
2. Introduce notch filters at the front end.
3. Consider mitigation of RFI by passive microwave barriers around the RAS site against terrestrial based transmitters to conserve the elevation mask.
4. Define specific 1-GHz sub-bands in the $2-14$ GHz range as the future VGOS observation bands. This would enable the design of new four-band receivers which would be insensitive to other occupied parts in the range of $2-14$ GHz.
5. Develop software for RFI detection and excision.

References

Jessner 2013. A. Jessner "Conservation of spectrum for scientific services: The radio-astronomical perspective", URSI Radio Science Bulletin, N. 346, pages 6–11, 2013.

UN-Resolution 69/266. United Nations 69/266, "A global geodetic reference frame for sustainable development" http://www.un.org/en/ga/search/view_doc.asp?symbol=A/RES/69/266 February 26, 2015.

Directive 2007/2/EC. Directive 2007/2/EC of the European Parliament and of the Council, "Establishing an Infrastructure for Spatial Information in the European Community (INSPIRE)" https://eur-lex.europa.eu/legal-content/EN/TXT/PDF/?uri=CELEX:32007L0002&from=EN March 14, 2007.

ITU-R TF.460. ITU-R Rec. TF.460-6, "Standard-frequency and time-signal emissions", ITU, Geneva, 2002. https://www.itu.int/rec/R-REC-TF.460/en

ITU-R RA.769-2. ITU-R Rec. P.769-2: "Protection criteria used for radio astronomical measurements", ITU, Geneva, 2003. https://www.itu.int/rec/R-REC-RA.769/en

ITU IMT-2020. ITU IMT-2020, "ITU towards IMT for 2020 and beyond". https://www.itu.int/en/ITU-R/study-groups/rsg5/rwp5d/imt-2020/Pages/default.aspx

Draft ECC Report 281. CEPT, "Analysis of the suitability of the regulatory technical conditions for 5G MFCN operation in the 3400-3800 MHz band", 2018. www.cept.org/files/9522/Draft ECC Report 281 PF_1.docx

Winkel, Jessner 2018. Winkel, B., Jessner, A., "Spectrum management and compatibility studies with Python", Adv. Radio Sci., 16, pages 177–194, 2018. https://doi.org/10.5194/ars-16-177-2018,

ITU-Rec. P.452-16. ITU-R Rec. P.452-16, "Prediction procedure for the evaluation of interference between stations on the surface of the Earth at frequencies above about 0.1 GHz", ITU, Geneva, 2015. https://www.itu.int/rec/R-REC-P.452/en

Farr et al. 2007. Farr, T. G. et al. "THE SHUTTLE RADAR TOPOGRAPHY MISSION" [2007] Rev Geophys 45, doi:10.1029/2005RG000183. https://agupubs.onlinelibrary.wiley.com/doi/epdf/10.1029/2005RG000183

BGeoRG. "Bundesgeoreferenzdatengesetz - BGeoRG" http://www.gesetze-im-internet.de/bgeorg/BGeoRG.pdf

Hase et al. 2016. Hase, H., Tornatore, V., Corey, B., "How to Register a VGOS Radio Telescope at ITU and Why It Is Important", Proceedings of the IVS-GM2016, 2016. https://ivscc.gsfc.nasa.gov/publications/gm2016/011_hase_etal.pdf

Design Trade-offs in Feed Systems for Ultra-wideband VLBI Observations

Jonas Flygare, Miroslav Pantaleev, John Conway, Michael Lindqvist, Rüdiger Haas

Abstract Due to the advanced capability of today's ultra-wideband feed systems and low-noise amplifiers, interesting upgrades for future VLBI receiver and telescope design should be considered. Multiple input parameters need to be taken into account for optimal sensitivity and applications of the future astronomical and geodetic observational systems. In this paper we present an overview of some trade-offs for wideband systems between SEFD, bandwidth, and telescope reflector optics. We evaluate receiver bandwidths from 3.5:1 to 10.3:1 bandwidth within the frequency range 1.5–24 GHz in different configurations. Due to potential RFI pollution of the lower frequencies we present potential feed upgrades for the most common reflector geometries of VGOS and EVN telescopes that mitigate this problem. The results of this work is relevant for future VLBI stations and telescope design in general.

Keywords SEFD, VLBI, ultra wideband, VGOS, Quad-Ridge Flared Horn

1 Introduction

The VLBI Global Observing System (VGOS) network typically uses frequencies over 2–18 GHz with receiver bandwidth ratios of 6:1. The benefit of wideband feed systems is that continuous observational bandwidth will be available, at the expense of absolute system equivalent flux density (SEFD) over frequency. Despite this trade-off, with current state-of-the-art low-noise amplifiers (LNA) and highly optimized feed antennas, a good sensitivity (SEFD) level can still be achieved.

Onsala Space Observatory: Department of Space, Earth and Environment, Chalmers University of Technology, S-43992, Onsala, Sweden.
Email: jonas.flygare@chalmers.se

Fig. 1 Onsala Twin Telescope (OTT) on the left and center; Onsala 25-m telescope on the right.

The research project BRoad-bAND (BRAND), funded by EU Horizon 2020 RadioNet, will cover a decade in frequency over 1.5–15.5 GHz with a single-pixel feed [1]. This receiver system will enable continuous observations within the European VLBI Network (EVN) over L-, S-, C-, X-, and Ku-band. We evaluate the BRAND feed with simulations in a VGOS reflector, the Onsala Twin Telescope (OTT) [2], see Figure 1, and compare to the current system installed on one of the telscopes [3]. Due to the radio frequency interference (RFI) pollution at L- and S-band frequencies and the probable release of more frequencies for 5G telecommunication, potential new frequency bands should also be investigated. With respect to this, we present the high-frequency quad-ridge flared horn (QRFH) developed for the Square Kilometre Array (SKA) project covering 4.6–24 GHz [4] and evaluate it in the VGOS reflector through simulations. These feeds are optimized for reflectors with low focal length

over diameter ratio, f/D, which corresponds to a large half-subtended opening angle, θ_e, see Figure 2. Since many of the EVN telescopes are reflectors with high f/D, we include a feed system over 4.4–15.5 GHz designed for the Onsala 20-m telescope to compare. In this paper we use measured feed beam patterns for the current OTT QRFH over 3–18 GHz and for the SKA Band B QRFH over 4.6–24 GHz. The feed beam patterns for the BRAND QRFH over 1.5–15.5 GHz and the 4.4–15.5 GHz system for Onsala 20-m telescope are simulated. The measured patterns show good agreement with simulated. The patterns are used in the system simulator for the full telescope beam pattern simulations described in the next section.

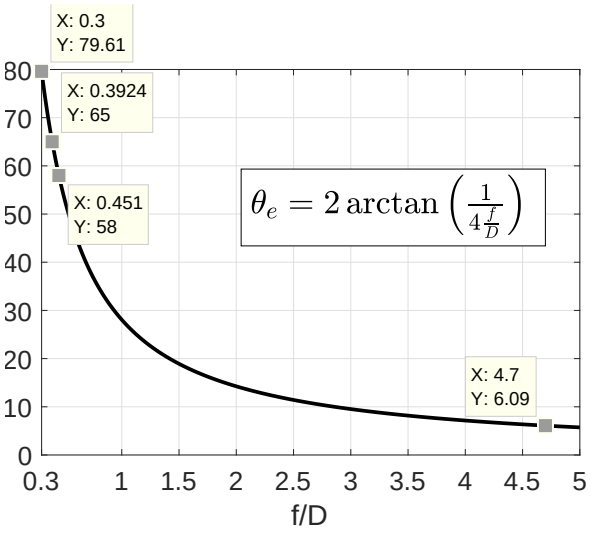

Fig. 2 Half-subtended angle θ_e seen from the feed-point, plotted against corresponding effective f/D for the reflector geometry.

2 Analysis

In the analysis we compare four different reflector geometries that are illustrated in Figure 3. The corresponding θ_e are highlighted in Figure 2 with the largest being $\theta_e = 79.61^\circ$ for the prime-focus reflector and the Cassegrain dual-reflector the smallest $\theta_e = 6.09^\circ$. The Gregorian ring-focus (VGOS) represents $\theta_e = 65^\circ$ and the Gregorian offset $\theta_e = 58^\circ$.

For accurate SEFD analysis we use a full system simulator [5] that uses physical optics (PO) + physical

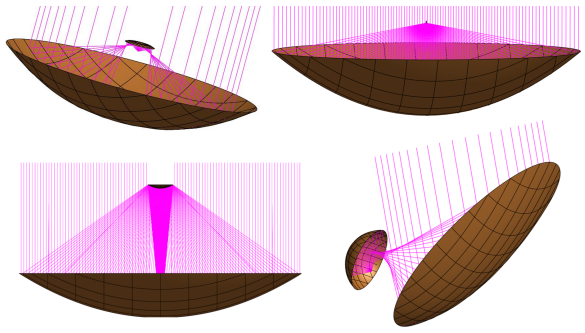

Fig. 3 (Top-left) Gregorian ring-focus axial-symmetric dual-reflector, common concept for VGOS; (Top-right) Primary-focus axial-symmetric reflector; (Bot-left) Cassegrain axial-symmetric dual-reflector, common concept within EVN; (Bot-right) Gregorian offset dual-reflector, common concept for new generation astronomy arrays (e.g., SKA, ngVLA).

theory of diffraction (PTD) to calculate the full telescope beam pattern, $G(\theta,\phi,f)$. The telescope reflector is fed with either simulated or measured feed beam patterns. The full telescope beam pattern is used to weight the surrounding sky noise temperature, $T(\theta,\phi,f)$, in a full-sphere integration to calculate the antenna noise temperature, T_A, see Equation 1. One key component in T_A is the amount of spill-over noise picked up from the 300 K ground noise temperature.

$$T_A = \frac{\int\int_{4\pi} G(\theta,\phi,f)T(\theta,\phi,f)\sin\theta\,\mathrm{d}\theta\,\mathrm{d}\phi}{\int\int_{4\pi} G(\theta,\phi,f)\sin\theta\,\mathrm{d}\theta\,\mathrm{d}\phi}. \quad (1)$$

For the feed models analyzed in this paper a very high radiation efficiency is achieved. Therefore we assume a simple model for the total system noise: $T_{sys} = T_A + T_{REC}$. T_{REC} represents the noise of the complete receiver chain. In Figure 4 we present two different re-

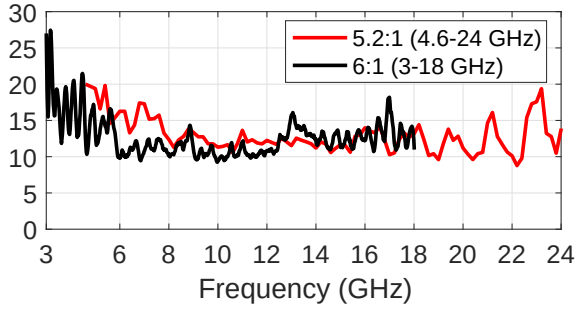

Fig. 4 Measured receiver noise temperatures, T_{REC}, for two different wideband systems in Onsala.

ceiver setups measured with Y-factor tests in Onsala that show good noise performance over wide frequency bandwidth.

From the telescope main-beam gain, G, we can calculate the effective area of the reflector as $A_{eff} = (G\lambda^2)/(4\pi)$. Finally, it is straightforward to calculate SEFD according to

$$SEFD = \frac{2k_B T_{sys}}{A_{eff}}, \quad (2)$$

where k_B is the Boltzmann constant. For accurate estimation we include appropriate degradation of SEFD due to the aperture blockage for the respective reflector geometry (not applicable for offset reflectors).

3 Wideband System Performance

In Figure 5 we present simulated aperture efficiency, $\eta_a = A_{eff}/A_{phy}$, of the receiver systems on different reflectors. A_{phy} is the available physical area of the reflector. The 10.3:1 feed was successfully designed for the prime-focus configuration with a challenging $\theta_e = 79.61°$ to illuminate. Therefore, in the VGOS reflector at the low-frequency end it is over-illuminating (lower η_a) but matches better at high frequency when the feed beamwidth is slightly narrowed. The 5.2:1 feed show fairly smooth η_a over bandwidth in the VGOS reflector. In Figure 6 we present the simulated SEFD at elevation $\theta = 30°$ for the wideband systems applicable to the VGOS reflector. Simulation of one of the current OTT receivers is represented with the green dash-dotted line over 3–18 GHz. An alternative 5.2:1 system is presented over 3.5–18 GHz for a possible mitigation of RFI below the 3.5 GHz. Due to the waveguide structure of the QRFH feed, it acts as a high-pass filter for frequencies below the cut-off. The receiver systems show excellent simulated SEFD performance where the ones with less than decade bandwidth show SEFD better than 1,000 Jy over most of the respective frequency band.

Another interesting aspect of these receiver systems is how the performance scales with size of the main reflector. Within the EVN, main-reflector diameters range up to 100 m. The OTT VGOS reflector measures 13.2 m, whilst the SKA offset Gregorian reflector is 15 m in effective diameter. SEFD scales inversely

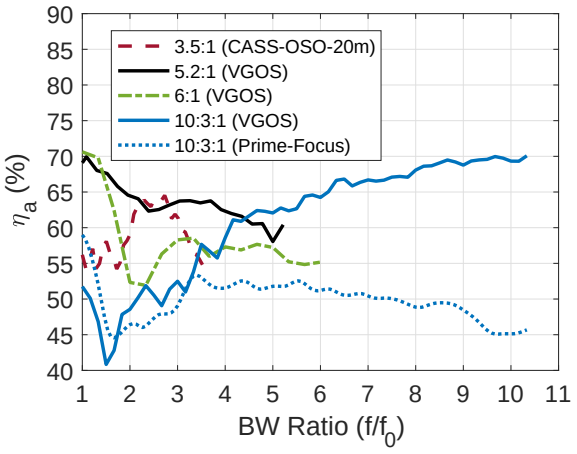

Fig. 5 Simulated aperture efficiency for different receiver systems in different reflector geometries. The bandwidth is normalized to the lowest frequency f_0.

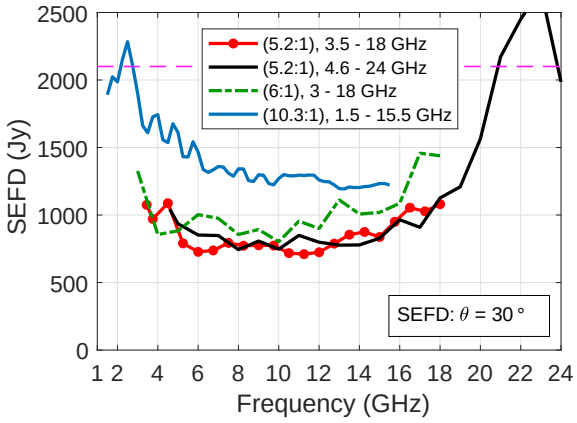

Fig. 6 Simulated SEFD for four different receiver systems in the OTT 13.2-m reflector (VGOS). Elevation: $\theta = 30°$, purple-dashed line represents the 2,100 Jy specification.

proportional to $A_{eff} = \eta_a A_{phy}$ (Equation 2). The physical main-reflector area can be written $A_{phy} = \pi(D_m/2)^2$ where D_m is the main-reflector diameter. In Figure 7 and Figure 8 we present SEFD as a contour plot over frequency and telescope main-reflector diameter, for the different receiver systems on different reflectors. The homogeneously dark red colored area represents SEFD higher than 2,100 Jy and does not fulfill VGOS specifications. For the VGOS type reflector in Figure 7 the 4.6–24 GHz system is on equal or better than the 3–18 GHz receiver on OTT, for overlapping frequencies. As mentioned, the higher cut-off frequency at 4.6 GHz mititgates potential LNA saturation from

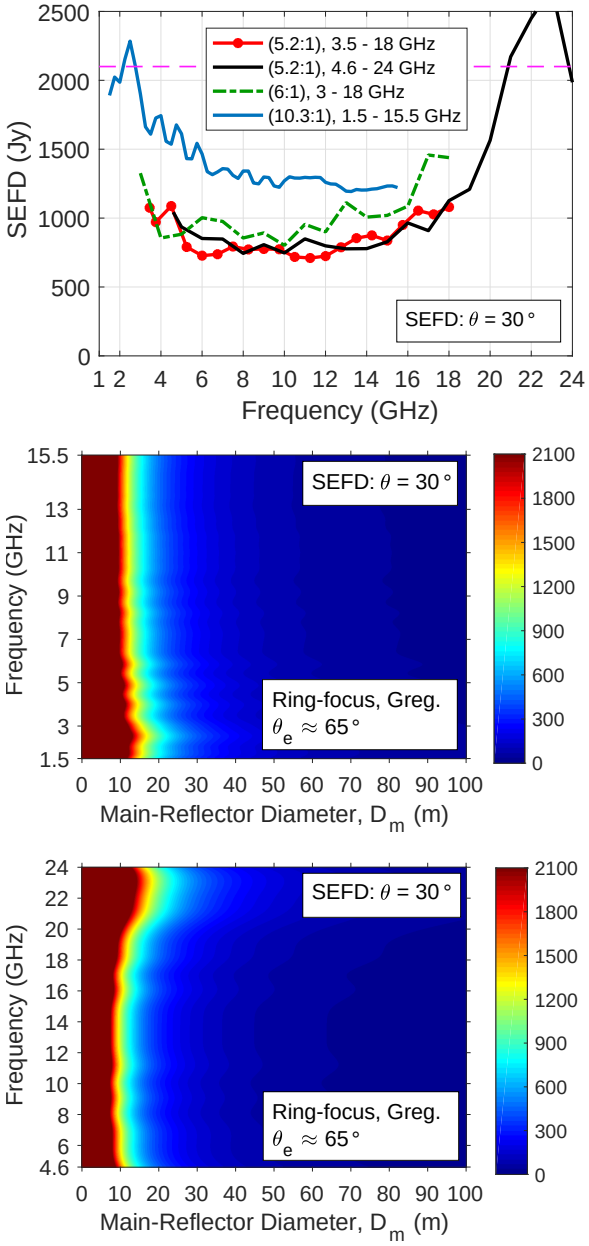

Fig. 7 Simulated SEFD (contour) for three receiver systems evaluated in Gregorian ring-focus type reflector (VGOS), plotted against main-reflector diameter size (x-axis) and frequency (y-axis). (Top) Current OTT, 6:1 bandwidth, 3–18 GHz; (Mid) BRAND, 10.3:1 bandwidth, 1.5–15.5 GHz; (Bot.) SKA Band B, 5.2:1, 4.6–24 GHz.

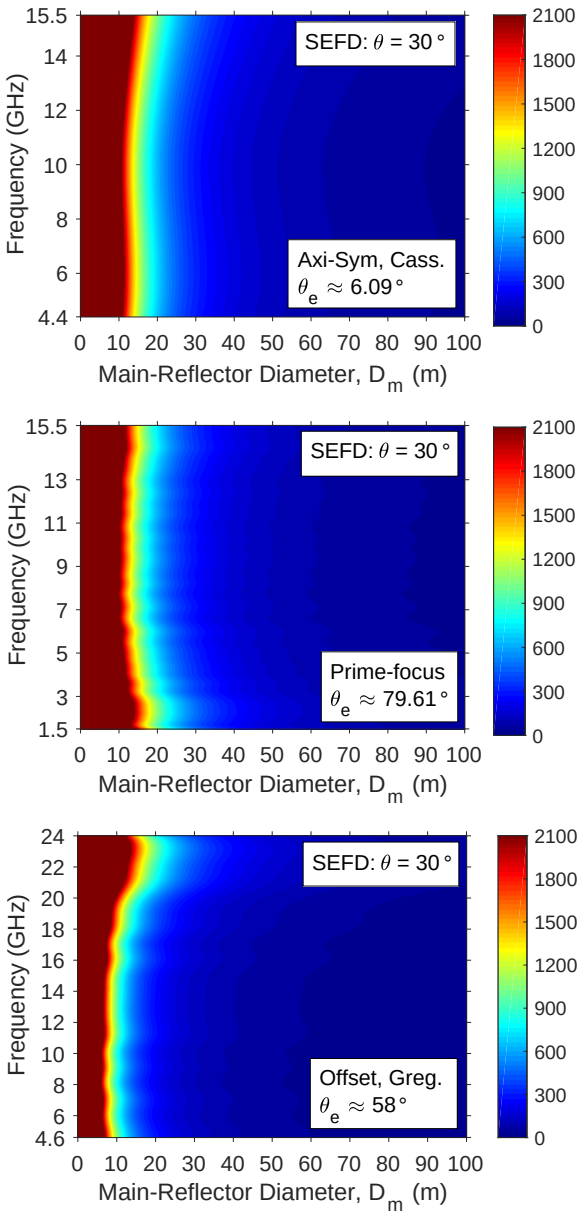

Fig. 8 Simulated SEFD (contour) for three receiver systems evaluated in three different reflector types, plotted against main-reflector diameter size (x-axis) and frequency (y-axis). (Top) Cassegrain dual-reflector, wideband system, 3.5:1 bandwidth, 4.4–15.5 GHz; (Mid) Prime-focus reflector, BRAND, 10.3:1 bandwidth, 1.5–15.5 GHz; (Bot.) Shaped Offset Gregorian reflector, SKA Band B, 5.2:1, 4.6–24 GHz.

the lower bands whilst the inclusion of the water-line at 22 GHz within the band introduces another possibility. In [6] we investigate theoretically this receiver system as a potential line-of-sight water vapor radiometer on the telescope. From simulation results, we expect a performance close to that of the dedicated water vapor radiometers of today. The obvious benefit is to have accurate water vapor measurements in the telescope line-

of-sight during observations with no separate system needed.

In general the receiver systems simulate better than specification on reflector diameters of 10–13 m for the Gregorian ring-focus type used in VGOS. The 1.5–15.5 GHz system can achieve similar SEFD for a 15-m dish in both Gregorian ring-focus and prime-focus reflectors, see middle plot in Figures 7 and 8, respectively. The best SEFD using the smallest reflector diameter is found in the highly shaped offset Gregorian reflector in the bottom row of Figure 8. This is expected as the feed is optimized specifically for this low-spillover reflector. For the Cassegrain dual-reflector system shown in the top row of Figure 8 the required reflector diameter is larger to achieve the same SEFD. This is due to the difficulty in designing feeds for a small θ_e over a large bandwidth without sacrificing aperture efficiency η_a. This type of feed in a standard horn configuration generally needs to be very large, which makes it difficult to fit in the receiver cabin as well. However, this result shows good performance over the 3.5:1 bandwidth which overlaps with VGOS frequencies. This configuration also has a higher cut-off frequency to mitigate low-frequency RFI pollution and is suitable for reflectors with small θ_e, which is common within the EVN. The frequency band available would allow for joint VLBI observations with VGOS.

4 Conclusions

We present different receiver systems applicable especially to the VGOS-type Gregorian ring-focus reflector. The presented receiver systems are evaluated through simulation with respect to main-reflector diameter and bandwidth for VGOS and other common reflector geometries. The 4.6–24 GHz allows for an interesting upgrade option in future VGOS receivers with a less RFI-polluted frequency band. SEFD performance can be expected in the same order as current VGOS systems, with the possibility of line-of-sight WVR in parallel with observation (further studied in [6]). A receiver system overlapping VGOS frequencies and suitable for Cassegrain dual-reflectors with high f/D (e.g., EVN) was also presented and evaluated. Finally we include the 10.3:1 receiver developed for radio astronomy (BRAND) over 1.5–15.5 GHz. This option enables a decade in available bandwidth with a substantial overlap with VGOS frequencies, further enabling joint observations between these systems.

Acknowledgements

The authors thank the ÅForsk Foundation for funding a travel grant for Jonas Flygare to attend the IVS 2018 conference and presenting this work.

References

1. J. Flygare, M. Pantaleev, and S. Olvhammar, “BRAND: Ultra-Wideband Feed Development for the European VLBI Network - A Dielectrically Loaded Decade Bandwidth Quad-Ridge Flared Horn” in *Proc. 12th Euro. Conf. Antennas Propag. (EuCAP2018)*, London, UK, April 2018.
2. G. Elgered, R. Haas, J. Conway, R. Hammargren, L. Helldner, T. Hobiger, M. Pantaleev, L. Wennerbäck, “The Onsala Twin Telescopes Project” in *Proc. 23rd EVGA Working Meeting (EVGA2017)*, Gothenburg, Sweden, May 2017.
3. J. Flygare, M. Pantaleev, B. Billade, M. Dahlgren, L. Helldner, and R. Haas, “Sensitivity and antenna noise temperature analysis of the feed system for the Onsala twin telescopes” in *Proc. 23rd EVGA Working Meeting (EVGA2017)*, Gothenburg, Sweden, May 2017.
4. B. Dong, J. Yang, J. Dahlström, J. Flygare, M. Pantaleev, and B. Billade, “Optimization and Realization of Quadruple-ridge Flared Horn with New Spline-defined Profiles as a High-efficiency Feed for Reflectors over 4.6-24 GHz”, *IEEE Trans. Antennas. Propag.*, August 2017 (accepted for publ.).
5. M. V. Ivashina, O. Iupikov, R. Maaskant, W. A. Van Cappellen, and T. Oosterloo, “An optimal beamforming strategy for wide-field surveys with phased-array-fed reflector antennas” in *IEEE Trans. Antennas Propag.,* vol. 59, no. 6, pp. 1864-1875, 2011.
6. J. Flygare, M. Pantaleev, J. Conway, M. Lindqvist, L. Helldner, M. Dahlgren, R. Haas, and P. Forkman, “Ultra-wideband feed systems for the EVN and SKA - evaluated for VGOS” in *Proc. 10th Int. VLBI Service for Geodesy and Astrometry (IVS) General Meeting*, Longyearbyen, Svalbard/Norway, June, 2018.

Ultra-wideband Feed Systems for the EVN and SKA - Evaluated for VGOS

Jonas Flygare, Miroslav Pantaleev, John Conway, Michael Lindqvist, Leif Helldner, Magnus Dahlgren, Rüdiger Haas, Peter Forkman

Abstract The design of the Square Kilometer Array (SKA) project for radio astronomy is now materializing at a rapid speed; the EU Horizon 2020 RadioNet project BRoad-bAND (BRAND) has the ambition of delivering a decade bandwidth receiver for EVN. The ultra-wideband quad-ridge flared horn (QRFH) feed systems developed for these projects show good performance within the geodetic VLBI Global Observing System (VGOS) frame due to the overlapping frequency bands and reflector geometries. We estimate, through simulation, the system equivalent flux density (SEFD) of the two feed systems in the VGOS reflector and compare it to the existing system installed on one of the 13.2-m diameter reflectors of the Onsala twin telescopes (OTT). The two frequency bands analyzed cover $1.5-15.5$ GHz and $4.6-24$ GHz. Both systems show an SEFD better than 1,000 Jy over large parts of the respective frequency band — comparable to the $3-18$ GHz feed systems. For the SKA QRFH over $4.6-24$ GHz, the water vapor absorption line at 22 GHz is within the operational band; therefore we study the application of water-vapor radiometry in line-of-sight of the telescope.

Keywords VGOS, Water-vapor radiometry, EVN, SKA, QRFH

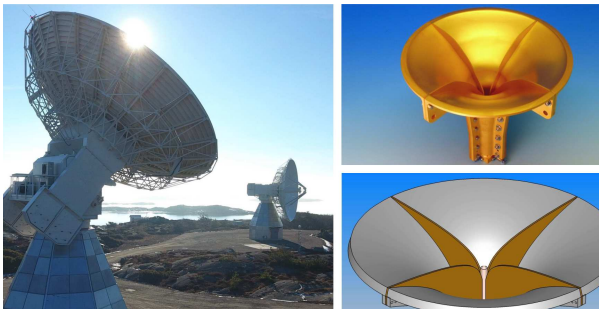

Fig. 1 (Left) Onsala Twin Telescopes, part of the VGOS network; (top right) SKA Band B QRFH: $4.6-24$ GHz; (bottom right) BRAND EVN QRFH: $1.5-15.5$ GHz.

1 Introduction

The ultra-wideband (UWB) Band B [2] feed was designed for $4.6-24$ GHz in the Square Kilometre Array (SKA) project as an option to extend the high-frequency limit beyond 13.8 GHz. UWB receivers enable large continuous bandwidth but also enable lower cost, less maintenance, and less complexity for a large telescope array compared to multiple narrowband receivers. The EU Horizon 2020 RadioNet project BRoad-bAND (BRAND) [3] for EVN has the ambition of offering a full decade receiver system that can replace multiple systems over L-, S-, C-, X-, and Ku-band with one receiver. Wideband feed systems are already installed and operational on the Onsala twin telescopes (OTT) within the VGOS network [1]. In Figure 1 (right) we present the two UWB quad-ridge flared horn (QRFH) feeds developed for these projects.

Onsala Space Observatory: Department of Space, Earth and Environment, Chalmers University of Technology

Due to the relatively large half-subtended angles these feeds were designed for, it is interesting to compare the system performance. We use the VGOS axial-symmetric ring-focus reflector in this comparison due to its relevance for the IVS community. The SKA QRFH excludes the generally RFI-polluted $2-4$ GHz band, due to the low-frequency cut-off property of the waveguide-based QRFH. An interesting application of the high-frequency limit of 24 GHz is the possibility of doing line-of-sight water-vapor radiometry on the telescope during observation. We compare this approach with dedicated water-vapor radiometers based on simulations. This offers an interesting upgrade of future frequency bands for VGOS.

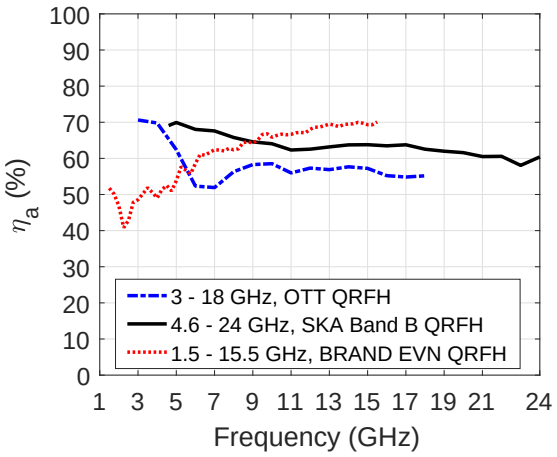

Fig. 2 Simulated aperture efficiency, η_a, over frequency for the three receiver systems in the OTT reflector.

2 System SEFD Performance

In Figures 2 through 4, we present the simulated system performance in the 13.2-m OTT reflector for the introduced receiver systems. We compare the performance to the current $3-18$ GHz QRFH system for OTT [1]. The OTT QRFH and SKA Band B QRFH results are based on measured beam patterns and receiver noise temperature determined through Y-factor tests with state of the art UWB low noise amplifiers (LNA). For the calculation of antenna noise temperature, T_A, a system simulator using physical optics (PO) and physical theory of diffraction (PTD) was used [4]. All three receiver setups show a system equivalent flux density (SEFD) better than 1,000 Jy over large parts of their respective frequency band for zenith ($\theta = 90^\circ$) in Figure 3. The elevation (θ) dependence of T_A is clearly seen in Figure 4, which degrades the SEFD closer to the horizon, specifically around the water-line at 22 GHz.

3 Water-Vapor Radiometry in Telescope Line-of-sight with High-frequency QRFH

Water-vapor radiometry (WVR) in line-of-sight (LOS) of the telescope, as previously investigated in [5], is an interesting application of high-frequency wide-band feed. We present a theoretical study estimating the zenith integrated cloud water (ICW) and zenith integrated water vapor (IWV) using the sky brightness temperatures at two frequencies in the $15-35$ GHz range. A similar study has previously been performed [6].

Vertical profiles of pressure, temperature, humidity, and cloud water are taken from the ERA-Interim reanalysis [7]. Data for two years (four times a day) at a grid point close to the Onsala Space Observatory have been used in the investigation. ARTS (Atmospheric Radiative Transfer System; [8]; [9]) was used to calculate the sky brightness temperatures from the ERA-Interim vertical profiles. ARTS is a general forward model for observations of thermal emission, often used for microwave applications. In the ARTS setup, [10] was used for the absorption of water-vapor and oxygen, [11] for the absorption of nitrogen, [12] for the air refractive index, and [13] for the absorption of liquid cloud water. In the $15-35$ GHz frequency range, scattering can be omitted as long as the droplets are smaller than about 0.5 mm. The simulations are therefore valid during clear or cloudy conditions but not during rainy weather. No mapping functions are needed because the ray tracing calculations include the Earth's curvature. The ERA-Interim data was used to derive IWV and ICW, and ARTS was used to simulate the sky brightness temperatures at certain elevations assuming a narrow beam. Figure 5 (top) shows the simulated sky brightness temperatures, T_b, at elevation $\theta = 30^\circ$ (two air-masses) for the two-year ERA-Interim data set. The peak around $20-25$ GHz is due to the absorption line of water-vapor at 22 GHz, while the general upward

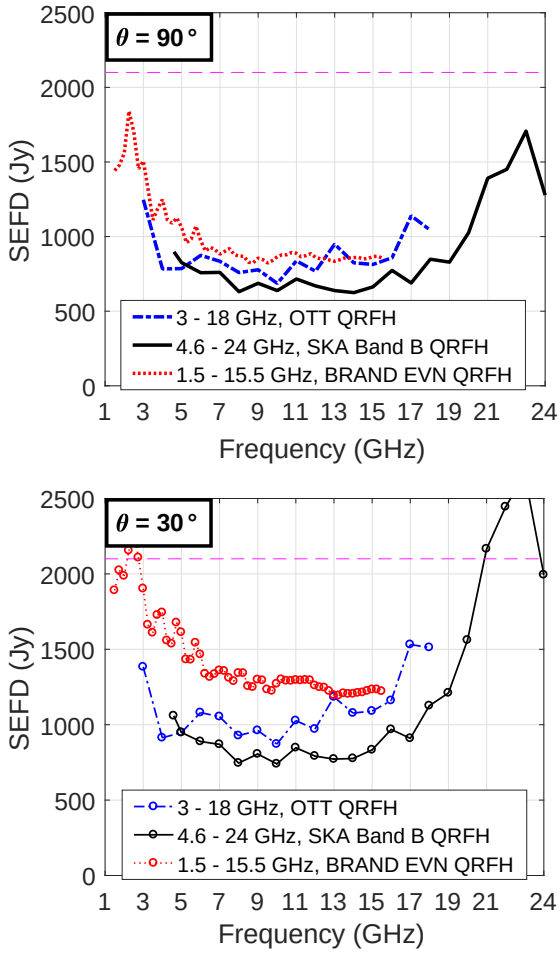

Fig. 3 Simulated SEFD over frequency at elevations $\theta = 90°$ (top) and $\theta = 30°$ (bottom) for the three receiver systems in the OTT reflector. Purple dashed line: 2,100 Jy.

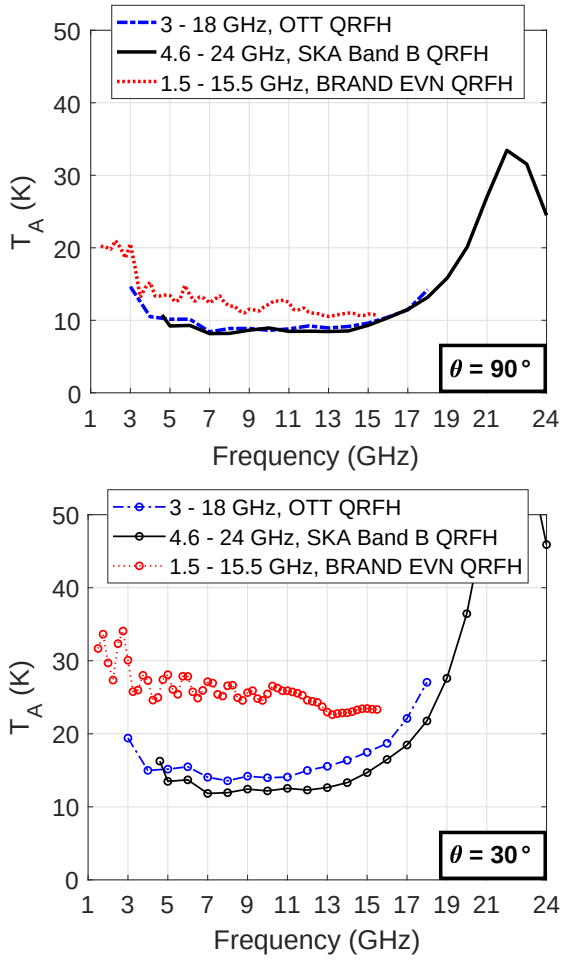

Fig. 4 Simulated T_A over frequency at elevations $\theta = 90°$ (top) and $\theta = 30°$ (bottom) for the three receiver systems in the OTT reflector.

slope of the spectra is affected by the absorption of liquid cloud water. The brightness temperatures in the $20-25$ GHz range are most sensitive to IWV, while frequencies above 30 GHz are most sensitive to ICW (where the general slope is not affected by the 22 GHz line), but frequencies below 20 GHz are also quite sensitive to ICW. IWV and ICW were estimated by polynomial expressions using the sky brightness temperatures (T_{b1} and T_{b2}) at two different frequencies (f1 and f2) for a given elevation. For IWV a second order polynomial was used:

$$IWV = a_0 + a_1 T_{b1} + a_2 T_{b2} + a_3 T_{b1}^2 + a_4 T_{b2}^2 + a_5 T_{b1} T_{b2} \quad (1)$$

For ICW a higher order polynomial was needed to generate a good fit:

$$ICW = b_0 + b_1 T_{b1} + b_2 T_{b2} + b_3 T_{b1}^2 + b_4 T_{b2}^2 + b_5 T_{b1} T_{b2} + b_6 T_{b1}^3 + b_7 T_{b2}^3 \quad (2)$$

The coefficients a_{1-5} and b_{1-7} were calculated using the method of least squares. Noise (σ_{T_b}) was added to the sky brightness temperatures, to simulate atmospheric variations and calibration noise. The polynomials in (1) and (2) were used to get the retrieved values of IWV and ICW. Finally the standard deviations between perfect fit and retrieved values were calculated.

Two-channel water-vapor radiometers were used for decades to estimate zenith wet delay as well as IWV and ICW. WVRs often use a frequency pair where the first channel is close to 21 or 24 GHz and the second is close to 31 GHz. In our study we first used f1 = 21 GHz and calculated the standard deviations when f2 varied between 15 and 35 GHz. As expected the frequency pair 21 and 31 GHz gave small retrieval errors, but the frequency pair 21 and 17 GHz also gave quite small retrieval errors. In the next step, f1 was set to 17 GHz, f2 varied between 15 and 35 GHz, and the calculations were done for different levels of atmospheric noise. It was then found that the frequency pair 17 and 23.4 GHz was a good choice, see Figure 5 (bottom). Finally the obtained results for the frequency pair 17/23.4 GHz were compared to 21/31 GHz. This comparison indicates that it is possible to use a frequency pair within the frequency range of the 4.6 – 24 GHz QRFH to obtain IWV and ICW to almost the same accuracy compared to a typical WVR, see Figure 6 (σ_{T_b} : 0.4 K). It is, however, important to note that this comparison is only valid if the calibrations of the 21/31 GHz and 17/23.4 GHz systems are performed to the same level of accuracy. Preliminary data indicate that the sky brightness temperatures at 17 and 23.4 GHz also can be used to estimate the slant wet delay, which can be very useful for VLBI observations. This will be discussed in an upcoming paper.

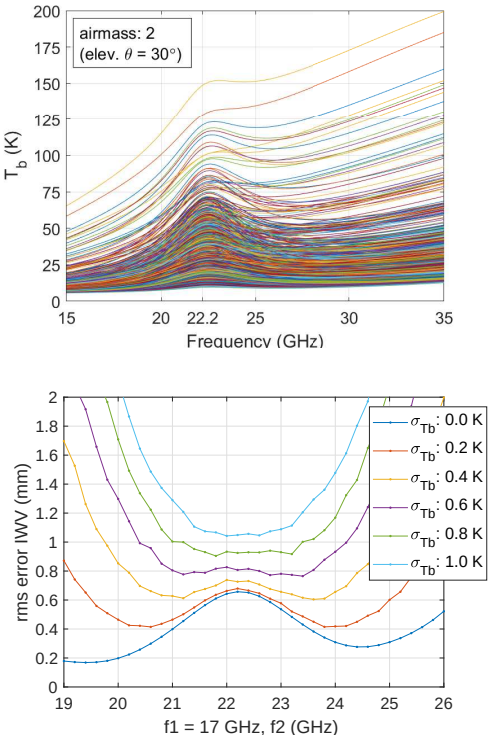

Fig. 5 (Top) Brightness temperature, T_b, of the sky at the Onsala site varying with ICW and IWV content; (bottom) RMS error in IWV varying with the choice of upper frequency channel, f2, and assumed σ_{T_b} rms noise error.

4 Conclusions

Simulations of the wideband systems developed for SKA and BRAND show SEFD performance similar to the current OTT system. The high-frequency limit of the 4.6 – 24 GHz QRFH presents an interesting application with telescope line-of-sight water-vapor radiometry during standard VLBI observations. This system will be set up and tested in the near future. RFI could potentially pollute the lower frequencies of VGOS, so the high cut-off frequency offered here may be beneficial in future systems.

Acknowledgements

The authors thank the ÅForsk Foundation for funding a travel grant for Jonas Flygare to attend the IVS 2018 conference and present this work.

References

1. J. Flygare et al., “Sensitivity and antenna noise temperature analysis of the feed system for the Onsala twin telescopes” in *Proc. 23rd EVGA Working Meeting (EVGA2017)*, Gothenburg, Sweden, May 2017.
2. B. Dong et al., “Optimization and Realization of Quadruple-ridge Flared Horn with New Spline-defined Profiles as a High-efficiency Feed for Reflectors over 4.6-24 GHz”, *IEEE Trans. Antennas. Propag.*, August 2017 (accepted for publ.).
3. J. Flygare, M. Pantaleev, and S. Olvhammar, “BRAND: Ultra-Wideband Feed Development for the European VLBI Network - A Dielectrically Loaded Decade Bandwidth

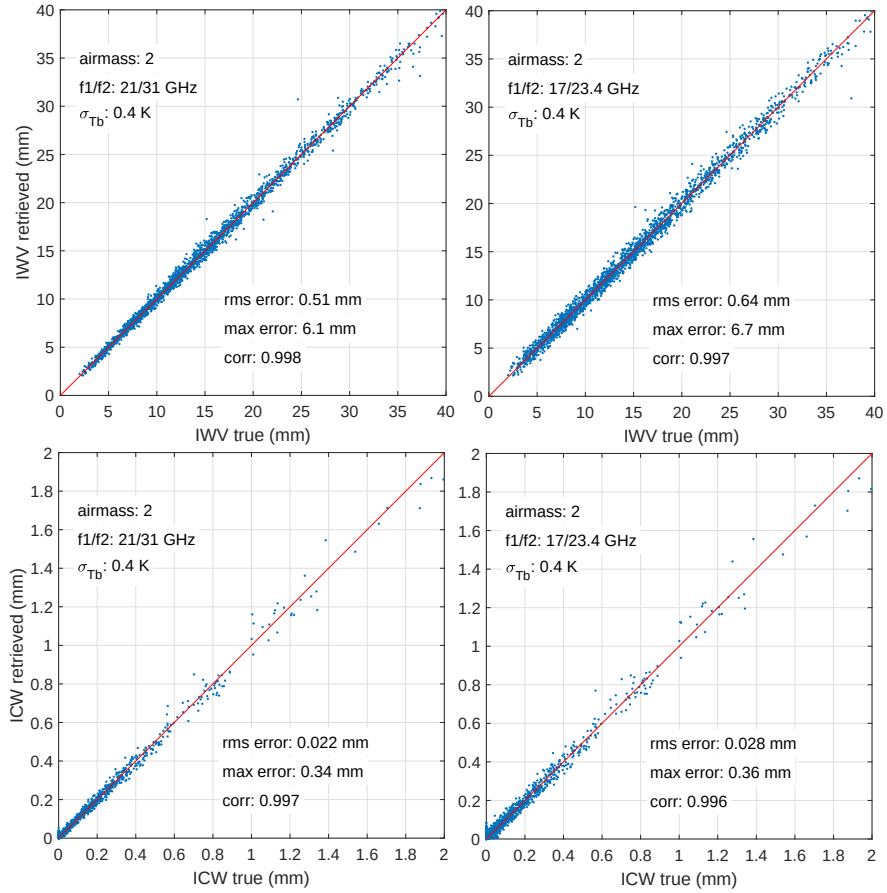

Fig. 6 (Top) IWV; (bottom) ICW; (left) simulated retrieved vs. true for the 21/31 GHz dedicated radiometer frequency channels; (right) simulated retrieved vs. true for the wideband feed 17/23.4 GHz frequency channels. $\sigma_{T_b} = 0.4$ K, $\theta = 30°$.

Quad-Ridge Flared Horn" in *Proc. 12th Euro. Conf. Antennas Propag. (EuCAP2018)*, London, UK, April 2018.

4. M. V. Ivashina et al., "An optimal beamforming strategy for wide-field surveys with phased-array-fed reflector antennas" in *IEEE Trans. Antennas Propag.,* vol. 59, no. 6, pp. 1864-1875, 2011.
5. B. J. Butler, "22 GHz Water Vapor Radiometry at the VLA", in *Imaging at Radio through Submillimeter Wavelengths, ASP Conf. Proc.*, Vol. 217, *ASP*, ISBN 1-58381-049-8, 2000., p.338, 2000.
6. P. Eriksson and G. Elgered, "Development of miniaturized microwave ground radiometers for satcom ground stations: Retrieval approach", *unpublished report*, patrick.eriksson@chalmers.se, 2016.
7. D. P. Dee et al., "The ERA-Interim reanalysis: configuration and performance of the data assimilation system", *Q.J.R. Meteorol. Soc.*, 137: 553-597, 2011.
8. S. A. Buehler et al., "ARTS, the Atmospheric Radiative Transfer Simulator", *J. Quant. Spectrosc. Radiat. Transfer*, 91:65-93, 2005.
9. P. Eriksson et al., "ARTS, the atmospheric radiative transfer simulator", version 2. *J. Quant. Spectrosc. Radiat.* Transfer, 112:1551-1558, 2011.
10. P. W. Rosenkranz., "Water vapor microwave continuum absorption: A comparison of measurements and models." *Radio Sci.*, 33(4):919-928, 1998 (correction in 34, 1025, 1999).
11. P. W. Rosenkranz., "Absorption of microwaves by atmospheric gases." In *Atmospheric remote sens. microw. radiometry*, pages 37-90. John Wiley & Sons, 1993.
12. M. Bevis et al., "GPS meteorology: Mapping zenith wet delays onto precipitable water", *J. Appl. Meteorol.*, 33:379-386, 1994.
13. H. J. Liebe, G. A. Hufford, and M. G. Cotton, "Propagation modeling of moist air and suspended water/ice particles at frequencies below 1000 GHz". In *AGARD 52nd Specialists Meeting of the Electromagn. Wave Propag. Panel*, Palma de Mallorca, Spain, May 1993.

New Observing Modes for the DBBC3

Gino Tuccari[1], Walter Alef[1], Sven Dornbusch[1], Rüdiger Haas[2], Karl-Åke Johansson[2], Helge Rottmann[1], Alan Roy[1], Michael Wunderlich[1]

Abstract The DBBC3 was further enhanced by introducing new modes. Three different firmwares have recently been implemented for observing: Direct Sampling Conversion (DSC), arbitrary selection of bands (OCT), and Digital Down Conversion (DDC). These modes cover all the requirements of astronomical, VGOS, and legacy geodetic VLBI for the time being and the immediate future. In addition, the DBBC3 offers unsurpassed compatibility to the relatively large number of other existing VLBI backends. A number of test observations were performed in the last months to achieve the best performance of the VGOS modes, and similar tests are planned for the EVN network. At the same time the DBBC3 is an important platform for additional new modes to be implemented for the BRAND receiver. Several DBBC3 systems are deployed in the field and more are under construction, with the number of 4-GHz bands ranging from two up to eight with resulting output data rates from 32 Gbps to 128 Gbps.

Keywords DBBC3, digital backend

1 Introduction

The DBBC3 backend system for VLBI was developed with the support of the Radionet3 joint research activity under the DIVA project. Partners in this development have been the Italian INAF (Istituto Nazionale di Astrofisica), the German MPIfR (Max Planck Institute for Radio Astronomy), and the Swedish OSO (Onsala Space Observatory). The backend was developed initially for astronomy with the aim to improve the EVN network data rate and bandwidth. As a natural consequence, it could also be devoted to the EHT (Event Horizon Telescope) and to geodetic VLBI both in the new broadband VGOS network and with the legacy S/X stations.

The DBBC3 constitutes the third generation member of the DBBC family, following the DBBC2 which is still the most widely adopted digital backend in VLBI. The DBBC3 is an evolutionary product that is backwards compatible with the DBBC2 in several ways: observing modes, control software, and parts of the hardware. In principle it is possible to upgrade a DBBC2 system to a DBBC3 by replacing some key parts, but reusing many elements of the existing system including the housing and basically all of the general pieces.

The DBBC3 offers a selection between one and eight IFs, each a maximum of 4 GHz wide to produce a maximum data rate of 16 to 128 Gbps when operating at 2-bit. The hardware is capable of producing a maximum of 512 Gbps when operating with output samples of 8-bit.

A number of modes were commissioned:

- **DSC:** 4 GHz full band/IF;
- **DDC:** 8 BBC/IF with bandwidth in the output channels ranging between 32 and 1 MHz for legacy modes;
- **OCT_S:** 1 x 1 GHz selectable in 4 GHz; and
- **OCT_D:** 2 x 2 GHz in 4 GHz.

A number of additional modes were developed needing to be commissioned and further modes are under development. The goal is to achieve the best possible

[1]Max Planck Institute for Radio Astronomy
[2]Chalmers University of Technology

compatibility with all the other existing VLBI backend systems in the world and to introduce new modes not yet available in other backends that are deemed greatly useful and desired by the scientific community.

2 DBBC3 Components

The enclosure of a DBBC3 system is, as mentioned, exactly the same as used in the previous versions of the DBBC backend family and so are many ancillary parts such as the cooling section, the power supply, the control computer, and the DBBC stack structure, where a number of boards are connected to one another in a block to perform the main functionalities. Even if a specific board is different from one generation to the next, there is full mechanical and electrical compatibility from the power supply point of view.

The first main active component is the GCoMo2, the second version of the GCoMo analog conditioning module, whose functionality is to adapt the receiver to the sampling process. The new GCoMo2 provides an improved bandwidth over the 4-GHz band. The unit is made to match the receiver electronics with a lot of flexibility with internal and external components; this is very useful to be able to adapt to the various receiver implementations of the radio telescopes. It still can measure the full input band total power before sending the signal to the samplers. The samplers' functionality is operating in the first Nyquist zone; then a direct input of 0–4 GHz is dedicated to a mode that allows full support for the adaptation at the first Nyquist zone of any 4-GHz piece of band in the range from 4 to 15 GHz.

The second element in the processing chain for each 4 GHz piece of band is the ADB3L sampler board. This sampler is the third generation of samplers in the DBBC family and is capable of sampling a band of 4,096 MHz making use of four separate sampler devices accommodated in the same board adjacent to each other. A number of calibration procedures have been implemented in hardware, firmware, and software presenting at the end for the user very simple commands to keep under control elements such as the offset, gain, and delay of the four samplers avoiding artifacts and optimizing the behavior of the sampling process. Several original methods were developed in order to achieve this goal.

Fig. 1 Front view of the DBBC3.

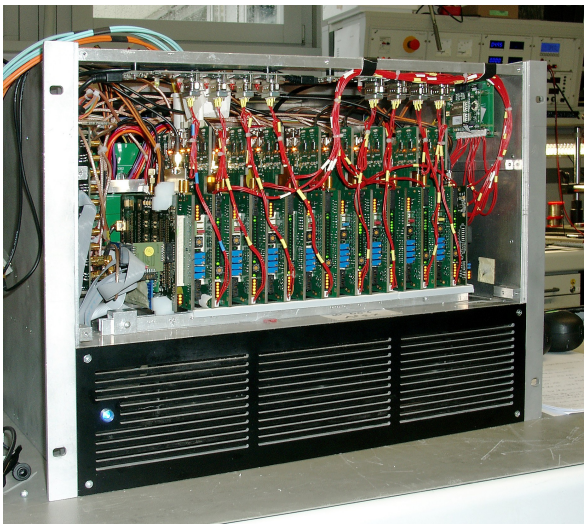

Fig. 2 DBBC3 VGOS model with eight IFs.

Finally, the last main element is represented by the CORE3H board. Here the data is received by the samplers in digital format and the band forming is done. The functionality is realized by making use of a very high end FPGA device adopting different firmware codes for different observing modes. The data output is handled by four 10 GE transceivers on the board; however, if a higher output data rate is required (up to a maximum of 512 Gbps), a maximum of eight transceiver slots could be populated. The control of the functionalities is assured by three different communication channels: a parallel PCI bus line, an RS232 serial communication link, another RS232 serial channel

for a dedicated GPS receiver system. The control software is very similar to the DBBC2, but it is, of course, adapted to the many more resources available. For instance, in DDC mode the maximum number of BBC units is 128 (in legacy mode), while it was 16 in the DBBC2.

3 Observing Modes

For each IF processed in the system, different modes can be realized depending on the type of observation to be performed. The difference comes from the use of a different firmware inside the FPGA elements of the system, which is highly flexible in this respect.

The samplers produce the digital version of the input band coming from the receivers requiring still to be processed to create frequency channels in tuning, bandwidth, number, and format to be compatible with the VLBI standards as well as with any other VLBI backend and the processing VLBI correlators. The entire process and preparation of the output data format to be recorded or to be transferred electronically directly to the correlators is then realized inside the processing boards (CORE3H) making use of a collection of different firmwares to be loaded on the boards as required by the type of observation.

As mentioned, a number of modes were developed:

- DSC (direct sampling conversion): 4 GHz full band/IF, using this mode it is possible to record a large received bandwidth ranging from 4 GHz up to 32 GHz;
- OCT_S (octopus single band): some examples
  - 0–2, 2–4 GHz
  - 0–1, 1–2, 2–3, 3–4 GHz
  - 0.5–1.0, 1.0–1.5, ..., 3.5–4.0 GHz
  - many others possible;
- OCT_D (octopus double band): some examples
  - 2 x 2 GHz
  - 2 x 1 GHz
  - 2 x 512 MHz
  - 1 x 2 GHz + 1 x 1 GHz
  - many others possible;
- DDC (digital tunable down conversion):
  - V type (VGOS), eight BBC/IF with bandwidth 32 MHz U&L, max 64 BBC in a system;
  - V type (VGOS), 12 BBC/IF with bandwidth 32 MHz (for six IFs systems) U&L, max 96 BBC in a system;
  - L type (legacy), 16 BBC/IF with bandwidth 32-16-8-4-2 MHz U&L, max 128 BBC in a system;
  - H type (high band, under development), 16 BBC/IF with bandwidth 128-64-32-16-8 MHz;
  - P type (tunable PFB, under development), 32 bands tunable 64-32-16-8-4 MHz PFB block in 4 GHz.

For all the configurations an automatic threshold calibration is available for 2-bit output during runtime. The DDC-VGOS mode was the first of its kind and it was widely debugged by the Onsala team over several months. The many improvements were possible due to the large amount of tests performed at that observatory within 24-hour VGOS Test sessions as well as outside of them. The Onsala site is anticipated to function as the main testbed for introducing any new version in the field.

Initial Results from the MIKES-Metsähovi Time and Frequency Link for the VGOS Radio Telescope

Guifré Molera Calvés [1], Anders Wallin [2], Jyri Näränen [1], Thomas Fordell [2]

Abstract VLBI relies on the precision of Hydrogen maser clocks at each station to provide accurate time and frequency for their observations. Recent developments allow us to use distributed clocks via optical fiber links in order to provide these time signals at any remote radio telescope. Here in this paper, we discuss the distribution of the official Finnish UTC clock time to operate the new VGOS radio telescope at Metsähovi.

Keywords VGOS, Time & frequency link, White Rabbit switch, fiber-optic

1 Introduction

Correlation of data obtained by Very Long Baseline Interferometry (VLBI) radio telescopes located around the globe relies on very precise information about the arrival time of the radio signals. VLBI stations also require a very stable frequency reference (at 5 or 10 MHz) for operating most of their instrumentation. These stations use a local Hydrogen maser (H-maser) as a reference clock. We are developing a 'remote maser' concept for VLBI that synchronizes participant stations to the same reference clock via optical fibers [1]. In this paper, we report on the first results from a 50 km optical fiber time and frequency link between the National Metrology Institute VTT MIKES and the Metsähovi Geodetic Research Station.

1. Finnish Geospatial Research Institute FGI, National Land Survey

2. Technical Research Centre of Finland Ltd VTT, Centre for Metrology MIKES

In summer 2018 the Finnish Geospatial Research Institute (FGI), part of the National Land Survey of Finland (NLS), began the construction of a new VGOS radio telescope at Metsähovi. FGI had been participating in the IVS campaigns for over a decade already but did not have its own radio telescope. Instead, FGI rented observing time from the astronomical radio telescope of Aalto Metsähovi Radio Observatory (MRO). The construction of this new antenna will provide a new station dedicated 24/7 to global geodetic observations. More information about the status of the radio telescope at Metsähovi can be found at [2].

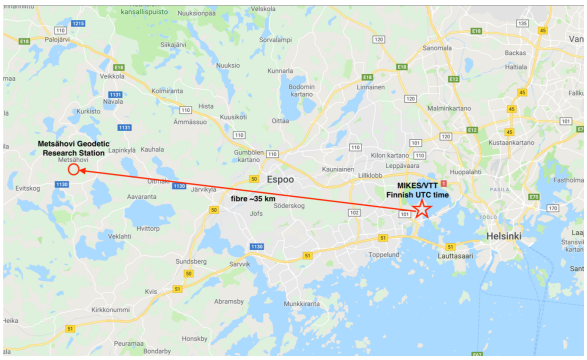

Fig. 1 Metsähovi is located 50 km from Helsinki. VTT MIKES is in Otaniemi, next to Aalto University and 40 km from Metsähovi. The official Finnish UTC time and frequency signal is provided to the station via an optic fiber.

The location of the new VGOS radio telescope at Metsähovi and VTT MIKES can be seen in Figure 1. Both institutes are separated by a distance of 40 km; however, they are linked with several pairs of dark fibers thanks to the Finnish University and Research Network (FUNET), part of CSC - IT Center for Sci-

ence LTD. The link was originally installed to provide a 10 Gbps connection to the radio telescope.

2 Configuration

The experiments are conducted with the White Rabbit (WR) extensions to the Precision Time Protocol (PTP) [1]. The White Rabbit switch provides precision timing and high accuracy synchronization based on an Ethernet-based network. The so-called WRS master distributes the clock, 1 pps signal, and a fixed 5 or 10 MHz frequency signal to all the nodes in the network using a hierarchical architecture. The basic configuration used during the first tests is shown in Figure 2.

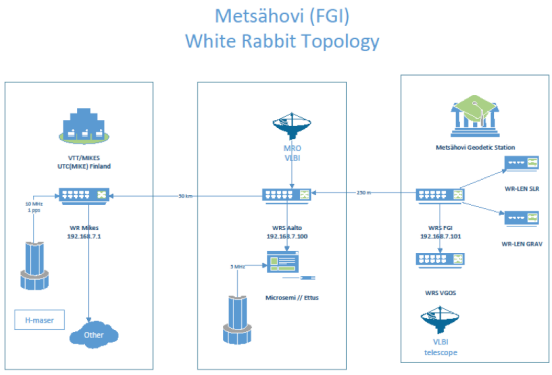

Fig. 2 Current set up to distribute the standard Finnish UTC time and frequency reference to the Metsähovi station and to the future VGOS radio telescope.

The WRS master is located at VTT MIKES and is directly connected to one of their Hydrogen masers. The WRS master distributes the time and frequency signals via optic fiber to a number of WRS nodes (also known as WRS slaves). For instance, the two WRS existing at Metsähovi are configured as WRS slaves. There is a pair of dark fibers that directly links VTT MIKES to Aalto MRO. These fibers are shared for the 10 Gbps data transmission connection and the time and frequency link. Additional fibers between MRO and FGI were installed in order to extend the White Rabbit network within Metsähovi facilities. The FGI and MRO facilities are located within a radius of 300 m.

[1] www.sevensols.com

The White Rabbit units are configured with a Dense Wavelength Division Multiplexing (DWDM) Small Form-factor Pluggable transceiver (SFP) in bi-directional mode, allowing proper transfer of the optical wavelengths over long-distance fibers. The round-trip time of the optical link was monitored over a period of one year. The first estimations indicate that asymmetry of the link contributes less than 500 ps to the uncertainty of time-transfer.

The standard configuration of a White Rabbit switch (see Figure 3 (i)) was upgraded with the Low Jitter Daughterboard (LJD) modification to the WRS (see Figure 3 (ii)) [3]. The installation of the LJD board improves significantly the stability of the internal clock of the standard WRS. The measurement set up at Metsähovi is shown in Figure 4.

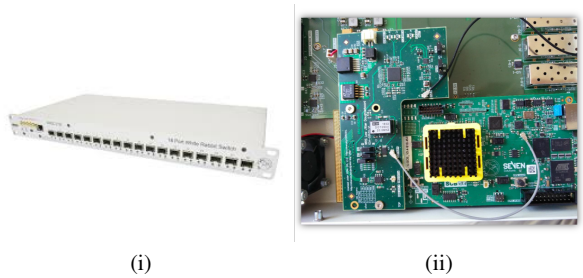

(i) (ii)

Fig. 3 (i) Standard WRS capable of the distribution of time and frequency signals up to 15 nodes. (ii) Modification to the WRS, which improves the stability of the clock and frequency signal.

Fig. 4 Current set up arranged at Aalto Metsähovi radio observatory where the time and frequency signals provided by the VTT MIKES are being compared with the local Hydrogen masers.

Three White Rabbit LEN extension units were purchased this year for testing purposes. The units are a

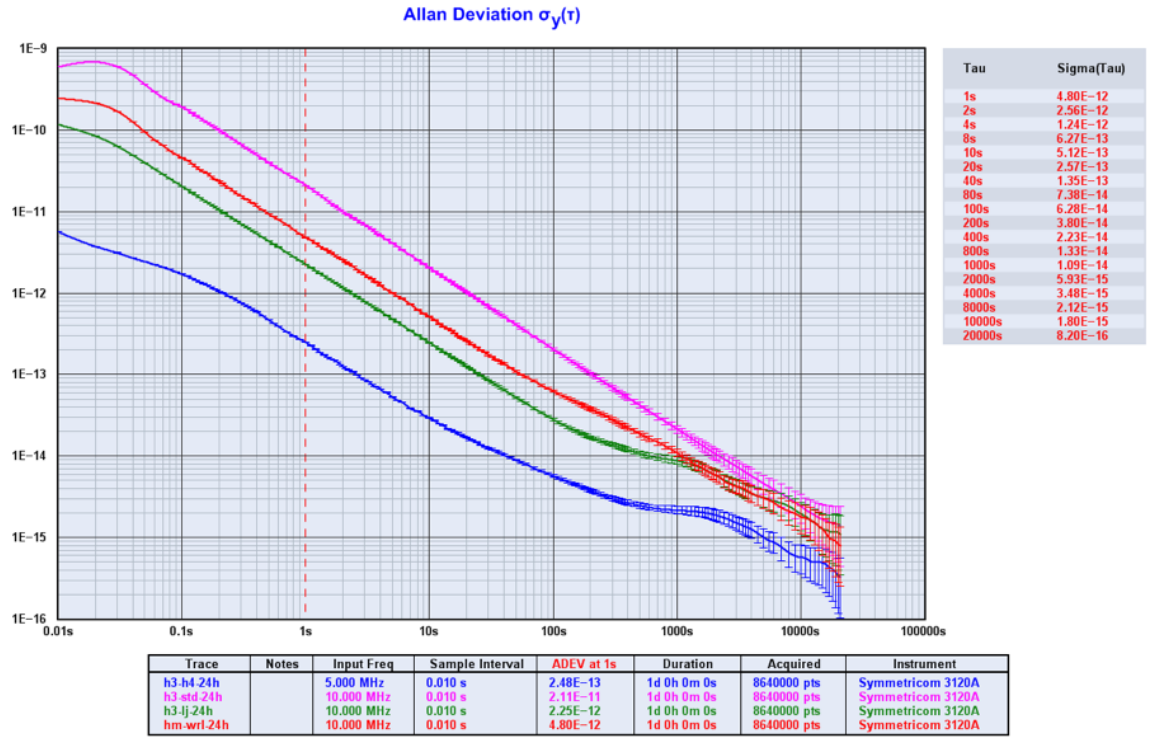

Fig. 5 Allan deviation of the H-maser vs. Standard WR (pink), H-maser vs. WR-LEN (red), and H-maser vs. WRS with the modified Low Jitter Board (green), and the H-maser (blue). The analysis was conducted with a Symmetricom 3120A phase meter.

cost-effective solution to extend internally at FGI the 10 MHz and 1 pps or IRIG-B signal between the different scientific instruments at Metsähovi. The dimensions of these units are relatively smaller than standard WR switches, and their performance is slightly higher.

3 Results

The 1 pps signal was closely monitored for the last year and a half. The 1 pps signal provided by the standard WRS and the WRS + LJD have been compared with the local Hydrogen masers. Statistics of the signals are extracted every minute for all possible measurement sets. The real-time information can be followed from the VTT MIKES web site [2].

Comparisons of the frequency signal (5 and 10 MHz) with the local H-masers were also conducted. The phase noise and Allan deviation analysis have been analyzed regularly over periods of 24 to 100 h using a phase meter. We used the Symmetricom 3120A for these tests. Figure 5 shows the Allan deviation of the H-maser compared to the standard White Rabbit switch (in pink), the H-maser vs. the WR-LEN (in red), the H-maser vs. the WRS + LJD (in green), and finally two of the H-masers from Aalto Metsähovi (in blue). The performance of the WRS + LJD is one order of magnitude better than the standard WRS and one order of magnitude worse than a Hydrogen maser. The results show that the random errors are reduced to the level of 1e-12 at 1s (0.5 Hz BW). This performance is perfectly suitable to fulfill the requirements for VLBI Global Observing System (VGOS) and sufficient for all but the most demanding applications [4].

4 Future Work

A high-performance remote maser concept is currently being developed at VTT MIKES. This new frequency

[2] http://monitor.mikes.fi/mets_aalto/

transfer technique [5] is under design in order to improve the current performance of WR-PTP and reduce the random errors to the 1e-13 level, that of active H-masers used worldwide for continuous timekeeping. The concept can be simplified to the schematics shown in Figure 6. A Morion MV317 voltage controlled oscillator is operated 'symmetrically' in a phase-locked loop (PLL), which compensates for drifts in the optical fiber link. Phase detection is done at the highest frequency present in the system. Frequency multipliers/dividers and a clean-up oscillator could be added to the remote end.

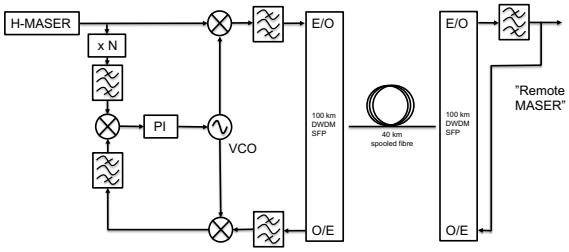

Fig. 6 A Morion MV317 voltage controlled oscillator is operated 'symmetrically' in a phase-locked loop, which compensates for drifts in the medium (fiber). Phase detection is done at the highest frequency present in the system.

Initial tests were conducted in the laboratory with satisfactory results. The system consists of a receiver and transceiver transmission over a spool of 40 km of fiber. The Allan deviation of the reference or noise floor is shown in black, the performance of an H-maser is shown in blue, and finally the received signal after the fiber spool is shown in red.

Further experiments will start in the fall of 2018, when the system will be deployed over the fiber between the radio telescope and the VTT MIKES. Successful results on these tests are expected by the end of 2019. The time is in agreement with the current schedule of operations for the VGOS radio telescope.

5 Conclusions

The definitive goal is that this time transfer project will support the geodetic measurements at the Metsähovi Geodetic Research Station. The new link, together with the atomic clocks of the Aalto MRO, also improves the

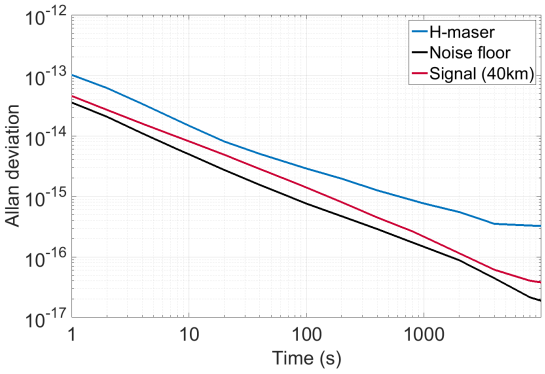

Fig. 7 Allan deviation of the reference or noise floor (black) and the received signal after propagating 50 km in a fiber spool (red). Also shown is the performance of the H-maser (blue). For the measurements all signals have been divided down to 10 MHz.

time and frequency precision for all the instrumentation at the station. Finally, the link opens as well new opportunities for connecting the UTC (MIKE) atomic time scale to other international geodetic observation networks such as IGS.

Future work will continue to exploit the White Rabbit technology for the time and frequency link of a geodetic station, while focusing on improving the concept of the high-performance remote-maser concept.

References

1. Clivati et al., A coherent fiber link for very long baseline interferometry IEEE Trans. Ultrason., Ferroelect., Freq. Contr., 2015, 62,
2. Zubko, N., Molera Calvés, G. et al.,'Status Update of the Metsähovi VGOS radio telescope', PoS IVS GM 2018.
3. M. Rizzi et al., "WRS Low Jitter Daughterboard", Open Hardware repository, https://www.ohwr.org/projects/wrs-low-jitter
4. Wallin, A.E. et al., Improved systematic and random errors for long-distance time-transfer using PTP White Rabbit, EFTF2018.
5. Fordell, T., Wallin, A.E., "A simple High-Performance Remote-Maser concept", ETFT2018.

Session 2

VGOS Technique and Observations

Development of a Wide Bandwidth VLBI System at Kashima

Kazuhiro Takefuji [1], Hideki Ujihara [1], Masanori Tsutsumi [1], Tetsuro Kondo [1,2], Shingo Hasegawa [1], Yuka Miyauchi [1], Eiji Kawai [1], Mamoru Sekido [1]

Abstract We have been developing a wide bandwidth VLBI system for Time and Frequency (T&F) comparisons. Two compact 2.4-meter antenna systems were installed and tested at NICT headquarters in Koganei, Tokyo and at the National Metrology Institute of Japan (NMIJ) in Tsukuba, Ibaraki until 2017. The two compact VLBI stations were indirectly connected via joint VLBI observations with the Kashima 34-meter antenna. In 2018, in collaboration with the Italian National Research Institute of Metrology (INRiM) and the Medicina VLBI station of INAF, we decided to relocate one compact antenna system to Medicina for T&F comparisons via VLBI observations between NICT in Japan and INRiM in Italy. The disadvantage of the lower sensitivity of the compact antenna is compensated for by the higher data acquisition rate, the wide frequency range of the observations, and the joint observations with a high sensitivity antenna. We have developed a broadband feed and a direct sampling system, allowing to use the frequency range from 3.2 to 14.4 GHz for VLBI observations.

Keywords Broadband VLBI, VGOS, T&F

1 Broadband System Development at Kashima

Three stations have installed a broadband frontend and backend system, consisting of a NINJA feed from 3.2 GHz to 14.4 GHz and a 16-GHz K6/GALAS direct sampler. Currently we have installed two types of broadband feeds at Kashima 34-m: firstly, since December 2013, an IGUANA-H from 6.5 to 15 GHz and, secondly, a NINJA feed from 3.2 to 14.4 GHz (SEFD $\sim$1,500 Jy) since July 2015. A modified NINJA feed 3–15 GHz was installed at all three stations in 2016. In paricular, the NINJA feed for the Kashima 34-meter radio telescope was specifically designed to realize a sharp beam pattern within 17 degrees to illuminate the sub-reflector. Two polarization sky signals after the amplifiers are transferred by optical converters with WDM to the observation room. We have installed a direct sampling system to make the entire system simple. The K6/GALAS direct sampler (see Table 1 for specifications) realized a relatively high-speed sampling at 16 GHz. After the quantization of the analog signals, the streams are digitally down-converted. Currently K6/GALAS has four ADCs, the first IF inputs the lower 8-GHz range and the second IF inputs the upper 8-GHz range, which covers the whole frequency allocation of VGOS [1]. Because the RF signal is directly digitized without analog frequency conversion, the phase differences between the output channels are fixed at the sampling stage. Thus, high precision delays can be derived with high stability by broadband bandwidth synthesis.

Table 1 Specifications of the K6/GALAS direct sampler.

Frequency range	0.01 to 24 GHz
Number of analog inputs	2
Sampling rate	16,384 or 12,800 MHz
Quantization	3 bit
DBBC	1-GHz bandwidth, 2 bit, 4 streams
10GbE protocol	VDIF / VTP / UDP / IP

1. National Institute of Information and Communications Technology (NICT)
2. Shanghai Astronomical Observatory (SHAO), Chinese Academy of Sciences

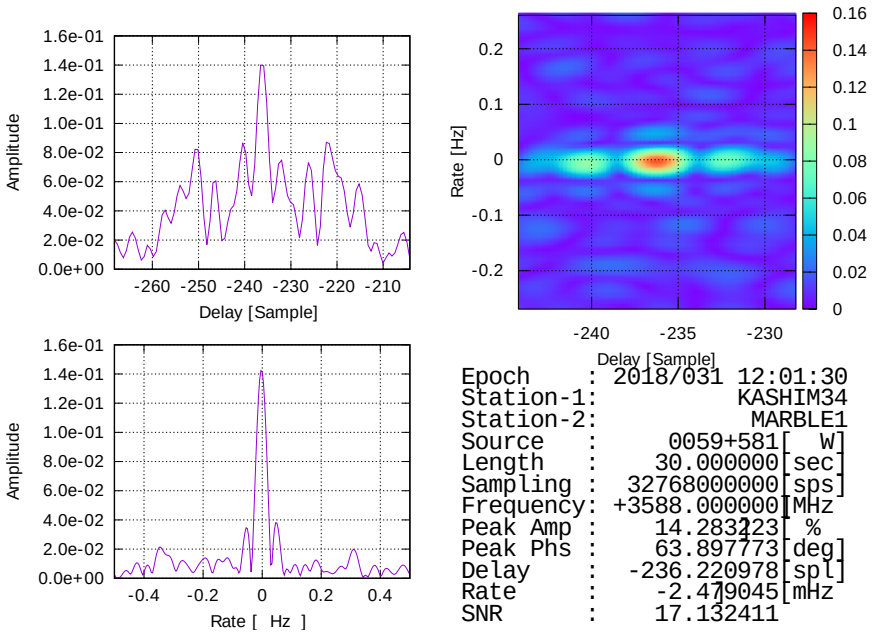

Fig. 1 Fringe plot between the compact #1 and 34-meter antennas after wide bandwidth synthesis. The width of the delay resolution function is only 70 ps.

After the correlation, we determined a reference scan as a reference with a strong source from all scans for the wide bandwidth synthesis (WBWS). All scans were corrected using the reference scan; then residual delays and delay rates were estimated by calculating a search function. Finally, differential TEC values were estimated [2]. Figure 1 shows the fringe taken in early 2018 between the compact #1 and 34-meter antennas with the frequency sequence of 3.2 GHz, 4.8 GHz, 9.6 GHz, and 12.8 GHz. The compact antenna located in Koganei, Tokyo might have the worst RFI environment in the world. Then we adapted the system to the environment by several counter measures, such as installation of a feed with a sharp cut-off frequency, an analog filter bank system, and filtering after the software correlation, to reduce the impact of strong RFI.

2 Time and Frequency Transfer by VLBI

The National Institute of Information and Communications Technology (NICT) has not only been developing a VLBI observation system in its function as an IVS-TDC, but it also has maintained and kept the Japanese time standard. Recently NICT, AIST, and Tokyo University have been developing an optical-lattice clock for the next generation time standard towards the redefinition of "the Second." Thus, it is necessary to compare with distant clocks of other countries on international baselines using several techniques. In case of two stations being as close as a few hundred kilometers, optical-fiber transmission is the best technique for the comparison. However, for distant station comparisons over thousands of kilometers a space technique is needed, e.g., GNSS, Two-Way Satellite Time and Frequency Transfer (TWSTFT), or VLBI. Thus, we would like to apply the VLBI technique to the intercontinental T&F.

With regards to the Time and Frequency transfer (T&F) by VLBI, the order of 10^{-16} in a few days is targeted. Since our two MARBLE antennas are quite small for VLBI, it is necessary to have a broadband system and to make effective use of it, e.g., by employing the VLBI Global Observing System (VGOS).

For the next-generation system of geodetic VLBI, VGOS was specified with fast moving antennas and broadband receivers. Several antennas that meet the VGOS requirements have been constructed (e.g., GGAO and Westford in the United States; one in Hobart, Australia and one in New Zealand; the

TWIN radio telescopes in Germany (Wettzell, TTW), Norway, and Sweden (Onsala, OTT); the RAEGE telescopes at Yebes in Spain and on Santa Maria in Portugal; three VGOS antennas of the QUAZAR network in Russia; and the Ishioka telescope in Japan).

NICT/Kashima is also developing a broadband system from 3.2 GHz to 14.4 GHz for the Kashima 34-meter antenna and two small and transportable antennas (see Figure 2). The broadband project is called "GALA-V."

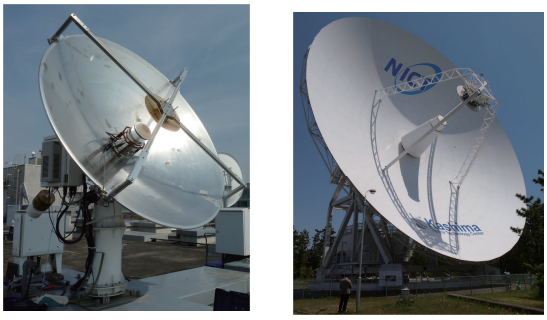

Fig. 2 The broadband compact #2 (MARBLE2) in Tokyo (left) and the Kashima 34-meter antenna in Ibaraki (right).

We measure the frequency difference between the compact antennas by using the large telescope indirectly. The big advantage of adopting this method is that we omit the large telescope effects (e.g., gravity and thermal deformation, cable delay). When the large telescope is labeled O and two compacts are A and B, then the delay model between the two compacts can be expresseded as

$$\tau_{AB} = \tau_{OA} - \tau_{OB} - \dot{\tau}_{AB} \times \tau_{OA}. \quad (1)$$

The delays that involve the large telescope τ_{OA} and τ_{OB} will disappear. Figures 3 and 4 show the $\pm$500 ps clock behavior between each compact antenna and the 34-meter antenna for an experiment that was carried out in 2014. After performing the epoch conversion (Equation 1), the clock variation was reduced to $\pm$100 ps in this case.

With regard to the postfit residuals after the subtraction of two delays $\tau_{OA} - \tau_{OB}$, the RMS of the residuals (typically 10 to 20 ps) shows almost the same value or it increased slightly. If the residuals are dominated by Gaussian noise, the RMS of the residuals will increase

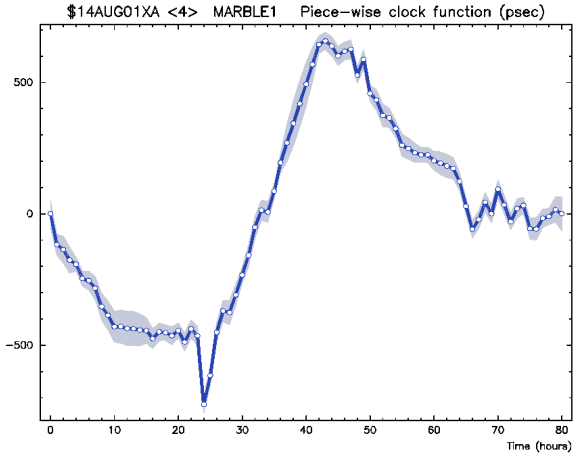

Fig. 3 The clock behavior between compact #1 and the 34-meter.

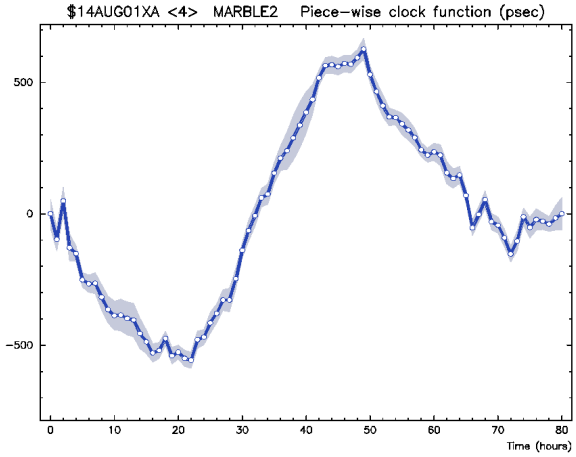

Fig. 4 The clock behavior between compact #2 and the 34-meter.

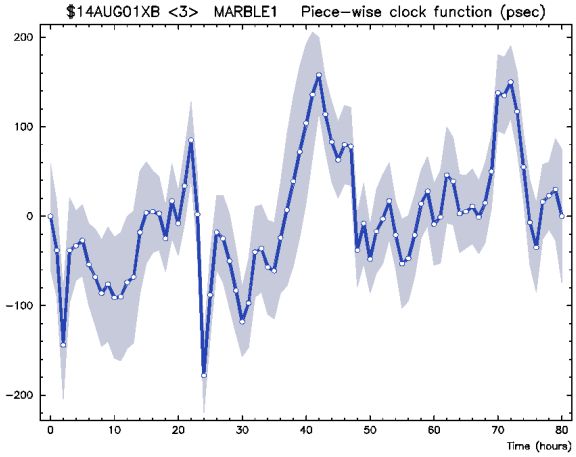

Fig. 5 Clock behavior between compact #1 and compact #2 after subtracting Figure 3 from Figure 4 based on Equation (1).

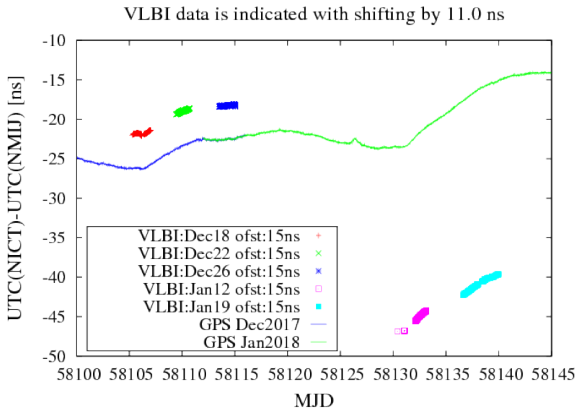

Fig. 6 Clock comparison between GPS and VLBI for UTC(NICT)–UTC(NMIJ).

Fig. 7 Relocated compact telescope in Medicina, Italy.

by a factor of $\sqrt{2}$. Therefore, we think that the residuals hit the atmosphere limit.

Figure 6 shows a clock comparison between GPS and VLBI for one month between NICT in Tokyo and NMIJ in Tsukuba. In this period, we carried out five 24-hour experiments with the wide bandwidth system. The data volume of the 24-hour observation amounts to about 150 TB (each station 50 TB). We performed a heavy correlation work for a few days. The VLBI result during the observation had a jump due to a feed replacement. However, once the system was fixed, we confirmed that the VLBI result had good agreement with GPS.

3 T&F between Japan and Italy

In the summer of 2018, we removed our compact telescope from Tsukuba and installed it in Medicina, Italy (Figure 7). Medicina and Turin are connected via optical fiber. The reference signal from INRiM in Turin can synchronize the Hydrogen maser in Medicina. The system works perfectly and the first fringe was obtained while we were still visiting Italy. We are now investigating compact and strong radio sources. We will carry out T&F measurements using VLBI starting in the fall of 2018.

References

1. K.Takefuji, “Performance of Direct Sampler K6/GALAS,” IVS NICT-TDC News 36, pp. 20–22, 2016, `http://www2.nict.go.jp/sts/stmg/ivstdc/news_36/pdf/tdcnews_36.pdf`.
2. T. Kondo and K. Takefuji, An algorithm of wideband bandwidth synthesis for geodetic VLBI, *Radio Sci., Vol. 51*, doi:10.1002/2016RS006070, 2016.

Current Status of VGOS Observation wtih Ishioka VLBI Station

Takahiro Wakasugi, Shinobu Kurihara, Haruka Ueshiba, Michiko Umei, Masafumi Ishigaki, Hiroshi Munekane

Abstract The Geospatial Information Authority of Japan (GSI) constructed a new VLBI facility at Ishioka in 2014 which meets the VGOS requirements. The Ishioka VLBI station is regularly involved in international VLBI observation sessions with S/X-band, is one of the leading stations of IVS after taking over the role of the Tsukuba VLBI station, and is in preparation for regular VGOS operations. From November through December 2017, IVS performed the Continuous VLBI Campaign 2017 (CONT17), which included not only 15-day conventional S/X-band observation sessions but also five-day continuous broadband observation sessions that were compatible with the VGOS frequency setup for the first time. The Ishioka VLBI station was involved in the preceding VGOS Trials and in CONT17 with five other VGOS stations as the only station with the VGOS setup in Asia-Oceania. This report summarizes the current status of the Ishioka VLBI station, especially with respect to the broadband observations in the CONT17 campaign.

Keywords Ishioka, Tsukuba, VGOS, broadband

1 Introduction

The Geospatial Information Authority of Japan (GSI) started the construction of a new geodetic VLBI station at Ishioka in 2011. Ishioka is located about 17 km northeast of Tsukuba, where the headquarters of GSI is located. The location of the new station was selected by considering some requirements such as ground stability, good sky coverage, the condition of relatively less RFI, availability of a power supply and high speed network, and accessibility to the GSI headquarters.

The VLBI station is designed for the next-generation VLBI system called VGOS. It is equipped with a fast-slewing telescope with a diameter of 13.2 m, a proper optical system, a high speed data acquisition system, and two hydrogen masers in an observing building.

In addition, the site is equipped with gravity measurement equipment and continuously operating GNSS reference stations to contribute to the Global Geodetic Observing System (GGOS) as a core observatory (Figure 1) [1].

2 Regular S/X-band Observation Sessions

GSI started the operation of the Ishioka VLBI station in February 2015 in parallel with the Tsukuba station, which had been the main VLBI station of GSI since 1998. The Ishioka station and the Tsukuba station were involved in more than 50 IVS S/X-band regular observation sessions during the overlapping operational period until the end of 2016. Figure 2 shows the baseline length between the Kokee Park station in Hawaii, USA and the two stations in Japan. Results of the Kokee-Ishioka baseline were converted to the Kokee-Tsukuba baseline by using the Tsukuba-Ishioka baseline vector derived from the parallel operation over a year and a half. One can observe a good geodetic connection between Tsukuba and Ishioka.

The UT1 Intensive series, which rapidly measures the UT1-UTC parameter, is one of the most significant services of the IVS. GSI started the weekend

Geospatial Information Authority of Japan

Fig. 1 The panoramic view of the new geodetic observing site at Ishioka.

Intensive sessions (INT2) in 2002 with the Tsukuba-Wettzell baseline. The whole process from data transfer to analysis is conducted by unmanned operation at GSI. Results are then submitted to the IVS and the IERS within a few minutes from the end of each session. Thus, INT2s contribute to monitoring the irregular fluctuation of UT1-UTC and improving the accuracy of the prediction value [2].

Ishioka started trial observations for UT1-UTC in October 2016 in order to take over the role of Tsukuba. The comparison of UT1-UTC estimation with respect to the IERS final solution are shown in Figure 3. The results derived from the Ishioka-Wettzell baseline are consistent with those from the Tsukuba-Wettzell baseline.

As a result, GSI terminated the operation of Tsukuba at the end of 2016, and Ishioka took over the role of Tsukuba at the beginning of 2017.

3 Broadband Experiments

The compatibility of the broadband observing system of Ishioka with overseas VGOS systems was confirmed in September 2016 through some broadband experiments [3]. The first continuous broadband observation for five days was performed in December 2017 as a part of the continuous VLBI campaign observation (CONT). Ishioka carried out this campaign observation as one of the six VGOS stations in the world (Figure 4).

In order to receive broadband data, it is necessary to replace the tri-band feed for the S/X-band system with a QRFH. Additional data storage was also prepared because the total amount of data was expected to be around 80 TB during the five-day observation. Since observation started at 8:00 a.m. every day and finished at 7:30 the next day in local time, GSI staff went to the Ishioka station at 7:00 a.m., checked the recording system and the observation status, connected new data storage, and ran a schedule file during this switching time. Thanks to these efforts, Ishioka successfully finished CONT17 without any trouble, and all data were e-transferred to MIT Haystack for correlation.

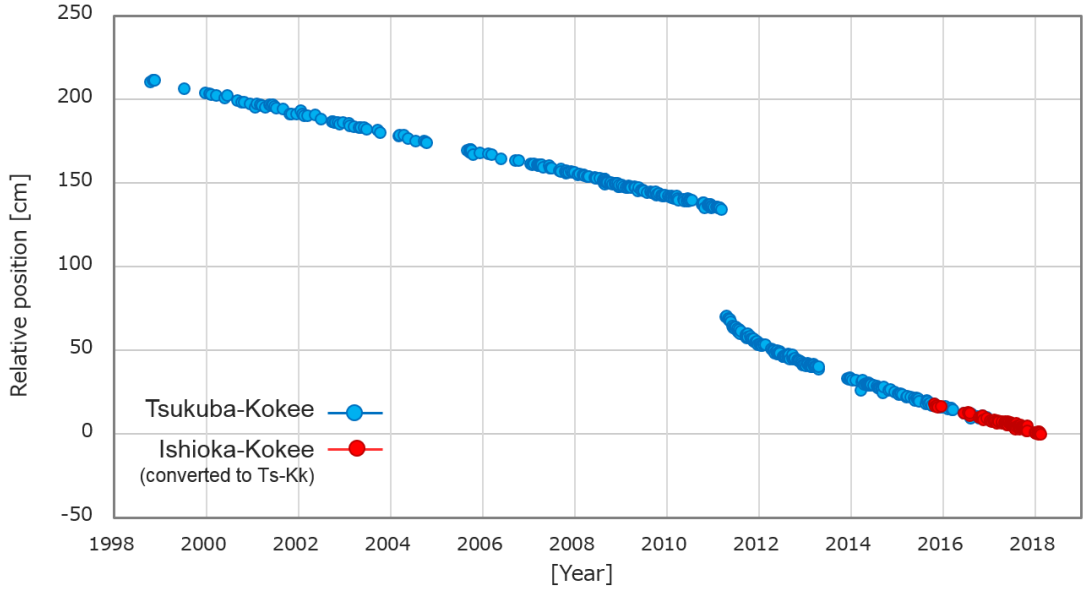

Fig. 2 The baseline length between Tsukuba-Kokee and Ishioka-Kokee obtained from S/X-band observation sessions. The length of Ishioka-Kokee was converted to the Tsukuba-Kokee baseline by using the Tsukuba-Ishioka baseline vector derived from 2015 through the end of 2016.

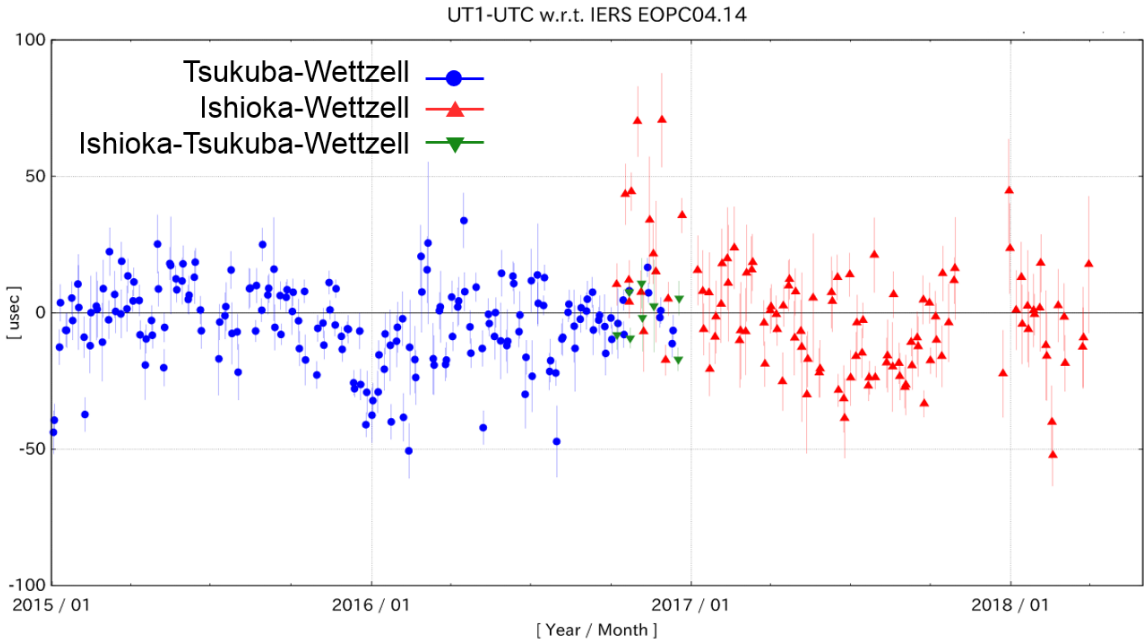

Fig. 3 The estimated UT1-UTC with the Tsukuba-Wettzell baseline and the Ishioka-Wettzell baseline, with respect to the IERS final solution.

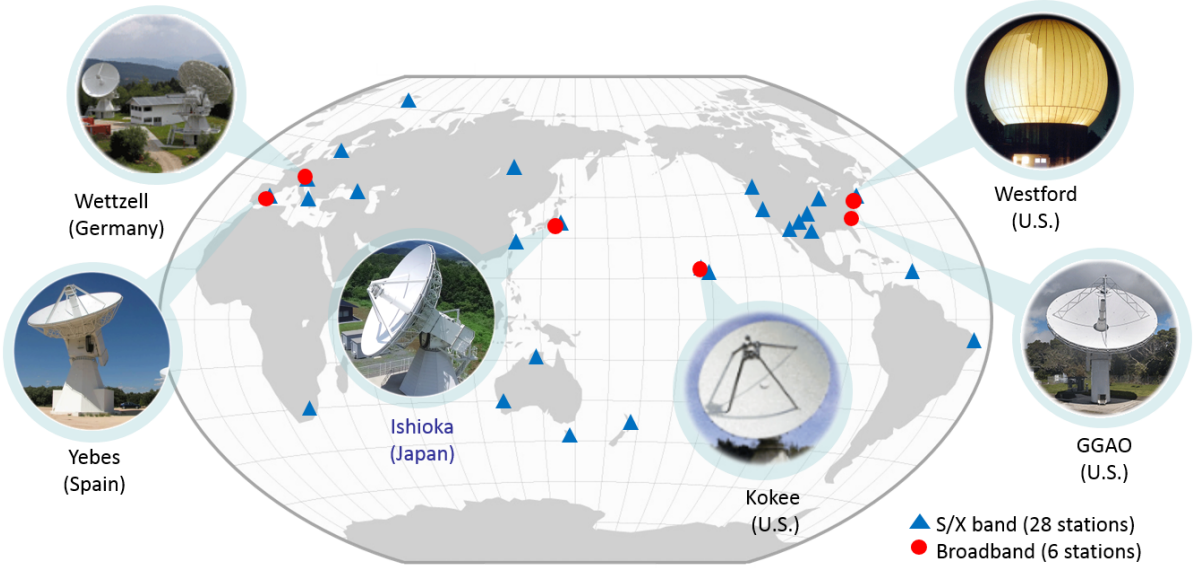

Fig. 4 Six VGOS stations involved in CONT17.

GSI has interest in VGOS not only as an observing station but also as a correlator. We tested the correlation of the Ishioka-Yebes baseline with the K5 correlation software, which was developed by NICT, with the cooperation of the Spanish IGN for provision of Yebes data. Fringes were successfully detected on each channel, and it is confirmed that the K5 software is applicable to VDIF format data.

4 Future Perspective

Ishioka will continue legacy S/X-band observation sessions for a while in order to establish relative positions with existing stations in the world. On the other hand, the development and the operation of the broadband system are very significant challenges. Ishioka is involved in VGOS experiments from June to mid-September 2018. Then the station will gradually transit to VGOS observations while keeping pace with overseas stations.

GSI will also continue test correlation of VGOS data and its validation and will investigate feasibility as a future VGOS correlator.

5 Conclusions

GSI constructed a new geodetic VLBI station at Ishioka in 2014 and started its operation in 2015 in parallel with Tsukuba. Through the overlapping operations until the end of 2016, a reliable geodetic connection between Tsukuba and Ishioka was established. Accompanying the termination of operations and demolishment of Tsukuba, Ishioka took over the roles of Tsukuba, such as the IVS Intensive sessions for the rapid estimation of UT1-UTC.

Ishioka succeeded in carrying out the first continuous broadband observation of CONT17 as one of the six VGOS stations in December 2017. In addition, GSI started VGOS correlation testing with K5 correlation software. We continue to move VGOS forward through these contributions.

Acknowledgements

We thank Mamoru Sekido and Kazuhiro Takefuji from NICT for general support for VGOS observation, Pedro Elosegui and Chester Ruszczyk from MIT Haystack for general support for VGOS observation and correlation, Pablo de Vicente and Javier Gonzalez Garcia from IGN Spain for providing the CONT17

data of Yebes, and Tetsuro Kondo and Fengchun Shu for useful comments for VGOS correlation.

References

1. Ishimoto, M., M. Umei, T. Wakasugi, R. Kawabata, T. Toyoda, B. Miyahara, and Y. Fukuzaki. Status on the Ishioka Geodetic Observing Station. *IVS NICT-TDC News*, 36, 9–12, 2016.
2. Wakasugi, T. and T. Hara. Tsukuba VLBI Analysis Center. *International VLBI Service for Geodesy and Astrometry 2015+2016 Biennial Report*, edited by K. D. Baver, D. Behrend, and K. L. Armstrong, NASA/TP-2017-219021, 272–275, 2017.
3. Wakasugi, T. M. Umei, T. Toyoda, M. Ishimoto, R. Kawabata, and B. Miyahara. VGOS development for Ishioka 13-m antenna. *Proceedings of the 23rd European VLBI Group for Geodesy and Astrometry Working Meeting*, 84–87, 2017.

Current Results of the VERA K/Q-band Fringe Survey: Performance of the 8-Gbps Recording System and its Effectiveness

Takaaki Jike [1], Tomoaki Oyama [1], Takumi Nagayama [1], Aya Yamauchi [1]

Abstract VERA (VLBI Exploration of Radio Astrometry) started a K/Q-band continuum radio source fringe survey using an 8-Gbps recording system in January 2016. The main purposes of these experiments are the establishment of analysis procedures for highly sensitive VLBI (Very Long Baseline Interferometry) data, increasing the observable radio sources for VERA, and confirming the effect on the analysis results of the reduction of white noise error. The radio sources for observation are selected from the VLBA (Very Long Baseline Array) Calibrator List; some 5,196 radio sources, which are distributed in the range of −45 to 90 degrees of Celestial declination, are listed as observable candidates. The frequency fluctuation from atmospheric refraction and the instability of phase lock oscillators are corrected by smoothing, using a Moving-Average Filter, to inhibit a decrease of the correlation coefficient during the integration period. By May 2018, 3,252 sources in K-band and 2,941 sources in Q-band were observed. When the fringe detection was realized with signal-to-noise ratios of seven or more, the number of radio sources that met the fringe detection criterion was 2,608 in K-band and 1,725 in Q-band. From the delays of the 8-Gbps recorded VLBI data, the azimuthal anomaly of residual delays (including anisotropy of atmospheric excess pass delay) was confirmed.

Keywords VERA, 8-Gbps recording

1. Mizusawa VLBI Observatory, National Astronomical Observatory of Japan

1 Introduction

VERA is a Japanese VLBI project dedicated to phase-referencing astrometry. This project aims at determining annual parallaxes and proper motions of Galactic MASER (Microwave Amplification by Stimulated Emission of Radiation) emitting areas in the precision of a few tens of microarcseconds with reference to a nearby quasar on the celestial sphere.

A new sampling and recording system with a more than 8-Gbps rate capability is developed corresponding to a wide-band receiving system, and experimental fringe search observations have been carried out to confirm the fringe detection performance of this system. Serving as this experiment, VERA started a K/Q-band continuum radio source fringe survey using an 8-Gbps recording system in January 2016. The purposes of this experiment are reservation of the radio sources suitable for phase referencing by improving fringe detection sensitivity, establishment of the way for obtaining accurate fringes from wide band VLBI data, and fundamental research for the next plan for Mizusawa. Obtaining accurate fringes improves reliability also for geodetic and astrometric parameter estimation.

In this report, we present the results of the fringe survey performed by May 2018 and the fringe detection performance of the 8-Gbps recording system.

2 Formation of Data

The radio sources which become observable candidates are selected from the VLBA Calibrator List (http://www.vlba.nrao.edu/astro/calib). The distribution of observable radio sources on the celestial sphere

is shown in Figure 1, and the restrictions for selecting radio sources are shown in Table 1.

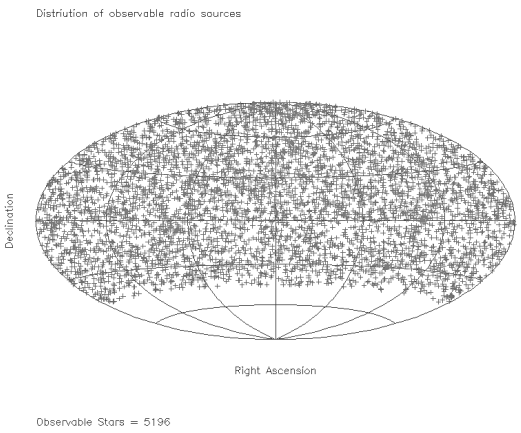

Fig. 1 Distribution of observable radio sources.

Table 1 Restrictions for selecting radio sources.

Version of main radio source list	160107
Total number of observable radio sources	5,196
Range of Right Ascension	0–24 hour
Range of Declination	−45 – 90 deg

A series of observations was carried out only in the VERA network. Specifications of the observation system which refer to fringe detection sensitivity are shown in Table 2. ADS3000+ and VSREC are adopted to the sampling—recording system. Observations were performed separately for each frequency band.

Table 2 Specifications of observation system.

Frequency Band Code	K	Q
Received Freq. band (GHz)	21.5–23.5	42.4–44.4
Typical SEFD (Jy)	439	848
Sampling and Filtering Mode	1,024 MHz, 2 bit, 4 stream	
Recording Bit Rate (Mbps)	8,196	

Correlation processing was done by the Mizusawa Software Correlator. Table 3 shows the settings of the correlation and fringe search. The basic package of fringe search software is regularly used in order to estimate delays from VERA internal geodetic VLBI data, and this software was given additional reconstruction for processing of this wide-band and highly sensitive VLBI data.

One of the main reconstructions is correcting the temporal fluctuations of fringe phases whose causes are frequency variations from atmospheric refraction and instability of the local reference frequency. The temporal fluctuations of fringe phases become large in proportion to frequency. Because the K- and Q-bands are high frequency, the temporal fluctuations of fringe phases are remarkable. The fluctuations degrade the coherency, and the fringe is dispersed along the rate direction; therefore, a suitable correlation amplitude corresponding to the integration time is not obtained. In order to remove the long-periodic component of fluctuations, smoothing by Low Pass Filter (LPF) was executed on the fluctuations. At the first onset, as one of the most fundamental digital LPFs, the Moving Average Filter was adopted for smoothing. The averaging period is nine seconds, which was estimated by Modified Allan Standard Deviation of phase temporal fluctuations. It was confirmed that the period from seven to eleven seconds is the zone where the character of fluctuations shifts from random walk to bias instability (Figure 2), almost in a fringe with a signal-to-noise ratio of 20.0 or more. Integration is again carried out, with modification of the phase along the smoothed line like the solid line shown in Figure 3.

Table 3 Correlation and fringe search settings.

Correlator Type	FX
The number of spectrum channels / stream	512
Frequency resolution / channel	1 MHz
Total correlated bandwidth	2048 MHz
Accumulation period	1 second
Effective integration bandwidth	1920 MHz
Integration period / 1 scan	128 seconds
Peak search method	2-D parabolic fitting

When the phase fluctuations of Figure 3 were modified, the signal-to-noise ratio of the fringes after fluctuation modification was 1.4 times larger in comparison to the one before modification. It is necessary to take care of the effect that coherency of noise increases. Before and after the smoothing process, the root mean square of the fringe phase differences was 0.67° at the central epoch in the integration time range; the large difference with respect to the estimation of the averaged fringe phase was not confirmed.

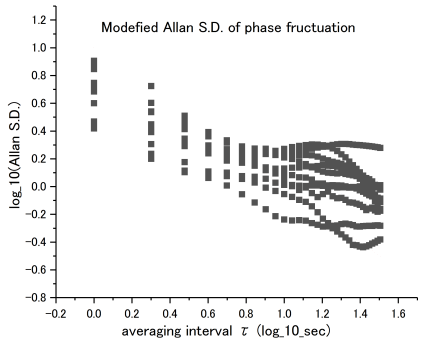

Fig. 2 Modified Allan Standard Deviations of fringe phase fluctuations.

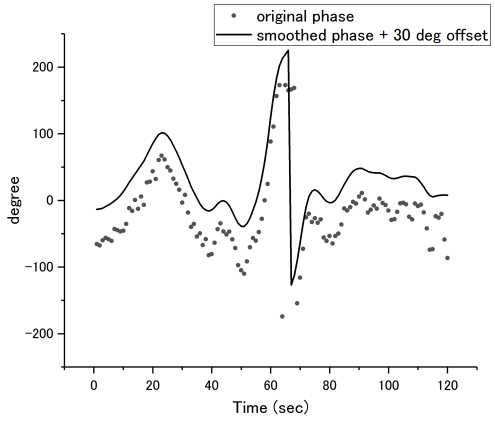

Fig. 3 Temporal fluctuation of fringe phases and smoothed line.

3 The Borderline of Fringe Recognition

The signal-to-noise ratio (S/N) is used for recognition of fringe detection as a standard. Usually, the analysis of VERA internal geodetic VLBI sets the criterion for recognition of fringe detection; the delay estimated from fringes with 7.0 or more S/N is used for parameter estimation. The Delay Deviation Score (*DDS*) is adopted in order to investigate the relationship between S/N and the accuracy of fringe tracking parameters. The delays used for estimation of the standard deviation in the calculation process of *DDS* are obtained from fringes with 7.0 or more S/N, applying the fringe recognition criterion of geodetic VLBI, and this is expressed by the following equations.

$$DDS = \{10(dly_{obs} - dly_{apr} - dly_{clk})/\sigma_{dly}\} + 50, \quad (1)$$

where dly_{obs} is the observed delay, dly_{apr} is the a-priori delay used for fringe tracking, dly_{clk} is the clock offset residual, σ_{dly} is the standard deviation of $dly_{SN7} - dly_{apr} - dly_{clk}$, and dly_{SN7} is dly_{obs} with 7.0 or more S/N. It is expected that *DDS* will congregate between 40 and 60 (the 1σ zone), when an accurate fringe tracking parameter is used for correlation processing. Therefore, when *DDS* of a fringe goes into the 1σ zone, it leads to the increase in probability that the S/N of this fringe is the signal-to-noise ratio of the fringe brought about from the signal of the radio source.

The relationship between S/N and *DDS* is shown in Figure 4. When S/N becomes 6.5 or more, *DDS*s congregate remarkably near the 1σ zone, and this tendency is the same with K- and Q-band. In order to show in detail the *DDS* distribution near where the concentration ratio changes, Figure 5 shows the ratios of fringes which fulfill specific restrictions. The ratio (R_{DDS}) is given as a percentage as follows,

$$R_{DDS} = \{n(S_{(DDS)} \cap S_{(S/N)})/n(S_{(S/N)})\} \times 100. \quad (2)$$

$S_{(DDS)}$ and $S_{(S/N)}$ in Equation 2 are the sets with restrictions expressed in the following,

$$\begin{aligned} S_{(DDS)} &= \{DDS \,|\, 40 \le DDS \le 50\}, \\ S_{(S/N)} &= \{S/N \,|\, SNR_1 \le S/N < SNR_2\}, \end{aligned} \quad (3)$$

where SNR_1 and SNR_2 are specific values of the signal-to-noise ratio showing the range of restrictions. As S/N increases from 5.5 to 7.0, the increasing rate of R_{DDS} becomes rapid; on the other hand, when S/N becomes larger than 7.0, the increasing rate of R_{DDS} declines. Therefore, when S/N is 7.0 or more, a fringe is mostly recognized to be detected, and when $6.0 \le S/N < 7.0$, recognition of fringe detection is marginal.

Even if S/N is high, several percent of radio sources remove *DDS* from the 1σ zone. A *DDS* which has a large gap from the 1σ zone arises from mistakes of fringe tracking. It is considered that the causes of fringe tracking mistakes are an instable reference frequency, inaccuracy of geometrical delay from the uncertainty of the radio source positions and ground-station positions, and error of the atmospheric excess pass delay model. Accumulation of fringe tracking errors decreases the correlation coefficient. It is required to re-

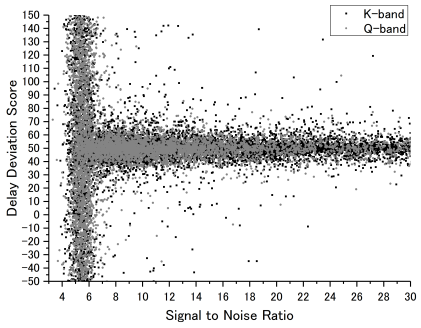

Fig. 4 Distribution of delay deviation score with respect to signal-to-noise ratio.

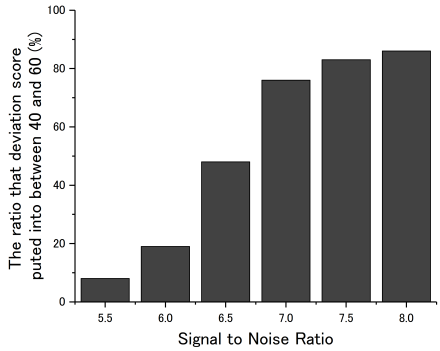

Fig. 5 The ratios of fringes with specific S/N score *DDS*s between 40 and 60.

duce these factors that obstruct accurate fringe tracking in order to obtain a more accurate fringe.

4 Results of Fringe Detection

In fringe survey observation, several fringe results are obtained from one radio source. The maximum signal-to-noise ratio in these fringe results is adopted as the decision of fringe detection. Table 4 shows the fringe detection results of the fringe search observations performed by May 2018. The fringes with 7.0 or more S/N were obtained from 80% of K- and 59% of Q-band radio sources.

For checking the minimum of the correlation flux density, Figure 6 shows the frequency distribution of less than 1.0 Jy correlation flux density. The minimum

Table 4 Fringe detection result.

	Number of sources	
Frequency Band Code	K	Q
Total number of observed	3,252	2,941
Fringe is detected	2,608	1,725
Fringe is marginal	378	730

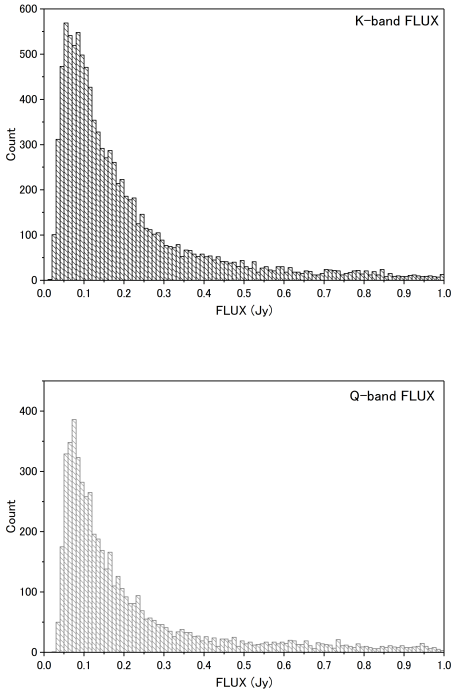

Fig. 6 Frequency distributions of less than 1.0 Jy correlation flux density.

flux density is 25 mJy in K- and 35 mJy in Q-band. The coherence loss factor used in order to estimate these correlation flux densities was 0.87. However, this factor is an ideal value for two-bit sampling and is not the actual value estimated corresponding to the efficiency of our wide band observation system, so these flux densities are provisional.

5 Azimuthal Anisotropy of Atmospheric Excess Pass Delay

A fringe tracking mistake removes the *DDS* from the 1σ zone, and it is surmised that one of the main causes

of fringe tracking mistakes is prediction errors of the atmospheric excess pass delay. Estimation of the atmospheric excess pass delay correction applied to the mapping function is effective for bringing the *DDS* close within the 1σ zone. However, although an observed delay with a few picoseconds of theoretical white noise error is obtained from 8-Gbps recording VLBI data, the root mean square of the post-fit-residual delay remained 14.0 picoseconds [1]. It is expected that the excess pass delays which do not suit the azimuthal-isotropic mapping function model are mixed in these residuals.

In order to confirm the azimuthal anisotropy of atmospheric excess path delay, we tried to get the distributions of $dly_{grad}(= dly_{rsd}/GMFW)$ in alignment with the azimuth. The used delays were obtained from VERA K-band internal geodetic VLBI using the OCTAD-OCTADISK2 8-Gbps sampling-recording system on November 27, 2017; theoretical white noise delay errors were a few picoseconds. The delay residual (dly_{rsd}), which is mainly constructed from the atmospheric excess pass delay error, has the following proportional relationship to the Global Mapping Function Wet-term ($GMFW$),

$$\begin{aligned} dly_{rsd} &= dly_{obs} - dly_{prdc} \\ &\approx dly_{grad} \times GMFW, \end{aligned} \tag{4}$$

where $dly_{prdc} = dly_{calc} + dly_{clk} + dly_{zpdc} \times GMFW$, dly_{calc} is the predicted delay from *CALC*, and dly_{zpdc} is the correction value of the zenith pass delay. The Global Mapping Function is also used to calculate the atmospheric excess pass delay in *CALC*. The distribution of dly_{grad} arranged in accordance with azimuth is shown in Figure 7. The major distribution form of dly_{grad} appears like a sine or triangle wave. It is considered that the biggest sine wave function is made into a cause of the horizontal deviation of the station position, and the anisotropy of the atmospheric excess pass delay is mixed with the remainder after removal of the delays by the error of the station position.

However, the anisotropy of excess path delay static in time cannot by itself explain all of the delay residual variation. Even if the gradient difference is ~ 0, about 50 picoseconds of scatter is confirmed. Temporal variation of the anisotropy and other error sources that correlated with the zenith and azimuth angle are taken into consideration; for example, collaboration of the position and the structure effect of radio sources, and excess path delay error. Complexity of atmospheric structure and its timing variation also become error sources.

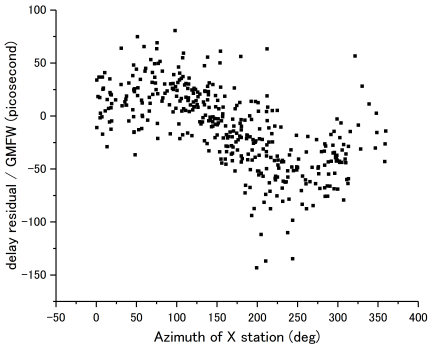

Fig. 7 The distribution of the atmospheric excess pass delay gradient in alignment with azimuth.

6 Conclusions

The wide-band fringe survey detected fringes from the VLBA Calibrator List. Detection of a fringe is recognized in a fringe with an S/N of seven or more. The detection percentage of fringes with S/N of seven or more is 80% in K- and 49% in Q-band. The minimum correlation flux density is 0.25 mJy in K-band and 0.40 mJy in Q-band. From delays of the 8-Gbps recorded VLBI data, the azimuthal anomaly residual delays, including atmospheric excess pass delay, was confirmed.

References

1. T. Jike, “VERA Geodetic VLBI with Newly Developed High-speed Sampler and Recorder”, In D. Behrend, K. Baver, and K. Armstrong, editors, IVS 2016 General Meeting Proceedings “New Horizons with VGOS”, NASA/CP-2016-219016, pages 159–162, 2016.

VieSched++: A new Scheduling Tool in VieVS

Matthias Schartner, Johannes Böhm

Abstract Scheduling is an integral part of every VLBI experiment. The task of a scheduler is to create the sequence of observed sources for each station. Because the amount of possible source sequences is extremely high, selecting the best sequence is a challenging problem and can be exploited for optimization. Typically scheduling software is used to automate this process. With the VGOS era approaching, high demands are posed on scheduling software. We present a new scheduling software called VieSched++ as part of the Vienna VLBI and Satellite Software (VieVS) [3] which is able to fulfill those requirements. This software follows many new ideas concerning the algorithms used to create schedules and support various new features. It is written from scratch, keeping VGOS requirements in mind. First results using the new scheduling software look very promising.

Keywords Scheduling, VieSched++, VieVS

1 Introduction

For the analysis of VLBI sessions several different software packages exist, like the Vienna VLBI and Satellite Software (VieVS), Calc/Solve, OCCAM, C5++, Where, and many more. But, when it comes to scheduling, most of the IVS sessions are scheduled using only one software package called SKED [4], which was developed by NASA/GSFC. Those schedules are usually not cross-validated against results from other software packages. In Vienna, we had developed our own scheduling tool [11] as part of VieVS which is successfully applied for scheduling geodetic VLBI sessions, especially for the AUSCOPE [5] network. While schedules generated with this software tool were considered good, the software had some limitations considering the flexibility, and – most importantly – it was not capable of scheduling VGOS [8] experiments. Based on the experience we gained with our previous software, we have started to develop a new scheduling tool from scratch as part of VieVS called VieSched++.

Technische Universität Wien

2 Concept

VieSched++ is written in C++ using a fully object-oriented software design. The software consists of two parts, the scheduler and a graphical user interface (GUI). It makes use of many modern software development approaches and supports multithreading for increased performance. It is a multi-platform application and is successfully tested on Linux and Windows using different compilers.

The scheduler supports all features required in geodesy and astrometry like optimization of sky coverage (Section 3.4), tagalong mode, fillin mode (see Section 3.2), subnetting, and basic support for twin telescopes. The output is available in both .skd and .vex format. Besides the schedule files, an operation notes file, helpful log files, and other files with statistical information can be generated as well as an empty NGS file which can be directly used in the VieVS VLBI package to simulate the schedule. The scheduler is controlled by a simple .xml document which can be set up by the GUI or by hand. To make

the software more consistent with today's schedules, VieSched++ supports the sked catalogs.

Great care was taken to ensure that the software and the GUI are very intuitive and therefore easy to use. Installing the software should also be easy because it has only a small amount of dependencies. For the scheduler, only the Standards of Fundamental Astronomy (SOFA) [10] libraries need to be linked. Other pre-requirements are the boost C++ header files and OpenMP for the multithreading support. While it is sufficient to only include the boost header files, it is recommended to link the boost libraries for additional features. The Qt libraries are required for the GUI. To further simplify the installation process, a CMake file for the scheduler and a qmake file for the GUI are provided.

While the main purpose of the GUI is the creation of the .xml documents required for the scheduler, it comes with many additional features like a schedule analyzer and comparison tools between different schedules and between schedules and station log files. Although VieSched++ is a standalone tool of the VieVS package, the interaction between VieSched++ and the VieVS VLBI software is straightforward, and results from the scheduler can be directly used.

3 Algorithms

All algorithms used in VieSched++ are redesigned from scratch. In the following subsections, some major differences compared to other software packages are shown and their usefulness is discussed.

3.1 Multi-scheduling

With VieSched++ it is recommended to not only generate one schedule for a session but create many schedules with different parameters. This can be automatically achieved using our multi-scheduling support. There are many parameters which can be used in every scheduling software to fine tune a schedule, such as the maximum allowed slew time per station, the time between observations to the same source, or the maximum allowed idle time for slow antennas. At the same time, it is difficult to decide which scan is the best at a certain time and therefore should be scheduled. To measure this, usually multiple quantities are combined like the improvement in the sky coverage, the number of expected observations, the duration of the scan, and many more. Additional parameters combine these quantities to decide which scan should be scheduled. Together this leads to a huge variety of parameters which can be used to fine tune a schedule. Different networks with different stations benefit greatly from customized scheduling parameters [9]. The multi-scheduling tool helps in this process to create an optimized schedule with customized parameters. Instead of only scheduling one schedule at a time it creates many schedules automatically by varying some scheduling parameters. The multithread support reduces the processing time significantly. It is possible to compare the huge amount of schedules based on statistics in the GUI to pick the best schedule. Furthermore, the output can be used directly in the VieVS VLBI software to simulate the sessions in order to get a better comparison of the schedules based on repeatability of geodetic parameters. Altogether this increases the quality of the schedules significantly.

3.2 Recursive Scan Selection / Fillin Modes

In geodetic VLBI schedules, a concept named fillin modes is used to minimize the amount of idle time per station. Usually, there are two main reasons why idle time in a schedule occurs. First, most stations have very different slew rates, and therefore some stations have to wait for others to finish slewing before a scan can be started. Second, most stations have different sensitivities and therefore observing times which lead to some stations finishing a scan earlier than others. Thus, a so called fillin mode tries to minimize the idle time by scheduling more scans in between the main scans with a reduced amount of stations which would otherwise be idling. Most scheduling software follows a sequential scan selection, which means they start at the beginning of the session and schedule scan after scan increasing in time. If some stations finish way before others additional fillin mode scans are introduced to reduce the idle time. The downside of this approach is that it only reduces idle time based on shorter ob-

serving times which occur after an observation and not based on different slew times before an observation.

With VieSched++ this is not necessarily the case. Figure 1 illustrates how the recursive scan selection in the standard case works. First, the scheduler decides to

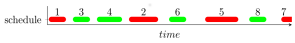

Fig. 1 Recursive scan selection. Red (dark) lines indicate observing times for main scans. Green (light) lines indicate observing times for recursively selected scans. Numbers show the order in which these scans are selected.

schedule scan number 1 at the beginning of the session. The next scheduled scan is scan number 2. Now the software checks if it is possible to squeeze in another scan between 1 and 2. This might be possible for some stations which are faster slewing or are more sensitive and therefore require less observing time. If a new scan is possible it is scheduled as scan number 3. Again the software checks if it is possible to squeeze in another scan, this time between scan 1 and 3. If not, the software checks if it is possible to add a scan between scan 3 and 2. If scan number 4 is possible the software tries to squeeze in another scan between 3 and 4 and 4 and 2. If no more scans are possible it will continue with scan 5 and the process starts over again. Following this algorithm, the whole session is scheduled, and the idle time of both different slew times and different observing times is reduced.

While this is the most basic case it is also possible to start the schedule at any time. Figure 2 illustrates another case. This time the scheduler starts with the most important scans for this session.

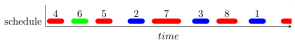

Fig. 2 Recursive scan selection. First, scans which are assumed to have the highest impact (blue: scans 1, 2, and 3) are scheduled. Afterward, the gaps between those scans are filled (see Figure 1).

For example, those could be scans during Intensive sessions that will be close to the edges of the commonly visible sky. It is assumed that these observations have the highest impact on the result [1], [12]. After fixing the most important scans the gaps in between are recursively filled.

Another use is the so-called fillin mode a posteriori, where the schedule is first created without any recursion and the recursive scan selection happens after the schedule reaches the end time. In the case of Figure 1 the scheduler would first select the scans 1, 2, 5 and 7 and afterwards fill the gaps in between. This works particularly well in the case of multiple tagalong stations (see Section 4).

3.3 Station-, Source-, and Baseline-based Parameters

To increase the flexibility of the scheduler it is possible, but not necessary, to give every station, source, or baseline its own optimization parameters. This can be helpful if you have a network with very different stations. For fast slewing, smaller antennas it might bring an improvement to schedule them differently than slower, bigger antennas and give them, for example, a different maximum allowed slew distance. The same is true for sources. If you have a set of calibration sources it might bring a benefit to schedule them differently than your target sources and set a different minimum required signal to noise ratio or a different minimum time between two scans to the same source. On top of that, it is possible that these parameters can change in time. This might be helpful if your session has a special science goal like relativistic experiments and your session consists of multiple phases. With this technique, it is further possible to start and end the tagalong mode of stations during a session. For example, this is done by the CONT campaign for stations participating in Intensive sessions [2]. It is also possible to follow custom scheduling designs like the Austral star mode [6].

3.4 Sky Coverage

One major disadvantage of the previous VieVS scheduling tool was the representation of the sky coverage. There, the sky is divided into thirteen areas. If an observation is inside one of these areas, the area is assumed to be saturated and further observations in a certain time epoch that are in the same area are assumed to have no improvement on the sky coverage. This representation fails if observations are close to the edges of the areas. As with other software packages in VieSched++, the sky is no longer divided into distinct

areas, but instead the angular distance between the new and previous observations is taken into account.

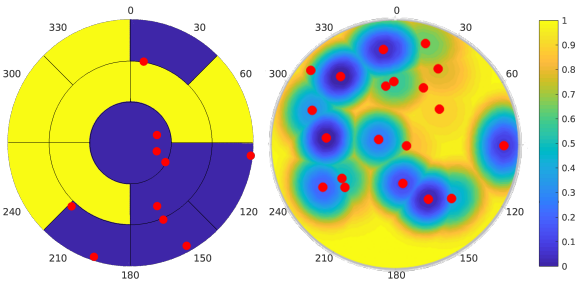

Fig. 3 Comparing the old sky coverage model with 13 areas (left) and the new implementation using angular distance and time as parameters. Red dots mark observations.

Several parameters can be used to describe the model. Figure 3 compares the old representation with the new one when decreasing the saturation of the sky coverage with the distance from the observation and with time.

4 Results

The usefulness of the new scheduling algorithms is discussed using the first CONT17 VGOS schedule CONTB1701. From a scheduling point of view, CONTB1701 is very special. According to personal email communication, four out of eight stations are scheduled in tagalong mode (see Table 1).

Table 1 Example of scheduled CONT17 VGOS network. Four stations were part of a core network, four stations were scheduled in tagalong mode. The schedule is limited by two slow core stations.

CONTB1701		**slew rate**	**idle**	**scans**
GGAO12M	**core**	**300/66**	15%	1178
ISHIOKA	tag	720/360	**74%**	412
KOKEE12M	core	720/300	**80%**	363
ONSA13NE	tag	720/360	**61%**	736
ONSA13SW	tag	720/360	**61%**	735
RAEGYEB	core	720/360	**58%**	722
WESTFORD	**core**	**200/120**	10%	1078
WETTZ13S	tag	720/360	**73%**	509

While most of the stations are very fast slewing antennas with a slew rate of 720 degrees per minute in azimuth and 360 degrees per minute slew rate in elevation, two antennas are considerably slower. Both of this antennas are part of the main scheduling network. Additionally, one of those two slower stations, GGAO12M, is given double weight in the scheduling software.

This results in a schedule which is completely limited by the two slow antennas in the core network, which can be seen by comparing the number of scans and amount of idle time in Table 1.

With the recursive scan selection and especially the fillin mode a posteriori it is possible to create a schedule which is better suited for the full network while keeping the results from the core network intact. Using the multi scheduling feature (see Section 3.1), more than 100 different schedules were created and compared to pick the best one. The schedules are automatically created in three phases:

1. a first schedule is created using only the core stations,
2. the other stations are tagged along, and
3. the fillin mode a posteriori (see Section 3.2) is used to minimize idle time and increase number of scans.

Table 2 summarizes results achieved with this new procedure. The number of scans and the number of observations are considerably higher using VieSched++ compared to the submitted CONTB1701 schedule, both by looking only at the core network and by analyzing the full network. Even more observations can be scheduled using the fillin mode a posteriori mode.

Table 2 Comparison of the number of scans and simulated repeatabilities. Different sub-networks are investigated. *Core* means only the four core stations are used, *full* means all stations are used, and *fi a post* stands for fillin mode a posteriori.

	CONTB1701	VieSched++
scans core network	1180	1365
scans + fi a post		**2508**
obs core network	3267	5007
core + tagalong	12985	18540
core + tag + fi a post		**23771**
coord core network	9.8	**3.7** [*mm*]
coord full	4.7	**2.2** [*mm*]
xpol core network	831	**645** [μas]
xpol full	357	**114** [μas]
dut1 core network	50.5	**31.9** [μs]
dut1 full	17.0	**4.8** [μs]

Using the VieVS VLBI software, simulations were carried out to compare the effect on geodetic parameters. Table 2 lists repeatability values based on 300 simulations of the submitted CONTB1701 schedule and the schedule created with VieSched++. The simulations were carried out like standard SX observations and are based on a structure constant C_n of $1.8 \cdot 10^{-7} m^{-1/3}$ and a scale height of 2 km for the description of tropospheric turbulence, an Allan Standard Deviation of 10^{-14} after 50 minutes for the clocks, and an additional white noise of 30 picoseconds per observation [7].

Based on the simulations, a significant improvement can be seen by using the schedule created using VieSched++.

5 Conclusion

VieSched++ is a new modern VLBI scheduling software written in C++ and redesigned from scratch. It supports all necessary features to create geodetic and astrometric VLBI schedules. Many new ideas are implemented to increase the quality of created schedules as well as the flexibility of the software. One main goal is to automate the creation of highly optimized schedules. A GUI can be used to set up the schedule and analyze results.

Based on simulations, schedules created with VieSched++ look very promising. While still being developed, the software already runs very stably and can be used easily. It is planned to further optimize the implemented algorithms, as well as to add new features such as a tree-based scan selection and quality of life improvements.

References

1. K. Baver, J. Gipson, M. S. Carter, K. Kingham. Assessment of the First Use of the Uniform Sky Strategy in Scheduling the Operational IVS-INT01 Sessions (2012). International VLBI Service for Geodesy and Astrometry 2012 General Meeting Proceedings, NASA/CP-2012-217504, 251—255.
2. D. Behrend. Continuous VLBI Scheduling: The CONT14 Example (2015). Proceedings of the 22nd European VLBI Group for Geodesy and Astrometry Working Meeting.
3. J. Böhm, S. Böhm, J. Boisits, A. Girdiuk, J. Gruber, A. Hellerschmied, H. Krásná, D. Landskron, M. Madzak, D. Mayer, J. McCallum, L. McCallum, M. Schartner, K. Teke. Vienna VLBI and Satellite Software (VieVS) for Geodesy and Astrometry (2018). Publications of the Astronomical Society of the Pacific, 130(986), 044503, 1-6.
4. J. Gipson. Sked - VLBI Scheduling Software (2016). NASA Goddard Space Flight Center, ftp://gemini.gsfc.nasa.gov/-pub/sked/sked_Manual_v2012May09.pdf.
5. J.E.J. Lovell, J.N. McCallum, P.B. Reid, P.M. McCulloch, B.E. Baynes, J.M. Dickey, S.S. Shabala, C.S. Watson, O. Titov, R. Ruddick, R. Twilley, C. Reynolds, S.J. Tingay, P. Shield, R. Adada, S.P. Ellingsen, J.S. Morgan, H.E. Bignall. The AuScope geodetic VLBI array (2013). J Geod, 87, 527—538.
6. L. McCallum, D. Mayer, K. Le Bail, M. Schartner, J. McCallum, J. Lovell, O. Titov, S. Fengchun, G. Sergei. Star Scheduling Mode - A New Observing Strategy for Monitoring Weak Southern Radio Sources with the AuScope VLBI Array (2017). Publications of the Astronomical Society of Australia, 34, E063. doi:10.1017/pasa.2017.58.
7. A. Pany, J. Böhm, D. MacMillan, H. Schuh, T. Nilsson, J. Wresnik. Monte Carlo simulations of the impact of troposphere, clock and measurement errors on the repeatability of VLBI positions (2011). Journal of Geodesy, 85(1), doi:10.1007/s00190-010-0415-1, 39—50.
8. B. Petrachenko, A. Niell, D. Behrend, B. Corey, J. Böhm, P. Charlot, A. Collioud, J. Gipson, R. Haas, T. Hobiger, Y. Koyama, D. MacMillan, Z. Malkin, T. Nilsson, A. Pany, G. Tuccari, A. Whitney, and J. Wresnik. Design Aspects of the VLBI2010 System - Progress Report of the IVS VLBI2010 Committee (2009). NASA/TM-2009-214180.
9. M. Schartner, J. Böhm, D. Mayer, L. McCallum, A. Hellerschmied. Recent developments in scheduling with VieVS (2017). Proceedings of the 23rd European VLBI Group for Geodesy and Astrometry Working Meeting.
10. IAU SOFA Board, IAU SOFA Software Collection (2018), Issue 2018-01-30, http://www.iausofa.org.
11. J. Sun, J. Böhm, T. Nilsson, H. Krásná, S. Böhm, H. Schuh. New VLBI2010 scheduling strategies and implications on the terrestrial reference frames (2014). J Geod, 88(5), 449—461.
12. M. Uunila, A. Nothnagel, J. Leek. Influence of Source Constellations on UT1 Derived from IVS INT1 Sessions (2012). International VLBI Service for Geodesy and Astrometry 2012 General Meeting Proceedings. NASA/CP-2012-217504, 395—399.

The “Smart Observatory” for Autonomous and Remote Observations

Alexander Neidhardt [1], Johann Bachem [2], Matthias Schönberger [2], Katharina Kirschbauer [2], Johann Eckl [2]

Abstract “Internet-of-things”, “Industry 4.0”, and “Smart Factory” are key words of new, technical revolutions in industry. Over the past years, similar techniques were also developed for geodetic observatories at different places, using available micro-controller boards and software solutions for monitoring and control of telescopes. Transferring these techniques into a concept of a “Smart Observatory”, autonomous and self-organizing operations become possible. Therefore, engineers at the Wettzell observatory started to implement and integrate such techniques into their systems. A key feature is the autonomous, state-driven processing of schedules from autonomous fetching and preparation of schedules, the operation of observations, and the finalization and transfer of the data. Another key technology is the Central Site Monitoring to fulfill aspects of safety and security to protect humans and the technique itself from harmful situations. A third essential part for whole networks is a Central Coordination (& Control). Developments for this globally available state information are funded within the project “JUMPING JIVE” from the European Union’s Horizon 2020 research and innovation program. This paper describes the current state of the developments at Wettzell.

Keywords automation, smart observatory, central monitoring

1. Technische Universität München, Forschungseinrichtung Satellitengeodäsie, Geodätisches Observatorium Wettzell
2. Bundesamt für Kartographie und Geodäsie, Geodätisches Observatorium Wettzell

1 Introduction

The consequence of an increasing number of antennas in the global VLBI network is increasing costs for operation and maintenance. A local estimation of workload at the Wettzell observatory — planning observations which run 24 hours, 7 days per week — showed that the available staff is not enough. The key feature to solve this dilemma is automation ([Neidhardt(2017)] page 505 f.). While the estimation discussed the principle of shared observations where the responsibility for a session is handed from observatory to observatory to always keep one responsible human operator, administrative regulations, and restrictions, reduce the realization of such a plan to a minimum. But mechatronics and computer techniques are meanwhile sophisticated enough to run sessions completely autonomously.

2 Autonomous Observations

The staff at the Wettzell observatory continuously improves existing scripts to extend automated support of routine tasks. Currently, a script “autodrudg.pl” is used to fetch schedule files from the central data servers, to prepare them for the local session, and to adapt specific parameters to local implementations. Further scripts are tested to support other tasks of an operator during a session. The goal is to prepare everything for an automated and at least autonomous operation of radio telescopes including:

1. Checking for sessions
2. Local prioritization and planning
3. Fetching of session schedules

4. Local preparation (drudg)
5. Local adaption and recorder selection
6. Automatic startup
7. Observation status notification
8. Quality and alarm management
9. Post-processing and archiving

A test version of the script "autodrudg.pl" mentioned above is able to search for new schedule files in IVS, European VLBI Network (EVN), and domestic schedule archives via File Transfer Protocol (FTP). There are additional plans to include combined master plans with session details and prioritization to optimize the search. The script downloads the files, runs the program "drudg" of the NASA Field System with predefined settings, and, for example, adapts recorder settings to select a specific server location for the recording on Flexbuff systems. This optional location reduces manual copying from Mark 5 modules to e-VLBI servers. The results of this first step are antenna-specific "SNAP" and "PROC" files for the NASA Field System, which can be used to run the observations.

Using these SNAP files, a list of startup commands can be created which are time-tagged so that the NASA Field System calls them at the predefined time. This means, that the session automatically starts at an individual antenna at the right time. The rest of the observation is already automated by the Field System.

While information like dewar, cable, and meteorology monitoring are already integrated into the Field System, additional, centralized site monitoring also collects these data in parallel. Trigger levels are used to identify the health state of the system (see next section). Additionally, available sensors at the Wettzell observatory also support automatic status notifications. Cloud coverage can be derived from Nubiscope data. Different rain sensors offer status information about rain situations. Several wind sensors support the detection of necessary wind stow scenarios. Derived offsets between the clocks compared to one observatory-wide master clock allow automatic identification of clock jumps. All data can be combined to create regular status entries in the log file or to produce start, emergency, and stop e-mails sent to the Data Centers.

After finishing an observation, an additional script does the post-processing, including the sending of log files to central services, to bring the antenna into stow position, or to archive local, session-specific files.

Currently, several tasks are still in the hands of the operators, because the scripts are not yet combined into one system. Nevertheless, several tests showed good performance, so that the implementation is promising. To reach the goal of complete autonomy, most of the safety and security relevant tasks were implemented in the antenna control unit and therefore certified by an external company. It is quite important to keep the overview about the health state of each radio telescope and connected equipment.

3 Central Site Monitoring

While automatic observations are already more or less possible, a very important aspect is the collection and interpretation of system data to permanently derive the health status. The current risk planning and management knows four priorities of hazards:

1. hazards to humans: humans can be hurt or killed
2. hazards to systems: system can be damaged or destroyed
3. hazards to products: sessions/data can be corrupted or completely lost
4. hazards to product quality: data sets can be bad or unusable

While the systems must always keep a safe and secure situation without interaction, sensor and system parameters are permanently collected, explored, and logged (see Figure 1). For example, when rack temperatures reach a maximum limit, the automatic emergency system of the racks opens the doors while the parameters are independently collected and interpreted to notify staff or the security guard at the entrance gate. To do this, the monitoring enterprise software "ZABBIX" is used ([Zabbix(2018)]).

All collected data sets are logically grouped and hierarchically combined, so that triggers which identify critical severity states can directly be assigned to locations (see Figure 2). The current monitoring system just uses three severity states: "not classified" (system is ok), "warning" (system is stable but a parameter reached a limit), and "high" (system reached a critical state and requires human interaction). Some of the triggers are also a combination of conditions with different values, so that consecutive errors can be defined.

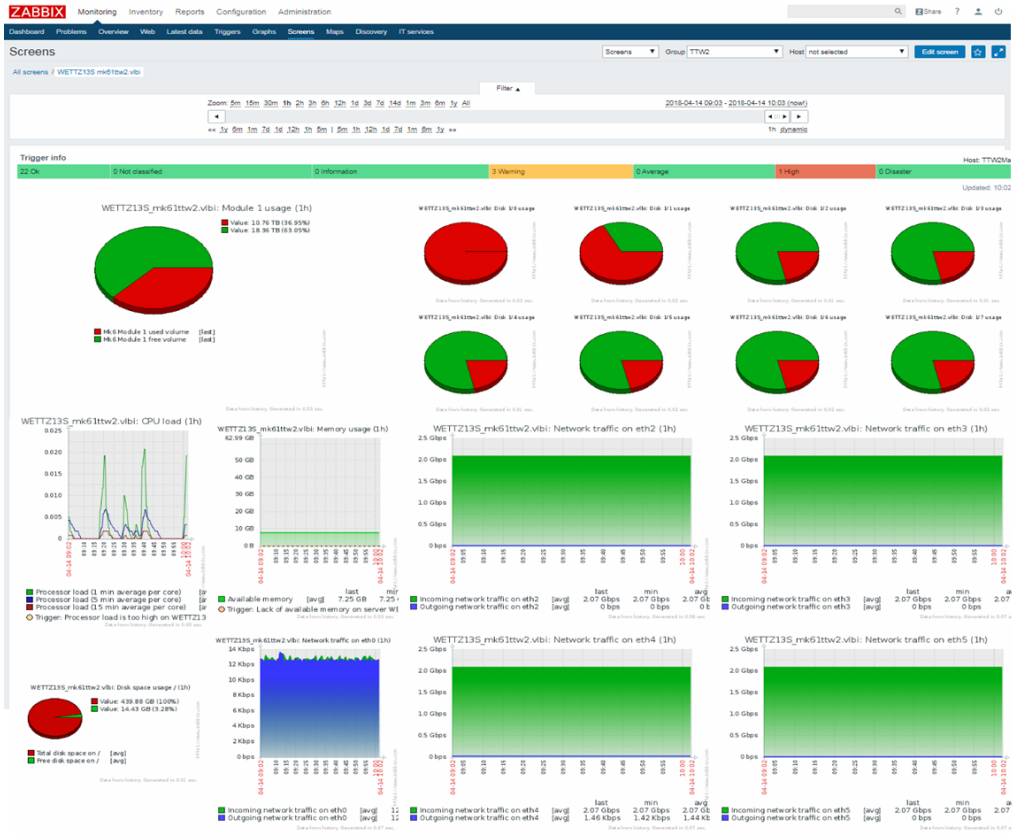

Fig. 1 The central system monitoring Web page for a Mark 6 at the Wettzell observatory.

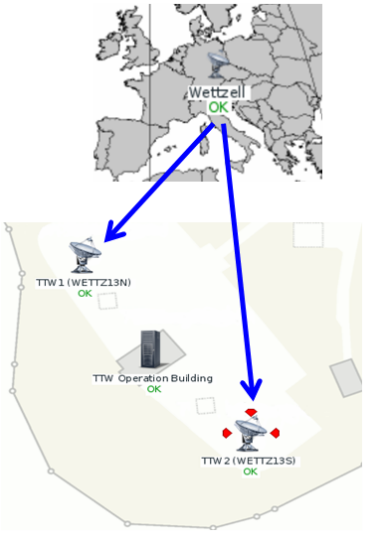

Fig. 2 Hierarchical and logical grouping of system trigger.

The states are presented on maps, which are interactive network diagrams showing relationships and structures of monitored systems. Additionally, it is possible to send out e-mails or short messages via mobile phone. Staff at the Wettzell observatory made some experiments with the Private Branch Exchange (PBX) software “Asterisk”, to send out converted Voice-over-IP messages over a Session Initiation Protocol (SIP) connection. Using the text-to-speech program “pico2wave”, text messages with error information can be sent as audio messages to phones. Staff which is on stand-by for emergency duties can receive such calls. These operators can use the ZABBIX front-end to get more details about the situation and the remote control software “e-RemoteCtrl” ([Neidhardt(2013)]; e.g., also in the new Web-based version) to get remote access to the system. Most of the problems can be solved with this remote maintenance.

4 Central Coordination (& Control)

Having central site monitoring also opens the door to global monitoring of complete VLBI networks with several antennas. If system health states and also quality parameters are available at a Data Center, it is possible to plan capacities or to react to changed conditions, e.g. if one site is influenced by bad weather. Attempts like dynamic observing (see [Lovell(2016)]) necessarily require complete information about network stations to run central negotiations and to prioritize tasks. Responsible schedulers, correlator staff, or analysts can be informed automatically to improve the quality of sessions. Received data can be stored and archived for later analysis.

Archiving data is also the intention of a central server for seamless, auxiliary data ([Neidhardt(2015)]). Because not all telescopes support ZABBIX, "e-RemoteCtrl" supports a way to send out data in the form of Web pages to be parsed and organized by scripts on the central server. Tests with the antennas of the Wettzell observatory are promising. Values which are available in the shared memory of the NASA Field System can be used. ZABBIX is used for a simple plotting of the data on the central server, while the data are also stored in daily files to be used or converted for further analysis steps.

5 Conclusions and Outlook

The telescopes of the Wettzell observatory are on a good path to be operated in a completely autonomous way. Central monitoring always gives a complete overview of the system details and does the notification if critical limits are reached. Safety and security issues are managed by the antennas. The central monitoring has huge benefit for the whole VLBI network, to support sophisticated observation strategies. Similar solutions are currently also implemented for the laser ranging systems of the Wettzell observatory. All of these techniques together are the basis for a "smart observatory", which also makes some decisions without interaction of a human being.

Acknowledgements

Some of the work is part of the project "Jumping JIVE", which received funding from the European Union's Horizon 2020 research and innovation program under grant agreement No. 730884.

References

[Lovell(2016)] Lovell, J.; Plank, L.; McCallum, J.; Iles, E.; Shabala, S. Dynamic Observing with the AuScope VLBI array 5th International VLBI Technology Workshop - MIT Haystack Observatory, https://www.haystack.mit.edu/workshop/ivtw2016/presentations/jlovell_ivtw2016.pdf, Download 2018-09-17.

[Neidhardt(2013)] Neidhardt, A.; Ettl, M.; Mühlbauer, M.; Kronschnabl, G.; Alef, W.; Himwich, E.; Beaudoin, C.; Plötz, C.; Lovell, J.: Safe and secure remote control for the Twin Radio Telescope Wettzell. Proceedings of the 21st meeting of the European VLBI Group for Geodesy and Astrometry, 2013.

[Neidhardt(2015)] Neidhardt, A.; Lovell, J.; Kirschbauer, K.; Schönberger, M.; Himwich, E.; McCallum, J.; Plötz, Ch.; Quick, J. Results from a test realization of a system monitoring for seamless auxiliary data. Proceedings of the 22nd European VLBI Group for Geodesy and Astrometry Working Meeting, 2015.

[Neidhardt(2017)] Neidhardt, A. Applied Computer Science for GGOS Observatories. Communication, Coordination and Automation of Future Geodetic Infrastructures. ISBN 978-3-319-40137-9. Springer International Publishing Switzerland, 2017.

[Zabbix(2018)] Zabbix LLC The Ultimate Enterprise - class Monitoring Platform https://www.zabbix.com/, Download 2018-09-13.

Communication, Coordination, and Automation for Future Geodetic Infrastructures

Alexander Neidhardt [1]

Abstract In the second half of 2017, a Springer book was published explaining ideas, implementations, and solutions for future geodetic infrastructures. It explains seven years of technical research in computer science applied to systems of space geodetic techniques. The main focus is laid on stable and safe scientific software, an extended common software toolbox, autonomous production cells, and remote access and monitoring. The book addresses students as well as engineers at the observatories. These stations are seen as multi-agent systems which operate worldwide and are centrally coordinated to offer their geodetic products of the Global Geodetic Observing System (GGOS).

Keywords GGOS, infrastructure, automation, control, communication, coordination

1 Introduction

In August 2017, Springer published the textbook "Applied Computer Science for GGOS Observatories: Communication, Coordination and Automation of Future Geodetic Infrastructures" (ISBN-10: 3319401378) in Earth Sciences, Geography and Environment in English language. It is the first edition available as hardcover and eBook covering questions of the Global Geodetic Observing System (GGOS) with state-of-the-art methods from computer science on 546 pages. Real examples from the Geodetic Observatory Wettzell are taken to explain strategies and solutions to implement software for modern observatories with a focus on remote and autonomous operations [Springer(2017)]. The following sections are related to the book [Neidhardt(2017)].

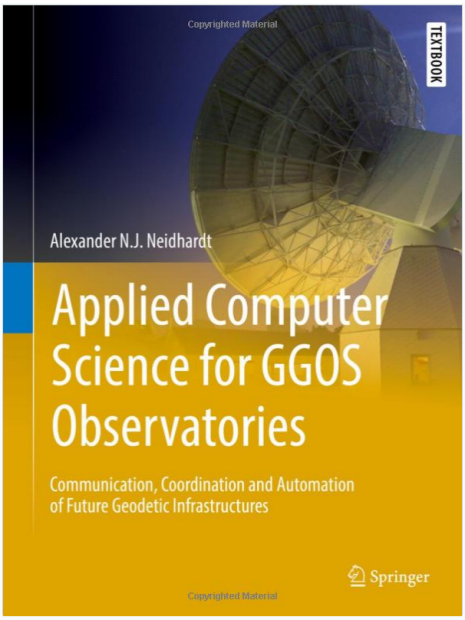

Fig. 1 The cover of the textbook.

2 Content of the Book

The book has seven chapters. After a short introduction, the second chapter explains aspects and solutions for writing safe and stable code in the field of scientific environments. Programming languages are dis-

1. Technische Universität München, Forschungseinrichtung Satellitengeodäsie, Geodätisches Observatorium Wettzell, Sackenrieder Str. 25, D-93444 Bad Kötzting, Germany

cussed. The style (coding layout and code policies) which is used for writing the source code is essential to keep the programs comprehensive. A big issue is the inclusion of existing legacy code using suitable converter classes with clear interfaces to keep "older" code more manageable. Automatic document generators help to implement an agile documentation landscape. High-quality, test-driven developments use unit tests, static inspections, and dynamic analysis to get a suitable test coverage. Test metrics provide quantitative classifiers for software quality. Continuous integration offers daily overviews. Code repositories use version management systems to track all changes and updates. This ideally supports agile development.

The third chapter shows methods to create code toolboxes as re-usable code basis. Software is decomposed into modules and components partly using generative ways to support parametrized applications. This splits a development into domain and application engineering, so that most of the engineers can use predefined, parametrized domains, e.g., for communication over network, for specific tasks to implement their own applications. Remote procedure calls standardize this communication and also all related tasks. The results are remote function calls which look similar to local calls. They organize data conversion, implement call semantics, and guarantee safety and security. The result is a middleware for the controlling of distributed systems.

The fourth chapter puts the focus on operating of geodetic antenna systems showing the aspects of a controlling system on the example of a laser ranging system. Designing of control tasks means a mapping of real structures to software units. An intelligent management of hardware includes different layers of feedback loops which use data from sensors to make decisions for the commanding of actuators. Every hardware is represented in form of standardized software stubs. Autonomous production cells using autonomous software cells provide techniques for planning, controlling, user interfacing, hardware driving, and failure managing. A coordination cell uses metrics for static and dynamic planning. Separate autonomous hardware cells control the individual hardware. All data are organized in a hybrid, autonomous data management cell. A parallel system monitoring is used to fulfill safety criteria and to show state overviews.

The fifth chapter extends the local control systems with remote functionality and access using the existing software "NASA Field System" controling radio telescopes as an example. It is feasible to extend such an existing system with functionalities for remote access to support orders from external partners and offer reports to them. Because worldwide networks do not guarantee continuous access, systems have to increase their ability to run completely autonomously. This can be implemented using multi-agent systems where each agent uses an internal feedback loop. An agent can control existing software, like the NASA Field System, as legacy code. Additional requirements, like Web cameras, remotely controled switches, and a suitable graphical remote interface, extend the local architecture to replace the senses of an operator at the system. Remote access requires network security using role-based access control and ciphering algorithms, restricted network enclaves, and different types of firewalls.

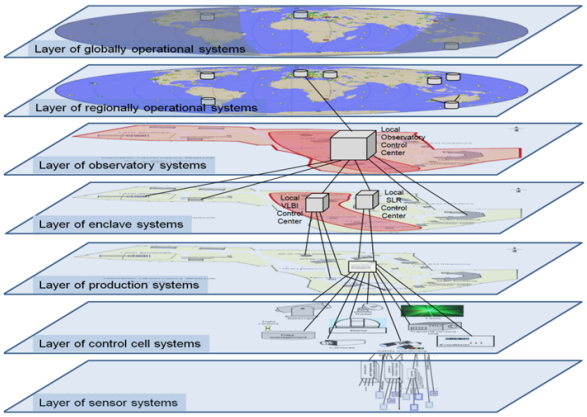

Fig. 2 Communication and coordination layers for GGOS products [Neidhardt(2017)].

A final, sixth chapter before the outlook section summarizes all techniques to a world-wide method of coordination, communication, and automation of GGOS workflows. It names the operational deficits having the GGOS products as parallel workflows without operational interaction. A layered hierarchy is explained to interact between the systems of the different services. Finally, statistics are shown to explain the essential need of automation for the realization of continuous operations with different world-wide telescopes.

The outlook shows that GGOS networking between autonomous agents explained in the book can be compared to Internet-of-the-Things or Industry 4.0 where

cyber-physical systems are a consequence of modern workflows in industry.

3 VLBI-related Topics

Especially chapter five has a strong relationship to VLBI-relevant tasks. It describes the idea of multi-agent systems, which might be the future for automated computer auctions to automatically plan and assign resources to an optimal offer. While this is more or less future, concrete implementations extend the existing software "NASA Field System" to read, control, and manipulate the lower-level communication to the hardware devices as well as the higher-level interaction with the operator. It is like creating a control "parentheses" around the NASA Field System which can also be used to bypass it but especially to monitor all levels of the interaction. Using such an environment enables the access to the data and control from remote over computer networks. Therefore, an important aspect is security. Security touches different levels using different methods from simple user accounts with passwords to specified operator roles and access rights to higher level control tasks. It also requires methods for the architecture of networks and secure sub-networks.

Besides implementations around the NASA Field System, monitoring aspects also touches the field of VLBI. VLBI is currently the only GGOS technique which strongly requires a tight cooperation of telescopes around the world. Therefore, coordination of such networks and a real-time status during the observation is more and more an essential requirement. Industrial-like monitoring techniques with centralized archives are explained in Section 4.7 of the book, where the starting point was a white paper created at the beginning of the discussions about a Monitoring and Control Infrastructure (MCI) (see also [Ettl(2010)]). Meanwhile, different systems were developed and are in use. This means that the focus turned to a centralized collection and archiving of monitoring of seamless, auxiliary data from different sources ([Neidhardt(2015)]). This task is touched by the "Jumping JIVE" project, funded by the European Union, where a centralized monitoring infrastructure has to be established for the European VLBI Network (EVN).

4 Conclusions and Impact

The book is an interesting combination of applied computer science with the applications of geodesy. It is helpful for students, but also for engineers at the observatories. A valuable aspect is the impact to other disciplines. Meanwhile, the chapters of the book were downloaded over 4,600 times while computer scientists build the largest group of readers [Bookmetrix(2018)]. The projects described in the book are still ongoing. For example, the follow-on of the monitoring system is currently funded by the European Union's Horizon 2020 research and innovation program. The implementations of the designs are also under finalization for the laser ranging system and the automation of the VLBI system of the Geodetic Observatory Wettzell. Therefore, there is a huge relation to real applications of different fields.

Acknowledgements

Thanks to all contributors, mentors, the Springer team, and the institutions operating the Geodetic Observatory Wettzell.

References

[Bookmetrix(2018)] Bookmetrix. Applied Computer Science for GGOS Observatories - 2017. Springer Nature. Springer-Verlag GmbH, Heidelberg, Germany, http://www.bookmetrix.com/detail/book/7b9e5134-fded-4569-a89f-b3fbe35f1b51#downloads, Download 2018-09-06.

[Ettl(2010)] Ettl, M.; Neidhardt, A.; Mühlbauer, M.; Plötz, C.; Beaudoin, C.: The Wettzell system monitoring concept and first realizations; in: Behrend, D.; Baver, K. D. (eds.) VLBI2010: From Vision to Reality, IVS 2010 General Meeting Proceedings, NASA/CP?2010?215864, pp 444-448, NASA, Goddard Space Flight Center, 2010.

[Neidhardt(2015)] Neidhardt, A.; Lovell, J.; Kirschbauer, K.; Schönberger, M.; Himwich, E.; McCallum, J.; Plötz, Ch.; Quick, J. Results from a test realization of a system monitoring for seamless auxiliary data. Proceedings of the 22nd European VLBI Group for Geodesy and Astrometry Working Meeting, 2015.

[Neidhardt(2017)] A. Neidhardt. Applied Computer Science for GGOS Observatories. Communication, Coordination and Automation of Future Geodetic Infrastructures. ISBN 978-

3-319-40137-9. Springer International Publishing Switzerland, 2017.

[Springer(2017)] Springer Int. Book Web page "Applied Computer Science for GGOS Observatories." Springer International Publishing Switzerland, https://www.springer.com/de/book/9783319401379, Download 2018-09-06.

A New Generation of Wettzell's Remote Access to the NASA Field System using Web-based Techniques

Alexander Neidhardt

Abstract The origin of the remote control software e-RemoteCtrl for VLBI antennas was in the year 2008. After ten years, it is still the only software to operate the NASA Field System remotely implementing secure and save techniques. The software is in use at several sites, but there have been almost no official releases over the past years. But, there is still an on-going development of the software at the Geodetic Observatory Wettzell. To support the requirements of "smart observations" reducing the required manpower for operator tasks, the e-RemoteCtrl server was extended with its own web server to enable a web-based monitoring access using just a simple web browser. It is not yet a complete replacement of the classic graphical e-RemoteCtrl client user interface, but it is a first step to converting a VLBI antenna to a web-enabled device.

Keywords NASA Field System, web interface, monitoring

1 Introduction

The operational data from IVS or other telescope networks (e.g., the EVN) are interesting for operations, diagnostics, and analysis. Such data are written to log files for each observation session and copied to a central File Transfer Protocol (FTP) server after a session ends. Currently, there is still no real-time information available showing the telescope's health state. There were some attempts, like the real-time extension to IVS Live web pages [Neidhardt(2014)], struggling with software and security problems to get the data with Secure Copy (SCP) from the observatory to the central web page. Besides monitoring of health states of telescopes, a continuous data set of seamless auxiliary data (like meteorological sensor data, clock data) which are produced in addition to the actual observation data would be appreciated by analysts. The IVS started a task force to discuss and implement the continuous collecting of such data in real-time [Neidhardt(2015)]. With the experience from the previous live monitoring implementations, staff at the Wettzell observatory started to first implement a technical solution for the monitoring before more decisions can be made about which data should be collected from the IVS sites. On the way to becoming a "smart observatory" where operational tasks are mainly managed by computers, real-time monitoring is a synergy between reacting to critical health states and the collection of seamless, auxiliary data. Therefore, e-RemoteCtrl software was extended to support both. The result is a web-based access to the NASA Field System using web pages and an Internet browser.

2 The Data Sender on the NASA Field System Computer: e-RemoteCtrl Software

The e-RemoteCtrl software was extended with a web server functionality. It has good performance to serve a few different users but cannot be compared to specialized web servers, like Apache. The server reads template files containing Hypertext Markup Language (HTML) code including tags representing monitoring

1. Technische Universität München, Forschungseinrichtung Satellitengeodäsie, Geodätisches Observatorium Wettzell, Sackenrieder Str. 25, D-93444 Bad Kötzting, Germany

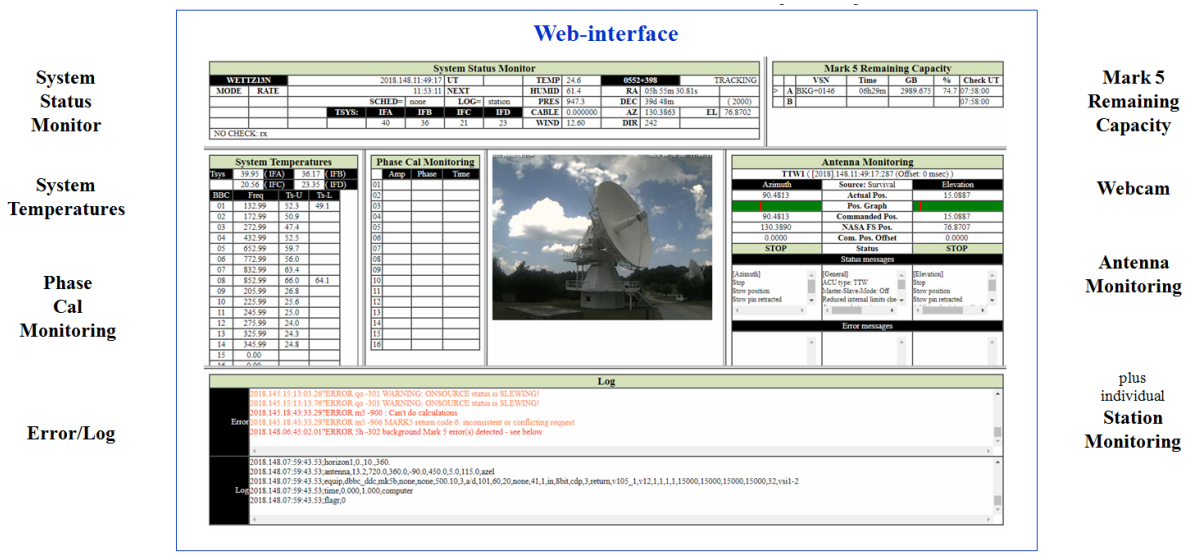

Fig. 1 The new web interface to the NASA Field System.

values with a keyword. The tags are predefined words in the form of HTML comments. The rest of the HTML structure can be changed individually. HTML was explicitly chosen instead of other web-based protocols (like e.g., JavaScript Object Notation (JSON)), to enable two aspects with one implementation: a new, modern, and straightforward Graphical User Interface (GUI) for the NASA Field System and a standardized format to exchange data with a central monitoring archive using web ports.

The HTML GUI uses a flat structure. The main page is defined in "FieldSystemMonitoring.html". It contains a frame with sub-pages for individual monitoring screens. Each single sub-page consists of two files: an IFRAME page (e.g., "SystemStatusMonitor_iframe.html") and a content page (e.g., "SystemStatusMonitor.html"). The IFRAME-file is used to manage the updates with up to several milliseconds update time avoiding white flashing between the reloads of the pages. The white flashing usually shows up with different browsers (e.g., Chrome, MS Internet Explorer, etc.). This behavior is annoying and not useful for GUIs. The content web page contains the actual data and layout structures. This setup of the web pages reduces the use of Javascript and other active elements to a minimum to limit maintenance tasks and security issues. It also separates predefined control tasks of the web pages from layout and data presentation which can be designed individually by each telescope site.

The new GUI only requires the e-RemoteCtrl server. The latest release can be requested from the author of this paper (neidhardt@fs.wettzell.de). After unpacking the code archive and building the executable, the configuration file must be edited. Especially the two-letter-code of the antenna and the section "<WebServer>" with the settings for the web server are important. After adapting the configuration, the program "ercd" can be started with the path to the configuration file as an argument. The latest software release already contains a set of web pages, so that the GUI (see Figure 1) can already be accessed on the defined port using an Internet browser connecting to the IP address of the NASA Field System PC via Hypertext Transfer Protocol (HTTP).

The server reads the HTML templates and replaces the tags representing monitoring values with the corresponding numbers read from the shared memory or log file of the NASA Field System. For example, "<!−−PRESSURE−−>" might be replaced by "<!−−PRESSURE−−> 941.9 <!−−−−>", where the number is the air pressure from the Field System shared memory. Therefore, Internet browsers just see the value, while scripts and programs of the central seamless, auxiliary data server can search for the tag and extract the single number. Meanwhile,

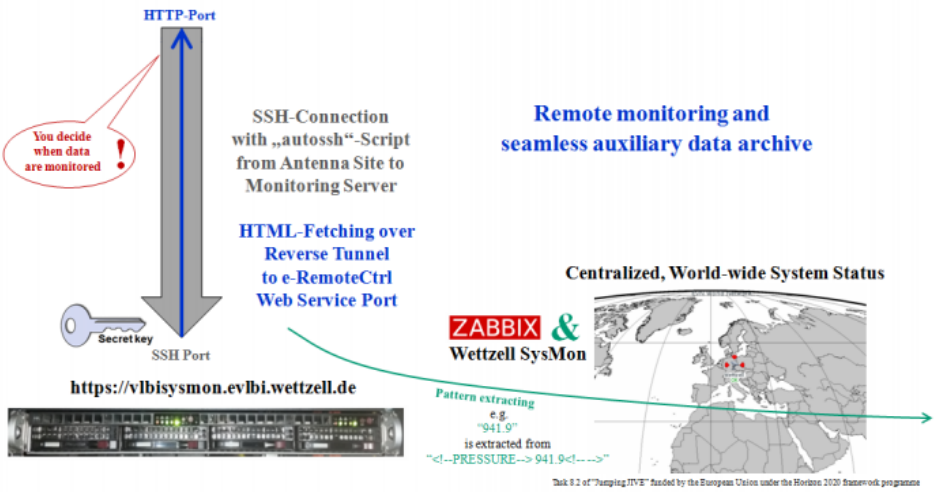

Fig. 2 The way to the central monitoring archive.

172 parameters from the NASA Field System can be streamed with this technique. Each number is assigned to a time tag created from the NASA Field System time and hidden in an HTML comment, so that always the original time of the value creation on the Field System PC is applied.

3 Supporting a Centralized Monitoring Archive

While the local HTTP access is designed for local operations within a secure network of an observatory, a central monitoring server at the Wettzell observatory offers world-wide access to the data using Hypertext Transfer Protocol Secure (HTTPS).

To enable a secure way of data exchange between an antenna site and the central server, the NASA Field System PC must open an SSH connection to the central monitoring server (see Figure 2). Therefore, the staff at an observatory gets an SSH key to open an SSH connection to the central server. The authentication with a key is the only way to do the login on the monitoring server. The SSH connection is used to open a reverse tunnel from the monitoring server to the NASA Field System to access only the HTTP server port. It is also possible to open further reverse ports if other features are wished. Therefore, the local staff always keeps control of whether data can be monitored by opening and closing the SSH connection, as well as which data are available by writing their own web pages with the tags of just the enabled values.

After a successful connection to the monitoring server at Wettzell, a script on that machine starts to request all web pages of the site once per second. The server runs Zabbix 3.2.4 [Zabbix(2018)]. Zabbix is a monitoring platform supporting the collecting and presentation of monitoring data. Scripts on the server are used to extract the HTML values. The scripts are triggered by ZABBIX hosts, where also individual update times can be defined to import an individual value into the ZABBIX database. The script also supports Wettzell's version of the Monitoring and Control Infrastructure (MCI) software "SysMon" ([Ettl(2010)]) and can be used to create archive files with individual, time-tagged values (currently as a test version).

A template definition of a presentation screen combines graphs of the history of the most important values (see Figure 3). Each site is also registered on a world map. Trigger levels are used to convert limits into health states shown as colored severity states. Staff from the observatories can get access to these web pages by requesting a user account for the Zabbix web front-end. It is easy to extend the monitoring archive with web pages for additional telescope sites using the template definition.

Fig. 3 ZABBIX screen with graphs of the most important data from the NASA Field System.

4 Conclusions

The new release of the e-RemoteCtrl software not only supports central monitoring attempts, it can also be used by staff to easily check the NASA Field System during observation sessions using a web browser. Using the central monitoring archive, such web pages can be accessed from anywhere, and real-time data can be used to get snapshots of the health states of VLBI networks.

Acknowledgements

Jumping JIVE has received funding from the European Union's Horizon 2020 research and innovation program under grant agreement No. 730884.

References

[Ettl(2010)] Ettl, M.; Neidhardt, A.; Mühlbauer, M.; Plötz, C.; Beaudoin, C.: The Wettzell system monitoring concept and first realizations; in: Behrend, D.; Baver, K. D. (eds.) VLBI2010: From Vision to Reality, IVS 2010 General Meeting Proceedings, NASA/CP-2010-215864, pp 444—448, NASA, Goddard Space Flight Center, 2010.

[Neidhardt(2014)] Neidhardt, A.; Collioud, A. Real-time data streams from "e-RemoteCtrl" to central VLBI network status monitoring services like "IVS Live". IVS 2014 General Meeting Proceedings - "VGOS: The New VLBI Network", pp 262—266, Science Press (Beijing), ISBN 978-7-03-042974-2, 2014.

[Neidhardt(2015)] Neidhardt, A.; Lovell, J.; Kirschbauer, K.; Schönberger, M.; Himwich, E.; McCallum, J.; Plötz, Ch.; Quick, J. Results from a test realization of a system monitoring for seamless auxiliary data. Proceedings of the 22nd European VLBI Group for Geodesy and Astrometry Working Meeting, 2015.

[Neidhardt(2017)] A. Neidhardt. Applied Computer Science for GGOS Observatories. Communication, Coordination and Automation of Future Geodetic Infrastructures. ISBN 978-3-319-40137-9. Springer International Publishing, Switzerland, 2017.

[Zabbix(2018)] Zabbix LLC The Ultimate Enterprise - class Monitoring Platform, https://www.zabbix.com/, Download 2018-09-13.

Investigating Quasar Structure in VGOS with Simulations

Simin Salarpour, Lucia McCallum, Stanislav Shabala, Jamie McCallum

Abstract Quasar structure is a well-known issue that can be important in determining accurate celestial and terrestrial reference frames. So far, no good strategy to address this issue has been found. A complication is that the structure of quasars can, and often does, evolve with time. Furthermore, the variability and structure of flat-spectrum radio-loud quasars used in geodetic VLBI is highly frequency-dependent. This poses a challenge for next-generation (VGOS) systems currently being built around the world, which aim to observe over a wide range of 2–14 GHz. The structure effects for the same quasar can be very different at different frequencies in this range. On the other hand, we understand the astrophysics of quasars relatively well. In this research, we model the frequency-dependent quasar structure by using the extracted information from real images. To quantify the effects of the changing quasar structure in VGOS observations, the source structure module of the Vienna VLBI Software (VieVS) is extended. In this work we are focusing on a single source (J0136+4751) to explore strategies and calculate the effects of source structure as a function of frequency and time for varying geometries. Ultimately, we hope to address issues related to source structure as seen in Australian and global VGOS observations.

1 Introduction

By measuring the position of radio sources with Very Long Baseline Interferometry (VLBI), the International Celestial Reference Frame (ICRF) is defined. Usually assumed to be point-like, extragalactic sources are often known to have extended structures on the scale of milliarcseconds [2, 5]. In addition, structure varies with time and frequency, possibly restricting the determination of source positions [11, 14, 16]. Further, source structure can cause systematic errors in station positions at the millimeter level [15], although other errors are currently more significant in legacy VLBI. Despite many efforts, so far there is no standard procedure to determine and correct for source structure effects. While this may be acceptable for legacy VLBI, it is an important risk for the broadband method. The greatest concern is associated with phase connection when source structure considerably varies over the broadband frequencies.

The suggested VGOS broadband system uses four bands in the range of 2–14 GHz, each of them 1 GHz wide. Hereby, placement of frequency bands may affect the ability of phase connection [12]. Some initial work on how to handle source structure in VGOS has been done by Niell [8, 9].

In this project, we develop the idea introduced by Niell and enhance it with the information taken from real images. We also expand the current source structure module of VieVS [1, 15], allowing for VGOS simulations and possibly even corrections of source structure effects. The other perspective is developing tools and routines to predict source structure as seen in VGOS (test) observations with the AuScope/AOV array and working on mitigation strategies.

2 Enhancing the Approach of Niell

As previously mentioned, the possibility of connecting phase across the broadband can be affected by rapid

University of Tasmania, School of Natural Sciences

phase variation of the source itself as a function of frequency. In 2006, Niell did first investigations by using previously published source characteristics [6] as well as some common assumptions.

Starting from a source image using a Gaussian fitting algorithm, one can get the position, size, and brightness of individual components of this source (so-called clean components). The Fourier Transform of the so-called brightness distribution leads to the visibility function. From this, one can calculate the source structure phase as a function of observing frequency. While extracting clean components from source images traditionally has been done manually, we have tried to automate this process. Using various downloading and processing scripts allows us to conduct large-scale investigations.

Coming back to the idea of Niell, we can now replace some of his assumptions with the parameters derived from real images, such as maximum flux density (S_0), position parameters of each components like distance and position angle from the origin (r, θ), major axis (a), axial ratio (b/a), and position angle of major axis (ϕ).

One of the sources that we investigate for this purpose is 0133+476 (J0136+4751) which is an ICRF2-defining source and is well observed (1,450 sessions from the year 2000). We study the mentioned ICRF2 source since based on its images in S (2.3 GHz), X (8.6 GHz), and U (15.4 GHz) bands; it shows source structure evolution during the time that allows us to consider it as a nonpoint-like source. In this research, we have used the Astrogeo VLBI image database (http://astrogeo.org/) to collect 162 available images of 0133+476, which are taken in S, X and, U frequency bands.

Although we are aware that our automated routines for image processing may still have some limitations, they seem to work well for first applications. The following Table 1 is an example for our selected source.

Following the algorithm described by Niell [8] and using the parameters shown in Table 1 we can reproduce his investigations. By further combining this with the VieVS source structure module, we can do this for arbitrary frequencies and different geometries (Figures 1 and 2). As is well known, the observed source structure depends on the projected baseline, which itself is the product of baseline length and its orientation in space. The two figures show that baseline criteria, such as length and angle, can dramatically influ-

Table 1 Extracted parameters from source image. Source Name: J0136+4751, Observation Date: 2015 March 17, Image Frequency: 8.7 GHz, RA: 24.2441 degrees, DEC: 47.8581 degrees, FITS file generator: Alexandr Pushkarev, Instrument used: VLBA, Database: Astrogeo Center.

S_0 (Jy)	r (mas)	θ (degree)	a (mas)	b/a	ϕ (degree)
1.84	0.0	0.0	3.01	0.31	45.19
0.09	2.63	-35.19	2.91	0.37	44.53
0.08	0.79	-55.39	2.79	0.23	44.42

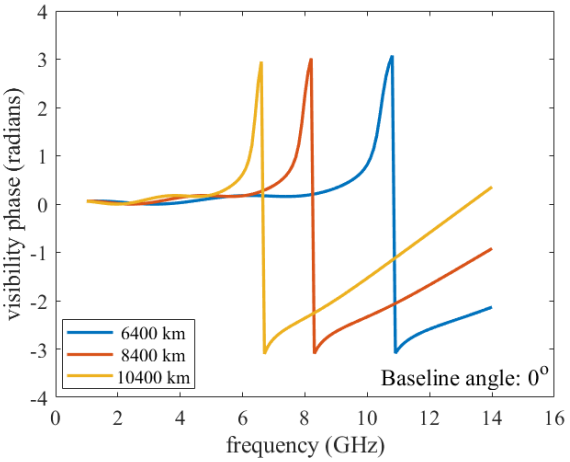

Fig. 1 Visibility phase as a function of frequency for baseline lengths of 6,400 km (blue), 8,400 km (red), and 10,400 km (yellow). Varying the baseline length with a fixed angle (0°) causes a shift in frequency. Adopted source model is as in Table 1.

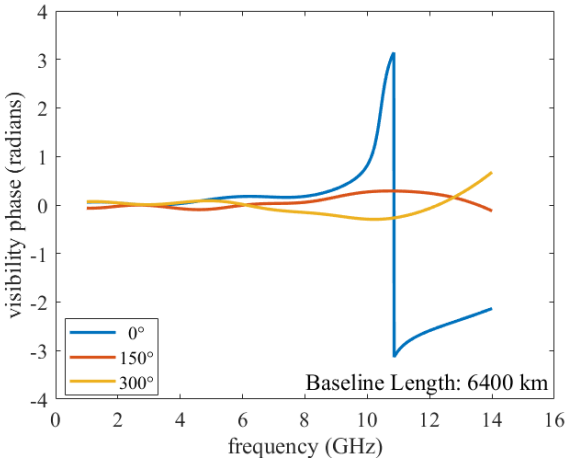

Fig. 2 Visibility phase as a function of frequency for baseline angles of 0° (blue), 150° (red), and 300° (yellow). Varying baseline angle with a fixed baseline length (6,400 km) makes big changes in phases.

ence the source phase. For example, it is clear from Figure 1 that the overall trend is similar and baseline length variation only changes the frequency at which the phase starts varying rapidly. Figure 2 is an example of dramatic source phase change over the VGOS frequency band when the baseline angle is varied. Such a rapid phase change can cause serious problems for the VGOS broadband delay.

3 What Images Can Tell Us About Source Structure in VGOS Bands

A well-known problem with source structure is their evolution with time and frequency. Unfortunately, we do not have enough images in all frequency bands and at all times to correct observed delays using contemporaneous images in each case.

3.1 Time Variability

Our automated routines help us to create time series of flux densities, structure indices, and delay for each source based on the available image in different reference frequencies. As an example, Figures 3 and 4 show the time series of flux density and structure index of our candidate source using X-band images.

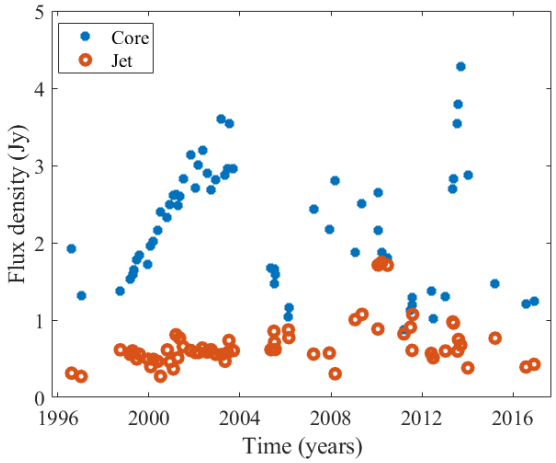

Fig. 3 Changes in flux density of core and jet as a function of time show that we cannot consider this source as a point-like source.

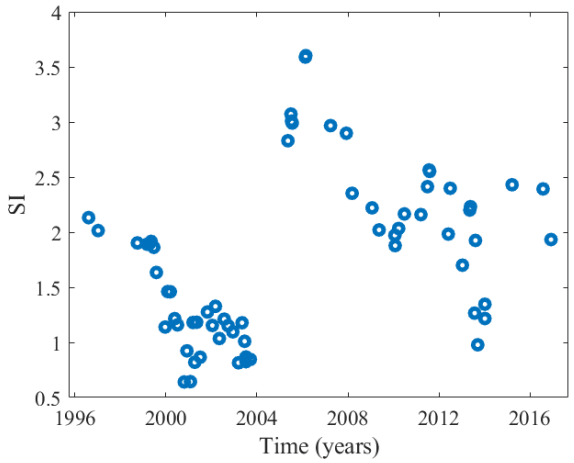

Fig. 4 Source structure index as a function of time for X-band images. X-band structure index varies from 0.5 to 3.5 during the time. This source is a good candidate to study source structure effects.

For core-dominated emission, the core shift effect means that light curves at different frequencies will be shifted in time. Higher frequencies (closer to the true jet base) will arrive before lower frequencies. For non-accelerating jets (which do not exist in reality), we expect the time lag to go as 1/freq (see [14] and [7]). In any case, two high frequencies separated by the same number of GHz will have a smaller time lag than two low frequencies separated by the same amount.

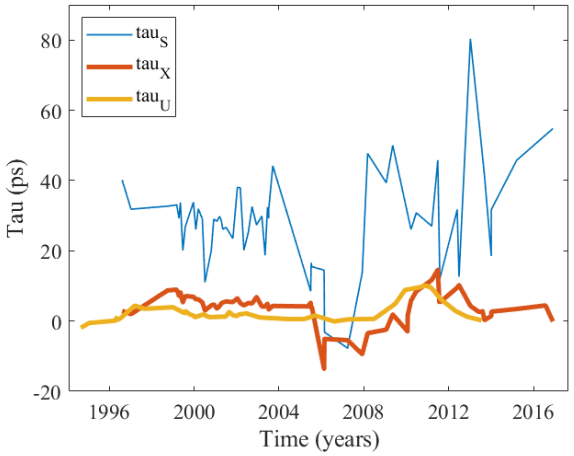

Fig. 5 Delay as a function of time for S, X, and U band in their own reference frequencies (2.3, 8.6, and 15.4 GHz).

This fits our findings: in Figure 5, we have used S-, X-, and U-band images to compare the structure de-

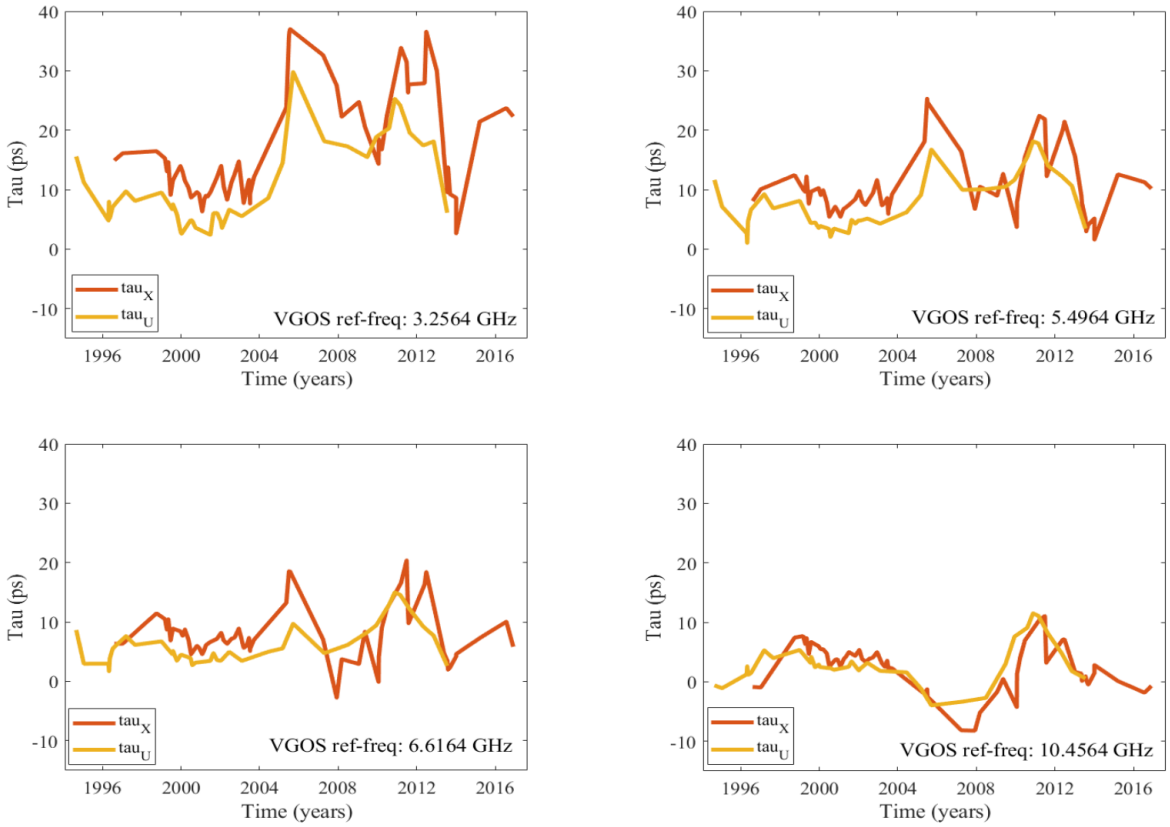

Fig. 6 Delay as a function of time using different X-band and U-band images for source 0133+476 in VGOS reference frequencies. In these figures, the source structure is a fixed parameter with the reference frequency of the image.

lays as function of time in their own reference frequencies. We find that there is a good correlation between X- and U-band images. The S-band delays appear less correlated with either U- or X-band, than U and X with each other. As expected, because U and X frequencies are actually quite close, the structure is similar. On the other hand, the delays resulting from S-band images are very variable, which may be due to the low resolution of S-band images. As a consequence, we decided not to use the S-band images for further investigations.

3.2 Application of Images at Different Frequencies

Most images are available in S, X, and possibly higher frequencies, commonly used for astrometry. So the question is how does the source behave over the whole VGOS frequency range? How far of the image's reference frequency is it safe to use the structure information for other frequencies? While this is not a guarantee, because we actually do not have other frequency bands' images, a preliminary conclusion tells us that we can use X- or U-band images as proxy for the whole VGOS frequency range. We have used X-band (or U-band) images for the Hobart12–Ishioka baseline (8,096 km) using the actual geometry at the image reference time to derive the structure delay at four VGOS bands. When using the VGOS reference frequency that is closer to the image frequency (in either X- and U-band) we get good agreement. In Figure 6, even though similar trends can be seen for both X- and U-band delay for all the VGOS reference frequencies, there still exist minor differences between the two lines. However, as the VGOS reference frequency approaches the image frequencies for each band, these minor differences become less. This can be especially seen in VGOS frequency 10.4564 GHz. We therefore conclude that we can use source information available in either X- or U-

band to be suitable for investigating source structure effects in all VGOS bands.

4 Next Steps

The approach developed here can be applied to more well observed sources with multiple images and for various reference frequencies. The established connection with the VieVS structure module further allows investigations using real geometries and actually observed schedules. More work also needs to be done on improving our routines for automatically deriving the source models. At UTAS, we also plan to connect these theoretical investigations with real observations. The ongoing VGOS tests on the Hobart12–Ishioka baseline are a good testbed, as are the VGOS results from CONT17 reported by Elosegui [4].

5 Conclusions

Using new, automated procedures for deriving source models allows us to take the next step in investigating source structure in VGOS.

The overall aim of these investigations is to identify the critical parameters which we need to know about; how they are expected to change with time; and, ultimately, how to observe sources with VGOS, so that they do not adversely influence (or even prohibit) geodetic and astrometric results.

References

1. Böhm, J., Böhm, S., Boisits, J., Girdiuk, A., Gruber, J., Hellerschmied, A., Krásná, H., Landskron, D., Madzak, M., Mayer, D., and others (2018). Publications of the Astronomical Society of the Pacific. 130(986), 044503.
2. Charlot, P. (1990) Radio-source structure in astrometric and geodetic very long baseline interferometry. The Astronomical Journal. 99, 1309.
3. Collioud, A., Charlot, P. (2009). The Bordeaux VLBI image database. Proceedings of the 19th European VLBI for Geodesy and Astrometry Working Meeting, Bordeaux. (*https://www.researchgate.net/profile/Arnaud_Collioud/publication/252870783_The_Bordeaux_VLBI_Image_Database/links/5575602108ae7521586aa474/The-Bordeaux-VLBI-Image-Database.pdf*)
4. Elosegui, P. (2018). An early exploration of VGOS data, precision, and accuracy. 10th IVS General Meeting (this issue) (*https://ivs2018.kartverket.no/event/1/contributions/73/attachments/12/12/S2-T06_elosegui.pdf*)
5. Fey, A. L., Clegg, A. W., Fomalont, E. B. (1996). VLBA Observations of Radio Reference Frame Sources. I. The Astrophysical Journal Supplement Series, 105, 299.
6. Fey, A. L., Charlot, P. (2000). VLBA Observation of radio reference frame sources. III. Astrometric suitability of an additional 225 sources. THE ASTROPHYSICAL JOURNAL SUPPLEMENT SERIES, 128(1), 17.
7. Kudryavtseva, NA., Gabuzda, DC., Aller, MF., Aller, HD. (2011) A new method for estimating frequency-dependent core shifts in active galactic nucleus jets. MNRAS 415, 1631.
8. Niell, A. (2006). Source Structure Simulation. IVS Memorandum 2006-017v01 (*https://ivscc.gsfc.nasa.gov/publications/memos/ivs-2006-017v01.pdf*).
9. Niell, A. (2006). Source Structure Examples. IVS Memorandum 2006-018v01 (*https://ivscc.gsfc.nasa.gov/publications/memos/ivs-2006-018v01.pdf*).
10. Plank, L., Lovell, J., Shabala, S., Böhm, J., Titov, O. (2015). Challenges for geodetic VLBI in the southern hemisphere. Advances in Space Research, 56, 304.
11. Plank, L., Shabala, S., McCallum, J., Krasna, H., Petrachenko, B., Rastorgueva-Foi, E., Lovell, J. (2016). On the estimation of a celestial reference frame in the presence of source structure. MNRAS, 455, 343.
12. Petrachenko, B., Charlot, P., Collioud, A., Searle, A. (2016). International VLBI Service for Geodesy and Astrometry 2016 General Meeting Proceedings "New Horizons with VGOS", Eds. Dirk Behrend, Karen D. Baver, Kyla L. Armstrong, NASA/CP-2016-219016, p. 82–86.
13. Schuh, H. (2000). Geodetic analysis overview. International VLBI Service for Geodesy and Astrometry 2000 General Meeting Proceedings. (*https://ntrs.nasa.gov/archive/nasa/casi.ntrs.nasa.gov/20000074683.pdf*)
14. Shabala, S., Rogers, J., McCallum, J., Titov, O., Blanchard, J., Lovell, J., Watson, C. (2014). The effects of frequency-dependent quasar variability on the celestial reference frame. Journal of Geodesy,88(6), 575.
15. Shabala, S., McCallum, J., Plank, L., Böhm, J. (2015). Simulating the effects of quasar structure on parameters from geodetic VLBI. Journal of Geodesy, 89(9), 873.
16. Tornatore, V., Charlot, P. (2007). The impact of radio source structure on European geodetic VLBI measurements. Journal of Geodesy, 81, 469.

Session 3

Legacy S/X and Mixed Legacy/VGOS Operations

Organizing the Continuous VLBI Campaign 2017 (CONT17)

Dirk Behrend[1], Cynthia Thomas[1], John Gipson[1], Ed Himwich[1]

Abstract The Continuous VLBI Campaign 2017 (CONT17) was observed from November 28 to December 12, 2017. Unlike previous CONT campaigns organized under the auspices of the IVS, CONT17 was not a single-network effort but featured three independent observing networks. Two legacy S/X networks of nominally 14 stations each observed in parallel for the full 15 days of the campaign. This was made possible in large part by the participation of the ten-station VLBA network of the LBO. Furthermore, for the five-day period from December 4-8, 2017 a six-station broadband network continuously recorded VGOS data. The different networks will help probe the accuracy of the VLBI estimates of the EOP and investigate possible network biases. In this paper, we describe the coordination effort undertaken to make CONT17 a successful endeavor. This includes the assignment of stations to the three networks based on EOP simulations, analysis of media, e-transfer, and correlation resources, as well as schedule writing, among other things.

Keywords CONT17, legacy S/X, VGOS, VLBA

1 Introduction

The Continuous VLBI Campaign 2017 (CONT17) is the continuation of a series of very successful continuous VLBI campaigns that have been organized and observed since 1994. For a more detailed summary of the various CONT efforts the reader is referred to [4].

[1]NVI, Inc.

A prominent feature of the CONT17 campaign was the utilization of three independent VLBI networks: two global legacy S/X networks and one northern hemisphere VGOS network. Having independently measured parameters for the same period enables us to get an estimate of their accuracy and to uncover possible biases originating from the station selection of the networks.

The CONT17 effort was an ambitious endeavor that necessitated the use of many resources. In this paper we try to touch on the organizational side of CONT17 and provide insights into the work of the Coordinating Center. This includes the preparatory work and the general handling of resources such as station observing time, correlator time, media usage, and data transport, among others.

2 Some History

Prior to CONT17, five continuous VLBI campaigns were organized under the auspices of the IVS (i.e., after 1999) (see Table 1).

Table 1 History of CONT campaigns in the IVS era.

Campaign	Network size	Observation month	Observation length
CONT02	8 stations	Oct. 2002	15 days
CONT05	11 stations	Sept. 2005	15 days
CONT08	11 stations	Aug. 2008	15 days
CONT11	14 stations	Sept. 2011	15 days
CONT14	17 stations	May 2014	15 days

The network size increased significantly from 2002 to 2014, more than doubling the number of participat-

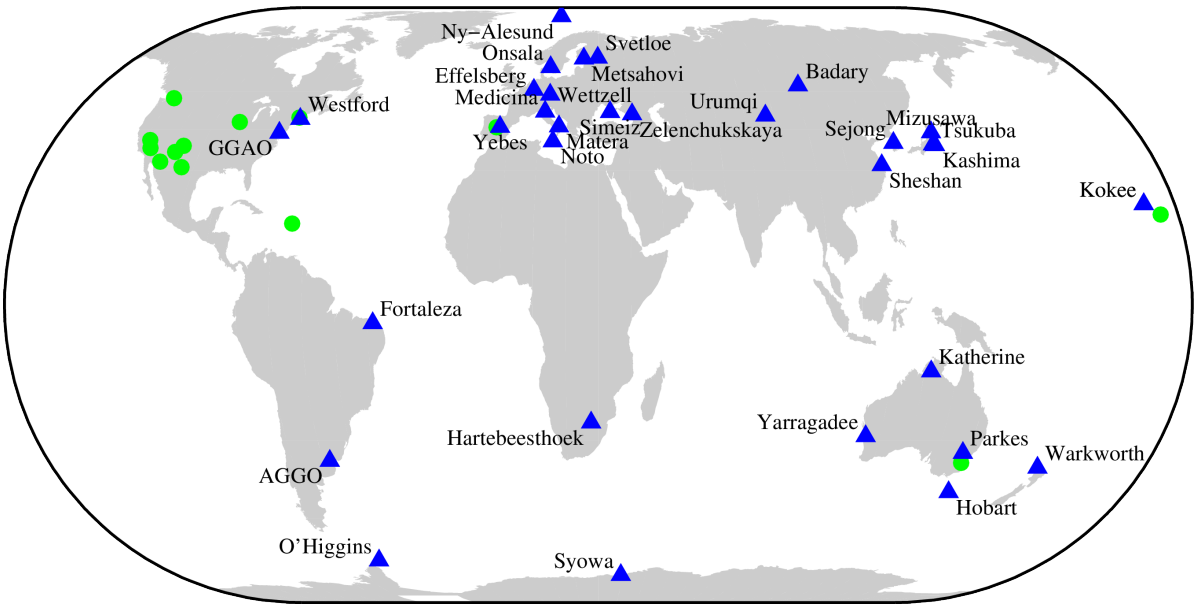

Fig. 1 Map of IVS Network Stations (blue triangles ▲) and cooperating VLBI sites (green circles ●) as of 2016. These 42 stations constituted the available station pool that might participate in the CONT17 effort as of that time.

ing stations. Most of the campaigns were observed in the second half of the calendar year (the sole exception being CONT14), and all CONTs took data for 15 days.

The spacing between the CONT campaigns is roughly three years. The reason for this can be traced back to a decision by the Observing Program Committee (OPC) in 2005. CONT campaigns should not be observed more frequently than every three years, because the strain on the resources (mostly stations and correlators) was considered too taxing. This, of course, holds for the legacy S/X stations; but it also puts into perspective the VGOS goal of 24/7/365 continuous observing in the future. Following the three-year rule, the next CONT campaign would be in the year 2020.

The first actual mention of a CONT17 campaign was made at the IVS General Meeting in Shanghai, China in 2014 (see, e.g., [1]), with two possible scenarios mentioned:

- to observe a campaign with a legacy S/X network in parallel to a VGOS network;
- to observe a campaign with a mixed network of legacy S/X and VGOS stations.

The implementation of either would depend on the station availability and thus also on the observing time frame.

3 Observing Period

Serious discussion about CONT17 commenced in early 2016. The Coordinating Center internally discussed the possible time frame for the campaign and decided on late 2017 (or early 2018). In April 2016, CONT17 was on the agenda of an OPC meeting for the first time. Then the Coordinating Center contacted various VLBI groups (e.g., EVN, GMVA, JIVE) to determine a time period with the least conflict potential. Based on these discussions the actual observing period was fixed to November 28 – December 12, 2017.

4 Station and Correlation Resources

The discussions about the time frame triggered interest in the Very Large Baseline Array (VLBA) being part of the CONT17 effort. The VLBA was being reorganized at the time to be managed by the Long Baseline Observatory (LBO) starting 1 October 2016; hence, the actual inclusion procedure was still unclear.

The Coordinating Center sent out the Call for Participation in CONT17 to the stations in June 2016 together with the station time request for the Master

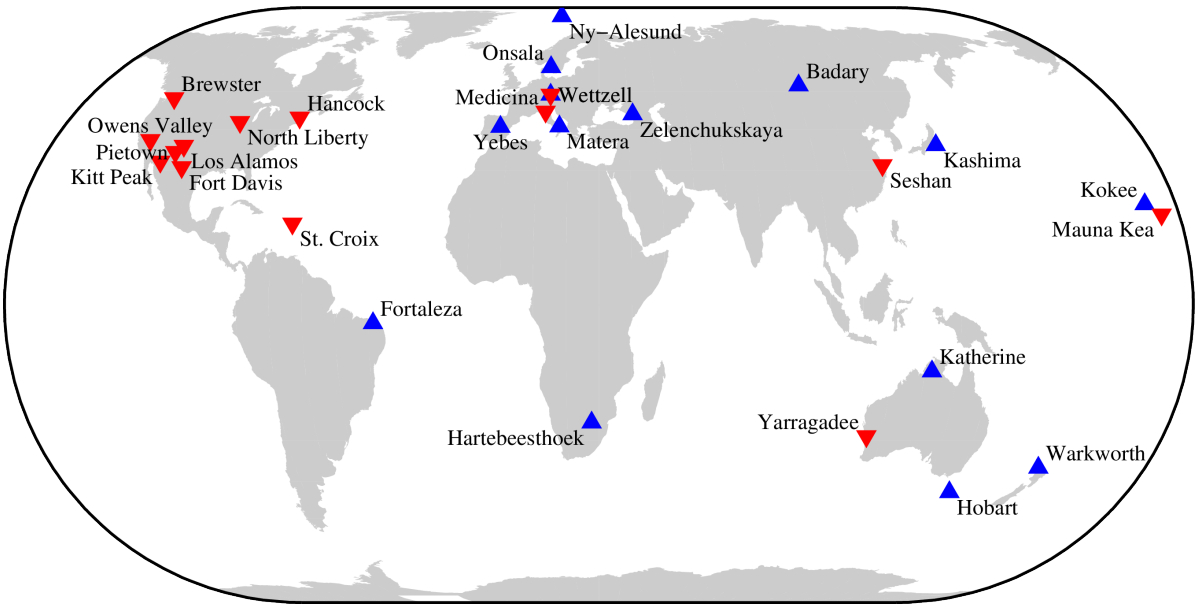

Fig. 2 The two legacy S/X networks of CONT17: the Legacy-1 network is depicted by blue triangles ▲ and the Legacy-2 network by red inverted triangles ▼. Twenty-seven stations at 26 sites participated in the S/X portion of CONT17.

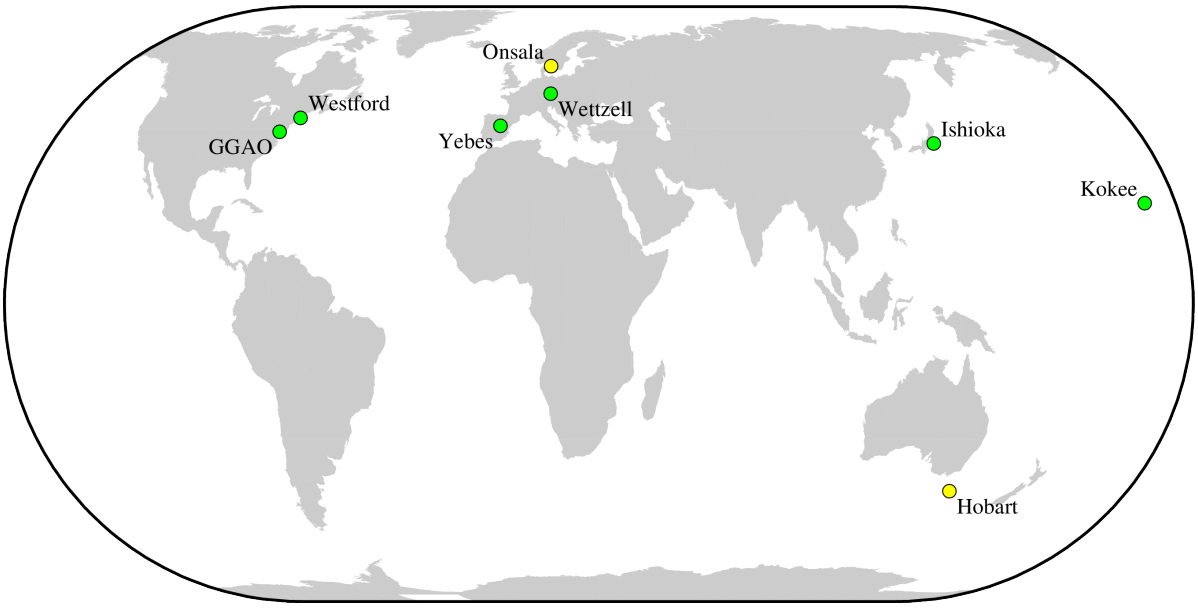

Fig. 3 The six-station VGOS demonstration network (VGOS-Demo, green circles ●) of CONT17. The broadband signal chain roll-out for Onsala and Hobart (yellow circles ●) was not completed on time for an official inclusion in the campaign.

Schedule 2017. In response, some 19 IVS Network Stations (S/X and VGOS) agreed to participate. The participation of the VLBA had to be requested through a proposal to the USNO VLBA Telescope Allocation Committee (TAC). The GSFC VLBI Group made several EOP simulations with varying networks, setups, and parameters/options. A proposal "Using the VLBA in CONT17 as a probe of the accuracy of VLBI estimates of EOP" was submitted to the TAC in late December 2016 and approved about a month later. With

the approval of the proposal, the decision was made to have two legacy S/X networks and one VGOS network for CONT17.

The plans for CONT17 were presented at the EVGA meeting in Gothenburg, Sweden in May 2017. As a consequence, two additional stations (Kashima and Seshan) requested to be added to the networks. Following several additional simulations, the final networks were determined as depicted in Figures 2 and 3. Thus, by mid-2017 the observing networks, consisting of two legacy S/X networks of nominally 14 stations each and one VGOS broadband network of up to eight stations, as well as the observing period were settled.

Three correlators were involved in the bulk of the CONT17 processing (cf. Table 2). In addition, the Washington Correlator assisted by reducing the work load on the Bonn Correlator prior to and after CONT17, taking over the correlation of regular IVS sessions (e.g., R1 sessions) from mid-November 2017 through the end of April 2018.

Table 2 Data rates and correlators of the CONT17 networks.

Network	#stations	Data rate	Correlator	Comment
Legacy-1	14	512 Mbps	Bonn	—
Legacy-2	14	256 Mbps	Socorro	VLBA
VGOS-Demo	6	8 Gbps	Haystack	—

The limitations of the media pool, e-transfer capacities, and data storage (at the correlators) largely determined which data rates were possible for the observing networks. The Legacy-1 network used the same mode as was used in CONT14, that is, a 512-Mbps mode. For Legacy-2, a 256-Mbps recording mode was chosen; while a 2-Gbps mode similar to the VCS-II survey would have been possible for the VLBA stations, this mode was too risky for the four geodetic stations. The observing mode for the VGOS network was identical to the one used for the VGOS test sessions.

Table 3 Data storage and data transport resources.

Network	e-transfer	Module shipment	Storage type	Volume per day
Legacy-1	12 stations	Matera, Kokee	Mark 5, FlexBuff	40.6 TB
Legacy-2	—	all stations	Mark 5	23.8 TB
VGOS-Demo	Ishioka	five stations	Mark 6	132 TB

The Bonn Correlator arranged to have 600 TB of storage space available for the Legacy-1 network. A contingency RAID was built using eight 32-TB Mark 6 modules. In this setup, Bonn was able to support twelve stations with e-transfer of data; two stations had to ship their Mark 5 modules physically (see Table 3). All stations of the Legacy-2 network had to ship their modules physically to Socorro. For the VGOS-Demo, only one out of the six stations e-transferred their data to Haystack.

5 Schedule Writing and Source Selection

The individual observing schedules were written using NASA's scheduling software *sked* [3]. The schedulers for each network as well as some general features are compiled in Table 4; there were altogether four schedulers involved. For the legacy S/X schedules the observing was organized in 24-hour time periods from 0–24 UT. This was done to be compatible with the other space-geodetic techniques.

Table 4 Preparation of observation schedules.

Network	Scheduler	Change-over time	General technique
Legacy-1	Dirk Behrend, Cynthia Thomas	3 min	complete period, then cut into days
Legacy-2	David Gordon	5 min	individual days
VGOS-Demo	Alex Burns	15 min	individual days

From the full 24 hours the schedule changeover time needs to be subtracted. That means that, for instance, the Legacy-1 network had no more observations after 23:57:00 UT of each day (except for the final day). To eliminate operational difficulties at stations with both legacy S/X and VGOS antennas, the VGOS sessions started at 23 UT, one hour before the S/X sessions. The last day of the VGOS-Demo portion was then scheduled for 25 hours. Hence, in the processing stage it would be possible to rearrange the data to the 0–24 UT time span.

For the scheduling of the Legacy-1 network the same scheme was employed as for CONT14 (see [2]). The full 15 days of CONT17 were written in a single schedule file (with gaps of three minutes at the end of each UT day); then this file was broken up into indi-

vidual observing days. Because the cable-wrap information was carried forward across the day boundaries, this allowed very brief changeover times (necessary for changing schedules at the stations). The Legacy-2 and VGOS-Demo schedules were written as independent single days.

As the observation of the Intensive sessions for UT1 determination had precedence over the CONT17 observing, stations participating in Intensives were removed from the CONT17 observations during Int1, Int2, and Ru-I Intensives. No Int3 Intensive was observed during CONT17. As the VLBA Intensives are dynamically scheduled, no slots were freed in the Legacy-2 network, and the loss of observations was simply accepted.

The final list of sources used for scheduling contained 92 sources. The source selection was the work of Karine Le Bail and was done by applying three criteria:

- Flux values ≥ 0.25 Jy in S- and X-band (August 2017 flux values);
- Failure rate in 2017 $\leq 20\%$ in S- and X-band;
- Structure index (SI) better than 3.

This resulted in a list of 142 sources. From this list the best 90 sources were selected using *sked*'s BESTSOURCE command. Finally, two southern sources were added back manually for better sky coverage; they had a failure rate of 24% in 2017.

6 Preliminary EOP Results

As part of the resource allocation process described in Section 4, a number of simulation runs using the *Solve* software were done to determine the optimal networks. Table 5 summarizes the EOP formal errors for the three CONT17 networks plus the results using the actual data for CONT11 and CONT14 (using the same control file in *Solve*). Note that no station velocities were estimated, and thus the results are too optimistic. But the intrinsic measurement precision is represented correctly, allowing intercomparison of the results from the different networks and different times. Behrend et al. (2014) explains in more detail the impact of estimating station velocities in the covariance simulations [1] .

Hence, from the simulations it was expected that the CONT17 legacy S/X networks would have similar EOP formal errors as CONT11, which also sported a 14-station network of global extent. As the simulated data represented the ideal case of 100% successful observing, the final results were anticipated to be slightly worse depending on the level of missed observations.

Table 5 Simulated EOP formal errors derived from a covariance analysis without station velocity estimation for the three CONT17 networks and the actual data for CONT11 and CONT14.

Network	#stat	$\sigma_{X\,pole}$ [µas]	$\sigma_{Y\,pole}$ [µas]	σ_{UT1} [µs]	σ_{ψ} [µas]	σ_{ε} [µas]
Legacy-1	14	13.0	13.7	0.9	14.4	13.1
Legacy-2	14	15.0	17.5	0.8	15.0	14.3
VGOS-Demo	8	22.1	22.5	0.8	17.2	18.1
CONT11	14	12.9	13.1	0.7	13.4	13.8
CONT14	17	12.6	12.3	0.7	14.2	13.2

The slightly inferior EOP formal errors for the VGOS-Demo network are mostly due to the limited geographic range of this network. As the simulation was done with the originally planned eight-station network (including Onsala and Hobart), the actual EOP formal errors for the VGOS portion of CONT17 will be higher.

Two stations dropped from the original VGOS-Demo network. The VLBA station of St. Croix was not available for the Legacy-2 network because of the aftermath of Hurricane Maria. Furthermore, Seshan had a failure about mid-way through observing the campaign and thus missed the second half of CONT17.

The data transport and correlation of the CONT17 legacy S/X data was quite fast. The elapsed time from the end of the last observation to having all CONT17 data correlated took about 77 days for Legacy-1 and some 21 days for Legacy-2. This compares to 138 days for CONT11 and 51 days for CONT14. The jump in processing speed from 2011 to 2014 can largely be attributed to the changeover from hardware correlator to software correlator. The (relative) increase of the elapsed time from CONT14 to CONT17 Legacy-1 is an indication of still remaning bottlenecks in the e-transfer of data.

Based on a Goddard solution (2016a) but without estimating station velocities, Figure 4 shows the EOP uncertainties for the continuous VLBI campaigns since 2002. As for the simulation results, the formal errors are too optimistic but they are intercomparable between the campaigns. (More realistic numbers for the actual accuracy may be obtained by multiplying with a factor between 1.5 and 1.8 depending on the distance

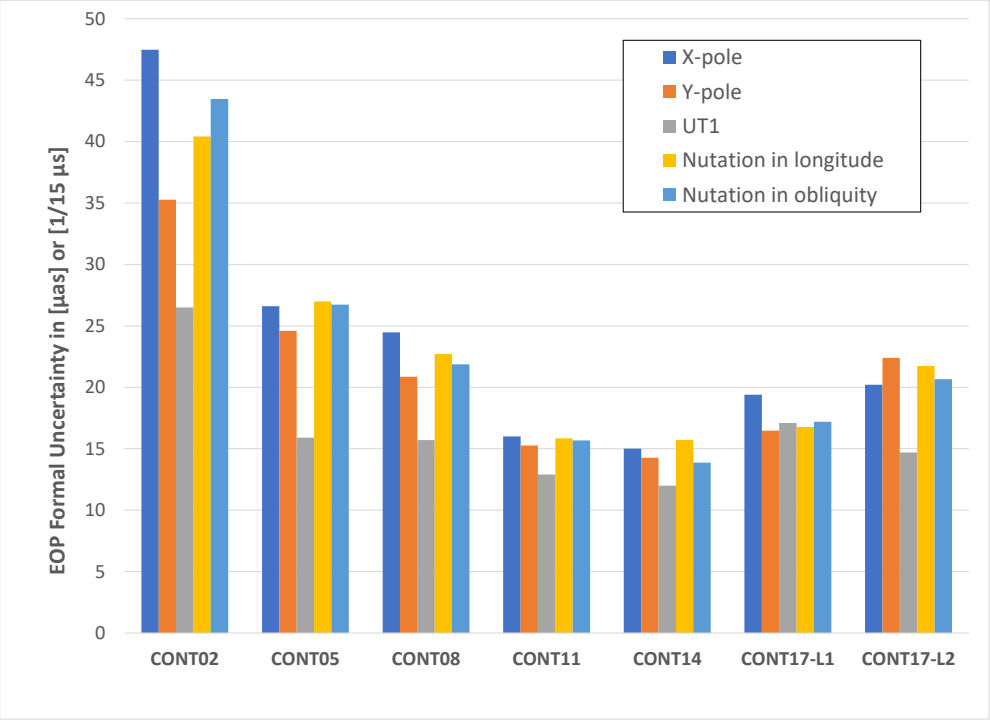

Fig. 4 EOP uncertainties for the CONT campaigns since 2002 based on a Goddard solution (2016a) with no station velocity estimation.

from the midpoint of the overall data span.) The actual, unscaled EOP formal errors are in reasonable agreement with the simulation results. The actual Legacy-1 EOP uncertainties are marginally worse than found in the simulation; this can easily be explained by the loss of observations. Likewise, the slightly worse performance of Legacy-2 is a direct result of the decrease in the number of observations and the geographic coverage (i.e., loss of the VLBA station at St. Croix).

The overall best continuous VLBI campaign in terms of formal errors is CONT14. This comes as no surprise, as it had the largest network size (17 stations) and best geographic distribution. CONT11 is only slightly worse with its 14-station network. As the CONT17 Legacy-1 and Legacy-2 networks were formed as a compromise to define two global networks, their performance did not reach the level of CONT11. But they performed better than the CONT02, CONT05, and CONT08 networks, which had a weaker global distribution and size.

The early results for the Legacy-1 and Legacy-2 networks indicate that the two networks are consistent with each other at the 1.5-sigma level. That is, there is likely no bias between larger global networks. This needs to be looked at in more detail.

7 Acknowledgement in Publications

It is essential that contributors to the success of CONT17 be acknowledged in publications that make use of CONT17 data. An acknowledgement to this effect assists the VLBI components in securing continued funding for their activities. The IVS Directing Board, thus, established a data policy for CONT17 that includes a request to add a specific acknowledgement text to CONT17 publications. The text is available at the CONT17 Web page at `https://ivscc.gsfc.nasa.gov/program/cont17/` and is also included at the end of this paper as the acknowledgements section.

The availability of the CONT17 data is initially restricted. For a period of six months after the completion of the correlation the full set of CONT17 session days is only accessible to involved parties. Following

the half-year data embargo period, the CONT17 data fully become publicly available through the IVS Data Centers.

8 Conclusions and Outlook

The preparation of the CONT17 campaign started as early as Feburary/March 2016, i.e., more than 1.5 years prior to the actual observing. It is the first continuous VLBI campaign that made use of three different networks. The independent networks allow probing of the accuracy of the EOP estimates, in particular of UT1 and nutation. During the IVS era, CONT17 was the first continuous VLBI campaign that included the VLBA.

It seems likely that CONT17 will remain the largest legacy S/X CONT effort, as stations start to convert to the VGOS system (e.g., the AuScope antennas at Hobart, Katherine, and Yarragadee). Prior to the complete changeover to the VGOS, a final CONT campaign in 2020 (CONT20) could be organized that will be based on a mixed network of S/X and VGOS stations. Once VGOS is operational, continuous VLBI observing will be the standard mode of operations.

Acknowledgements

We are grateful to all parties that contributed to the success of the CONT17 campaign, in particular to the IVS Coordinating Center at NASA Goddard Space Flight Center (GSFC) for taking the bulk of the organizational load, to the GSFC VLBI group for preparing the legacy S/X observing schedules, and MIT Haystack Observatory for the VGOS observing schedules, to the IVS observing stations at Badary and Zelenchukskaya (both Institute for Applied Astronomy, IAA, St. Petersburg, Russia), Fortaleza (Rádio Observatório Espacial do Nordeste, ROEN; Center of Radio Astronomy and Astrophysics, Engineering School, Mackenzie Presbyterian University, Sao Paulo and Brazilian Instituto Nacional de Pesquisas Espaciais, INPE, Brazil), GGAO (MIT Haystack Observatory and NASA GSFC, USA), Hartebeesthoek (Hartebeesthoek Radio Astronomy Observatory, National Research Foundation, South Africa), the AuScope stations of Hobart, Katherine, and Yarragadee (Geoscience Australia, University of Tasmania), Ishioka (Geospatial Information Authority of Japan), Kashima (National Institute of Information and Communications Technology, Japan), Kokee Park (U.S. Naval Observatory and NASA GSFC, USA), Matera (Agencia Spatiale Italiana, Italy), Medicina (Istituto di Radioastronomia, Italy), Ny-Ålesund (Kartverket, Norway), Onsala (Onsala Space Observatory, Chalmers University of Technology, Sweden), Seshan (Shanghai Astronomical Observatory, China), Warkworth (Auckland University of Technology, New Zealand), Westford (MIT Haystack Observatory), Wettzell (Bundesamt für Kartographie und Geodäsie and Technische Universität München, Germany), and Yebes (Instituto Geográfico Nacional, Spain) plus the Very Long Baseline Array (VLBA) stations of the Long Baseline Observatory (LBO) for carrying out the observations under the U.S. Naval Observatory's time allocation, to the staff at the MPIfR/BKG correlator center, the VLBA correlator at Socorro, and the MIT Haystack Observatory correlator for performing the correlations and the fringe fitting of the data, and to the IVS Data Centers at BKG (Leipzig, Germany), Observatoire de Paris (France), and NASA CDDIS (Greenbelt, MD, USA) for the central data holds.

References

1. D. Behrend, C. Thomas, E. Himwich, and D. MacMillan. CONT14: Preparation and Prospects. *IVS 2014 General Meeting Proceedings 'VGOS: The New VLBI Network'*, edited by D. Behrend, K. D. Baver, and K. L. Armstrong, Science Press (Beijing), ISBN 978-7-03-042974-2, pp. 196–200, 2014.
2. D. Behrend. Continuous VLBI Scheduling: The CONT14 Example. *Proceedings of the 22nd European VLBI Group for Geodesy and Astrometry Working Meeting*, edited by R. Haas and F. Colomer, Ponta Delgada, Azores, ISBN 978-989-20-6191-7, pp. 145–149, 2015.
3. J. Gipson. Sked. VLBI Scheduling Software. Web document https://vlbi.gsfc.nasa.gov/files_user_manuals/sked/SkedManual_v2016Dec09.pdf, 2016.
4. C. Thomas, D. Behrend, and D. MacMillan. From CONT to VGOS: the Evolution of the CONT Campaigns. *IVS 2016 General Meeting Proceedings 'New Horizons with VGOS'*, edited by D. Behrend, K. D. Baver, and K. L. Armstrong, NASA/CP-2016-219016, pp. 127–131, 2016.

Implementation and First Results of the Local Wettzell VLBI Correlator GOWL

Apurva Phogat [1], Christian Plötz [1], Torben Schüler [1,5], Hayo Hase [1], Gerhard Kronschnabl [1], Alexander Neidhardt [2], Jan Kodet [2], Ulrich Schreiber [2], Walter Alef [3], Helge Rottmann [3], Laura La Porta [4], Simone Bernhart [4]

Abstract The Geodetic Observatory Wettzell (GOW), jointly operated by the Federal Agency for Cartography and Geodesy (BKG) and the Technical University of Munich is equipped with three radio telescopes for Very Long Baseline Interferometry (VLBI). Extended local correlation capabilities, however, have been missing at the Observatory so far. A computing cluster forming the GO Wettzell Local Correlator (GOWL) was installed in September 2017 as well as the Distributed FX (DiFX) software correlation package and the Haystack Observatory Post processing System (HOPS) for fringe fitting and post processing of the correlated output. Data pre-processing, including ambiguity resolution (if necessary) as well as the generation of the geodetic database and NGS card files, is carried out with nuSolve. The final analysis is either performed with our local processing software (LEVIKA short baseline analysis) or with the Vienna VLBI and Satellite (VieVS) software. We present an overview of the correlation capabilities and results obtained so far. Regarding the local ties at Wettzell, we have been studying the local baseline between RTW (20 m) and TTW1 (13.2 m) in detail since 2016. These local sessions are usually scheduled with VieVS. Here we report on the method and first results of the local baseline estimated with VLBI and then compare with local tie measurements. Moreover, we also present initial results from the AGGO radio telescope testing as well as from individually scheduled sessions including the O'Higgins VLBI telescope at Antarctica. Finally, we want to present different observing prospects and future plans.

Keywords VLBI correlation and analysis, local ties, Wettzell triple radio telescope, scheduling

1. Geodetic Observatory Wettzell, Federal Agency for Cartography and Geodesy (BKG), Sackenrieder Str. 25, D-93444 Bad Kötzting, Germany
2. Geodetic Observatory Wettzell, Technische Universität München, Sackenrieder Str. 25, D-93444 Bad Kötzting, Germany
3. Max Planck Institute for Radioastronomy, Auf dem Hügel 69, 53121 Bonn, Germany
4. Reichert GmbH / Federal Agency for Cartography and Geodesy (BKG), Auf dem Hügel 69, 53121 Bonn, Germany
5. University of the Federal Armed Forces Munich, Faculty of Aerospace Engineering, Werner-Heisenberg-Weg 39, D-85577 Neubiberg, Germany

1 Short Baseline Sessions

Short baseline measurements at GOW are observed between RTW and TTW1 (Figure 1). Both telescopes are currently participating in IVS sessions in legacy (S/X band) mode. Due to the presence of the phase calibration signal with the same bandwidth and spacing on both telescopes, the baseline is not usable and rejected during the analysis process. The local sessions are conducted with phase cal switched off on one of the observing telescopes to avoid interference by the phase calibration signal and to make the baseline usable for geodetic analysis. For acquiring sufficient signal-to-noise ratio and fringe quality the manual phase cal mode is applied for the same telescope in the fringe fitting process. Both telescopes are connected to separate clocks during the local sessions. One of the advantages of scheduling short baseline observations is that the number of observed sources is very high because of very good sky coverage. Keeping in mind the number of sessions observed by Wettzell telescopes on a regu-

Fig. 1 View of the GOW with RTW and TTW1.

lar basis, the scheduling software is optimized to gain the maximum number of scans possible in an hour to reduce the total observation time. Various scheduling modes used in official IVS sessions are tested and observed.

2 Long Baseline Sessions

For getting familiar with long baseline correlation and analysis, sessions with partner telescopes in the southern hemisphere (Figure 2) are also organized and observed. The long baseline sessions require ambiguity

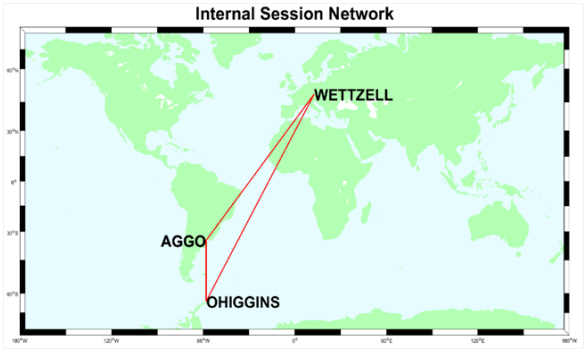

Fig. 2 Local network for long baseline sessions.

resolution and ionospheric correction before estimating geodetic parameters which includes earth orientation, station coordinates, tropospheric correction, and clock offsets. These sessions are dedicated to assuring the quality of VLBI data at the AGGO Observatory, La Plata, Argentina and the Receiving Station O'Higgins, Antarctica. Several tests were conducted in the past with variable durations for testing the VLBI system at AGGO to assess the readiness of the telescope for observing on a regular basis. A list of long baseline sessions observed so far with AGGO and O'Higgins since January 2018 are listed in Table 1. The operation of and data transfer from the GARS O'Higgins telescope is done remotely from GOW. Few trial sessions between

Table 1 List of local long baseline sessions.

Session name	Participating telescope	Duration (Hour)	No. of scans
WB015N	Ag, Wz	1	8
WB072I	Ag, Wz	5	11
WB087I	Ag, Oh, Wz	9	92
WB106S	Ag, Wn	24	221
WB136Q	Ag, Wn, Wz	24	455

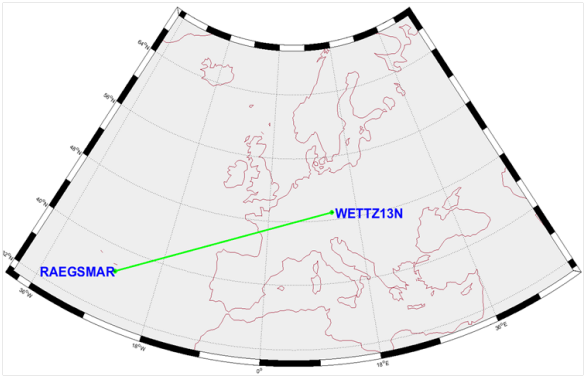

Fig. 3 Baseline for proposed European ΔUT1 estimation.

WETTZ13N and RAEGSMAR are also observed for the determination of ΔUT1 between fast moving telescopes. Both participating telescopes as shown in Figure 3 are within European territory; hence, these sessions are titled as the European Intensive sessions. The hardware configuration for both the telescopes is very similar as they are built as per the VLBI2010 [Niell et al., 2005] specifications (fast moving, small dish, broader frequency coverage). The number of observed scans is much higher in this case as compared to other Intensive sessions as a consequence of better sky coverage [Boehm et al., 2018].

3 Scheduling, Correlation, and Analysis

Before scheduling a local session they have to be requested via BKG CVC [Schüler et al., 2018b] to keep

track of the status of each session and proper communication between scheduler, operator, correlator, and analyst. The Vienna VLBI and Satellite Software (VieVS 3.0) [Sun et al., (2012)] and Sked [Gipson et al., 2012] are installed for scheduling local sessions. Figure 4 depicts the statistics of local sessions scheduled in the last two years. It is clearly seen that the short baseline sessions between TTW1 [Schüler et al., (2015)] and RTW are in the majority as compared to the long baseline sessions. The baseline between O'Higgins and Wettzell was scheduled a few times in the past to monitor the health of the VLBI system in Antarctica and to collect data sets for educational purposes. Including TTW2 in the short baseline network is one of the priorties and it is still under investigation and testing. After schedule

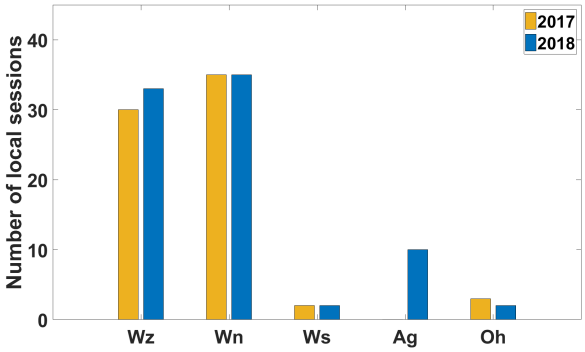

Fig. 4 Local session statistics.

Fig. 5 Image of the computing cluster installed at the TWIN operations room with the spare nodes.

preparation and observation, raw data is transferred in real time via a 10-Gbps optical link to the high speed data recorder and streamer (flexbuff) with total storage space of 100 TB. It is connected to the computing cluster (Figure 5) on which the DiFX [Deller et al., (2011)] and the HOPS package is installed. Fringe fitting software (HOPS) accounts for insufficiencies in the correlator model and integrates the interferometer signal. Data transmission to and from the observatory is done via a 1-Gbps Internet link. The local correlator GOWL serves three main purposes:

1. It is primarily designed for relative positioning of the three Wettzell radio telescopes, i.e., to derive the local ties between the three telescopes from VLBI raw data in addition to the conventional terrestrial surveys carried out.
2. The local correlator closes the gap between the observation work and geodetic analysis. The closure of this missing piece in the measurement/analysis chain is important to provide timely quality feedback to the VLBI engineers regarding the status of their telescopes.
3. Finally, GOWL serves as a critical backup infrastructure. This means that it is not foreseen to carry out routine operational work, which resides with the Bonn Correlator operated at the Max-Planck-Institute for Radio Astronomy, but is available in case of dedicated and special needs.

Thereafter, the fringe fitted output is processed in νSolve [Bolotin et al., (2014)] to produce vgosDB and NGS (ASCII) card files for an individual session. These ASCII files are input to VieVS and the in-house short baseline software (LEVIKA) [Schüler et al., 2018a] developed for estimating station coordinates and comparing them with the results of local survey measurements. In case of a long baseline session, station coordinates and other geodetic parameter estimation is done either by νSolve or by VieVS [Boehm et al., (2012)].

4 Results

Radio frequency interference (RFI) is another limiting factor for short baseline observations. Most of the scans in S-Band are affected by RFI mainly due to overlapping with Wi-Fi and other telecommunication signals. This causes a hindrance in terms of accessing the data quality of the affected channels as they have to be flagged in the correlation process and are not contributing in further analysis. Figure 6 depicts the output after post-processing a VLBI session where the local baseline is also included. When S-band is se-

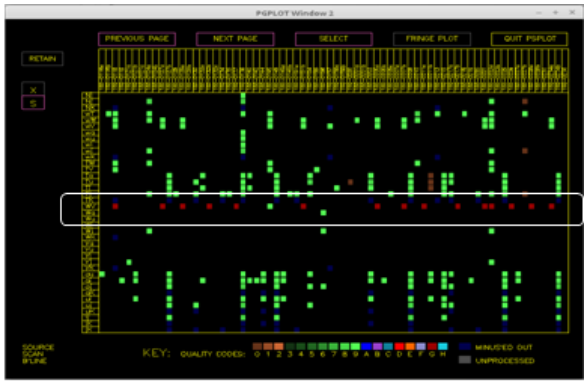

Fig. 6 This figure is produced using post-processing software showing the fringe quality of all the scans (x-axis) corresponding to S-band for all participating baselines (y-axis). The quality code or fringe quality is represented by different colors. Green is an indicator of fringe quality between three to nine, G-code is shown in red, and blue represent scans for which correlation was not attempted due to problems at the station.

lected, the local baseline is visible with red dots for most of the scans which are an annotation for G-code. G-code for a scan is an indication that the fringe amplitude is less than 0.5 times the mean amplitude of the received signal which is in most of the cases due to internal or external interferences. For a 123-m baseline an additional delay due to ionosphere is considered negligible; hence, observing with S-band is of no real importance except quality control. This makes the further procedure simpler as only group delays from X-band are used for analyzing the sessions. Figure 7 il-

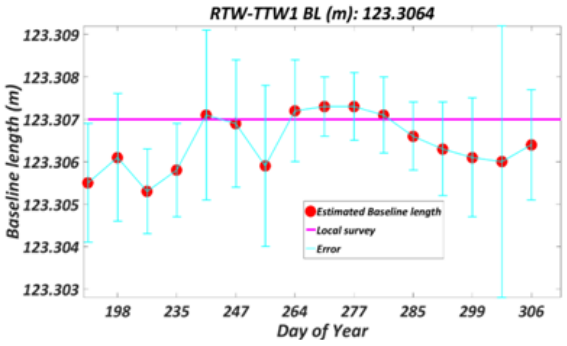

Fig. 7 3-D distance estimated with local sessions between RTW and TTW1 with the mean offset of 0.6 mm from the local survey measurement taken in the year 2017.

lustrates the analysis results from the sessions observed in 2017. Red dots represent the baseline length (3-D) estimated from an individual session with error bars (uncertainties) in cyan. The local survey measurement result is delineated in pink. Improvement in terms of estimated baseline length is expected after implementation of a common clock framework between all three telescopes. The common clock will provide equal delays in the time regime if all systematic biases are correctly addressed. Figure 8 gives an overview of the sta-

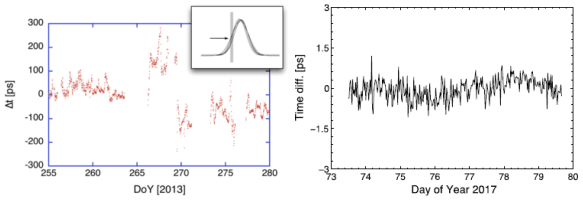

Fig. 8 Stability of pps signal transferred via coaxial cable (left) and optical fiber cable (right) is illustrated in this figure.

bility of the pulse per second signals when transferred using coaxial cable and optical cable. The dataset for these tests was collected by transferring the pps signals between two buildings at the Geodetic Observatory Wettzell [Schreiber et al., 2018] to make a comparison between the two approaches.

5 Conclusions and Outlook

The availability of a correlation capability fulfills multiple roles and it is of the utmost importance in terms of quality assurance. Further research and development work is being carried out on a regular basis at all three VLBI sites. Geodetic sessions are conducted on a regular basis to estimate baseline length between all the possible telescopes operated by GOW. Results presented in this paper show sub-millimeter accuracy of the baseline length between RTW and TTW1. Further improvement is foreseen after the implementation of a common clock. The comparison between the time transfer via coaxial cable and optical fiber gives a clear picture about the stability of both methods. The pps signal transmission via optical fiber seems to have a better stability in contrast to the coaxial cable.

The introduction of TTW2 into the short baseline network is in the initial stages. The availability of the Eleven feed with the possibility to observe only with linearly polarized signal makes it challenging to in-

clude it into the network where all the other telescopes are equipped with a receiving unit with the capability to observe a circularly polarized signal only. Several tests were conducted in the past to accomplish common clock modes and it is likely that there will be more tests in the future for finalizing the most efficient scheme amongst the two. The absence of the phase calibration signal in one of the telescopes for each short baseline session also deteriorates the results. There are a few solutions suggested to avoid such a set-up for short baseline observation and this is also in the list of future work to further improve the solution. A tri-band feed is installed at the TTW1, giving the possibility to observe with Ka-band in addition to S and X frequency bands. Incorporating Ka-band channels with the existing setup will be part of future research. Considering the fact that the hardware design of RAEGSMAR is similar to WETTZ13N, this scientific work will be part of the European Intensive sessions.

6 Acknowledgements

The authors would like to gratefully acknowledge the software correlator (DiFX) used for correlating the dataset presented in this paper. The software correlator was developed at the Swinburne University of Technology as part of the Australian Major National Research Facilities Programme and operated under license.

References

[Niell et al., 2005] A. Niell, A. Whitney, B. Petrachenko, W. Schlter, N. Vandenberg, H. Hase, Y. Koyama, C. Ma, H. Schuh & G. Tuccari. VLBI2010: Current and future requirements for geodetic VLBI systems, International VLBI Service for Geodesy and Astrometry, 2005, pp. 13–40.

[Boehm et al., 2018] J. Boehm, R. Bolano, S.G. Espada, J. Gonzalez, J. Gruber, G. Kronschnabl, A. Neidhardt, A. Phogat, C. Ploetz, M. Schartner, T. Schueler, P.D. Vicente. European Intensive Sessions for the Estimation of Universal Time, In Proceedings of the IVS 2018 General Meeting, Svalbard, Norway, 3-6 June 2018.

[Schüler et al., 2018a] T. Schüler, C. Plötz & A. Phogat. LEVIKA SBA - Wettzell Radio-Telescope Positioning with a Tailor-Made Analysis Software, In Proceedings of the IVS 2018 General Meeting, Svalbard, Norway, 3-6 June 2018.

[Sun et al., (2012)] J. Sun, T. Nilsson, J. Boehm & H. Schuh. New observing strategies with twin telescopes for geodetic vlbi, Proceedings, 2012 pp. 28–32.

[Gipson et al., 2012] J. Gipson. Sked: VLBI Scheduling Software, Program Reference Manual, Goddard Space Flight Center, 2012.

[Deller et al., (2011)] A. T. Deller, W. F. Brisken, C. J. Phillips, J. Morgan, W. Alef, R. Cappallo, E. Middelberg, J. D. Romney, H. Rottmann, S. J. Tingay & R. Wayth. DiFX-2: A More Flexible, Efficient, Robust, and Powerful Software Correlator, PASP, 2011, 123, 275–287.

[Bolotin et al., (2014)] S. Bolotin, K. Baver, J. Gipson, D. Gordon & D. MacMillan. The VLBI Data Analysis Software nuSolve: Development Progress and Plans for the Future, General Meeting Proceedings: VGOS: The New VLBI Network, 2014, Beijing, China, pp. 253–257. ISBN 978-7-03-042974-2.

[Schüler et al., 2018b] T. Schüler, C. Plötz & A. Phogat. BKG CVC The Central VLBI Observation Coordination Facility at the Geodetic Observatory Wettzell, In Proceedings of the IVS 2018 General Meeting, Svalbard, Norway, 3-6 June 2018.

[Boehm et al., (2012)] J. Boehm, S. Boehm, T. Nilsson, A. Pany, L. Plank, H. Spicakova, K. Teke & H. Schuh. The new Vienna VLBI Software VieVS, Geodesy for Planet Earth, 2012, Berlin, Heidelberg, pp. 1007–1011.

[Schüler et al., (2015)] T. Schüler, G. Kronschnabl, C. Plötz, A. Neidhardt, A. Bertarini, S. Bernhart, L. La Porta, S. Halsig, & A. Nothnagel. Initial Results Obtained with the First TWIN VLBI Radio Telescope at the Geodetic Observatory Wettzell, Sensors 2015, 15(8), 18767-18800. DOI10.3390/s150818767. Available online: http://www.mdpi.com/1424-8220/15/8/18767 (accessed on 19 August 2015).

[Schreiber et al., 2018] KU. Schreiber, J. Kodet. The Application of Coherent Local Time for Optical Time Transfer and the Quantification of Systematic Errors in Satellite Laser Ranging. Space Science Reviews, 2018, pp. 22.

The Bonn Correlator: Status Report

Laura La Porta [1,2], Walter Alef [3], Simone Bernhart [1,2], A. Müskens [4], Axel Nothnagel [4], Helge Rottmann [3], Torben Schüler [2], Jan Wagner [3]

Abstract We present a status report of the Bonn correlator. After discussing some technical aspects concerning the cluster and its performance, we will introduce the people working at the correlator, as well as the ongoing projects and duties, focusing on geodesy.

Keywords VLBI correlation, DiFX, VGOS

1 Introduction

The Bonn correlator is operated jointly by the Max Planck Institute for Radioastronomy (MPIfR) in Bonn and by the Federal Agency for Cartography and Geodesy (Bundesamt für Kartographie und Geodäsie, BKG), with the support of the Institute of Geodesy and Geoinformation (IGG) of the Bonn University. The MPIfR hosts the correlator facility and shares with the BKG the costs of the cluster, of most of the staff and of the internet connectivity. The IGG contributes to the connectivity of the cluster and pays one member of the geodetic staff. Since January 2017 the personnel responsible for the correlation of geodetic sessions have been employed by the BKG via a private contractor, the Reichert GmbH.

1. Reichert GmbH
2. Bundesamt für Kartographie und Geodäsie
3. Max-Planck-Institut für Radioastronomie
4. Institut für Geodäsie und Geoinformation der Rheinische Friedrich-Wilhelms Universität Bonn

2 The HPC Cluster

We run the Distributed FX software correlator at Bonn ([Deller et al. 2011]), of which we have various versions at our disposal. In particular, a branch version developed by J. Anderson for Radioastron experiments exists ([Bruni et al. 2014]). For production we use the latest stable DiFX release, and before switching to a newer DiFX version we perform a comparison of the resulting observables. Currently we are using DiFX 2.5.2, for both geodesy and astronomy. The correlator is running on a High Performance Computing (HPC) cluster, which was renewed in 2015 to match both VGOS and mm-VLBI requirements and consists of:

- 68 nodes with 20 compute cores each, for a total of 1,360 cores, which provide a computing power about ten times larger than that available with the old cluster;
- three head nodes which allow execution of several correlations in parallel (up to three parallel correlations were tested, and no reduction in speed was observed);
- 56 Gbps Infiniband interconnect between all nodes;
- 1.348 PB of disk space organized in RAID units (each with redundancy), of which 1.2 PB are combined in a BeeGFS parallel cluster file system;
- 14 Mark 5 playback units; and
- eight Mark 6 playback units each with four bays.

The raw data are recorded at the stations on Mark 5 or Mark 6 modules or on flexbuff. For geodetic experiments the data are mostly e-transferred to the HPC cluster, connected to the Internet through two 1-Gbit lines, one of which belongs to the Bonn University. Various data formats have already been correlated in Bonn: Mk4, Mk5, DVP, and VDIF. A native playback

Fig. 1 New HPC cluster at MPIfR seen through a glass wall.

mode for Mark 6 modules is about 90% ready. A feature to correlate multiple datastreams per station was implemented and is now routinely used, e.g., for the Event Horizon Telescope (EHT) sessions.

The correlated data can be exported to FITS and HOPS (mk4) format. The post-processing may be done with AIPS, PIMA, and HOPS, which is the standard tool for geodesy. The correlator outputs and other important files (e.g., vex and v2d files) are backed up daily on the HPC cluster. The final products are archived on the MPIfR archive server, where they will be kept for at least ten years.

The EXPAD and COMEDIA tools have been extended to help bookkeeping of the experiments correlated in Bonn by collecting all relevant information (observation date, participating stations, modules, status of the experiment) stored in the local database (difxdb).

3 Staff at the Bonn Correlator

The MPIfR staff at the Bonn correlator belongs to the VLBI technical development group, headed by W. Alef. Its members are H. Rottmann, A. Roy, J. Wagner, Y. Pidopryhora, M. Lisakov, S. Dornbusch, and G. Tuccari, who has a guest contract. In addition to the scientific staff, there are one technician, R. Märtens, one engineer, M. Wunderlich, and two operators, H. Sturm and H. Fuchs. The group is responsible for keeping the cluster software up to date, for hardware maintenance and repair, as well as for IT support and software correlator improvements (H. Rottmann and J. Wagner are DiFX developers).

The group members are involved in several projects. A. Roy is responsible for the Atacama Pathfinder EXperiment (APEX) and H. Rottmann for the beamformer of the Atacama Large Millimeter/submillimeter Array. G. Tuccari is the leader for the Digital Base Band Converters (DBBCs) and the Fila10G and, together with W. Alef, for the development of a new BRoad bAND (BRAND) receiver. J. Wagner, Y. Pidopryhora, and M. Lisakov take care of the correlation of astronomical experiments, which are focused on very high resolution imaging. About five Radioastron sessions are correlated in Bonn every year. Those sessions involve up to 38 antennas and baseline lengths of several Earth diameters. Two Global Millimeter VLBI Array (GMVA) sessions with up to 21 antennas are also correlated in Bonn. The data rate ranges between 2 Gbps and 8 Gbps, depending on

Fig. 2 View of the Mark 5 and Mark 6 units through a glass wall.

whether ALMA is participating in the observations or not, so that the amount of stored data can be as large as 700 TB. In addition, half a session of the Event Horizon Telescope (EHT) is correlated in Bonn, namely the data at 230 GHz (1 mm), which includes left and right circular polarization over a 4 GHz bandwidth. Last but not least, the group performs several tests for development of digital VLBI backends.

The geodesy group at the Bonn correlator is composed of about 2.3 FTEs. A. Müskens is mainly concerned with the schedules of various IVS sessions, namely of INT3, EURO, T2, and OHIG, which he generates with the SKED software ([Gipson 2010]). S. Bernhart and L. La Porta are responsible for the remaining activities. They coordinate the data logistics, prepare and supervise the correlation, carry out the post-processing and deliver the resulting observables to the IVS repository in the form of databases, which are suited for the subsequent geodetic analysis software packages. The IVS sessions correlated in 2017 are 45 R1, six EURO, six T2, 44 INT3, four OHIG, and five days of CONT17. Since May of this year those databases have been produced solely via the vgosDB-make software ([Bolotin et al. 2016]) in VGOS format.

Aside from these standard duties, they provide the stations with feedback on their performance and support tests of the VLBI systems, in particular for the Wettzell Observatory. They also participate in IVS activities by cooperating on various subjects, for example the determination of peculiar clock offsets for the various stations or the verification of the distributed correlation as a possible approach for sharing the work load among correlators during the VGOS era (read next section for further details).

As a final remark, the Bonn correlator is a natural test-bench for the DiFX software and for the e-transfer protocols, so that all its personnel contribute to debugging those tools.

4 Bonn as an IVS Correlator

4.1 CONT17

The Legacy-1 S/X network of the IVS CONTinous VLBI campaign 2017 was correlated in Bonn. Standard activities were stopped a couple of weeks before CONT17 to prepare storage space and organize the logistics of data transfers. We stored about 500 TB, which were mostly e-transferred to Bonn (only three stations sent modules). The cluster BeeGFS failed at the beginning of the campaign, so that we relied solely on three RAIDs for storing and correlating the Rapid-like sessions (C1701-R1, C1703-R4, C1707-R4, and C1714-R1). As a consequence the correlation ran much slower (by a factor of three) w.r.t. normal, and we had to pause e-transfers until the beginning of January when the cluster BeeGFS was completely restored. Nevertheless, we managed to submit the databases of the Rapid-like sessions within the usual two to three week latency time. The final correlation of CONT17 was completed during February.

It took some time before we resumed our normal activities (at the beginning of May), due to some doubts concerning the global set of clock parameters used for the final correlation. The following discussions concluded that the set of clocks was correct and no re-correlation was necessary.

The effective processing time of the CONT17 campaign was enormously reduced with respect to CONT14, thanks to the capabilities of the new cluster. The computing time for 24 hours of data was about a factor of three higher for CONT14, also due to the larger number of modules involved in the correlation (Mk5 units often had to be reset).

4.2 Distributed Correlation

A possible way to deal with the huge workload foreseen for VGOS could be to share it among several correlators by dividing the sessions into time blocks. Each correlator would receive only part of the raw data for a given session. Upon request of the IVS Directing Board we organized for testing such an approach, together with five other correlators (Onsala, Warkworth, Hobart, Seshan, and Vienna). We agreed on a common DiFX and HOPS version and performed the test for session R1840, which belongs to the IVS sessions regularly processed in Bonn.

As Bonn is the main correlator, we prepared and sent to our colleagues the vex and v2d files to be used for correlation, as well as the control file for fringe-fitting the data. We then collected the DiFX and Fourfit outputs of the branch correlators to compare them with ours. Verification of results is ongoing. We will generate a new database for R1840 by combining the output of the main and the branch correlators. R. Haas will perform a geodetic analysis of that database and compare the outcome with that of the original database, which contains only the outputs of the Bonn correlator.

The main downside of a distributed correlation is that the data logistics becomes more complicated. The raw data should be distributed to the various correlation centers, which should later upload their products to the main correlator.

4.3 Pipeline for Geodetic Post-Processing

Currently, there are no standard procedures for geodetic post-processing, although the IVS correlators all use the HOPS package for producing the databases holding the VLBI observables. There are a number of differences in terms of data handling, which may have an effect on the produced results and should therefore be investigated further.

An important aspect is the clock to be used for correlation. In Bonn we select a few scans both at the beginning and at the end of a session to determine the residual delay and delay rate of each station with respect to a reference station, which is usually Wettzell. At the USNO Washington correlator (WACO), the standard practice was until lately to choose a scan in the middle of the session instead. As a consequence the reference time of the clock model was different for IVS-R1 sessions, correlated in Bonn, and IVS-R4 sessions, correlated at USNO.

Other relevant aspects concern the post-processing of the data. Analysts should define best-practice guidelines for dealing with problematic data and, in particular, for channel flagging (the data are often affected by interferences) and for phase cal corrections (additive phases, manual pcal). The handling of Kokee Park phase-cal is still inconsistent between correlators.

4.4 Conclusions

The Bonn correlator is ready for the VGOS era, as has been demonstrated by the successful routine correlation of astronomical experiments with comparable data rates (e.g., the EHT at 32 Gbps).

The real challenge for VGOS will not be the computing power, but rather the data logistics. It is unlikely that stations and correlators will have at disposal adequate internet connections for e-transferring the amount of raw data generated in a VGOS session. Stations will likely have to ship their modules to the correlators, which is rather expensive. Furthermore, the foreseen duty cycle (24 hours per day on consecutive days) will require a rich media pool to provide stations with enough modules to keep observing while part of the raw data is being sent to the correlators.

References

[Deller et al. 2011] A. T. Deller, W. F. Brisken, C. J. Phillips, J. Morgan, W. Alef, R. Cappallo, E. Middelberg, J. D. Romney, H. Rottmann, S. J. Tingay & R. Wayth. DiFX-2: A More Flexible, Efficient, Robust, and Powerful Software Correlator, PASP, 2011, 123, 275-287

[Bruni et al. 2014] G. Bruni, J. Anderson, W. Alef, A. Lobanov, & A. J. Zensus. Space-VLBI with RadioAstron: new correlator capabilities at MPIfR, in Proceedings of the 12th European VLBI Network Symposium and Users Meeting, Cagliari, Italy, 2014, ID: 119

[Gipson 2010] J. Gipson An Introduction to Sked, in Proceedings of the 6th IVS General Meeting, Hobart, TAS, Australia, NASA/CP-2010-215864, pp. 77-84, 2010.

[Bolotin et al. 2016] S. Bolotin, K. Baver, J. Gipson, D. Gordon, & D. MacMillan Transition to the vgosDB Format, in Proceedings of the 9th IVS General Meeting, Johannesburg, South Africa, NASA/CP-2016-219016, pp. 222-224, 2016.

VLBI Correlation Activities at TU Wien

Jakob Gruber [1], Johannes Böhm [1], David Mayer [1], Jamie McCallum [2]

Abstract Geodetic VLBI correlation poses a new challenge in the current VLBI activities at the research area Higher Geodesy at Technische Universität Wien (TU Wien). We are using the Distributed FX (DiFX) software correlator and the Haystack Observatory Postprocessing System (HOPS) on the Vienna Scientific Cluster 3 (VSC-3), which is a supercomputer located at TU Wien. We provide more technical details about the VSC-3 and information about activities related to correlation at TU Wien. Furthermore, we present tools to directly access the correlation and fringe-fitting output database with the Vienna VLBI and Satellite Software (VieVS) using the vgosDb format and we discuss post-correlation processing aspects in VieVS based on currently correlated experiments.

Keywords VLBI correlation, Vienna Scientific Cluster

1 Introduction

VLBI correlation refers to the process of determining the difference in signal arrival times at two stations by comparing the recorded bit streams. These bit streams are characterized by very high sampling rates, ranging from several hundred Mbps to a few Gbps. Thus, for the realization of VLBI correlation, a high performance computing environment is convenient to carry out the correlation task efficiently and a large disk space is required to store all the recorded bit streams of various VLBI stations. Additionally, a stable link with high data rates is needed to transfer the data to the correlator. At TU Wien, we are capable of scheduling VLBI observations and estimating geodetic parameters with the Vienna VLBI and Satellite Software VieVS [1]. With the installation of a VLBI correlation infrastructure, we establish an additional element in the VLBI processing chain (see Table 1) allowing us to contribute with a wider field of capabilities to the VLBI community. This will become even more important with the increasing amount of data due to the VGOS observing scenario.

We installed the Distributed FX-style Correlator (DiFX [3]) on the Vienna Scientific Cluster 3 (VSC-3), a collaboration of several Austrian universities that provides supercomputer resources and corresponding services to their users. Technical details and inital performance tests of the VSC-3 are described in [2]. Here, we focus on data transfer capabilities, further performance studies of the VSC-3, the VLBI data processing pipeline at TU Wien, and current correlation activities.

Table 1 Core tasks in the VLBI processing chain with current and planned realizations.

VLBI task	current status	plan
Scheduling	VieVS	VieVS
Observation	–	–
Correlation	DiFX	DiFX
Fringe-fitting	HOPS/PIMA	HOPS/PIMA
Post-correlation	*v*Solve	VieVS
Analysis	VieVS	VieVS

1. Technische Universität Wien
2. University of Tasmania

2 Data Transfer Capabilities of the VSC-3

The VSC-3 is located in Vienna and linked to the Gigabit European Academic Network (GEANT). GEANT is a pan-European data and communication network that spans connections to 38 countries in Europe and other regions in the world with data transfer rates up to several backed-up 10-Gbps links. The VSC-3 can be accessed by five login nodes sharing the 10-Gbps link, which means that each of the login nodes of the VSC-3 can be accessed with 2 Gbps on average. For the data transfer of VLBI baseband data we make use of the jive5ab software package developed by H. Verkouter.

To avoid several data transfers through the same login node, we split up the data transfer into streams (usually one per station) and transfer the data through several login nodes in parallel to make efficient use of the VSC-3 network infrastructure. One of our main tasks of the VSC-3 is the correlation of data from the AUSTRAL network. For the data transfer between Hobart and Vienna, the pull method is used to retrieve the data and it is split up into several data streams—one per login node. With this concept, any bottlenecks of transmission via a single login node in Vienna are avoided and a total download rate of 1.8 Gbps from Hobart can be achieved effectively.

3 Correlation Processing Performance of the VSC-3

High performance clusters like the VSC-3 offer a large amount of cores which can be used on a shared basis with other users for processing intensive tasks, e.g., VLBI correlation. To some extent, the user can decide how many cores should be used for the processing task. As shown in [2], the correlation software DiFX scales up to approximately six nodes at the VSC-3 for an AUSTRAL session; therefore, we usually request six nodes for the correlation of those sessions because the use of more nodes does not decrease the processing time. The DiFX software architecture is well designed to efficiently process the baseband data of all stations that contribute to only one single scan.

However, to make efficient use of more cores we test a parallel scan processing strategy. While in a serial scan processing strategy all the processing power is assigned to one single scan, a parallel scan processing strategy spreads all the processing power efficiently to several scans.

3.1 Methodology and Realization

In contrast to the MPI parallelization within one single scan, parallelization of several scans can be realized with the concept of job arrays provided by the Slurm workload manager. In the method described here, each job of the Slurm array refers to the execution of a DiFX job for a single VLBI scan. The Slurm job array allows the execution of several jobs in parallel making it possible to correlate several VLBI scans in parallel and make efficient use of more cores. In this performance test we change the number of scans that are correlated simultaneously to evaluate possible impacts on the correlation processing time. The relation of the number of scans processed in parallel and the correlation processing time is estimated. Furthermore, this test reveals if the network data traffic and disk work load reach a critical point where latency becomes an issue and the VSC-3 network and disk infrastructure cannot be used anymore within a certain test setup.

3.2 Test Setup

We use real observed data from two single baseline experiments: a four-hour session with the local baseline in HartRAO called SBL500 and a one-hour intensive-style session. Since SBL500 was observed in 2-Gbps recording mode, it is a very handy experiment to evaluate the data load on the system due to the very high recording rate. Only scans with 30-sec duration are used to ensure consistency between the scans which are processed in parallel. This means that 66 scans were used for correlation. In the DiFX correlation setup, 1-sec integration times are selected along with 128 channels for the spectral resolution. The second experiment used in this performance test is a one-hour VLBI session with the new VGOS antennas in Wettzell and Santa Maria with 73 scans (session v012). This session is dedicated to an ESA project for the independent generation of Earth Orientation Parameters (EOP). Since this kind of session has an even greater value when an-

alyzed in near real-time, testing the correlation time performance for this session has important practical reasons. It is recorded with 256 Mbps and consists of mainly 20-sec scans. In the DiFX correlation setup, a 1-sec integration time is selected and 64 channels are used for the spectral resolution.

3.3 Results

In this performance test the impact of the additional workload due to simultaneously loaded data of parallel scan processing is evaluated. A clear correlation between number of scans processed in parallel and the processing time can be found (see Figure 1).

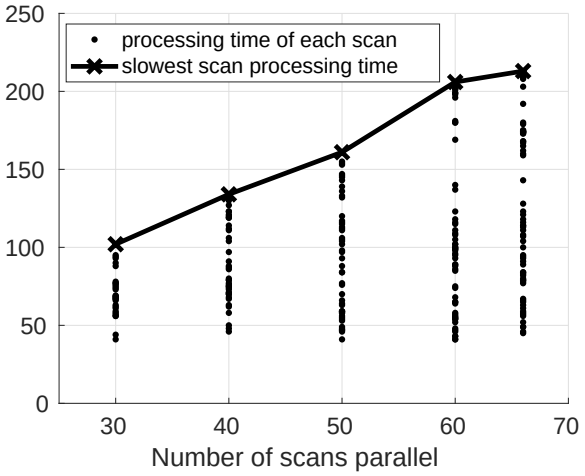

Fig. 1 Processing time. DiFX processing time on the VSC-3 with respect to number of scans which are processed in parallel using the SLURM job array.

This might be mainly due to the additional data traffic in the VSC-3 network and due to the increased reading processes on the BeeGFS file system of the VSC-3. While this test using the SBL500 session basically shows that the VSC-3 is capable of processing a high number of scans in parallel (in this case up to 66 scans), it also reveals that the total processing time increases as well. This means that the amount of data which is processed per unit time does not increase effectively. The effective throughput is characterized by the processing rate, which shows how much data is processed in one second. The processing rate for the SBL500 session is depicted in Figure 2 and shows that there is no improvement in data rates when using an increased number of scans processed in parallel.

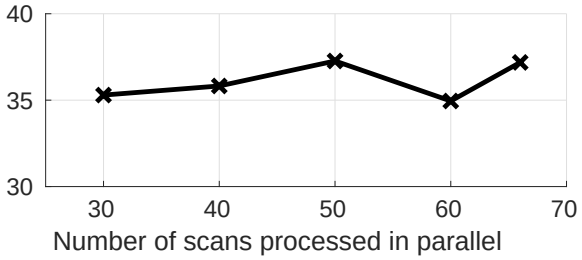

Fig. 2 Processing rate. Relation between processing rate and number of scans processed in parallel.

The data rate performance is flat with a value of around 36 Gbps between 30 and 66 scans in parallel. This means there is no increase in efficiency when going from 30 to 66 scans in parallel as almost the same amount of data is processed in the same time. However, it still needs to be evaluated at which point the data rate performance does not improve any more. There might be a point for a certain number of scans processed in parallel below 30 at which the VSC-3 stops scaling. Below this number the data rate might efficiently increase with an increasing number of scans until it reaches the 36-Gbps level. In any case, with a total rate of 36 Gbps the VSC-3 is also capable to process large VLBI networks with high recording rates in real-time. Furthermore, this test shows that the VSC-3 is capable of processing in total 990 GB (66 scans x two stations x 2 Gbps x 30-sec scans) at once without completely overloading the hard drive and the network.

Of great interest is the parallel scan strategy for intensive sessions because we want to keep the latency of the delivery of correlation results as short as possible. For this purpose we apply the parallel scan processing strategy for the v012 session and run all scans of this session in parallel. Usually, the processing time for a single scan of this certain recording setup with one node takes 16 sec for processing. Due to the small total amount of loaded data in comparison to the SBL500 session with 2 Gbps, the parallel scan processing strategy is very effective for one-hour sessions such as the v012 European intensive session. Using the parallel scan processing strategy a total processing time for the whole session of 22 sec can be achieved. With this value we completely remove the bottleneck for real-time processing of VLBI intensive sessions from the

correlation task, and other tasks are crucial for a fast provision of intensive session results like data transfer speed.

4 VLBI Data Processing Pipeline at TU Wien

Once the incoming radiation is received, digitized by the VLBI stations, and transmitted to the correlator such as the VSC-3, several processing steps need to be carried out to finally obtain geodetic parameters, e.g., station coordinates, Earth orientation parameters, and atmospheric parameters. The processing steps can be split up into four core tasks. First the digital baseband data needs to be correlated to generate so-called visibilities. Thereafter, a multiband delay is estimated out of several single-band visibilities. This process is called fringe-fitting. In the legacy S/X system a multiband delay is estimated per band (X- and S-band). However, these observations are affected by large systematic errors (several tens to hundreds of nanoseconds) including clock jumps, unresolved ambiguities, and delays due to the dispersive medium (the ionosphere). The correction of those systematic errors is carried out within the task of post-correlation processing. In this step essential database updates such as the addition of cable delay information and meteorological parameters and data flagging are carried out. Post-correlation processing yields the fundamental observations which are free of large systematic influences and then used for geodetic parameter estimation. Several individual software packages are required to carry out all the processing steps from baseband data to the final geodetic parameters. At TU Wien, we implemented DiFX for correlation, HOPS and PIMA for fringe-fitting, and νSolve for post-correlation processing in our working environment in addition to our Vienna VLBI and Satellite Software (VieVS). Currently, we use νSolve for post-correlation processing and geodetic parameter estimation to verify the correlation and fringe-fitting results because it provides valuable insights of the correlation/fringe-fitting results.

Additionally, we are working on a post-correlation processing toolbox to directly access the fringe-fitting output with VieVS. We have developed a tool to convert the fringe-fitting output to vgosDb. This tool is capable of reading fourfit binary output files (type-1, 2, 3, 4) as well as PIMA ascii output, and it produces a vgosDb file which also takes the cable delay and meteorological information from station field log files into account. It is realized mainly with Matlab and makes heavy use of the NetCDF library. A verification was carried out with the νSolve tool vgosDbMake of correlated AUA sessions and it was applied to the analysis of the European intensive sessions. Other components, which will be implemented in this post-correlation toolbox, are ambiguity correction algorithms, ionospheric delay correction and data flagging tools. With such a toolbox we can realize a more independent data flow in VieVS and we gain experience with algorithms that are necessary for the post-correlation processing tasks. Furthermore, we can better evaluate the impact of correlation/fringe-fitting models and configuration setups on geodetic parameter estimation.

5 Correlation Activities at TU Wien

Several different types of VLBI sessions were correlated, mostly for scientific geodetic and astrometric purposes, such as official IVS sessions dedicated to the VLBI SOuthern Astrometry Project (SOAP) using the AuScope array plus the local baselines at Hartebeesthoek and Warkworth. For the first time both New Zealand antennas participated simultaneously. Those sessions are correlated on a monthly basis and the results are published via the IVS. Besides the AUA sessions from the SOAP program, satellite observations with VLBI telescopes were correlated as well as other specific VLBI sessions such as the short baseline session (SBL500) using the local baseline at Hartebeesthoek. Furthermore, we carry out the correlation of one-hour Intensive sessions with the northern VGOS antenna at Wettzell and Santa Maria. These sessions represent a reasonable test case to work on an highly automated processing pipeline to provide geodetic products in near real-time. This involves methods and algorithms to process the data with minimized manual interactions on the one hand, and on the other hand it uses the total potential of transfer speed and correlation capabilities as described in Sections 2 and 3. We also want to note here that a successful comparison against the Washington correlator was carried out.

6 Conclusion and Outlook

We describe various fields of work with respect to VLBI correlation activities at TU Wien. In particular, we show data transfer capabilities of the 10-Gbps links of the VSC-3 into the GEANT network, with a tested download rate of 1.8 Gbps from a flexbuff at the University of Tasmania. A method for parallel scan processing with DiFX is described to efficiently use the processing power of a supercomputer like the VSC-3. With such a method it is possible to achieve a total correlation processing throughput of up to 36 Gbps.

To get a more independent data flow we are working on a post-correlation processing toolbox in VieVS. At this point we can carry out a data base conversion from the fringe-fitting output of fourfit and PIMA to vgosDb. Furthermore, we are correlating official IVS sessions on a regular basis from the AUSTRAL network. The correlation results of the VSC-3 were successfully compared against the correlation results of the Washington correlator, which shows no significant differences. At the moment we are in the progress of becoming an official IVS Correlation Center and we will carry out further correlation of IVS sessions on a regular basis in the future. As a university we are also interested in research topics within the correlation, fringe-fitting, and post-correlation tasks. We are highly interested in data processing of VGOS data and we plan to develop a generator for simulated digitized VLBI baseband data in the VDIF format.

In early 2019, we will gain access to dedicated storage of 1 PB and 250 private cores on a new realization within the Vienna Scientific Cluster family (VSC-4). We will carry out performance tests and efficiency analyses on the VSC-4 as well and we will work on a refined processing pipeline. Finally, we are working on spreading the correlation knowledge to all members of the TU Wien VLBI group.

Acknowledgements

The correlation has been carried out on the Vienna Scientific Cluster (VSC-3). We acknowledge the Austrian Science Fund (FWF) for supporting our work in projects SORTS (I 2204) and VGOS Squared (P 31625).

References

1. J. Böhm, S. Böhm, J. Boisits, A. Girdiuk, J. Gruber, A. Hellerschmied, H. Krásná, D. Landskron, M. Madzak, D. Mayer, J. McCallum, L. McCallum, M. Schartner, K. Teke. Vienna VLBI and Satellite Software (VieVS) for Geodesy and Astrometry. *Publications of the Astronomical Society of the Pacific*, 130(986), 044503, 16, 2018.
2. J. Gruber, J. Böhm, and J. McCallum. Geodetic VLBI Correlation at the Vienna Scientific Cluster. In R. Haas and G. Elgered, editors, *Proceedings of the 23rd European VLBI Group for Geodesy and Astrometry (EVGA) Working Meeting*, Chalmers University of Technology, 2017, ISBN: 978-91-88041-10-4, pages 140–144.
3. A.T Deller, S.J. Tingay, M. Bailes, C. West. DiFX: A Software Correlator for Very Long Baseline Interferometry Using Multiprocessor Computing Environments. *Publications of the Astronomical Society of the Pacific*, 119, 318336, 2007.

Geodetic Capabilities at the JIVE SFXC Correlator

Francisco Colomer [1,2], Mark Kettenis [1], Robert M. Campbell [1], Patrick Charlot [3], Arpad Szomoru [1]

Abstract We are implementing geodetic capabilities for the EVN SFXC correlator at JIVE, as part of the EC H2020 JUMPING JIVE project (JJ WP6). The correlator is now capable of processing complex geodetic-like schedules with many subarrays. Moreover, SFXC output is converted into Mk4 format, that includes the correlator model ("totals") and measures phase-cal values. Tests are being performed at JIVE to process geodetic VLBI data, with the main goal of improving the accuracy with which positions of non-IVS EVN stations are known.

Keywords Correlation, legacy S/X, VGOS

1 Introduction

Astronomers typically use the European VLBI Network (EVN) for self-calibrated or phase-referenced imaging, or for phase-referenced relative astrometry, and the VLBI processors at the Joint Institute for VLBI ERIC (JIVE) were developed with these priorities in mind. The data produced by the EVN software correlator at JIVE (SFXC) now contain visibility phases residual to the a priori correlator model (based on CALC10). The correlator model, although it can be linked to the output visibilities, has not yet been included in the files that the astronomer receives. The few EVN experiments that have conducted absolute astrometry have usually been correlated up to now at the MPIfR/BKG correlator in Bonn.

1. Joint Institute for VLBI ERIC (JIVE)
2. Instituto Geográfico Nacional (IGN)
3. Laboratoire d'Astrophysique de Bordeaux

The EVN also contains some telescopes that are not able to participate in standard IVS programs due to a lack of S/X receivers. There were two experiments that were able to estimate positions for these stations from single-band observations:

- TP001: A dedicated geodesy-like C-band experiment (23–24 November 2000) including Torun, JodrellBand_Mark2, Westerbork_RT7, and Onsala_85′, plus other EVN telescopes that have regularly participated in geodetic programs (Charlot et al., 2001; 2002). The estimates of the positions of these antennas in ITRF2000 derived from TP001, plus station velocities computed in NNR-NUVEL-1A (DeMetz et al., 1994), were included in the NRAO `sched` station location catalog. Positions for the MERLIN out-stations were derived from the Jb_Mark2 position via baseline solutions from the MERLIN correlator. At the time, there was a desire to repeat such an observation at K-band once Torun obtained a receiver (Tr participated in K-band sessions starting in February 2013).
- EP066: A K-band experiment (27–29 October 2009) underlying the EVN Galactic Plane Survey (Petrov 2012). It also provided a more precise estimate for the Jb_Mark2 antenna, at the time the only of the above telescopes with K-band capability. (The TP001 position carried forward with the modeled station velocity was consistent at the 1–2σ level.)

A preliminary assessment of the astrometric quality of SFXC was carried out by L. Petrov and the JIVE staff in the summer of 2015. Four stations from R1680 were re-correlated, and the combination of the standard residual visibilities plus the correlator-model "de-

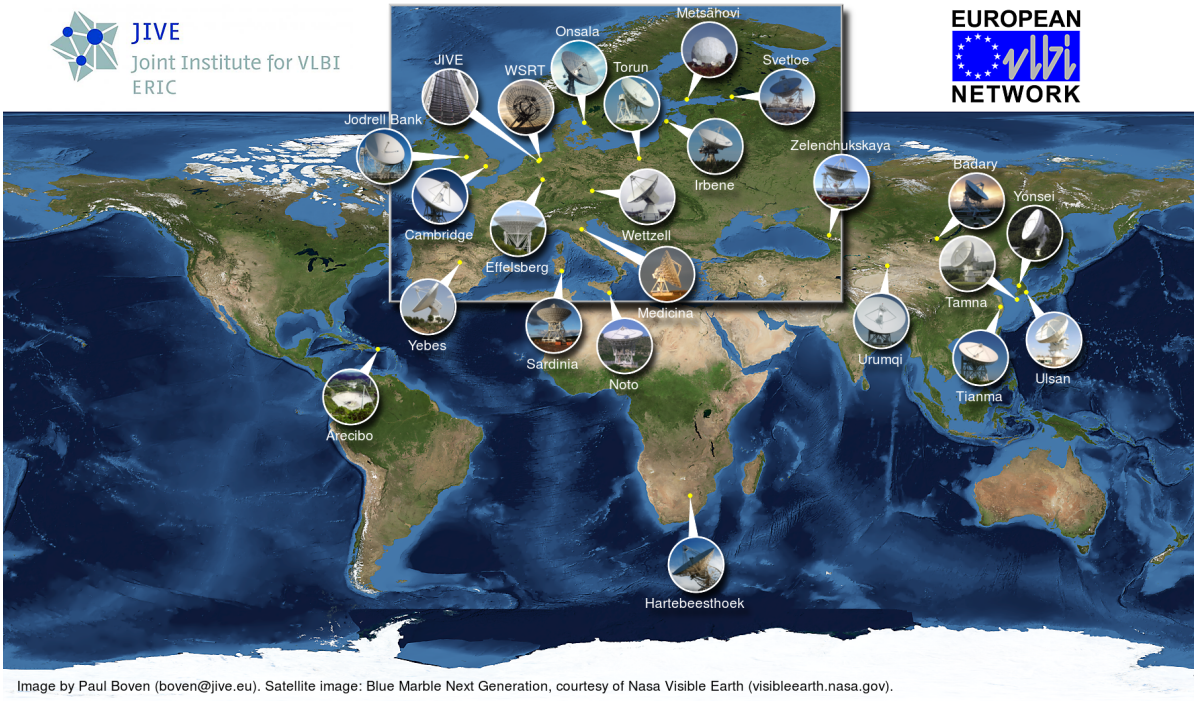

Fig. 1 The European VLBI Network (EVN) and JIVE.

lay files" was compared to the original IVS geodetic correlation. The success of this comparison motivated the pursuit of ways to incorporate model information into SFXC output in a manner that users could directly accommodate.

2 JUMPING JIVE Design & Progress

JIVE and collaborators are involved in the EC H2020-INFRADEV-2016-1 project "JUMPING JIVE" (see `http://jumping.jive.eu`), in which Work Package 6 focuses on developing geodetic capabilities for SFXC. It comprises three tasks:

1. Provide the ability to process sub-netted schedules.
2. Attach the correlator model and phase-cal information directly into the correlator output.
3. Conduct a K-band geodetic-style experiment to provide a new estimate of station positions for non-geodetic EVN telescopes—as a result of such an experiment some telescopes would obtain an empirical station velocity estimate (Jb_Mark2, Torun) and some would obtain their first position estimated directly from VLBI (e-MERLIN out-stations). There are also some telescopes that do not appear in standard global station-location catalogs (Sardinia, KVN). This experiment would provide an end-to-end test of the new geodetic capabilities. Use of K-band does preclude participation of the EVN telescopes Westerbork, Irbene, and Kunming.

The first task has already been accomplished. Since SFXC was designed for astronomy, one of the underlying assumptions in its control system was that time-range suffices as the identifier of what data to accept from the assembled telescopes to treat as a scan. This leads to ambiguity if there are multiple scans at any given time, as can be the case with sub-netting. JIVE added an optional scan label into the control file that drives SFXC, which, if present, would break any such ambiguity by allowing look-ups that pertain to the subset of telescopes involved in the specified scan and to a sub-interval within the requested time-range for each individual telescope. JIVE also modified "runjob", the GUI interface that sits between the correlator operators and SFXC, to always provide such a label in the control files it generates, consistent with the scans selected

by the operators for correlation within a job. Testing these modifications again used data from R1680, comparing correlations run with the original SFXC system after removing the sub-netting from the schedule manually (i.e., splitting the schedule into two non-sub-netted parts, and correlating each separately; for an example see Figure 2) against those run with the modified SFXC system in a single pass using the original sub-netted schedule. The new system produced the same net correlator output as did the union of the two passes of the original system (i.e., nothing missing or extraneous), with consistent values for the complex visibilities in both. (Note that the correlation of R1680 used for the preliminary assessment discussed above followed the manual de-sub-netting route.)

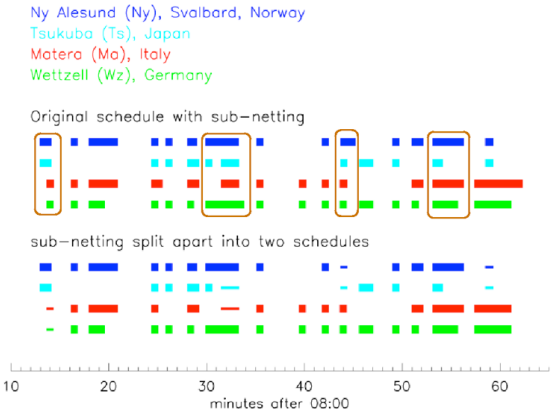

Fig. 2 Schematic of scans over one hour in R1680. Scans with sub-netting among the four antennas in the original schedule are circled in brown (top half). The width of the time-ranges per station in the bottom half denote which station/scans were split off into a separate schedule to remove sub-netting to allow correlation in the original system (thin bars split off).

Within the second task, CNRS/Bordeaux and JIVE decided on mark4 as the file format to pursue initially to allow processing of the data with the Haystack Observatory Processing System (HOPS) software. JIVE has designed and implemented programs to create and populate the mark4-file format output with visibilities from SFXC and the appropriate correlator-model information. The correlator model used by SFXC interpolates the delays computed with one-second sampling from CALC10 via Akima splines. The model is translated into the representation supported in the mark4 data format by fitting a fifth order polynomial to the

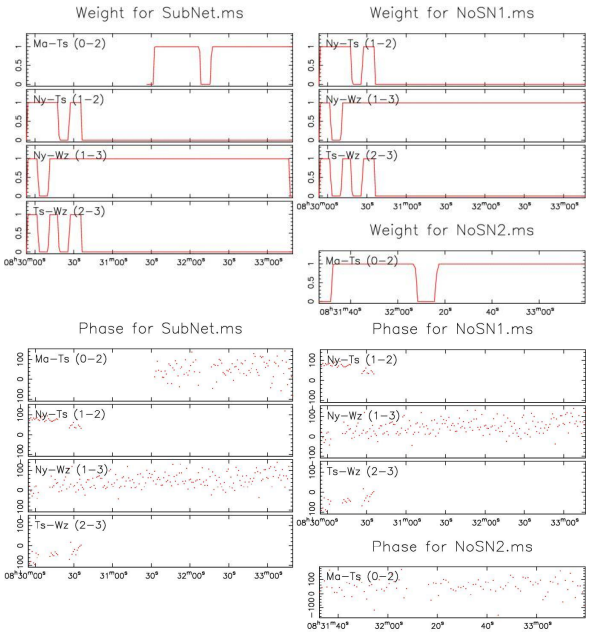

Fig. 3 Weight (top) and phase (bottom) as a function of time for an instance of sub-netting, with panels from the single-pass run in the new system to the left, and the two-pass, de-sub-netted run in the original system to the right.

results from evaluating the Akima splines at regular intervals. The difference between these two models is smaller than $1 \cdot 10^{-15} s$ at any point within an accumulation period. Phase-cal information, used to align phases in the various observed sub-bands to estimate meaningful multi-band delays without a separate fringing step, is also now included (standard astronomical analysis does not use these). Initial testing at JIVE has successfully loaded the resulting mark4-format data into HOPS and compared results to correlations of the same data run through the DiFX correlator. (The path to include model-related information in FITS-IDI tables, as had been done by the VLBA hardware correlator, is not being pursued at this time, although it is not ruled out for the future.)

The geodetic-style EVN experiment forming the basis of the third task has been proposed and observed (EC065; 13–14 June 2018). During the course of preparing the observing schedule, some limitations in the sub-band tunability were uncovered in the e-MERLIN out-stations (two sub-bands of 64 MHz, such that the separation between them is a multiple of 64 MHz) and KVN stations (limited to separations of integral steps of the combined LSB+USB

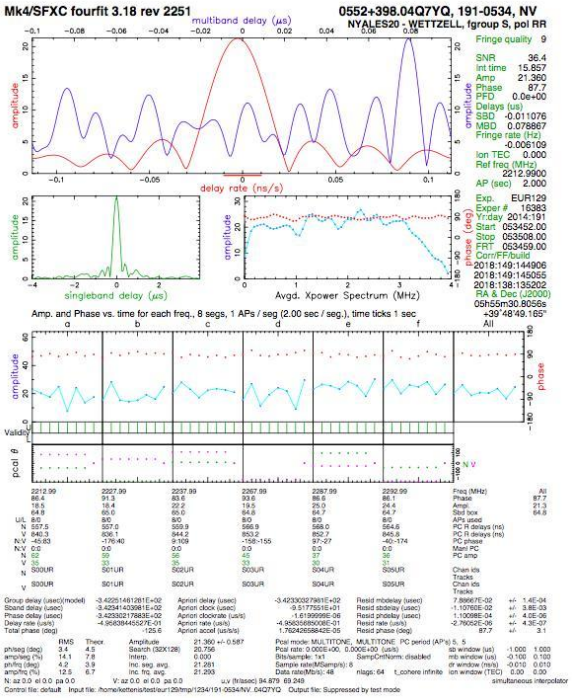

Fig. 4 HOPS fourfit plot of a scan from geodetic observation EUR129 re-correlated with SFXC.

bandwidth), which affected the freedom to sculpt the delay-response function. Initial feedback from the stations suggests that only one KVN telescope was able to participate, and Tianma/Urumqi were both unable to join because of Chang-E4 obligations. High winds may have affected pointing at the UK telescopes (Jb_Mark2, four e-MERLIN out-stations).

3 Future Prospects

A validated path for SFXC to provide "totals" in its output data in a standard fashion would lower the threshold to EVN experiments pursuing absolute astrometry choosing to correlate at JIVE. For such purpose, providing the correlator model in the default FITS-IDI output would be essential. Since the representation of the correlator model is very similar to the representation used in the mark4 data format, providing this information should be relatively easy. An approach to attach the required tables using the Python PyFITS module is being considered. This approach has been used sucessfully to attach system temperature measurements and weather information to FITS-IDI files.

Future broadband data, in VGOS or in astronomical observations, will have to properly estimate the ionospheric contribution. Current developments in radio astronomy (such as "RINGS", WP7 in EC H2020 project RADIONET, see `https://www.radionet-org.eu`) provide interesting synergies that should be explored.

Acknowledgements

This research is supported by the "JUMPING JIVE" project, funded by the European Unions Horizon 2020 research and innovation programme under grant agreement No. 730884.

References

1. Charlot, P., Campbell, R., Alef, W. et al. 2001, "ITRF2000 Positions of Non-geodetic Telescopes in the EVN", in Proc. 15th WMEVGA, eds. D. Behrend and A. Rius, Institut d'Estudis Espacials de Catalunya, CSIC, Barcelona, p. 194.
2. Charlot, P., Campbell, R., Alef, W. et al. 2002, "Improved Positions of Non-geodetic EVN Telescopes", in Proc. 6th EVN Symposium, eds. E. Ros, R.W. Porcas, A.P. Lobanov, and J.A. Zensus, MPIfR, Bonn, p. 9.
3. DeMets, C., Gordon, R.G., Argus, D.F., & Stein, S. 1994, GRL, 21, 2191.
4. Keimpema, A, Kettenis, M.M., Pogrebenko, S.V. et al. 2015, "The SFXC software correlator for very long baseline interferometry: algorithms and implementation", Experimental Astronomy, 39, 259.
5. Petrov, L. 2012, "The EVN Galactic Plane Survey—EGaPS", MNRAS, 419, 1097.

Washington Correlator Status 2018

Andrew Sargent [1], David Hall [1], Phillip Haftings [1], Matthew Hardin [2], Khalil Suliman [2]

Abstract This report summarizes the activities of the Washington Correlator for the IVS General Meeting. The Washington Correlator primarily supports Earth Orientation and astrometric observations by providing correlated output of IVS VLBI experiments.

Keywords Correlator, WACO

1 General Information

The Washington Correlator (WACO) is located at and staffed by the United States Naval Observatory (USNO) in Washington, DC, USA. The correlator is sponsored and funded by the National Earth Orientation Service (NEOS), which is a joint effort of USNO, NASA and NOAA. Dedicated to processing geodetic and astrometric VLBI observations, the facility spent 100 percent of its time on these sessions in 2017 and 2018. All of the weekly IVS-R4 sessions and all of the daily IVS-INT01 Intensives were processed at WACO. Additionally, WACO correlated some IVS-CRDS and IVS-CRF sessions, as well as daily VLBA Intensive sessions. The facility houses the WACO DiFX correlator.

2 Activities

The correlator staff is primarily responsible for the IVS-R4 and the IVS-INT01 Intensive sessions. From November 2017 through April 2018, WACO was responsible for correlating both the IVS-R1 and IVS-R4 sessions while the Bonn Astro/Geo Correlator worked through the correlation of the CONT17 sessions. In total, WACO correlated 21 IVS-R1 sessions starting with R1818 and through R1839 until Bonn resumed correlation of IVS-R1 sessions.

Daily Intensive observations from Kokee Park and Wettzell are routinely transferred via e-VLBI. 24-hour sessions from AGGO, Badary, Fortaleza, HartRAO, Hobart, Ishioka, Katherine, Kokee Park, Matera, Medicina, Noto, Ny-Ålesund, Urumqi, Warkworth, Wettzell and Wettzell North, Yebes, Yarragadee, and Zelenchukskaya are also transferred to USNO, with about 35% of the data shipped on Mark 5 diskpacks and the remainder transferred over high-speed networks.

Table 1 Experiments correlated as of 1 August 2018.

Experiment	2017	2018 (Scheduled)
IVS-R4	50	28 (52)
IVS-INT01	233	131 (231)
IVS-R1	4	17
IVS-CRDS	3	2 (5)
IVS-CRF	0	1 (1)

WACO continues the testing and repair of the Mark 5 modules and has started efforts to stand up Mark 6 units and diskpacks. WACO has four Mark 6 units which are usable but not yet online. Out of an initial 128 Mark 6 diskpacks, 32 were shipped to Kokee Park. The correlator staff conditioned the remaining 96 diskpacks and started shipping modules out in late 2017.

1. United States Naval Observatory
2. Universities Space Research Association

3 Current Setup

WACO has a dedicated 1 Gbps line for e-transfers and a combined internal and external disk space of around 545 TB to store all data. For incoming data, either e-VLBI or diskpack, 180 TB of storage space was recently added to bring the externally accessible disk space to around 278 TB. In the internal network, WACO has a lustre file system used for correlation with 192 TB and another 79 TB of storage space for backups and local use.

The correlator is made up of several multi-core processing nodes with a combined total of 512 single-threaded cores. Each node has a high-speed fiber line to the lustre file system for data processing and an ethernet line for node management. Additional and identical nodes are used for all post-correlation processing.

Table 2 lists software WACO uses in production. DiFX is used to correlate all IVS data, and WACO uses HOPS and SKED for post-correlation processing. Calc/Solve and nuSolve are used to generate both Mk III and VGOS-style correlation databases, respectively. Tsunami and jive5ab are used for e-transfer of VLBI data. In addition to the versions of the software listed in Table 2, WACO maintains older versions for legacy support.

Table 2 Software used at WACO as of 1 August 2018.

Software	Version	Used for
DiFX	2.4	Correlation
HOPS	3.17	Fringing
SKED	2018Jul05	Predicted SNR
Calc/Solve	2018Jul13	V001 Database Creation
vgosDbMake	0.5.2	V001 Database Creation
Tsunami	v1.1 build 42	e-transfer
jive5ab	2.8.1	e-transfer

A performance test was conducted using the WACO correlator in early 2018. Figure 1 shows the usual plot of correlation time decreasing as processing power is increased. The use of more processing cores is especially advantageous for multi-station scans, but eventually correlation speed becomes limited by disk IO speed over pure processing power.

4 Hardware Refresh

WACO is in the process of configuring a new software correlator which is expected to be up and running in the near future. The current DiFX correlator was configured in 2014, and it can take four to six hours to correlate a typical IVS-R4 experiment. The new correlator will at least double the speed of the current setup and will consist of upgraded hardware, more lustre system storage hosts, and more processing nodes which can be used for simultaneous correlations. Upgraded backend machines and workstations are in the works, as well as a smaller correlator configured for testing purposes. Finally, the high-speed internet line is planned to be upgraded to around 3-4 Gbps.

5 Staff

The Washington Correlator is under the management and scientific direction of the Earth Orientation Department of the U.S. Naval Observatory. As of November 2016, the VLBI division is now fully staffed with two new astronomer positions and a contract for two FTE correlator scientists.

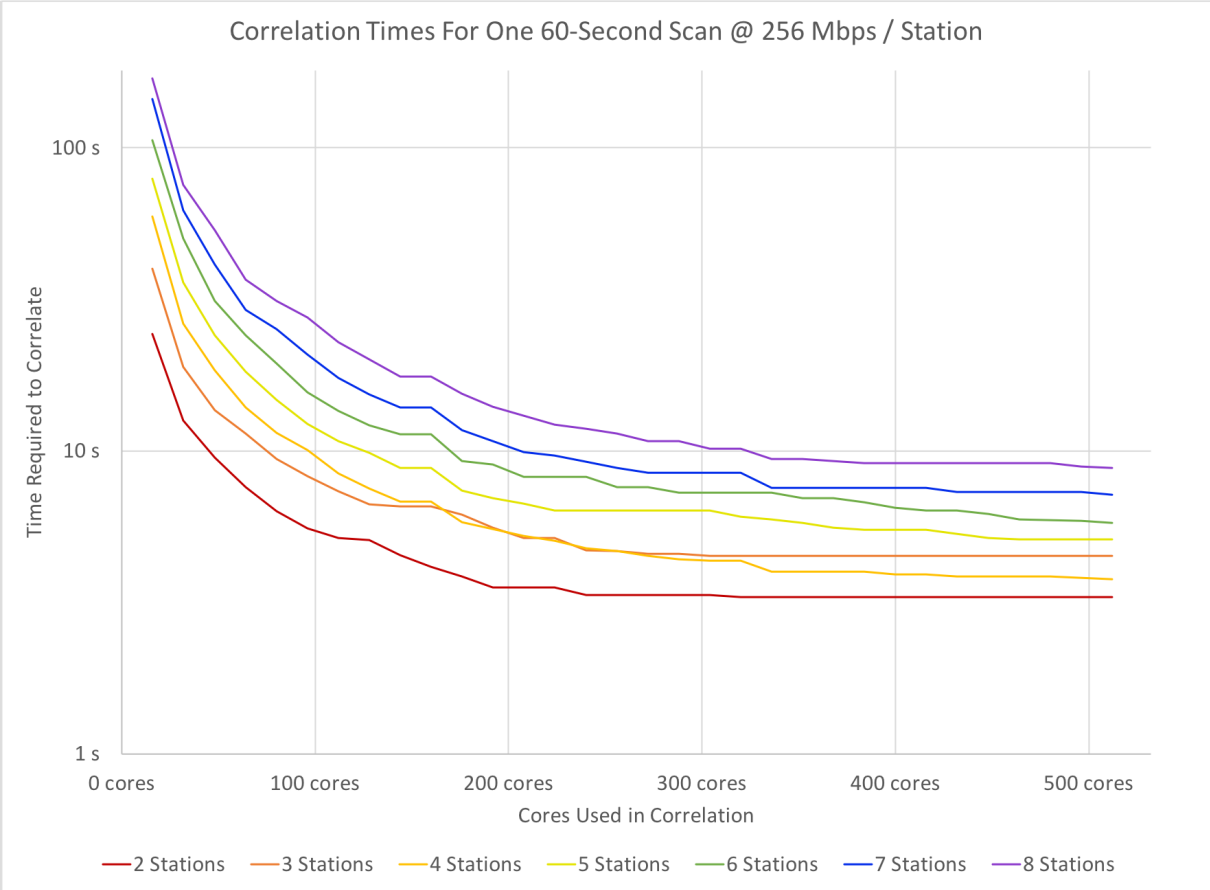

Fig. 1 WACO Performance Test

An S/X Compatible VGOS System for the AuScope Array

Jamie McCallum [1], Lucia McCallum [1]

Abstract Work is underway of upgrading the AuScope VLBI Array to VGOS. This is done by replacing the current S/X legacy observing chain with the new VGOS receivers on the existing telescopes. As of now, the conversion to VGOS will mean that the AuScope telescopes cannot contribute to the legacy VLBI, leaving a major gap in the global network. In this contribution we report on our efforts to support legacy S/X VLBI using the new VGOS receiver at the Hobart 12-m telescope. Despite some existing problems with the new back-ends as well as in antenna sensitivity, in principle the legacy observing mode can be covered. We report on a few test experiments, where data collected with the VGOS receiver at Hobart was successfully correlated and processed, revealing promising results. Details are given on the observing setup, the adopted processing chain and first results. Following those initial tests, a more extensive test series, the AUM (Australian mixed-mode sessions), was initiated. Some details about this program are provided.

Keywords AuScope VLBI Array, VGOS, mixed-mode operations, AUM sessions, AUSTRALs

1 Introduction

The AuScope VLBI array [1] consists of three 12-m telescopes, which were built as a dedicated geodetic facility. Compared to current VGOS specifications, the AuScope telescopes are of a slow type, with slewing speeds of fives respectively 1.5 deg/s in azimuth and elevation. The telescopes in Hobart (Hb), Katherine (Ke), and Yarragadee (Yg) have been operating with S/X receivers using recording modes of up to 1 Gbps since 2012. Since 2014, the telescopes have been regularly participating in global and regional IVS sessions, producing one of the most dense time series of VLBI telescopes.

1. University of Tasmania, Australia

1.1 VGOS Upgrade

While the AuScope VLBI array had already originally been designed for VGOS, the actual receiver upgrade began in 2015. Starting in Hobart, a prototype wideband feed was installed, tested, and improved with the final version of the feed installed in mid-2017. The wideband receiver was designed and built by Callisto, using Stirling cycle cooling. It is equipped with the QRFH feed.

The new VGOS system, which is planned to be installed at all three sites, has evolved to a three frequency band system using a DBBC3 and Flexbuff for the back-end. As illustrated in Figure 1, signals above 3 GHz are sent through a high-pass filter and then via the RF over fiber (RFoF) link to the control room. The frequencies below 3 GHz are mixed with a 1,900-MHz local oscillator signal and sent via the old coax connection.

In the control room, the VGOS signal is split and, using 4-GHz filters, can be input into the DBBC3. Our DBBC3s have six inputs which will be used for three frequency bands at dual polarization. Using the DDC mode, this allows for full VGOS compatibility. In Figure 2, the three overlapping 4-GHz-wide bands are shown.

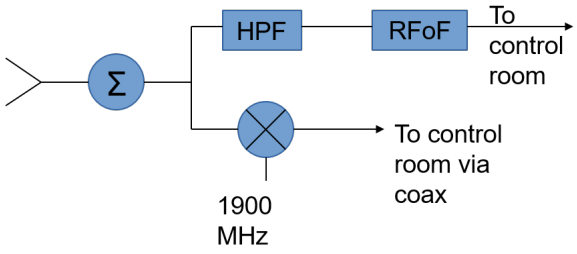

Fig. 1 Signal chain of the new VGOS system installed at Hobart. While the VGOS signals are sent through a high-pass filter (HPF) and are transported at sky frequencies via a fiber connection (RFoF) to the control room, signals below 3 GHz are down-mixed and sent via the old coax cable to the control room.

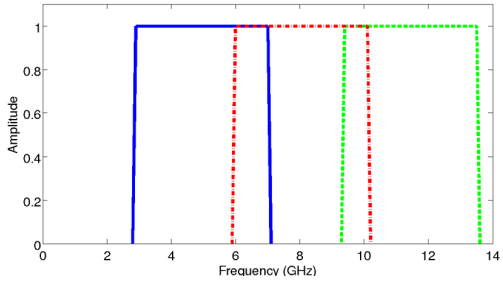

Fig. 2 For AuScope VGOS, we use three input frequencies at 4 GHz into the DBBC3. Using the DDC mode, this allows for full VGOS compatibility.

1.2 One or the Other

Contrary to most other VGOS stations, where new telescopes are built at existing IVS sites, in the case of AuScope the VGOS telescopes will replace the legacy ones. This means that legacy and VGOS operations cannot be done at the same time. Moreover, the implementation itself as well as the necessary testing of the new VGOS chain causes significant down-times of the Australian stations, as shown in Figure 3 for Hb.

The either-or situation puts us in a similar position as Ishioka. With global VGOS operations just taking off (at a current cadence of 2–4 weeks, with geodetic results pending), the question to be asked is when is the right time to upgrade the remaining two telescopes (Ke and Yg). In particular, since as soon as we start this upgrade, nearly the whole Australian continent will disappear from the legacy operations. This leaves a considerable gap in the global network and will without doubt negatively impact the geodetic products of VLBI. The core mandate of the AuScope VLBI

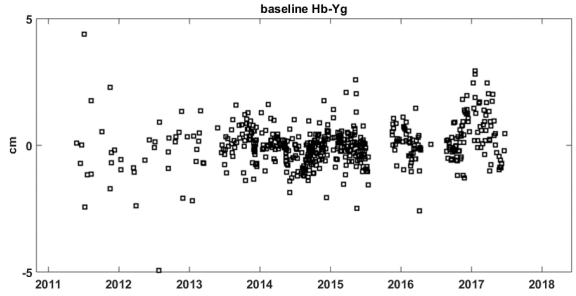

Fig. 3 Starting in 2014, the Hb–Yg baseline used to be one of the most dense baseline time series in VLBI. Multiple tests of the VGOS prototype receiver in 2015 and 2016 as well as the final installation in 2017 cause significant interruptions. Data source: CCIVS.

network is to contribute to global geodesy and positioning, so how will this mission be served best?

2 Idea

Our idea to overcome the issue of too much down-times in the transitioning phase are mixed-mode operations. This means, trying to operate the new VGOS receivers in legacy mode.

Are those two systems compatible?

- **Frequency coverage**
  The nominal operating range of the QRFH feed is approx. 2–14 GHz. Despite the usual problem of severe RFI in Hobart—which make local Ho–Hb tests impossible—sensitivity in S-band appears reasonable. The legacy X-band is covered by our 6–10 GHz filter and we achieve reliable fringes in the Ho-Hb baseline. For recording X-band, we only need two (for dual-polarization) inputs for the DBBC3.[1]
- **Polarization**
  While in legacy VLBI we typically use the right-hand-circularly polarized signal (RCP), the VGOS signal comes in two linear polarizations. Hence, one needs to handle the cross-polarization products to get full sensitivity or take a $\sqrt{2}$ loss in sensitivity.
- **S-band signal**
  In our system, the S-band signal is down-converted after the LNA and sent over the coax, while the

[1] This enabled us to test the mixed mode despite the fact that not all six DBBC3 inputs were fully functional at that time.

3–14 GHz signal travels over the fiber connection to the control room. If we want to use and combine both frequencies, we have to take the possibility of different and varying cable delays into account.

3 Test Observations

In May 2018, a few tests of this mixed-mode observations were done. AUSX01 ran over a weekend, using a simple automated schedule, cycling through a list of strong sources with Hb, Ke, and Yg. Ke and Yg used the 1-Gbps AUSTRAL mode [2], with 16x16 MHz channels and S-band restricted to 2.2–2.3 GHz. Hb recorded three VDIF streams using 32-MHz channels. The X-band was recorded through the DBBC3 and the S-band through a DBBC2 using the DDC mode with v105E firmware. Due to a lack of automated scripts, the VEX entries for Hb were created by hand. The observations themselves were steered through the FS plus some additional scripts.

The correlation was performed in one pass, using zoom bands for Hb. The subsequent fringe fitting was done in Fourfit. Figures 4 and 5 show the results of the fringe fitting for S- and X-band, respectively.

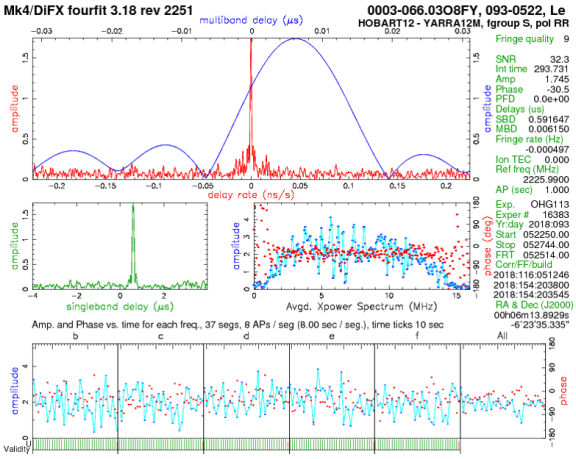

Fig. 4 Fourfit output of AUSX01 for S-band on the Hb–Yg baseline. An SNR of 32 was achieved on a five-minute scan of 093-0522.

We achieved good fringes in both bands and all polarization products. As a comment, for AIPS compatibility the X and Y polarizations at Hb are labelled as

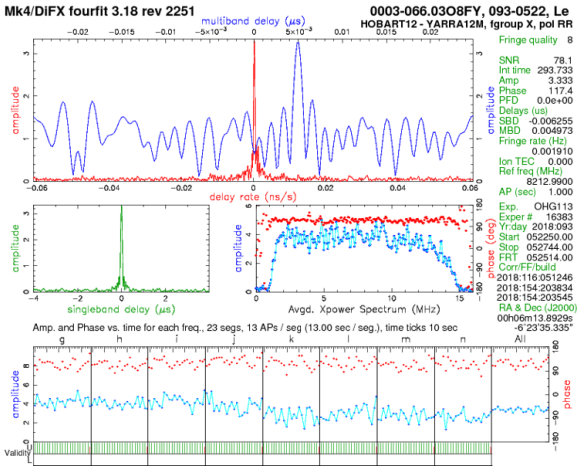

Fig. 5 Fourfit output of AUSX01 for X-band on the Hb–Yg baseline. An SNR of 78 was achieved on a five-minute scan of 093-0522.

R and L. A manual phase calibration correction was applied to each polarization separately.

In a next step, the different polarization products were then combined in Fourfit using XR + YR with the results further compiled into a database for analysis in NuSolve. Due to the different signal paths for the S- and X-band signal at Hobart (as mentioned above), we found a large (approximately 0.5 μas) offset between the two bands. While it would be possible to remove such offset as an a priori delay offset in the fringe fitting step, in this test we let it soak up in the clock model. Besides this, further inspection of the results did not reveal any obvious deficiencies.

In a second test, Hb12 *shadowed* the last half of the r1840 schedule. Again, we recorded 32-MHz channels and used zoom bands in correlation. Due to a hardware limitation in the DBBC2, no S-band channels above 2.3 GHz were observed. If those are then absent in the VEX file, this caused difficulties in the channel labelling in difx2mark4. In order to resolve this and ensure consistent labelling (e.g., a-f for S-band and n-g for X-band), *fake* channels had to be added in the VEX file.

In a final test, Hb12 was scheduled in AUA044 as a tag-along station. This time the new DBBC3 DDC_L firmware was used, allowing to observe matching 16-MHz channels at X-band. As previously, S-band was recorded using the DBBC2 in DDC mode. Unfortunately, there were power failures just before and during the experiment and a patching error for

the S-band data. While X-band fringes were found, S-band data was not successful. However, this test was useful in confirming a working DDC_L mode, which will avoid the issue of unnecessary excess data in the future.

4 Summary

The either VGOS or legacy situation for the AuScope VLBI array poses a significant risk of maintaining a good geodetic measurement history. Establishing a working mixed operation mode was identified as a solution to this situation.

In this contribution we describe a few tests of S/X compatibility that were performed using the new VGOS receiver and signal chain installed at Hobart. We found that the correlation of a single station with a linear polarized feed against the legacy RCP stations is straightforward. The fringe-fitting in this case seems to yield stable results.

5 Outlook

While the results presented above are motivating, we are aware that further, more detailed investigations will be necessary before a mixed-mode station could for example be added into an R1/R4 session in order to maintain good global results.

For this reason, the AUM sessions are currently being conducted. A series of ten 24-hour experiments have been scheduled from July through September 2018 (see Table 1). The observation setup is similar to AUA044, using Ke and Yg in legacy and Hb in VGOS mode.

Table 1 AUM session schedule.

sess name	date	time	network	scheduler	correlation
AUM001	Tue Jul 31	17:30	HbKeYg	VIEN	UTAS
AUM002	Wed Aug 01	18:00	HbKeYg	VIEN	UTAS
AUM003	Wed Aug 08	18:00	HbKeYg	VIEN	UTAS
AUM004	Wed Aug 15	18:00	HbKeYg	VIEN	UTAS
AUM005	Sat Aug 18	16:00	HbKeYg	VIEN	UTAS
AUM006	Sun Aug 19	16:30	HbKeYg	VIEN	UTAS
AUM007	Sat Aug 31	19:00	HbKeYg	VIEN	UTAS
AUM008	Wed Sep 12	18:00	HbKeYg	VIEN	UTAS
AUM009	Wed Sep 19	18:00	HbKeYg	VIEN	UTAS
AUM010	Mon Sep 24	16:30	HbKeYg	VIEN	UTAS

First data of these experiments has arrived in Hobart and correlation is underway. These experiments are further a great motivation to improve the scheduling and implementation of VGOS observations as well as improving the sensitivity and reliability of the new VGOS system in Hobart. Hopefully we can report on successful results soon.

Besides that, we are also carrying out tests to improve the performance of the receiver system and we intend to use the AUM series to provide a cross-check on the results.

References

1. J. Lovell et al., “The AuScope geodetic VLBI array”, Journal of Geodesy, 87:527-538, doi:10.1007/s00190-013-0626-3, 2013.
2. L. Plank et al., “The AUSTRAL observing program”, Journal of Geodesy, doi:10.1007/s00190-016-0949-y, 2016.

Half the Time: An Overview of the LBO-USNO Timeshare Agreement

Megan C. Johnson[1], Alan Fey[1], Bryan Dorland[1], Christopher Dieck[1], Nicole Geiger[1], Lucas Hunt[1,2], John Spitzak[1,3]

Abstract We present an overview of the Long Baseline Observatory (LBO) — United States Naval Observatory (USNO) 50% timeshare agreement. The USNO has contributed 50% of the operations costs to the LBO in exchange for 50% of the time on the VLBA since January 2017. The USNO uses the majority of this time allotment for observations related to Celestial and Terrestrial Reference Frame work and Earth Orientation Parameters, including maintenance and improvements in preparation for the upcoming release of the ICRF3, source structure studies, and daily Intensive and geodetic observations. In addition, USNO supports scientific research observations related to our mission objectives. Here, we present a summary of our supported projects on the VLBA and our thoughts and ideas for potential future applications of the VLBA.

Keywords VLBA, LBO, USNO

1 Introduction

The Very Long Baseline Array (VLBA) is a radio interferometer that consists of ten identical antennas, eight of which are placed across the continental United States; one antenna is located on Mauna Kea (MK) in Hawai'i, and one antenna is on St. Croix (SC) in the Virgin Islands. The array contains a maximum baseline length of 8,611 km (MK–SC), which makes it a unique and highly beneficial instrument for geodetic and astrometric observations.

1. United States Naval Observatory
2. George Mason University
3. Computational Physics Incorporated

Upon announcement by the National Science Foundation that it would be divesting in the VLBA, the National Radio Astronomical Observatory (NRAO) financially separated the VLBA from its other assets, which in turn resulted in the formation of a separate, independent management facility named the Long Baseline Observatory (LBO), whose sole purpose was to manage the VLBA. The LBO was launched on 1 October 2016 and actively sought funding partners to sustain the VLBA's scientific endeavors. Due to the unique capabilities of the VLBA and its abilities to meet mission requirements, the United States Naval Observatory (USNO) entered into a 50% timeshare agreement beginning on 1 January 2017. In exchange for 50% of the funding costs of the VLBA, the USNO is given 50% of the time on the telescope. In this paper, we provide an update of the LBO—USNO 50% timeshare agreement.

2 USNO Mission Goals and VLBA Observations

The USNO is one of the official data Analysis Centers for the International VLBI Service for Geodesy and Astrometry (IVS) and, as such, contributes data products to the VLBI community. In addition, the USNO has requirements to contribute to the maintenance and improvement of the Celestial Reference Frame (CRF), Earth Orientation Parameters (EOP), and daily measurements of UT1−UTC. Thus, long baseline radio interferometry is essential to meet our mission objectives. The USNO uses the 50% timeshare allocation on the VLBA primarily for meeting mission requirements

and uses three sets of operational observations to accomplish these goals.

The first series of observations called "daily Intensive observations" are used to measure UT1−UTC from group delay measurements on a single VLBA baseline. These data are obtained at a cadence offset from the IVS daily Intensive observation series. USNO uses the primary VLBA baseline, Mauna Kea–Pie Town (MK–PT) with backup stations St. Croix (SC) for MK and Los Alamos (LA) for PT, thus providing secondary baselines MK–LA, PT–SC, and LA–SC. During the St. Croix outage caused by hurricane Maria, USNO implemented a tertiary backup baseline utilizing the maximum continental extent of the VLBA, which is the Hancock–Owens Valley (HN–OV) baseline. These daily Intensive observations are supplemented by a second operational series called the "fortnightly observations" that are made once a fortnight, i.e., bi-weekly, for the purpose of monitoring baseline quality and stability. The fortnightly series uses all six VLBA antennas that participate in the daily Intensive observations. Finally, the third operational series that USNO supports on the VLBA is called the "RDV 24-hour EOP observations." This series is primarily for making geodetic measurements to produce state-of-the-art EOPs, but the observations have also been maximized for producing images of the sources used in all of our operational observations. The RDV experiments utilize the entire VLBA plus several other VLBI antennas for high sensitivity and good uv-coverage for imaging.

USNO also supports observations for CRF, EOP, and UT1−UTC research. A few examples of these types of observations are shown in Table 1. The project led by Dr. Aletha de Witt contributed ∼99% of the K-band CRF data for the ICRF-3 that was recently adopted by the IAU in August 2018. The S-/X-band CRF observations led by co-principal investigators Dr. David Gordon and Dr. Alan Fey improved the astrometric quality for more than 4,000 sources. These observations are also being used to produce images that will be made publicly available in the USNO Radio Reference Frame Image Database, which is currently being redesigned. The CONT17 observations are part of a large undertaking by the IVS community to produce the most accurate EOPs available. These observations occurred at the end of November 2017 and ran continuously for 15 consecutive 24-hour days.

Finally, USNO permits a small fraction of the time allocation for basic astronomical research. These observations are for USNO staff astronomers to enhance their basic scientific research programs. There are a myriad of observations that USNO has supported under this category, although the total amount of time observed for these programs constitutes less than 5% of the total observing time obtained to date.

Table 1 USNO VLBA time allocation summary from January 2017 through May 2018.

Project Name	Project Type	Total Hrs Requested	Total Hrs Observed
Daily Intensive Obs	Operational	750.75	894.27[a]
Fortnightly Obs	Operational	36	33.81
RDV 24 Hour EOP Obs	Operational	216	216
K-band CRF Obs PI: Aletha de Witt	CRF Research	624	471.63[b]
S-/X-band CRF Obs PIs: David Gordon/ Alan Fey	CRF/EOP Research	720	621.72
CONT17 PI: David Gordon	EOP Research	360	358.69
Other Astronomical Obs	Basic Research	142	104.97
Total Allotment = 3523.6 hrs	**Total Hours:**	**2848.75**	**2701.09**

Notes: [a]The additional hours observed are for testing a tertiary backup baseline, HN-OV. [b]Backlog of hours from CONT17, bad weather. In addition, May hours are not included.

3 USNO Time Allocation Process

USNO is in agreement with the LBO to not become a back door for astronomical observations that would otherwise belong under the open skies VLBA proposal mechanism. Thus, to ensure the scientific integrity of the telescope, USNO has devised an internal Telescope Allocation Committee (TAC) that meets monthly to review all proposals for time on the VLBA through the USNO 50% timeshare allocation. Figure 1 outlines the sequence for obtaining time on the VLBA through USNO. All projects that are executed through the USNO 50% timeshare allocation are required to submit an observing proposal. Proposals are due by the first of the month. The TAC meets on the third Tuesday of the month, and the outcome of the proposal is then communicated to the authors within a few days of the

TAC meeting. If the proposal is successful and time is granted, then the project is included in the observation request that is sent to the LBO on the last day of the month. The observations will be executed in the month plus one following the observation request. For example, the observation request submitted on the last day of May 2018 requests time for the month of July 2018. This gives the LBO one entire month to fold the USNO observations into their dynamical scheduling system.

The USNO TAC developed a ranking system for proposals, which gives a higher ranking to USNO mission-related projects over other types of research proposals. USNO does support external proposals that have USNO mission-related objectives like the K-band observations that are entirely externally led. For any questions about applying for time on the VLBA through the USNO 50% timeshare allocation, or to request the USNO proposal form, readers can contact the first author at megan.johnson@navy.mil.

Fig. 1 Schematic of the observing cadence for obtaining VLBA observations through the USNO 50% timeshare allocation.

4 VLBA Updates and Future Prospects

Due to the success of obtaining financial partners like USNO, the VLBA will be folded back under the NRAO umbrella later this year. This will bring a renewed stability to the future of the VLBA, which will hopefully provide a solid path to upgrading the telescope. The extent to which such an upgrade will be accomplished is not yet known; however, there are already encouraging signs that an upgrade may be possible. One such sign stems from the recent US congressional agreement to fund refurbishment to the SC station that was damaged during hurricane Maria. Under this funding provision, the SC station will be given fiber optic connections along with rust mitigation, painting of the antenna structure, and an EPA-compliant generator. With fiber optic connections enabled at the SC station, USNO looks to implement a three-station daily Intensive observation with MK, PT, and SC that will make use of the longest baseline extent of the VLBA and simultaneously mitigate the need for multiple backup baselines.

Some of the other upgrade possibilities for the VLBA include upgrading to wide bandwidth capabilities, installing new wide-band receivers, and installing fiber optic connections to all ten antennas. USNO is interested in expanding CRF research into higher frequencies as source structure is expected to be more point-like at these higher frequencies which in turn would produce a more accurate CRF. If wide bandwidth capabilities are implemented, then a set of ten new Ka-band receivers with frequency coverage from 26.5 – 40 GHz would be optimal for this area of CRF research. USNO is also interested in exploring new wide bandwidth X-band receivers similar to those currently on the Jansky VLA, possibly with a dichroic to the C-band receiver or a dichroic from the Ka-band receivers, if both are feasible to fund. Installing fiber optic links to all ten antennas is another important upgrade feature that USNO is interested in as this will enable fast data transfer rates and therefore enable correlation in a more timely manner.

5 Summary

In summary, the LBO–USNO 50% timeshare agreement has been mutually beneficial to the VLBA and the USNO. The USNO values the capabilities of the VLBA and recognizes its importance to the astrometric and geodetic community. The prospects for the future of the VLBA look promising, and we look forward to seeing what the future brings.

Current Activities and Plans of the AOV - Asia-Oceania VLBI Group

Lucia McCallum [1], Takahiro Wakasugi [2], Fengchun Shu [3]

Abstract Founded in 2014, the Asia-Oceania VLBI group for Geodesy and Astrometry (AOV) has been active in fostering collaboration and pushing progress in our region. Since 2015, 18 AOV sessions have been scheduled, observed, correlated, and analyzed by AOV member institutions. Furthermore, 12 sessions follow in 2018. Two AOV meetings have been held in the region, and we have also undergone a successful re-election of the AOV representatives, the Chair and Secretary positions, in 2017. In this contribution we report on the recent activities within the AOV, current topics, and plans for the future. An overview of the AOV sessions is given, including a summary of the aims and results. A proof for the success of the AOV initiative is a number of small collaborations in correlation and VGOS testing. Details on these projects are provided. Overall, the aim of this contribution is to inform the IVS community about our activities and invite interested colleagues to join the AOV in individual projects, observations, and meetings.

Keywords Asia-Oceania VLBI group, AOV sessions

1 Introduction

Founded in 2014, the Asia-Oceania VLBI group for Geodesy and Astrometry (AOV) has been active in fostering collaboration and pushing progress in our region. The motivation for running dedicated AOV sessions is to maintain the knowledge of scheduling and correlation amongst the member groups. Finally, the similar time zones and reduced spatial distances may help to allow more frequent meetings and visits amongst collaborators, also enabling more students with limited travel budgets to experience international liaisons, which we consider the backbone of global VLBI. That said, we also invite interested stations and people outside the AOV region to join the AOV sessions and activities.

Fig. 1 AOV station network.

2 AOV Sessions

The first AOV session took place in 2015, as part of the IVS observing program. The primary motivation for the AOV sessions is to keep and extend the skill set within the institutes of the AOV. This includes the capability of generating new observing modes and frequencies that are compatible for all participating stations and frequency ranges, on the one hand, and making optimal use of modern hardware on the other. The

1. University of Tasmania, Australia
2. GSI, Japan
3. Shanghai Astronomical Observatory, China

scheduling of these sessions is split between three institutes (GSI, SHAO, and UTAS), and the correlation amongst two (GSI and SHAO).

Initially at a cadence of six sessions per year in 2015, 2016, and 2017, in 2018 the number was increased to one session per month. As visible in Figure 2, a high of 13 participating telescopes was reached in AOV010. Subject to compatibility of all stations, new AOV modes were developed with most AOV sessions now being observed at a 1 Gbps mode, with 512 MHz channels at two bit sampling.

While conducting the experiments alone is one of our aims, the sessions do follow specific targets. In principle one can distinguish between geodetic, astrometric and research and development (R&D) sessions. Suggestions for the latter are welcome at any time.

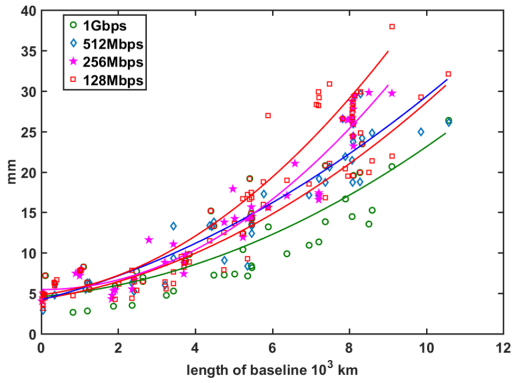

Fig. 3 Simulated baseline length repeatabilities for AOV schedules. Different colors and symbols represent different observing modes used in the sessions. The solid lines are fitted second-order polynomials. Despite variations in the station network that may affect this simulated comparison, we expect improved results using the 1 Gbps mode (shown with green circles).

2.1 Results

- **Geodesy**
  The geodetic sessions are scheduled with the aim of achieving a high number of observations, but also accounting for the large variety of telescopes in the network. While the Antarctic station Syowa or the more astrometrically used telescopes of the VERA network have restrictions in available bandwidth or recording, pairing up small and fast (e.g. AuScope, Ishioka) telescopes with large and sensitive but rather slow ones (e.g. Hobart26, Urumqi, Tianma65) is not a trivial task. A few hardware upgrades and the development of new observing modes now allow us to run most geodetic experiments at a 1 Gbps mode using two bit sampling of 512 MHz wide bands.
  While real-time EOP extraction was used in a few AOV experiments in 2015, deriving those parameters from a regional network is challenging. Geodetically more useful results are baseline lengths and station coordinates. In Figure 3 we show simulated baseline length repeatabilities for AOV schedules with different recording rates. Despite variations in the station network, we expect improved results using the 1 Gbps mode.
- **Astrometry**
  Multiple AOV sessions had an astrometric focus. There are several telescopes with high sensitivity in the region, which regularly could be arranged to join the AOV sessions. Most prominently, these are the Tianma65 or the Parkes telescopes, allowing for special aims of the AOV sessions.
  Emphasis has been put on the ecliptic plane (for deep space navigation) and middle southern sources which are invisible to the VLBA. An overview of the target sources is shown in Figure 4.

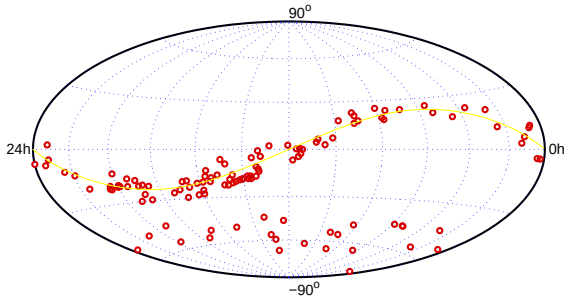

Fig. 4 Astrometric target sources of the AOV sessions. Efforts are focussed on an ecliptic plane survey as well as middle southern sources that are invisible to the VLBA.

- **R&D**
  AOV operations are notable for their responsivity. Multiple sessions were organized flexibly, on short notice via informal e-mail exchange. This allows reacting on short notice to the availability of heavily booked telescopes or tailoring sched-

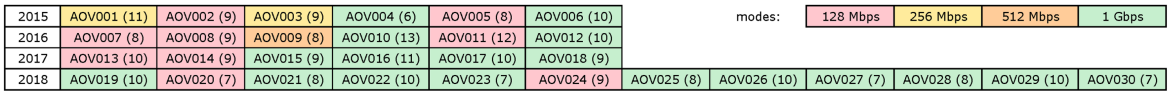

Fig. 2 AOV sessions (and number of stations), color-coded with the observing mode (128 Mbps: AOV002, 005, 007, 008, 011, 013, 014, 020, and 024; 256 Mbps: AOV001 and 003; 512 Mbps: AOV009, and 1 Gbps: AOV004, 006, 010, 012, 015 through 019, 021 through 023, and 025 through 030).

ules to special constellations or observing targets. For example, in AOV022 the three Russian stations Badary, Svetloe, and Zelenchukskaya joined in observations aimed at testing relativity.
Informal communication also enabled AOV network stations to join observations of the Chang'E-3 lander, additional stations to join the Australian AUA sessions, e.g. AUA020 [1], or the Chinese geodetic sessions.

2.2 APSG Sessions

The primary purpose of the APSG sessions is to monitor the relative motions of the plates in the Asia-Pacific region. After some discussion about ceasing these sessions within the IVS, the APSG sessions' scheduling and correlation is now handled by SHAO, under their commitment to the AOV region from 2015 onwards.

3 AOV Meetings and Governance

Regular meetings, an elected structure, and good communication are considered to be essential for the success of the AOV. All relevant information is distributed via dedicated e-mail lists and published at our website: `www.auscope.phys.utas.edu.au/aov`. A few highlights of the previous years are:

- **1st AOV Science and Technology Meeting, November 19-20, 2015, Hobart, Australia**
  An inaugural meeting with about 20 participants and 15 talks. A meeting within the region quickly revealed its benefits, with engaged discussions and keen plans for future collaboration. A key outcome of this meeting was the plan of further AOV meetings at a 1.5 year cadence, preferably hosted by member institutions in alternating hemispheres. The program, copies of the talks, and the meeting minutes are available on the AOV website (see above).
- **March 2017: new Chair and Secretary elected**
  Following the retirements from VLBI by both the AOV chair (Jim Lovell) and the Secretary (Ryoji Kawabata) in early 2017, new elections were held. Takahiro Wakasugi from GSI Japan was elected for the new chair, and he appointed Lucia McCallum from the University of Tasmania for the role of Secretary.
- **2nd General Meeting of the AOV, July 31 to August 1, 2017, Kobe, Japan**
  The second AOV meeting was held as a side meeting of the 2017 IAG-IASPEI conference in Kobe, Japan. While participation of the southern hemisphere was a bit lower this time, a group of around 15 contributed to a successful meeting (see group picture in Figure 5). Noteworthy results are the decision to double the number of AOV sessions per year from six to 12, or the agreement for some common VGOS projects (see below). Furthermore, the meeting program was enhanced with a keynote speech by the IVS chair, Axel Nothnagel, about synergy aspects of the AOV and IVS, as well as an invited talk by John Dawson from Geoscience Australia, on collaboration with the UN-GGIM-AP WG1. It was also a pleasure to welcome both masters and PhD students at this meeting. For details on the program, the talks and meeting minutes the interested reader once more is referred to our website.
- **AOV Retreat, March 6-8, 2018, Hobart, Australia: Chair and Secretary**
  In March 2018, the Chair visited his Secretary in Hobart. During this two-day retreat, some of the agenda items were details of the 3rd AOV meeting (see below), the status of the ongoing AOV operations, representation at the upcoming IVS GM in

Fig. 5 Participants of the second AOV meeting, held in Kobe, Japan.

Svalbard, as well as future VGOS activities within the AOV.

- **3rd Meeting of the AOV, November 9-10, 2018, Canberra, Australia**
  The next AOV meeting will be held in Canberra, hosted by Geoscience Australia and coinciding with the ILRS Workshop. Registration was opened, and the meeting Web site went online in August. Following the tradition of the previous meeting, one day will be dedicated to discussions within the VLBI experts, while the second day will consist of reports, scientific talks, and invited presentations, also with the intention of attracting a wider audience from different fields and techniques.

4 VGOS and the AOV

The AOV is working together on VGOS observations. The testing so far has contributed to the quality checking of VGOS equipment and the accumulation of operational knowledge. In particular we tested modes and compatibility between the DBBC-3 (in Hobart) and the Japanese GALA-V system (at Ishioka and Kashima). Correlation was performed at NICT and in Hobart, investigating group delays obtained with zoom-bands and FOURFIT and those from the Japanese full-bandwidth processing. This has prompted active development of the DBBC in Hobart, testing multiple frequency bands and polarization combinations using the DBBC's OCT-mode.

With the now established procedures for scheduling and data transfers, further tests are planned within the next months. Focus will be given to polarization combinations and source structure studies, as well as further development on correlation and post-correlation procedures (at SHAO).

References

1. O. Titov, A. Girdiuk, S.B. Lambert, J. Lovell, J. McCallum, S. Shabala, L. McCallum, D. Mayer, M. Schartner, A. deWitt, F. Shu, A. Melnikov, D. Ivanov, A. Mikhailov, S. Yi, B. Soja, B. Xia, and T. Jiang, "Testing general relativity with geodetic VLBI - What a single, specially designed experiment can teach us", Astronomy and Astrophysics, man. no. 33459, doi:10.1051/0004-6361/201833459, 2018.

BKG CVC - The Central VLBI Observation Coordination Office of the Federal Agency for Cartography and Geodesy at the Geodetic Observatory Wettzell

T. Schüler [1,2], C. Plötz [1], A. Phogat [1]

Abstract The Federal Agency for Cartography and Geodesy (BKG) is operating three radiotelescopes at Wettzell, one telescope at the Argentinean-German-Geodetic Observatory (AGGO) together with Argentinean partners from the research organization CONICET, and one telescope at O'Higgins, Antarctica (BKG holds a share of 20% for geodetic VLBI, with primary operation by the German DLR for satellite communications). Apart from this geodetic base infrastructure, BKG is co-financing the VLBI correlator at the Max-Planck-Institute for Radioastronomy at Bonn, including a separate contract for geodetic correlation services. A local VLBI correlator was installed at the Geodetic Observatory Wettzell in September 2017. Finally, VLBI data analysis and data combination are carried out both at Frankfurt and Leipzig. One important component missing at BKG in the past was a Central VLBI Observation Coordination Facility (CVC). It was implemented at the Geodetic Observatory Wettzell during 2017 in order to better organize domestic VLBI sessions. A total of 28 domestic sessions were coordinated within that year, also featuring dedicated sessions for O'Higgins with up to six telescopes. This contribution portrays the individual VLBI components operated by BKG with a special focus on the VLBI observing and coordination tool. The current realization state is depicted.

Keywords VLBI session coordination, central VLBI coordination, IVS Master Schedule, domestic VLBI sessions, local baselines, integration of VLBI sessions

1. Geodetic Observatory Wettzell, Federal Agency for Cartography and Geodesy (BKG)
2. University of the Federal Armed Forces Munich, Faculty of Aerospace Engineering

1 Background and Motivation

For many years, the Geodetic Observatory Wettzell has been almost exclusively observing sessions for the International VLBI Service for Geodesy and Astrometry (IVS). A few extra sessions per year have been attributed to the European VLBI Network (EVN) requiring a minimum extra coordination effort. This situation has changed with the implementation of the local VLBI correlator *GOWL* at Wettzell [Phogat et al., 2018]. The primary purposes of the local correlator are

1. *Local ties:* The determination of connection vectors between the local radio-telescopes from VLBI data in addition to terrestrial measurements.
2. *Quality assurance:* The regular execution of experiments between all BKG-operated telescopes for quality assurance of the VLBI data.

The increase of in-house sessions triggered a need for better coordination of all VLBI activities. The primary aim is to blend the international sessions (mainly IVS) seamlessly with the domestic ones in order to avoid scheduling conflicts. Further purposes are related to a proper prioritization of both sessions and correlation activities as well as performance monitoring and evaluation.

2 Scope of Effort and Capabilities of Coordination Tool

The following activities are carried out within the scope of the Central VLBI Observation Coordination Office (CVC):

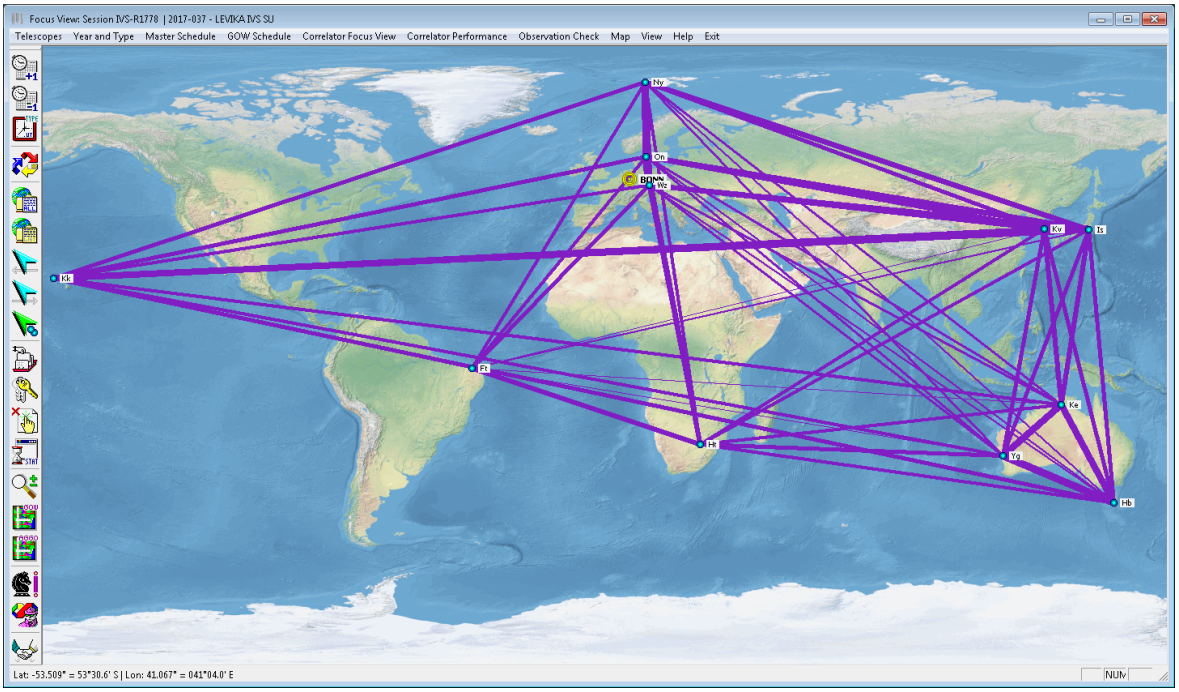

Fig. 1 Screenshot of the VLBI coordination tool. The map overlay is a selected IVS Rapid R1 network. The width of the lines indicates the number of scans commonly observed on the respective baseline.

2.1 Coordination of VLBI Sessions

Firstly, the domestic local sessions for relative radio-telescope positioning (*VLBI ties*) require coordination with the internationally scheduled sessions. Currently, three types of (master) schedules issued by the IVS are taken into consideration:

- *IVS Master Schedule:* This table contains the various sessions coordinated by the IVS with a standard duration of 24 hours, e.g. Rapids, T2 sessions, Research & Development sessions, and others.
- *IVS Intensives:* The short hourly sessions aiming at rapid determination of UT1 coordinated by the IVS.
- *VGOS Pilot Test:* The experimental VGOS test schedule including the evolving network of VGOS telescopes.

All tables are updated daily via FTP by the coordination software and combined with the domestic schedule. The domestic session is plan currently comprised of:

- *Local sessions:* Local Wettzell radio-telescope sessions.
- *Test and quality assurance sessions:* These sessions are not limited to the telescopes at Wettzell but also include AGGO, Argentina and O'Higgins, Antarctica. The purposes are quality assurance and initial testing, i.e. for AGGO. Partner telescopes can be involved in these activities upon need and availability.
- *Special densification programs:* Sessions foreseen to improve performance of remote telescopes such as O'Higgins.
- *Externally handled sessions:* All sessions not directly handled at GO Wettzell, but under participation of BKG-operated telescopes. Although not many of these sessions are foreseen per year, coordination at one central place is essential in order to avoid confusion. Such sessions include EVN and RadioAstron support as well as other special activities, e.g. test sessions for European UT1 estimation, etc.

The coordination tool can blend the domestic sessions seamlessly into the existing IVS schedules. A priority can be assigned to each of these sessions so that a well mapped-out allocation of resources for the execution of the sessions can be assured.

Geodetic Observatory Wettzell

2017 Domestic Sessions

	Date	Day	DoY	Start	Duration	Session Name	DBC	Network	Correlator	Schedule	Issued by
	07.06.2017	Wed	158	18:00	24 h	GOW1715818 (W158AS) Group ID: 251017	X9	Wz Wn Oh **Session observed; data not yet available at correlator.**	GOWL	GOWL	PLOE
	13.06.2017	Tue	164	18:00	24 h	GOW1716418 (W164AS) Group ID: 251017	X9	Wz Wn Oh Ht Ke Yg **Session observed; data not yet available at correlator.**	GOWL	GOWL	PLOE
	21.06.2017	Wed	172	18:00	24 h	GOW1717218 (W172AS) Group ID: 251017	X9	Wz Wn Oh Ht Ke Yg **Session observed; data not yet available at correlator.**	GOWL	GOWL	PLOE
	05.07.2017	Wed	186	20:00	22 h	GOW1718620 (W186AU) Group ID: 289417	X9	Wz Wn **Data analyzed - session is closed.**	GOWL	BONN	NEID
	10.07.2017	Mon	191	09:00	7 h	GOW1719109 (WA191J) Group ID: 81917	XA	Wz Wn **Data analyzed - session is closed.**	GOWL	GOWL	APUR
	17.07.2017	Mon	198	09:00	6 h	GOW1719809 (WA198J) Group ID: 81917	XA	Wz Wn **Data analyzed - session is closed.**	GOWL	GOWL	APUR
	24.07.2017	Mon	205	10:00	6 h	GOW1720510 (WA205K) Group ID: 221917	X9	Wz Wn **Data analyzed - session is closed.**	GOWL	GOWL	APUR

Fig. 2 Web-based output of domestic sessions. Brief status information is shown. Further details can be browsed on user request, see the following two figures.

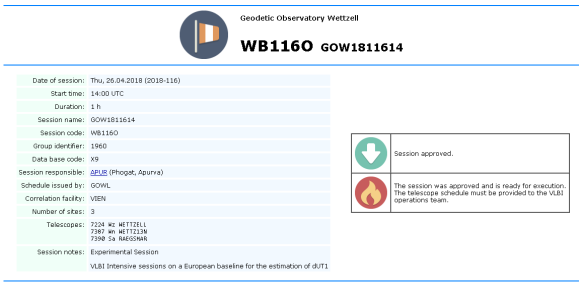

Geodetic Observatory Wettzell

WB116O GOW1811614

Date of session:	Thu, 26.04.2018 (2018-116)
Start time:	14:00 UTC
Duration:	1 h
Session name:	GOW1811614
Session code:	WB116O
Group identifier:	1960
Data base code:	X9
Session responsible:	APUR (Phogat, Apurva)
Schedule issued by:	GOWL
Correlation facility:	VIEN
Number of sites:	3
Telescopes:	7224 Wz WETTZELL 7307 Wn WETTZ13N 7390 Sa RAEGSMAR
Session notes:	Experimental Session VLBI intensive sessions on a European baseline for the estimation of dUT1

Session approved.

The session was approved and is ready for execution. The telescope schedule must be provided to the VLBI operations team.

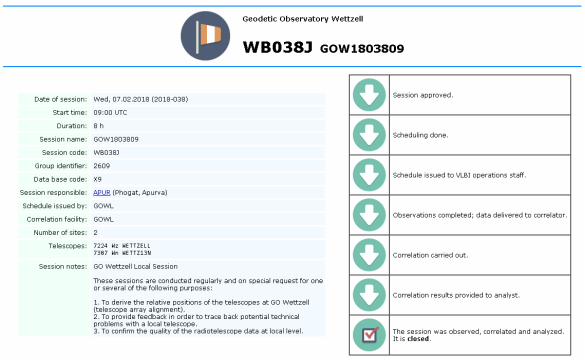

Geodetic Observatory Wettzell

WB038J GOW1803809

Date of session:	Wed, 07.02.2018 (2018-038)
Start time:	09:00 UTC
Duration:	8 h
Session name:	GOW1803809
Session code:	WB038J
Group identifier:	2609
Data base code:	X9
Session responsible:	APUR (Phogat, Apurva)
Schedule issued by:	GOWL
Correlation facility:	GOWL
Number of sites:	2
Telescopes:	7224 Wz WETTZELL 7307 Wn WETTZ13N
Session notes:	GO Wettzell Local Session These sessions are conducted regularly and on special request for one or several of the following purposes: 1. To derive the relative positions of the telescopes at GO Wettzell (telescope array alignment). 2. To provide feedback in order to trace back potential technical problems with a local telescope. 3. To confirm the quality of the radiotelescope data at local level.

Session approved.

Scheduling done.

Schedule issued to VLBI operations staff.

Observations completed; data delivered to correlator.

Correlation carried out.

Correlation results provided to analyst.

The session was observed, correlated and analyzed. It is **closed**.

Fig. 3 Example of session details (web page view) for an open session that has not been planned in detail (schedule is still to be issued) nor executed yet.

Fig. 4 Example of session details displayed on the web page upon user request. This example illustrates the complete planning, measurement, and analysis chain for a selected local session at Wettzell.

Figure 2 shows a fragment of the intranet web output of the coordination tool showing some 2017 domestic sessions. The plan consists of some local sessions between the two telescopes Wettzell North (Wn, TWIN 1) and Wettzell 20 m (Wz, RTW) and three international sessions coordinated to improve the position accuracy of the O'Higgins telescope at Antarctica including partner telescopes from South Africa (Ht) and Australia (Ke, Yg). Figure 3 portrays the details the user can browse for each domestic session, featuring its status on the right. Figure 4 illustrates a fully completed session with all planning, observing, and analysis steps carried out.

Note that all functions and details are, of course, directly accessible via the graphical user interface of the coordination tool developed (see Figure 5, for instance). The web-based output is generated to provide

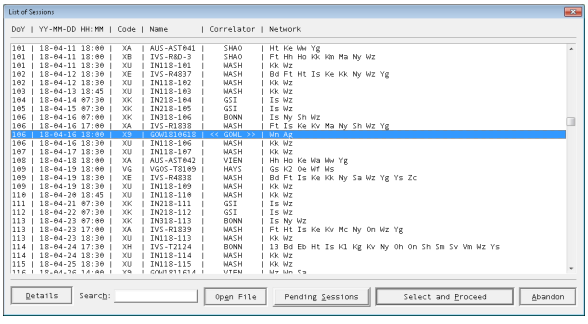

Fig. 5 List of sessions as displayed in the coordination tool. This screenshot shows the blended view containing all international IVS, as well as domestic, sessions at a glance.

essential pieces of information to operators as well as correlation and analysis staff. It is automatically updated daily and each time a change to the domestic schedule is made.

2.2 High-Level Coordination of Correlation Activities

Similarly to the coordination of observations, sessions can be assigned for VLBI correlation to either the local correlator *GOWL* at Wettzell or the Bonn correlator under contract to BKG. The priority scheme includes four levels.

2.3 Workload and Performance Monitoring

The following functionality is available to monitor the workload of both the radio-telescopes as well as the correlation facilities:

- The load on the correlation facilities can be figured out easily with the coordination tool. Three main workload figures are available:
  1. *Simplified Correlator Load*: This figure is based on the available IVS schedules. Separate figures for the Master and the Intensives Schedule and a combined figure are provided. The session duration is considered.
  2. *Correlation Station Load*: This workload figure takes the size of the network into consideration, because a larger network contains substantially more baselines to be correlated (the number of baselines is a quadratic function of the number of stations in the network).
  3. *Correlator Baseline Load*: This figure requires the analysis of all NGS card files available for the period under investigation. The number of scans on the various baselines successfully correlated is analyzed in order to provide feedback based on real output rather than planning information.
- Performance monitoring of the telescope includes
  1. annual analyses of the number of observations (group delays or scans) successfully collected,
  2. corresponding individual baseline statistics and
  3. the analysis of group delay standard deviations (precision figures) as obtained at the correlation stage.

2.4 Communication

Communication functions with the planning, operations, correlation, and analysis staff, as well as extra functions for communication with the correlation facilities are implemented into the coordination software.

Bookkeeping is available in the messaging system so that coordination activities are not limited to single individuals, but can be taken over by different persons according to their availability.

2.5 Observation and Correlation Resource Planning and Commitments

The coordination software is also an aid for mutual agreements between BKG and the IVS Coordinating Center. The corresponding support functions provide observation information about the actual and the previous years at a glance in order to easily derive the observation commitment for the following year.

The domestic sessions already planned are automatically communicated, as well as the holidays (at Wettzell, Bavaria, Germany) and the maintenance days, if already fixed.

3 Injection of Domestic Sessions

New domestic observations can be easily added to the list of sessions taking the current plans into consideration. The following steps summarize this procedure:

1. The focus telescopes must be selected. A selection list is supplied for typical sessions. The list is associated to a default set of telescopes. For certain networks, an individual selection can be performed directly afterwards, too. *Example:* The network Wettzell - AGGO - O'Higgins may include several telescopes at Wettzell or just a single one.

In order to remain flexible, the individual selection is supported in that case.

2. The free observation windows for the selected telescopes will be displayed in a dialog as shown in Figure 6.

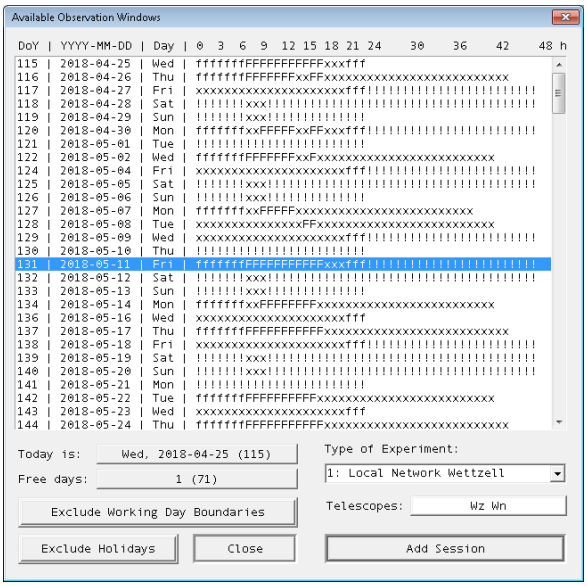

Fig. 6 List of free observation time windows for the selected telescopes Wn (Wettzell North, TWIN 1) and Wz (Wettzell, RTW 20 m) to add a new domestic session. Symbols: F = free observation time during regular working hours (at Wettzell), f = possible observation at less fortunate times, ! = holiday , x = blocked by existing session, X = maintenance day.

3. After selection of the desired day, some details of the session can be defined according to Figure 7. The exact start and end time (integer hours) can be defined, as well as the session responsibility and the scheduling and correlation institutions. Finally, session notes can be inserted to supply further details as needed for successful preparation, observation, and correlation, i.e. sampling and bit rates, subchannel setup, operation modes like common clock and phase calibration, etc.
4. Once these details are defined, a summary dialog box will be displayed for finalization. After confirmation, the window will be added to the list of sessions to be approved.
5. The request and approval system makes sure that each session or group of sessions is reviewed by the head of operations or the head of the observatory prior to scheduling and execution.

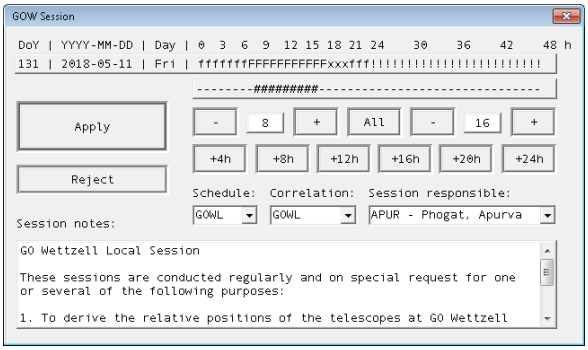

Fig. 7 Setting the details of a new domestic session at the planning stage.

The processing status can be updated any time after approval of the session. The following update states are currently implemented in the coordination tool:

- Schedule submitted to observer
- Observation session finished
- Measured data available at correlation facility
- Data correlated and ready for geodetic analysis
- Analysis completed.

References

[Phogat et al., 2018] A. Phogat, C. Plötz, T. Schüler, H. Hase, G. Kronschnabl, A. Neidhardt, J. Kodet, U. Schreiber, W. Alef, H. Rottmann, L. La Porta, S. Bernhart. Implementation and First Results of the Local Wettzell VLBI Correlator GOWL. In: Proceedings of the IVS 2018 General Meeting, Svalbard, Norway, 3-6 June 2018, this volume.

LEVIKA SBA – Wettzell Radio-Telescope Positioning With a Tailor-Made Analysis Software

Torben Schüler [1,2], Christian Plötz [1], Apurva Phogat [1]

Abstract The Geodetic Observatory Wettzell features three radio-telescopes dedicated to Geodesy: the 20-m telescope Wz (internally called RTW – Ratioteleskop Wettzell) has been in operation since 1984, and the two 13.2-m TWIN telescopes. Wn (TWIN 1, called "Wettzell North" by the IVS Coordinating Center) and Ws (Wettzell South) are VGOS-capable and were inaugurated in 2013. Wn is currently equipped with a triband receiving system (S/X/Ka) and regularly participates in routine IVS operations. Ws is equipped with a VGOS Elevenfeed and participates in the VGOS Pilot Test phase. Together, these three telescopes form a local triangle. The analysis software LEVIKA SBA (Short Baseline Analysis) was developed at the Observatory for local VLBI data adjustment. It serves the primary purpose of determining the relative positions of the three telescopes from original VLBI data and comparing these results with the local tie vectors from the precision engineering network regularly surveyed at Wettzell. In addition, the software was developed as part of a quality management initiative, in order to provide timely feedback to the engineers and operators regarding the health status of the overall system. Since telescopes with substantially different receiving systems are present at Wettzell, mixed-mode observations and analysis are of importance. This contribution depicts the analysis software, its functional basics and presents selected analysis results.

1. Geodetic Observatory Wettzell, Federal Agency for Cartography and Geodesy (BKG), Sackenrieder Str. 25, D-93444 Bad Kötzting, Germany
2. University of the Federal Armed Forces Munich, Faculty of Aerospace Engineering, Werner-Heisenberg-Weg 39, D-85577 Neubiberg, Germany

Keywords Short baseline VLBI analysis, relative local radio telescope positioning, local ties

1 Motivation

The three radio-telescopes Wz, Wn, and Ws at Wettzell are surveyed regularly by terrestrial measurement equipment. The antenna reference point of the new TWIN telescopes Wn and Ws is not directly accessible and requires—though partly automatized—a major effort. However, the ties (connection vectors) between the telescopes can also be determined from the VLBI observations, and these "local VLBI ties" can be compared with the terrestrial ties.

The local VLBI correlator *GOWL* was installed at Wettzell for this very purpose. Local data quality assurance sessions require an a analysis software that is easy to use in order to warrant a rapid feedback to the VLBI engineers. Consequently, the development of a small, but straightforward baseline adjustment tool was fostered.

2 Equations & Observations

LEVIKA SBA processes VLBI group delay observations for any band separately. A geocentric formulation [Campbell, 2000] of the equations is preferred and fully sufficient for this purpose. The associated observation equation reads according to [Lu et al., 2014]:

$$\tau_G = -\frac{1}{c}\left(b_x cos(t)cos(\delta) - b_y sin(t)cos(\delta) + b_z sin(\delta)\right)$$

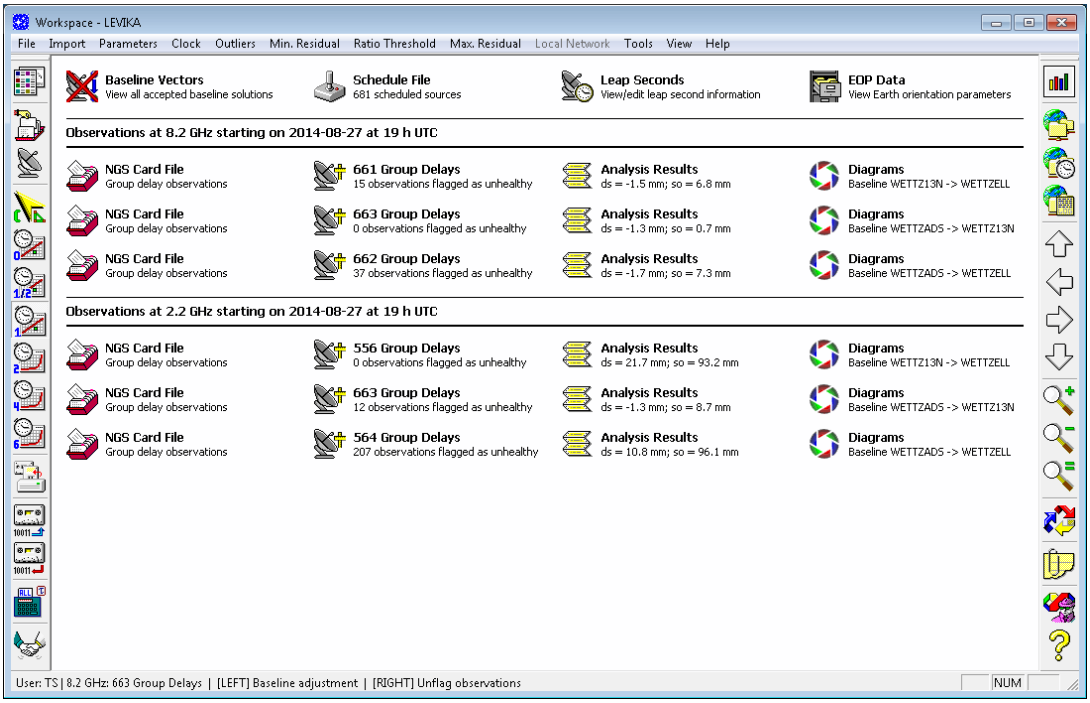

Fig. 1 LEVIKA SBA desktop screenshot. The short baseline analysis module of the LEVIKA software in support of local VLBI correlation is flexible in terms of group delay processing since each frequency band can be analyzed independently. This desktop shows three different setups for two different frequencies (X- and S-band). The baseline WETTADS to WETTZ13N is a zero baseline, the others refer to baseline Wn (TWIN 1) – Wz (RTW).

where τ_G is the group delay measurement, c is the speed of light, $b_{x,y,z}$ are the baseline components (coordinate vector) between the two telescopes, t is the hour angle, and δ is the declination of the radio source.

Figure 1 portrays the LEVIKA SBA desktop view displaying the different data sets analyzed during a local 24-hour session. You can see both data collected at X- (upper part) and S-band (lower part). The number of available and healthy observations in X-band is higher than in S-band (e.g., 661 group delays versus 556 delays). The reason is that S-band observations suffer from interference, yielding high correlation peaks on local baselines due to spatial correlation of the interference signatures. There is one exception: baseline WETTADS – WETTZ13N shows high numbers. This is a zero baseline; i.e., both groups of measurements refer to Wn/TWIN 1 and were sampled in parallel with a DBBC2 digital backend (refer to WETTZ13N) as well as an ADS3000+ sampler (refer to WETTADS). Environmental interference from mobile phone networks and similar differences cancel out in that case.

It is worth mentioning the following notes on observations and reductions:

- The *retarded baseline effect* [Brouwer, 1985] is compensated. It reaches significant values even over baseline as short as those at Wettzell (in the range of 100 m).
- Only *group delays* are currently processed in the software. The analysis of *phase delays* sounds attractive due to the high precision. However, our experience so far indicates that system-internal effects still dominate the error budget so that a smaller standard deviation of the observables will not lead to an increased accuracy of the baseline components.
- *Delay rates* were initially processed in the software. Though this type of observation usually yields centimeter precision of the baseline components in the end, the residuals showed height fluctuations and were difficult to interpret. It was therefore decided to exclude delay rates from analysis, because the added value in terms of quality feedback to the VLBI engineers is not clear.

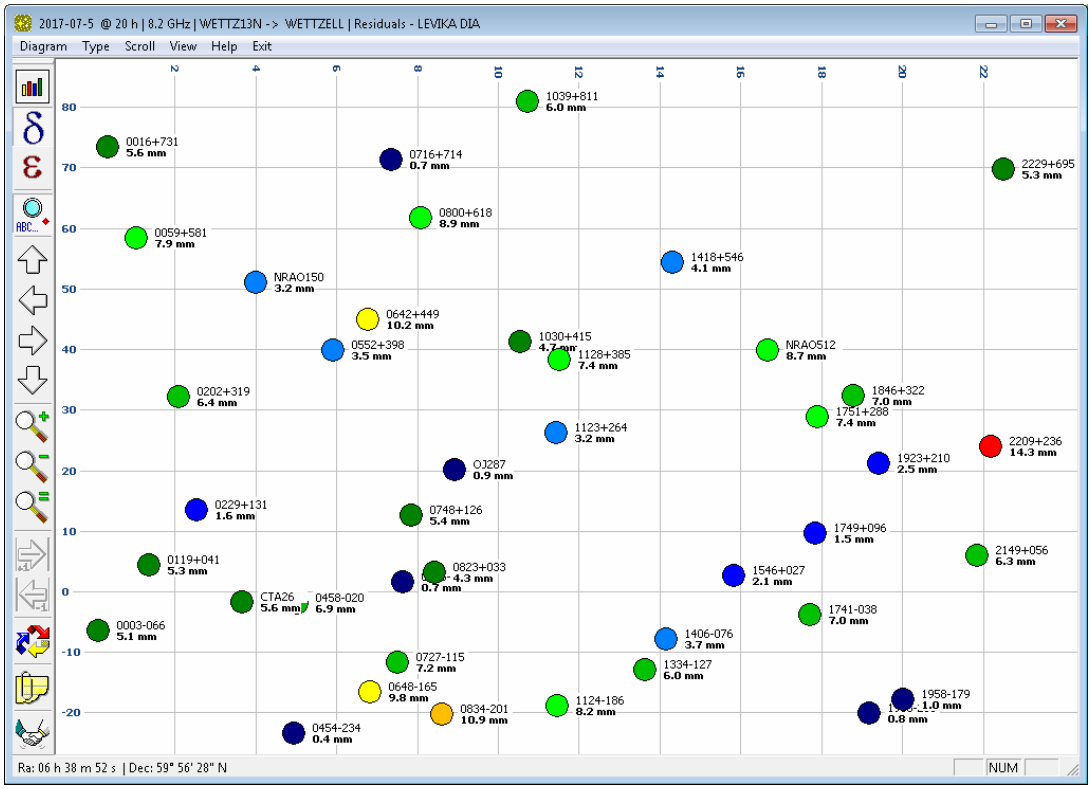

Fig. 2 Various graphical outputs are supported by LEVIKA SBA. This screenshot portrays the maximum residuals per radio source scanned (in metric units). The x-axis is the right ascension, the y-axis is the declination of the radio source. The data were derived from a local WHISP experiment lasting 24 hours. All sources scheduled are actually shown in the image.

- *Tropospheric propagation delays* are accounted for. The height difference between the reference points of Wz (RTW) and Wn (TWIN 1) is only 3.4 m. Approximately 8 m of height difference map into less than 3 mm of hydrostatic delay difference in zenith direction [Saastamoinen, 1972]. Though the hydrostatic delay effect is small, it is already at a magnitude to induce systematic errors. We can clearly see that the VLBI short baseline solutions deteriorate slightly with respect to the height when tropospheric corrections are disabled. Also note that the delay error at an elevation of 5° is ten times higher compared to zenith direction. In default mode, the total delay is compensated using a so-called "blind model", i.e., tropospheric correction based on climatology, but properly accounting for height reduction. Either the WAAS-model [RTCA, 2009] can be used or the in-house model TropGrid2 [Schueler, 2014]. Though TropGrid2 is considerably more sophisticated in terms of parametrization and made of a database comprising nine years of numerical weather model data, we hardly observe any differences in the adjustment results.

Figure 2 illustrates the (maximum) residuals for a local 24-hour experiment in X-band. One and the same radio source is usually scanned several times during such a session. Only the maximum residual is displayed in this right ascension – declination view. Individual residuals can be shown in an azimuth-elevation view. Further graphical outputs comprise the outlier ratio, the statistical redundancy of each observation, the clock drift time series, and a histogram of the residuals.

3 Parameters

LEVIKA SBA can handle the following set of parameters:

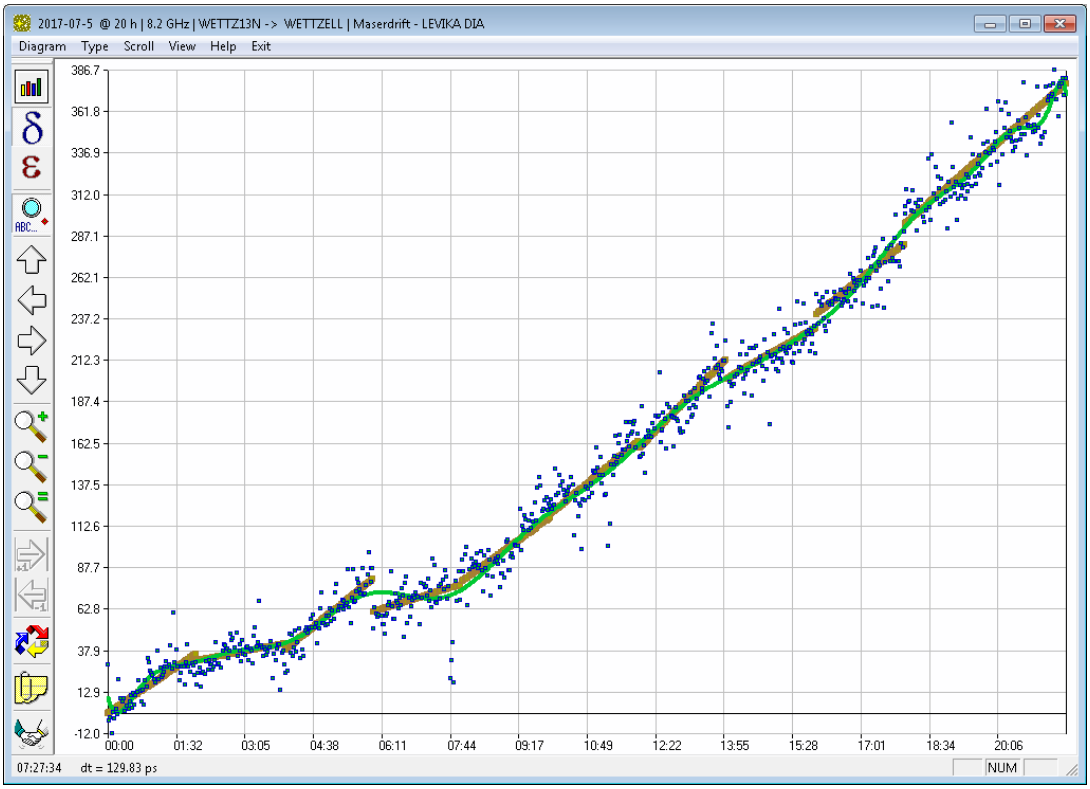

Fig. 3 Diagram of the master clock drift behavior. The software estimates piece-wise independent linear compensation functions shown in brownish color. The dots indicate the associated clock residuals of each scan. The green line is the result of smoothing (Chebychev polynomial).

- *Baseline vector*: Naturally speaking, the coordinate components are the primary set of unknowns we are interested in. However, it can also be justified to fix them in case quality assurance is of primary concern, since the terrestrial survey is very precise. In that case, the user can constrain the coordinates in the software (tight constraint = fixed as constants).
- *Zenith tropospheric delay*: Though applying a tropospheric correction model is sufficient in the vast majority of the cases, the software can estimate the zenith delay difference between both telescopes. The motivation to include this option stems from the fact that the tropospheric wet delay features a scale height of just 1.4 km compared to 8 km for the pressure (hydrostatic delay). Consequently, subtle variations of humidity between the two telescopes might result in noticeable delay errors. However, as mentioned just before, we have not yet observed session results yielding clearly significant tropospheric delay parameters. The tropospheric model compensation is always enabled, i.e., only a residual tropospheric delay difference will be estimated.
- *Clock drift*: Clock drift compensation is carried out using piece-wise linear functions. The resolution (time span) and the exact start of each independent linear function can be chosen by the user. The drift can be disabled for common clock experiments.

All other input data such as radio source locations, pole positions, and length-of-day information is injected as tight constraints into the analysis.

Figure 3 shows the clock error drift during a 24-hour session in units of picoseconds (x-axis is time in format hh:mm UTC). The hydrogen maser is apparently drifting over a bit less than 0.4 ns during that period. The clock error scatter is well within small bounds (though we wish to even reduce it further) and can be compensated by linear drift functions well in most cases (an exception can be seen around 06:11 UTC).

4 Clock Jumps and Outlier Handling

Initially, the software had no handling of clock jumps, because such events used to be extremely rare at Wettzell at that time (2014 to 2017). The situation worsened when we experimented with common clock modes so that an interactive as well as an automatic clock jump detection algorithm were implemented. Effectively, clock jump handling only requires to adapt the start times of the nearest clock drift compensation function properly.

Several outlier detection and handling methods are available. A minimum residual can be specified for X- and S-band observations separately. The outlier detector will only investigate residuals higher than this threshold. A conventional outlier detector based on à posteriori statistics is used [Pope, 1976]. This detector is implemented as an iterative algorithm rejecting the highest-probable outlier during each iteration. In addition, an "erazer" is usually activated. It deletes the residuals exceeding a pre-defined threshold. Though this type of outlier rejection should not be necessary in theory, we observed one session that essentially required such an additional step to yield good results in automatic processing mode, i.e., the outlier detector failed to identify one remaining unhealthy observation.

5 Results and Outlook

A number of local experiments have been performed at the local baseline Wn-Wz so far. The 3D distance compares well to the local precision survey and is at the sub-millimeter level on average. Further details can be found in [Schueler et al., 2016] and [Phogat et al., 2018]. However, note that deviations in height can accumulate to few millimeters.

Development of the LEVIKA short baseline analysis tool has been completed. A few outstanding points comprise the network combination module taking the temperature compensation into account.

References

[Campbell, 2000] J. Campbell. From Quasars to Benchmarks: VLBI Ties Heaven to Earth. International VLBI Service for Geodesy and Astrometry 2000 General Meeting Proceedings, Kötzting, Germany, February 21–24, edited by Nancy R. Vandenberg and Karen D. Baver, NASA/CP-2000-209893, 2000, p. 19–34.

[Lu et al., 2014] Z. Lu, Y. Qu, S. Qiao. Geodesy: Introduction to Geodetic Datum and Geodetic Systems. Springer, ISBN 978-3-642-41245-5.

[Brouwer, 1985] F.J.J. Brouwer. On the Principles, Assumptions and Methods of Geodetic Very Long Baseline Interferometry. Publications on Geodesy; Netherlands Geodetic Commission: Delft, The Netherlands, 1985; Volume 7, Number 4.

[Saastamoinen, 1972] J. Saastamoinen. Atmospheric Correction for the Troposphere and Stratosphere in Radioranging of Satellites. In: Use of Artificial Satellites for Geodesy. Geophys. Monogr. Ser. Edited by Henriksen, S.W., et al., 15, 247-251, American Geophysical Union, Washington D.C. 15: 2-1. doi: 10.1029/GM015p0247.

[RTCA, 2009] RTCA. RTCA DO-316: Minimum Operational Performance Standard (MOPS) for Global Positioning System/Aircraft Based Augmentation System Airborne Equipment. RTCA, Inc., 2009, 214 pages, https://standards.globalspec.com/std/1199977/rtca-do-316.

[Schueler, 2014] T. Schüler. The TropGrid2 standard tropospheric correction model. GPS Solut (2014) 18: 123. https://doi.org/10.1007/s10291-013-0316-x.

[Pope, 1976] A.J. Pope. The Statistics and Residuals and the Detection of Outliers. NOAA Technical Report NOS 65 NGS 1, Geodetic Research and Development Laboratory, National Geodetic Survey, Rockville, MD, USA, 1976.

[Schueler et al., 2016] T. Schüler, C. Plötz, S. Mähler, T. Klügel, A. Neidhardt, A. Bertarini, S. Halsig, A. Nothnagel, M. Lösler, C. Eschelbach, J. Anderson First Local Ties from Data of the Wettzell Triple Radio Telescope Array. IVS 2016 General Meeting Proceedings, pp. 149–153. Edited by Dirk Behrend, Karen D. Baver, and Kyla L. Armstrong, NASA/CP-2016-219016, 2016.

[Phogat et al., 2018] A. Phogat, C. Plötz, T. Schüler, H. Hase, G. Kronschnabl, A. Neidhardt, J. Kodet, U. Schreiber, W. Alef, H. Rottmann, L. La Porta, S. Bernhart. Implementation and First Results of the Local Wettzell VLBI Correlator GOWL. In Proceedings of the IVS 2018 General Meeting, Svalbard, Norway, 3–6 June 2018.

Comparision of the Masers at the Geodetic Observatory Wettzell

C.Bürkel [1], J. Kodet [2], G. Kronschnabel [1], C. Plötz [1], U. Schreiber [2], T. Schüler [1,3]

Abstract The Geodetic Observatory Wettzell operates three hydrogen masers as a part of the Wettzell atomic clock ensemble. The long term evolution of the masers is continuously measured. For the investigation of the short term behavior, a 14-day measurement campaign was carried out. The results presented in this paper are in good accordance with previous measurements and the specifications of the maser. With regard to improvements in the time and frequency department of the observatory, the results also show that steering should have no influence on the short term stability of the maser.

Keywords Time and frequency, hydrogen maser, Allan deviation

1 Introduction

The Geodetic Observatory Wettzell features a time laboratory with five commercial Caesium clocks and three hydrogen masers. All clocks take part in the calculation of UTC and are reported regularly to the BIPM. The UTC at the observatory *UTC(IFAG)* is realized with a commercial caesium clock.

The maser ensemble at the observatory helps to improve the short term stability of the local time with respect to more long term stable caesium clocks. The masers are primarily used as a stable frequency source for VLBI observations of the radio telescopes at the observatory. Due to the construction of two new telescopes (TWIN), one maser of the ensemble was installed in the TWIN operations building and serves as a common clock for both TWIN1 (Wn) and TWIN2 (Ws).

In the future, the maser ensemble is foreseen to provide a common clock for all three telescopes to provide geodetic and local VLBI measurements. Due to the separation of the maser ensemble to different buildings and environments, these comparisons have become necessary.

The results from this comparison will contribute to the project of using a steered hydrogen maser for generating the local representation of UTC at the observatory and the improvement of a local composite clock for the observatory, combining caesium clocks, hydrogen masers, and a cold rubidium clock.

2 Measuring Method

The measurement method we used for the comparison of the masers is called the triangular method. These method allows us to derive the performance of each oscillator on its own [Schlüter (1988)].

The triangular method needs three different oscillators which are compared to each other simultaneously (Figure 1).

In this measurement oscillator A is compared to oscillator B, oscillator B to oscillator C, and oscillator C to oscillator A. The simultaneous measurement is necessary to get a set of data that overlaps in time.

1. Geodetic Observatory Wettzell, Federal Agency for Cartography and Geodesy (BKG)
2. Geodetic Observatory Wettzell, Technische Universität München
3. University of the Federal Armed Forces Munich, Faculty of Aerospace Engineering

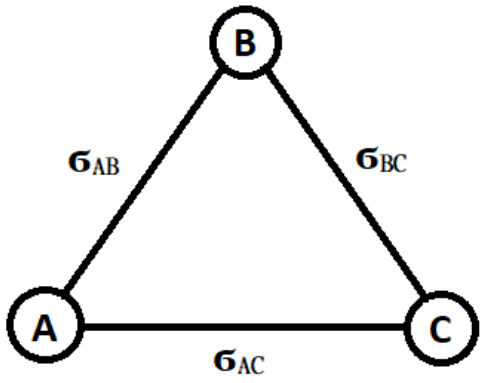

Fig. 1 Schematic draw of a triangular measurement.

Out of the measured data, the Allan variance of an oscillator pair can be calculated. The Allan variance, also known as two-sample variance, is a measure of the frequency stability in oscillators. The Allan variance is defined as [Allan et al. (1966)]:

$$\sigma_y^2(\tau) = \frac{1}{2}\langle (y_{n+1} - y_n)^2 \rangle \tag{1}$$

where τ is the observation period and y_n is the nth fractional frequency average over the observation time τ. Just as with standard deviation and variance, the Allan deviation is defined as the square root of the Allan variance:

$$\sigma_y(\tau) = \sqrt{\sigma_y^2(\tau)} \tag{2}$$

With respect to the three oscillators, the measurement leads to the three different Allan deviations σ_{AB}, σ_{BC} and σ_{AC}.

For derivation of the single Allan deviations σ_A, σ_B, and σ_C we can use the law of cosines. If the oscillators are independent then the correlation between the oscillators is zero and we can simplify the law of cosines to the Pythagorean theorem:

$$\sigma_{AB}^2 = \sigma_A^2 + \sigma_B^2 \tag{3}$$

$$\sigma_{AC}^2 = \sigma_A^2 + \sigma_C^2 \tag{4}$$

$$\sigma_{BC}^2 = \sigma_B^2 + \sigma_C^2 \tag{5}$$

The equations solve the following equation, as σ_{AB}, σ_{BC}, and σ_{AC} are known, and, after using the square root, the Allan deviation is extracted from the reference oscillators:

$$\sigma_A = \sqrt{\frac{1}{2}\left(\sigma_{AB}^2 + \sigma_{AC}^2 - \sigma_{BC}^2\right)} \tag{6}$$

The same can be done for σ_B and σ_C. Then the Allan deviation of each single oscillator can be calculated.

3 Measurement Set Up

We were interested in such a measurement because of the fact that our maser clock ensemble is not located in one single building. One maser is separated from the other two by a distance of around 100 m and is in a different building. The maser was relocated; before that, all three masers were at the same building next to each other. In previous measurements we had measured our masers with the same method. Therefore we were interested in whether the relocation had any influence on the maser ensemble's performance.

The measurement took place at the RTW operations building (close to the 20-m telescope Wz), the home of the two masers EFOS18 and EFOS39. The single new maser EFOS60 in the TWIN operations building is connected via a coaxial cable to the other two masers. We were also interested in whether the long cable connection matters with respect to the stability outcome.

Our measurement campaign had a length of 14 days, starting on 2017/12/22 and ending on 2018/01/05. The measurements were performed with a Vremja 314 frequency comparator at a frequency of 100 MHz.

During the measurement, our continuous PPS measurements of the masers were also running. Hence, we can get the long term behavior of the masers and could get a good picture of the drift evolution of our maser ensemble. These PPS measurements are rather simple; every three hours, the PPS signal of a maser is measured against our realization of UTC.

4 Results

The two-week continuous measurement campaign showed the following results: out of the measured frequency differences, the Allan deviations calculated after the described method were calculated. Due to the two-week measurement, a sample time of 10^5 s could

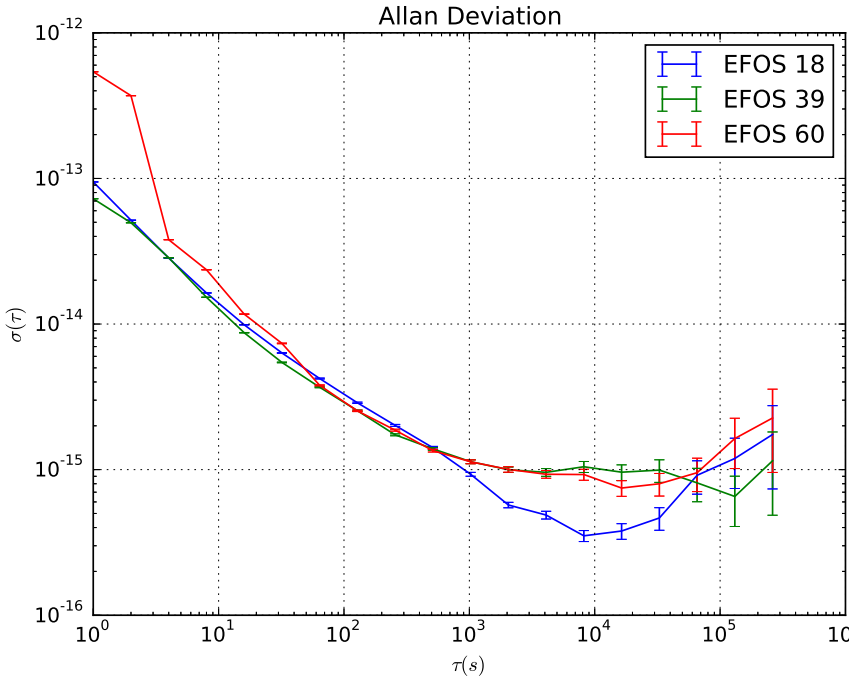

Fig. 2 Allan deviation of the Wettzell maser ensemble EFOS 18 (blue line, middle starting value), EFOS 39 (green line, lowest starting value), and EFOS 60 (red line, highest starting value). The shown graphs are calculated from a 15-day data set, which was measured from 2013/04/03 to 2013/04/18.

be reached for the Allan deviation calculation. For the calculation of the Allan deviation, the Allan tools for python were used [Wallin et al. (2018)].

All three masers show nearly the same expected behavior (Figure 3):

1. Starting with a stability of 10^{-13} at a sampling time of 1 s, we can show that the stability is in the range of the specification of the EFOS masers. The best performance in the 1 s regime is shown by EFOS 39 with a stability of $8 \cdot 10^{-14}$.
2. In the short term regime from 10 s to 1000 s the masers show a $\frac{1}{\sqrt{\tau}}$ behavior. The stability improves from a low value of 10^{-14} at 10 s to a high value of 10^{-16} at 1000 s.
3. After 1000 s of sampling time all masers reach the flicker floor at a stability of $8 \cdot 10^{-16}$. This stability is slightly better than mentioned in the specifications.

In comparison to previous measurements (Figure 2), calculated after the same method, we see no huge differences between the two measurement campaigns. In particular, EFOS 60 did not change in its performance after the relocation.

The PPS measurements (Figure 4) show a constant linear drift for EFOS 18 and EFOS 39. Only EFOS 60 shows some changes in its drift behavior during the two week period, and it is clear there is no linear behavior. Even the sign changes during the campaign.

5 Conclusion

The maser ensemble at the geodetic observatory Wettzell shows the specified behavior of stability (Figure 2), in some cases better than predicted.

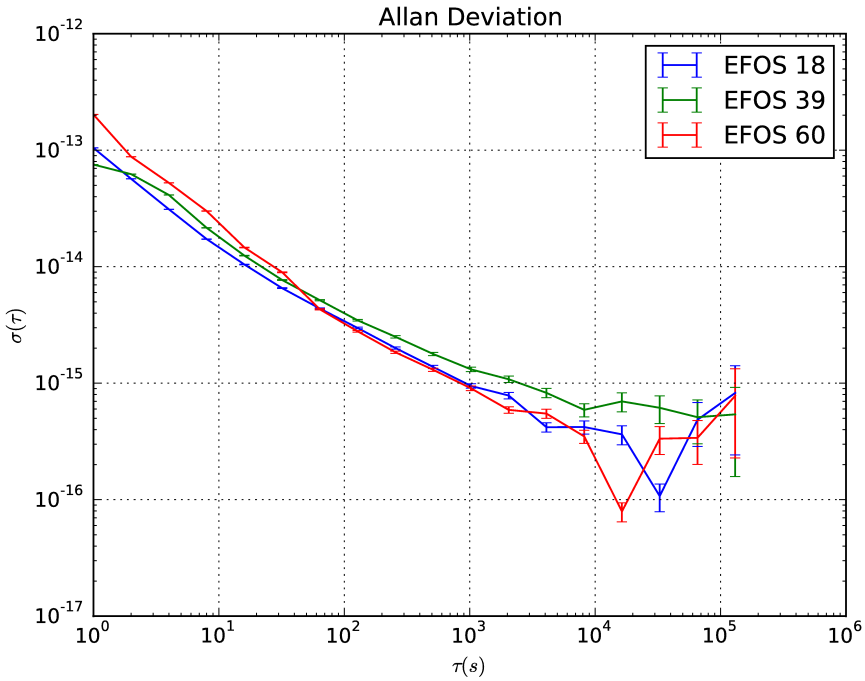

Fig. 3 Allan deviation of the Wettzell maser ensemble EFOS 18 (blue line, middle starting value), EFOS 39 (green line, lowest starting value), and EFOS 60 (red line, highest starting value). The shown graphs are calculated from a 14-day data set which was measured from 2017/12/22 to 2018/01/05.

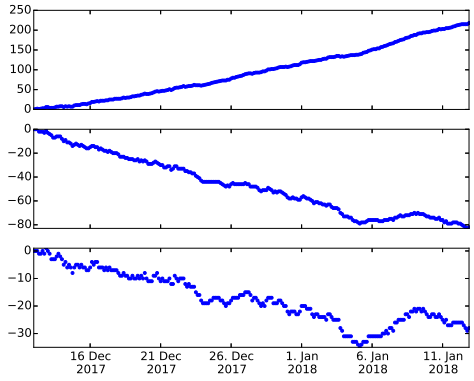

Fig. 4 The drift evolution of Wettzell's maser ensemble: EFOS 18 (upper panel), EFOS 39 (middle panel), and EFOS 60 (lower panel). The evolution of Δt is derived from the measured PPS signals over the time period from 2017/12/13 through 2018/01/12.

The long distance between the maser EFOS 60 and the two others had no effect on the measurement during the campaign. Therefore the distance between the masers should have no influence on measurements such as common clock VLBI measurements with the Wettzell radio telescopes.

The change in the drift behavior of EFOS 60 during the measurement campaign showed no influence on the resulting Allan deviation and had no effect on the short term stability of the maser. This short term stability is required to provide good VLBI measurements. Hence, we assume that a steered maser with small corrections to the drift should have no influence on the short term stability and its usage as a frequency source for our measurements such as VLBI and SLR.

The steered maser could be used as a backbone of the whole time and frequency system of the observatory. In a combination of our optical time and frequency distribution system, a new time measurement system, and the steered maser, we should improve our time and frequency performance for the whole observatory, and the performance of SLR, VLBI, and GNSS measurements should improve as well.

References

[Schlüter (1988)] Schlüter, W., Zeit und Frequenz im Meßverfahren der Geodäsie., Deutsche Geodaetische Kommission Bayer. Akad. Wiss., 337, 1988.

[Allan et al. (1966)] Allan, D. W., Statistics of atomic frequency standards, IEEE Proceedings, 54, Feb. 1966 DOI10.1109/PROC.1966.4634.

[Wallin et al. (2018)] Wallin, A. E. E., Price, D. C., Carson, C. G., and Meynadier, F., allantools: Allan deviation calculation Software, Astrophysics Source Code Library, 2018.

Local Radio Telescope Ties from the Wettzell Precision Engineering Surveying Network

Torben Schüler [1,2], Thomas Klügel [1], Swetlana Mähler [1], Christian Plötz [1]

Abstract The Geodetic Observatory Wettzell is a fundamental station of Geodesy and a GGOS Core Site. This co-location site features all systems of the space-geodetic techniques, i.e., three VLBI telescopes, two operational SLR telescopes, various GNSS receivers, a DORIS beacon, and a ring laser gyro for instantaneous measurement of the Earth rotation. The existence of a geodetic co-location site is justified by the need to synergistically combine the various techniques in order to derive all geodetic parameters of interest which are needed to realize the reference system. Although VLBI is the only technique capable of providing the full set of Earth orientation parameters, the determination of the geo-center (the origin of our coordinate system) is not possible at all, and SLR will be needed for this purpose. GNSS, in the end, provides easy access to the terrestrial reference frame. These synergies can only be exploited for Geodesy if precise geometric links between the reference points of the various systems are known, the so-called "local ties". At Wettzell, these vectors are derived from a local precision engineering surveying network that is covering the entire observatory yielding a point precision around 0.2 to 0.4 mm for the majority of the points. This contribution will outline the methodology to derive the local tie vectors and to transform them into the ECEF system, present the latest results, and compare them with alternative methods like the direct local VLBI data analysis.

1. Geodetic Observatory Wettzell, Federal Agency for Cartography and Geodesy (BKG), Sackenrieder Str. 25, D-93444 Bad Kötzting, Germany
2. University of the Federal Armed Forces Munich, Faculty of Aerospace Engineering, Werner-Heisenberg-Weg 39, D-85577 Neubiberg, Germany

Keywords Local ties, precise engineering network, terrestrial surveying, network transformation

1 Local Terrestrial Network Wettzell

The local network at the Geodetic Observatory Wettzell is regularly surveyed in order to monitor the local stability at the site and, most importantly, to provide the local ties for ITRF computation. The term "local ties" denotes the connection vectors between the various systems of the space geodetic techniques co-located at Wettzell, namely

- the three VLBI telescopes Wz (7,224, RTW, 20 m), Wn (7,387, TWIN 1), and Ws (7,388, TWIN 2),
- the two SLR stations WLRS (8,834) and SOSW,
- a number of GNSS reference stations (in particular WTZR, an IGS station),
- the DORIS beacon, and
- the two SAR corner reflectors (for support of interferometric SAR applications).

As a final product, the local ties are basically a set of Earth-Centered Earth-Fixed (ECEF) coordinates provided in standard SINEX (Solution-Independent Exchange) format.

This contribution refers to the local network solution of 2012 which was used to derive the ties employed in the realization of ITRF 2014. Although more recent network measurements exist, this one is still the official release. Figure 1 portrays the local network. It covers the entire GO Wettzell. The new TWIN VLBI telescopes are located in the southern part of the network and surrounded by surveying pillars. The old SLR system WLRS is located in the center of the net,

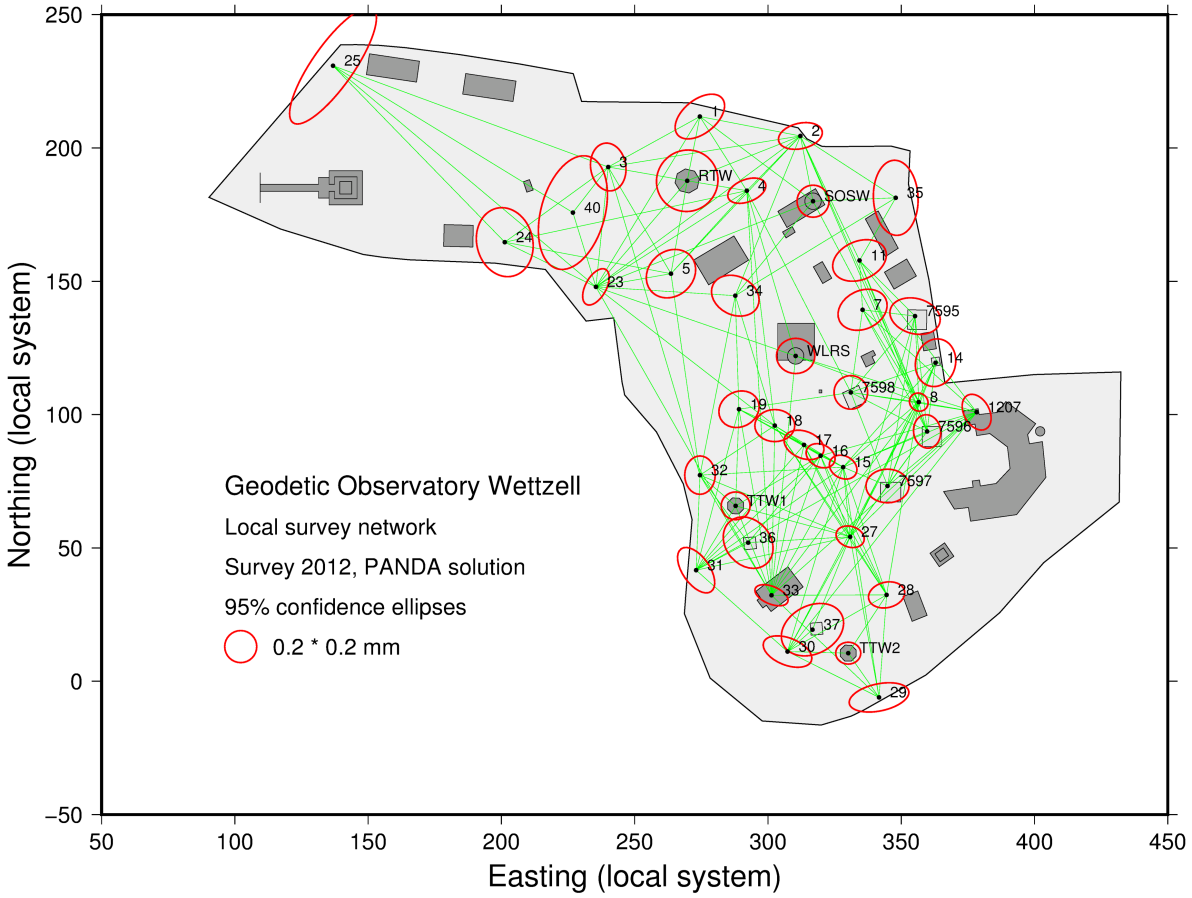

Fig. 1 Local precision engineering surveying network of the Geodetic Observatory Wettzell with a selected set of observations (baselines measured by terrestrial total station) and confidence ellipses (precision at a level of 95% probability). This network plot is related to the measurement epoch 2012 that was used to derive the local ties for the computation of ITRF 2014.

whereas the old VLBI telescope Wz (RTW, 20 m) and the new SLR station SOSW are visible at the northern periphery of the network.

2 Procedures and Notes on Processing

Deriving highly precise coordinates from terrestrial measurements is a discipline of craftsmanship and requires meeting rigorous surveying procedures. Though it is not possible to go into any details in this paper, it is worth mentioning the following notes:

- *Terrestrial survey:* The precise terrestrial survey is carried out in a local coordinate system. The radial coordinate channel is supported by precision levelling wherever feasible. The local network adjustment is currently carried out in 3D mode.
- *Surveying equipment:* The terrestrial measurements are carried out using a precision total station with an angular standard deviation of $\sigma_r = 0.5''$ (one single direction observation) and a distance precision of $\sigma_s = 0.6$ mm. In addition, a precise digital levelling device with an invar rod is in use.
- *System reference points:* Several reference points are not directly accessible, e.g., those of the new TWIN telescopes. Separate procedures are employed to indirectly determine these points [Maehler et al., 2018]. In these cases, zenith angle measurements contribute in major parts to the determination of the height component, because spirit levelling is not a practicable means. The reference points of the TWIN telescopes are regularly mon-

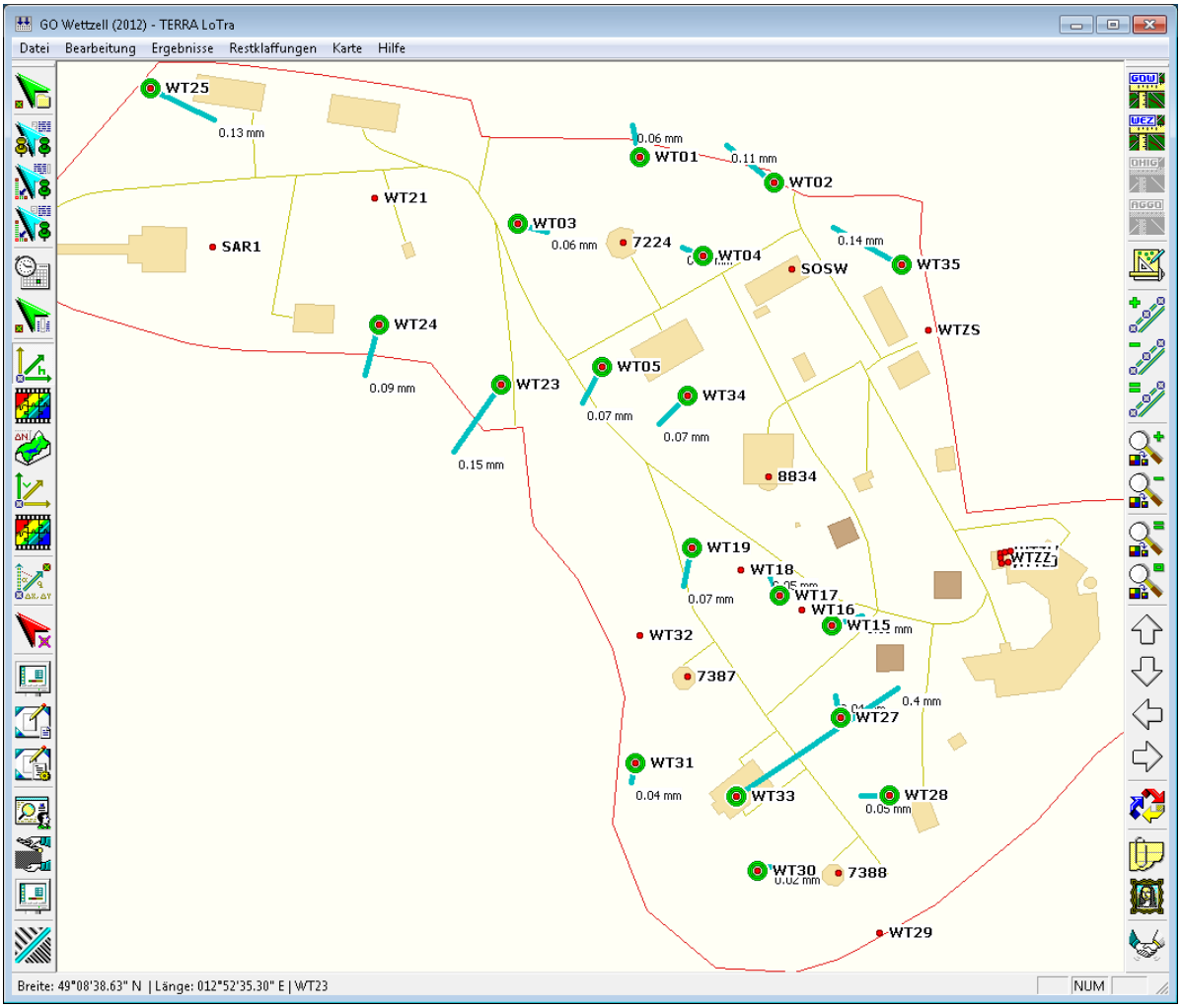

Fig. 2 Horizontal residuals à posteriori for the transformation points showing a very good agreement between the local survey and the GPS positioning results (thanks to manual screening of the GPS residuals).

itored. A monitoring session close in time to the network survey was used to inject the associated data into the overall network adjustment.

- *GPS control network:* A number of survey pillars were occupied by GPS yielding a set of identical points. The control points were used to derive transformation parameters in order to refer the local coordinates to ECEF. The GPS measurements were collected for at least 24 hours or longer (1.5 days). The same antenna type was used at both the central point and on the control points in order to avoid/to minimize antenna phase center uncertainties.
- *Manual screening of GPS residuals:* Most importantly, we used an in-house GNSS processing software that is optimized for interactive data editing. Manual editing of all GPS baselines was carried out removing suspected unhealthy data. This is a tedious and highly long, drawn-out effort, but many of the control point locations were optimized for terrestrial surveying rather than GPS observing. As a consequence, signal blocking, multipath, and also signal bending were visible in the data. Figure 2 nicely illustrates that the major effort of manual editing was worth being spent. Automatic outlier removal yields approximately three times less precise results than manual data editing.

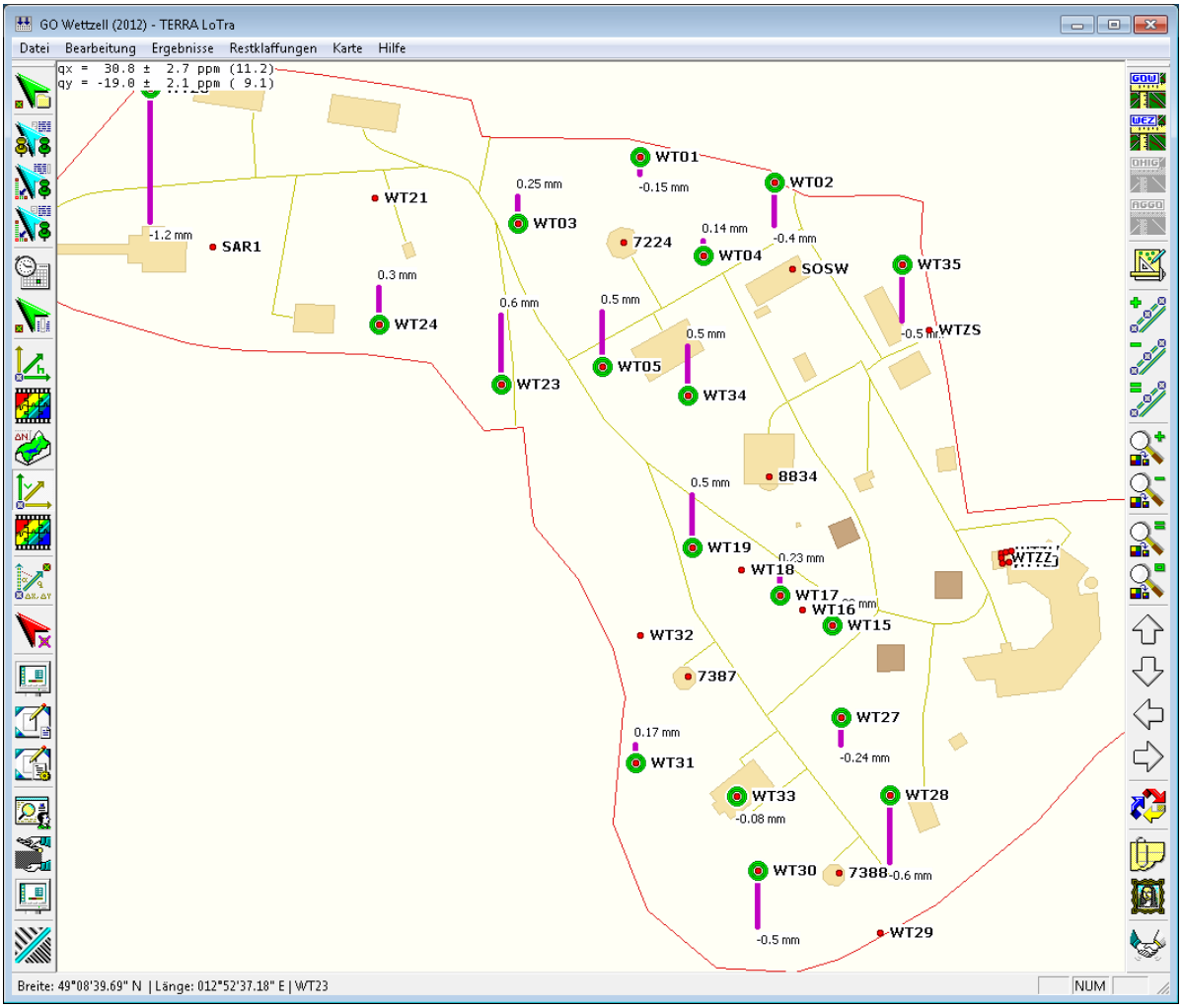

Fig. 3 Vertical residuals à posteriori for the transformation points. It was essential to estimate a pair of horizontal gradients in addition to the vertical offset in order to reduce these residuals to a level coinciding with the measurement precision. The gradient components are numerically given in the upper left part of the screen-shot.

3 Transformation Approach

We strictly separated the horizontal and vertical coordinates and derived independent sets of transformation parameters. This procedure is necessary at Wettzell due to a special treatment of the radial channel, possibly due to changes of the geoidal separation over relatively small horizontal distances.

The horizontal transformation coefficients consist of a classical set of datum transformation parameters, i.e., two translations, one net rotation, and a scaling factor. Figure 2 reveals small residuals, not to say a fantastic agreement, except for pillar WT33 on the TWIN operating building's terrace which is not a perfect geodetic monument, and surrounded by the telescopes yielding GPS signal blockage and related effects. The other points usually stay around 0.1 to 0.2 mm. These nice results should not hide the fact that a theoretical control point on the GNSS tower (where WTZZ and WTZR are located with WTZR being an important point for ITRF computation) would, most likely, have revealed a higher residual due to extrapolation geometry.

The vertical transformation might consist of a mere offset describing the average geoid height in the area. Whilst this approach appears to be suitable for O'Higgins as well as TIGO, the spatial variation of the geoid at Wettzell is significant, and a horizontal

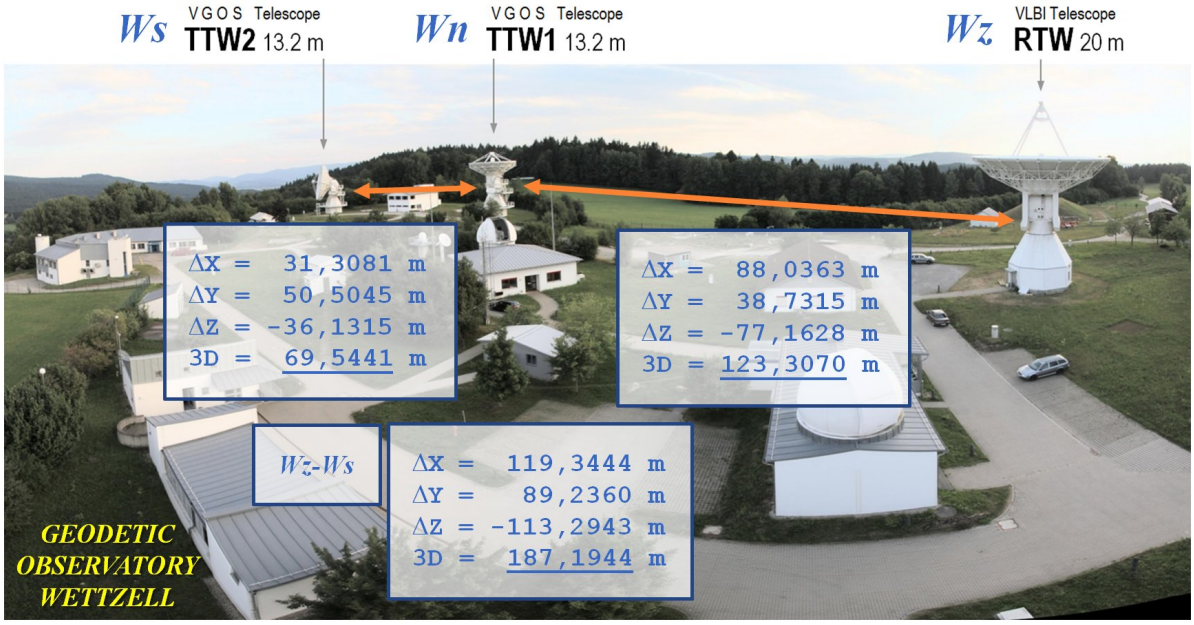

Fig. 4 Local ties for the three Wettzell VLBI telescopes from terrestrial surveying (official local ties solution for ITRF2014).

gradient even persists when newest geoid models are employed. Consequently, the vertical transformation parameters are the vertical offset plus a pair of horizontal gradients, amounting to a considerable value of approximately 30 ppm, i.e., 3 cm of change in geoid height over one km of horizontal distance. As can be seen in Figure 3, the vertical residuals are higher compared to the horizontal ones. This is the nature of GPS: GPS is less precise in height (extrapolation geometry) compared to horizontal coordinates (interpolation geometry). Nevertheless, the residuals usually stay below the desired limit of 1 mm for the majority of the points. WT25 features a discrepancy of -1.2 mm, but this point is not of concern for the VLBI and SLR reference points.

4 Results and Future Work

The results of the local tie vectors between the three Wettzell telescopes are illustrated in Figure 4. We have carried out short baseline VLBI group delay analysis for baseline Wz-Wn [Phogat et al., 2018] and can confirm an agreement between VLBI and terrestrial residuals in the sub-millimeter domain for the 3D distance, though a few millimeters can be seen in the height component. However, we suspect that the major source of uncertainty is currently within the VLBI systems.

Although the precision of the local survey network at Wettzell is sufficient at the moment, a number of small improvements are foreseen in the near future. One topic requiring attention is the computation of a local fine structure geoid and the derivation of deflections of the vertical in order to verify the nature of the significant changes in the geoidal separation over Wettzell. Furthermore, network configuration enhancements can reduce precision losses at the GNSS tower due to extrapolation, and experiments with direct datum parameter injection like scale and azimuth are envisaged.

References

[Maehler et al., 2018] S. Mähler, T. Klügel, M. Lösler, T. Schüler. Permanentes Referenzpunkt-Monitoring der TWIN-Radioteleskope am Geodätischen Observatorium Wettzell. Allgemeine Vermessungsnachrichten 127 (7).

[Phogat et al., 2018] A. Phogat, C. Plötz, T. Schüler, H. Hase, G. Kronschnabl, A. Neidhardt, J. Kodet, U. Schreiber, W. Alef, H. Rottmann, L. La Porta, S. Bernhart. Implementation and First Results of the Local Wettzell VLBI Correlator GOWL. In Proceedings of the IVS 2018 General Meeting, Svalbard, Norway, 3–6 June 2018.

Antenna Parameters and Local Tie between HartRAO 15-m and 26-m Antennas

Marisa Nickola [1,2], Aletha de Witt [1], Hana Krásná [3,4], Ludwig Combrinck [1,2], Johannes Böhm [3], Matthias Schartner [3], Christopher Jacobs [5]

Abstract In preparation for upcoming VGOS operations at HartRAO with the accompanying GGOS requirement of 1 mm accuracy in station coordinates and global baselines, a first short baseline experiment between the HartRAO 26-m legacy antenna and the co-located 15-m antenna was conducted and is described here. Antenna parameters of the HartRAO 26-m and 15-m telescopes are investigated—data from geodetic VLBI sessions are analyzed with VieVS to further estimate the antenna axis offset as well as possible seasonal variations thereof. CONT campaigns in which HartRAO participated are analyzed to compare the antenna axis offset.

Keywords VLBI, ITRF, Local tie, Axis offset

1 Introduction

In order to improve the accuracy of site coordinates and geodetic VLBI results, accurate antenna axis offsets (AO) and local ties are required. For the Global Geodetic Observing System (GGOS) goal of $\pm$ 1 mm accuracy to be achievable on global baselines (Beutler et al., 2009), it must be achievable on short baselines at least. Recently, an experiment was conducted at the Hartebeesthoek Radio Astronomy Observatory (HartRAO) on the short baseline between the HartRAO 26-m legacy antenna and co-located 15-m antenna with a view to testing this accuracy. Experiments such as these provide an opportunity to build an error budget for short baseline ties between the HartRAO antennas (including the newly built VGOS antenna) and to improve our understanding of the HartRAO complex. Running off the same clock under the same atmosphere from the same location provides a laboratory for investigating VLBI instrumental effects and antenna structure, as most geophysical and atmospheric effects mostly cancel in common mode on short baselines. The first such short baseline experiment at HartRAO is described in the sections to follow.

An antenna AO exists for radio telescopes where the rotation axes do not intersect, and AO models have to be applied for such telescopes. The AO causes geometric and dry tropospheric delays which have to be considered in VLBI analysis. Geodetic VLBI sessions are analyzed with the Vienna VLBI Software (VieVS) (Böhm et al., 2018) to estimate AO values for the HartRAO 26-m and 15-m antennas.

2 Short Baseline Experiment

A first short baseline experiment between the HartRAO 26-m legacy antenna and the co-located 15-m antenna (baseline = 113 m) was conducted on the 11th of May 2018. Unfortunately, the antennas could not be run off the same clock for this first short baseline experiment, but co-location ensured common local geophysics and atmosphere at least. VieVS was used to schedule the four hour session, SBL500. ICRF-2 defining sources were observed at X-band at 2 Gbps per station. Phasecal was turned off for the 26-m antenna, which carries

1. Hartebeesthoek Radio Astronomy Observatory (HartRAO)
2. University of Pretoria (UP)
3. Technische Universität Wien (TUW)
4. Astronomical Institute of Czech Academy of Sciences (ASU)
5. California Institute of Technology, Jet Propulsion Laboratory/NASA

less cable length from receiver to backend, in order to avoid corrupting the cross-correlation. The session ran from 22 UT on the 11th of May until 2 UT the following morning, well away from sunset and sunrise to ensure temperature stability. This is necessary to minimize thermally induced changes in cables, LNAs and downconverters as well as thermal expansion of the antennas.

Scans were scheduled to cover the full range of azimuth, elevation and cable wrap. Sweeping the full range of azimuth allows for determining east and north baseline components, while sweeping the full range of elevation separates the vertical from the troposphere. Scans were scheduled so that the antennas would nod up and down in elevation in 15° steps (from 10° to 70°) as they sweep in azimuth in 30° steps. Following this approach, the older 26-m legacy antenna does not waste much time on long slews. The first scan was scheduled at a higher elevation of 55° for calibration purposes and an azimuth of 115°. It was endeavored to schedule scans over the full range of mutual visibility for the HA-Dec mounted 26-m antenna and the Az-El mounted 15-m antenna. However, for southerly azimuths, it was not possible to observe many sources at low elevations due to the 26-m antenna's polar mount.

The 15-m antenna with its faster slew rate (Az = 2° s^{-1}, El=1° s^{-1}) had to wait for the slower 26-m legacy antenna (slew rate: HA = 0.5° s^{-1}, Dec = 0.5° s^{-1}) for a considerable amount of time. The only idle time experienced by the 26-m antenna was whilst waiting for the 15-m Az-El antenna to complete two cable wrap slews, lasting 211 and 220 seconds, respectively. A pre-observation time of ten seconds, to allow for settling time and calibration, and an observation time of 30 seconds per scan were scheduled. The schedule produced 95 scans and 880 GB of data per antenna. The SBL500 session has now been correlated by the Vienna correlator and will be analyzed in due course.

3 Antenna Axis Offsets

The rotation axes of the HartRAO 26-m equatorially mounted Cassegrain radio telescope do not intersect and are offset by ∼6.7 m. Its VLBI reference point is represented by the intersection of the fixed Hour Angle (HA) axis with the perpendicular plane containing the moving Declination (Dec) axis. The rotation axes of the HartRAO 15-m Azimuth-Elevation (Az-El) mounted radio telescope also do not intersect and are offset by ∼1.5 m. Its VLBI reference point is represented by the intersection of the fixed azimuth axis with the perpendicular plane containing the moving elevation axis. In October 2008, the south polar bearing of the 26-m antenna failed, and operations resumed only after bearing repair in August 2010. In October 2012, the 15 m was commissioned as a geodetic VLBI antenna.

Krásná et al. (2014), Nickola et al. (2015), and Nilsson et al. (2016) estimated the antenna AO values for the HartRAO 26 m by making use of VieVS in a global solution of geodetic VLBI sessions. The AO was estimated for sessions from before and after bearing repair as well as for the entire period of the 26-m antenna's operation (or a significant portion thereof). These VieVS estimated AO values failed to agree with values estimated with other VLBI analyses and measurements from ground surveys. Results from a co-location survey (taken to be the more accurate) performed in 2014 have since become available. Currently, additional geodetic VLBI sessions are analyzed using VieVS to estimate the AO of both the 26-m and 15-m antennas for comparison with previous values and values measured in the 2014 co-location survey as well as to further investigate possible seasonal variations in AO.

3.1 Comparison

Antenna AO values for the HartRAO 26-m antenna as determined by ground survey and estimated by VLBI solution are displayed in Table 1. The AO values from before the bearing repair (ground surveys and VLBI) are given in the top section of the table (taken from Combrinck and Merry (1997)) with the addition of the measurement from the co-location survey in 2014 after the bearing repair. The second section provides the VieVS estimates obtained by Krásná et al. (2014) for before and after bearing repair as well as for the entire period from 1986 (start of geodetic VLBI observations on the 26-m antenna) until the end of 2013. The third section provides the VieVS estimate obtained by Nickola et al. (2015) for after bearing repair with the addition of sessions from 2014. The values obtained in the current study, given in the bottom section of the

table, used VieVS to estimate the AO also before and after bearing repair but with the addition of sessions for 2015. The AO was also estimated for the entire period from 1986 to the end of 2015. The AO value estimated in the current study for before the bearing repair agrees within the formal error with the a priori value (= 6695.3 mm), whilst the value for after bearing repair differs by nearly a centimeter from the a priori value. The AO value estimated in the current study for the entire period from 1986 to the end of 2015 also does not agree within the formal error with the a priori value. Except for the value from the current study for before bearing repair, the 26 m AO values estimated with VieVS and reported by Krásná et al. (2014), Nickola et al. (2015), Nilsson et al. (2016), and in the current study, differ by several millimeters from the a priori value. This a priori value was however corroborated during a co-location survey in February 2014 (Muller and Poyard, 2015).

Antenna AO values for the HartRAO 15-m antenna as determined by ground survey and estimated by VLBI solution are displayed in Table 2. The AO values, obtained by using either method, are given in the top section of the table. The bottom section provides the VieVS estimates obtained by Krásná et al. (2014), Nickola et al. (2015), and in the current study for the periods indicated. While the VieVS estimates of Krásná et al. (2014), Nilsson et al. (2016), and of the current study agree within the formal error with the a priori value, all these estimates, as well as the estimate of Nickola et al. (2015) and, most importantly, the a priori value itself (determined by VLBI analysis), differ by several millimeters from the value measured during the co-location survey of 2014 (Muller and Poyard, 2015).

The difference between the a priori value and VieVS estimated value of the AO for the Continuous (CONT) VLBI campaigns in which HartRAO participated (CONTnn, nn=year) are displayed in Table 3. The CONT02, CONT05 and CONT08 campaigns were all observed with the 26-m antenna before bearing repair, whilst CONT11 was observed after bearing repair. CONT14 was observed by the 15-m antenna. None of the VieVS estimates for the CONT campaigns before bearing repair agree within the formal error with each other. Only the VieVS estimate for CONT05 agrees within the formal error with the a priori value. None of the VieVS estimates for any of the CONT campaigns agree within the formal error with the 2014 ground survey measurement. The VieVS estimate for the CONT14 campaign of the 15-m antenna does not agree within the formal error with either the a priori value or the 2014 ground survey measurement.

Table 1 HartRAO 26 m antenna axis offset determined by independent techniques (a priori value = 6695.3 mm).

Method	Determined by	Value (mm)
Standard value	JPL (1961)	6706
Conventional survey	M. Newling (1993)	6695 ± 3
VLBI solution	C. Ma (1995)	6693.6 ± 2.5
VLBI solution	M. Eubanks (1995)	6692.5 ± 1.5
HartRAO GPS	L. Combrinck (1995)	6695.6 ± 2.3
VLBI solution	C. Ma (1996)	6688.8 ± 1.8
Local tie survey	Michel et al. (2005)	6695 ± 2.5
Local tie survey	Muller and Poyard (2014)	6694.0
VieVS solutions:		
Before repair -		
1986-2008.8		6699.2 ± 0.5
After repair -	Krásná et al. (2014)	
2010.8-2014.0		6707.3 ± 0.8
1986-2014.0		6703.1 ± 0.5
VieVS solution:		
After repair -		
2010.8-2014.11	Nickola et al. (2015)	6707.9 ± 0.7
(180 sessions)		
VieVS solutions:		
Before repair -		
1986.1-2008.9		6697.8 ± 2
(757 sessions)		
After repair -	Current study	
2010.8-2015.12		6705.5 ± 0.7
(227 sessions)		
1986.1-2015.12		6700.5 ± 1.3
(984 sessions)		

Table 2 HartRAO 15 m antenna axis offset determined by independent techniques (a priori value = 1494.1 mm).

Method	Determined by	Value (mm)
GPS survey	A. Combrinck (2007)	1495
VLBI solution	D. MacMillan (2014)	1494.1 ± 2.6
Local tie survey	Muller and Poyard (2014)	1490.9
VieVS solutions:		
2012.10-2013.9	Krásná et al. (2014)	1495.0 ± 3.4
(12 sessions)		
2012.10-2015.03	Nickola et al. (2015)	1499.8 ± 1.1
(134 sessions)		
2012.10-2015.12	Current study	1496.5 ± 0.8
(272 sessions)		

Table 3 HartRAO 26 m and 15 m difference in antenna axis offset (dAO) between a priori value and VieVS estimated value for the CONT campaigns.

Campaign	dAO (mm)
26 m: CONT02 (Oct 2002)	13.67 ± 2.65
26 m: CONT05 (Sep 2005)	1.41 ± 1.53
26 m: CONT08 (Aug 2008)	4.47 ± 1.43
26 m: CONT11 (Sep 2011)	13.71 ± 1.60
15 m: CONT14 (May 2014)	-9.01 ± 2.44

3.2 Seasonal Variation

In Table 4 and Table 5, the sessions in which the 26-m antenna participated during various periods (before and after bearing repair, entire period) are divided into seasonal groupings and into two six month periods, respectively, to investigate the possibility of seasonal variations in antenna AO. The difference in AO between the a priori value and VieVS estimates from the current study for after bearing repair are also compared with the corresponding differences reported in Nickola et al. (2015).

In Table 6 and Table 7, the sessions in which the 15-m antenna participated are divided into seasonal groupings and into two six month periods, respectively, to investigate the possibility of seasonal variations in antenna AO. The difference in AO between the a priori value and VieVS estimates from the current study are also compared with the corresponding differences reported in Nickola et al. (2015).

In the current study, for the period before the bearing repair on the 26-m antenna, the largest deviation occurs in winter. For the period after bearing repair, the largest deviation occurs in summer, and the smallest deviation in autumn, similar to the findings of Nickola et al. (2015). Over the entire period, spring and summer produce the largest deviations. For before and after bearing repair as well as over the entire period, the largest deviation occurs September to February, again corresponding to the finding of Nickola et al. (2015). For the 15 m, the largest deviations occur in spring and summer and September to February, all corresponding to the findings of Nickola et al. (2015).

In general, differences between a priori AO and VieVS estimates from the current study are smaller than corresponding differences reported by Nickola et al. (2015).

Table 4 HartRAO 26 m difference in antenna axis offset (dAO) between a priori AO value (= 6695.3 mm) and VieVS estimated value for specified months/seasons.

Month/Season	Before repair	After repair	All
Summer - DecJanFeb			
Current study:	1986.1-2008.9	2010.8-2015.12	1986.1-2015.12
26 m dAO (mm)	4.70 ± 0.92	12.55 ± 1.41	7.03 ± 0.77
No. of sessions	230	59	289
2015 study:		2010.8-2014.11	
26 m dAO (mm)		17.30 ± 1.67	
No. of sessions		46	
Autumn - MarAprMay			
Current study:	1986.1-2008.9	2010.8-2015.12	1986.1-2015.12
26 m dAO (mm)	4.26 ± 1.07	3.45 ± 1.69	3.94 ± 0.90
No. of sessions	160	37	197
2015 study:		2010.8-2014.11	
26 m dAO (mm)		5.77 ± 1.97	
No. of sessions		31	
Winter - JunJulAug			
Current study:	1986.1-2008.9	2010.8-2015.12	1986.1-2015.12
26 m dAO (mm)	-2.12 ± 6.26	9.78 ± 1.40	1.49 ± 4.51
No. of sessions	179	54	232
2015 study:		2010.8-2014.11	
26 m dAO (mm)		13.25 ± 1.56	
No. of sessions		44	
Spring - SepOctNov			
Current study:	1986.1-2008.9	2010.8-2015.12	1986.1-2015.12
26 m dAO (mm)	4.67 ± 0.82	10.88 ± 1.04	7.64 ± 0.66
No. of sessions	189	77	266
2015 study:		2010.8-2014.11	
26 m dAO (mm)		12.03 ± 1.06	
No. of sessions		59	

4 Conclusions

The antenna AO values show statistically significant differences between various data sets that are not well understood. For the VieVS estimated AO values of the 26-m antenna, there appears to be a significant change from before to after bearing repair, but this is not reflected in the corresponding ground survey values. For both the 26-m and 15-m antennas, the AO estimated with VieVS differ considerably from the values measured during the 2014 co-location survey. Possible correlation of AO with station position, tropospheric delay, clock parameters, structural deformation, hydrology loading etc. needs to be investigated.

With regard to the short baseline sessions, future efforts will be directed towards running the 26-m and

Table 5 HartRAO 26 m difference in antenna axis offset (dAO) between a priori AO value (= 6695.3 mm) and VieVS estimated value for specified six month period.

Month/Season	Before repair	After repair	All
Spring and Summer - Sep - Feb			
Current study:	1986.1-2008.9	2010.8-2015.12	1986.1-2015.12
26 m dAO (mm)	4.85 ± 0.61	11.46 ± 0.83	7.50 ± 0.50
No. of sessions	419	136	555
2015 study:		2010.8-2014.11	
26 m dAO (mm)		13.14 ± 0.91	
No. of sessions		105	
Autumn and Winter - Mar - Aug			
Current study:	1986.1-2008.9	2010.8-2015.12	1986.1-2015.12
26 m dAO (mm)	0.06 ± 3.75	7.32 ± 1.07	2.04 ± 2.72
No. of sessions	338	91	429
2015 study:		2010.8-2014.11	
26 m dAO (mm)		9.75 ± 1.23	
No. of sessions		75	

Table 6 HartRAO 15 m difference in antenna axis offset (dAO) between a priori AO value (= 1495.0 mm) and VieVS estimated value for specified months/seasons.

Month/Season	Current study 2012.10-2015.12	2015 study 2012.10-2014.11
Summer - DecJanFeb		
15 m dAO (mm)	5.46 ± 1.68	7.09 ± 2.12
No. of sessions	73	42
Autumn - MarAprMay		
15 m dAO (mm)	-2.88 ± 1.58	1.41 ± 2.22
No. of sessions	57	27
Winter - JunJulAug		
15 m dAO (mm)	-2.81 ± 1.51	6.67 ± 2.37
No. of sessions	64	27
Spring - SepOctNov		
15 m dAO (mm)	5.96 ± 1.56	6.02 ± 2.47
No. of sessions	78	38

15-m antennas off the same clock and conducting these short baseline sessions at least once a month to detect possible seasonal variations. An error budget for short baseline ties will be drawn up, and each term will be investigated. The newly built VGOS antenna also needs to be accurately tied to the 26-m legacy antenna.

Table 7 HartRAO 15 m difference in antenna axis offset (dAO) between a priori AO value (= 1495.0 mm) and VieVS estimated value for specified six month period.

Month/Season	Current study 2012.10-2015.12	2015 study 2012.10-2014.11
Spring and Summer - Sep - Feb		
15 m dAO (mm)	5.73 ± 1.14	7.11 ± 3.78
No. of sessions	151	80
Autumn and Winter - Mar - Aug		
15 m dAO (mm)	-2.73 ± 1.09	3.74 ± 1.64
No. of sessions	121	54

Acknowledgements

 A portion of this research was carried out at the Jet Propulsion Laboratory, California Institute of Technology, under a contract with the National Aeronautics and Space Administration. The authors acknowledge the IVS and all its components for providing VLBI data (Nothnagel et al., 2015). The authors wish to thank Jakob Gruber (TU Wien) and Jonathan Quick (HartRAO) for their contribution to the first HartRAO short baseline session.

References

1. G. Beutler et al. Global Geodetic Observing System - Meeting the Requirements of a Global Society on a Changing Planet in 2020. *Towards GGOS in 2020*, Chapter 10, 273–281, 2009.
2. J. Böhm et al. Vienna VLBI and Satellite Software (VieVS) for Geodesy and Astrometry. *Publications of the Astronomical Society of the Pacific*,130(986), 10.1088/1538-3873/aaa22b, 044503, 2018.
3. W.L. Combrinck and C.L. Merry. Very long baseline interferometry antenna axis offset and intersection determination using GPS. *J. Geophys Res.*, 102(B11):24741–24744, 1997.
4. H. Krásná, M. Nickola, and J. Böhm. Axis offset estimation of VLBI telescopes. *IVS 2014 General Meeting*, Shanghai, 339–343, 2014.
5. J.M. Muller and J-C. Poyard. Hartebeesthoek local tie survey. *IGN report*, 2015.
6. M. Nickola et al. Determining HartRAO antenna parameters with VieVS. *EVGA 2015 Working Meeting*, 140–144, 2015.
7. T. Nilsson et al. Antenna axis offsets and their impact on VLBI derived reference frames. *REFAG 2014*, International Association of Geodesy Symposia, 146, 53-58, 2016.
8. A. Nothnagel et al. The IVS data input to ITRF2014. *International VLBI Service for Geodesy and Astrometry*, doi:10.5580/GFZ.1.1.2015.002, 2015.

Session 4

VLBI Core Products and Their Improvements

Galactic Aberration in VLBI Analysis:
Findings of IVS WG8

Daniel MacMillan [1], Alan Fey [2], John Gipson [1], David Gordon [1], Chris Jacobs [3], Hana Krásná [4], Sébastien Lambert [5], Chopo Ma [6], Zinovy Malkin [7], Oleg Titov [8], Guangli Wang [9],Minghui Xu [9], Norbert Zacharias [2]

Abstract The IVS Working Group on Galactic Aberration (WG8) was established to investigate issues related to incorporating the effect of galactic aberration in IVS analysis. Secular aberration drift is caused by the acceleration of the Solar System barycenter. It is mainly due to the rotation of the barycenter about the center of the Milky Way galaxy. Studies made by working group members have shown that aberration can be estimated from VLBI geodetic data. The VLBI estimates of the aberration amplitude are in the range 5.1 to 6.4 μas/yr. These estimates are close to independent estimates of 4.8 to 5.4 μas/yr that were derived from astrometric measurements of proper motions and parallaxes of masers in the Milky Way galaxy. For the recommended aberration constant, a geodetic value 5.8 μas/yr based on data until May 2018 was chosen by the Working Group in order to be consistent with geodetic VLBI applications, specifically for the generation of the ICRF3 solution. In this paper, we discuss the investigation of the Working Group and its findings.

Keywords Galactic aberration, ICRF, Proper motion

1. NVI Inc. at NASA/GSFC
2. United States Naval Observatory
3. Jet Propulsion Laboratory
4. Technische Universität Wien
5. Paris Observatory
6. NASA Goddard Space Flight Center
7. Pulkovo Observatory
8. Geoscience Australia
9. Shanghai Astronomical Observatory

1 Introduction

The IVS Working Group on Galactic Aberration (WG8) was established by the IVS Directing Board at its meeting in November 2015 with the work beginning in 2016. The purpose of the group was to investigate the issues related to incorporating the effect of galactic aberration in IVS analysis. Based on this investigation, the WG was tasked to formulate a recommendation for an aberration correction model to be applied in IVS data analysis and to be provided to the ICRF3 Working Group.

Secular aberration drift is caused by the acceleration of the Solar System barycenter. It is mainly due to the rotation of the barycenter about the center of the Milky Way galaxy as illustrated in Figure 1. This motion induces an apparent proper motion of extragalactic objects observed by VLBI. It was predicted theoretically to have a dipolar structure with an amplitude of 4-6 μas/yr (see e.g., [1], [6], [5]).

Figure 2 shows the proper motion induced by galactic aberration [13] where the aberration amplitude was 6.4 μas/yr. The proper motion vectors stream away from the anti-galactic center towards the galactic center in a dipolar pattern where the maximum proper motion occurs for sources that are 90 $^\circ$ away from the galactic center (RA = 266.4°, DEC = -28.9°).

The effect of aberration is to cause apparent source positions to change over time. Several studies in recent years, which we discuss in Section 2, have shown that aberration can be estimated from VLBI geodetic data. The VLBI estimates of the aberration amplitude are in the range 5-7 μas/yr. These estimates are reasonably close to independently determined estimates of 4.8-5.5 μas/yr that can be derived from recent astrometric measurements of proper motions and parallaxes of masers

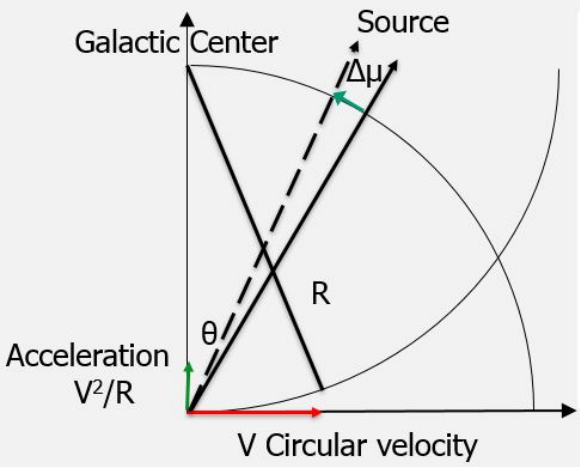

Fig. 1 Galactic aberration. Induced proper motion $\Delta\mu$ of a source is V^2/(Rc) sin θ.

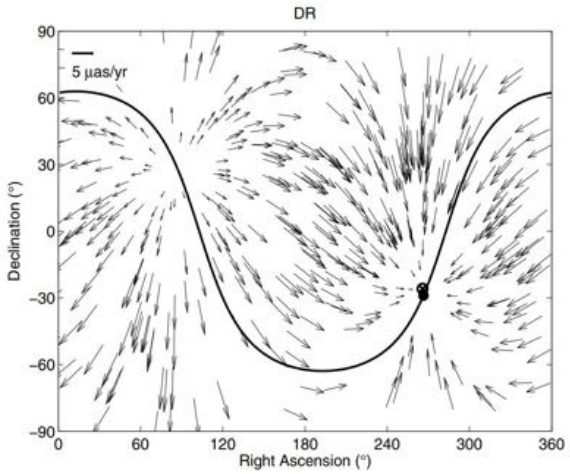

Fig. 2 Aberration proper motion (Titov and Lambert, 2013).

in the Milky Way galaxy. Although the effect of aberration is small, it is not negligible in terms of future micro-arcsecond astrometry. The systematic drift due to an aberration drift of 5 μas/yr would lead to a dipole systematic error of 100 μas after 20 years. One of the effects of applying an aberration model is to change the source positions for a given reference epoch. If the reference epoch of the aberration model is J2000, when the correction is defined to be zero, the aberration corrections to radio source positions at J2000 are as large as 40–50 μas depending on the source coordinates. This arises from the distribution of the median epochs of observation of the sources observed by VLBI over the last three decades. The correction increases as the temporal difference between the median epoch and the reference epoch increases.

Generally the aberration vector estimates from most of the VLBI WG member solutions have components not directed toward the galactic center, which are at most 25% of the aberration amplitude. The WG investigated whether this could be due to how VLBI analysis is performed. Among the issues investigated were 1) dependence of aberration estimates on experiment sessions included in solutions, 2) dependence on sources included, and 3) dependence on solution parametrizations.

The primary objective of the WG was to determine a value of the secular aberration drift constant to be applied in an a priori model of aberration. The application of an a priori model of aberration will most importantly account for the systematic error that is committed without the model. Clearly the dipole systematic due to aberration is significant compared to the CRF noise floor, which in the case of ICRF2 was 40 μas.

The ICRF realizes the International Celestial Reference System (ICRS) by the positions of a set of defining sources that are assumed to have no measurable proper motion. An underlying issue is that applying apparent proper motion corrections due to aberration in VLBI analysis could require a redefinition of the ICRS. However, a redefinition of the ICRS is not something that the IVS can do as it would have to be done by the International Astronomical Union (IAU). The working group found that it was not necessary to redefine the ICRS. We can simply apply an aberration proper motion correction in VLBI analysis by a procedure that is similar to that followed in VLBI analysis to account for other effects like precession or annual aberration (see Section 4). For non-VLBI applications requiring source positions at an epoch other than J2000, one would need to apply the galactic aberration model proper motions with reference epoch J2000 to the source positions given in a catalog generated with the model.

In Sections 2 and 3, we discuss possible choices of the model aberration constant: 1) a geodetic VLBI determined value, 2) a value determined from recent parallax and proper motion measurements of galactic masers, and 3) an average of the two techniques. Then in Section 4, we consider the effects of applying aberration to estimates of source positions from VLBI analysis.

2 Geodetic VLBI Solutions

Figure 3 shows the proper motion field computed from source position time series where the RA and DEC uncertainties were better than 50 μas/yr. These observed proper motions can be as large as a few hundred μas/yr, which are likely due to apparent motion caused by source structure effects. In contrast, systematic galactic aberration proper motions are less than 6 μas/yr. To estimate the systematic effect, one has to assume that source structure effects are random over the sky.

A change in the source direction away from the nominal direction $\mathbf{s_0}$ due to the aberration acceleration $\mathbf{A}$ in a time interval Δt can be expressed as

$$\Delta \mathbf{s} = \frac{\mathbf{s_0} \times (\mathbf{A}\Delta t \times \mathbf{s_0})}{c} \quad (1)$$

The components of the aberration proper motion $\Delta/\mathbf{s}\Delta t$ for a source at right ascension and declination (α, δ) are

$$\Delta\mu_\alpha cos\delta = \frac{1}{c}(-A_1 sin\alpha + A_2 cos\alpha) \quad (2)$$

$$\Delta\mu_\delta = \frac{1}{c}(-A_1 cos\alpha sin\delta - A_2 sin\alpha sin\delta + A_3 cos\delta) \quad (3)$$

Over the last several years, members of our working group made several solutions for the galactic acceleration vector $\mathbf{A}$ using Calc/Solve and VieVS. Table 1 shows the estimates and uncertainties of the galactic center component $\mathbf{A_G}$, the magnitude $|\mathbf{A}|$ of the vector, and the direction of the vector that was estimated for each solution. We usually inflate Calc/Solve parameter estimate uncertainties by a factor of 1.5, which was derived in decimation studies (for example, [3]). To be consistent, the uncertainties of all the amplitudes in the table were all scaled up by this factor.

The global Calc/Solve solutions estimated the components of $\mathbf{A}$ as additional global parameters using the userpartial feature of Calc/Solve ([14] and Xu et al., 2017; [7] and MacMillan, 2016). For the Calc/Solve time series solutions ([12] and [13]), $\mathbf{A}$ was estimated in three steps: 1) estimate source position time series in Calc/Solve solutions, 2) estimate source apparent proper motions from these time series, and 3) estimate $\mathbf{A}$ from these proper motions.

For the scale solution, [11] expanded Equation (1) so that the aberration delay becomes

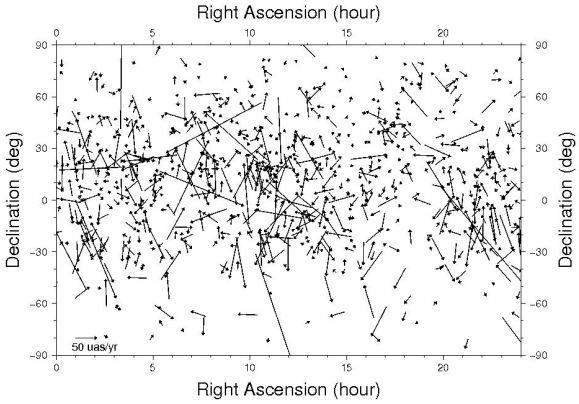

Fig. 3 Proper motion field computed from source position time series (with RA and DEC uncertainties better than 50 μas).

$$\Delta\tau = -\frac{\mathbf{B}\cdot\Delta\mathbf{s}}{c} = -\frac{\mathbf{B}\cdot\mathbf{A}\Delta t}{c} - \frac{F\Delta t\mathbf{B}\cdot\mathbf{s_0}}{c} \quad (4)$$

$$F \equiv -\frac{\mathbf{A}\cdot\mathbf{s}_0}{c}. \quad (5)$$

A global scale factor parameter F was estimated for each source using only the second term in (4), and $\mathbf{A}$ was then derived from the estimated scale factor parameters for all sources using the expression above for F. In the Calc/Solve global solutions, no such separation was made, and $\mathbf{A}$ was estimated essentially from the proper motions of all the sources. An advantage of the method in [11] is that it allows one to estimate $\mathbf{A}$ from different subsets of all sources and thereby remove poorly determined sources from the estimation.

Most of the VLBI estimates of $\mathbf{A}$ have relatively small components (less than 25% of $|\mathbf{A}|$) not in the Galactic center direction. An exception is the first solution of Xu et al., [14], where the component of the acceleration $\mathbf{A}$ perpendicular to the Galactic plane was 46% of $|\mathbf{A}|$. They suggested several hypothetical mechanisms that could explain this estimate, for example, a companion star orbiting the Sun. A second solution of Xu et al. made in 2017 has significantly smaller components not in the direction of the Galactic center. Further investigation of possible physical means for producing non-galactic center components could provide a bound for the VLBI estimates of these components. For the recommended model, we will just consider the Galactic center component A_G of the estimates of the aberration acceleration vector.

Table 1 Geodetic VLBI Aberration Estimates.

		A_G	σ	$\lvert A\rvert$	σ	RA	σ	DEC	σ
		μas/yr		μas/yr		deg		deg	
Titov et al. (2011)	1990-2010	6.3	1.4	6.4	1.5	263	11	-20	12
Titov+Lambert(2013)	1979-2013	6.4	1.1	6.4	1.1	266	7	-26	7
Xu (2013)	1980-2011	5.2	0.5	5.8	0.5	243	4	-11	4
Xu (2017)	1980-2016	6.0	0.3	6.1	0.3	271	2	-21	3
MacMillan (2014)	1979-2014	5.3	0.4	5.6	0.4	267	4	-11	6
MacMillan (2017)	1979-2016	5.7	0.3	5.8	0.3	273	3	-22	5
Titov+ Krasna (2018)	1979-2016	6.0	0.3	6.1	0.3	260	2	-18	4
Titov+Krasna (2018)	1979-2016	5.4	0.6	5.4	0.6	273	4	-27	8
Titov+Krasna (2018)	1979-2016	5.1	0.3	5.2	0.3	281	3	-35	3

3 Galactic Astrometry Estimates

Aberration can also be derived from recent (2009–2017) stellar astronomy measurements (e.g., [10], [8], [2]). These measurements are trigonometric parallaxes and proper motions of masers in high-mass star-forming regions in the Milky Way galaxy. The measurements were made using the Very Long Baseline Array (VLBA), the European VLBI network (EVN), and the Japanese VLBI Exploration of Radio Astronomy Project (VERA). The most recent investigation noted here [8] used a maser sample of 136 sources. Using these parallax and proper motion measurements, different investigators have derived models of the galaxy. Among the parameters of these models are the radial distance R (kpc) to the galactic center and circular rotation speed V (km/s) of the solar system barycenter. Based on the estimated parameters R and V and their uncertainties from each investigator, one can determine the aberration constant A_G=V^2/(Rc) and its uncertainty. Table 2 shows the resulting estimates of the aberration constant A_G. Based on the uncertainties of R and V, the formal uncertainties of A_G are in the range 0.3-0.8 μas/yr.

4 Application of Aberration in Geodetic VLBI Solutions

In this section, we discuss how the aberration correction should be applied to determine a new ICRF catalog. One can simply run a solution with an aberration correction that has a reference epoch of t_0 = J2000. The estimated positions will then be self-consistent with the correction. The aberration contributions to the a priori source positions are

$$\Delta\alpha(\alpha,\delta) = \Delta\mu_\alpha(t-t_0) \quad (6)$$

$$\Delta\delta(\alpha,\delta) = \Delta\mu_\delta(t-t_0) \quad (7)$$

where the aberration proper motions ($\Delta\mu_\alpha\cos\delta$, $\Delta\mu_\delta$) are given above in (2) and (3). For non-VLBI applications requiring positions at epoch t, the catalog positions at J2000 would be corrected by applying the Galactic aberration model correction for epoch t.

We have investigated what is the effect of the aberration on estimated source positions. Figures 4, 5, 6, and 7 show the Calc/Solve differences in source positions (RA, DEC) versus RA and DEC when the aberration constant A_G is a nominal 5 μas/yr. The variation (scatter) of the differences at RA or DEC in these plots is due to the fact that the difference in the mean epoch from the reference epoch (e.g., J2000) varies significantly over the set of sources. In this case the sources in the source NNR (no net rotation) constraint were uniformly weighted.

5 IAU Recommendation

Possible options for the IVS working group recommendation for the aberration constant AG are: 1) VLBI weighted mean, 2) galactic astronomy weighted mean, and 3) the average of 1) and 2). If the two were equally weighted A_G = 5.3 $\pm$ 0.3 μas/yr. The average of the two sets of measurements differ from the means of each group by at most 0.4 μas/yr which is less than 10% of the aberration effect. If we are uncertain about which

Table 2 Galactic Astronomy Derived Estimates.

	A_G	σ	V	σ	R	σ	masers
	μas/yr		km/s		kpc		
Reid (2009)	5.4	0.08	254	16	8.40	0.60	18
Brunthaler (2011)	5.1	0.3	246	7	8.30	0.23	18
Honma (2012)	4.9	0.6	238	14	8.05	0.45	52
Reid (2014)	4.8	0.3	240	8	8.34	0.16	103
Rastorguev (2017)	4.8	0.3	238	7	8.24	0.12	136

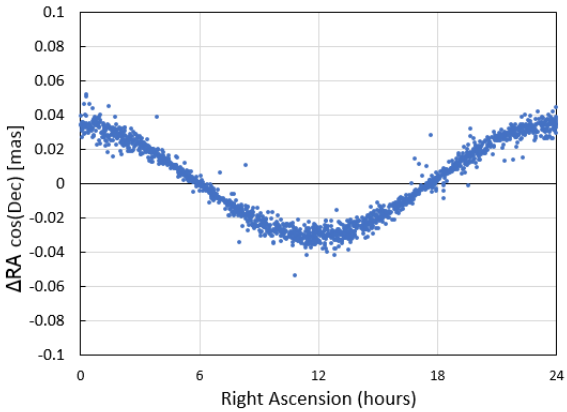

Fig. 4 Aberration effect on right ascension versus right ascension with an aberration constant of 5 μas/yr.

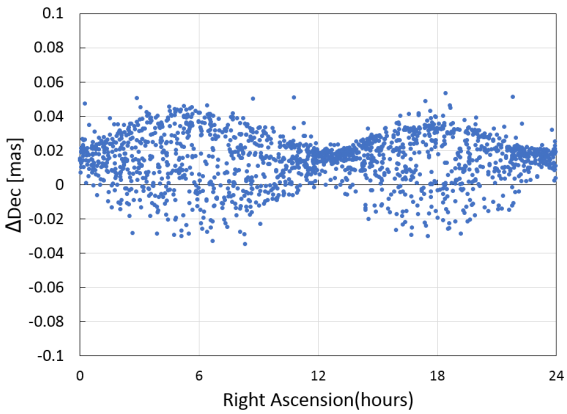

Fig. 6 Aberration effect on declination versus right ascension with an aberration constant of 5 μas/yr.

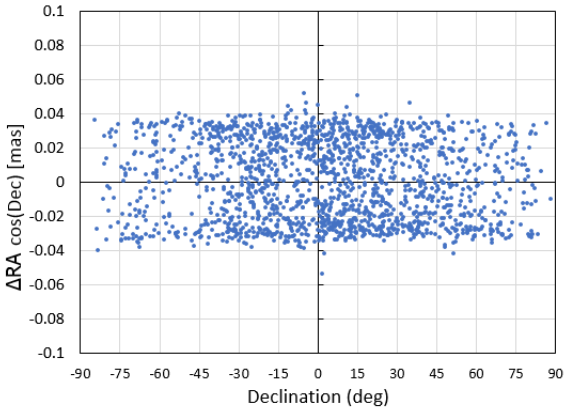

Fig. 5 Aberration effect on right ascension versus declination with an aberration constant of 5 μas/yr.

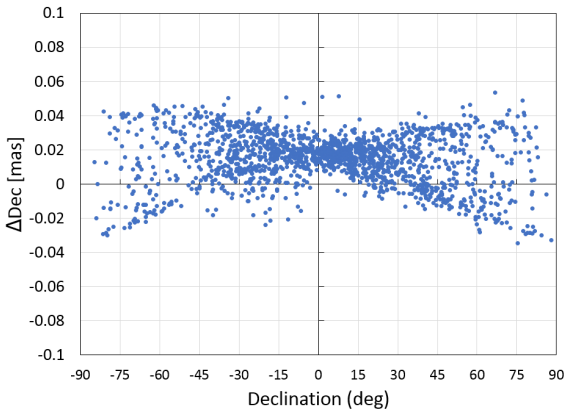

Fig. 7 Aberration effect on declination versus declination with an aberration constant of 5 μas/yr.

group of measurements may be biased from the truth, this would appear to be the best option.

However, we recommend that the IAU ICRF3 working group should use option 1) for the value of A_G when a galactic aberration contribution is applied. The rationale is that since the correction was derived via geodetic VLBI solutions, it should be applied in the analysis of geodetic VLBI sessions, specifically for the ICRF3 solution, in order to be self-consistent. Since none of the solutions reported in Table 1 used all of the available data, a new Calc/Solve global solution was run using all of the data used for the

ICRF3 solution (from 1979 through May 2018). The resulting estimated aberration constant 5.8 μas/yr is not significantly different from the value from the solution (MacMillan, 2016) that used data until 2016. This aberration constant was taken to be the final recommended value.

6 Conclusions

The Working Group recommended an aberration constant derived only from geodetic VLBI data analysis in order to be consistent with geodetic VLBI solutions (and specifically for the ICRF3 solution) rather than averaging geodetic and galactic astronomy estimates. The ICRF3 was derived using an aberration constant estimated using all the data used for the ICRF3 solution, which was about two more years of data than any of the previous VLBI solutions. The recommended value of 5.8 μas/yr is reasonably close to the constant derived from recent Galactic astronomy measurements. An issue that remains to be studied further is to understand the cause of non-galactic center components of the estimated aberration vector estimates from the different WG solutions although their magnitudes are generally less than 25% of $|\mathbf{A}|$. This could be due to some unmodeled physical aberration effect or possibly to how the VLBI analysis was done.

Acknowledgements

Dan MacMillan acknowledges support from NASA contracts NNG12HP00C and NNG17HS00C.

References

1. U. Bastian, In M. A. Perryman and F. Van Leeuwen, editors, Proc. RG0-ESA Workshop on Future Possibilities for Astrometry in Space, ESA SP-379, 99, 1995.
2. A. Brunthaler, M. J. Reid, K. M. Menten, et al. The bar and spiral structure legacy (BeSSeL) survey: Mapping the Milky Way with VLBI astrometry. *AN*, 332(5), 461, 2011.
3. A. Fey, D. Gordon, C. S. Jacobs, et al. The second realization of the international celestial reference frame by very long baseline interferometry. *AJ*, 150, 58, 2015.
4. M. Honma, T. Nagayama, K. Ando, et al. Fundamental parameters of the Milky Way Galaxy based on VLBI astrometry. *PASJ*, 135, 64, 2012.
5. S. M. Kopeikin and V. V. Makarov. Astrometric effects of secular aberration. *AJ*, 131, 1471, 2006.
6. J. Kovalevsky. Aberration in proper motions. *A&A*, 404, 743, 2003.
7. D. S. MacMillan. Determination of galactic aberration from VLBI measurements and its effect on VLBI reference frames and Earth orientation parameters. In AGU Meeting abstracts, San Francisco, CA, 2014.
8. A. S. Rastorguev, N. D. Utkin, M. V. Zabolotskikh, et al. Galactic masers: kinematics, spiral structure and the disk dynamic state. *Astrophys. Bull.*, 72, 122, 2017.
9. M. J. Reid, K. M. Menten, X. W. Zheng, et al. Trigonometric parallaxes of massive star- forming regions. VI. Galactic structure, fundamental parameters, and noncircular motions. *ApJ*, 700, 137, 2009.
10. M. J. Reid, K. M. Menten, A. Brunthaler, et al. Trigonometric parallaxes of high mass star forming regions: the structure and kinematics of the Milky Way. *ApJ*, 783, 130, 2014.
11. O. Titov and H. Krásná. Measurement of the solar system acceleration using the Earth scale factor. *A&A*, A36, doi.org/10.1051/0004-6361/201731901, 610, 2018.
12. O. Titov, S. B. Lambert, and A. -M. Gontier. VLBI measurement of the secular aberration drift. *A&A*, A91, 529, 2011.
13. O. Titov and S. B. Lambert. Improved VLBI measurement of the solar system acceleration. *A&A*, A95, 559, 2013.
14. M. H. Xu, G. L. Wang, and M. Zhao. The solar acceleration obtained by VLBI observations. *A&A*, A135, 544, 2012.

The Effect of Galactic Aberration on the CRF

David Mayer [1], Sébastien Lambert [2], Johannes Böhm [1], Hana Krásná [1,3], Niu Liu [2,4]

Abstract We compare two Celestial Reference Frame (CRF) solutions made from Very Long Baseline Interferometry (VLBI) group delay observations in S/X band using vector spherical harmonics. In both solutions the same data set was used which consists of almost all observations since 1979 until the beginning of 2018. The same parameterization and models were used with the exception that in one of the solutions the effect of galactic aberration (GA) was corrected. The other solution serves as a reference. We show that the deformation of a CRF estimated with the whole set of VLBI observations can be described by a systematic dipole displacement with an amplitude of about 35 μas.

Keywords CRF, Galacto-centric acceleration, vector spherical harmonics

1 Introduction

The solar system is rotating around the galactic center. This introduces a galacto-centric acceleration, which, in turn, imprints itself as an apparent proper motion of celestial objects. The term galactic aberration (GA) is used for this effect. On the one hand, this is a problem for Very Long Baseline Interferometry (VLBI), since the sources are assumed stationary, which should be corrected. On the other hand, since quasars are very stable reference objects, which do not have detectable proper motions, we can use VLBI to assess this phenomenon. Several papers were published with the aim of estimating GA from Very Long Baseline Interferometry (VLBI) data (see, e.g., [12, 16, 13, 14]). They report values ranging from 5.2 ± 0.2 to 6.4 ± 1.1 with the center of the Galaxy at $17^{\mathrm{h}}45^{\mathrm{m}}40^{\mathrm{s}}$ in right ascension and $-29°00'28''$ in declination. The International VLBI Service for Geodesy and Astrometry (IVS) initiated a working group, which was tasked with the investigation of this effect. At the IVS General Meeting in 2018, the working group presented their recommendations. The GA was estimated with 5.6 μas per year and it was recommended to remove this effect at the modeling stage, see [9]. However, for consistency reasons this value was recalculated using the data set, which was used for the calculations of the International Celestial Reference Frame 3 (ICRF3), see [4]. The fully consistent (with ICRF3) estimate of GA was found to be 5.8 μas per year. The ICRF3, which is the newly recommended international celestial reference frame, utilizes this value to model the effect of GA. In order to correct a time dependent effect an epoch has to be chosen. The average mean epoch of sources in S/X band published in ICRF3 is December 2012 and the epoch for which GA is corrected is 2015. The same value of 5.8 μas per year with the same epoch of 2015 was used in the CRF solution evaluated here. We can expect that the correction of GA has some systematic effect on the celestial reference frame. This systematic is imprinted onto the difference vectors between two solutions, one where GA was corrected and one where it was not.

In order to quantify this effect the method of vector spherical harmonics, see [10], is used. Global features of the differences such as a rotation of the catalogs and the so-called glide parameters are reflected in degree 1. Degree 2 describes the quadrupole deformations between the catalogs. The whole transformation reads:

1. Technische Universität Wien, Austria
2. Observatoire de Paris, France,
3. Czech Academy of Sciences, Czech Republic
4. School of Astronomy & Space Science, China

$$
\begin{aligned}
\Delta\alpha\cos\delta &= R_1\cos\alpha\sin\delta + R_2\sin\alpha\sin\delta - R_3\cos\delta \\
&\quad - D_1\sin\alpha + D_2\cos\alpha \\
&\quad + a_{20}^{M}\sin 2\delta \\
&\quad + \left(a_{21}^{E,\mathrm{Re}}\sin\alpha + a_{21}^{E,\mathrm{Im}}\cos\alpha\right)\sin\delta \qquad (1)\\
&\quad - \left(a_{21}^{M,\mathrm{Re}}\cos\alpha - a_{21}^{M,\mathrm{Im}}\sin\alpha\right)\cos 2\delta \\
&\quad - 2\left(a_{22}^{E,\mathrm{Re}}\sin 2\alpha + a_{22}^{E,\mathrm{Im}}\cos 2\alpha\right)\cos\delta \\
&\quad - \left(a_{22}^{M,\mathrm{Re}}\cos 2\alpha - a_{22}^{M,\mathrm{Im}}\sin 2\alpha\right)\sin 2\delta, \\
\Delta\delta &= -R_1\sin\alpha + R_2\cos\alpha \\
&\quad - D_1\cos\alpha\sin\delta - D_2\sin\alpha\sin\delta + D_3\cos\delta \\
&\quad + a_{20}^{E}\sin 2\delta \\
&\quad - \left(a_{21}^{E,\mathrm{Re}}\cos\alpha - a_{21}^{E,\mathrm{Im}}\sin\alpha\right)\cos 2\delta \qquad (2)\\
&\quad - \left(a_{21}^{M,\mathrm{Re}}\sin\alpha + a_{21}^{M,\mathrm{Im}}\cos\alpha\right)\sin\delta \\
&\quad - \left(a_{22}^{E,\mathrm{Re}}\cos 2\alpha - a_{22}^{E,\mathrm{Im}}\sin 2\alpha\right)\sin 2\delta \\
&\quad + 2\left(a_{22}^{M,\mathrm{Re}}\sin 2\alpha + a_{22}^{M,\mathrm{Im}}\cos 2\alpha\right)\cos\delta
\end{aligned}
$$

where R_i are the three rotation parameters, D_i are the three glide parameters, and $a_{lm}^{M,E}$ are the quadrupole parameters of electric (E) and magnetic (M) type.

2 Data

The data used for this comparison is equivalent to the data set used for the S/X band solution within ICRF3. It spans almost 40 years from 1979 until the beginning of 2018 with 6,000 observing sessions. More than 100 stations collected about 12 million group delay observations from more than 4,500 sources.

3 Analysis

Two celestial reference frames were estimated with the software VieVS [3]. Single sessions were analyzed first and the normal equation system from each session was saved. The normal equation systems were then stacked in a following global solution, which results in a global celestial and terrestrial reference frame.

Generally, the IERS 2010 Conventions [11] were used for a priori modeling. The following provides a short overview of parameters that were used in the single session analysis:

- ITRF2014 (see [1]) and ICRF2 (see [5] and [6]) were used as a priori Terrestrial Reference Frame (TRF) and CRF, respectively.
- The Vienna Mapping Function (VMF1), see [2], was used as mapping function, the DAO model was used for a priori gradients, see [7] and [8], and the atmospheric pressure loading (APLO) model by [15] was used.
- Clocks were estimated as quadratic functions with piece wise linear offsets (PWLO) every hour.
- Troposphere delays were estimated as zenith wet delays and north/east gradients every 30 min and six hours, respectively. Absolute constraints were used for the gradients in order to prevent unrealistic values.
- Earth orientation parameters (EOP) were estimated every 48h with tight relative constraints between these offsets, effectively constraining them to a single offset.
- Sources, which have less than three observations, were excluded at the observation level.

In the global solution, the following parameters were used:

- Stations with a short observing history were reduced, which means that their position was estimated session-wise.
- Known breaks from earthquakes and other sources were introduced.
- Velocity constraints for stations at the same site are introduced.
- Station positions and velocities are estimated, the datum is set to 21 well-behaved stations.
- The special handling sources were reduced. Note that this is different in the ICRF3 solution where all sources are estimated as global parameters.
- Source coordinates are estimated with the 295 ICRF2 datum sources being used to define the frame. Note that this is different for the ICRF3 where a new set of 303 sources is used to define the frame.

As mentioned before, in one of the two solutions the GA is corrected, in the other it is not. This is the only difference between these solutions.

4 Results and Discussion

When the Vector Spherical Harmonic (VSH) decomposition is performed on the difference vector field of the two solutions, the parameters listed in Table 1 are found. The formal errors of the VSH parameters are generally lower than 0.1 μas. Looking at Table 1 one can immediately see the parameters most affected by GA which are the D_2 and D_3 parameters.

The apparent proper motion field, which can be expected from GA, resembles a flow from a source (galactic anti-center) to a sink (Galactic Center). In the VSH, the glide parameters describe a similar dipole pattern with a flow from a source to a diametrically opposed sink. The D_2 parameter describes a dipole with the poles at 18^{h} (note that this is almost exactly the same right ascension as the Galactic Center) and 6^{h} in right ascension and zero in declination, while the D_3 parameter describes a dipole with poles at $\pm 90^{\circ}$ declination and zero right ascension. Therefore, a combination of D_2 and D_3 is sufficient to describe most of the effect of GA.

Other parameters do show a small (couple of μas) variation as well. However, when looking at the correlation between the parameters, it can be seen that some of these parameters are correlated with factors as high as 0.46, see Table 3. This is most likely the reason for the other small parameters. One explanation for the correlations is the uneven distribution of the sources on the celestial sphere.

We can calculate the amplitude and direction of the glide (D_1, D_2, and D_3 parameters). This is listed in Table 2. One can see that the estimated direction is very close to the anti-center of the Galaxy.

This becomes even more evident when the glide is plotted on the celestial sphere, see Figure 1. One can see that the direction of the glide points almost exactly to the center of the Milky Way.

5 Conclusions

We created two CRF solutions with parameterization close to ICRF3 with the difference that in one of those solutions the effect of galacto-centric acceleration is corrected. Using a vector spherical harmonic decomposition of the difference vector field of these solutions we can show that correcting GA affects the glide parameters. In particular, the D_2 and D_3 parameters are affected by GA with a difference of 30 μas and 15 μas,

Table 1 VHS parameters of degree 2 between the Vienna CRF solution with correction of GA and without correction of GA.

	[μas]
R_1	-6 ± 0.1
R_2	$+3 \pm 0.1$
R_3	-3 ± 0.0
D_1	$+2 \pm 0.1$
D_2	$+31 \pm 0.1$
D_3	$+15 \pm 0.1$
$a^{e}_{2,0}$	$+4 \pm 0.1$
$a^{m}_{2,0}$	$+0 \pm 0.1$
$a^{e,Re}_{2,1}$	-0 ± 0.1
$a^{e,Im}_{2,1}$	$+2 \pm 0.1$
$a^{m,Re}_{2,1}$	-2 ± 0.1
$a^{m,Im}_{2,1}$	$+0 \pm 0.1$
$a^{e,Re}_{2,2}$	-0 ± 0.0
$a^{e,Im}_{2,2}$	$+0 \pm 0.0$
$a^{m,Re}_{2,2}$	$+0 \pm 0.0$
$a^{m,Im}_{2,2}$	$+0 \pm 0.0$

Table 2 Amplitude and direction of glide between the Vienna CRF solution with correction of GA and without correction of GA.

	[μas]
Glide Amplitude	$+35 \pm 0.1$
Glide RA	$+86 \pm 0.1$
Glide DEC	$+25 \pm 0.1$

Table 3 Correlation of VSH parameters between the Vienna CRF solution with correction of GA and without correction of GA. To improve readability the correlations between the quadrupole parameters are omitted. The largest correlation between quadrupole parameters is -0.25.

	R_1	R_2	R_3	D_1	D_2	D_3
R_2	$+0.12$					
R_3	-0.13	-0.16				
D_1	$+0.03$	$+0.43$	-0.07			
D_2	-0.46	-0.03	$+0.04$	-0.07		
D_3	$+0.01$	-0.02	$+0.01$	$+0.03$	$+0.08$	
$a^{e}_{2,0}$	$+0.01$	$+0.02$	$+0.00$	-0.03	-0.00	-0.36
$a^{m}_{2,0}$	-0.03	-0.07	$+0.33$	-0.17	$+0.14$	$+0.00$
$a^{e,Re}_{2,1}$	-0.00	$+0.02$	$+0.01$	$+0.32$	$+0.04$	$+0.01$
$a^{e,Im}_{2,1}$	$+0.06$	-0.02	$+0.00$	-0.03	-0.37	-0.01
$a^{m,Re}_{2,1}$	-0.40	-0.03	$+0.04$	-0.08	$+0.29$	-0.07
$a^{m,Im}_{2,1}$	$+0.04$	$+0.37$	-0.05	$+0.40$	-0.08	-0.08
$a^{e,Re}_{2,2}$	$+0.02$	-0.03	-0.00	-0.02	$+0.01$	$+0.04$
$a^{e,Im}_{2,2}$	$+0.02$	$+0.01$	$+0.02$	$+0.07$	$+0.03$	$+0.05$
$a^{m,Re}_{2,2}$	-0.02	-0.01	-0.02	-0.08	-0.07	-0.15
$a^{m,Im}_{2,2}$	-0.02	-0.03	-0.03	-0.09	$+0.08$	$+0.15$

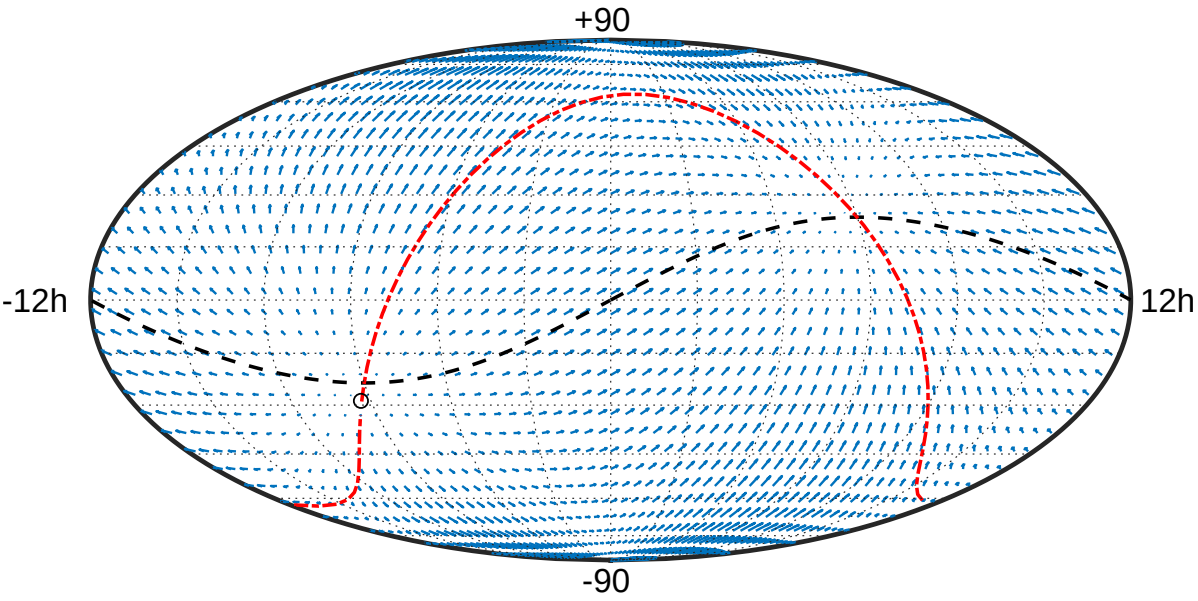

Fig. 1 Glide between the Vienna CRF solution with correction of GA and without correction of GA. The largest arrow has a size of 35 µas. The ecliptic is plotted in black and the galactic plane is plotted in red. The center of the galaxy is denoted as a black circle.

respectively. Other parameters show a small dependence of a couple of µas. However, since correlations of up to 0.46 between the parameters exist these small transformation parameters are most likely not a real effect.

References

1. Altamimi, Z., Rebischung, P., Métivier, L. and Collilieux, X. ITRF2014: A new release of the international terrestrial reference frame modeling nonlinear station motions. *Journal of Geophysical Research: Solid Earth*, 121(8), 6109–6131, 2016. http://dx.doi.org/10.1002/2016JB013098
2. Böhm, J., Werl, B. and Schuh, H. Troposphere mapping functions for GPS and very long baseline interferometry from european centre for medium-range weather forecasts operational analysis data. *Journal of Geophysical Research: Solid Earth*, 111 (B2), 2006. http://dx.doi.org/10.1029/2005JB003629
3. Böhm, J. et al. Vienna VLBI and Satellite Software (VieVS) for Geodesy and Astrometry. *Publications of the Astronomical Society of the Pacific*, 130(986), 2018. http://stacks.iop.org/1538-3873/130/i=986/a=044503
4. Charlot, P. et al. The Third Realization of the International Celestial Reference Frame by Very Long Baseline Interferometry. *A&A*, to be submitted, 2018.
5. Fey, A. L. et al. The Second Realization of the International Celestial Reference Frame by Very Long Baseline Interferometry. *The Astronomical Journal*, 150(2), 58, 2015. http://stacks.iop.org/1538-3881/150/i=2/a=58
6. Ma, C. et al. The Second Realization of the International Celestial Reference Frame by Very Long Baseline Interferometry. *IERS Technical Note 35*, 2009. https://www.iers.org/IERS/EN/Publications/TechnicalNotes/tn35.html
7. MacMillan, D. S. Atmospheric gradients from very long baseline interferometry observations. *Geophysical Research Letters*, 22(9), 1041–1044, 1995. http://dx.doi.org/10.1029/95GL00887
8. MacMillan, D. S. and Ma, C. Atmospheric gradients and the VLBI terrestrial and celestial reference frames. *Geophysical Research Letters*, 24(4), 453–456, 1997. http://dx.doi.org/10.1029/97GL00143
9. MacMillan, D. S. et al. Final Report of the IVS Working Group 8 (WG8) on Galactic Aberration, 2018.
10. Mignard, F. and Klioner, S. Analysis of astrometric catalogues with vector spherical harmonics. *A&A*, 547, A59, 2012. https://doi.org/10.1051/0004-6361/201219927
11. Petit, G. and Luzum, B., eds. IERS Technical Note No. 36. *IERS Conventions 2010*, Frankfurt am Main: Verlag des Bundesamts für Kartographie und Geodäsie, 2010. http://iers-conventions.obspm.fr/updates/2010updatesinfo.php
12. Titov, O., Lambert, S. B. and Gontier, A.-M. VLBI measurement of the secular aberration drift. *A&A*, 529, A91, 2011. https://doi.org/10.1051/0004-6361/201015718
13. Titov, O. and Lambert, S. Improved vlbi measurement of the solar system acceleration. *A&A*, 559, A95,2013. https://doi.org/10.1051/0004-6361/201321806

14. Titov, O. and Krásná, H. Measurement of the solar system acceleration using the earth scale factor. *A&A*, 610, A36, 2018. https://doi.org/10.1051/0004-6361/201731901
15. Wijaya, D., Böhm, J., Karbon, M., Krásná, H. and Schuh, H. Atmospheric Pressure Loading. *Atmospheric Effects in Space Geodesy*, Springer Berlin Heidelberg, Berlin, Heidelberg, pp. 137–157, 2013 http://dx.doi.org/10.1007/978-3-642-36932-2_4
16. Xu, M. H., Wang, G. L. and Zhao, M. The solar acceleration obtained by VLBI observations *A&A*, 544, A135, 2012. https://doi.org/10.1051/0004-6361/201219593

Effect of VLBI Observation Network on Source Stability

Karine Le Bail [1], David Gordon [1]

Abstract The observing network changes depending on the type of session and the availability of stations. Some factors that affect the session network are the nature of the session (geodesy, astronomy), the strength and/or the location of the target sources, and the maintenance or repair of certain antennas. The observation frequency varies from weekly (R1 and R4 sessions) to a few irregular times a year (R&D, CRF, and CRDS sessions). Because of such network disparities and irregularities, a given source is observed irregularly and we expect its time series to reflect some non-stationarity. This study aims at investigating the question: Does the observing network have an effect on source stability? We isolated position determination depending on different types of sessions and determined the type and level of noise using the Allan variance. We show the results particularly for the source 3C418, emphasizing on the differences between R1 and R4 sessions. The source 3C418 is one of the sources used regularly in geodesy sessions. It was initially chosen because it was a strong and compact source. In the last part of this paper, we show the temporal change in behavior in its time series over the past two years. This demonstrates the importance of observing and monitoring all sources regularly.

Keywords Radio source position time series, statistical characterization, Allan variance

1. NVI, Inc./NASA Goddard Space Flight Center, USA

1 Introduction

The problem we face in VLBI is the continuous evolution of the entire system we study: the radio sources are evolving, the observing instrument or data are changing with time, and the sampling is not homogeneous.

Le Bail and Gordon 2010 [1] and Le Bail et al. 2014 [2] discussed the source 3C418 and showed that the source exhibits different statistical characteristics depending on the studied time period. When considering the period 1988–1993, the noise of the source position time series is a flicker noise at a one-year level of 180 μas for right ascension (R.A.) and 300 μas for declination (DEC). When considering the period 1997–2005, the noise is a white noise at a one-year level of 70 μas for R.A. and 110 μas for DEC. One cause could be the technique and analysis improvement over the years such as improvements to the instrumentation or data processing. A second cause is that the source may change with time.

Another cause for inhomogeneity is the network. From one observation to another, the source is observed by different stations. We investigate how this impacts the source position determination. We studied different sources but decided to focus on 3C418. In Section 2, we extract from its position time series the points corresponding to the same type of sessions (e.g., R1, R4, RDV). In Section 3, we study the different extracted time series with the Allan variance and determine the type and level of noise. Section 4 is a discussion on the change of the behavior of 3C418 in the past two years and presents a tool that could help monitor all VLBI sources to detect such changes.

2 The Example of the Source 3C418 in Various Sessions since 2002

The set of VLBI position time series we analyzed in this paper was produced with the Calc/Solve software at GSFC. It used VLBI sessions from August 3, 1979 through March 26, 2018, for a total of 6,182 sessions, including all of the VCS1-6, VCS-II, and UF001 A-T/UG002 A-C VLBA sessions. It contains 4,529 sources, including the VCS sources.

There are significant variations in the number of sessions per source: 222 sources were observed successfully in only one session, 3,569 sources in five or less sessions, and 3,747 sources in less than ten sessions. Only 782 sources, 17% of the set, were observed in ten or more sessions. Some sources have a long observation history like OJ287 (4,361 sessions covering the period April 1980 to March 2018) and 0552+398 (4,589 sessions covering the period August 1979 to March 2018).

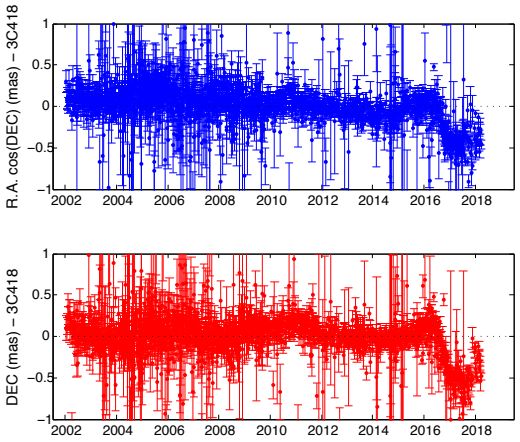

Fig. 1 Position time series of the source 3C418 over the period January 2002 to March 2018.

In this study, we will focus on the source 3C418. This source was observed in 1,969 sessions total during the period from June 1982 to March 2018. Since we are interested in the weekly IVS sessions R1 and R4, we restrain the studied period to January 2002 to March 2018 which represents 1,621 sessions (see Figure 1).

Over this period, 3C418 was observed in 592 R1 sessions, 618 R4 sessions, 75 R&D sessions, 51 RDV sessions, 55 EURO sessions, 20 APSG sessions, 11 AOV sessions, 63 T2 sessions, two AUA sessions, two AUG sessions, and 127 various others. We show the position time series obtained when extracting points corresponding to R1, R4, and RDV sessions in Figure 2.

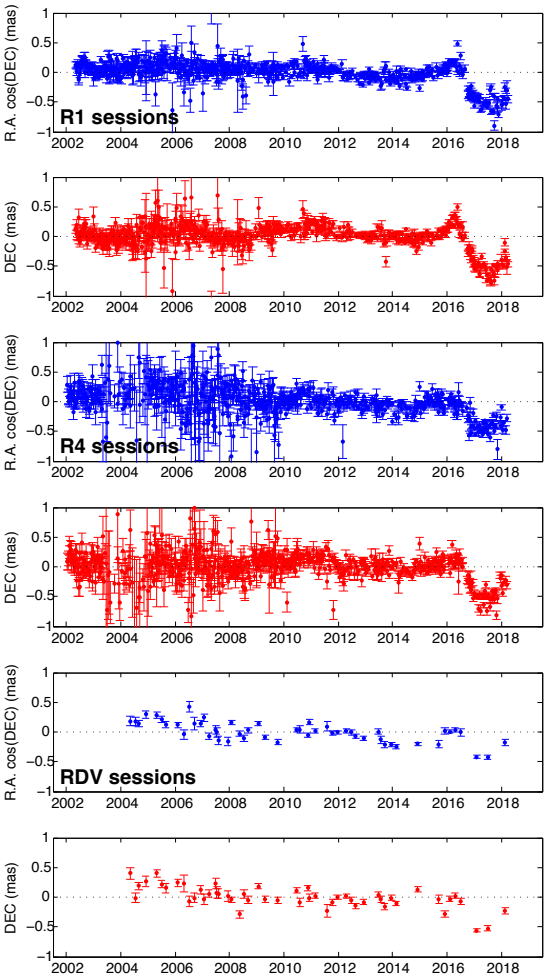

Fig. 2 Position time series of the source 3C418 differentiated by type of sessions (top two plots: R1 sessions, middle two plots: R4 sessions, bottom two plots: RDV sessions) over the period January 2002 to March 2018.

The three time series show the same behavior for the source, even though the formal errors of the R4 sessions are generally larger than the formal errors of the R1 sessions, which are larger than the RDV formal errors. This could be explained by the number of observations per session: the average number of observations used to estimate the position for each session is 84 for the R4 sessions, 171 for the R1 sessions, and 275 for the RDV sessions. The time series, obtained when

extracting only R1 or R4 sessions, have more points than the time series of RDV sessions, which allows the access to more details.

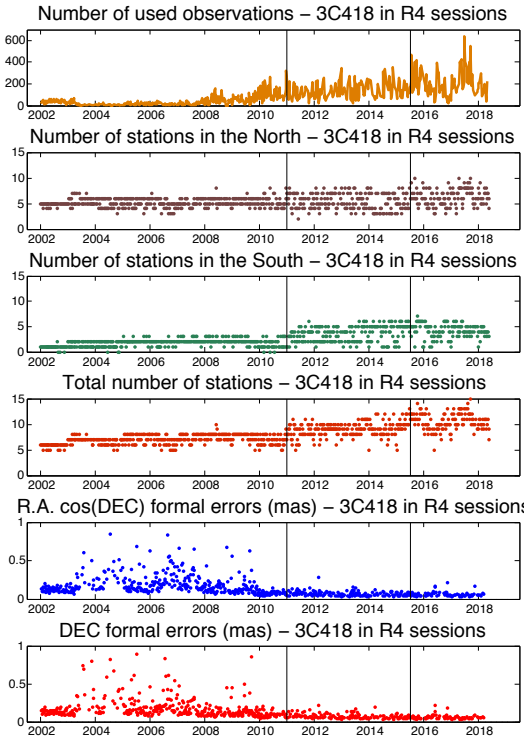

Fig. 3 Observation numbers (top), station numbers (center), and formal errors of the source 3C418 in R4 sessions from 2002 to 2018.

The position formal errors for the R1 and R4 sessions improve over time. If we look at the R4 sessions specifically (see Figure 3), the number of used observations in the solution increase significantly, while the formal errors decrease. The increase in the number of observations is partially explained by the increase in the number of stations, which is dominated by the increased use of stations in the south. If we divide the observation period into three different periods (2002–2011, 2011–2015.5, and 2015.5–2018.3), the average number of stations in the south is 1.7 for the first period, than doubles for the second period (3.4), and reaches 4.3 for the third period, while the average number of stations in the north increases from 5.2 for the first period to 6.2 for the third period. Thomas et al. 2018 [3] investigate the differences between R1 and R4 sessions and highlight some possible reasons that explain the formal error discrepancies between different periods.

There is no such variation in the position formal errors of the RDV sessions: the formal errors remain comparable over the period 2002.0–2018.3. This is because the RDV sessions have the VLBA network as a base of its network which is ten stations in the northern hemisphere. To this network, up to ten geodetic stations capable of recording VLBA modes were added at the beginning of the campaign, then up to six stations from 2009, the number of stations varying from session to session. In July 2009, the recording mode changed from 1-bit to 2-bit sampling.

3 Statistical Characterization of 3C418 Position Time Series

To obtain the type and the level of noise, we use the Allan variance. If $(x_i)_i$ are the measurements and τ the sampling time, the Allan variance at τ is defined by: $\sigma^2(\tau) = \frac{1}{2} < (\widehat{x_{i+1}} - \widehat{x_i}) >^2$. The type of noise is obtained by computing the slope of the Allan variance curve in a plot $(log_{10}(\sigma^2(\tau)), log_{10}(\tau))$. A slope of -1 indicates white noise, 0 indicates flicker noise, and $+1$ indicates random walk.

To be able to use the Allan variance, the time series have to be equally spaced. For this reason, the time series were first yearly averaged.

Figure 4 shows the Allan variance processed on yearly averaged time series of R1, R4, RDV, and all sessions time series. The plot points are all within the same range: the level and type of noise for each session types are very similar. But three points are not sufficient to determine significantly the type of noise.

Table 1 Type and level of noise determined by the Allan variance on weekly averaged time series.

Session type	Slope and sigma	
	Right Ascension	Declination
All sessions	-0.40 ± 0.09	-0.27 ± 0.08
R1	-0.21 ± 0.07	-0.15 ± 0.07
R4	-0.34 ± 0.08	-0.17 ± 0.02
Session type	Allan variance (7 days) in microas	
	Right Ascension	Declination
All sessions	87.14 ± 0.17	92.70 ± 0.18
R1	78.36 ± 0.16	91.12 ± 0.18
R4	142.60 ± 0.28	133.70 ± 0.27

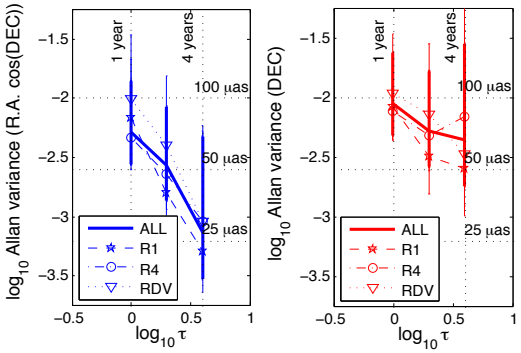

Fig. 4 Allan variance graphs processed on yearly averaged time series. All sessions, R1 sessions, R4 sessions, and RDV sessions.

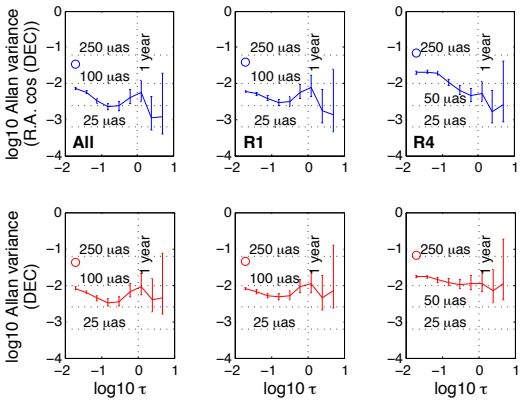

Fig. 5 Allan variance graphs processed on weekly averaged time series. Left: All sessions. Center: R1 sessions. Right: R4 sessions. The circle at $\tau = 7$ days indicates the standard deviation of the time series.

Figure 5 shows the Allan variance processed on weekly averaged time series of R1, R4, and all session time series. Other kinds of sessions, e.g. RDVs, do not occur frequently enough to compute a weekly average. Table 1 gives the type and level of noise determined by the Allan variance plot. For the R.A. component, the slopes vary between -0.21 ± 0.07 for the R1 sessions and -0.34 ± 0.08 for the R4 sessions, and for the DEC component, between -0.15 ± 0.07 for the R1 sessions and -0.17 ± 0.02 for the R4 sessions. These slopes give a similar conclusion for the type of noise—the time series exhibit a flicker noise. As expected from Section 2, the level of noise of the R4 sessions is higher than the level of noise of the R1 sessions for both components. This seems to impact the Allan variance plots for sampling times lower than $\tau = 1$ year, as seen in Figure 5.

4 Discussion: Temporal Evolution of 3C418

The position time series of 3C418 are remarkable because of the change in behavior. To track where the evolution impacts the statistical characterization of the source, we studied the time series on different time periods. As an initial time period, we take 2002.0 to 2006.3 and process the Allan variance on this period. Then we add six months of data and process the Allan variance on this new period. We follow the same procedure until we reconstruct the entire series. Each Allan variance processing provides the slope of the Allan variance for R.A. and DEC that determine the type of noise and the Allan standard deviation at 64 weeks for R.A. and DEC that determine the level of noise (see Figure 6). In Figure 6, we added the regular standard deviation for comparison.

The conclusions are similar for both components. The type of noise is determined as white noise until late 2016 when the type of noise shifts to flicker noise. At the same time, the Allan standard deviations as well as the standard deviations increase rapidly. The standard deviations are between 180 µas and 200 µas when processed on the entire time series, and are between 120 µas and 140 µas when processed on the period 2002.0–2006.3.

The source 3C418 is a source used as a base in geodetic session scheduling: it was initially chosen because it was a stable and compact source. If evaluated now, the source statistical characterization would not make a good candidate.

5 Conclusions

This study shows that the statistical characterization of sources is influenced by the level of noise of the time series. This level of noise depends on the type of sessions used to observe the sources: R4 sessions have position formal errors larger than R1 sessions, which have larger formal errors than RDV sessions.

Another difficulty for determining the type of noise is the unpredictable temporal evolution of the source. This study showed that 3C418 had a stable position (stable means in this context a predictable position not

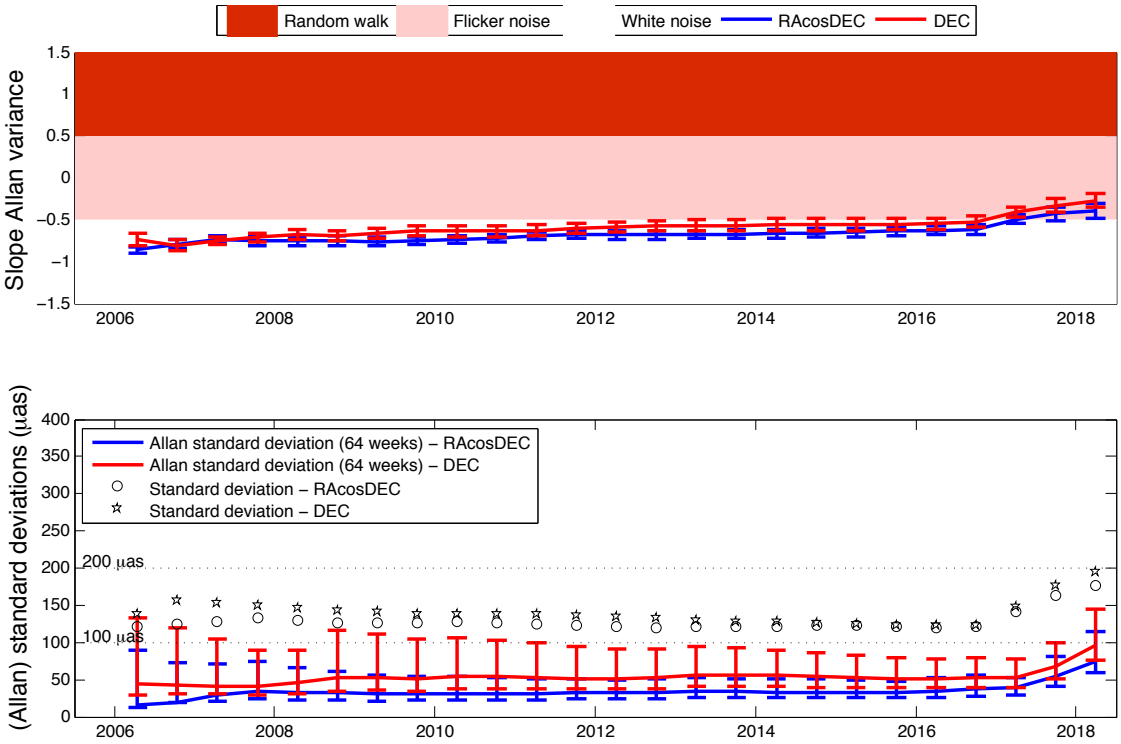

Fig. 6 Level and type of noise of 3C418 in function of the period. The initial period is 2002.0–2006.3 (first points on the left side of the graphs). Each additional points correspond to the previous period incremented by six months of data.

changing with time) from 2002 until 2016, when the source position changed abruptly.

This demonstrates we need to observe sources more often and regularly to monitor them more precisely.

This method could be developed as a tool to monitor source time series type and level of noise. To be complete, this tool should also provide quantities as these:

1. level of noise using the Allan variance at different sampling time, type of noise using the Allan variance on regularized series averaged on different periods from 7 days to 1 year (this is significant when the source is sufficiently observed);
2. level of noise using the regular standard deviation, drift of the time series,... (quantities that could be computed even with a low number of observations);
3. Structure Index SI from Fey & Charlot 1997 [4], time series of flux values,... (quantities to indicate the physical nature of the source).

References

1. K. Le Bail, and D. Gordon, "Time-dependent Selection of an Optimal Set of Sources to Define a Stable Celestial Reference", In D. Behrend and K. D. Baver, editors, International VLBI Service for Geodesy and Astrometry 2010 General Meeting Proceedings, NASA/CP-2010-215864, pages 280–284, 2010.
2. K. Le Bail, D. Gordon, and J. M. Gipson. Evaluation of the Stability of ICRF2 in the Past Five Years Using the Allan Variance. In D. Behrend, K. Baver, and Kyla Armstrong editors, *IVS 2014 General Meeting Proceedings, "VGOS: The New VLBI Network"*, Science Press (Beijing), ISBN 978-7-03-042974-2, pages 395–398, 2014.
3. C. Thomas, D. MacMillan, and K. Le Bail. Performance of the Operational IVS-R1 and IVS-R4 Sessions. In D. Behrend, K. Baver, and Kyla Armstrong editors, *IVS 2018 General Meeting Proceedings, "Global Geodesy and the Role of VGOS – Fundamental to Sustainable Development"*.
4. A. L. Fey, and P. Charlot, "VLBA Observations of Radio Reference Frame Sources. II. Astrometric Suitability Based on Observed Structure", In *The Astrophysical Journal Supplement Series*, 111:1, doi:10.1086/313017, pages 95–142, 1997.

Insight into Astrophysical Phenomena from VLBI Source Position Instabilities

César Gattano, Patrick Charlot

Abstract Most of the radio sources observed by VLBI, some used as defining sources in the International Celestial Reference Frame [ICRF2], show instabilities in position. These instabilities may be caused by astrophysical phenomena occurring in the central VLBI region of these objects (i.e., active galactic nuclei). On this basis, we have begun to characterize the signal included in the available VLBI position time series. Often, position instabilities happen along a preferred direction. There are cases, however, where two directions are distinguishable. The first scenario is consistent with a regular emergence of jet components from the VLBI core; hence, causing shifts of the radio emission centroid. On the other hand, the second scenario may give clues to the presence of a second black hole within the system that has its own activity offset from that of the first black hole. Comparing these directions with the orientation derived from radio-optical position offset brings further insights into astrophysical phenomena within active galactic nuclei.

Keywords Astrometry, celestial frame, source stability

1 Introduction

Active Galactic Nuclei [AGN] are currently the most appropriate sources in the Universe to define stable fiducial marks on the celestial sphere. The reason is that they show no apparent proper motion due to their extragalactic distance from us.

Laboratoire d'Astrophysique de Bordeaux, Université de Bordeaux, OASU, CNRS

However, when we have a look at their position evolution, we often note astrometric instabilities, i.e., systematic variations regarding the measurement uncertainty (see Section 3). Such instabilities vary from source to source, generally in the range 0.1–1 mas and characterize the astrometric behavior of the source. A recent study [3] revealed that among the most observed sources with VLBI, only 5% have a stable astrometric behavior and this fraction cannot be increased much even if loosening the criteria that define stability.

This variability may have two origins. First, it may be an effect of the observing system (i.e., extrinsic to the source) imperfectly taken into account during the data reduction. On the other hand, VLBI, due to its resolving power, is sensitive to the source apparent structure despite their cosmic distances. Indeed, at the milliarcsecond resolution, sources are not point-like, neither do they present a symmetric structure in radio. The photometric variability, sometimes correlated with the astrometric variability, provides hints in favor of source intrinsic effects [13]. The interest in astro-geodesy is to observe sources with the least astrometric variability. Our study aims to extract and collect information that may help to identify these appropriate sources.

2 Preliminary Global Analysis

First, we searched for source astrophysical and observational parameters that may discriminate between sources with stable or unstable observed behavior. We used the VLBI source classification of Gattano et al. [3], built by using the Allan standard deviation to characterize the source behavior. It is divided into three categories: AV0 (stable), AV1 (intermediate),

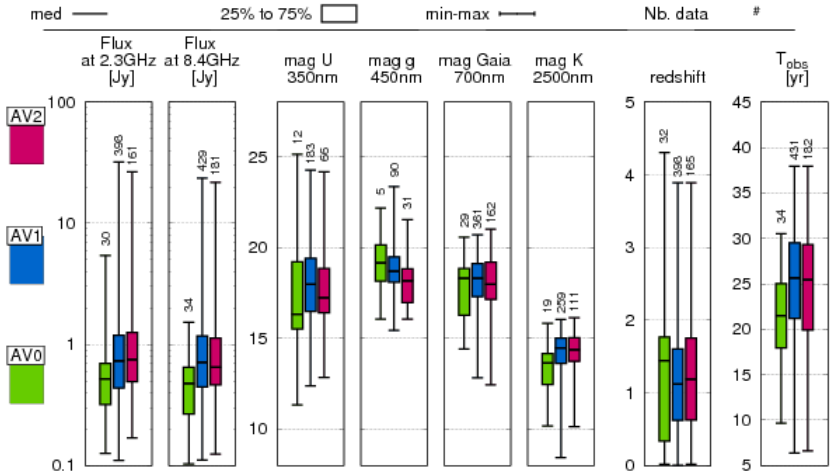

Fig. 1 Distribution of 647 well observed VLBI sources considering the Gattano et al. [3] source classification and regarding several source parameters independently. AV0 sources (green) are sources presenting a stable astrometric behavior, whereas AV2 sources (red) present an unstable astrometric behavior. AV1 sources (blue) are intermediate. Each candlestick gives, from bottom to top, the minimum, the first-second quartile boundary (25%), the median (50%), the third-fourth quartile boundary (75%), and the maximum for each distribution.

and AV2 (unstable). Astrophysical parameters were retrieved from the fourth version of the Large Quasar Astrometric Catalog [4] that gathers 443,725 sources including information from the SDSS DR12Q [9] and Gaia DR1 [7].

The parameter-by-parameter analysis is illustrated in Figure 1. The trends observed are that stable sources are fainter in radio, brighter in infra-red, and less observed. Unstable sources are brighter in mag g. No particular trend was observed for the other magnitudes or regarding morphological optical indices. Also, the redshift is not necessarily higher for stable sources. These results are not systematic, as the different candlesticks largely overlap between source categories.

Although interesting, this initial study does not provide help for the identification of the most stable sources. For this purpose, we need to go into further details regarding the relationship between source astrophysics and astrometric instabilities.

3 VLBI Source Position Time Series

We used VLBI source position time series computed in Gattano et al. [3, Section 2]. We only considered 197 sources observed in at least 200 sessions. This number was arbitrarily chosen in consideration of the reduction process. This process aims to filter the high frequency part of the signal presumed to be mainly associated with the observing system.

For each time series, we used a starting window of 32 years and we counted the number of position measurements y_i within it. If greater than 100, we split that window into two half-length windows and proceeded again. When the number of points within a window was between 50 and 100, the average was computed and a new point $\bar{y}_i$ was added to the reduced position time series. If the number of points dropped below 50, the window was ignored. In the end, we obtained reduced time series containing from two to several tens of $\bar{y}_i$ points for each source.

4 Orientation Analysis

Source orientation may be derived in several ways. First, VLBI source images can provide a direction that links two source components if as many are visible. Second, source positions in radio and in optical are sometimes offset in a certain direction. A recent study [10, 6] compared such two directions for thousands of VLBI sources, leading to the conclusion that significant radio-optical offsets favor the jet direction (as revealed by VLBI images) and giving clues as to the existence of an optical jet structure at the parsec scale.

Also, it is possible to extract from our reduced source coordinate time series the direction along which source astrometric instabilities occur, a third direction in the puzzle. To extract the angle θ of this direction, we built the total orientation Probability Density Function [PDF] by considering pairs of successive positions $\left(\overline{\Delta\alpha\cos\delta}_i, \overline{\Delta\delta}_i\right)$ and $\left(\overline{\Delta\alpha\cos\delta}_{i+1}, \overline{\Delta\delta}_{i+1}\right)$ equivalent to vectors (ρ_i, θ_i). Each pair contributed to the PDF by a Gaussian function centered on the orientation θ_i,

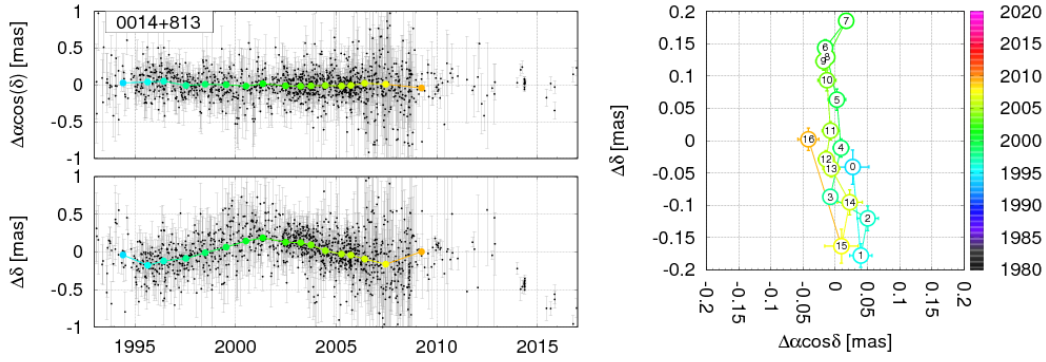

Fig. 2 **(top left)** Position time series of source 0014+813 in black (error bars in gray). The associated reduced time series is given by the colored dots. **(top right)** 2D-representation of the astrometric instability: trajectory drawn from the reduced time series on the local plane centered on the mean position of the source. **(right)** Distribution of the instantaneous directions (from successive positions in the reduced time series). The inset gives the total orientation probability density function in black and its Gaussian fit in red (see Section 4).

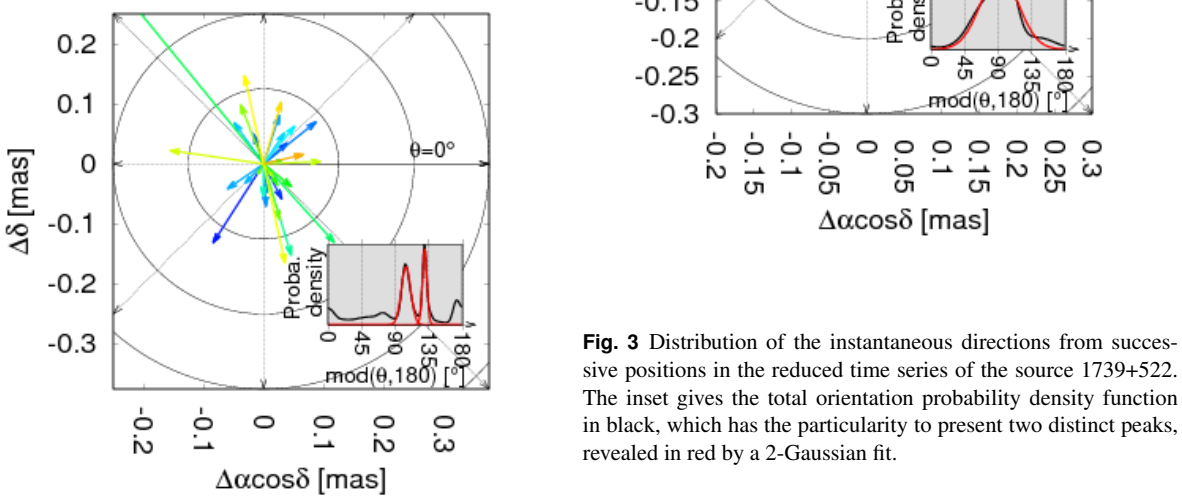

Fig. 3 Distribution of the instantaneous directions from successive positions in the reduced time series of the source 1739+522. The inset gives the total orientation probability density function in black, which has the particularity to present two distinct peaks, revealed in red by a 2-Gaussian fit.

with half-width at half-maximum equal to σ_{θ_i} and an amplitude equal to the ratio between the length ρ_i of the offset and σ_{ρ_i}. The uncertainties σ_{θ_i} and σ_{ρ_i} are computed by error propagation from the coordinates' uncertainties. The built function is finally normalized to respect the property of unit integral.

Then, given this produced orientation PDF, we fitted a global Gaussian function, which provides the preferred orientation θ, its uncertainty σ_θ, and a degree of confidence P_{orient} on θ equal to the integral of the fitted Gaussian function. Figure 2 shows our results for the source 0014+813 ($\theta = 92 \pm 25°$ with 95% of confidence). For some sources, multiple directions can be distinguished. This is the case for the source 1739+522 presented in Figure 3 for which two preferred directions are found : $\theta_A = 105 \pm 6°$ and $\theta_B = 130 \pm 3°$ with 57% of confidence in total.

Results for sources observed in more than 200 sessions are presented in Figure 4. The first plot shows that, with a $P_{orient} \geq 0.8$ threshold, already 60% of the sources have a preferred direction. Secondary orientations appear at $P_{orient} = 0.5$. Approximately 20% of the sources may be subject to a secondary orientation.

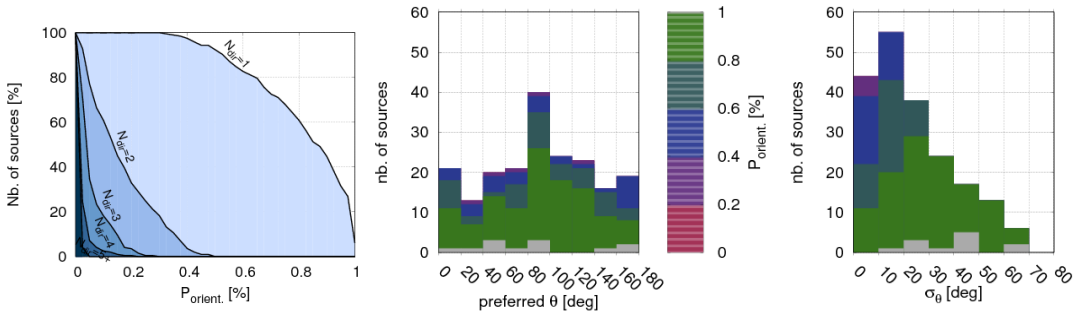

Fig. 4 **(left)** Cumulative histograms of sources with N_{dir} orientations found in the reduced time series as the threshold on the degree of confidence P_{orient} decreases from 1 to 0. **(middle)** Histogram of the source primary orientation found in the reduced time series. The color indicates different intervals of P_{orient}. **(right)** Histogram of the associated uncertainties on the source primary orientation.

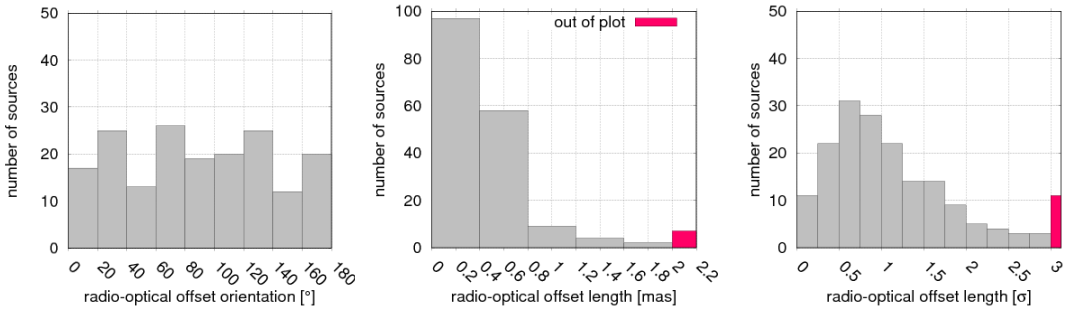

Fig. 5 **(left)** Histogram of the source radio-optical offset orientations. **(middle)** Histogram of lengths in milli-arcseconds. **(right)** Histogram of lengths normalized to the formal errors. The right pink bars also cumulate offsets that are outside the plots.

Nevertheless, the uncertainty on the derived orientation is not so small as seen in the third plot of Figure 4. The distribution peaks at 10–20° and the maximum is greater than 60°. Also, the distribution of the source preferred orientation presents an excess along the declination direction. This is unnatural as sources should be randomly oriented on the celestial sphere. This is probably due to an effect of the observing system, despite the aforementioned low-pass filter.

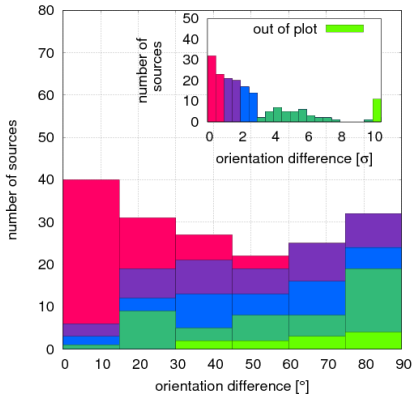

Fig. 6 Comparison between astrometric instability primary directions and radio-optical offset directions. The abscissas give the difference between these two directions in degrees and with respect to the difference uncertainty σ. Each color indicates the level of significance of the direction difference.

In parallel, we focused on the VLBI-Gaia radio-optical offsets. The 2nd data release of Gaia was oriented on a prototype of the ICRF3 [8] thanks to 2,820 VLBI sources with a sufficiently bright optical counterpart. Among the 197 VLBI sources we studied, 177 were found in this subset and we computed their radio-optical offsets. Figure 5 presents the resulting distribution.

The first plot confirms the natural homogeneous distribution of the offset orientations. The distribution with respect to the length shows that most of the offsets are small (more than 50% are less than 0.4 mas). Moreover, only eleven offsets are significant regarding their uncertainty.

5 Comparison and Conclusions

Two astrophysical phenomena may be responsible for the observed radio emission centroid instabilities. First, the source structure may present several components (see for example the Bordeaux Image VLBI Database[1]): one is the main radio core, the others are knots, generally moving along the jet from the main core. The whole configuration of core and knots may be explained by physical process within the jet [5]. Second, the presence of a black hole binary system within the AGN may affect the structure of the source due to two distinct sites of activities. The hypothesis was developed from the mergers between galaxies [1]. Some sources were studied under this hypothesis [12, 2, 11].

Our interpretation of the results is that, when one preferred direction is found for a source, it is probable that the astrometric instabilities follow the evolution of the knot configuration and, therefore, it is aligned with the jet direction. Future comparisons with VLBI images available in the aforementioned database will be useful to test this hypothesis. On the other hand, sources where astrometric instabilities occur along several preferred directions are good candidates for searching binary black hole systems.

Finally, Figure 6 compares the derived directions based on the above mentioned (i.e., from astrometric instabilities) with the radio-optical offsets. Small differences are in general non-significant and characterize a population of sources where those two directions are aligned. If they are also aligned with the jet, the optical centroid is located in the jet. Conversely, sources which show significant differences have values for these differences preferentially near 90°. Hence, if it is the astrometric instability that occurs along the jet, then the radio-optical offset is across the jet and the optical counterpart may be preferably dominated by the accretion disk or the host galaxy. But if it is the radio-optical offset that is aligned with the jet, the astrometric instability occurs across the jet, which is in favor of the search of potential binary black hole.

Adding the source structure orientation from VLBI images to our result will be useful to get further insights into those possibilities.

[1] → http://astrophy.u-bordeaux.fr/BVID/

Acknowledgements

This work was supported by a CNES post-doctoral grant. César Gattano is grateful to the IAG, the CNFGG, and the OASU for supporting the trip and thus allowing the presentation of this work at the IVS General Meeting.

References

1. Begelman, M. C.; Blandford, R. D. & Rees, M. J., Massive black hole binaries in active galactic nuclei, Nature, 1980, 287, 307–309.
2. Britzen, S. et al., On the origin of compact radio sources. The binary black hole model applied to the gamma-bright quasar PKS 0420-014, A&A, 2001, 374, 784–799.
3. Gattano, C.; Lambert, S. B. & Le Bail, K., Extragalactic radio source stability and VLBI celestial reference frame: insights from the Allan standard deviation, A&A, 2018, forthcoming paper.
4. Gattano, C. et al., LQAC-4: Fourth release of the Large Quasar Astrometric Catalogue. Compilation of 443 725 objects including cross-identifications with Gaia DR1, A&A, 2018, 614, A140.
5. Hervet, O. et al., Shocks in relativistic transverse stratified jets. A new paradigm for radio-loud AGN, A&A, 2017, 606, A103.
6. Kovalev, Y. Y.; Petrov, L. & Plavin, A. V., VLBI-Gaia offsets favor parsec-scale jet direction in active galactic nuclei, A&A, 2017, 598, L1.
7. Lindegren, L. and Gaia Collab., Gaia Data Release 1. Astrometry: one billion positions, two million proper motions and parallaxes, A&A, 2016, 595, A4.
8. Lindegren, L. and Gaia Collab., Gaia Data Release 2. The astrometric solution, A&A, 2018, 616, A2.
9. Pris, I. et al., The Sloan Digital Sky Survey Quasar Catalog: Twelfth data release, A&A, 2017, 597, A79.
10. Petrov, L. & Kovalev, Y. Y., On significance of VLBI/Gaia position offsets, MNRAS, 2017, 467, L71–L75.
11. Roland, J. et al., Binary black holes in nuclei of extragalactic radio sources, A&A, 2013, 557, A85.
12. Roos, N.; Kaastra, J. S. & Hummel, C. A., A massive binary black hole in 1928 + 738 ?, Astroph. J., 1993, 409, 130–133.
13. Shabala, S. S. et al., The effects of frequency-dependent quasar variability on the celestial reference frame, J. Geod., 2014, 88, 575–586.

Realization of Celestial Reference Frames using the Allan Variance Classification

C. Gattano, P. Charlot

Abstract Recently [5], a new classification of VLBI radio sources was built on the basis of their astrometric stability revealed by the use of the Allan standard deviation. In such a classification, sources are divided into three groups depending on the nature of the noise content in the astrometric time series. The global level of noise then orders sources within each group. In this proceedings, we present several strategies on the basis of this classification to realize celestial reference frames, i.e. for selecting the set of defining sources used to define the fundamental axes of the frame. This set of sources is usually constrained in the data reduction by a no-net rotation constraint. Using two tools developed to determine the stability of realized frames, one that analyzes the stability of the annual realizations of a given frame and another that analyzes the coherence of random sub-frames, we determine the best usage of this classification.

Keywords Astrometry, celestial reference frame, Allan standard deviation

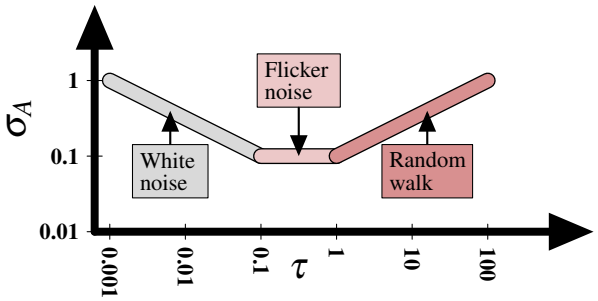

Noise type	Slope in log-log scale	Exponent p in $S_y(f) \propto f^p$	Noise color
Random walk	0.5	-2	Red
Flicker noise	0	-1	Pink
White noise	-0.5	0	White

Table 1 Correspondence between the type of noise, associated with a color given by the exponent of the power law-type spectral density function, and the drift observed in the Allan standard deviation as a function of the timescale represented in a log scale.

1 Introduction

The Allan standard deviation [1] provides a means for measuring the amplitude of the noise as a function of the data averaging timescale from a measurement time series, such as the monitoring of VLBI radio source positions. Initially conceived to characterize the stability of time and frequency standards, the Allan standard deviation has been used in geodesy for about two decades and was raised in several studies aiming at selecting suitable radio sources to define stable celestial frame axes [6, 2, 3, 7] (see also [9] and references therein).

The slope of the Allan standard deviation as a function of the data averaging timescale (in logarithmic scales) discriminates between several types of noise that may coexist in the time series (see the illustration of Table 1). Noise types are separated into two categories:

- Noise types indicating a stable behavior of the series: as the timescale increases, the estimated standard deviation decreases

Laboratoire d'Astrophysique de Bordeaux, Université de Bordeaux, OASU, CNRS

- Noise types indicating an unstable behavior of the series: as the timescale increases, the estimated standard deviation increases as well

The stability of a time series may result from a combination of behaviors associated to different timescale ranges. This principle is at the basis of a recent classification of VLBI radio sources following their assessed astrometric stability from coordinate time series. In the following section, we briefly summarize the principle and the result of this classification. Details are given by Gattano et al. [5].

2 Classification of VLBI Radio Sources

The set of sources is split into three categories following the sequence of the dominating noise at each timescale, i.e. with respect to the behavior of the data at those timescales:

- **AV0** sources with the most stable astrometric behavior. The condition to be classified as AV0 is not to be dominated by unstable noise (slope larger than +0.25, see Table 1) such as red noise at any timescale.
- **AV1** intermediate astrometric stability. AV1 is dominated by unstable noise at some timescales, but stable noise (slope lower than -0.25, see Table 1) such as white noise dominates on the longest timescales appreciable considering the observational history of the source.
- **AV2** sources with the least stable behavior. All sources for which the longest timescales are dominated by an unstable noise.

Right ascension and declination are studied separately. The source category is obtained by keeping only the worst category. Additionally, the global level of noise is evaluated taking into account the straight line that maximizes the Allan standard deviation graph (see the blue line in Figure 1). By doing so, it is possible to order sources within each category by increasing level of noise.

In parallel, a statistical validation test is used to determine the probability that the detected slope results from a white noise process even if it is not -0.5 (due to the irregularity of the sampling). It is based on Monte-Carlo simulations of 1,000 white noise draws distributed on the original sampling of the tested time series. The scatter of their corresponding Allan standard deviations provides an empirical error (see Figure 1 for example). Thanks to this test, each of the un-

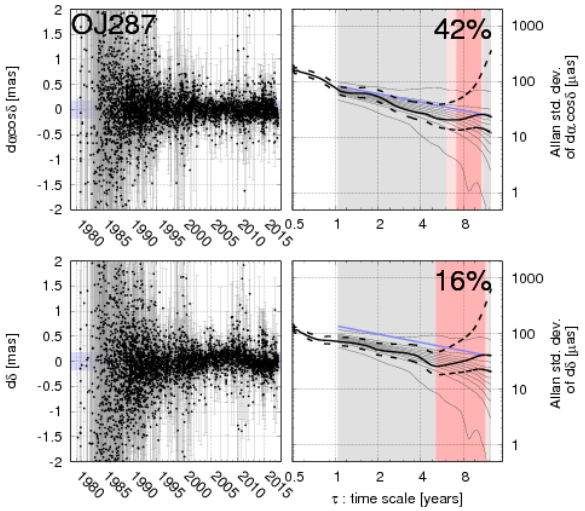

Fig. 1 (Left) Astrometric offset with respect to the mean position computed for each VLBI session. (Right) Allan standard deviation of the regularized time series over time scale τ. The log-log diagram is plotted with a black solid line with its uncertainties at 90% as black dashed lines. The colored background indicates the behavior of the noise at each time scale (more details are in Section 1). The blue straight line is the lowest line that maximizes the diagram down to $\tau = 1$ year. It leads to the global noise level of the source (more details are in Section 2). The grey solid lines are the dispersion of the Monte-Carlo test (more details are in Section 2). How much the black diagram remains within the dispersion lines provides the indicated probabilities on the top right corners. They are compared with the threshold of the rehabilitation process.

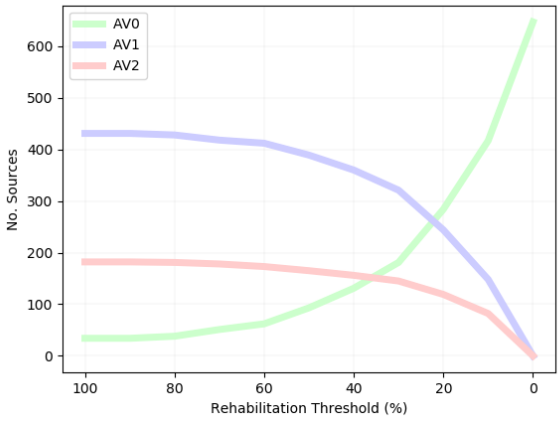

Fig. 2 Evaluation of the source distribution within the classification with respect to the chosen rehabilitation threshold (more details on the text on right).

stable sources (AV1/2) has therefore a certain probability to be in fact a stable source (AV0) offering the possibility to rehabilitate some sources for which their probability is greater (on both coordinates) than a given threshold. Figure 2 shows the evolution of the classification as the threshold varies.

3 Stategies to Select Defining Sources

We establish several strategies to realize celestial reference frames by selecting the set of defining sources. Table 2 below sums up the criteria for each strategy:

- N is the number of defining sources to be selected;
- P_{rehab} is the chosen rehabilitation threshold (see Section 2);
- σ_{AV0}, σ_{AV1}, and σ_{AV2} are upper limits for the noise level in each category (10 mas enables exclusion of all sources);
- $prior = 0$ gives the priority on the source class (data behavior) for the selection and then on the noise level. $prior = 1$ is reversed.

No. sol.	N	P_{rehab} [%]	σ_{AV0} [mas]	σ_{AV1} [mas]	σ_{AV2} [mas]	$prior$
GROUP 1: Only AV0 sources						
1	100	50	10	0	0	0
2	100	25	10	0	0	0
3	200	25	10	0	0	0
4	100	0	10	0	0	0
5	200	0	10	0	0	0
6	300	0	10	0	0	0
7	400	0	10	0	0	0
8	500	0	10	0	0	0
GROUP 2: First AV0, then AV1, no AV2						
9	200	50	10	10	0	0
10	300	50	10	10	0	0
11	300	25	10	10	0	0
GROUP 3: smallest level of noise						
12	100	-	10	10	10	1
13	200	-	10	10	10	1
14	300	-	10	10	10	1
15	400	-	10	10	10	1
16	500	-	10	10	10	1
GROUP 4: smallest level of noise but no AV2						
27	100	50	10	10	0	1
28	200	50	10	10	0	1
29	300	50	10	10	0	1
30	100	25	10	10	0	1
31	200	25	10	10	0	1
32	300	25	10	10	0	1
33	100	0	10	10	0	1
34	200	0	10	10	0	1
35	300	0	10	10	0	1
36	400	0	10	10	0	1
37	500	0	10	10	0	1

Table 2 List of realization strategies of celestial reference frames based on the classification of Gattano et al. [5]. See the text for the meaning of each column. The representative of each group is highlighted in light blue.

For each solution, the criteria are used within the following way.

First, we rehabilitated AV1/2 sources into the AV0 category regarding the chosen P_{rehab} threshold. Then, we excluded sources in each category which have a level of noise greater than the chosen σ_{AVi}. Then, if $prior = 0$, we selected the first N remaining AV0 sources. When there are no more AV0 sources, we continue with the remaining AV1 sources and then the remaining AV2 sources. If $prior = 1$, we first gathered all remaining sources and ordered them according to their noise level. Then, we selected the first N ones.

4 Method to Analyze the Stability of Celestial Reference Frames

We developed two statistical tools to assess the stability of celestial reference frames. Each of these is associated with a different concept of the stability of a frame.

4.1 Stability over Time

The Allan standard deviation analysis revealed that only a limited number of sources have stable behavior (see Figure 2). Every other one shows a perceptible variability affecting its astrometric position. Consequently, "how far can we state the non-rotation or non-deformation of the frame over time?" is a fundamental question when investigating the stability of the celestial reference frame. One difficulty is that we do not have the capability to measure the true stability of the frame because we cannot observe frequently the whole subset of defining sources.

Through the source observational history, we can nevertheless get some insights into the frame stabilities over time. We quantified this insight on an an-

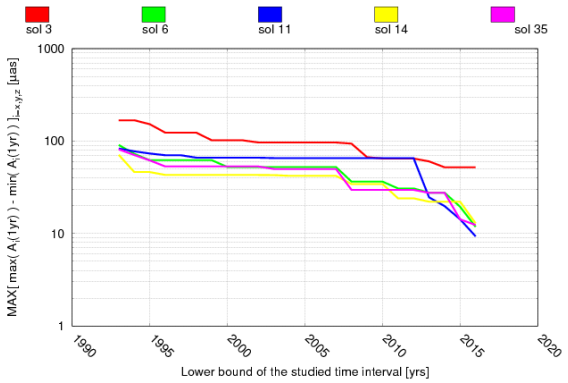

Fig. 3 Comparison of the quantifiable part of the annual stability between representatives of each solution group (see Section 3). From annual rotation time series $A_i(t)$ ($i = x$ for rotation around (Ox) axis, $i = y$ around (Oy), and $i = z$ around (Oz)), we chose the comparison criterion as the maximum between the largest differences within each of the three time series. The comparison criterion is computed on a time interval delimited by a chosen epoch up to the most recent date in the data. The value of this lower limit is given in abscissa and the related comparison criterion in ordinate in μas.

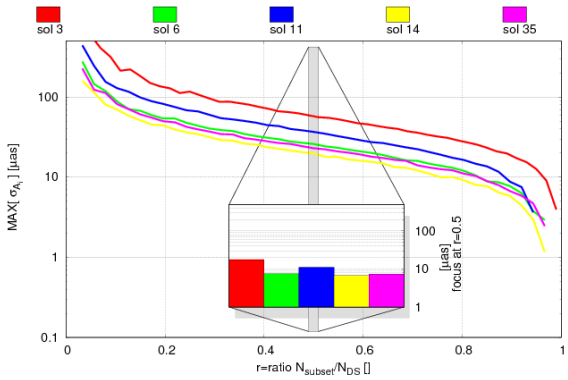

Fig. 4 Comparison of the sub-frame orientation dispersion between representatives of each solution group (see Section 3). The comparison criterion is set on the maximum between the three standard deviations σ_{A_i} ($i = x$ for rotation around (Ox) axis, $i = y$ around (Oy), and $i = z$ around (Oz)) of the thousand random sub-frames of size $N_{subset} \in [0 : N_{DS}]$, N_{DS} being the total number of defining sources of the complete frame.

nual basis by computing annual versions of celestial frame solutions by means of the annually-averaged positions of the observed sources. Then, we assessed the differences between these annual frames by comparing the rotation parameters $A_x(t)$, $A_y(t)$, and $A_z(t)$ between these frames. Finally, the stability is derived from the maximum of the differences on a time-interval with a given lower limit. In Figure 3, we show one of the three rotation parameters with the largest difference depending on the chosen lower time limit. For legibility, we only plot representatives of each group of solutions.

4.2 Sub-frames Orientation Coherence

On the other hand, only a subset of N sources among the set of N_{DS} defining sources is observed during a VLBI session, and the frame orientation within the session is determined to a certain extent by this sub-frame. "Whether the sub-frame has statistically the same orientation as the complete frame" is also an important question when dealing with frame stability.

Therefore, we randomly drew a thousand times N_{subset} sources from the total set of N_{DS} defining sources of a celestial frame solution (see Section 3). In other words, we got a thousand random sub-frames of identical size. We computed their statistical relative differences in orientation and retrieved the standard deviation on each rotation parameter A_x, A_y, and A_z. We repeated the process with different values of ratio N_{subset}/N_{DS} and drew the function of this standard deviation with respect to the ratio N_{subset}/N_{DS} (see Figure 4). For legibility, we only plot representatives of each group of solutions in Figure 4.

As a result, it is the height of this function with respect to the standard deviation axis which differs, more than the shape of curve. The height may be different between axes of different celestial frames but also between the three axes of the same frame. The most stable celestial frame shows the lowest height when considering all the three axes together, which means the lowest dispersion between the set of random sub-frames.

5 Results and Discussion

Based on the two statistical tools used (see Section 4), we note that the "sol 3", representative of the group *"Only AV0 sources"* is curiously the least stable celestial frame. AV0 sources, although having a stable behavior, present in general a higher level of noise. As the whole set of defining sources in "sol 3" are AV0, this explains its last position in the comparison.

On the opposite end, "sol 14", as the representative of the group where only the level of noise of the sources is taken into account to select defining sources, is the most stable celestial frame in the comparison. This leads to the conclusion that, for the realization of a celestial frame at a determined epoch, the dominant information to take into account is the noise level of the sources. The data behavior only comes in second rank for the selection of defining sources.

The ranking between representative solutions goes in the same sense:

- "sol 11" better than "sol 3" shows the advantage of taking AV1 sources into account, and
- "sol 14" better than "sol 35" shows the disadvantage of excluding AV2 sources;

as well as the differences between solutions within each group:

- "sol 5" (non-plotted) better than "sol 3", "sol 11" better than "sol 10" (non-plotted), and "sol 35" best of its group show the advantage to lowering the rehabilitation threshold P_{rehab} to its minimum value, 0%, which is equivalent to making the division AV0/AV1/AV2 meaningless.

Another conclusion is the confirmation that a total of about 300 sources is enough to obtain optimal stability performance in the realization of a celestial reference.

By the time we wrote those lines, the IAU working group in charge of the realization of the third version of the international celestial reference frame finalized its work, and the resulting ICRF3 was adopted by the IAU during the XXX General Assembly as the next celestial reference frame (which will come into effect on the 1st of January, 2019).

In the meantime, what was not addressed in this study, as well as during the realization of the two previous versions of ICRF [8, 4], is the assessment, at the time of realization, of the defining source behavior impact on the future evolution of the celestial frame. In other words, is it possible to assess, when selecting the defining sources, their effect on the frame stability due to individual instabilities that may come in the future? Data behavior revealed by the use of the Allan standard deviation might be of great help in this task, but further investigations are needed to confirm this possibility. The almost 40 years of VLBI observations should be of great value for such studies.

Acknowledgements

This work has been supported by a CNES post-doctoral grant. César Gattano is grateful to the IAG, the CNFGG and the OASU for supporting the trip and thus allowing the presentation of this work at the IVS General Meeting.

References

1. Allan, D. W., Statistics of atomic frequency standards, IEEE Proceedings, 1966, 54, 221-230.
2. Feissel-Vernier, M., Selecting stable extragalactic compact radio sources from the permanent astrogeodetic VLBI program, A&A, 2003, 403, 105-110.
3. Feissel-Vernier, M.; de Viron, O. & Le Bail, K., Stability of VLBI, SLR, DORIS, and GPS positioning, Earth, Planets, and Space, 2007, 59, 475-497.
4. Fey, A. L.; Gordon, D.; Jacobs, C. S.; Ma, C.; Gaume, R. A.; Arias, E. F.; Bianco, G.; Boboltz, D. A.; Böckmann, S.; Bolotin, S.; Charlot, P.; Collioud, A.; Engelhardt, G.; Gipson, J.; Gontier, A.-M.; Heinkelmann, R.; Kurdubov, S.; Lambert, S.; Lytvyn, S.; MacMillan, D. S.; Malkin, Z.; Nothnagel, A.; Ojha, R.; Skurikhina, E.; Sokolova, J.; Souchay, J.; Sovers, O. J.; Tesmer, V.; Titov, O.; Wang, G. & Zharov, V., The Second Realization of the International Celestial Reference Frame by Very Long Baseline Interferometry, Astron. J., 2015, 150, 58.
5. Gattano, C.; Lambert, S. B. & Le Bail, K., Extragalactic radio source stability and VLBI celestial reference frame: insights from the Allan standard deviation, A&A, 2018, accepted.
6. Gontier, A.-M.; Le Bail, K.; Feissel, M. & Eubanks, T. M., Stability of the extragalactic VLBI reference frame, A&A, 2001, 375, 661-669.
7. Le Bail, K.; Gordon, D. & Ma, C., Selecting Sources that Define a Stable Celestial Reference Frame with the Allan Variance, International VLBI Service for Geodesy and Astrometry 2016 General Meeting Proceedings: "New Horizons with VGOS", Eds. Dirk Behrend, Karen D. Baver, Kyla L. Armstrong, NASA/CP-2016-219016, p. 288-291, 2016.
8. Ma, C.; Arias, E. F.; Eubanks, T. M.; Fey, A. L.; Gontier, A.-M.; Jacobs, C. S.; Sovers, O. J.; Archinal, B. A. & Charlot, P., The International Celestial Reference Frame as Realized by Very Long Baseline Interferometry, Astron. J., 1998, 116, 516-546.
9. Malkin, Z., Application of the Allan Variance to Time Series Analysis in Astrometry and Geodesy: A Review, IEEE Transactions on Ultrasonics Ferroelectrics and Frequency Control, 2016, 63, 582-589.

Improving the S/X Celestial Reference Frame in the South

Aletha de Witt [1], Karine Le Bail [2], Christopher Jacobs [3], David Gordon [2], David Mayer [4], Matthias Schartner [4], Sayan Basu [1]

Abstract We believe that the S/X celestial reference frame (CRF) can be improved in the far-south by a factor of 2 in density and a factor of 2.5 in precision. We have started a collaboration to meet these goals. We have increased the data rates on existing IVS astrometric sessions in the south from 256 Mbps to 1 Gbps. We will use this sensitivity to detect weaker sources and to improve the precision of sources in the southern S/X CRF, while simultaneously increasing the number of sources, in particular the overlap with other frames such as K- and Ka-band in the radio and the *Gaia* frame in the optical. VLBI observations in the southern celestial hemisphere have always been more difficult both because there are fewer radio telescopes in the south than in the north and because there are fewer known reference sources in the south. There have been many efforts in recent years to increase the number of known reference sources in the south, in particular the LBA calibrator Survey (LCS), which has already produced a significant improvement at X-band. The ICRF-3 is expected to make significant improvements in the south; however, the south has not yet reached parity with the north and much work remains to be done. Therefore, dedicated astrometric and imaging observations have already begun to improve the southern CRF at S/X-bands.

Keywords Astrometry, VLBI, Celestial Reference Frame, Southern Hemisphere, quasars

1. Hartebeesthoek Radio Astronomy Observatory (HartRAO), South Africa
2. NVI, Inc./NASA Goddard Space Flight Center, USA
3. Jet Propulsion Laboratory, California Institute of Technology/NASA, USA
4. Technische Universität Wien, Austria

1 Introduction

Geodetic and astrometric VLBI observations have always been more difficult in the south, with the availability of antennas being the most limiting factor. The second realization of the International Celestial Reference Frame (ICRF-2 [7]) was dominated by data from the north. However, despite many efforts to improve the north/south imbalance of observations (e.g., the AUSTRAL observing program that was started in 2011 [9]), current radio astrometry catalogs are still weak in the south, with a significant hemisphere disparity in source distribution and density.

In recent years there have been many efforts to increase the number of known reference sources in the south, with the most significant contribution coming from the Australian Long Baseline Array (LBA) Calibrator Survey (LCS, [8]), that observed more than 1,500 candidate extragalactic radio sources, (declination below -30°), from 16 VLBI experiments with the LBA at 8.4 GHz.

In 2012, the need for a more uniform spatial coverage of sources and uniform accuracy in source coordinates led to the formation of an International Astronomical Union (IAU) working group, with the goal of the realization of the next generation celestial reference frame (ICRF-3, [6]). Specific emphasis was placed on improving the southern CRF as well extending the frame to higher radio frequencies, chiefly at 24 GHz (K-band [4]) and 32 GHz (Ka-band [5]). Although the ICRF-3 is expected to show significant improvements in the south, the south has not yet reached parity with the north and much work remains to be done.

It is well known that the effect of source structure on astrometric VLBI positions can be significant and that structure and flux density variability are directly

related to the precision of geodetic solutions [3, 10]. It is therefore important to map the structures of these sources on a regular basis. There have, however, only been a few imaging sessions of reference sources in the south and dedicated campaigns to map and monitor source structure have proven difficult to obtain. However, recent investigations to image source structure from existing astrometric and geodetic observations in the south have shown that dedicated imaging campaigns may indeed be possible [1].

In this paper we present the current status of the S/X CRF as well as our proposed plans to improve the S/X CRF in the south. We also present some recent results from these efforts, including a multi-epoch campaign to image source structures in the south.

2 Current Status: North Versus South

At present there are only a few VLBI-capable radio telescopes in the Southern Hemisphere and even fewer that regularly participate in astrometric and geodetic VLBI experiments. The Very Long Baseline Array (VLBA) significantly contributes to CRF work in the north, but unfortunately there is no VLBA to compensate in the south. Currently there are only five radio telescopes in the south that regularly participate in astrometric experiments (∼12% of total); a 15 & 26-m telescope in South Africa, three 12-m telescopes and one 26-m in Australia, and one 12-m telescope in New Zealand. There are two radio telescopes in Antarctica, but these are very small in size and can only detect a few of the brightest sources. There is also a radio telescope in Brazil, but it is close to the equator and does not contribute significantly to southern observations.

In Figure 1 we show the evolution of geodetic and astrometric observations for the period 03 August 1979 to 27 March 2018. The plot shows the distribution of northern-only baselines, southern-only baselines, and north-south or mixed baselines. The distribution has evolved from mainly northern-only baselines to ∼10% southern-only and almost 20% mixed baselines.

The growth of astrometric and geodetic observations between the period 03 August 1979 and 27 March 2018 are shown in Figure 2. Southern-only baselines and mixed baselines have increased noticeably in recent years, but still represent only ∼15% of the total number of baselines.

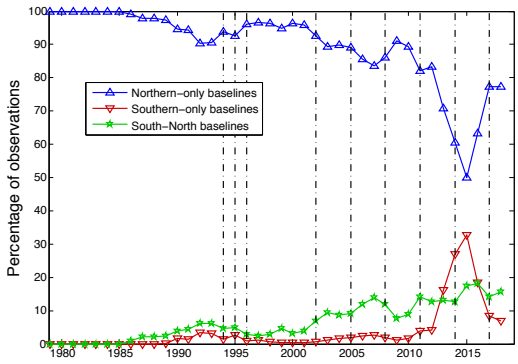

Fig. 1 The evolution of the observation distribution from 3 August 1979 to 27 March 2018 between northern-only baselines (blue traingles), southern-only baselines (red inverted triangles), and mixed baselines (green stars).

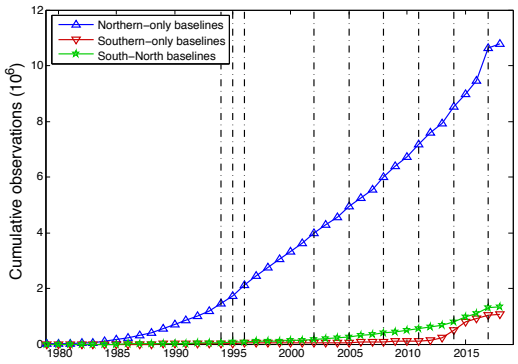

Fig. 2 Cumulative growth of northern-only observations (blue traingles), southern-only baselines (red inverted triangles), and mixed baseline observations (green stars) for the period 03 August 1979 to 27 March 2018.

The ICRF-2 is based on high precision Very Long Baseline Interferometric (VLBI) measurements of positions of 3,414 extragalactic radio sources. This includes the 295 defining sources which determine the orientation of the frame axes. The ICRF-2 has a noise floor of 40 µas in the individual source coordinates, and an axis stability of 10 µas. The positions were determined from dual-frequency VLBI observations at 2.3 GHz (S-band) and 8.4 GHz (X-band), mostly organized under the auspices of the International VLBI Service for Geodesy and Astrometry (IVS).

The ICRF-2 was generated from 4,726 VLBI sessions and 6.5 million measurements acquired for geodetic and astrometric purposes between 1979 and 2009 and was dominated by data from the north (e.g., Figures 1 & 2). The most recent S/X astrometric so-

lution (sx-gsfc-180521, David Gordon) was generated from 6,206 VLBI sessions and 13.2 million measurements from all available sessions up to 27 March 2018, and includes significantly more southern-only and north-south baseline observations than the ICRF-2.

The sky distribution plot of the formal position uncertainties, from the most recent S/X CRF, is shown in Figure 3. Although this solution shows significant improvement over the ICRF-2, it is clear that we still need more sources in the south and that we also need to improve the spatial coverage, especially for declinations south of -30°. Both the number of sources and the average number of observations per source are a factor of 2 less in the far-south ($\leq -30^\circ$) compared to the far-north. The median formal uncertainties are a factor of 1.5 weaker in $\alpha\cos(\delta)$ in the far-south and a factor of 2.7 weaker in δ. It is evident from these plots that we need more southern baseline observations as well as more north-south baselines.

From the most recent S/X CRF we identified 124 sources (37 ICRF-2 defining sources) in the far-south (below -45° south), with no VLBI images—almost half the total number of sources in the far-south! Multi-epoch maps are essential to assess the astrometric suitability of CRF sources. Extended intrinsic source structures can introduce significant errors in the VLBI measurements, thereby degrading the accuracy of the estimated source positions. The lack of images will severely limit the potential for further improvements in the accuracy of VLBI source positions in the far-south and thus the improved stability of future S/X-band CRFs.

3 Proposed Plans and Progress to Date

3.1 Increase Data Rates

Currently the only dedicated astrometric programs at S/X in the Southern Hemisphere are the IVS Celestial Reference Frame (IVS-CRF) and Celestial Reference Frame Deep South (IVS-CRDS) sessions. Up until 2017, the data rates of these were only 128 Mbps for the IVS-CRF sessions and 256 Mbps for the IVS-CRDS sessions and included only observations of ICRF-2 defining sources. We propose to increase the data rates of these sessions by a factor of 4 or more by increasing the data rate to 1–2 Gbps. This in turn will allow an increase in the sensitivity by a factor of 2 or more, which will allow the detection of weaker sources down to $\sim$350 mJy or less. Scheduling will also become more efficient, since there will be more sources to choose from and scan times will be shorter, which will result in more scans and/or sources per schedule.

We tested and implemented a 1-Gbps observing mode for the IVS-CRDS sessions and a 1-Gbps narrow-band mode was tested for the IVS-CRF sessions. The IVS-CRDS sessions were officially upgraded to 1 Gbps mode starting with crds93 on 24 January 2018. The IVS-CRF sessions switched to 1 Gbps on 4 April 2018 with crf106.

3.2 Scheduling Optimized for Astrometry

We propose to change the scheduling of the IVS-CRF and IVS-CRDS sessions to be optimized for astrometry and imaging instead of geodesy. This would imply using the full network of stations when possible for every scan and with no sub-netting as is used routinely for geodesy schedules. There should also be at least 3–8 scans per source spread evenly over hour angle range, to allow for optimal *u-v* coverage for imaging without compromising the astrometric goals of the experiment. The schedule should also include blocks with tropospheric calibrators, that will also be used as astrometric ties and for amplitude calibration for imaging. In addition, we propose astrometric sessions be scheduled as part of a campaign rather than individual sessions. This will ensure that each source will receive the required amount of observing time and that the ultimate astrometric goals of the project be reached.

We have optimized the scheduling of all of the IVS-CRDS sessions from crds93 onwards. Figure 4 compares the *u-v* coverage for a source observed in both crds68 (27 November 2013) and crds94 (21 March 2018). The improvement in *u-v* coverage going from two scans (crds68) to seven scans (crds94) is clearly evident from these two plots. The overall number of sources also increased from 38 to 51 and the overall number of scans from 144 to 304, from crds68 to crds94.

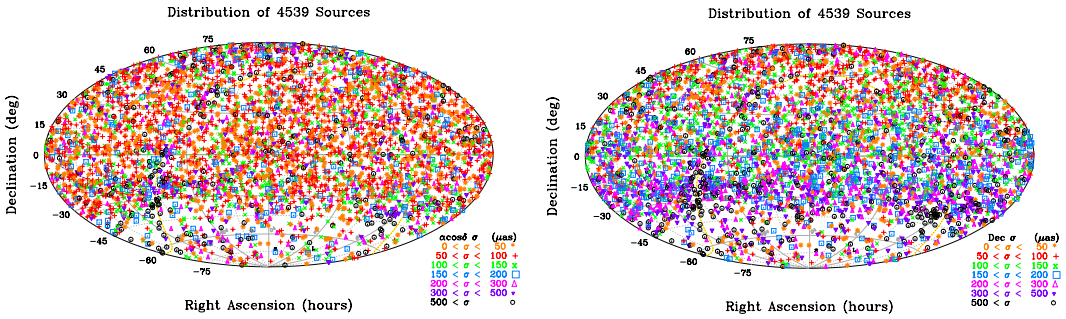

Fig. 3 The distribution of sources from the most recent S/X astrometric solution (sx-gsfc-180521) showing the formal uncertainties in $\alpha\cos(\delta)$ on the left and δ on the right.

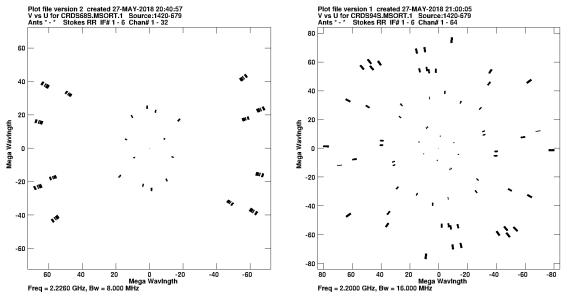

Fig. 4 The *u-v* plane coverage for the source 1420-679, observed in different IVS-CRDS sessions. The *u-v* coverage plot on the left is from the crds68 session (27 November 2013) and the plot on the right, showing a much improved sampling of the *u-v* plane, is from the crds94 session (21 March 2018). In both sessions five antennas participated. In crds68 the source was only observed in two scans and in the crds94 it was observed in seven scans.

3.3 Improve Precision

Up to 2017, only ICRF-2 defining sources were observed in IVS-CRF and IVS-CRDS sessions. We propose to re-observe all southern sources in the current S/X CRF to improve the source position accuracy in both coordinates. We propose to improve the overall precision by a factor of 2.5 in the south. From the 1,344 sources south of -15°, we have 1,091 sources with ≤ 10 observing sessions. We will prioritize the 216 of these sources with flux density > 350 mJy that will be easily detectable with current instruments and data rates. Since December 2017, we started to include some of these 216 sources as part of the IVS-CRDS and IVS-CRF sessions.

3.4 Improve Density and Spatial Coverage

We propose to improve the far-south by a factor of 2 in density by expanding the source list in the south, specifically in the far-south (below -30° south). In addition, we also propose to improve the overlap with K- and Ka-band frames and the *Gaia* optical frame. We identified $\sim$80 K- and Ka-band sources that are not in the current S/X frame at declinations south of -15°. From these we have $\sim$20 sources with flux density > 350 mJy at S/X-band. In addition, we also propose follow-up observations of candidate CRF sources brighter than 350 mJy from the pool of LCS sources. Priority will be given to $\sim$1/2 of the target sources that have a counterpart with *Gaia*. Since December 2017, we started to include those K- and Ka-band sources that are not currently in the S/X CRF into the IVS-CRDS sessions.

3.5 Imaging

We propose to produce multi-epoch maps at both 2.3 and 8.4 GHz for all sources observed in the IVS-CRDS and IVS-CRF sessions. These maps will be used to quantify the non-pointlike structure and jet directions in these CRF sources. First priority will be given to those 124 sources in the far-south with no VLBI images. In Figure 5 we show representative contour plots from recent imaging results obtained from the crds94 session from 21 March 2018 [2].

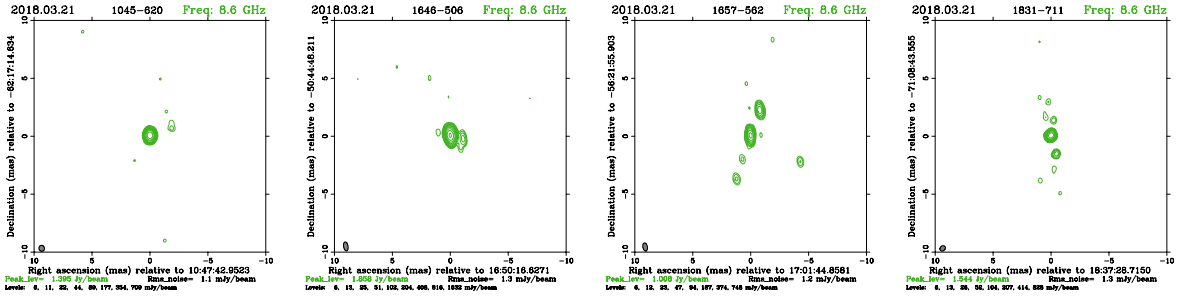

Fig. 5 From left to right, contour plots for sources 1045-620, 1646-506, 1657-582, and 1831-711 at 8.6 GHz from 21 March 2018 (crds94). North is Up and East is to the Left. The FWHM beamsize is graphically indicated in the bottom left corner [2].

4 Conclusions

Our goal is to improve the S/X-band frame in the south by at least a factor of 2 in density and 2.5 in precision, to be about as good as the north.

In order to achieve this, we propose to increase the data rate of southern IVS sessions to at least 1 Gbps and to optimize the scheduling of these sessions for astrometry and imaging versus geodesy. We further propose to increase the number of well observed sources (Nsess $>$ 10) in the south and to increase both the number of southern-only and north-south baseline observations. We also propose to expand the southern source list and improve spatial coverage. In addition, we propose multi-epoch imaging of southern CRF sources to quantify non-pointlike structure and measure jet directions.

Our initial steps are succeeding: all IVS southern astrometric sessions are now at 1 Gbps, non-defining sources were added to the IVS-CRDS and IVS-CRF source list, and we produced first imaging results from and IVS-CRDS sessions at 1 Gbps.

Acknowledgements

Copyright 2018. All rights reserved. U.S. Government sponsorship acknowledged for part of this research. HartRAO is a facility of the National Research Foundation (NRF) of South Africa. The Hobart telescope is operated by the University of Tasmania and this research has been supported by AuScope Ltd., funded under the National Collaborative Research Infrastructure Strategy (NCRIS).

References

1. S. Basu et al., How Good is the Deep Southern Sky, in D. Behrend, K. D. Baver, K. L. Armstrong (eds.), *IVS 2016 General Meeting Proceedings: "New Horizons with VGOS"*, p. 312–316, 2016.
2. S. Basu et al., VLBI Imaging Observations of Potential ICRF-3 Defining Sources in the South. *MNRAS*, in preparation, 2018.
3. P. Charlot., Radio-source Structure in Astrometric and Geodetic Very Long Baseline Interferometry, *AJ*, 99, 1309, 1990.
4. A. de Witt et al., K-band Celestial Reference Frame: Can it be Better than S/X?, in R. Haas & G. Elgered (eds.), *Proceedings of the 23rd EVGA Working Meeting, May 2017, Gothenburg, Sweden*, pp. 181–185, 2017.
5. C. Jacobs et al., Celestial Reference Frame at X/KA-Band (8.4/32 GHz) for Deep Space Navigation, *23rd International Symposium on Space Flight Dynamics, Pasadena CA, 30 Oct 2012*, 14 pages, id.1, 2012
6. C. Jacobs et al., ICRF-3: Roadmap to the Next Generation ICRF, in N. Capitaine (eds.), *Proceedings of the Journées 2013, 16-18 September 2013*, p. 51–56, 2014.
7. C. Ma et al., The Second Realization of the International Celestial Reference Frame by Very Long Baseline Interferometry, *IERS Technical Note 35*, 29, 2009.
8. L. Petrov et al., The LBA Calibrator Survey of Southern Compact Extragalactic Radio Sources - LCS1, *MNRAS*, 414, 2528, 2011
9. L. Plank et al., The AUSTRAL VLBI Observing Program, *Journal of Geodesy*, 91, 7, p. 803–817, 2017.
10. S. Shabala et al., Quasar Structure Effects on the VLBI Reference Frame: The Case of 1144-379, In D. Behrend and K.D. Baver (eds.), *Seventh IVS General Meeting*, 329, 2012.

New VLBI Solutions at Analysis Center DGFI-TUM

Matthias Glomsda, Younghee Kwak, Michael Gerstl, Detlef Angermann, Florian Seitz

Abstract The Deutsches Geodätisches Forschungsinstitut at Technische Universität München (DGFI-TUM) is one of the Analysis Centers (AC) of the International VLBI Service for Geodesy and Astrometry (IVS). In this regard, it provides solutions consisting of Earth Orientation Parameters (EOP), station coordinates and radio source positions for observations obtained from Very Long Baseline Interferometry (VLBI). Until recently, the official solutions were computed with the external VLBI software OCCAM. In 2018, after successful completion of internal and third-party validations, DGFI-TUM started contributing to the IVS with the Radio Interferometry component of its proprietary DGFI Orbit and Geodetic parameter estimation Software (DOGS-RI). In this work, we will summarize the model approaches followed by DOGS-RI and provide analysis results from our latest contributions to extend the quality assessment of DGFI-TUM's new VLBI solutions.

Keywords VLBI Analysis Software, DOGS-RI, IVS

1 Introduction

Since 2008, the Deutsches Geodätisches Forschungsinstitut at Technische Universität München (DGFI-TUM) has been an operational Analysis Center (AC) of the International VLBI Service for Geodesy and Astrometry (IVS, [6]). It provides *daily SINEX* files to the IVS Combination Centers (CC), which contain solutions for the various Very Long Baseline Interferometry (VLBI) experiments conducted. These solutions are given in the form of unconstrained and datum-free normal equations (NEQ), which were established to estimate the following geodetic variables: Earth Orientation Parameters (EOP), the positions of the observing VLBI stations, and the positions of the extra-galactic radio sources (quasars) which were aimed for in the corresponding VLBI session. Based on these NEQ, generated by several Analysis Centers, the Combination Centers can compute the values for the geodetic parameters. This is either done for each AC separately or in a combinatory approach, where the single NEQ are stacked (in terms of a weighted sum) to produce an averaged solution.

The distinct solutions (i.e. *daily SINEX* files) of the AC can be found online[1] and are labelled by names like *gsf2016a*: the first three letters represent the AC (in this example the *Goddard Space Flight Center*), the four digit number is the year in which the solution was provided for the first time, and the last letter reflects the particular quarter of the latter ($a = 1$, $b = 2$, $c = 3$, $d = 4$). Until March 2017, DGFI-TUM used its own branch of the analysis software *OCCAM* (see [9]) to process VLBI sessions (*dgf2009a*). During the last years, however, we implemented a proprietary VLBI analysis tool as part of the DGFI Orbit and Geodetic parameter estimation Software package (DOGS, see [2]). The new component is called DOGS-RI (Radio Interferometry), and since February 2018 it has been used to generate DGFI-TUM's official IVS contribution *dgf2018a*.

In Section 2, we will describe DOGS-RI and the features of the new solution *dgf2018a*. The initial validation of the results of DOGS-RI is described in [5],

Deutsches Geodätisches Forschungsinstitut der Technischen Universität München

[1] ftp://cddis.gsfc.nasa.gov/vlbi/ivsproducts/daily_sinex/

but since the actual IVS contribution has a different setup, we will show some recent assessments of the latter in Section 3. In Section 4, the current development status of our VLBI analysis software is summarized, before we finalize this document with conclusions in Section 5.

2 VLBI Analysis with DOGS-RI

The DGFI Orbit and Geodetic parameter estimation Software (DOGS) now consists of three major parts:

- **DOGS-RI** (Radio Interferometry) processes VLBI experiments,
- **DOGS-OC** (Orbit Computation) performs Precise Orbit Determination (POD) based on satellite observations (currently SLR and DORIS), and
- **DOGS-CS** (Combination & Solution) aggregates the distinct results of any space geodetic technique (if available in DOGS- or SINEX format) on the normal equation level.

Figure 1 presents a schematic overview of the interaction of DOGS's components. The programming language is Fortran 2003, so DOGS can make use of standard procedures and subroutines already available for geodetic and astrometric applications, like the SOFA-library [3]. All parts share common models and subroutines to ensure a consistent combination of solutions within DOGS.

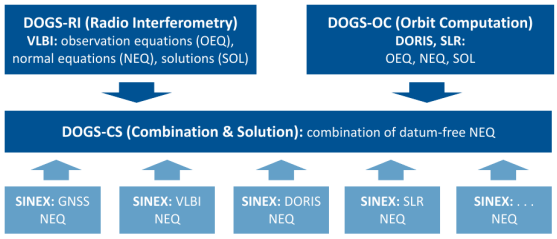

Fig. 1 Consistent combination of various space geodetic techniques with DOGS. Light blue boxes refer to external data.

The VLBI component DOGS-RI is based on a two-step least-squares minimization (the classic Gauss-Markov model) with intermediate outlier detection. Next to station and quasar coordinates and EOP, also tropospheric (zenith and gradient delays) and station clock parameters can be estimated. Optionally, various constraints and datum conditions can be applied. To support the post-processing of equations and solutions, DOGS-RI offers three different output formats, including the binary DOGS-CS format and the SINEX format. DOGS-RI provides great flexibility by containing a wide range of geophysical and signal delay models of previous and current IERS Conventions [7]. Furthermore, a multitude of mathematical functions and interpolation types is available for the representation of estimated parameters. The current setup for solution *dgf2018a* in comparison to that of *dgf2009a* is listed in Table 1.

Table 1 Settings for the IVS contributions by DGFI-TUM.

component	**dgf2018a**	**dgf2009a**
software	DOGS-RI	OCCAM @ DGFI-TUM
observation data format	NGS (Mk3)	NGS (Mk3)
precession / nutation	IAU 2006/2000A	MHB 2000 (IAU 2000A)
nutation parameters	ΔX_{CIP}, ΔY_{CIP} (CIO based)	$\Delta\psi$, $\Delta\varepsilon$ (equinox based)
a-priori TRF	ITRF2014	VTRF2008
a-priori EOP	IERS 14 C04	IERS 08 C04
a-priori gradients	GSFC / TU Vienna	zero
IERS Conventions	2010	2003
atmosphere loading	Petrov & Boy [8]	n/a
tidal ocean loading	FES2004 (with CoM correction)	FES2004 (w/o CoM correction)
tropospheric mapping fct.	VMF1	VMF1
delay model	IERS 2010	IERS 1992

3 Assessment of Solution dgf2018a

Before DGFI-TUM could contribute *dgf2018a*, the results of DOGS-RI had to be validated. At a first stage, our new software took part in the VLBI Analysis Software Comparison Campaign [4]. Then, an intermediate solution was provided to the Combination Centers (see [5]). Only after the latter was approved, DGFI-TUM started to provide the current, finally official solution.

The intermediate solution had a setup which was slightly different from *dgf2018a*, in particular with respect to the a-priori EOP and TRF. Hence, we re-assessed the quality of our official solution by comparing it to those of some other Analysis Centers. In

the following, we will look at EOP, station and quasar coordinates. Several ACs not only provide normal equations in their *daily SINEX* files but also estimates for the geodetic parameters themselves. Hence, we could simply extract the latter from the corresponding files. Our own estimates are not available in SINEX format, but they are available in the local output files of DOGS-RI.

Earth Orientation Parameters

We perform the common test of subtracting the single AC values of an EOP from the corresponding value of the official IERS 14 C04 series. This is done epoch-wise for every available session between January 2005 and March 2018 per Analysis Center, with exceptionally high differences being removed as outliers. Figure 2 shows the time series of differences between the single AC values of the EOP $\Delta UT1(0h) = UT1 - UTC$ and its IERS 14 C04 value.

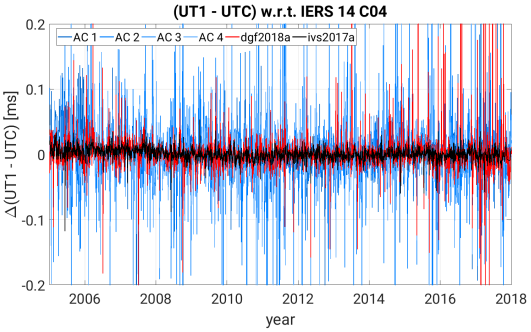

Fig. 2 Time series of the differences between EOP (UT1 – UTC) per AC and the IERS 14 C04 reference value.

ivs2017a is the solution of the IVS Combination Center at *Bundesamt für Kartographie und Geodäsie* (BKG), which provides parameters estimated from a weighted sum of the individual AC's normal equations. As the IERS 14 C04 series is also obtained from a combination of single solutions (see [1]), it can be expected that the deviations will be smallest for *ivs2017a*. The deviations of DOGS-RI, however, have a magnitude similar to those of the other Analysis Centers used in the comparison. This pattern is valid for all EOP, which is also indicated by the weighted means and weighted RMS per EOP and AC as listed in Tables 2 and 3. There, we see that the minimum weighted RMS per EOP is always given by the combined solution *ivs2017a*, and our solution *dgf2018a* stays within the range of the other AC's values, while the weighted means all show comparable magnitudes. (N/A means that the corresponding EOP could not be extracted from the *daily SINEX* files.)

Table 2 Weighted mean for differences to the IERS 14 C04 series. The units for $\Delta UT1$ and LOD are ms and ms/d, respectively. For all the others, they are mas (or mas/d for the rates).

EOP	AC1	AC2	AC3	AC4	dgf2018a	ivs2017a
x_{pol}	0.0574	0.0061	0.0123	-0.0087	-0.0194	0.0030
$\dot{x}_{pol}$	0.0248	0.0258	0.0202	0.0148	0.0283	0.0260
y_{pol}	0.2577	-0.0200	-0.0346	-0.0176	-0.0096	-0.0098
$\dot{y}_{pol}$	0.0133	-0.0003	-0.0000	0.0105	0.0132	0.0073
$\Delta UT1$	0.0020	-0.0004	-0.0013	-0.0052	-0.0023	-0.0008
LOD	-0.0003	-0.0010	-0.0011	0.0020	0.0012	-0.0014
ΔX_{CIP}	n/a	n/a	n/a	0.0234	0.0200	0.0066
ΔY_{CIP}	n/a	n/a	n/a	-0.0069	-0.0047	-0.0076

Table 3 Weighted RMS for differences to the IERS 14 C04 series. The units are the same as in Table 2.

EOP	AC1	AC2	AC3	AC4	dgf2018a	ivs2017a
x_{pol}	0.1652	0.1507	0.1322	0.1558	0.1479	0.0801
$\dot{x}_{pol}$	0.2965	0.2579	0.2732	0.3173	0.2911	0.2320
y_{pol}	0.1939	0.1617	0.1346	0.1765	0.1570	0.0763
$\dot{y}_{pol}$	0.2884	0.2540	0.2685	0.3221	0.2910	0.2307
$\Delta UT1$	0.0154	0.0185	0.0148	0.0164	0.0144	0.0097
LOD	0.0194	0.0173	0.0177	0.0186	0.0189	0.0162
ΔX_{CIP}	n/a	n/a	n/a	0.1680	0.1375	0.0329
ΔY_{CIP}	n/a	n/a	n/a	0.1528	0.1385	0.0358

Station Coordinates

The Cartesian coordinates of the observing stations can be extracted from the Analysis Centers' *daily SINEX* files, too (except for the combined solution *ivs2017a*). We transformed the global (x, y, z) coordinates into local Cartesian ones (North, East, Up) and compared the absolute values directly instead of computing differences to some reference frame. Figure 3 exemplarily shows the time series of the local coordinates for the radio telescope in Ny-Ålesund (NYALES20), again for different ACs and the available VLBI sessions between January 2005 and March 2018. The coordinates estimated by DOGS-RI are in line with those of the other ACs, which generally agree well except for the vertical (Up) component. To highlight the differences in the latter, we apply a linear fit to each time series and plot the corresponding functions (confined to the most recent years) in Figure 4. The spread in the vertical component is mainly created by

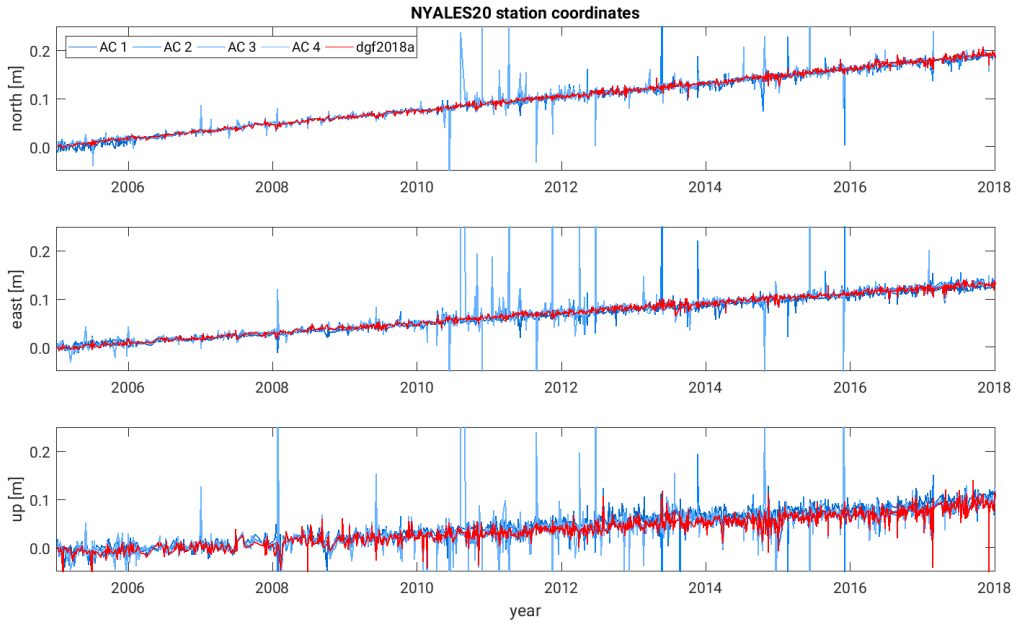

Fig. 3 Local Cartesian coordinates of the VLBI station in Ny-Ålesund per Analysis Center.

the solution of one of the other Analysis Centers, while DGFI-TUM's solution *dgf2018a* matches the results of the remaining ones. We found a similar behavior for other VLBI stations as well.

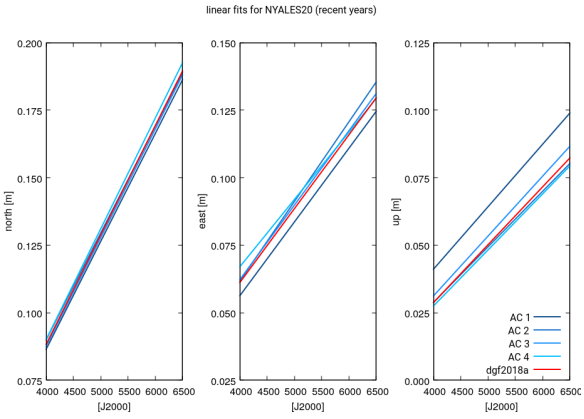

Fig. 4 Linear fit to the local (NEU) coordinates for Ny-Ålesund.

Quasar Coordinates

Finally, we compare the positions estimated for the radio sources in terms of right ascension and declination. These could again be directly extracted from the *daily SINEX* files, at least for most of the Analysis Centers. As an example, Figure 5 shows the time series for the ICRF2 defining source *3C446*. Also for this type of geodetic parameter, the results of DOGS-RI are in line with those of the other VLBI analysis softwares.

4 Ongoing Development

DOGS-RI is permanently updated and extended to incorporate the recent developments in VLBI. The most important modification currently is the inclusion of the new *vgosDB* format. Apart from minor issues and final tests, DOGS-RI is basically able to cope with vgosDB. Further projects for the future are, for example, an automatic detection of jumps in station clocks and a more advanced outlier identification routine.

5 Conclusions

dgf2018a is DGFI-TUM's new official contribution of normal equations to the IVS for estimating geodetic parameters from VLBI experiments. It is now generated with the VLBI analysis tool DOGS-RI, which is part

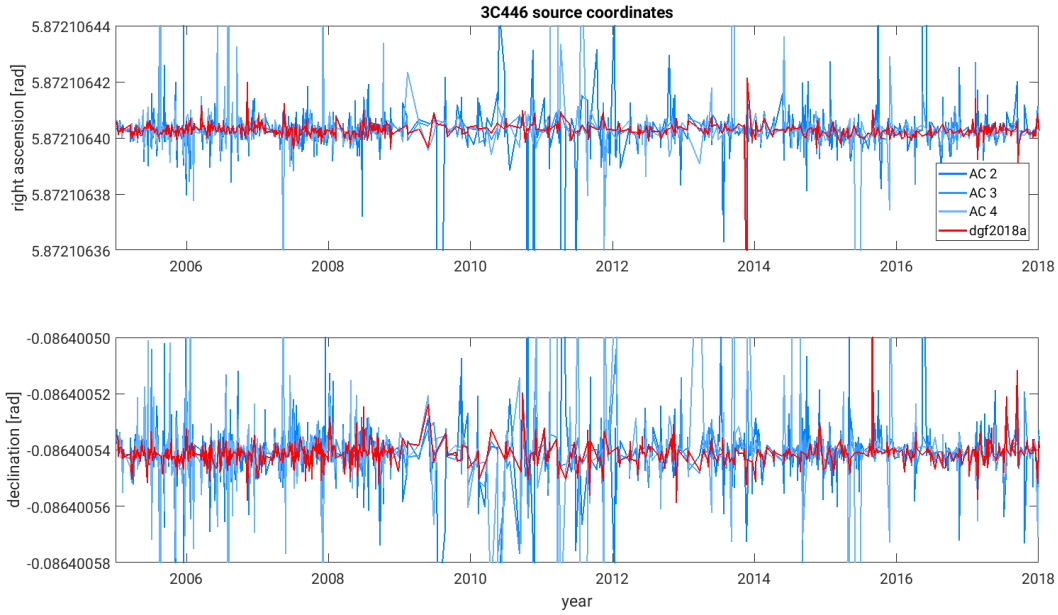

Fig. 5 Coordinates of ICRF2 defining source 3C446 as estimated by different Analysis Centers.

of our proprietary software package DOGS. The latter makes use of the most recent IERS Conventions, and it could be shown in numerous tests that its solutions agree well with those of other IVS Analysis Centers. The vgosDB format will soon be supported.

Acknowledgements

We acknowledge the efforts of the various members of the IVS [6] (here in particular the Analysis Centers and the Combination Center at BKG) for generating and sharing their data, hence enabling us to compare and verify our solutions.

References

1. Bizouard C., Lambert S., Becker O., and Richard J. Y. (2017): *Combined solution C04 for Earth Rotation Parameters consistent with International Terrestrial Reference Frame 2014*. Preliminary draft of January 9, 2017.
2. Gerstl M., Kelm R., Müller H., and Ehrnsperger W. (2000): *DOGS-CS - Kombination und Lösung großer Gleichungssysteme*. Internal Report, DGFI-TUM, München.
3. IAU SOFA Board (2018): *IAU SOFA Software Collection*. Issue 2018-01-30, URL http://www.iausofa.org
4. Klopotek G., Artz T., Bellanger A., Bourda G., Gerstl M., Gordon D., Haas R., Halsig S., Hjelle G. A., Hobiger T., Hugentobler U., Iddink A., Kirkvik A. S., Lambert S., Plank L., Schmid R., Shu F., Titov O., Tong F., Wang G., Xu M., and Zheng W. (2016): *Results from the VLBI Analysis Software Comparison Campaign 2015*. In: D. Behrend, K. D. Baver, K. L. Armstrong (eds.), IVS 2016 General Meeting Proceedings, NASA/CP-2016-219016, pp. 203-207.
5. Kwak Y., Gerstl M., Blossfeld M., Angermann D., Schmid R., and Seitz M. (2017): *DOGS-RI: new VLBI analysis software at DGFI-TUM*. Proceedings of the 23rd EVGA Meeting, Gothenburg, Sweden.
6. Nothnagel A., Artz T., Behrend D., and Malkin Z. (2017): *International VLBI Service for Geodesy and Astrometry: Delivering high-quality products and embarking on observations of the next generation*. Journal of Geodesy, Vol. 91(7), pp. 711-721.
7. Petit G., and Luzum B. (2010): *IERS Conventions (2010)*. IERS Tech. Note 36, Verlag des Bundesamtes für Kartographie und Geodäsie, ISBN: 978-3-89888-989-6.
8. Petrov L., and Boy J.-P. (2004): *Study of the atmospheric pressure loading signal in very long baseline interferometry observations*. J. Geophys. Res., 109, B03405.
9. Titov O., Tesmer V., and Böhm J. (2004): *OCCAM v.6.0 software for VLBI data analysis*. In: N. Vandenberg and K. D. Baver (eds.), IVS 2004 General Meeting Proceedings, NASA/CP-2004-212255, pp. 267–271.

Making Where Available to the Community

Geir Arne Hjelle, Ann-Silje Kirkvik, Michael Dähnn, Ingrid Fausk

Abstract The Norwegian Mapping Authority is an associated Analysis Center within the IVS and is currently preparing to contribute VLBI analyses to the IVS with its new Where software. The software is being made available to the geodetic community under an open source MIT license. You can download Where from GitHub and try it for yourself. Where is written in Python and comes with a graphical tool called There that can be used to analyze results from Where and edit sessions. Furthermore, a geodetic Python library called Midgard is made available. This library contains components of Where that are useful in a wider setting. If you are doing any geodetic data analysis in Python, Midgard might be useful to you.

Keywords VLBI, Software, Python, Open source

1 Introduction

The Norwegian Mapping Authority (NMA) has been developing a new software for geodetic analysis over the last years [2, 3]. That software is called Where and is currently being used in NMA's bid for becoming an operational Analysis Center within the International VLBI Service for Geodesy and Astrometry (IVS) [4]. In addition NMA has made Where available to the community as open source software [1] under the MIT license.

The Where software is currently able to analyze single VLBI sessions, where ambiguities have already been resolved (level 4 databases). There are plans to extend the capabilities of the software going forward, including preliminary support for SLR and GNSS analyses.

The background for why NMA has developed a new software and which models are available, as well as early benchmarks and results, are covered in [3] and [4]. This note will focus more on how you can obtain and use the software yourself.

2 Overview of Where

The Where software is mainly written in Python[1]. It is cross platform and can run on Linux, macOS, and Windows. Where is available for download at

`kartverket.github.io/where/`

Where can do different kinds of analyses. Each kind of analysis is defined as a pipeline consisting of separate steps or stages. Currently, only the VLBI pipeline is publicly available, but work on other pipelines based on SLR and GNSS is underway.

Figure 1 illustrates the VLBI pipeline in the green, vertical box that contains arrows. Pipelines are based on a few simple principles:

- Stages in a pipeline are performed sequentially.
- The output from one stage is input to the next stage.
- The state of an analysis can be inspected at each stage.

While the pipelines are tailored to one particular kind of analysis, each stage relies on components that are common to all pipelines. This is illustrated as horizontal, blue boxes in Figure 1.

Norwegian Mapping Authority

[1] www.python.org

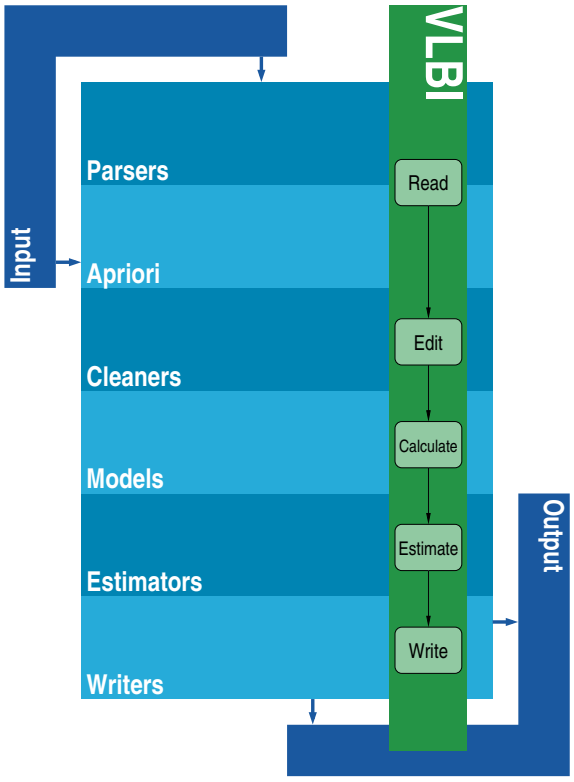

Fig. 1 The VLBI pipeline. The stages *Read*, *Edit*, *Calculate*, *Estimate*, and *Write* are performed sequentially to perform a VLBI analysis. Other pipelines can be defined that may reuse the common Where components: *Parsers*, *Apriori*, *Cleaners*, *Models*, *Estimators*, and *Writers*.

This architecture makes it easy to reuse code across techniques. For instance, different pipelines can use the same ITRF component for a priori station positions, the same ocean loading model for station displacements, or the same Kalman filter estimator.

Where comes bundled with a graphical tool for looking at and analyzing results from an analysis. This tool is called There. Figure 2 shows a screenshot of There in action. More information about There will be given in Section 5 below.

In an effort to make the functionality of Where as available as possible, components that can be reused outside Where pipelines are being separated into its own package called Midgard. While Midgard has its own web page[2], it is most easily installed through the

[2] kartverket.github.io/midgard/

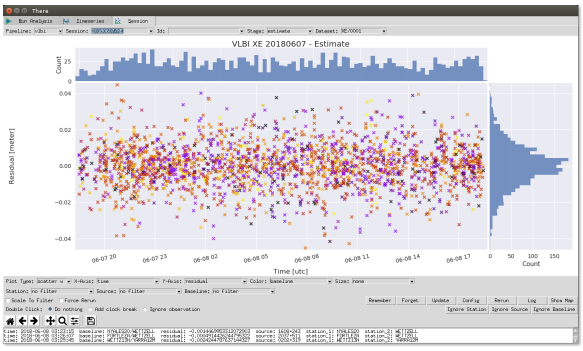

Fig. 2 The There graphical analysis tool. The plot shows post-fit residuals (after the *Estimate* stage) for the XE session on June 7, 2018. The colors indicate the baseline. That is, all residuals for the same baseline have the same color.

Python Package Index (PyPI)[3] using the standard Pip tool:

```
$ pip install midgard
```

Section 6 contains more information.

3 Try It Yourself

Where is available through the GitHub platform. GitHub[4] is a place for sharing code and working together on software development. In addition to downloading Where and using it for your own analysis, you may also contribute to the further development of the software. Get in touch[5] if you have any questions.

To start using Where you first need to install Python. We recommend the Anaconda Python distribution[6], as it bundles Python together with a lot of useful data science tools. Once you have Python on your system follow the instructions at the Where web page[7] to install the program.

Once the program is installed you can run an analysis. This is done with a command of the form

```
$ where 2018 6 7 --vlbi --session=XE
```

The date, pipeline, and session must be specified. When executed, this will perform a VLBI analysis with the default settings (see Section 4 below for more infor-

[3] pypi.org/project/midgard/

[4] github.com

[5] kartverket.github.io/where/pages/contact.html

[6] www.anaconda.com/download

[7] kartverket.github.io/where/installing.html

mation). The program will automatically download all auxilliary files needed to do the analysis.

All information about an analysis, including the configuration, a list of file dependencies, and intermediate and final results, are stored in a separate directory. While running the analysis, Where will by default print information about what it is doing to the console. The name of the analysis directory is printed at the top of this log, and the log is also stored to a file inside the analysis directory.

4 Changing the Analysis Parameters

Most aspects of a Where analysis are configurable. The default configuration is defined in configuration files[8]. You can change the default configuration for all analyses by creating a file called `where_local.conf` inside a directory called `.where` that resides in your home directory.

You can look at the configuration of an analysis by using the `where_setup` tool:

```
$ where_setup 2018 6 7 -v --session=XE
========================================
VLBI XE 2018-06-07

[vlbi]
atmospheric_tides               = cm
atmospheric_tides_cmc           = False
ephemerides                     = de430
...
```

Individual parameters can be changed by specifying them on the command line when running either `where` or `where_setup`:

```
$ where 2018 6 7 -v --session=XE \
        --ephemerides=de421
```

You can also use the `-E` (`--edit`) option to open and change the configuration in an editor:

```
$ where 2018 6 7 -v --session=XE -E
```

While NMA so far has used Where to analyze 24-hour R1 and R4 sessions, the software can analyze other kinds of VLBI sessions as well by changing the configuration appropriately. To easily work with different kinds of sessions, Where supports configuration profiles. You can for example analyze the XU intensive session on June 7, 2018 as follows:

```
$ where 2018 6 7 -v --session=XU \
        --profile=intensives
```

A graphical utility for setting up and changing the configuration is in preparation. It will be integrated into There later.

5 Running Analyses

To run a series of analyses you can use the `where_runner` tool. It will use master files[9] to call Where for all sessions in a specified time interval. For example, to analyze all sessions in January 2018 use the following:

```
$ where_runner 2018 1 1 2018 1 31 --vlbi
```

If you try to rerun an analysis you have already done, Where will by default do so in the same directory as before. Where is also lazy software, so it will not even do the analysis unless either the configuration or at least one of the input files have changed.

When comparing different models or settings you will be interested in running the same analysis twice and keeping the results. The way to do this is to label each of your analyses using the `--id` option:

```
$ where 2018 6 7 -v --session=XE \
        --id=vtrf \
        --reference_frames=vtrf
```

The results from an analysis can be inspected using the There graphical tool. Starting There is usually done only by specifying that you want to look at VLBI analyses (either `-v` or `--vlbi`):

```
$ there -v
```

This opens the There application. There is organised using tabs. Along the top you will see different tabs including *Timeseries* and *Session*.

The *Timeseries* is used to get an overview over all sessions that were analyzed. It can display many different summary parameters for each session, including residuals (see Figure 3), size of session, and estimated parameters. Clicking on a point gives more information in the status bar at the bottom of the window.

You can also choose *Go to session* and then double click on a point to investigate that session more closely. This will open the *Session* tab as in Figure 4.

The dropdown menus can be used to choose everything from plot type, to which variables to show, to

[8] github.com/kartverket/where/tree/master/config

[9] ivscc.gsfc.nasa.gov/program/control_files.html

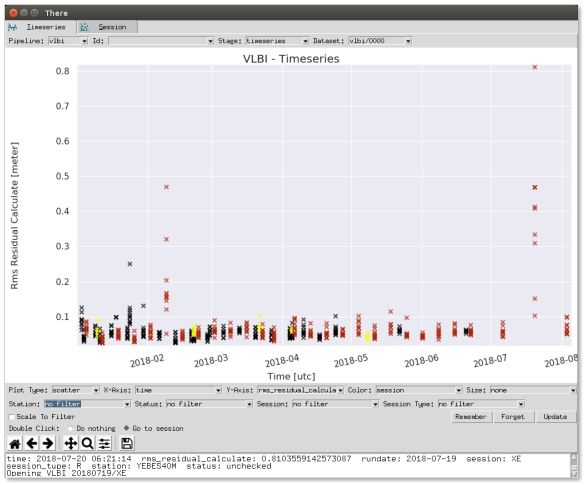

Fig. 3 An overview over analyzed sessions. The *Timeseries* tab shows aggregated information about many sessions. In this example you can see that a few sessions (including one in July 2018) have much higher residuals than is normal. The colors indicate session name.

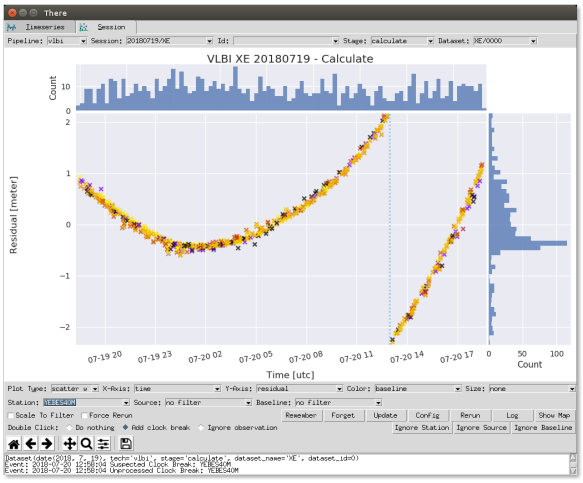

Fig. 4 Looking at the results from one analysis. The *Session* tab shows information about one particular session. The current plot shows prefit residuals for the XE session on July 19, 2018. The results have been filtered to only show the YEBES40M station. A clock break is clearly visible in the residuals at around 13:00 UTC and is marked with a blue dashed line.

filters that can be applied to the data. Each point represents one observation in the session. Clicking on a point shows information about that observation in the status bar.

You can edit a session from within There. As an example, consider Figure 4. There is a clock break at around 13:00 UTC that should be edited out. Where has preliminary support for detecting clock breaks by itself. To mark the clock break and rerun the analysis, you do the following:

- Choose *Add clock break.*
- Filter on the station in question, in this example YEBES40M.
- Double click in the plot where the clock break should be added. You might need to zoom in to do this precisely.
- Click the *Rerun* button.

After rerunning the analysis, There will update with the improved residuals.

Other editing operations, like ignoring single observations or all observations for stations, baselines, or sources are available directly in the There interface. However, more complicated editing can be done by opening the configuration file. This is most easily done by clicking the *Config* button.

One other option for getting insight about the results of an analysis is to plot the results on a map. Clicking the *Show Map* button in There will open an interactive map in your browser. The map shows all stations and baselines in the session. Colors are used to show the size of the residuals (green is smaller), while the size of circles and width of lines represent the number of observations for a given station or baseline.

The map illustrates the geometry of the solution. As it is interactive you can also zoom and pan and, for instance, look at local conditions at a site.

6 Reuse in Your Own Programs

If you are using Python for programming geodetic applications or analyzing geodetic data, Midgard might also be interesting to you directly.

Midgard is a library containing more general purpose geodetic functionality. Where uses Midgard extensively, and the plan is to move all parts of Where that can be reused to Midgard. Moving common components to Midgard is an ongoing process. Check the web page[10] for the current status.

You can use Midgard also if you are not using Where. In that case, first install Midgard using `pip`:

```
$ pip install midgard
```

[10] kartverket.github.io/midgard/

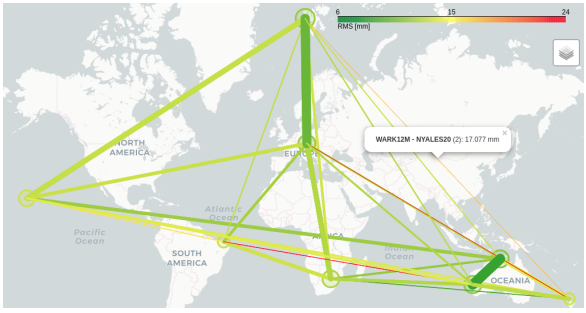

Fig. 5 Interactive map of one analysis. The colors indicate the size of the residuals on given stations and baselines. The size of a circle and the width of a line show how many observations were used for a station or baseline, respectively

You can then use Midgard in your own scripts. For instance, to read a Rinex file[11] you can do something such as:

```
>>> from midgard import parsers
>>> path = "ALGO00CAN_R_20121601000.rnx"
>>> parsers.parse_file("rinex3_obs", path)
```

More information about Midgard and examples of how to use it is available online.

7 Conclusions

At the time of writing, the latest available version of Where is v0.12.1. However, new development on Where is ongoing, and we plan to release version 1.0.0 within 2018. See the web page[12] for the latest updates.

Please get in touch[13] if you find Where useful or have any questions.

References

1. Hjelle, G. A., et al., Where: A scientific python package for geodetic analysis, in preparation.
2. Kirkvik, A.-S., Norwegian mapping authority analysis center biennial report 2015–2016, in Baver, K. D., Behrend, D., Armstrong, K. L. (eds.), *International VLBI Service for Geodesy and Astrometry 2015+2016 Biennial Report*, pages 245—248, NASA/TP-2017-219021, 2017.
3. Kirkvik, A.-S., et al., Where - a new software for geodetic analysis, in Haas, R., Elgered, G. (eds.), *Proceedings of the 23rd European VLBI Group for Geodesy and Astrometry Working Meeting*, 2017.
4. Kirkvik, A.-S., et al., NMA analysis center – progress report, in Armstrong, K. L., Behrend, D. Baver, K. D., IVS 2018 General Meeting Proceedings, 2018, this volume.

[11] en.wikipedia.org/wiki/RINEX

[12] kartverket.github.io/where/

[13] kartverket.github.io/where/pages/contact.html

Measurement of Earth's Nutation by VLBI: Direct Estimates from VLBI Delays and a Discussion on the Error

S. Lambert [1], I. Nurul-Huda [1], Y. Ziegler [1], J.-Y. Richard [1], N. Liu [1,2], C. Gattano [3], S. Rosat [4], C. Bizouard [1]

Abstract Accurate measurements of the Earth nutation by VLBI provide insights into the deformability of and the coupling mechanisms at the core-mantle and core-inner core boundaries. We propose here to adjust nutation amplitudes directly to VLBI delays, as opposed to the traditional method consisting of fitting nutation amplitudes to time-domain nutation series. However, the complexity of the VLBI analysis chain makes the formal error on the parameters somehow obscure and disconnected from a realistic error based on, e.g., empirical tests of robustness and errors on models. In this work, we address some striking differences between formal and empirical errors.

Keywords Earth rotation, VLBI

1 Introduction

Very Long Baseline Interferometry (VLBI) is the only technique that gives access to nutation and precession, that is, the variable orientation of the Earth's figure axis with respect to space. The amplitude of nutation depends on (i) the amplitude of the external gravitational potential arising from the Moon and the Sun, and (ii) the Earth deformational response to this potential. The latter can be expressed as a function of parameters describing the Earth's structure and rheology (e.g., flattening of the various layers, anelasticity coefficients, coupling constants). An accurate measurement of nutations allows therefore to perform geophysical studies related to the Earth interior (see, e.g., [15, 10, 8, 13, 14, 4] and references therein).

Mathews et al. ([10]), who published in 2002 the current conventional nutation model known as MHB 2000 or IAU 2000A, adjusted the so-called basic Earth parameters using an indirect method consisting of two steps: (1) fitting a finite number of amplitudes to nutation time series, and (2) fitting the geophysical parameters to the set of amplitudes. Implicitly, this method needs also the preliminary reduction of VLBI delays to obtain nutation time series, constituting a step (0). Later, [8] used a Bayesian approach to fitting directly the geophysical parameters in the time domain to the nutation time series, treating therefore the steps (1) and (2) of [10] together but still having no control on the nutation data themselves except a classical outlier elimination and a recalibration of the errors (see also [13, 14, 6]). Here, we propose to test a so-called 'direct' approach consisting of fitting directly the nutation amplitudes to VLBI delays, as a shortcut of steps (0) and (1). Such an approach avoids multiplying least-squares computations and ensures a rigorous error propagation from time delays to parameters. Beyond the feasibility of such an approach, we want to address the question of the precision of its results.

2 Analysis and Results

We processed all VLBI sessions between 1979 and 2018 with the Calc/Solve geodetic VLBI analysis soft-

1. SYRTE, Observatoire de Paris, Université PSL, CNRS, Sorbonne Université, LNE
2. School of Astronomy and Space Sciences, Nankin University
3. Laboratoire d'Astrophysique de Bordeaux, Université de Bordeaux
4. Institut de Physique du Globe de Strasbourg, Université de Strasbourg/EOST, CNRS

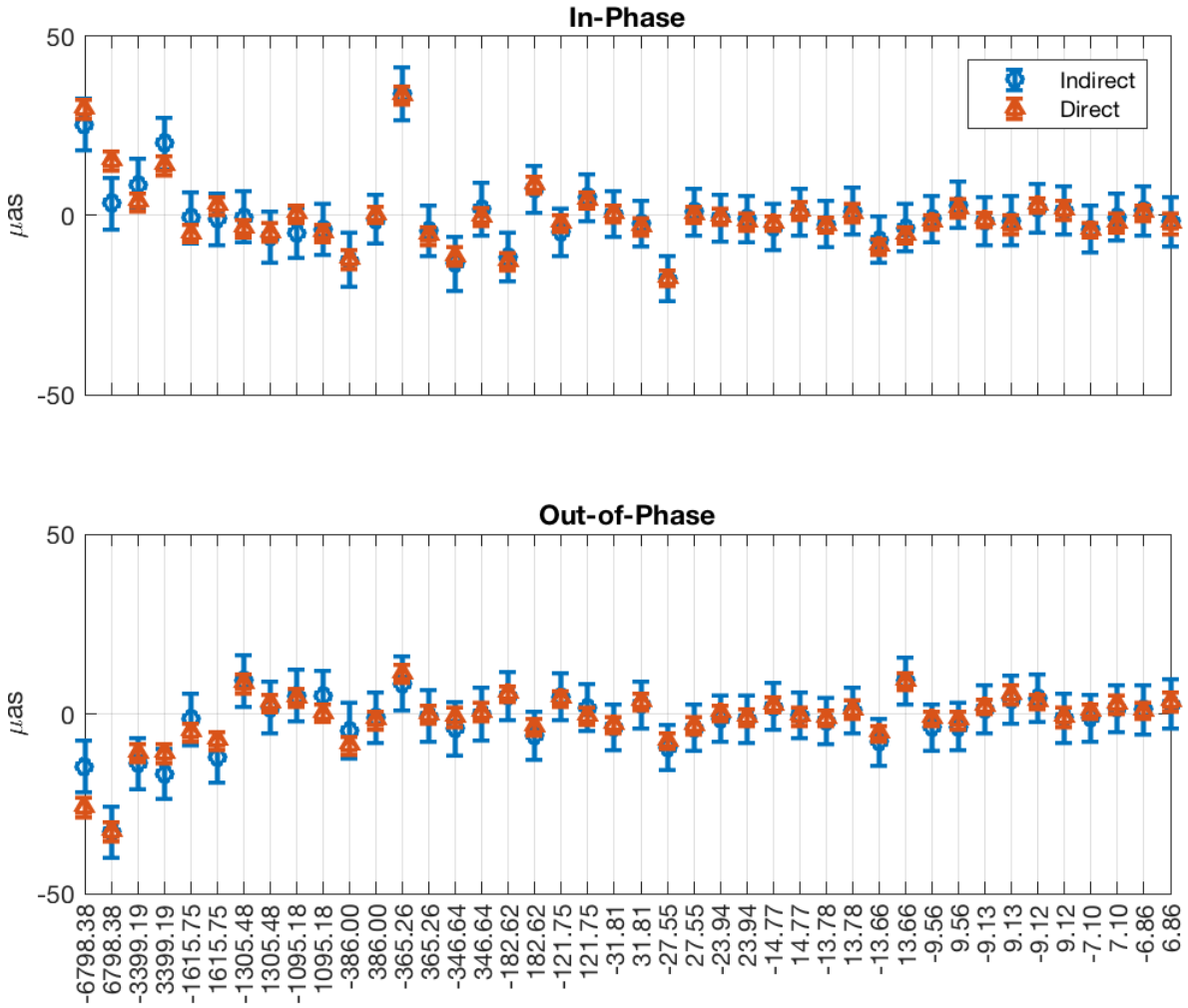

Fig. 1 The corrections to MHB 2000 obtained by the direct and the indirect approaches.

ware package using a standard configuration as described in the Paris Observatory analysis center Web site at http://ivsopar.obspm.fr/24h. In the so-called indirect approach, we estimated session-wise nutation offsets to MHB 2000. Then, we estimated the correction to the MHB 2000 amplitudes of the 42 periodic nutation terms whose periods are listed in [10] by applying simple weighted least-squares to the time series. Weights were taken as the inverse of the squared formal error. We also adjusted iteratively a noise floor and a scale factor to the formal errors (see [7, 14, 6]). In the so-called direct approach, we switched off the session-wise nutation estimates and, instead, added partial derivatives of the delay with respect to the amplitudes of the same 42 periodic nutation terms. The obtained amplitudes (corrections to MHB 2000) are shown in orange in Figure 1, superimposed onto the amplitudes obtained by the indirect approach. One can see that the amplitudes obtained by the two approaches are fairly consistent, except for the longest periods (18.6 and 9.3-yr) for which the amplitudes are likely more sensitive to the sparse data of the early VLBI years (typically before 1984). One can see also that the error bars of the direct solution are much smaller than the ones of the indirect solution by a factor of about 3 to 4. In both approaches, however, the formal errors are homogeneous across the periods: the uncertainty on the 18.6-yr is only very slightly larger than the one of

the weekly terms. Correlations between nutation amplitudes are largely the same in the two approaches. Both direct and indirect solutions returned a postfit rms of 26 ps and a chi-squared per degree of freedom of 0.94 indicating no further systematics. These results demonstrate that an empirical modeling of the nutations directly adjusted on VLBI delays is feasible.

Now, should we conclude that we have a much more precise result using the direct approach? There are at least two reasons for which one should take these small error bars with great care. The first reason is the existence of external contributions to the nutation that can be considered as unknown. The main one is the contribution of the atmosphere to the diurnal nutation that shows inconsistent values from one model to another (see, e.g., [1, 16, 17, 9]). As an example, we used the output of the two well-known global circulation models from NCEP/NCAR Reanalysis and ECMWF ERA Interim to estimate the atmospheric contribution to some nutations (Figure 2) and we showed that the two models do not deliver the same message. E.g., for the annual retrograde nutation, NCEP/NCAR and ECMWF differ by 100% at the level of 0.1 mas, which is several times the amplitude of the correction to this nutation as shown in Figure 1. As a consequence, one cannot consider seriously the VLBI estimate of the amplitude at better than 0.1 mas, although the formal error is ridiculously small: of a few 0.001 mas. This explains why [10] did not consider the annual nutation for constraining the computation of the basic Earth parameters.

The next reason for which one must consider the formal error with care is the robustness of the estimates. Indeed, the nutation amplitudes were obtained with a certain analysis configuration; but what would happen if one modifies this configuration, even slightly? [6] has derived some empirical errors by comparing the amplitudes of nutation adjusted on various nutation series computed by several IVS analysis centers and showed that the inconsistencies between series could be as large as several tens of µas and very inhomogeneous across the frequencies.

Another possible test of stability is similar to what was used to recalibrate the errors on radio source positions in the ICRF2 and ICRF3 works [5, 2]. It consists of splitting our session list into two groups of approximately the same number of observations. Different networks like R1/R4 and NEOS/CORE were also separated into different session lists. Although the number

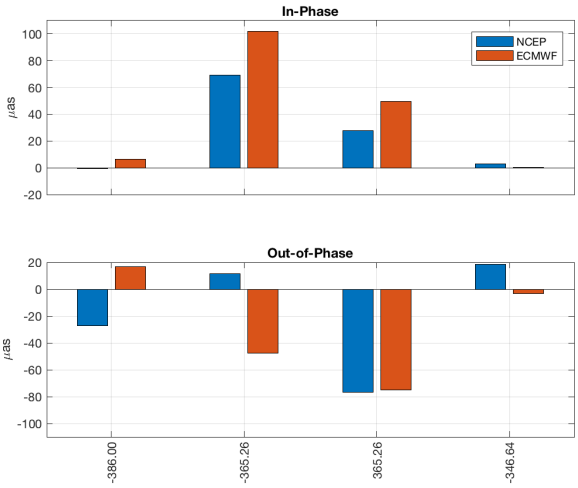

Fig. 2 The contribution of the diurnal variations in the atmospheric angular momentum to the nutation.

of observations is basically halved, the time domain information is not deeply changed with respect to the initial session list, especially for long periods. It seems therefore obvious that one should obtain results close to those obtained with the full session list. Then, we estimated the nutation amplitudes from the two session lists and computed the difference. This difference, that should be zero if the two session lists provided exactly the same result as the full session list, provides an external error characterizing the robustness of the amplitudes. We superimposed this external error onto the previous results of the direct and indirect approach in Figure 3. Interestingly, these external errors are much less homogeneous than the formal errors. For some unclear reasons, some nutation appear as very robust (external error within a few µas) while others are very unstable (external error up to 20 µas for the monthly and the semi-annual terms). The instability of some terms raises here the possibility of some unmodeled effect in the VLBI data reduction model like, e.g., a contribution of the subdaily polar motion ([12]).

3 Conclusion

This paper reports on the first step of a longer study currently undertaken at Paris Observatory in which we want to reestimate the basic Earth parameters of

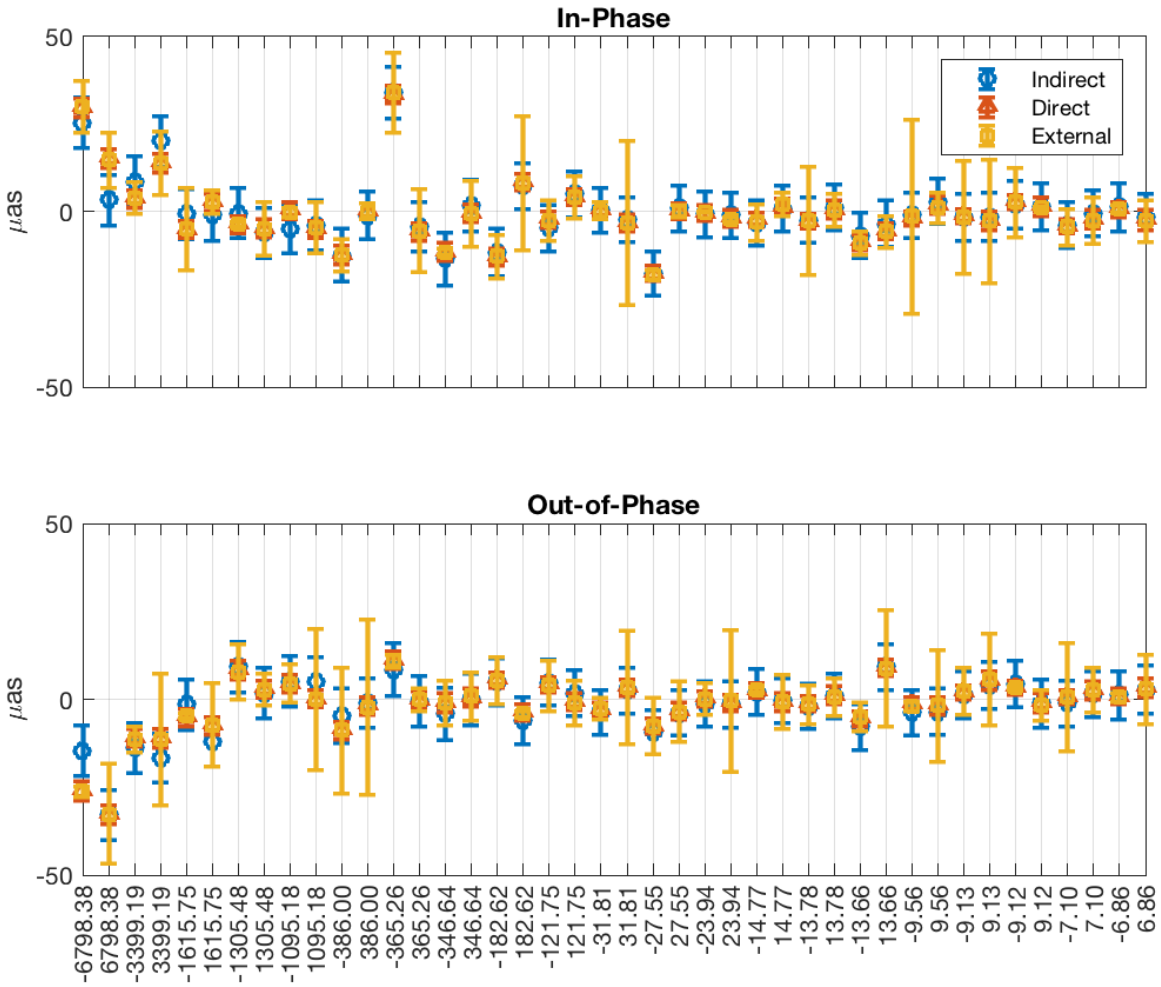

Fig. 3 Same as Figure 1 but with the external error superimposed.

[10] using several approaches (see [11, 18]). The fully-implemented direct approach consists of estimating the basic Earth parameters directly on VLBI delays ([11]), as opposed to a multi-step method used in various previous studies based on nutation time series ([10, 8, 13, 14]). Nevertheless, we aim at pointing out that there are numerous traps due to misinterpreted errors at various stages of the computation. Here, we showed that the direct approach is consistent with the indirect one for the estimation of nutation amplitude. But the formal errors on the amplitudes are somehow meaningless, or, at least, should be complemented by other errors arising from unknown contribution (e.g., atmosphere, oceans, correlation with the forced-free motion associated with the free core nutation, sensitivity to the analysis configuration and the observation list) obtained from, e.g., stability tests. These external errors could be used as weighting factors in further scientific exploitation of the nutation amplitudes.

References

1. C. Bizouard, A. Brzeziński, and S. Petrov. Diurnal atmospheric forcing and temporal variations of the nutation amplitudes. Journal of Geodesy, 72(10):561–577, 1998.
2. P. Charlot, C. S. Jacobs, D. Gordon, S. B. Lambert, J. Boehm, A. de Witt, A. Fey, R. Heinkelmann, E. Skurikhina, O. Titov, E. F. Arias, S. Bolotin, G. Bourda, C. Ma, Z. Malkin, A. Nothnagel, R. A. Gaume, D. Mayer, and D. S. MacMillan. The third realization of the International Celestial Reference Frame by very long baseline interferometry. Astronomy & Astrophysics, (in preparation), 2018.

3. V. Dehant, M. Feissel-Vernier, O. de Viron, C. Ma, M. Yseboodt, and C. Bizouard. Remaining error sources in the nutation at the submilliarc second level. Journal of Geophysical Research: Solid Earth, 108(B5), 2275, doi:10.1029/2002JB001763, 2003.
4. V. Dehant, R. Laguerre, J. Rekier, A. Rivoldini, S. A. Triana, A. Trinh, T. Van Hoolst, and P. Zhu. Understanding the effects of the core on the nutation of the Earth. Geodesy and Geodynamics, 8, pages 389–395, 2017.
5. A. L. Fey, D. Gordon, C. S. Jacobs, C. Ma, R. A. Gaume, E. F. Arias, G. Bianco, D. A. Boboltz, S. Böckmann, S. Bolotin, P. Charlot, A. Collioud, G. Engelhardt, J. Gipson, A.-M. Gontier, R. Heinkelmann, S. Kurdubov, S. Lambert, S. Lytvyn, D. S. MacMillan, Z. Malkin, A. Nothnagel, R. Ojha, E. Skurikhina, J. Sokolova, J. Souchay, O. J. Sovers, V. Tesmer, O. Titov, G. Wang, and V. Zharov. The Second Realization of the International Celestial Reference Frame by Very Long Baseline Interferometry. Astronomical Journal, 150:58, Aug. 2015.
6. C. Gattano, S. B. Lambert, and C. Bizouard. Observation of the Earth's nutation by the VLBI: how accurate is the geophysical signal. Journal of Geodesy, 91(7):849–856, 2016.
7. T. A. Herring, P. M. Mathews, and B. A. Buffett. Modeling of nutation-precession: Very long baseline interferometry results. Journal of Geophysical Research: Solid Earth, 107(B4):ETG 4–1–ETG 4–12, 2002.
8. L. Koot, A. Rivoldini, O. de Viron, and V. Dehant. Estimation of Earth interior parameters from a Bayesian inversion of very long baseline interferometry nutation time series. Journal of Geophysical Research: Solid Earth, 113, B08414, doi:10.1029/2007JB005409, 2008.
9. L. Koot and O. de Viron. Atmospheric contributions to nutations and implications for the estimation of deep Earth's properties from nutation observations. Geophysical Journal International, 185:1255–1265, June 2011.
10. P. M. Mathews, T. A. Herring, and B. A. Buffett. Modeling of nutation and precession: New nutation series for nonrigid Earth and insights into the Earth's interior. Journal of Geophysical Research: Solid Earth, 107(B4):ETG 3–1–ETG 3–26, 2002.
11. I. Nurul-Huda, Y. Ziegler, S. Lambert, and C. Bizouard, article in preparation
12. N. Panafidina, U. Hugentobler, M. Seitz, and H. Krásná. Influence of subdaily polar motion model on nutation offsets estimated by very long baseline interferometry. Journal of Geodesy, 91(12):1503–1512, 2017.
13. S. Rosat and S. B. Lambert. Free core nutation resonance parameters from VLBI and superconducting gravimeter data. Astronomy & Astrophysics, 503(1):287–291, 2009.
14. S. Rosat, S. Lambert, C. Gattano, and M. Calvo. Earth's core and inner-core resonances from analysis of VLBI nutation and superconducting gravimeter data. Geophysical Journal International, 208(1):211–220, 2017.
15. T. Sasao, S. Okubo, and M. Saito. A Simple Theory on Dynamical Effects of Stratified Fluid Core upon Nutational Motion of the Earth. In R. L. Duncombe, editor, Nutation and the Earth's Rotation, volume 78 of IAU Symposium, page 165, 1980.
16. O. de Viron, G. Schwarzbaum, F. Lott, and V. Dehant. Diurnal and subdiurnal effects of the atmosphere on the Earth rotation and geocenter motion. Journal of Geophysical Research: Solid Earth, 110(B11), 2005.
17. M. Yseboodt, O. de Viron, T. M. Chin, and V. Dehant. Atmospheric excitation of the Earth's nutation: Comparison of different atmospheric models. Journal of Geophysical Research: Solid Earth, 107(B2), 2002.
18. Y. Ziegler, S. Lambert, S. Rosat, and C. Bizouard, Toward reliable estimates of the free core and inner core parameters from a Bayesian inversion of VLBI and gravimetric data, this volume.

UT1 Formal Errors from the BA 50 Balanced Scheduling Strategy INT01 R&Ds

Karen Baver, John Gipson

Abstract The original operational IVS INT01 scheduling strategy (the "standard" strategy or STN) used as few as ∼30 strong but badly distributed sources, resulting in bad source and observation sky coverage at some times of the year. In response, in 2009, we proposed the Maximal Source Strategy (MSS) to maximize sky coverage by using all geodetic sources that are mutually visible at the primary INT01 stations. This yielded an operational INT01 MSS source set that had ∼90 sources but was, on average, weaker than the STN. Increasing sky coverage tends to decrease the UT1 formal error, while decreasing average source strength tends to increase the UT1 formal error by creating longer observations and scheduling fewer observations. To resolve this conflict, we investigated using *Sked*'s Bestsource command to select balanced source sets of varying sizes between the STN and MSS sizes, trying to select enough sources for good sky coverage but not enough to introduce too much weakness. We wanted to balance sky coverage and source strength to try to minimize the UT1 formal errors, while also considering balancing's effect on two other metrics. Our investigation led to the 50 source, balanced "Balanced 50" (BA 50) strategy. The IVS Observing Program Committee allocated six 2016 and 2017 R&D sessions for us to compare the BA 50 strategy to the MSS strategy, which had become the sole operational INT01 scheduling strategy in mid-2016. This paper reports the R&Ds' first results, focusing on their UT1 formal errors.

Keywords Intensives, UT1, sources, scheduling

NVI, Inc.

1 Introduction

The IVS observes one-hour INT01 sessions that provide rapid UT1-TAI estimates. The initial INT01 scheduling strategy, which we unofficially call the STN strategy, was to observe a strong but small, sparse source set whose size varied as sources were replaced due to flux changes. The STN was unevenly distributed and caused seasonal variations in observation coverage. As reported in [1] and [5], the size of an INT01 session's UT1 formal error is connected to the width of its azimuth observation coverage. The STN had narrow coverage and large UT1 formal errors at some times of the year, especially early October.

In 2009, we suggested improving source coverage by using all geodetic sources that are mutually visible at the two main INT01 stations, Kokee Park, Hawaii, USA and Wettzell, Germany, at some time during the year. We call this the Maximal Source Strategy (MSS). This improved the early October observation coverage and UT1 formal errors but raised the UT1 formal errors at some other times of the year, e.g., early to mid-November, presumably because the MSS had introduced weak sources, which take longer to observe and lead to fewer observations and, in turn, higher UT1 formal errors.

This indicated a need to balance the good strength but bad sky coverage of the, at minimum, ∼30 source STN source sets and the good sky coverage but weakness of the ∼90 source MSS source set that was ultimately used for operational INT01 observing. In 2014 we began to select source sets with varying numbers of sources and to use the balancing algorithm of the Bestsource command in *Sked*, the program that schedules INT01 sessions, to try to balance source strength and sky coverage and minimize the UT1 formal error,

while considering two other metrics. This led us to the Balanced 50 (BA 50) source strategy. The IVS Observing Program Committee (OPC) allocated six R&D sessions for us to test the BA 50 against the MSS. This paper reports the UT1 formal errors from these sessions.

Section 2 discusses the original STN strategy and its inadequate sky coverage. Section 3 discusses our first solution (the MSS strategy) and its introduction of weak sources. Section 4 discusses our new solution (the BA 50 strategy) and the six R&D sessions that tested it. Section 5 reports conclusions and a subsequent update.

2 Original STN Strategy

In 2004, Baver et al. [1] noted two INT01 sessions with equal numbers of observations (15) and almost equal session fits (31 ps vs. 32 ps) but very different UT1 formal errors. Figure 1 plots azimuth observation sky coverage at the sessions' stations, Kokee (left side of each plot pair) and Wettzell (right side). The session in Figure 1 (left pair) has good (wide) sky coverage and a good (low) UT1 formal error (13 μs), but the session in Figure 1 (right pair) has bad, narrow sky coverage and a very high UT1 formal error (49 μs). This was part of a pattern that Baver et al. found in two years of INT01 plots. So [1] noted that wide observation sky coverage is generally empirically connected to low UT1 formal errors (i.e., that narrow sky coverage is connected to high UT1 formal errors). Starting in 2012, Uunila et al., e.g. in [5], independently confirmed this connection.

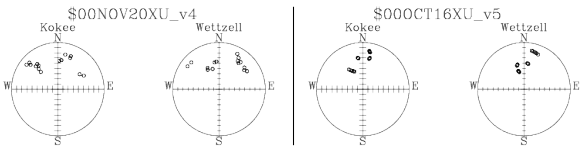

Fig. 1 Two INT01 sessions with similar numbers of observations and session fits but very different azimuth-elevation observation sky coverage and UT1 formal errors. Each plot pair shows Kokee (left) and Wettzell (right). Left pair: wide sky coverage and a low UT1 formal error (13 μs). Right pair: narrow sky coverage and a high UT1 formal error (49 μs). From [1].

Meanwhile, we had noticed a seasonal aspect to the varying observation coverage and in 2006 identified the cause: the strategy being used to observe sources in the INT01 sessions, the STN. The STN strategy consisted of observing strong but small sets of sources that contained, at minimum, ∼30 sources. The STN source sets were sparse and uneven, with large gaps, as shown in a right ascension and declination plot of a 27-source version from INT01 session i14315 (Figure 2 (left)). Because the Kokee–Wettzell baseline is long and INT01 sessions observe for only an hour, they observe a small, quasi-oval sky slice that moves during the year, sampling varying numbers and sets of sources. Figure 2 (center) and Figure 2 (right) show the areas of the sky observed at two times of the year, with dark circles showing mutually visible sources. Figure 2 (right), which represents mid-November, has wide source coverage, which enables wide observation coverage and promotes low UT1 formal errors. But Figure 2 (center), which represents early October, has narrow source coverage, which restricts the observations to a narrow part of the sky and leads to high UT1 formal errors. These cases represent the two extremes of the year, and the early October case illustrates the need to find additional sources for some times of the year.

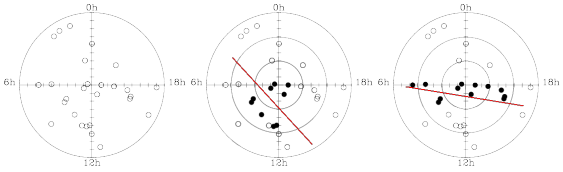

Fig. 2 Right ascension/declination plots of the i14315 STN source set. Left: source positions. Center: Mutual visibility (dark circles) on October 1 (18:30 UT) (narrow source coverage). Right: Mutual visibility on November 15 (18:30 UT) (wide source coverage). Plot edges are at 0°N, concentric circles mark 30°N and 60°N, and centers are at 90°N. The lines show the approximate width and orientation of the mutual visibility "ovals".

3 MSS Strategy

In 2009, we suggested the MSS strategy: improving source coverage in early October, and all year, by using all geodetic sources that are mutually visible at Wettzell and Kokee at some time during the year. We tested the MSS in nine 2009/2010 IVS R&D sessions. Then the IVS USNO NEOS Operation Center (USNO) began using the MSS strategy in operational INT01s in

mid-2010, alternating it with the STN every other day. In mid-2016 USNO began using only the MSS.

The pairs of right ascension and declination plots in Figure 3 show the i14315 STN (left side of each pair) and the i14316 MSS (right side) source sets. The MSS set is more extensive, with much smaller gaps. The left and right pairs of plots show mutually visible sources (dark circles) at 18:30 UT on October 1 and November 15, respectively. The October MSS mutual visibility (left pair, right side) is much wider than that of the October STN (left pair, left side), with sources added on each side of the STN mutual visibility area. But the STN November (right pair, left side) and MSS November (right pair, right side) mutual visibility areas are similar in width, indicating that the mid-November sky coverage did not need to be widened. Instead, using the MSS at that time mainly added redundancy by filling in gaps without widening coverage.

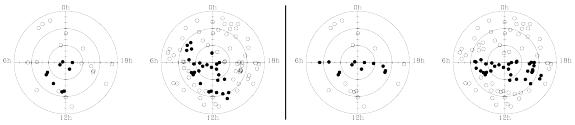

Fig. 3 i14315 STN and i14316 MSS mutual visibility (dark circles). Left pair: STN (left) and MSS (right) (October 1, 18:30 UT). Right pair: STN (left) and MSS (right) (November 15, 18:30 UT).

Figure 4 shows that the MSS solved the early October UT1 formal error problem. Figure 4 (left) plots the 2011 and 2012 STN UT1 formal errors, and two spikes show the very high early October UT1 formal errors. These spikes are absent in the MSS UT1 formal errors in Figure 4 (right). Also when the observed UT1 formal errors for the first half of October in both years are averaged, the MSS average (15.1 μs) is less than half that of the STN average (32.0 μs) [3].

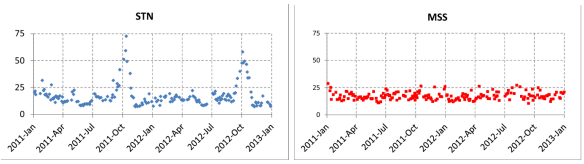

Fig. 4 UT1 formal errors from alternating 2011–2012 STN (left) and MSS (right) sessions. From [3].

But the UT1 formal errors at other times of the year increase with the MSS. In the first half of November, the MSS UT1 formal error average (12.0 μs) is 20% higher than the STN average (10.0 μs) [3]. This is a small trade-off for the large improvement in early October, but ideally the INT01 source strategy should provide as low UT1 formal errors as possible all year.

Our explanation in 2013 for the MSS' effect on the INT01 UT1 formal errors was as follows. Adding sources has two competing effects. First, at times of the year with narrow source coverage, adding sources at first widens the sky coverage and decreases the UT1 formal errors. But, when enough sources have been added to achieve wide enough coverage, adding more sources becomes redundant, and the UT1 formal errors are no longer improved. Meanwhile the additional sources are weaker and take longer to observe, leading to fewer observations and, in turn, higher UT1 formal errors. So at times of the year such as early October, adding sources should first lower the UT1 formal errors, then raise them. Meanwhile at times such as mid-November that already have wide enough source coverage with strong sources, any sources added will be redundant and weaker, so that adding sources will increase the UT1 formal errors from the start. In general, we expected that adding sources might lower, then raise the average UT1 formal error, and that there should be a balancing point where using the right number of sources would yield a minimum average UT1 formal error.

4 BA 50 Strategy

In 2014 we began to generate and evaluate source sets for a balance of sky coverage and strength through a) varying the number of sources and b) using the *Sked* Bestsource command, whose algorithm selects source sets balanced by sky coverage and strength. Ultimately we evaluated source sets with 30 to 90 sources, in increments of ten, to match the sizes of the minimal STN and the MSS source sets. The range was inclusive, because the Bestsource algorithm provided balance not found in the STN or MSS sets. In 2016, after considering the source sets' effects on the UT1 formal error and two other metrics, we selected 50 as the best number of sources. We call the new strategy the BA 50 (originally for "Best All 50" [2] but now for "BAlanced 50").

Figure 5 plots the INT01 i14315 STN source set (left), the BA 50 source set from R&D RD1608 (cen-

ter), and the i14316 MSS source set (right). The BA 50 set has extensive and fairly even sky coverage. Gaps exist but are much smaller than the STN gaps, and although the BA 50 is not as well filled at places as the MSS, it avoids the redundancy of the MSS, shown by overlapping sources. So the BA 50 offers the best compromise in sky coverage. Also, in the 2011 and 2012 operational INT01s, the average scheduled STN SNR was 130% that of the MSS, while in the 2016 and 2017 R&D schedules described in this paper, the average scheduled BA 50 SNR was 115% that of the MSS. This suggests that the strength of the tested BA 50 source sets falls between the strength of the tested STN and MSS source sets. So there is evidence that the BA 50 strategy balances sky coverage and source strength. Figure 6 verifies that the BA 50 provides as wide source coverage as the MSS in early October and mid-November and only removes redundant sources.

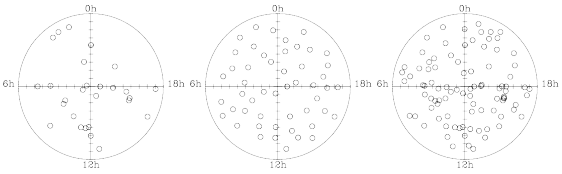

Fig. 5 Right ascension and declination source positions. Left: i14315 STN, center: RD1608 BA 50, and right: i14316 MSS.

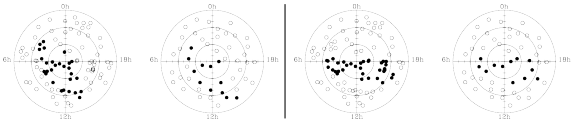

Fig. 6 i14316 MSS and RD1608 BA 50 mutual visibility. Left pair: MSS (left) and BA 50 (right) on October 1 (18:30 UT). Right pair: MSS (left) and BA 50 (right) on November 15 (18:30 UT).

We tested the BA 50 strategy in six 2016/2017 IVS R&D sessions, in which Wettzell and Kokee observed 24 one-hour pseudo-Intensives per R&D. The other stations, which varied, observed one 24-hour session that provided a single UT1 estimate and rate to use for an independent check of the pseudo-Intensives' UT1 estimates. We selected a different BA 50 source set for each R&D, using the most up-to-date source fluxes, and used it for every pseudo-Intensive in that R&D.

Table 1 shows the organization of the R&D pseudo-Intensives. The BA 50 alternates with the MSS in each R&D session, giving 72 MSS and 72 BA 50 pseudo-Intensives over which results can be averaged. The STN was no longer observed by the time of the R&D sessions and was excluded. We also needed to test the BA 50 and the MSS on sky areas observed by the INT01 sessions at different times of the year, especially early October and early and mid-November. The GST at which an INT01 session starts determines the area of the sky observed. So in each R&D, we started each pseudo-Intensive at one of 24 evenly spaced GSTs (00:00, 01:00, through 23:00). Within each GST's six pseudo-Intensives, we alternated the MSS and BA 50 strategies, giving three MSS and three BA 50 pseudo-Intensives per GST. GSTs 19, 21, and 22 approximated early October and early and mid-November observing, respectively.

Table 1 Organization of the one-hour R&D pseudo-Intensives.

GST	RD1608	RD1610	RD1701	RD1702	RD1706	RD1707
00:00	MSS	BA 50	MSS	BA 50	MSS	BA 50
01:00	BA 50	MSS	BA 50	MSS	BA 50	MSS
02:00	MSS	BA 50	MSS	BA 50	MSS	BA 50
			.....			
23:00	BA 50	MSS	BA 50	MSS	BA 50	MSS

Two types of UT1 formal errors are of interest. The predicted UT1 formal errors from the schedules show the most direct influence of using the two strategies, before unrelated effects, such as observation loss due to equipment failure, occur. The observed UT1 formal errors from the data are subject to the unrelated effects, but these formal errors must still be checked for any systematic BA 50 problems.

Table 2 (top) shows the predicted UT1 formal errors averaged over all MSS and all BA 50 schedules. The BA 50 improves the predicted errors' average by 1.4 μs (18%) and standard deviation by 0.5 μs (33%). Table 2 (bottom) shows the observed, averaged UT1 formal errors. The BA 50 improves the observed errors' average by 2.6 μs (19%) and standard deviation by 1.1 μs (17%). So the BA 50 strategy shows promise for improving the average UT1 formal errors.

With only three MSS and three BA 50 pseudo-Intensives per GST, there is not much data for drawing conclusions about the BA 50's effectiveness at individual GSTs. More data is needed. But Figure 7 (left), which plots the predicted UT1 formal errors for each GST, shows preliminary promise, because the BA 50

Table 2 Predicted and observed UT1 formal errors, in μs, averaged over all MSS and all BA 50 pseudo-Intensives.

A) Predicted	MSS	BA 50	Improvement
Average	7.9	6.5	1.4 (18%)
Standard deviation	1.5	1.0	0.5 (33%)
B) Observed	**MSS**	**BA 50**	**Improvement**
Average	13.4	10.8	2.6 (19%)
Standard deviation	6.3	5.2	1.1 (17%)

UT1 formal error average for a GST is lower than the corresponding MSS average for 21 of the 24 GSTs, and for the other three GSTs, it is either equal or only slightly higher. Without more data, it is hard to draw even a preliminary conclusion about the observed UT1 formal errors when broken down by GST, due to the low number of pseudo-Intensives per GST combined with the vulnerability of the sessions to problems not related to the strategies. So, we only include Figure 7 (right), the plot of the observed UT1 formal errors by GST, for completeness and note that it indicates that the BA 50 UT1 formal error average is lower than the MSS average at 18 of the 24 GSTs.

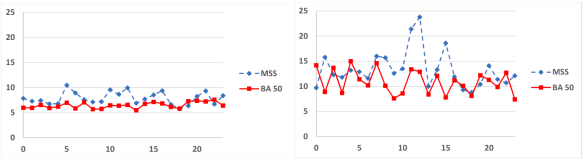

Fig. 7 Predicted (left) and observed (right) MSS (dashed line) and BA 50 (solid line) UT1 formal errors in μs averaged over individual GSTs.

Based on the averaged MSS and BA 50 UT1 formal errors, USNO has begun to schedule alternating MSS and BA 50 operational INT01 sessions on a trial basis.

5 Conclusions, Updates, and Acknowledgments

In 2014 we began to use source set size and a *Sked* algorithm to balance sky coverage and source strength to minimize UT1 formal errors and two other metrics. This led to the 2016 BA 50 strategy, which we tested against the MSS in six 2016 and 2017 R&Ds.

The R&Ds' sets of 72 MSS and 72 BA 50 R&D pseudo-intensives are large enough to conclude that the overall BA 50 UT1 formal errors are promising. The BA 50 improves the predicted and observed UT1 formal error averages and standard deviations by at least 17%. But there is not yet enough test data to draw meaningful conclusions about the BA 50's effect on the UT1 formal errors for individual areas of the sky. Meanwhile, based on the averaged MSS and BA 50 R&D UT1 formal errors, USNO has begun to schedule BA 50 operational INT01 sessions on a trial basis, alternating them with MSS sessions.

In late 2018, while preparing a related paper, we found a forgotten, unresolved 2016 result that contradicted our 2014 initial simulations, which had shown that the UT1 formal error increases with increasing source set size. New work to resolve the discrepancy showed that the 2014 results were atypical and that the UT1 formal error, at most, barely increases with increasing source set size. But balancing itself improves the UT1 formal error relative to both the STN and MSS strategies, and the BA 50 strategy remains useful.

We thank Chris Coughlin and the Kokee staff, Dr. Torben Schüler and the Wettzell staff, and Cynthia Thomas and the IVS OPC for their support of the six R&D sessions and their special requirements. We also thank the IVS for the use of its data [4].

References

1. Baver K, MacMillan D, Petrov L, Gordon D, Analysis of the VLBI Intensive Sessions. In: N. R. Vandenberg and K. D. Baver (eds.) *IVS 2004 General Meeting Proceedings*, NASA/CP-2004-212255, 394–398.
2. Baver K, Gipson J, Balancing Sky Coverage and Source Strength in the Improvement of the IVS-INT01 Sessions. In: D. Behrend, K. D. Baver, and K. L. Armstrong (eds.) *IVS 2014 General Meeting Proceedings*, Science Press (Beijing), ISBN 978-7-03-042974-2, 267–271.
3. Gipson J, Baver K, "Improvement of the IVS-INT01 Sessions by Source Selection: Development and Evaluation of the Maximal Source Strategy", J Geod (2016) 90(3):287-303, DOI 10.1007/s00190-015-0873-6.
4. Schuh H, Behrend D, "VLBI: A fascinating technique for geodesy and astrometry", Journal of Geodynamics, Vol. 61, pp. 68–80, October 2012. DOI 10.1016/j.jog.2012.07.007.
5. Uunila M, Nothnagel A, Leek J (2012) Influence of Source Constellations on UT1 Derived from IVS INT1 Sessions. In: D. Behrend and K. D. Baver (eds.), *IVS 2012 General Meeting Proceedings*, NASA/CP-2012-217504, 395–399.

European Intensive Sessions for the Estimation of UT1

Johannes Böhm [1], Ruben Bolaño [2], Susana Garcia-Espada [2], Javier González [2], Jakob Gruber [1], Gerhard Kronschnabl [3], Alexander Neidhardt [4], Apurva Phogat [3], Christian Plötz [3], Matthias Schartner [1], Erik Schönemann [5], Torben Schüler [3], Pablo de Vicente [2]

Abstract Global Navigation Satellite Systems (GNSS), such as the United States GPS, the Russian GLONASS, or the European Galileo, require accurate information about the difference between Universal Time 1 and Coordinated Universal Time (UT1–UTC) in real time for positioning and navigation purposes. This parameter can only be determined with Very Long Baseline Interferometry (VLBI), and the International VLBI Service for Geodesy and Astrometry (IVS) is providing UT1–UTC on a daily basis as derived from so-called one-hour Intensive sessions on long east-west baselines. Additionally, the U.S.A. and Russia run their own Intensive sessions and are thus not fully dependent on the UT1–UTC values from the IVS. We present the idea of European Intensive sessions on a baseline between Santa Maria (Azores, Spain) and Wettzell (Germany) and conclude from Monte Carlo simulations that we can achieve accuracies better than 40 microseconds. Real experiments to confirm those simulations are currently ongoing.

Keywords Intensive sessions, UT1–UTC, Galileo

1 Introduction

With the direct access to the International Celestial Reference Frame (ICRF), Very Long Baseline Interferometry (VLBI) is the only technique for the determination of Universal Time 1 (UT1), i.e., the Earth rotation angle with respect to Atomic Time (TAI) or the Coordinated Universal Time (UTC). The availability of this parameter with highest accuracy is essential for positioning and navigation applications on Earth and in space, because an error of one millisecond in UT1–UTC corresponds to an error of 0.5 meters at the equator and kilometers and more at distances to other planets like Mars. Satellite techniques like the Global Navigation Satellite Systems (GNSS) or Satellite Laser Ranging (SLR) are not capable of determining this parameter on their own because of the correlation of the ascending node of the satellite orbits and the Earth rotation angle which cannot be properly resolved.

The International VLBI Service for Geodesy and Astrometry (IVS) is providing UT1–UTC values, either determined from 24-hour sessions two to three times per week with an accuracy of 5 µs and a product delivery time of more than a week, or from special one-hour long Intensive sessions on a daily basis with an accuracy of 15–20 µs and a product delivery time of a day (Schlüter and Behrend, 2007 [7]). For the latter, the IVS is using long east-west baselines: currently Wettzell (Germany) to Kokee Park (Hawaii, U.S.A.) from Monday to Friday and Wettzell to Ishioka (Japan) from Saturday to Monday including Ny-Ålesund (Norway) and the northern dish of the new twin radio telescope in Wettzell on Monday.

Additionally, the U.S.A. and Russia are running their own national VLBI Intensive sessions for their GNSS, namely GPS and GLONASS, and are thus not fully dependent on UT1–UTC values from the IVS. In particular, the U.S.A. is using the Very Long Baseline Array (VLBA) with baselines from Mauna Kea (Hawaii) to stations Pie Town or Los Alamos, both in New Mexico. Now, they are considering additional

1. Technische Universität Wien
2. Observatorio de Yebes, IGN
3. Bundesamt für Kartographie und Geodäsie
4. Technische Universität München
5. ESA/ESOC

baselines including St. Croix on the Virgin Islands (Geiger et al., this issue). Russia runs the Quasar network for the determination of UT1–UTC with the stations Badary in the Karachaevo-Cherkessian Republic, Svetloe in the Leningrad Province, and Zelenchukskaya in the Buryatiya Republic. Figure 1 depicts those baselines and Table 1 lists the baseline lengths.

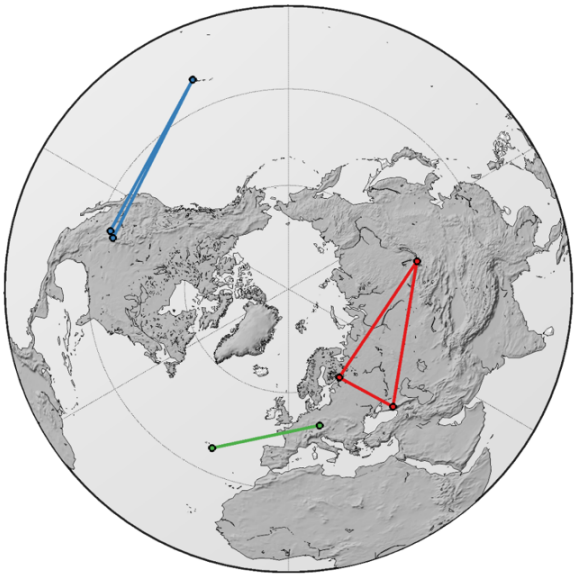

Fig. 1 VLBA baselines used by the U.S.A. (in blue) and the Russian Quasar baselines (in red). Additionally, the European baseline between Santa Maria (Azores) and Wettzell (Germany) is displayed in green.

Table 1 Lengths of the baselines illustrated in Figure 1.

From	To	Length
Mauna Kea	Pie Town	4,796 km
Mauna Kea	Los Alamos	4,970 km
Pie Town	Los Alamos	237 km
Badary	Zelenchukskaya	4,405 km
Badary	Svetloe	4,282 km
Zelenchukskaya	Svetloe	2,015 km
Santa Maria	Wettzell	3,286 km

In Europe, however, there is no similar dedicated activity for Galileo. Thus, we are investigating the possible use of a European baseline for the determination of UT1–UTC from daily one-hour Intensive sessions. In particular, we are considering observations on the baseline Santa Maria on the Azores (Sa) to the northern dish of the new twin radio telescope in Wettzell (Wn) with a baseline length of 3,286 km (Figure 1). This baseline is shorter than the longest baselines in the other networks listed in Table 1. While from a geometrical point of view with the need of a long east-west baseline for the determination of UT1–UTC, it is not as suitable as the other baselines; we can expect a better common visibility of the sky. Moreover, both telescopes are very fast antennas in the VGOS-style (Petrachenko et al., 2009 [6]) with slew rates of 360 and 720 degrees per minute in elevation and azimuth, respectively, allowing for short slewing times and a high number of observations. The diameters of the dishes with 13.2 m are smaller for Sa and Wn, thus yielding higher System Equivalent Flux Densities (SEFD) with reduced sensitivity. However, this should not be a disadvantage if strong sources are selected for observation when scheduling. Technical details of the radio telescopes are summarized in Table 2. The radio telescopes Sa and Wn are currently equipped with S/X/Ka-receivers but will be equipped with broadband receivers in the coming years. In this study, for simulations and real observations, observations at X- and S-band are used.

Table 2 Technical specifications of the radio telescopes in the VLBA and the Quasar network as well as for the telescopes Santa Maria (Sa) and the northern dish of the Wettzell twin telescope (Wn).

	VLBA	Quasar	Sa	Wn
Diameter in m	25	32	13.2	13.2
Slew rate az. in deg/min	90	60	720	720
Slew rate el. in deg/min	30	30	360	360
SEFD X-band in Jy	500	400	1600	1400
SEFD S-band in Jy	400	600	1700	1050

In the following sections, we describe simulations for European Intensive sessions in comparison to IVS Intensive sessions and present the current state of real observations on the baseline Santa Maria to Wettzell. Finally, we discuss future plans and opportunities with these new observations.

2 Monte Carlo Simulations

Many different schedules for the European Intensive sessions are generated with the scheduling tool (Schartner et al., this issue) of the Vienna VLBI and Satellite

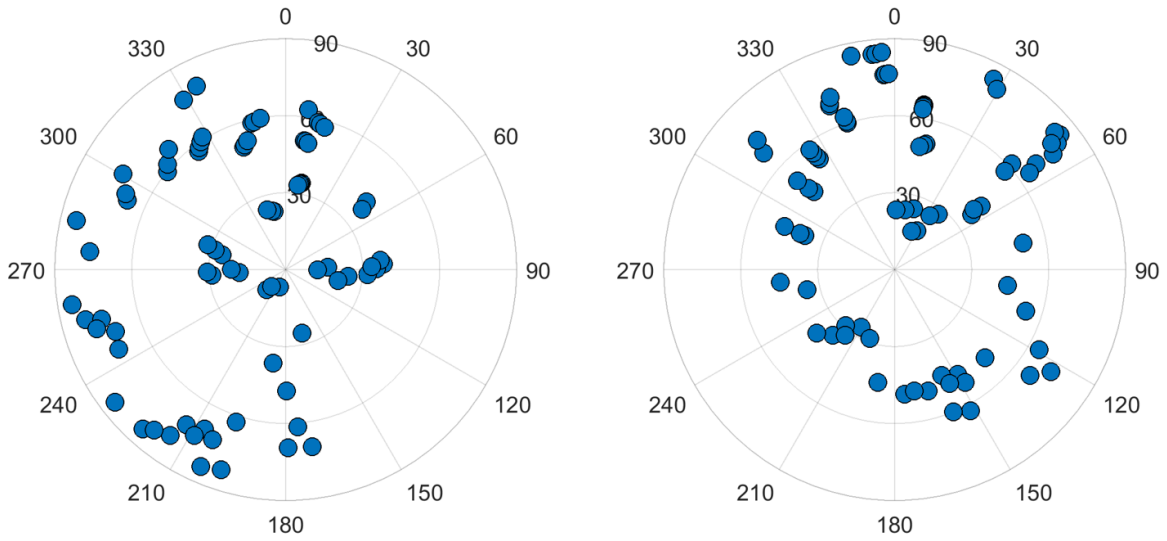

Fig. 2 Skyplot for the stations Wn (left) and Sa (right) of a one-hour European Intensive session. Due to the relatively short baseline we achieve a good sky distribution.

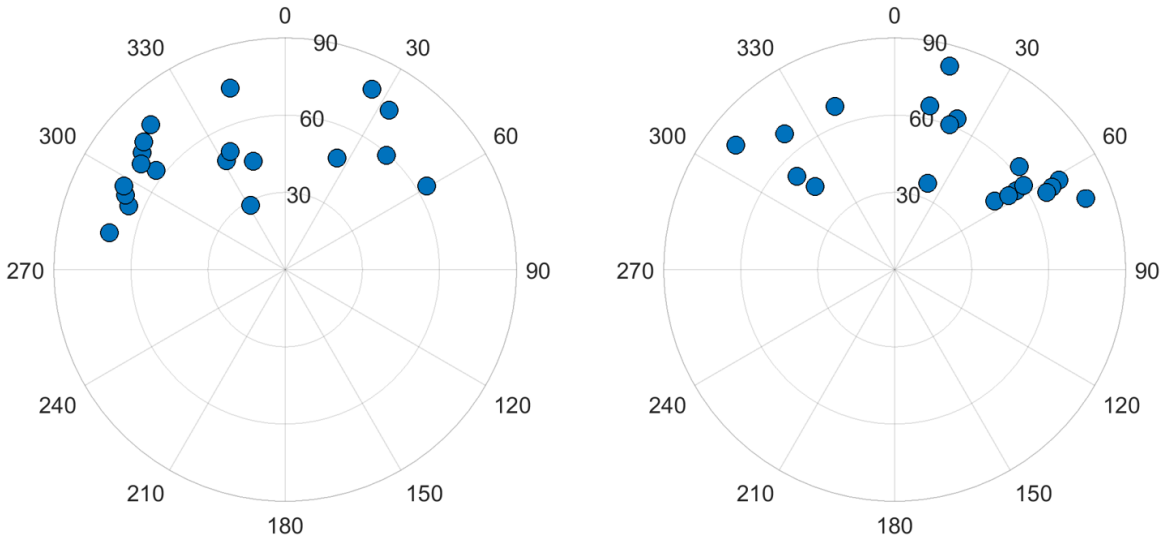

Fig. 3 Skyplot for the stations Wettzell and Kokee of an IVS Intensive session. Due to the long baseline of more than 10,000 kilometers, the part of the sky seen by both telescopes is rather small. On the other hand, from a geometrical point of view, a longer baseline is more sensitive to UT1.

Software (VieVS; Böhm et al., 2018 [1]). We assume a recording rate of 1 Gbit/s for observations in X- and S-Band and finally come up with 396 different schedules, differing in terms of weighting the parameters of sky coverage, scan duration, and minimum allowed source repeatability, and in terms of start time, which has a significant effect on the selection of sources. Without going into details here we want to stress that we are able to schedule 75 to 80 scans within one hour, which is considerably more than the current number of scans in IVS Intensive sessions (25 to 30 scans). The skyplots for one European session on the baseline Sa to Wn are shown in Figure 2, while the skyplots for a standard IVS Intensive session on the baseline Wettzell to Kokee are displayed in Figure 3 for comparison.

Based on the 396 schedules, 300 realizations are generated per schedule using a structure constant C_n of $1.8 \cdot 10^{-7} m^{-1/3}$ and a scale height of 2 km for the description of tropospheric turbulence, an Allan Standard Deviation of 10^{-14} at 50 minutes for the clocks and a white noise of 30 picoseconds per observation (Pany et al., 2011 [5]). The analysis of the simulated observations is also carried out with VieVS fixing station and source coordinates along with a priori values of polar motion and nutation. We estimate one linear clock between the two stations, constant zenith wet delay offsets for the stations, and a constant value of UT1–UTC for the session. Due to the higher number of scans and the good sky coverage for the European baseline, we also test the estimation of zenith wet delays every 30 minutes as piecewise linear offsets and the additional estimation of constant tropospheric gradients per station and session. Table 3 summarizes the simulation results in terms of repeatability and formal error. There is a notable decrease in the difference between repeatability and formal error when estimating a larger number of parameters and we reach a repeatability of less than 30 µs when estimating gradients.

Table 3 Results of UT1–UTC from simulated European Intensive sessions. The values are based on 396 (schedules) times 300 (realizations) sessions and different parametrization in terms of zenith wet delays (ZWD) and gradients.

	Repeatability	Mean formal error
60 min ZWD	34.6 µs	15.9 µs
30 min ZWD	33.0 µs	15.4 µs
60 min ZWD and gradients	26.9 µs	20.5 µs
30 min ZWD and gradients	26.3 µs	20.1 µs

In order to better assess and understand the numbers in Table 3, we also carry out identical Monte Carlo simulations for observed schedules of IVS Intensive sessions between Wettzell and Kokee. Based on the same simulation parameters and 300 realizations, we find a repeatability of 16.6 µs and a mean formal error of 12.7 µs. From comparisons against UT1–UTC parameters from 24-hour sessions during CONT08, Nilsson et al. (2011 [4]) found RMS values of about 23 µs, i.e., 40% above the repeatability of the simulated sessions. If we apply the same ratio on the repeatabilities of the European Intensive sessions, we arrive at UT1–UTC values better than 40 µs.

3 Real Experiments

After a first session on March 1, 2018 (V012), a series of six one-hour test experiments were observed between Sa and Wn in April and May 2018. Santa Maria (Sa) is a new station with first light in early 2018, and unfortunately our observations in April and May are affected by low SNR at X-band. On the other hand, we could use X-band data (without S-band data) of session V012 to work on the procedures necessary to derive UT1–UTC. We correlated the session with DiFX (Deller et al., 2007 [2]) on the Vienna Scientific Cluster (VSC-3) (Gruber et al., this issue) and used HOPS/Fourfit for fringe-fitting the data before writing vgosDB files with VieVS for 73 scans. However, at this stage the estimation of UT1–UTC is not yet possible, because we do not have accurate station coordinates of Sa and we lack the S-band information for the ionosphere calibration.

4 Conclusions and Outlook

Sophisticated simulations suggest that we can derive UT1–UTC from a European baseline between Santa Maria and Wettzell with an accuracy better than 40 µs. Although this is worse compared to standard IVS Intensive sessions, European Intensive sessions present a very valuable alternative or backup solution with even greater value if provided in near real time. Luzum and Nothnagel (2010 [3]) have demonstrated the positive impact on combination and prediction products of the International Earth Rotation and Reference Systems Service (IERS), if UT1–UTC estimates from Intensives between Wettzell, Tsukuba (Japan), and Ny-Ålesund are available eight hours after observation.

Currently, we are observing new test experiments of European Intensive sessions and we are optimistic to sort out final technical problems. We will then be able to estimate station coordinates of Sa and to determine a time series of UT1–UTC to finally confirm the expected accuracy. Thereafter, we will look into improved turnaround times between the observation and the provision of results. For example, Sekido et al. (2008 [8]) have reduced the turnaround time for Intensives between Kashima in Japan and Onsala in Sweden to less than 30 minutes. Of course, the availability of

accurate polar motion values for the analysis becomes a critical factor then.

In combination with length-of-day and polar motion values from GNSS and with forecast geophysical angular momentum functions, UT1–UTC values from European Intensives in near real time will certainly be a very valuable contribution to combined and predicted Earth orientation parameters.

Acknowledgements

The correlation has been carried out on the Vienna Scientific Cluster (VSC-3). TU Wien is partly funded by ESA for carrying out these studies.

References

1. J. Böhm, S. Böhm, J. Boisits, A. Girdiuk, J. Gruber, A. Hellerschmied, H. Krásná, D. Landskron, M. Madzak, D. Mayer, J. McCallum, L. McCallum, M. Schartner, K. Teke. Vienna VLBI and Satellite Software (VieVS) for Geodesy and Astrometry. *Publications of the Astronomical Society of the Pacific*, 130(986), 044503, 1–6, 2018.
2. A.T. Deller, S.J. Tingay, M. Bailes, C. West. DiFX: A Software Correlator for Very Long Baseline Interferometry Using Multiprocessor Computing Environments. *Publications of the Astronomical Society of the Pacific*, 119, 318–336, 2007.
3. B. Luzum and A. Nothnagel. Improved UT1 predictions through low-latency VLBI observations. *Journal of Geodesy*, 84, doi:10.1007/s00190-010-0372-8, 399-402, 2010.
4. T. Nilsson, J. Böhm, H. Schuh. Universal time from VLBI single-baseline observations during CONT08. *Journal of Geodesy*, 85(7), doi:10.1007/s00190-010-0436-9, 415–423, 2011.
5. A. Pany, J. Böhm, D. MacMillan, H. Schuh, T. Nilsson, J. Wresnik. Monte Carlo simulations of the impact of troposphere, clock and measurement errors on the repeatability of VLBI positions. *Journal of Geodesy*, 85(1), doi:10.1007/s00190-010-0415-1, 39–50, 2011.
6. B. Petrachenko, A. Niell, D. Behrend, B. Corey, J. Böhm, P. Charlot, A. Collioud, J. Gipson, R. Haas, T. Hobiger, Y. Koyama, D. MacMillan, Z. Malkin, T. Nilsson, A. Pany, G. Tuccari, A. Whitney, and J. Wresnik. Design Aspects of the VLBI2010 System - Progress Report of the IVS VLBI2010 Committee. NASA/TM-2009-214180, 2009.
7. W. Schlüter and D. Behrend. The International VLBI Service for Geodesy and Astrometry (IVS): current capabilities and future prospects. *Journal of Geodesy*, 81, doi:10.1007/s00190-006-0131-z, 379–387, 2007.
8. M. Sekido, H. Takiguchi, Y. Koyama, T. Kondo, R. Haas, J. Wagner, J. Ritakari, S. Kurihara, K. Kokado. Ultra-rapid UT1 measurement by e-VLBI. *Earth Planets Space*, 60, 865-870, 2008.

Intensifying the Intensives with the VLBA

Nicole P. Geiger, Alan Fey, Christopher Dieck, Megan Johnson

Abstract The U.S. Naval Observatory has, since late 2011, been observing a UT1−UTC Intensive series using the Very Long Baseline Array (VLBA). The primary baseline for these sessions is Mauna Kea – Pie Town (MkPt), using Los Alamos – St. Croix (LaSc) as secondary stations. The session observation times are offset by eight to 16 hours from the IVS Intensives. The VLBA Intensives series are observed at the standard S/X bands. In addition to the daily single baseline VLBA Intensives, VLBA fortnightly sessions using up to four VLBA antennas are observed to characterize the additional baselines. The stations that participate in the fortnightlies are Mauna Kea (Mk), Pie Town (Pt), Los Alamos (La), and St. Croix (Sc). During the period when Sc was offline due to Hurricane Maria damage, a tertiary Intensive was observed using Hancock – Owens Valley (HnOv). Hn and Ov were added to the fortnightlies. We present results of these UT1−UTC series to date and discuss future observing. One issue with the current observations is that the S-band can often be affected by RFI, which usually leads to dropped channels and increased noise in the data. To address the RFI in S-band, test observations are being done to characterize the performance of the VLBA using its more sensitive C-band. Potential future goals include extending the Intensives using three-station baselines to maximize the east-west array.

Keywords USNO, VLBA, Intensives

United States Naval Observatory

1 Introduction

The U.S. Naval Observatory (USNO) has contributed to the International VLBI Service for Geodesy and Astrometry (IVS) as an official Analysis Center for approximately 18 years. As such, the USNO is committed to maintaining and advancing the fields of Earth Orientation Parameters (EOP), the Celestial Reference Frame (CRF), and the measurements of UT1−UTC. The USNO regularly considers ways to contribute to these areas, specifically the measurement of UT1−UTC. One concept was to explore a UT1−UTC series that would act as a backup to the IVS Intensives. Since late 2011, the USNO has observed an Intensive series with the Very Long Baseline Array (VLBA), the VLBA Intensive series. The USNO entered into a 50% timeshare agreement with the Long Baseline Observatory (LBO) in January 2017. Currently, the VLBA Intensives are run as part of the standard operations under the 50% timeshare.

2 Observations

The Intensives are a UT1−UTC series with a primary VLBA baseline of Mauna Kea – Pie Town (MkPt), which has a distance of 4,796 km. In the event that either station is unable to observe, each has a backup. Sc is the backup for Mk, and La is the backup for Pt, producing the secondary baselines ScPt, MkLa, and ScLa. However, due to Hurricanes Irma and Maria, Sc experienced an outage between September 5, 2017 and March 10, 2018. During this outage, a tertiary Intensive series was observed between Hancock – Owens Valley (HnOv). This tertiary series utilized the longest con-

tinental VLBA baseline at 3,885 km. When Sc came back online after the hurricane, USNO was the first to confirm fringes and ensure that the antenna was functional. The Sc antenna is now at full operational capacity. In addition to the various Intensive series, there is also a fortnightly series. The fortnightly series is observed bi-weekly, i.e. once a fortnight. Observations began in late 2014, with the purpose of characterizing the VLBA baselines used in the Intensive series and monitoring them for stability and quality. Initially, there were four VLBA antennas that participated in the fortnightlies: Mk, Pt, La, and Sc. However, Hn and Ov started to be included in the fortnightly series when they were added as a tertiary baseline, bringing the number of VLBA stations to six.

3 VLBA Intensives Setup

In an effort to be as comparable as possible to the IVS daily Intensive series utilizing the baseline from Koke′e to Wettzell (KkWz), USNO uses the VLBA X-band receiver with a dichroic to the S-band receiver. The frequency overlap between the S-band receivers on the VLBA and the IVS antennas is similar. However, the X-band receivers have slightly different frequency coverages. The VLBA X-band receivers range from 8.0−8.8 GHz, while the IVS X-band receivers range from 8.1−8.9 GHz. The data are recorded using the VLBA polyphase filter bank (PFB) personality, which has a total of 16 32 MHz wide spectral windows. For the Intensive and fortnightly series, ten spectral windows are placed across the X-band, and six spectral windows are used across the S-band in single polarization. Figure 1 displays the frequency spacing of the PFB in both S- and X-band frequencies. Due to the fiber optic connections available on the Mk and Pt antennas, e-transfer of data to the Washington Correlator (WACO) is made after each session. However, for the secondary and tertiary stations, fiber optic connections are not yet available; thus, data is transferred via disk packs that are shipped through the mail. After correlation, the data are analyzed in νSolve.

4 Results

All sessions were analyzed and the results compared to C04. As expected, the weighted root mean square (wrms) difference for MkPt is about a factor of two times higher than the KkWz baseline, as can be seen in Figure 2. The KkWz baseline is just over 12,000 km. The longer the baseline, the better the precision, and thus a lower wrms. The VLBA Intensives often experience the well-known issue of high RFI in the S-band. High RFI can lead to dropped channels and increased noise. For instance, in a given observation two out of the six channels are regularly being dropped. Since the S-band is used to calibrate for the ionosphere, the measurement of what the ionosphere contributes to the group delay will not be as good. Therefore, RFI does affect the ionosphere calibration. It then becomes a question of how to deal with this high RFI. One solution to working around or eliminating the RFI in S-band is to observe in a completely different frequency. The C-band is the most sensitive receiver on the VLBA, with a range of 3.9–7.9 GHz. Currently, test sessions are being observed at C-band, see the paper by Dieck.

5 Summary

The VLBA Intensive series has been operational for seven years. Other VLBA sessions include the fortnightly series in which six stations participate. Comparison of the data from the VLBA Intensives to C04 shows a wrms that is approximately 2x higher than that of the IVS KkWz series. High RFI exists in the S-band with investigation into how to address the issue. One such possibility: a C-band session may eliminate this issue, and current test sessions are being observed. Looking to the future, the VLBA Intensives may be extended to three stations, namely Mk, Pt, and Sc, which maximizes the east-west array. The U.S. Naval Observatory is in the process of making the VLBA Intensives available to the IVS, and discussions are underway with the IVS Coordinating Center. However, there are some factors that need to be addressed, i.e.: What metadata do analysts need? What components need to be adjusted for SCHED vs. SKED? The USNO aims to contribute in providing more estimates of UT1−UTC

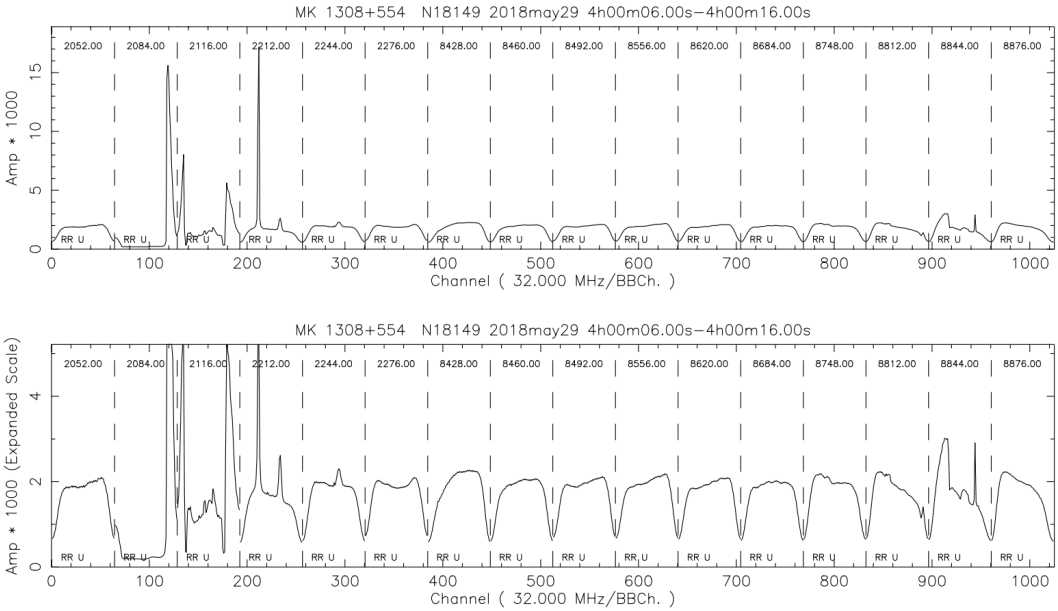

Fig. 1 The first six channels are S-band, and the remaining ten channels are X-band. The frequencies at the top of each panel are in MHz and are the lower edge of the channel. The bottom panel is the zoomed-in amplitude so the RFI in S-band can be seen.

and thus an increased frequency of Intensive observations.

Acknowledgements

The Long Baseline Observatory is a facility of the National Science Foundation operated under cooperative agreement by Associated Universities Inc. The authors acknowledge use of the Very Long Baseline Array under the U.S. Naval Observatory's time allocation. This work supports USNO's ongoing research into the celestial reference frame and geodesy.

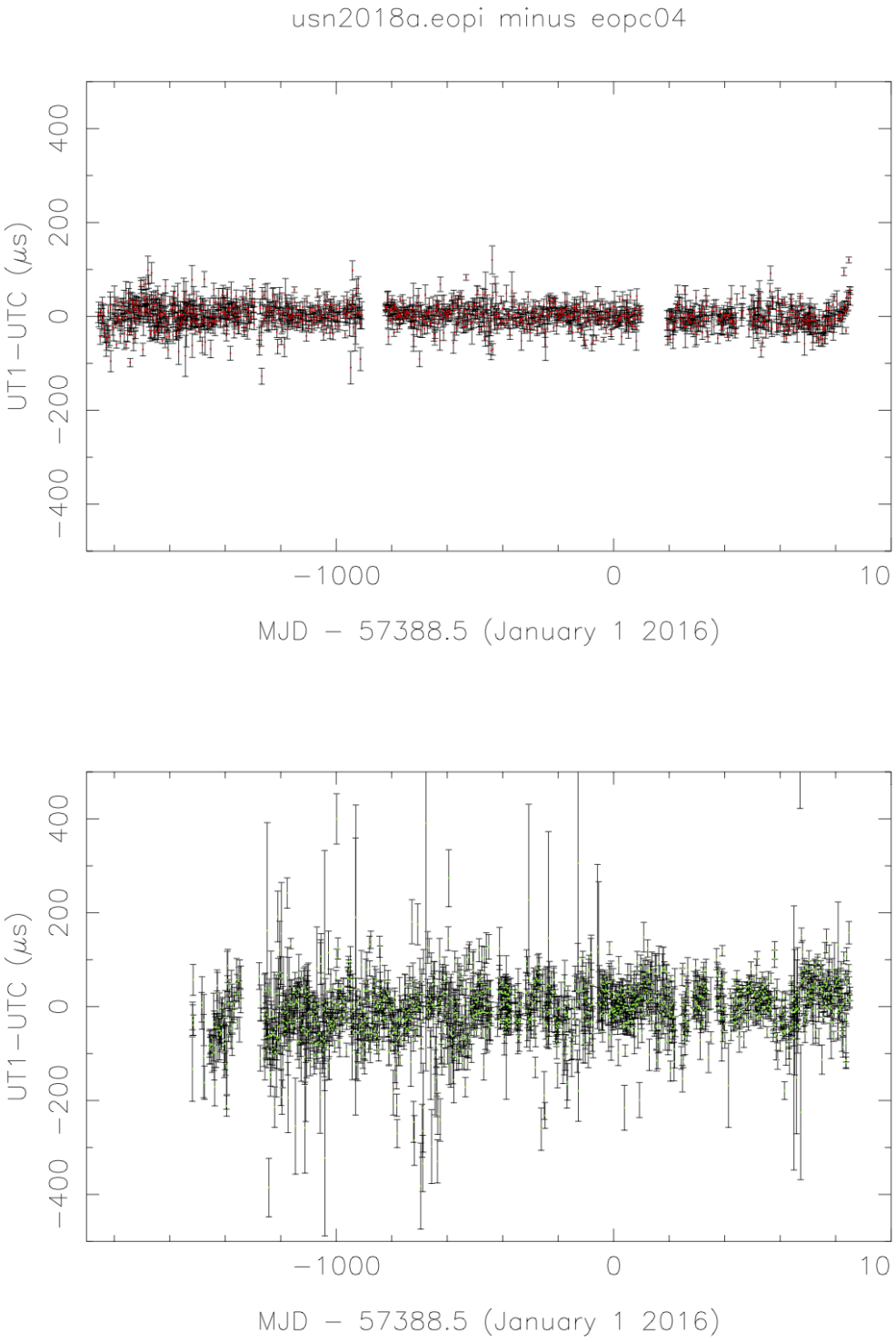

Fig. 2 Results compared to C04. The top plot displays the wrms for the IVS KkWz baseline. In comparison, the bottom plot shows the VLBA MkPt wrms.

Navigating Across the C-band
Experimental C-band Intensives with the VLBA

Christopher Dieck, Megan Johnson, Alan Fey, Nicole Geiger

Abstract The US Naval Observatory makes daily UT1 Intensive observations on the Mauna Kea–Pie Town (MkPt) baseline of the Very Long Baseline Array (VLBA) using the standard S/X bands in a bandwidth synthesis mode. These observations are increasingly negatively impacted by RFI in the S-band. The frequency range of the S-band receiver is no more than 256 MHz wide, restricting the ability to place the 32 MHz wide channels to avoid the RFI. The VLBA C-band receiver is more sensitive and has a wide frequency range (3.9–7.9 GHz) which allows for more flexibility in the placement of channels. To see if the difficulties encountered in the S-band can be overcome by using the C-band, we have undertaken two experiments using the C-band receiver on the Hancock–Owens Valley baseline of the VLBA. The first is a standard group delay observing setup accomplished by placing channels at the low and high ends of the C-band frequency range as analogs of the S- and X-bands. A major question here is whether the smaller frequency separation is sufficient for ionosphere calibration. The second is an attempt at broadband group delay measurement across the width of the C-band. Here we present the design of these sessions and preliminary results.

Keywords VLBA, C-band, Intensives, Broadband

United States Naval Observatory

1 Introduction

For several years the United States Naval Observatory (USNO) has been making daily Intensive observations using the Very Long Baseline Array (VLBA), which is operated by the Long Baseline Observatory. These 90 minute sessions use the Mauna Kea and Pie Town stations, which have optical fiber connections, allowing for fast data transfers resulting in latencies of less than half a day. So far, the session design was modeled on the IVS Intensive series. The setup uses six S-band channels and ten X-band channels in single polarization. Unlike in the IVS Intensives, the channels are 32 MHz wide, the widest that the VLBA can accommodate with 16 channels using the polyphase filter bank (PFB) personality, providing a total data rate of 2 Gbps. The VLBA scheduling software SCHED does not allow for a scan duration to be a function of the brightness of the source, so all scans record data on source for 16 seconds. This duration provides a good compromise between data volume and an adequate SNR for most sources.

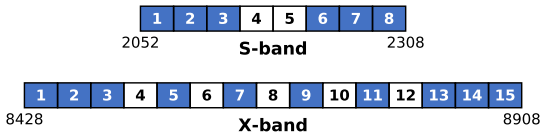

Fig. 1 The channel spacing for the current S/X VLBA Intensives, with the bounding frequencies labeled in MHz. The channels are 32 MHz wide, and those in blue are observed.

The existing setup has worked well but poses some problems as we look to the future. At the Mauna Kea and Pie Town stations, the available bandwidth of the S-band receiver is only 256 MHz, and, as can be seen in

Figure 1, there are only so many ways that six channels can be placed in this range. Currently, S-band channels 2 and 3 are regularly being dropped due to RFI, and there is no better way to arrange the channels in the available frequency space to retain a greater number of channels. Additionally, the RFI environment in the S-band is likely to deteriorate in the future as additional telecommunications infrastructure becomes operational. Furthermore, the available S-band bandwidth at the other eight VLBA stations is even less than that at Mauna Kea and Pie Town due to filters that are in place to keep RFI from swamping the amplifiers. If these observations were to be extended to other stations, which they already are for backup observations, S-band channel 1 would also be deselected because of the filters.

Currently, the most sensitive receiver available on the VLBA is the recently upgraded C-band receiver. It has a wide bandwidth of 4 GHz, spanning the frequency space between the S- and X-band receivers. These features make it a potential alternative to the S/X setup by using the low end of the C-band as an analog for the S-band and the high end of the C-band as an analog for the X-band. The purpose of the investigation described herein is to see whether or not Intensive sessions observed with the C-band receiver can perform as well as, or better than, the current S/X sessions and do so at all VLBA stations now and/or in the future.

2 Observations

2.1 Initial Test Session

Before embarking on a larger campaign to test the characteristics of sessions observed in the C-band, we first needed to test that such sessions could be scheduled, observed, correlated, fringed, and analyzed. To accomplish this, we ran a single observation in November of 2017 where everything was the same as the standard S/X setup except that the frequencies were different. The S-band became C-low, from 3,928–4,408 MHz, and the X-band became C-high, from 7,392–7,872 MHz.

This session was successfully shepherded through the process of making an estimate of UT1−UTC, and the values of UT1−UTC and its uncertainties were consistent with the other Intensive sessions observed around that time. However, given that the C-high and C-low mean frequencies are only separated by ∼3.5 GHz (compared to ∼6.5 GHz for the S/X mean frequencies) there may be an impact on the accuracy of the ionosphere correction. A small complication was that the Mark III database files required an atypical naming scheme to identify them as being associated with C-band data rather than S/X data. With only small obstacles and success in making the observation, further investigation was possible and warranted.

2.2 Typical Group Delay Sessions

After the initial test, we wanted to develop a setup from scratch that met some overarching design goals. First, we wanted to be able to compare the UT1−UTC value against another VLBA baseline that was observed at the same time. We also wanted a setup that mimicked the S/X approach and that kept as large a separation as possible between the two new subbands at the ends of the C-band. We also had to be careful about the channel spacing so that the fringe function would have a strong central peak with low side lobes. If possible, placing the channels so that the two subbands would have different ambiguity spacings would be a bonus.

Working within the constraints of the VLBA backends, we developed the following setup. The observations would be made on the longest east-to-west continental US baseline, Hancock–Owens Valley (HnOv), at the same time as the standard S/X MkPt VLBA daily Intensives. This meant that the difference between the UT1−UTC values would hopefully be able to be directly compared, and that the Intensive sessions were only interrupting the VLBA once. The digital down converter (DDC) personality allows for more flexible channel placement than the PFB personality, enabling us to achieve both different ambiguity spacings between bands and accessing the extremes of the range of the C-band receiver. However, this also limited us to using four 32 MHz channels with single polarization in each of the C-low and C-high bands.

To keep as many channels as possible towards the edges of the receiver's range while still keeping a reasonable fringe function, the channels were spaced using a Golomb ruler of order 4 and then placed at either end of the C-band. Though the channels at both C-low and C-high were still 32 MHz wide, the C-low chan-

nel edges were spaced at multiples of 40 MHz apart whereas the C-high channels were spaced at multiples of 32 MHz to make the ambiguity spacings different between the bands. The resulting fringe functions are shown in Figure 2. The lower edge frequencies of the C-low channels were 3,912, 3,952, 4,072, and 4,152 MHz while the lower edge frequencies of the C-high channels were 7,664, 7,728, 7,824, and 7,856 MHz, as shown in Figure 3. With only eight channels each 32 MHz wide in a single polarization, the data rate was 1 Gbps. Though not making up for the difference in data rate entirely, the scans were observed for twice as long as in the standard S/X setup, an on source duration of 32 seconds.

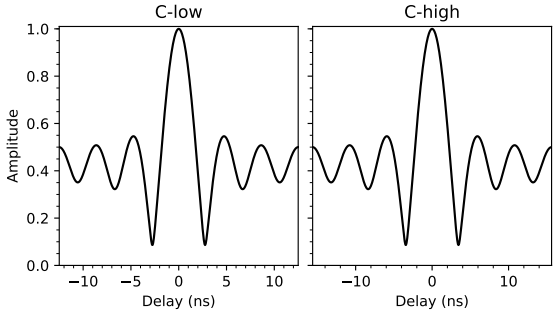

Fig. 2 The shapes of the normalized theoretical fringe functions of the typical group delay setup. The shape of the fringes is the same, but they have different widths, 25.0 ns for C-low and 31.25 ns for C-high.

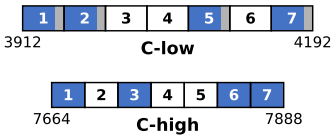

Fig. 3 The channel spacing for the C-band typical group delay setup, with the bounding frequencies labeled in MHz. The blue channels are those that were observed. The portion of the C-low channels that was not recorded is in gray. The widths of the channels are 40 MHz in C-low and 32 MHz in C-high.

2.3 Broadband Group Delay Sessions

In contrast to the typical group delay setup, we also wanted to develop a setup that would be better suited to fit the phase as a function of frequency across as much of the C-band as possible. Using the DDC personality we were able to place four channels, each 128 MHz wide, across the C-band with single polarization. However, rather than have them equally spaced, or some other particular placement, the channels had to be placed in pairs at the high and low ends of the C-band with a separation of 256 MHz between the channels in each pair, as shown in Figure 4. The data rate was 2 Gbps, so on source time was reduced back to 16 seconds. These observations were also observed at the same time as the standard S/X Intensives. With four 'bands' extracted from a wideband receiver, this setup is very similar to the full planned VGOS observations.

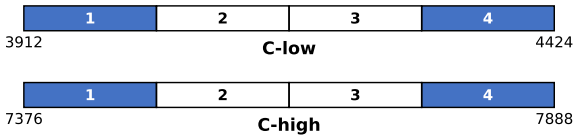

Fig. 4 The channel spacing for the C-band broadband group delay setup, with the bounding frequencies labeled in MHz. The channels are 128 MHz wide, and those in blue are observed.

3 Results

3.1 Typical Setup Results

The analysis of the sessions observed with the typical group delay setup is ongoing. There were 26 sessions observed from April 11 to June 28, 2018, of which ten were processed. These ten sessions were correlated, fringed, and packaged into the Mark III database format. From observation to having a database takes about two weeks. They were then analyzed in νSolve in the way that the IVS Intensives are analyzed. First, any ambiguities are resolved, and a group delay solution is fit at both the high and the low bands. Then the ionospheric corrections are calculated and applied, followed by scan uncertainty reweighting and outlier elimination. Of the ten analyzed sessions, only six have data that are useful for developing an understanding of the characteristics of the setup. The other four were either not observed at the same time as the S/X VLBA Intensive, the VLBA S/X Intensive used a baseline other

than MkPt, or the C-band session output was aberrant. The UT1−UTC values and uncertainties from these six sessions are given in Table 1 along with the uncertainties of the IVS Int1 and VLBA S/X Intensives for each of those days of the year.

Table 1 Analysis results and comparison of the group delay test sessions to the IVS and standard VLBA sessions on the same day of the year (doy). ΔUT1−UTC is the standard S/X VLBA session UT1−UTC minus the C-band session UT1−UTC. The rss is the root of the sum of the squares of the S/X and C-band σs.

DOY, 2018	IVS σ (μs)	S/X σ (μs)	C-band σ (μs)	ΔUT1−UTC (μs)	rss σ (μs)
111	7.0	20.6	13.4	94.3	24.6
115	6.5	13.0	33.4	81.7	35.8
124	6.8	7.1	34.4	−3.6	35.1
125	8.6	11.6	64.6	118.0	65.6
127	7.1	8.6	20.5	133.5	22.2
128	7.7	13.2	31.1	171.9	33.8
Mean	7.3	12.4	32.9	99.3	—

If we are to judge the success of these sessions based on their reported uncertainties, then they are not doing very well. With the mean uncertainty of the C-band sessions ∼2.5 times that of the standard VLBA S/X, this does not seem like a setup that would provide a better estimate of UT1−UTC than the one already in use. However, more sessions are necessary to make the statistics more meaningful. Also, the setup is better judged by the wrms of the UT1−UTC residuals to a reference series, such as the IERS Bulletin A.

Looking at the mean value of the difference in UT1−UTC from the S/X sessions to the C-band sessions, there is some systematic offset that needs to be taken into account. This is not unexpected because the measurements are made at different baselines. Additionally, the east-west component of the HnOv baseline is 3,856 km, where the same value for the MkPt baseline is 4,579 km. This difference in baseline length contributes to the increased uncertainty in the C-band sessions, so in addition to developing different statistics, it would be better if the C-band sessions were compared to the same baseline. Luckily, there are several months of standard S/X observations on the HnOv baseline from which to develop metrics for comparison. However, this comparison is left for future work.

Exploring an individual session, such as that from the 115th day of the year, we can see some other effects of the C-band setup. As noted above, the uncertainty

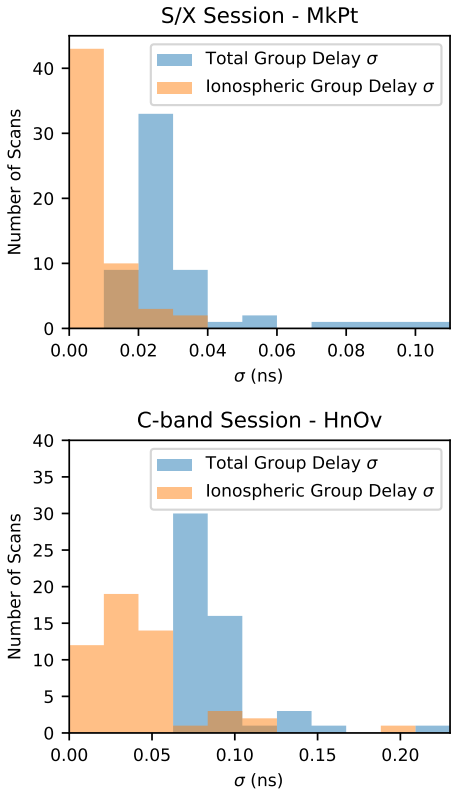

Fig. 5 Histograms showing the number of scans with total reweighted group delay uncertainties in blue and ionosphere correction uncertainties in orange for the MkPt S/X session (top) and the HnOv C-band typical session (bottom) on doy 115.

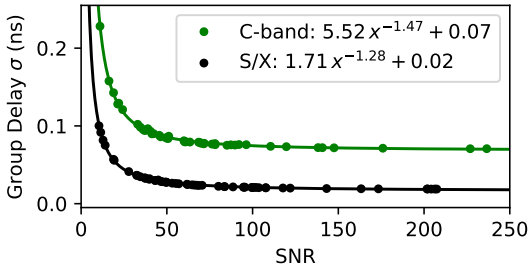

Fig. 6 Total reweighted group delay uncertainty per scan as a function of SNR for doy 115 for both the typical group delay setup on HnOv and the standard S/X session on MkPt. The functional form of the fit for both sessions is given in the legend.

is elevated over that of the S/X VLBA session. However, as is shown in Figure 5, the distribution is pretty similar; it is just the scale that is larger. This is corroborated by looking at the uncertainty as a function of scan

SNR, shown in Figure 6. One of the concerns regarding this setup design was whether or not the smaller distance between the two bands would allow for good ionospheric corrections. Figure 5 suggests that the uncertainty from the ionospheric correction in the C-band setup contributes more to the total uncertainty than in the S/X setup. This is supported by the mean of the ratio of the ionospheric correction uncertainty to the total uncertainty for each setup, which is 25.9% for the S/X setup and 43.0% for the C-band setup. It may be that C-high and C-low are too close together for useful ionosphere calibration in the typical setup.

3.2 Broadband Setup Results

For the broadband group delay setup, 15 observations were made, but only two have been processed. The processing of these two has been in the same manner as for the typical group delay. Though this was not the intended analysis when the setup was designed, it was executed to allow for a comparison between the analysis approaches. The output of these two sessions show uncertainties similar to the IVS Intensives, but the metrics are not very meaningful without a larger sample. The main conclusion from the analysis so far is that this setup shows promise, particularly over the typical C-band setup. All 15 sessions will be analyzed in this way and compared with the standard S/X and the typical C-band setups, but it is the potential to use each of the four channels on its own that makes this setup interesting, although new software may need to be developed.

4 Future Work

Though inconclusive at this stage of analysis, these initial results suggest that Intensives made with the C-band receiver on the VLBA may prove to be useful in the future. It appears that the broadband setup, rather than the traditional group delay setup, may be a better approach to incorporating the C-band. Before anything can be said with certainty, though, the analysis of the sessions already observed needs to be completed. There are also a few more calculations that can be applied to evaluate the results more effectively. For the typical group delay setup, calculating any bulk offset in UT1−UTC between the C-band series and the standard S/X series will allow for better comparison between the two. The uncertainties of the UT1−UTC estimates are dependent on the baseline length between the stations, and accounting for this when comparing the different session series will be illuminating.

With only 15 observations of the broadband setup, additional sessions will need to be obtained to achieve better statistics, perhaps with modifications to make the spacing of the channels within the band better suited to making an estimate of the differenced total electron content (dTEC). Additionally, we need to develop a way of using the four channels to actually do a broadband fit.

These analyses are currently based on the assumption that source positions defined in the X-band celestial reference frame are appropriate for use with observations made at C-high. The difference in mean frequency between these two bands is $\sim$1 GHz (8.6 GHz for X-band and 7.6 GHz for C-high). Though any induced offsets in UT1−UTC due to unaccounted shifts in the source position (e.g. core shift) are likely to be within the uncertainty, the validity of this assumption needs to be verified.

Regardless of the work that has yet to be performed, this investigation already demonstrates that the flexibility, rapid scheduling, and relatively short latency from observation to creating a database makes the VLBA a facility that can be effectively used to try out new approaches to geodetic and astrometric observations and data analysis. This could prove to be useful in the transition to and during the VGOS era.

Acknowledgements

The Long Baseline Observatory is a facility of the National Science Foundation operated under cooperative agreement by Associated Universities Inc. The authors acknowledge use of the Very Long Baseline Array under the US Naval Observatory's time allocation. This work supports USNO's ongoing research into the celestial reference frame and geodesy.

Performance of the Operational IVS-R1 and IVS-R4 Sessions

Cynthia C. Thomas, Daniel S. MacMillan, Karine O. Le Bail

Abstract This paper focuses on the performance of the operational IVS-R1 and IVS-R4 sessions from 2002 through 2017. The formal uncertainties of the IVS-R1 and IVS-R4 EOPs improved over the period of 2002 through 2017. We consider how much this improvement can be attributed to the increased size of the networks, changes in the data rate, the number of observed sources, and/or the scheduling parameters.

Keywords IVS-R1, IVS-R4, EOP

1 Introduction

In this paper we focus on the EOP (Earth Orientation Parameter) performance of the operational IVS-R1 and IVS-R4 sessions from 2002 through 2017. The IVS-R1 and IVS-R4 sessions began in January 2002 with a network of five to six stations and increased over time to a network size of 11 to 13 stations in 2017. There is significant variation in observed EOP precision over different time periods; for instance, the precision in the time period around the continuous observing campaign CONT14 was close to the precision of CONT14. We investigate the possible factors that could produce better or worse precision for the IVS-R1 and IVS-R4 networks from 2002 through 2017. Some factors that could help explain the variability in observed EOP precision are network station variation, media, data loss, and recording rate. All of these factors are examined in our analysis of the performance of the IVS-R1 and IVS-R4 series from 2002 through 2017.

NVI, Inc.

2 EOP Uncertainties of the IVS-R1 and IVS-R4 Sessions

The EOP uncertainty goal of the IVS program is 3.5 μs for UT1 and 100 μas for pole position. As shown in Figure 1, the formal uncertainties meet this goal and have improved over time. The moving average (one year) trend line for IVS-R1 pole position uncertainties decreases from 60 μas in early 2002 to 40 μas in late 2017. The moving average (one year) for IVS-R1 UT1 becomes more stable, but there is no significant linear trend. There is a more significant improvement over time in all EOP components for the IVS-R4 sessions. The moving average (one year) trend line for IVS-R4 X-pole position improves from 90 μas in early 2002 to 40 μas in late 2017 and from 70 μas in early 2002 to 40 μas in late 2017 for Y-pole. The UT1 uncertainties decrease from 3 μs to 2.5 μs over the 16-year period.

3 2014 & 2017 IVS-R1 & IVS-R4 & CONT Sessions

We wanted to know if the IVS-R1 and IVS-R4 sessions, scheduled before and after the CONT campaigns, had better formal uncertainties, since it is possible that the increase in station checkout before CONT campaigns could contribute to better performance for all sessions involving CONT stations. We see in Figure 2 that this is true during 2014 for the IVS-R1 sessions scheduled before and after CONT14. However, this did not occur during 2014 for the IVS-R4 sessions or any other CONT campaign for the IVS-R1 or IVS-R4 sessions. This appears to be an

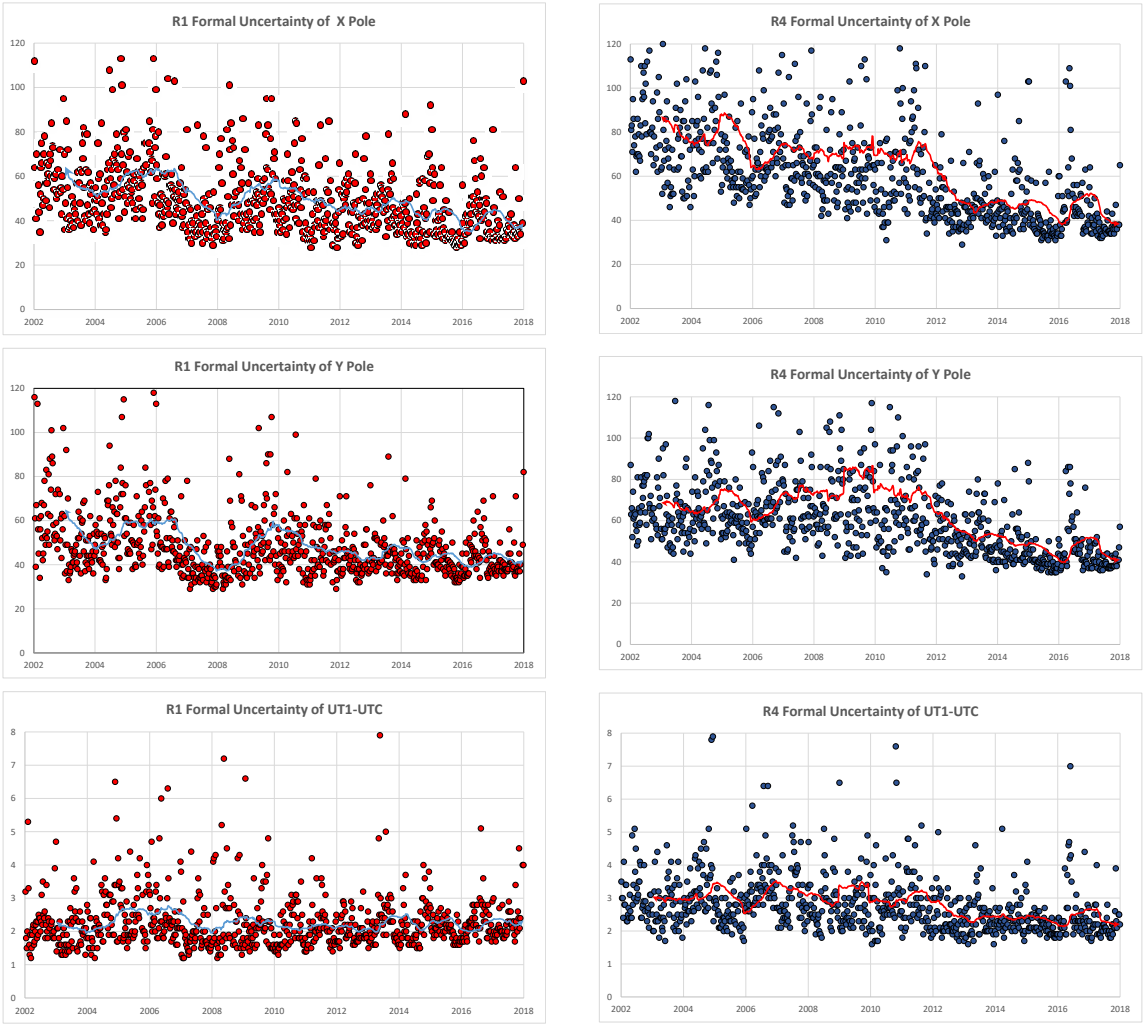

Fig. 1 IVS-R1 and IVS-R4 formal uncertainty of X-pole (µas), Y-pole(µas), and UT1 (µs) for the period of 2002 through 2017.

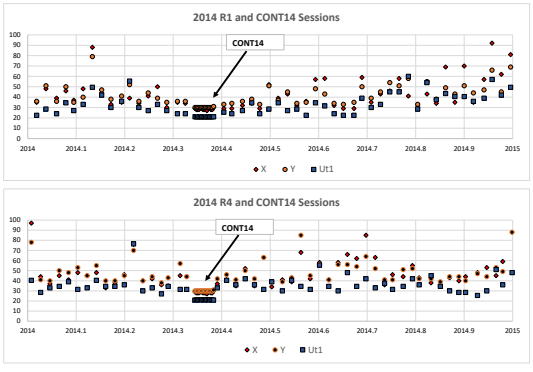

Fig. 2 2014 IVS-R1, IVS-R4, and CONT14 X-pole, Y-pole, and UT1 formal uncertainties (µas).

anomaly since it occurred only for CONT14 and for only one type of session.

4 EOP Uncertainties of the IVS-R1 and IVS-R4 Sessions with No Velocities Estimated

The standard VLBI solutions assume that you are doing a global estimate of station positions and velocities, and are estimating EOP on an arc-by-arc basis. Because of this, the uncertainties in the reference frame propagate into the EOP uncertainties. The reference frame has the least uncertainty in the middle of the data

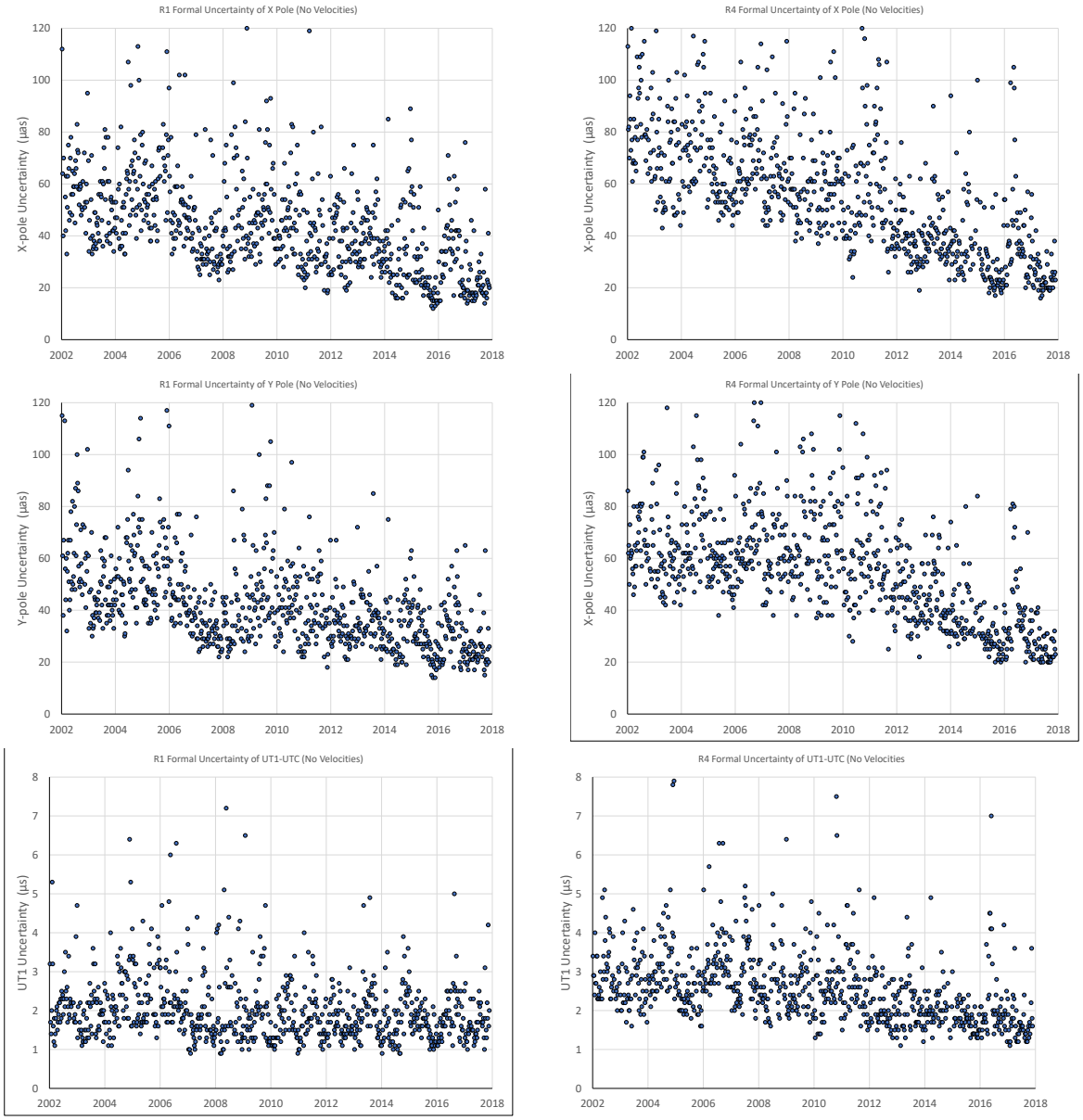

Fig. 3 IVS-R1 and IVS-R4 formal uncertainty of X-pole, Y-pole, and UT1 for the period of 2002 through 2017 – no velocities.

span, and increases towards the end. Because of this, even if the network and observing schedules remained the same, the EOP uncertainties would be larger towards the end of the observing span. An alternative way of studying the EOP uncertainties is to turn off reference frame estimation by turning off velocity estimation. The resulting EOPs are only influenced by the observing schedule and allow a truer comparison of EOP uncertainty at different epochs.

Figure 3 shows that the EOP formal uncertainties without velocity estimation improved from 2002 through 2017. The X-pole and Y-pole uncertainties for the IVS-R1 sessions improved by a factor of two and UT1 by a factor of about 1.5. There is a larger change with the IVS-R4 sessions where X-pole improves by a factor of three and Y-pole improves by a factor of two. UT1 improves by a factor of two.

5 Number of Observations Per Session

Figure 4 shows that the network size for both the IVS-R1 and IVS-R4 sessions increased. Depending on the network, the increased network also caused the number of observations to increase. The IVS-R1 first increased in network size in 2006, up to eight stations. There was a more significant increase in 2011 to ten stations and then 10+ stations in 2015. The IVS-R4 sessions first increased in network size in 2003, then 2011 to ten stations and later in 2014 to 11+ stations.

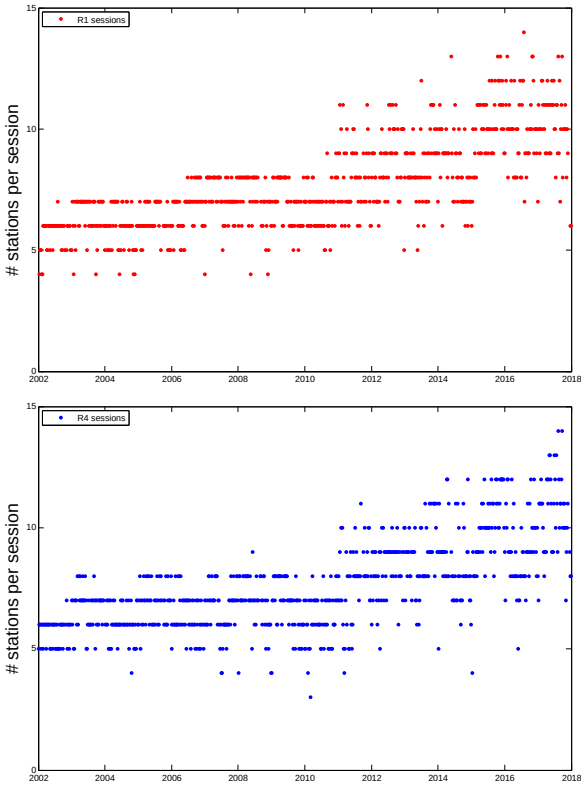

Fig. 4 IVS-R1 (top) and IVS-R4 (bottom) stations per session from 2002 to 2017.

Figure 5 displays the general increase in the number of obserations per session for the IVS-R1 and IVS-R4 sessions since 2002. There is an increase in session observations for the IVS-R1s that begin in August of 2006 and levels off until 2010. The August 2006 increase is consistent with the replacement of tapes with disks. Observations increased because tapes had required extra idle time due to tape turn-around and tape change. There is another increase starting in 2010 when AuScope stations were added to the IVS-R1 sessions. The number of observations continued to increase as Sejong was added to the network in the fall of 2014. Yebes-13.5m and Wettzell-North were tagged along and then added as regular stations in early and mid 2016, respectively. The increase starting at the end of 2015 can be attributed to an increase in the bit rate to 512 Mbps for the even IVS-R1 sessions.

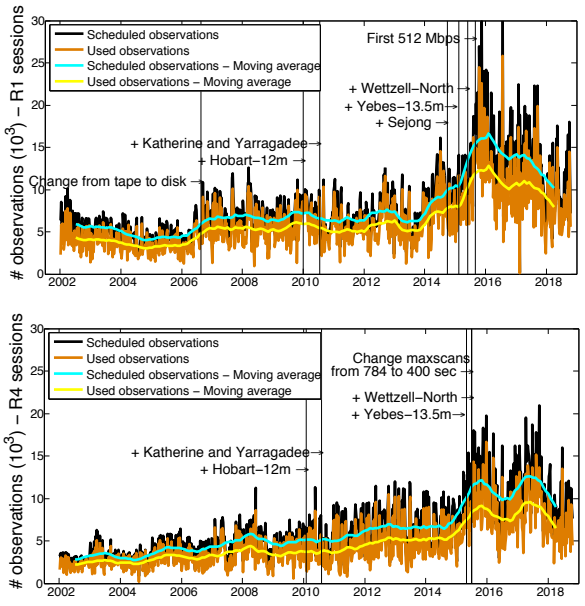

Fig. 5 Scheduled vs. good observations per IVS-R1 (top) and IVS-R4 (bottom) session (2002 through 2017).

The number of IVS-R4 observations increased steadily over time and the biggest increase came around mid 2014 to 2015 (Figure 5). The increase is primarily due to decreasing the maximum scan length from 784 to 400 seconds and the addition of Wettzell-North and Yebes-13.5m. We still need to investigate the reason for the short decrease in observations during 2016.

Figure 5 shows that, although the number of observations increased over the years for both the IVS-R1 and IVS-R4 sessions, the number of good observations decreased in 2016. The decrease in good IVS-R1 observations is especially large since the beginning of 2016, which needs to be studied to determine if the number of good observations can be increased. The number of successful IVS-R1 and IVS-R4 observations is on average about 80% of the observations scheduled

from 2002 through 2017. We need to investigate how to improve this success percentage.

6 Conclusions

The EOP formal uncertainties improved for both the IVS-R1 and IVS-R4 sessions since 2002. There are many interesting issues that still need to be studied regarding these data sets. Simulations are used to design future experiments and are based on scheduled data; it is possible that simulation procedures should be improved. The observation success rate for both IVS-R1s and IVS-R4s is about 80%. The main conclusion is that we need to investigate how to improve the success rate. Clearly the formal uncertainties of estimated EOP will be improved with more successful observations resulting from reducing the gap between scheduled and used observations. We also intend to further study the sessions where the performance of the IVS-R1 and IVS-R4 sessions were best, specifically the IVS-R1 sessions before and after CONT14.

Initial VLBI Data Analyses at the National Geographic Institute of Spain

E. Azcue [1], Y. Gomez-Espada [1], V. Puente [1], S. Garcia-Espada [2], J. Lopez-Ramasco [3], M. Valdes [1]

Abstract The National Geographic Institute of Spain (IGE) has been taking part in geodetic VLBI since 2008 through the participation of the Yebes 40-meter radio telescope in VLBI observation campaigns. It also encourages the continuous development of the RAEGE project for an Atlantic Network of Geodynamical and Space Stations, as part of the VLBI Geodetic Observing System. Currently, IGE is expanding its contribution to geodetic VLBI by taking its first steps in VLBI data analysis. We present in this work the results of the initial analyses carried out using VieVS 3.0 (University of Vienna) and Where (Norwegian Mapping Authority) as processing software. One-year series of Earth Orientation Parameters obtained from R1 and R4 IVS sessions are compared with IERS 14 C04 series and those from other VLBI Analysis Centers. In addition, secondary VLBI products such as zenith troposphere delay and clock offsets are also compared with GNSS-based products for stations in which VLBI and GNSS antennas' co-location make this analysis possible.

Keywords VLBI, VieVS, Where, EOP, GNSS

1 Introduction

The National Geographic Institute of Spain (IGE) has been taking part in geodetic VLBI over the last decades through the participation of the Astronomical Center of Yebes in VLBI observation campaigns. Regarding instrumentation, IGE encourages the development of the RAEGE project for an Atlantic Network of Geodynamical and Space Stations, as part of the VLBI Geodetic Observing System. As part of this project, VLBI antennas at Yebes (Spain) and Santa María (Azores) were installed. Currently, IGE is expanding its contribution to geodetic VLBI by taking its first steps in VLBI data analysis, whose results are shown in this work.

1. National Geographic Institute of Spain
2. RAEGE Santa Maria - National Geographic Institute of Spain
3. Astronomical Center of Yebes - National Geographic Institute of Spain

2 Goal

The aim of this work is to present the first VLBI data analysis results obtained at IGE. Several topics have been addressed during this work:

- Processing VLBI sessions for the same period of time by using different VLBI processing software; namely VieVS 3.0 (Boehm et al., 2018) and Where (Kirkvik et al., 2017).
- Comparing and contrasting the Earth Orientation Parameters (EOP) estimated by means of these programs and the solutions of other Analysis Centers with the IERS EOP 14 C04 series (Bizouard et al., 2018), which are used as a reference.
- Comparing the time series of the estimated station coordinates with the IVS combined solution (Schuh and Behrend, 2012).
- Validating the workflow and products obtained by comparing the VLBI troposphere estimation with the final IGS tropospheric Zenith Total Delay (ZTD) calculated with GNSS (Dow et al., 2009).

3 Strategy

IVS R1 and R4 sessions for the period spanning from October 2016 to October 2017 were used for the experimentation activities with the VLBI processing programs previously mentioned. The a priori models and configuration used in each software is reflected here, below.

1. IGE VieVS
   - Frames: ICRF2 and VTRF14
   - EOP: IERS Conventions 2010 and Bulletin A as initial value
   - Troposphere: VMF1 model
   - Geophysical models: solid tide, tidal ocean loading (FES2004), tidal atmosphere loading (Vienna model), thermal antenna deformation
   - Estimation model: weighted least squares
2. IGE Where
   - Frames: ICRF2 and VTRF14
   - EOP: IERS Conventions 2010 and Bulletin B as initial value
   - Troposphere: VMF1 model
   - Geophysical models: solid tide, tidal ocean loading (TPXO.7.2), thermal antenna deformation
   - Estimation model: Kalman filter

In both cases, the estimated parameters are EOP, station and source coordinates, station clock models, troposphere delay, and gradients.

4 Results

- EOP analysis

EOP estimations for the one-year period analyzed with VieVS 3.0 and Where software have been compared to IERS EOP 14 C04 using spline interpolation. The same comparison has been carried out using EOP estimated by other Analysis Centers such as BKG (Calc/Solve) and GFZ (VieVS) as well as with the IVS combined solution. These solutions were retrieved from IVS ftp. Figures 1 to 5 show the differences of each AC with respect to the IERS EOP 14 C04 series, and Table 1 includes a statistical summary of the differences.

- Time series of station coordinates

Station and source coordinates are part of the estimation process when dealing with VLBI observations. In order to validate other outputs obtained during the reprocessing campaign carried out by IGE, one-year time series of Wettzell station coordinates estimated with VieVS were compared with the IVS combined solution, which is available at IVS ftp through SINEX files. The same comparison has been performed using BKG and GFZ time series. The mean value and the standard deviation of each solution are provided in Table 2.

- ZTD estimation

The effect of the troposphere on GNSS and VLBI signals contributes as an additional delay in the measurement of the signal travelling. The magnitude of this delay depends on the temperature, pressure, and humidity as well as the antenna location. Taking advantage of GNSS and VLBI co-located antennas in Wettzell, VLBI-based ZTD estimated with VieVS has been compared to GNSS-based ZTD provided by IGS products. The mean value of the differences for the period analyzed is 4 mm, with a standard deviation of 7 mm.

5 Conclusions and Future Plans

The results presented in this poster lead to the following conclusions:

- Concerning EOP estimation, the accuracy of the IGE VieVS solution is within the same order of magnitude as other VLBI Analysis Centers. The IGE Where solution seems to be one order of magnitude better than other Analysis Centers regarding polar motion components. Additional tests are foreseen to confirm these outcomes.
- The accuracy in the estimation of other products derived from VLBI processing, such as station coordinates and troposphere delay, shows good agreement with other VLBI solutions and techniques (GNSS).

In light of these results, the IGE team is driven to gain more experience in VLBI processing and to continue reprocessing geodetic VLBI sessions. The ultimate aim is to contribute as much as possible to IVS activities.

6 Figures and Tables

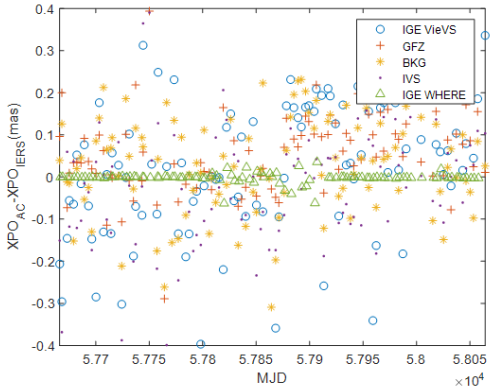

Fig. 1 X-pole differences with respect to IERS Bulletin B EOP (Oct '16-Oct '17).

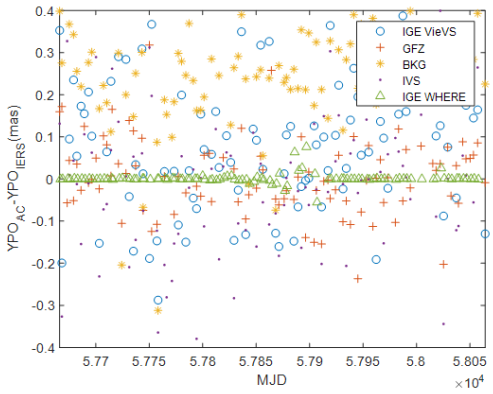

Fig. 2 Y-pole differences with respect to IERS Bulletin B EOP (Oct '16-Oct '17).

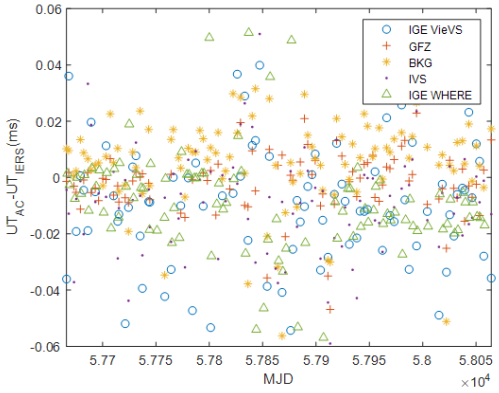

Fig. 3 UT1-UTC differences with respect to IERS Bulletin B EOP (Oct '16-Oct '17).

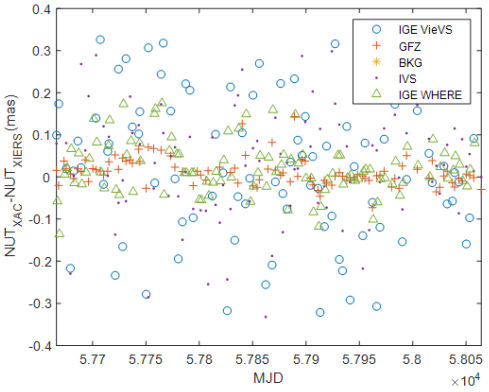

Fig. 4 dX differences with respect to IERS Bulletin B EOP (Oct '16-Oct '17).

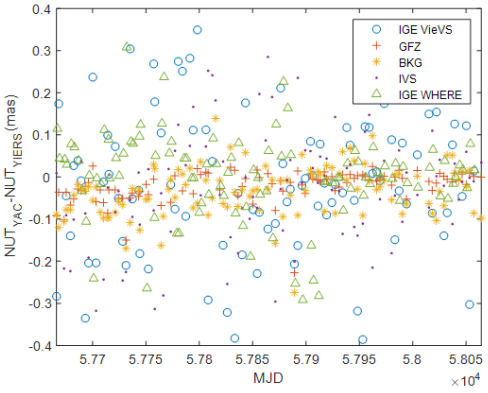

Fig. 5 dY differences with respect to IERS Bulletin B EOP (Oct '16-Oct '17).

Table 1 EOP differences statistics.

EOP	Solution	Samples	Mean	STD
X-Pole (mas)	IGE VieVS	108	0.156	0.206
	IGE Where	103	0.006	0.012
	BKG	109	0.112	0.169
	GFZ	109	0.178	0.558
	IVS	96	0.089	0.108
Y-Pole (mas)	IGE VieVS	108	0.198	0.258
	IGE Where	103	0.005	0.013
	BKG	109	0.314	0.172
	GFZ	109	0.207	0.579
	IVS	96	0.069	0.090
UT1-UTC (ms)	IGE VieVS	108	0.590	5.490
	IGE Where	103	0.021	0.032
	BKG	109	0.557	5.456
	GFZ	109	0.593	5.468
	IVS	96	0.017	0.082
dX (mas)	IGE VieVS	108	0.590	5.490
	IGE Where	103	0.021	0.032
	BKG	109	0.557	5.456
	GFZ	109	0.593	5.468
	IVS	96	0.017	0.082
dY (mas)	IGE VieVS	108	0.291	0.656
	IGE Where	103	0.048	0.062
	BKG	109	6.403	0.675
	GFZ	109	0.787	5.811
	IVS	96	0.024	0.033

Table 2 Difference in the norm of Wettzell coordinates.

Solution	Mean (m)	STD (m)
IGE VieVS	0.014	0.007
BKG	0.018	0.007
GFZ	0.013	0.016

References

1. IERS Conventions (2010), IERS Technical Note 36, Frankfurt am Main: Verlag des Bundesamts für Kartographie und Geodäsie, G. Petit and B. Luzum (eds.)
2. Bizouard C., Lambert S., Gattano C., Becker O., Richard J.Y., (2018). The IERS EOP 14 C04 solution for Earth orientation parameters consistent with ITRF 2014, Journal of Geodesy, August 2018.
3. Boehm J., et al. (2018), Vienna VLBI and Satellite Software (VieVS) for Geodesy and Astrometry, Publications of the Astronomical Society of the Pacific, Vol. 130(986), 044503.
4. Kirkvik A., et al. (2017), Where: A New Software for Geodetic Analysis, 23rd EVGA Working Meeting & 18th IVS Analysis Workshop.
5. Schuh H. and Behrend D. (2012), VLBI: A fascinating technique for geodesy and astrometry, Journal of Geodynamics, Vol. 61, pp. 68—80.
6. Dow, J.M., Neilan, R. E., and Rizos, C., (2009), The International GNSS Service in a changing landscape of Global Navigation Satellite Systems, Journal of Geodesy, Vol. 83, pp. 191—198.

NMA Analysis Center – Progress Report

Ann-Silje Kirkvik, Geir Arne Hjelle, Åsmund Skjæveland, Michael Dähnn, Ingrid Fausk

Abstract The Norwegian Mapping Authority is currently developing **Where**, a new software for geodetic analysis. The software will be used to analyze VLBI sessions and contribute to the rapid and other operational products of the International VLBI Service for Geodesy and Astrometry (IVS). All the components needed for the analysis of an individual VLBI session are finished in **Where** and the software is in its final testing phase. Together with the IVS Combination Center, the quality of the processed solutions are being evaluated and improved as problems are detected. The goal is to have a fully working version of the VLBI part of the software before the end of 2018.

Keywords VLBI, Where, software, analysis

1 Introduction

The Norwegian Mapping Authority (NMA) has been an Associate Analysis Center of the IVS [1, 9] since 2010. The original plan was to use the GEOSAT software [4] and become an operational Analysis Center, which regularly processes R1 and R4 sessions. As previously reported in the IVS 2015+2016 Biennial Report [5], the GEOSAT software was abandoned and a new software is under development. The new software is called **Where** [6]. The NMA plans to use this software to submit timely analyses to the IVS Combination Center (CCIVS).

Norwegian Mapping Authority

2 Motivation

The NMA has operated the VLBI station in Ny-Ålesund since the beginning of the 1990s with the first observations in 1994. The site is currently being upgraded with two new VLBI stations and an SLR station is planned to be added to the site by 2022. Several GNSS stations and a DORIS beacon already exist in Ny-Ålesund.

Ny-Ålesund is situated at 78.55°N, 11.56°E on the west coast of Spitsbergen, the largest island in the Svalbard archipelago. Ny-Ålesund is not open to the general public and professionals working there are limited to fixed term contracts. This naturally causes a high turnover and finding qualified personnel for a small field of science, such as VLBI and SLR, is a continuous challenge. Having qualified personnel in permanent positions at the head office is therefore essential. Creating, maintaining, and using an analysis software provides valuable compentence and insights into the field of VLBI for the group at the head office. Additionally, by becoming an Analysis Center, the NMA can finally analyze the data collected at Ny-Ålesund and provide direct feedback to the station on its performance.

3 Software

Figure 1 shows the architecture and basic pipeline for the analysis of a typical geodetic VLBI session. In 2017 the theoretical VLBI delay model of the **Where** software was confirmed to be comparable with other software packages [6]. This was done by utilizing the

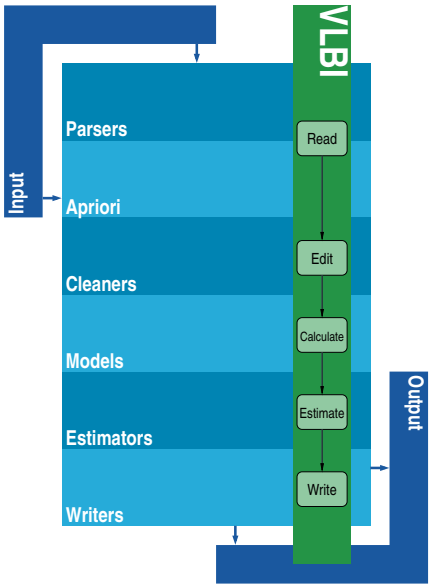

Fig. 1 **Where** architecture: The pipeline for the analysis of VLBI sessions.

data and analysis from the VLBI Analysis Software Comparison Campaign 2015 [7].

Where uses a Kalman filter with a Modified Bryson-Frazier smoother [2, 3] for estimation. Clocks and troposphere are modeled as continuous piecewise linear parameters. By default, the clocks and the wet troposphere are estimated with one linear segment per hour, while the horizontal gradients use one linear segment per six hours. Normal equations as requested by the IVS are created following the method of [8].

The **Where** software is available under an open source MIT license at `https://kartverket.github.io/where`.

4 Verification and Validation

Lately, a lot of effort has been put into analyzing sessions from 1994 to 2016 to identify clock breaks and other issues with the data. Furthermore, the estimator and writer components have been completed and a lot of testing has been done. Several solutions were submitted to the CCIVS for evaluation. Based on feedback from the CCIVS, several issues with the software were resolved. Table 1 summarizes the submitted solutions and their issues.

In March 2018 the first test solution was submitted to the CCIVS. It consisted of one year of sessions (2016) and contained estimates for Earth Orientation Parameters (EOP) and station coordinates. Briefly after, a solution with 23 years of processed sessions (1994–2016) was also submitted. The second solution also contained estimates for radio source coordinates. These solutions were processed by the same setup and version of the software.

However, there were some problems with the submitted solutions. First of all, the radio source names were wrong for those sources that are listed in the observation file with a different name than the official IERS name. This problem was resolved, but not yet verified by the CCIVS.

Secondly—and more worrisome—the estimates appeared to be extremely close to the a priori values. The first (and second) solution also contained large offsets in estimated station coordinates for some stations and the computed weight factor for the solution in the combination was too low.

The main problem was that when the Kalman filter iterated and removed outliers it did not estimate the parameters from scratch, but rather estimated a correction to the previous estimate. It was this correction to the previous estimate that was wrongly used to generate the normal equations.

The implementation of the creation of the normal equations also contained some minor bugs. All these mistakes were corrected in a new version of the software. A third solution with station coordinates and EOPs using sessions from 2013 to 2016 was then submitted at the end of May.

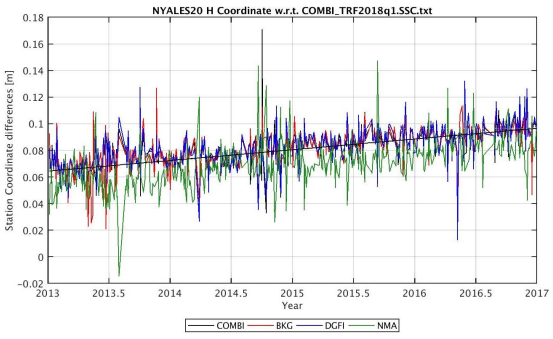

Fig. 2 Differences between the height component of NYALES20 and a reference frame solution from the third solution. Provided by Sabine Bachmann, BKG.

Table 1 Solutions submitted to the CCIVS for testing. The first column indicates the solution number and the second column shows which sessions were analyzed. All 24-hour sessions for a given year were submitted. The third column shows which parameters were included in the submitted normal equations. The fourth and fifth column describes the problems with the solutions and how these were improved in later solutions.

No.	Data	Parameters	Problems/Comments	Difference w.r.t. to previous solution
1	2016	Station coordinates EOP	Estimates too close to a priori Low weight factor in the combination	Initial solution
2	1994–2016	Station coordinates Source coordinates EOP	Same as above Problems with source names	Software unchanged
3	2013–2016	Station coordinates EOP	Wrong sign on estimates Worse weight factor in combination Offsets and high variability in EOP	Fixed bug that caused too small estimates
4	2002–2016	Station coordinates EOP	Variations in LOD Otherwise OK	Fixed bug with estimate sign Updated EOP C04 file Increased a priori standard deviations for EOP
5	2002–2016	Station coordinates Source coordinates EOP	Not analyzed yet	Fixed bug with LOD sign Corrected source names

The magnitude of the estimates now seemed to be reasonable and the estimates were no longer too optimistic. But they were still slightly different from the other Analysis Centers and the combined solution. They appeared to have the opposite sign. This can, for instance, be seen pretty clearly in the height component at Ny-Ålesund in Figure 2.

In addition, the offsets observed in the previous solutions and the weight factor became worse instead of better. This behavior is also consistent with the sign error. The problem was traced back to the residual vector that turned out to have the wrong sign.

There were also some problems with the EOPs. There was an offset in UT1–UTC and a large variability in the estimates for most of the parameters compared to the other Analysis Centers.

The sign error was corrected and an updated version of the a priori EOP 14 C04 file was downloaded, which had not been updated locally since September 2017. Since then, IERS has made several changes and fixed problems with this time series[1]. The latest change was in April 2018. Especially, the UT1–UTC time series had large differences. The standard deviations for the EOP used in the a priori covariance matrix in the Kalman filter were also increased, as some values were artificially low. The final values used are summarized in Table 2.

Table 2 Default a priori covariance matrix used in **Where**. The matrix is a diagonal matrix with σ^2 on the diagonal.

Parameter	σ
Constant parameters	
Station coordinates	1 m
UT1–UTC	10 ms
LOD	10 ms
Polar motion	100 mas
Polar motion rate	100 mas/d
Precession/Nutation	100 mas
Radio source coordinates	2.5×10^{-7} rad
Piecewise Linear Parameters (offset and rate)	
Clock	1 m and 1 m/h
Wet troposphere	1 m and 1 m/h
Horizontal gradients	1 m and 1 m/h

A fourth solution was submitted with processed sessions from 2002–2016 at the end of June. This time the results were more promising. The station coodinates and EOP estimates seemed to be comparable with other Analysis Centers. For instance, Figure 3 shows the height component at NYALES20, which clearly improved compared to Figure 2. Figure 4 shows the difference between the estimated UT1–UTC and the combined solution. Figure 5 shows the same but for LOD. The high variations in LOD are still a problem, but UT1–UTC and the other EOPs (not shown here) agree well with those from other Analysis Centers.

[1] http://hpiers.obspm.fr/iers/eop/eopc04/updateC04.txt

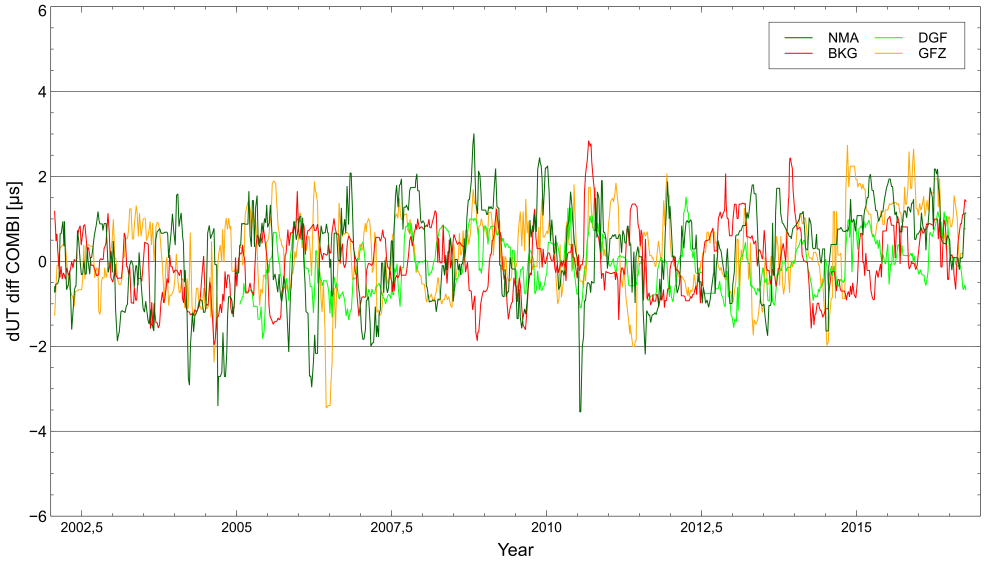

Fig. 4 Differences between UT1–UTC and the combined solution for different Analysis Centers from the fourth solution. Provided by Sabine Bachmann, BKG.

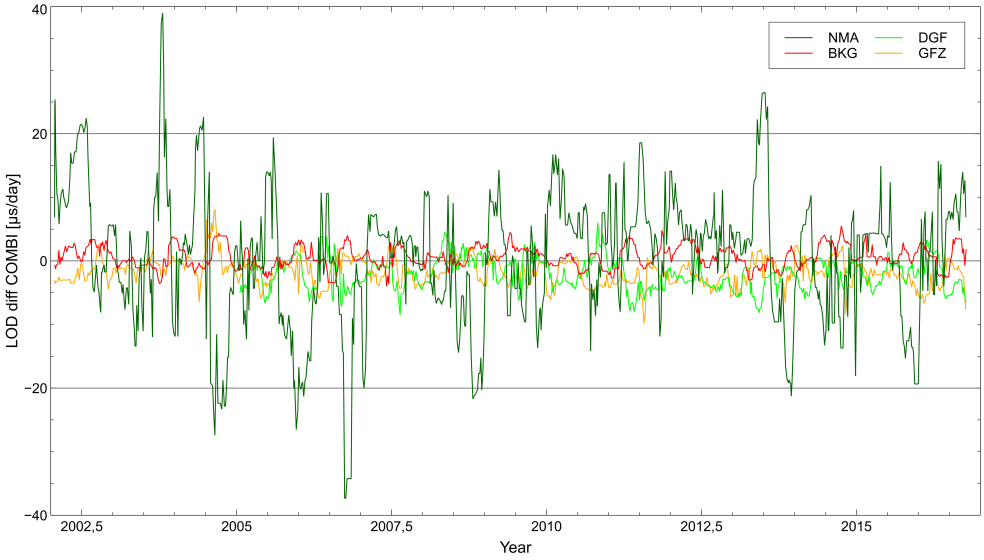

Fig. 5 Differences between LOD and the combined solution for different Analysis Centers from the fourth solution. Provided by Sabine Bachmann, BKG.

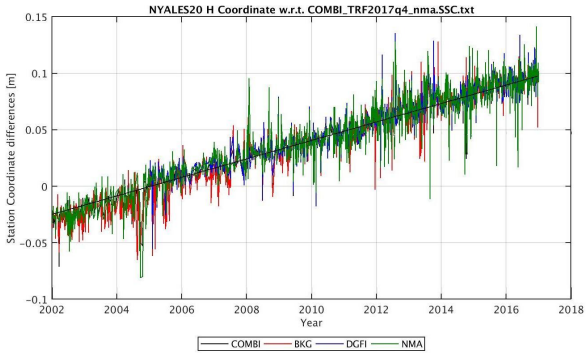

Fig. 3 Differences between the height component of NYALES20 and a reference frame solution from the fourth solution. Provided by Sabine Bachmann, BKG.

A sign error in the partial derivatives of the LOD parameter was discovered and the sesssions from 2002 to 2016 were processed again. This fifth and currently final solution was submitted in August, but has not yet been analyzed by the CCIVS. The LOD bugfix is expected to improve the LOD estimates, but it is still undecided how to compute a good a priori value for LOD, so a bit more work might be needed. In addition, this solution reintroduced radio source coordinates, but with correct source names. Feedback on the fifth solution is anticipated soon.

5 Future Work

The immediate plan is to continue to submit analyzed sessions to the CCIVS to improve the quality of the solution. When the estimates of station coordinates and the EOP seem reasonable, the source coordinates will be added again. Also, with the disappearance of the NGS card file format, the vgosDb file format parser needs to be tested more extensively and improved.

When the quality is approved, the next step is to start analyzing regularly the R1 and R4 sessions and to establish good routines for upholding the timeliness requirement. The plan is to start regular analysis by the end of 2018. This step will involve a different set of challenges such as automation of the analysis and having qualified personnel available during vacations.

In addition, outliers should be studied more closely. Some sessions do not have enough usable observations to estimate the full set of parameters. These sessions require special handling, which complicates the road to automating (as much as possible) the analysis.

Finally, models need to be updated as new conventions and analysis strategies are being implemented in preparation for the next international terrestrial reference frame solution projected for 2020.

Acknowledgements

Thanks to Sabine Bachmann (BKG) at the IVS Combination Center for analyzing our solutions and providing great feedback and insights.

References

1. Behrend, D., Data Handling within the International VLBI Service, *Data Science Journal*, 12, pp. WDS81–WDS84, 2013, doi:10.2481/dsj.WDS-011.
2. Bierman, G., *Factorization Methods for Discrete Sequential Estimation*, Dover Books on Mathematics Series, Dover Publications, 2006.
3. Gibbs, R. G., Square root modified bryson-frazier smoother, *IEEE Transactions on Automatic Control*, 56(2), pp. 452–456, 2011, doi:10.1109/TAC.2010.2089753.
4. Kierulf, H. P., et al., VLBI analysis with the multi-technique software GEOSAT, in Behrend, D., Baver, K. D. (eds.), *IVS 2010 General Meeting Proceedings "VLBI2010: From Vision to Reality"*, NASA/CP-2010-215864, pp. 207–211, 2010.
5. Kirkvik, A.-S., Norwegian mapping authority analysis center IVS biennial report 2015–2016, in Baver, K. D., Behrend, D., Armstrong, K. L. (eds.), *International VLBI Service for Geodesy and Astrometry 2015+2016 Biennial Report*, 2017.
6. Kirkvik, A.-S., et al., Where - a new software for geodetic analysis, in Haas, R., Elgered, G. (eds.), *Proceedings of the 23rd European VLBI Group for Geodesy and Astrometry Working Meeting*, 2017.
7. Klopotek, G., et al., Results from the VLBI analysis software comparison campaign 2015, in Behrend, D., Baver, K. D., Armstrong, K. L. (eds.), *IVS 2016 General Meeting Proceedings "New Horizons with VGOS"*, NASA/CP-2016-219016, pp. 203–207, 2016.
8. Mysen, E., On the equivalence of Kalman filtering and least-squares estimation, *Journal of Geodesy*, 91(1), pp. 41–52, 2017, doi:10.1007/s00190-016-0936-3.
9. Schuh, H., Behrend, D., VLBI: A fascinating technique for geodesy and astrometry, *Journal of Geodynamics*, 61, pp. 68–80, 2012, doi:https://doi.org/10.1016/j.jog.2012.07.007.

A Comprehensive Data Set of the State of the Atmosphere Around the Geodetic Observatory Wettzell During the CONT17 Campaign

Thomas Klügel [1], Armin Böer [1], Torben Schüler [1], Walter Schwarz [1]

Abstract During the last continuous VLBI campaign CONT17, a comprehensive data set reflecting the atmospheric conditions around the Geodetic Observatory Wettzell was created. The recorded atmospheric parameters comprised the meteorological quantities taken from the local meteo station close to the surface, temperatures up to 1,000 m above the surface from a temperature profiler, total vapor and liquid water content from a water vapor radiometer, and cloud coverage and temperatures from a nubiscope. Vertical profiles of pressure, temperature, and humidity from radiosonde ascents and numerical weather models complement the data set. The graphical representation and comparison show a good correlation in general, but also some disagreements at special weather situations. The accuracy as well as the temporal and spatial resolutions of the individual data sets are very different and represent a sound basis for further investigations. The data set is available online at https://doi.pangaea.de/10.1594/PANGAEA.895518.

Keywords VLBI, CONT17, Geodetic Observatory Wettzell, atmosphere

1 Introduction

Continuous VLBI observations are designed to obtain highly accurate VLBI data for detailed studies of high frequency Earth rotation variations, reference frame stability, and daily to sub-daily site motions. The last campaign, CONT17 [IVS 2017], covered a time span of 15 days between November 28 and December 12, 2017. During this time span, a comprehensive data set of atmospheric observations and weather model data were acquired at the Geodetic Observatory Wettzell, where three radio telescopes contributed to three different networks, which were established for this campaign. The data set is available to all the interested users in order to provide an optimal data base for the analysis and interpretation of the CONT17 VLBI data. In addition, it is a good data set for the validation and comparison of tropospheric parameters resulting from different space techniques with regard to the establishment of a common atmosphere at co-location sites.

1. Geodetic Observatory Wettzell, Federal Agency for Cartography and Geodesy (BKG), Sackenrieder Str. 25, D-93444 Bad Kötzting, Germany

2 Data Base

During the CONT17 campaign, all atmospheric sensors deployed at Wettzell yielded continuous time series, in particular:

- local meteo station (surface pressure, temperature, humidity, wind, and rain),
- temperature profiler (radiometric temperatures up to 1,000 m above surface),
- water vapor radiometer (integral water vapor and liquid water content),
- nubiscope (cloud distribution, temperature, and height of cloud base).

In addition, radiosonde balloons were launched twice per day at 8:00 and 14:00 UTC during the entire campaign providing pressure, temperature, humidity, and wind data up to 26 km in height. The average height reached was 19 km. The data set is augmented by

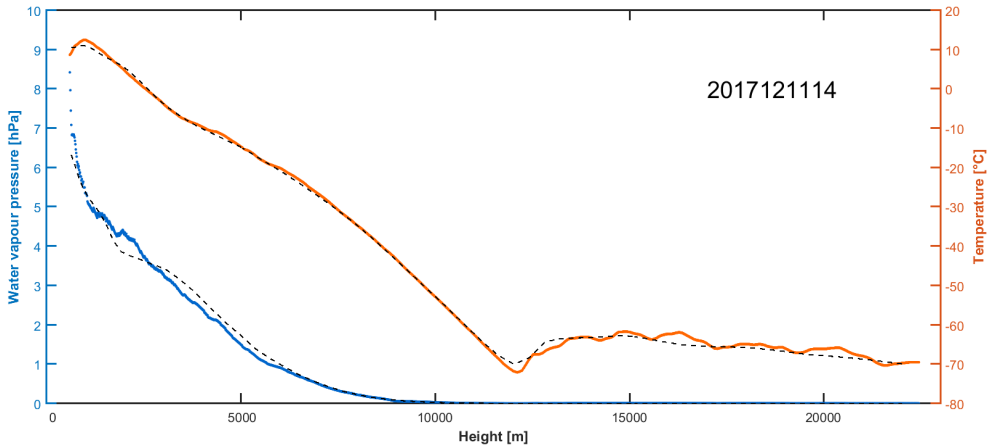

Fig. 1 Temperature (red) and water vapor pressure (blue) vs. height profiles of one particular radiosonde ascent as compared to the weather model profile at the launch location (dotted line).

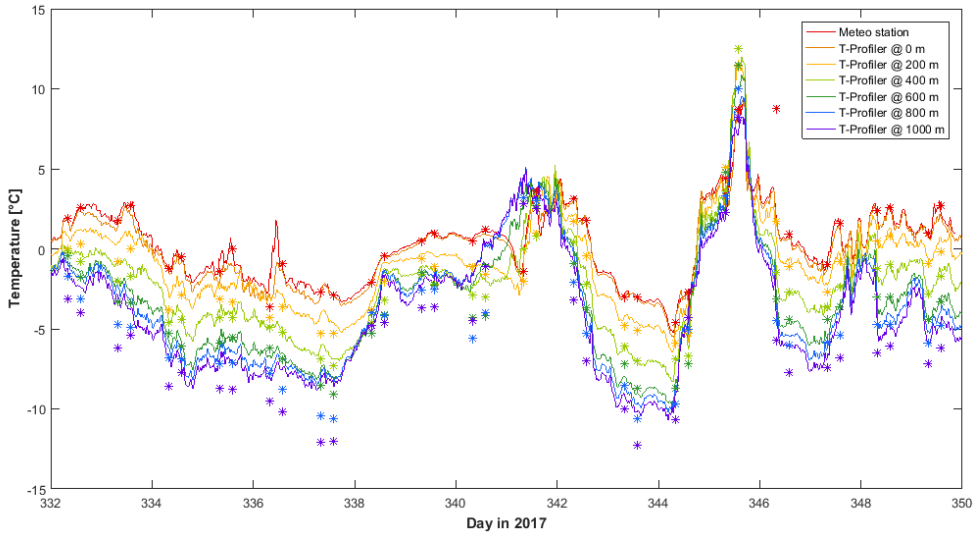

Fig. 2 Temperature profiler time series at particular heights compared to temperature record of meteo station and radiosonde data at equivalent heights (asterisks).

an excerpt of data from two different weather models. This comprises surface fluxes from the NCEP (National Center for Environmental Prediction), a global numerical weather model being interpolated to the location of Wettzell, and a set of 3-dimensional atmospheric state parameters from the ICON-EU model (ICOsahedral Nonhydrostatic model of EUrope) covering a 4-degree radius around Wettzell and a height of 22.5 km. This paper presents examples of some time series. A detailed description of the entire data set and the analysis procedure is given in [Klügel et al. 2018].

3 Results

All measurements plus the weather model data were compiled to obtain optimal information of the state of the atmosphere and to cross-check results from different sensors and models. The graphical representation and comparison show a good correlation in general, but it also shows some disagreements in special weather situations.

The vertical profiles recorded by the radiosondes are almost in good agreement to the ICON-EU model data at the Wettzell location. Some small scale pertur-

bations in the radiosonde data are not present in the model; however, the trend is always in accord. In the example shown in Figure 1, even the inversion close to the ground is indicated by the model, although in a less pronounced form.

Figure 2 depicts the traces of the temperature profiler at six different height levels and the ground temperature of the meteo station compared to temperatures measured by the radiosondes in the equivalent height. The profiler measures the blackbody thermal radiation of the atmosphere at a frequency of 56.6 GHz at varying elevations and computes the temperatures at different levels up to 1,000 m height in 50 m steps. While a good agreement is given at heights up to 400 m, the profiler systematically yields higher temperatures at higher levels; however, it provides a continuous record and helps identifying short-term features. As an example, the beginning and the end of the temperature inversions on days 341 and 354 can precisely be determined using the T-profiler. Figure 3 shows the time vs. height plot of the profiler records.

Data of the atmospheric water vapor content stem from radiosonde measurements and the water vapor radiometer (WVR). While the latter yields only the integral water vapor content given in the height of the eqivalent water column, the radiosondes provide the vertical distribution of water vapor; however, it is in a poor temporal resolution. Thus, the radiosonde humidity measurements were converted to a specific humidity and then integrated level-by-level up to the maximum height of the radiosonde ascent. Specific humidities from the ICON-EU model were treated in a similar way up to the upper model boundary. The comparison of the resulting integrated water vapor is shown in Figure 4. The overall agreement is good; however, the WVR produces outliers during periods of rain, which is a known issue due to droplets resting on the radiometer window. In general, the weather model slightly underestimates and the WVR slightly overestimates the water vapor content as measured by the radiosonde.

4 Conclusions

While the accuracy as well as the temporal and spatial resolutions of the individual data sets are very different, the data as a whole comprehensively characterizes the atmospheric conditions around Wettzell during the CONT17 campaign and represents a sound basis for further investigations. The complete data set is available online at https://doi.pangaea.de/10.1594/PANGAEA.895518

References

[IVS 2017] Continuous VLBI Campaign 2017. https://ivscc.gsfc.nasa.gov/program/cont17/ Last access: 30 October, 2018.

[Klügel et al. 2018] T. Klügel, A. Böer, T. Schüler, W. Schwarz. Atmospheric data set from the Geodetic Observatory Wettzell during the CONT17 VLBI campaign. Earth System Science Data (submitted).

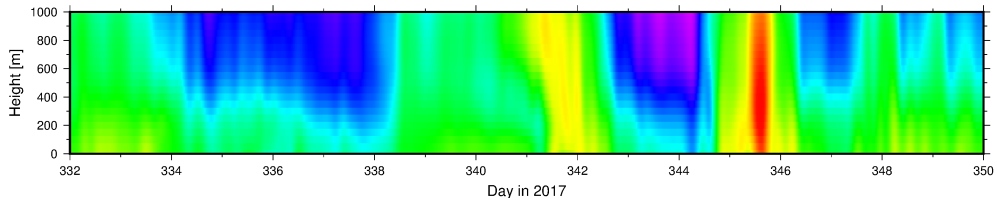

Fig. 3 Time vs. height plot of the temperature profiler records. The temperatures range from $+12°C$ (red) to $-10°C$ (violet).

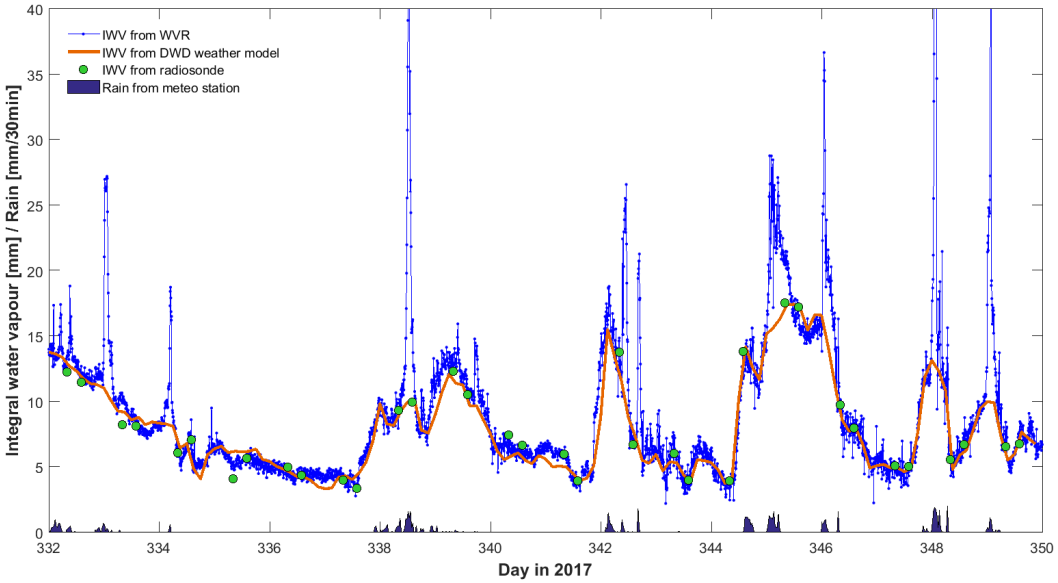

Fig. 4 Integrated water vapor (IWV) content as measured by the water vapor radiometer (WVR) compared to IWV values derived from weather model and radiosonde data. WVR spikes coincide with periods of rain.

Half-year Comparison of Precipitable Water Vapor Retrieved with Novel Ground-based Microwave Radiometer and GPS Receiver at Tsukuba and Numerical Weather Analysis Data

Ryuichi Ichikawa [1], Taketo Nagasaki [2], Osamu Tajima [3], Hiroshi Takiguchi [4], Kentaro Araki [5]

Abstract We have developed a state-of-the-art microwave radiometer named KUMODeS (KEK Universal Moisture and Oxygen Detection System) using millimeter-wave spectroscopy in order to monitor water vapor behavior. We have carried out comparative measurements of precipitable water vapor (PWV) in order to investigate the potential of KUMODeS/PWV measurements. Although further investigation is required to evaluate the performance of KUMODeS quantitatively, the preliminary results of PWV comparisons imply that the KUMODeS technology will be useful for retrieving the accurate behavior of water vapor with high temporal resolution.

Keywords water vapor radiometer, millimeter-wave spectroscopy, GNSS, precipitable water vapor

1 Introduction

Wet troposphere delay (wet delay) especially causes serious errors for precise positioning using GNSS and VLBI measurements as is well known in space geodesy. The wet delay issue is also important for improving the accuracy of GNSS-based time and frequency (T&F) transfer using GNSS. We have developed a state-of-the-art microwave radiometer named KUMODeS (KEK Universal Moisture and Oxygen Detection System) using millimeter-wave spectroscopy for the high-resolution and high-precision monitoring of water vapor behavior. We expect that KUMODeS will be a useful tool for space geodesy, T&F measurements, and related study fields. Thus, we have carried out comparative measurements of precipitable water vapor (PWV) in order to investigate the potential of KUMODeS/PWV measurements.

1. National Institute of Information and Communications Technology (NICT)
2. High Energy Accelerator Research Organization (KEK)
3. Kyoto University
4. Japan Aerospace Exploration Agency (JAXA)
5. Meteorological Research Institute, Japan Meteorological Agency

2 KUMODeS

The High Energy Accelerator Research Organization (KEK) has developed a state-of-the-art microwave radiometer named KUMODeS in order to observe the rapid increase in water vapor content within one hour, which is a sign of severe weather [2]. A commercial water vapor radiometer (conventional WVR) can only measure the temporal behavior of water vapor within 4–6 minutes.

But, this temporal resolution is insufficient to predict rapid cloud generation that causes heavy rain fall. KUMODeS has a millimeter-wave spectroscopy system for the high-resolution and high-precision monitoring of water vapor behavior. KUMODeS measures spectra using two receivers with frequency bands of 20–30 GHz and 50–60 GHz as shown in Figure 1. The low-noise amplifier of the first receiver and a cold calibration source are implemented in a cryostat, which is maintained at 10 K in order to improve the sensitivity in the detection of the characteristic broad peak of water vapor at around 22 GHz. The second receiver is used to measure the absorption peaks of oxygen ($\sim$60

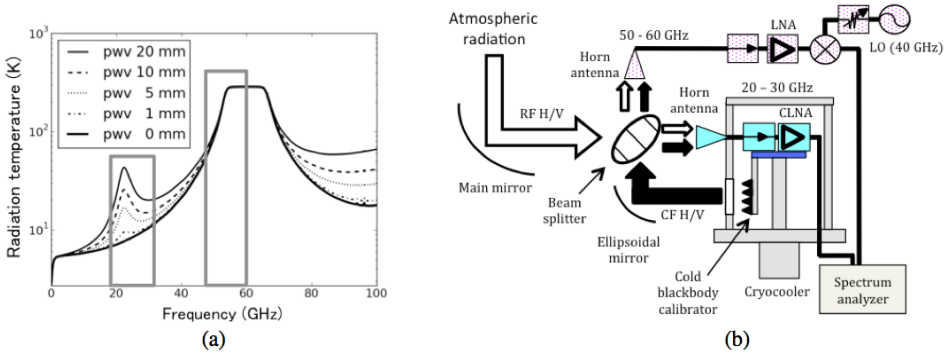

Fig. 1 (a) Effective temperature of atmospheric radiation as a function of observed frequency. (b) Conceptual overview of KUMODeS. Atmospheric radiation is divided into two frequency paths, 20–30 GHz and 50–60 GHz, by using a wire grid beam splitter [after Tajima et al., 2016 [2]].

GHz). More details about KUMODeS are shown in other papers [1, 2].

3 PWV Estimation by GPS

The GPS-based PWV is estimated reliably with 1–2 mm accuracy according to previous studies. In our comparison, GPS PWV values are retrieved from zenith wet delays (ZWDs), which are computed by subtracting zenith hydrostatic delays (ZHDs) from GPS-based zenith total delays (ZTDs). GPS-based ZTDs are estimated using conventional precise point positioning (PPP) processing. In this procedure, ZHDs are obtained from the in situ surface pressure and temperature.

4 Measurements

We performed KUMODeS- and GPS-based PWV measurements at Tsukuba from December 20, 2016 to July 15, 2017 (see Figure 2). Figure 3 shows an approximately half-year time series of PWV values derived from KUMODeS, GPS, and radiosonde (ROBS) observations. In addition, we also processed PWV variations using the operational local analysis (LA) technique developed by the Japan Meteorological Agency (JMA) during the events of a cold-front passage from December 20–24, 2016. Precipitation data at three stations around KEK are also demonstrated in the time series.

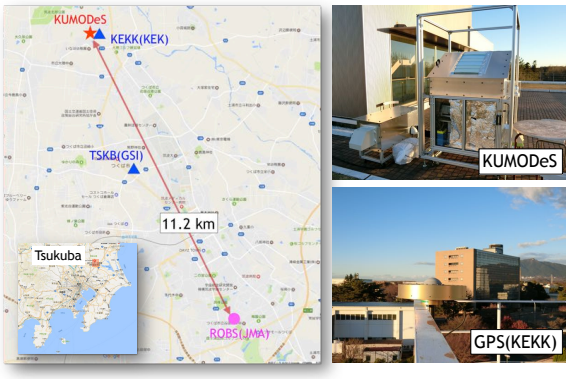

Fig. 2 Experimental setup. The KUMODeS station (star), the KEKK (KEK) and TSKB (GSI) GPS stations (triangles), and the JMA radiosonde launch site Tateno (circle) are indicated.

The PWV measurements derived from GPS and KUMODeS have temporal resolutions of 30 seconds and about two minutes, respectively. The estimates from the LA have a temporal resolution of one hour. The ROBS data is available every 12 hours.

Comparisons of about half a year of PWV values derived from KUMODeS, GPS, and ROBS show good agreement with the amplitudes and phase as shown in Figure 3. A comparison of time-series data obtained during the cold-front passage also shows good agreement between the PWV measurements retrieved from KUMODeS, GPS, and the LA between December 20 and 22, 2016. GPS-based PWV values highly correlate with KUMODeS-based PWV values except in rainy events as shown in Figure 4. Because we did not conduct in situ precipitation measurements

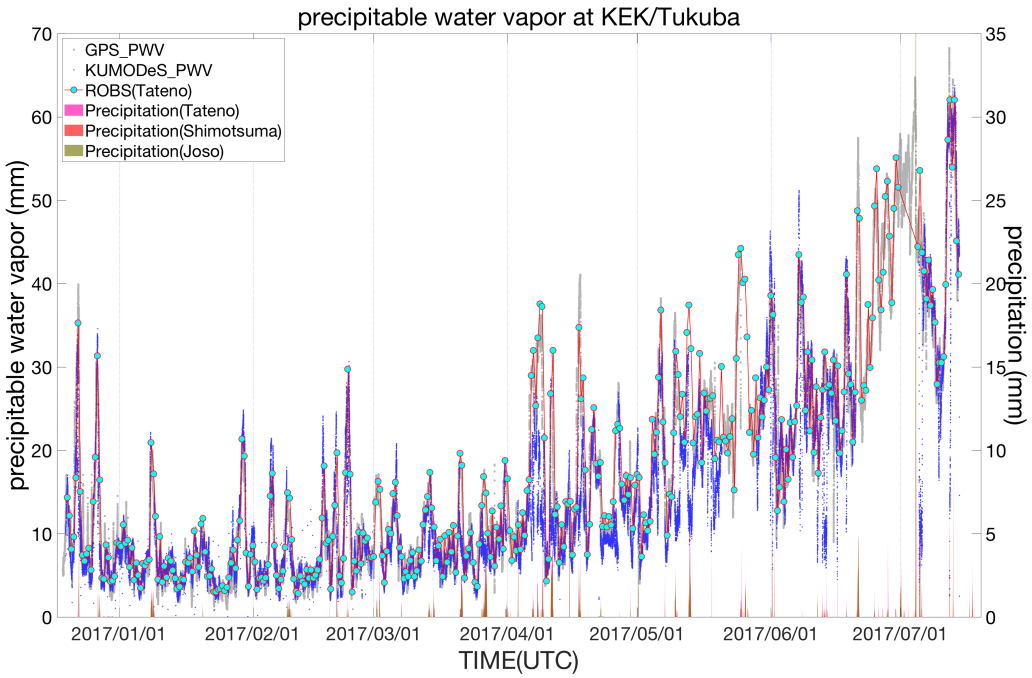

Fig. 3 Comparison of PWV values derived from KUMODeS (KEK), GPS (KEKK/KEK), and radiosonde (Tateno) in about six months during the period from December 20, 2016 to July 4, 2017. The precipitation data obtained around KEK are also shown in the time series.

near KUMODeS, we could not completely exclude the PWV estimates during rainy events from our comparisons. The correlation coefficient between the two data sets is 0.94.

5 Conclusions

We have developed a state-of-the-art microwave radiometer named KUMODeS using millimeter-wave spectroscopy. Although further investigation is required to evaluate the performance of KUMODeS quantitatively, the preliminary results of PWV comparisons imply the consistent performance and potential of KUMODeS technology.

6 Outlook

We have also developed a second prototype of KUMODeS. The characteristics of the second KUMODeS

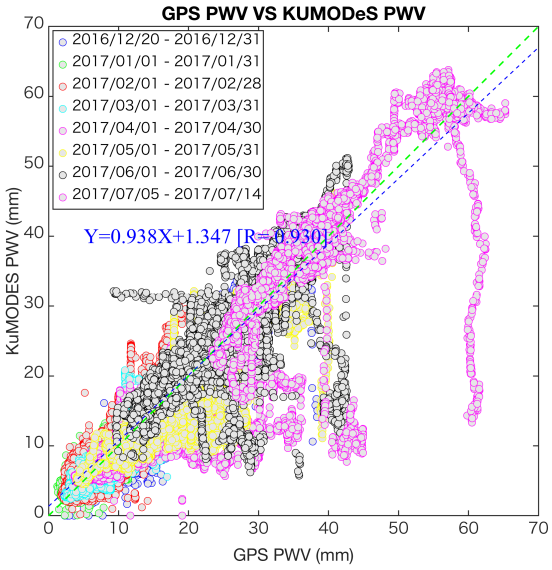

Fig. 4 Correlation plot. GPS PWV vs KUMODeS PWV estimates are shown. The regression curve for correlation and coefficients are also indicated in this figure.

prototype are compact form factor, light weight, and low power consumption. We are now planning to conduct test measurements using the second KUMODeS prototype in November 2018 (see Figure 5). In addition, we have started to develop a next-generation microwave radiometer that is suitable for field measurements such as monitoring volcanic activities and cumulonimbus cloud generation. We will implement accurate antenna pointing and azimuth-elevation driving in the new one. The new development will be completed at the end of the next fiscal year.

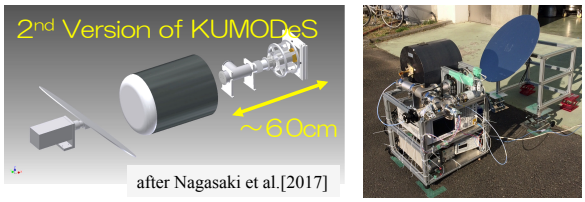

Fig. 5 Second prototype of KUMODeS [after Nagasaki et al., 2017 [3]].

Acknowledgements

This work was supported by JSPS KAKENHI Grant Number JP18H03828.

References

1. Nagasaki T., Araki K., Ishimoto H., Kominami K., and Tajima O., “Monitoring System for Atmospheric Water Vapor with a Ground-Based Multi-Band Radiometer: Meteorological Application of Radio Astronomy Technologies”, J. Low Temp. Phys., **184**, 674-679, https://doi.org/10.1007/s10909-015-1412-9, 2016.
2. Tajima O., Araki K., Ishimoto H., and Nagasaki T., “Sensing of the atmospheric water vapor with millimeter wave spectrometer KUMODeS”, 2016 Progress In Electromagnetic Research Symposium (PIERS), 4157-4161, doi: 10.1109/PIERS.2016.7735564, 2016.
3. Nagasaki T., Araki K., Ishimoto H., Ichikawa R., Takiguchi H., and Tajima O., “Long-term monitoring of water vapor by using a next generation microwave radiometer KUMODeS”, MTT38-P03, JPGU-AGU 2017, 2017.

Permanent Reference Point Monitoring of the TWIN Radio Telescopes at the Geodetic Observatory Wettzell

Swetlana Mähler [1], Thomas Klügel [1], Michael Lösler [2], Torben Schüler [1,3], Christian Plötz [1]

Abstract The reference point determination of VLBI telescopes is usually done every couple of years and allows for the identification of long-term drifts. In order to detect short-term motions like seasonal deformations, a monitoring system allowing more frequent measurements has to be established. At the Geodetic Observatory Wettzell a quasi-permanent reference point monitoring system was set up at the TWIN telescopes TTW-1 and TTW-2 in 2015 and 2013, respectively. The in-house software package called HEIMDALL allows the coordination of the VLBI and tacheometer schedules, the management of the moving targets, and the acquisition and storage of tacheometer and meteorological data in a database. The obtained data sets spanning a period of 1.5 and 3.5 years provide an insight into the three-dimensional motion of the invariant point. As expected, the largest motions occur in the vertical with an annual period, a maximum in the second half of July, and a peak-to-peak amplitude of nearly 2 mm. In addition, a weak seasonal signal of less than 1 mm is also visible in the horizontal component of both telescopes pointing towards southeast and showing a delay of two months with respect to the thermal peak. The correlation of the height variations with temperature records obtained from sensors inside the TTW-2 telescope structure yields correlation coefficients of up to 0.98 and coefficients of thermal expansion of 1.3 to 1.6 $\times 10^{-5}\,\mathrm{K}^{-1}$. These very high correlations allow the correction of thermoelastic height variations using the records of properly installed temperature sensors with RMS errors of the residuals of less than 0.15 mm.

Keywords Local ties, reference point, permanent monitoring, Geodetic Observatory Wettzell, TWIN radio telescopes

1 Introduction

The long-term stability of reference points of geodetic space techniques is crucial, since any temporal variation has a direct impact on the reference frame itself. Regular monitoring is thus an important task to prove the monument stability or to identify reference point motions. A local survey network being made up of deeply founded stable pillars provides the physical reference. A full survey is usually done every couple of years and allows for the identification of long-term drifts; however, short-term drifts like seasonal driven motions cannot be identified in this way. A quasi-continuous monitoring is required for this purpose.

While the terrestrial survey of reference points at non-rotating structures like GNSS and DORIS antennas or their reference markers can be done directly, the geometric reference point of VLBI and SLR telescopes has to be inferred indirectly. A convenient way to determine the reference point of VLBI antennas is the derivation of the invariant point (that is, the intersection of the azimuth and elevation axes) from numerous measurements of points on the moving telescope struc-

1. Geodetic Observatory Wettzell, Federal Agency for Cartography and Geodesy (BKG), Sackenrieder Str. 25, D-93444 Bad Kötzting, Germany
2. Faculty 1: Architecture, Civil Engineering, Geomatic, University of Applied Sciences Frankfurt, Nibelungenplatz 1, D-60318 Frankfurt am Main, Germany
3. University of the Federal Armed Forces Munich, Faculty of Aerospace Engineering, Werner-Heisenberg-Weg 39, D-85577 Neubiberg, Germany

ture. Since several hundred observations from different positions are usually done, a continuous monitoring is a time-consuming task. Therefore, an automated system was used for the permanent monitoring of the reference points. An appropriate procedure and corresponding software was tested and optimized during various campaigns at several radio telescopes; for instance, at Wettzell [Lösler 2008, Lossin et al. 2014], at Onsala [Lösler et al. 2013], and at Metsähovi [Kallio et al. 2016]. In this work, the Wettzell Twin Telescopes TTW-1 and TTW-2 were continously monitored over several years, yielding the most extensive data set in the context of reference point determination of radio telescopes.

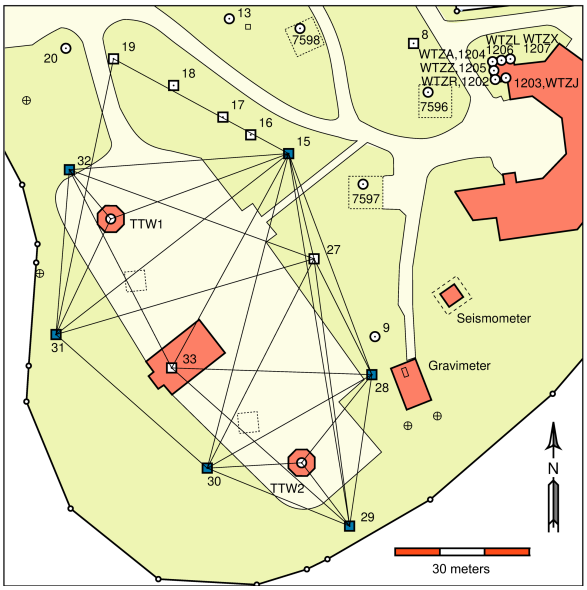

Fig. 1 Monitoring sub-network with used reference pillars, tacheometer positions (blue), and the telescope reference points.

2 3D-Monitoring Concept

For every reference point determination a full day of VLBI session time was required. A dedicated VLBI schedule was generated for this purpose, while a second schedule controls the tacheometer. Each telescope was observed from three different positions, which is a good compromise between accuracy and time consumption. The positions of the survey stations and the reference pillars, which are measured at regular intervals, are shown in Figure 1. There were 24 (TTW-1) and 26 (TTW-2) magnetic prisms attached to the telescopes back structure to serve as targets for the tacheometer measurements (Figure 2). The used in-house software package called HEIMDALL allows the coordination of the VLBI and tacheometer schedules, the management of the moving targets, and the acquisition and storage of the tacheometer and meteorological data in a database. Each session comprises about 700 single observations and takes nine hours per telescope. A detailed description of the measurement and analysis concept as well as the mathematical model is given in [Mähler et al. 2018, Lösler et al. 2013, Lösler 2008].

Fig. 2 Distribution of target prisms (bright spots) at TTW-2. The inset shows a prism in detail.

3 Results

The data sets obtained span a period of 1.5 and 3.5 years for TTW-1 and TTW-2, respectively. The standard deviations are in the order of 0.05–0.1 mm for the horizontal and 0.1–0.2 mm for the vertical component. The largest motions occur in the vertical with an annual period, a maximum in the second half of July, and a peak-to-peak amplitude of nearly 2 mm (Figure 3). In addition, a weak seasonal signal of less than 0.5 mm is also visible in the horizontal component of both telescopes.

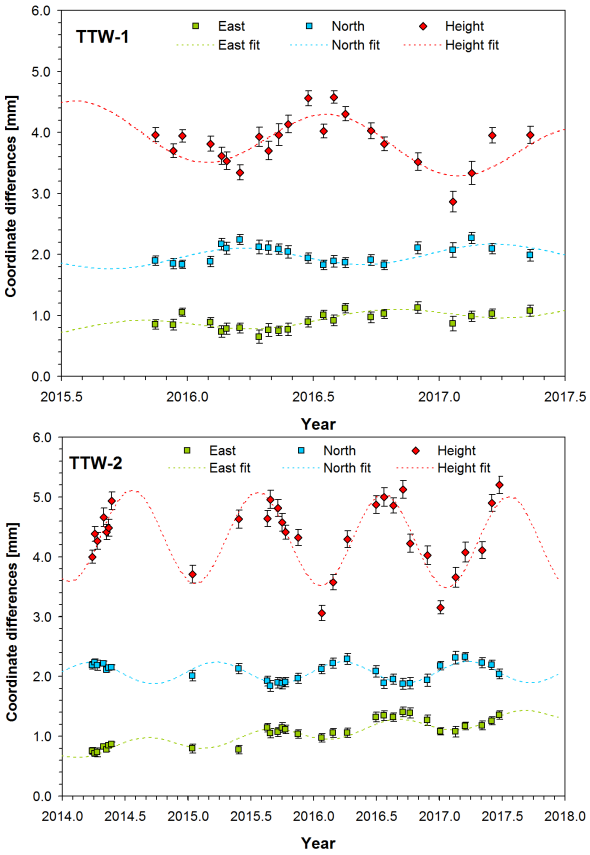

Fig. 3 Time series of the computed reference points for TTW-1 (above) and TTW-2 (below) with fitted annual sine curves. Series are vertically shifted, error bars are 1 sigma.

Phases and amplitudes of the annual signals and a linear drift were estimated using the approach

$$y = a + b \cdot t + c \cdot cos(\omega t) + d \cdot sin(\omega t)$$

with $\omega = 2\pi/year$ and the time t in years. The least-squares fit yields parameters given in Table 1. The offset a is irrelevant in this context. The linear drifts expressed by the parameter b are very small and only in the east component of both telescopes slightly significant. In contrast, the annual signal is significant in all components. The clear difference in the height component between both telescopes is not fully understood yet. It should be noted, however, that the short time span of 1.5 years at TTW-1 only allows a poor determination of the annual amplitude.

When combining the east and north components, the resulting amplitudes and directions of motions are very similar at both telescopes. The maximum occurs in the second half of September pointing towards the southeast with single amplitudes of 0.18 and 0.21 mm for TTW-1 and TTW-2, respectively.

Table 1 Parameters of the least-squares fits.

Component	b [mm/y]	c [mm]	d [mm]	Ampl [mm]	Phase [deg]	RMS err. [mm]
TTW1 East	0.18	0.031	−0.108	0.11	285.9	0.086
TTW1 North	0.07	0.037	0.147	0.15	76.0	0.091
TTW1 Height	−0.22	−0.405	−0.193	0.45	205.4	0.246
TTW2 East	0.15	−0.070	−0.105	0.13	236.4	0.066
TTW2 North	0.01	0.019	0.178	0.18	83.9	0.080
TTW2 Height	−0.03	−0.717	−0.284	0.77	201.6	0.232

4 Conclusions

The annual signal in the vertical component of both telescopes with its maximum at the thermal peak is compatible to the idea of thermoelastic deformations of the telescope structure. In order to confirm this assumption, linear regressions between temperature records from inside the telescope structure and the height variations were performed (Figure 4 and Table 2).

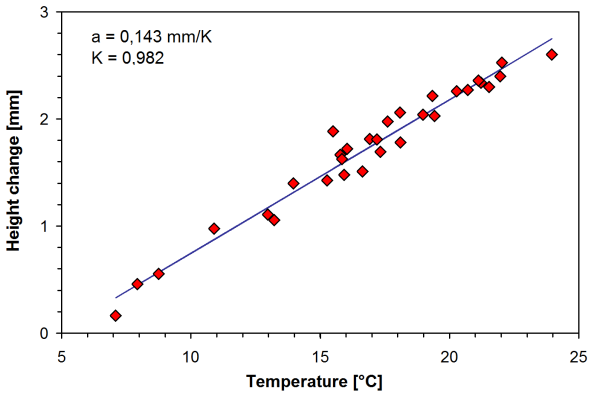

Fig. 4 Linear regression between the mean temperature record from the sensors T3E and T3W (see Table 2) and the measured height variations from TTW-2.

Correlation coefficients between 0.92 and 0.98 underline the strong linear relationship between temperature and height. The resulting slope parameter a translates into coefficients of thermal expansion between 1.3

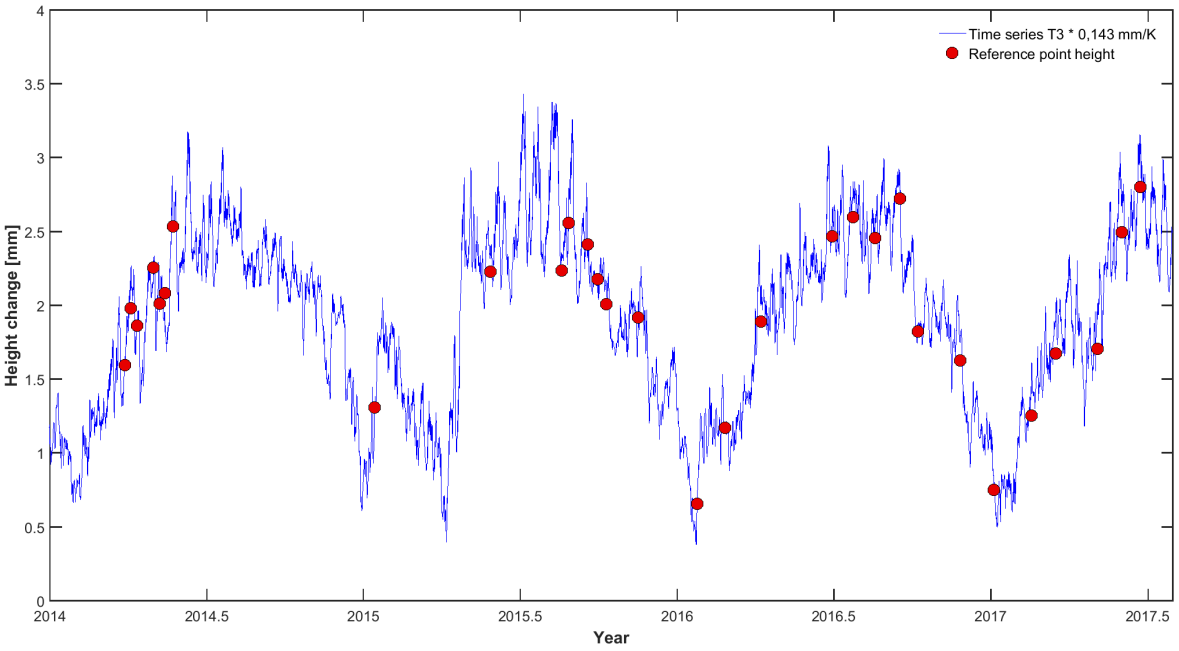

Fig. 5 Comparison of the reference point heights for TTW-2 and height variations resulting from temperature records taken in the wall of the TTW-2 tower.

Table 2 Regression parameters a and correlation coefficients r of linear least-squares fits between time series of different temperature sensors and measured height variations at TTW-2.

T-sensor	Position	a [mm/K]	r
T1E	Tower basement East	0.184	0.958
T1W	Tower basement West	0.163	0.951
T2E	Tower 1st floor East	0.181	0.940
T2W	Tower 1st floor West	0.190	0.925
T3E	Steel plate at tower top East	0.144	0.982
T3W	Steel plate at tower top West	0.143	0.980

and $1.6 \times 10^{-5}\,\mathrm{K}^{-1}$ when dividing by the total height of the telescope tower of 10.9 m.

Multiplying the regression coefficient of the most representative sensors T3E and T3W with their mean temperature record, the resulting linear expansion is opposed to the measured height variations in Figure 5. The height variations excellently fit the temperature time series and even identifies outliers as thermoelastic deformations. The resulting coefficient of thermal expansion of the best fitting time series (sensor T3) agree very well with common values for concrete and steel, which are in the order of $1.1\text{–}1.3 \times 10^{-5}\,K^{-1}$.

In the horizontal component, the origin of the annual signal is less clear. The delay of two months with respect to the thermal peak excludes an instantaneous thermoelastic distortion of the telescope structure as a direct cause. Small tilts of the telescopes' foundation caused by differential thermoelastic expansions in the underground could be a possible explanation of the seasonal horizontal motion of the reference point. However, the magnitude of motion being less than 0.5 mm is below the GGOS goal of 1 mm.

5 Outlook

The very high correlation between height and temperature allows the correction of height variations using the records of appropriately installed temperature sensors with RMS errors of the residuals of less than 0.15 mm. In this context the choice of the temperature measuring point is crucial, since it must represent the average internal temperature of the telescope structure. This height correction can also be applied to other radio telescopes using proper coefficients of thermal expansion or, in order to achieve higher accurary, performing a measuring campaign over 1–2 years using the monitoring system proposed in this paper to obtain these coefficients.

References

[Kallio et al. 2016] U. Kallio, M. Lösler, S. Bergstrand, R. Haas, C. Eschelbach. Automated simultaneous local ties with GNSS and robot tacheometer. Proceedings of the 9th IVS General Meeting "New Horizons with VGOS", NASA/CP-2016-219016, 154–158.

[Lösler 2008] M. Lösler. Reference point determination with a new mathematical model at the 20 m VLBI radio telescope in Wettzell. J Appl Geod, 2(4), 233–238. DOI 10.1515/JAG.2008.026.

[Lösler et al. 2013] M. Lösler, R. Haas, C. Eschelbach. Automated and Continual Determination of Radio Telescope Reference Points with Sub-mm Accuracy Results from a campaign at the Onsala Space Observatory. J Geod, 87(8): 791–804. DOI 10.1007/s00190-013-0647-y.

[Lossin et al. 2014] T. Lossin, M. Lösler, A. Neidhardt, R. Lehmann, S. Mähler. The usage of recursive parameter estimation in automated reference point determination. Proceedings of the 8th IVS General Meeting "VGOS: The New VLBI Network", 344–348. Science Press (Beijing).

[Mähler et al. 2018] S. Mähler, T. Klügel, M. Lösler, T. Schüler. Permanentes Referenzpunkt-Monitoring der TWIN-Radioteleskope am Geodätischen Observatorium Wettzell. Allgemeine Vermessungsnachrichten 127 (7): 209–219.

Session 5

Extending the Scope of VLBI Usage/Applications

Observing the APOD Satellite with the AuScope VLBI Network

Andreas Hellerschmied [1], Lucia McCallum [2], Jamie McCallum [2], Johannes Böhm [1], Jing Sun [3]

Abstract The Chinese APOD-A nano satellite, launched in September 2015, is the first LEO satellite co-locating three space-geodetic techniques including VLBI. Being equipped with a dual-frequency GNSS receiver, an SLR retro-reflector, and a VLBI beacon transmitting DOR tones in the S- and X-band, it can be considered as a first prototype of a geodetic co-location satellite in space. With the focus on VLBI observations we present a series of experiments carried out by the AuScope geodetic VLBI array in November 2016. These experiments represent first observations of a LEO satellite by VLBI radio telescopes with the goal of deriving baseline delays as common in the geodetic VLBI. In this paper we give an overview on the applied process chain that covers all tasks and aspects from scheduling and observations, over correlation and fringe fitting, to the actual data analysis. To stay as close as possible to the operational analysis scheme for geodetic VLBI sessions, we widely adopted the use of standard software such as DiFX for correlation and the Haystack Observatory Post-Processing System (HOPS). In the subsequent analysis of the derived delays in the Vienna VLBI and Satellite Software (VieVS) we find residuals in the range of a few nanoseconds. VieVS provides options to estimate a variety of geodetic parameters based on such data, including orbit offsets. The discussed experiments represent the first end-to-end realizations of VLBI observations of a tie satellite on a LEO orbit and are a valuable resource for future, more sophisticated space tie satellite missions in the style of E-GRASP/Eratosthenes.

1. Technische Universität Wien, Austria
2. University of Tasmania, Australia
3. National Astronomic Observatory, China

Keywords APOD, VLBI satellite tracking, AuScope

1 Introduction

The co-location of space-geodetic techniques (including VLBI) on Earth-orbiting satellites bears promising prospects regarding inter-technique ties. For example, observations of a satellite equipped with SLR, DORIS, VLBI, and GNSS capabilities would enable establishing technique ties in space, supplementary to the local ties at co-location sites on the ground used for the ITRF combination (e.g. Altamimi et al., 2016). Such an approach was followed by two major satellite missions, GRASP (Nerem and Draper, 2011) and E-GRASP/Eratosthenes (Biancale et al., 2017), which were proposed to NASA and ESA, respectively. Although their scientific significance was recognized, both missions were eventually not approved.

Contrary to the SLR, DORIS, and GNSS, which are routinely applied for satellite tracking, observations of satellites with geodetic VLBI systems (aiming at deriving observables in terms of group delays) are non-standard. Hence, suitable tracking and data processing schemes are still a matter of research. Over the past years different groups worked on improved satellite observation capabilities of VLBI and reported on successful tracking experiments. However, due to the lack of suitable targets for VLBI, mostly GNSS satellites were observed in the L-band, e.g. Plank et al. (2017), Hellerschmied et al. (2014), Tornatore et al. (2014), and Haas et al. (2017).

The first opportunity for carrying out satellite observations in the S- and X-band, which are routinely observed by geodetic VLBI and compatible to stan-

dard receiver equipment, was provided by the Chinese APOD-A nano satellite (hereinafter abbreviated as APOD). As described in Section 2, APOD can be considered as a first prototype of a co-location satellite in a low Earth orbit (LEO) including VLBI capabilities. In this paper we describe the only coordinated series of VLBI observations of APOD which was observed in November 2016 by the AuScope geodetic VLBI array (Lovell et al., 2013). The goal of this case study was to derive observables in terms of group delays — as is common in geodetic VLBI — based on observations of satellite signals and by applying standard observation and data processing schemes as far as possible. This proceedings contribution is a summary of a more detailed paper by Hellerschmied et al. (2018).

2 The APOD-A Nano Satellite

APOD-A nano is a Chinese cube satellite launched in September 2015 and controlled by the Beijing Aerospace Control Center (BACC). It orbits the Earth in a circular near-polar orbit with an inclination of about 97°. At the time the described observations were carried out the orbit altitude was about 450 km. The geodetic payload consists of a dual frequency GNSS receiver (capable of processing GPS and Beidou signals), an SLR retro-reflector, and a VLBI beacon emitting narrow-bandwidth DOR tones in the S- and X-band.

The structure of the VLBI signal in the S- and X-band is indicated in Figure 2. In both bands a carrier tone (long black lines) is symmetrically surrounded by four DOR tones (short black lines), yielding a total frequency span of 10.3 MHz in the S- and 38.3 MHz in the X-band.

Unfortunately, the on-board GNSS receiver which is used for the precise orbit determination (POD) by BACC partly failed in January 2016. Consequently, the accuracy of the final orbit solution (used for the calculation of theoretical near-field delays, required for the correlation and data analysis) dropped from the initial level of a few cm to the level of 10 to 20 m. Also, the orbit predictions used for tracking APOD with the AuScope antennas showed uncertainties of up to 1 km. These circumstances had wide-ranging consequences at different stages of this study.

More details about the APOD mission, the payload, the VLBI signal, and the POD are discussed by Sun et al. (2018).

3 Experiments

Table 1 APOD sessions observed in November 2016 by AuScope. The session durations and the experiment codes are listed in columns two and three, respectively.

Date	Duration	Exp. code	Stations	Targets
11.11.2016	33 min	316a	Ke, Yg	APOD, quasars
12.11.2016	41 min	317a	Ke, Hb	APOD, quasars
12.11.2016	35 min	317b	Ke, Yg, Hb	APOD, quasars
13.11.2016	26 min	318b	Ke, Yg, Hb	APOD, quasars
13.11.2016	26 min	318c	Ke, Hb	APOD, quasars
13.11.2016	23 min	318d	Ke, Yg	APOD, quasars
14.11.2016	40 min	319a	Ke, Yg, Hb	APOD, quasars
27.11.2016	24 h	a332	Ke, Yg, Hb	APOD, quasars

APOD was tracked by the three AuScope antennas — HOBART12 (Hb), KATH12M (Ke), and YARRA12M (Yg) — whenever there was common visibility by two antennas from November 11 to 14, 2016, yielding in total seven short sessions with durations of about 30 minutes (see Table 1). Throughout these sessions, first a block of about five strong quasars was observed, followed by one to two APOD tracks, and then again a block of quasars. The quasar observations were used to check the signal chains and to calculate the initial clock model for the correlation. Experiment a332 basically represents a geodetic 24-hour session with 761 scans of strong quasars (min. 0.65 Jy), intersected by four APOD scans.

3.1 Scheduling and Observations

All observations were planned by using a dedicated satellite scheduling program (Hellerschmied et al., 2017) which is implemented as a module in the Vienna VLBI and Satellite Software (VieVS; Böhm et al., 2018). VieVS generated VEX-formatted schedule files for controlling the receivers and the subsequent correlation process. Furthermore, VieVS was used to write tracking files containing azimuth and elevation positions of APOD in one second intervals, calculated

based on orbit predictions by BACC. These tracking files could be directly loaded by the AuScope antenna control units and enabled to track the fast moving LEO satellite continuously while data was recorded.

The experiment design was mainly determined by continental-wide baselines (between 2,360 and 3,432 km, see Figure 1) and the very low orbit of APOD (about 450 km), which significantly limited common visibility of the target. Hence, this observation geometry only enabled observing of single baseline scans during one to three overpasses per day. The situation is shown in Figure 1 for the Scans 168 and 169 in Experiment a332. APOD crossed Australia in the North-South (or vice versa) direction and was first observed on the baseline Hb-Yg for about 1.5 minutes (Scan 168), followed by a second scan on the baseline Yg-Ke (about a five minute duration). These two scans serve as a generic example for all further discussions in this paper.

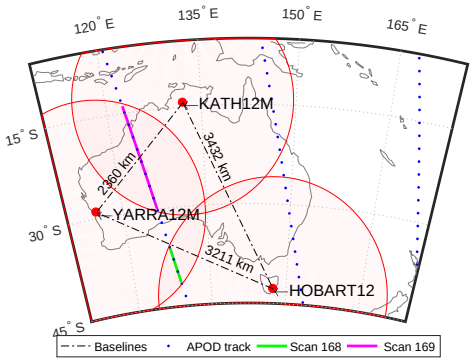

Fig. 1 Observation geometry in session a332. The antennas' projected fields of views are indicated by red circles. From Hellerschmied et al. (2018).

The observation mode aimed at goals: (1) to capture all APOD tones and (2) to allow the computation of reasonable multiband delays (MBD) based on observations of natural radio sources. For (2) a broad frequency span is needed. Hence, in total 16 16 MHz channels were recorded — six in the S- and ten in the X-band as indicated in Figure 2. All S-band tones of the APOD signal were recorded within one 16 MHz channel, whereas three channels were needed to record all X-band tones. A 2-bit sampling was used yielding a data rate of 64 Mbps per channel.

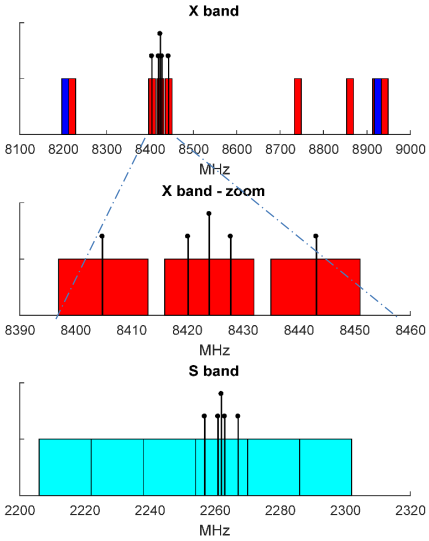

Fig. 2 Observation mode using ten 16 MHz channels in the X- and six in the S-band. APOD tones are indicated by black lines.

4 Correlation and Fringe Fitting

The recorded data was correlated with DiFX 2.5 (Deller et al., 2011) on the Vienna Scientific Cluster (VSC-3)[1]. For processing the APOD observations, the standard a priori delay model was replaced by a dedicated near-field delay model calculated in VieVS based on the final orbit solution by BACC. 32 kHz wide zoom bands centered on the DOR and carrier tones were used to extract the APOD signals from the recorded 16 MHz channels.

In the next step HOPS/fourfit[2] was used to calculate MBDs based on the correlated zoom band channels in the S- and X-band. We found smooth residual delays for both frequency bands in a range of typically ± 10 ns. The SNR is in general extremely high with values typically between 200 and 800.

5 Data Analysis

In order to mitigate the effects of the ionosphere, the ionosphere-free linear combination of the S- and X-band MBDs was calculated according to Alizadeh et al. (2013). In a first step, these values were ana-

[1] http://vsc.ac.at/systems/vsc-3/

[2] https://www.haystack.mit.edu/tech/vlbi/hops.html

lyzed in VieVS by investigating the observed minus computed (OMC) residuals. The theoretical delays were computed by applying the near-field delay model by Klioner (1991) and the VieVS default setup for geophysical modeling. Typically, the OMC residuals are on a level of about 10 ns. An example for two consecutive APOD scans is depicted in Figure 3. Investigations showed that the clear systematic signature (bent shape) can mostly be explained by an along-track offset in the orbit data which was used for modeling the computed delays. Taking into account the fact that the available orbit data is only accurate on the level of about 10 to 20 m, we concluded that it is mandatory to estimate orbit parameters. Otherwise, unmodeled orbit errors would propagate into other target estimates.

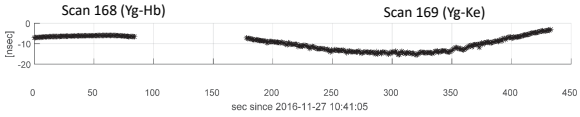

Fig. 3 Observed minus computed residuals of Scans 168 and 169 in Experiment a332.

In a simple test case, we estimated constant offsets for station clocks (Yg is the reference), zenith wet delays (ZWD), and the satellite orbit (three components) based on the OMC residuals plotted in Figure 3. The estimation results are shown in Table 2, and the post-fit residuals (WRMS of 9.5 cm) are depicted in Figure 4. Considering the rather non-ideal circumstances (weak observation geometry, low number of observations) the results are well within our expectations. Taking into account the low accuracy of the used orbit data, also the estimated orbit offsets meet our expectations — with the largest component (-7.8 m) in the along-track direction.

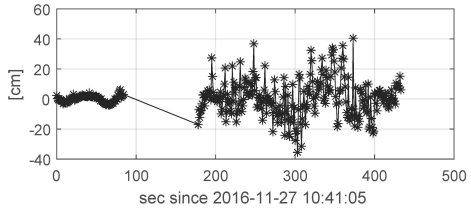

Fig. 4 Post-fit residuals of Scans 168 and 169 in Experiment a332.

Table 2 Estimation results from Scans 168 and 169 in Experiment a332.

Parameter	Estimates	Formal Errors
Clock offset, Hb	14.0 m	2.3 m
Clock offset, Ke	-1.1 m	1.9 m
ZWD, Hb	3.4 cm	1.7 cm
ZWD, Ke	14.3 cm	2.1 cm
ZWD, Yg	7.3 cm	1.7 cm
Orbit, radial	1.2 m	0.3 m
Orbit, along-track	-7.8 m	0.3 m
Orbit, cross-track	-1.9 m	1.3 m

6 Summary and Discussion

This paper describes a series of VLBI observations of the APOD-A nano satellite performed in November 2016 by the AuScope geodetic VLBI array. Although the observations were extremely challenging — mainly due to the low orbit of the satellite and its high speed — we were able to derive results in terms of OMC residuals on the nanosecond level. While the observations are still not sufficient to be used for actual frame tie studies, a simple test case proved that the parameter estimation in VieVS based on such data in principle works.

This case study also revealed some limitations. The available observation geometry (intra-continental baselines and the low orbit, see Figure 1) only allowed observing of a few single baseline scans per day. Hence, a denser tracking network would be needed to increase the number of observations. Furthermore, globally distributed tracking stations are a prerequisite to estimate reliable orbit parameters, as they would allow observing full orbit arcs.

For more details on this case study the authors refer to Hellerschmied et al. (2018).

Acknowledgements

This study made use of the AuScope VLBI infrastructure. It was supported by the Austrian Science Fund (FWF, projects SORTS I2204 and J3699-N29) and by the National Natural Science Foundation of China (Grant No. 11603001). We thank the Vienna Scientific Cluster (VSC-3) for supporting our VLBI work.

References

Alizadeh MM, Wijaya DD, Hobiger T, Weber R, Schuh H (2013) Ionospheric Effects on Microwave Signals. In: Böhm J, Schuh H (eds) Atmospheric Effects in Space Geodesy, Springer Berlin Heidelberg, Berlin, Heidelberg, 35–71, DOI 10.1007/978-3-642-36932-2_2

Altamimi Z, Rebischung P, Métivier L, Collilieux X (2016) ITRF2014: A new release of the International Terrestrial Reference Frame modeling nonlinear station motions. Journal of Geophysical Research: Solid Earth 121(8):6109–6131, DOI 10.1002/2016JB013098

Biancale A, Pollet A, Coulot D, Mandea M (2017) E-GRASP/Eratosthenes: a mission proposal for millimetric TRF realization. In: Conference Abstracts of the 19th EGU General Assembly, p 8752

Böhm J, Böhm S, Boisits J, Girdiuk A, Gruber J, Hellerschmied A, Krásná H, Landskron D, Madzak M, Mayer D, McCallum J, McCallum L, Schartner M, Teke K (2018) Vienna VLBI and Satellite Software (VieVS) for Geodesy and Astrometry. Publications of the Astronomical Society of the Pacific 130(986), DOI 10.1088/1538-3873/aaa22b

Deller AT, Brisken WF, Phillips CJ, Morgan J, Alef W, Cappallo R, Middelberg E, Romney J, Rottmann H, Tingay SJ, Wayth R (2011) DiFX-2: A More Flexible, Efficient, Robust, and Powerful Software Correlator. Publications of the Astronomical Society of the Pacific 123(901):275, DOI:10.1086/658907.

Haas R, Hobiger T, Klopotek G, Kareinen N, Yang J, Combrinck L, de Witt A, Nickola M (2017) VLBI with GNSS–signals on an Intercontinental Baseline – A progress report. In: Haas R, Elgered G (eds) Proceedings of the 23rd European VLBI Group for Geodesy and Astrometry Working Meeting, May, 2017, Gothenburg, Sweden, 117–121

Hellerschmied A, Plank L, Neidhardt A, Haas R, Böhm J, Plötz C, Kodet J (2014) Observing satellites with VLBI radio telescopes - practical realization at Wettzell. In: Behrend D, Baver K, Armstrong K (eds) IVS 2014 General Meeting Proceedings - "VGOS: The New VLBI Network", Science Press, 441–445

Hellerschmied A, Böhm J, Neidhardt A, Kodet J, Haas R, Plank L (2017) Scheduling VLBI Observations to Satellites with VieVS. In: van Dam T (ed) REFAG 2014: Proceedings of the IAG Commission 1 Symposium Kirchberg, Luxembourg, 13–17 October, 2014, Springer International Publishing, 59–64, DOI 10.1007/1345_2015_183

Hellerschmied A, McCallum L, McCallum J, Sun J, Böhm J, Cao J (2018) Observing APOD with the AuScope VLBI Array. Sensors 18(5), DOI 10.3390/s18051587

Klioner S (1991) General Relativistic Model of VLBI Observables. In: Alef W, Bernhart S, Nothnagel A (eds) Proceedings of the AGU Chapman Conference on Geodetic VLBI: Monitoring Global Change, Washington D.C., April 22-26, 1991, NOAA Technical Report NOS 137 NGS 49, 188–202

Lovell JEJ, McCallum JN, Reid PB, McCulloch PM, Baynes BE, Dickey JM, Shabala SS, Watson CS, Titov O, Ruddick R, Twilley R, Reynolds C, Tingay SJ, Shield P, Adada R, Ellingsen SP, Morgan JS, Bignall HE (2013) The AuScope geodetic VLBI array. Journal of Geodesy 87(6):527–538, DOI 10.1007/s00190-013-0626-3

Nerem RS, Draper RW (2011) Geodetic Reference Antenna in Space. GRASP proposal submitted in response to NNH11ZDA0120 prepared for National Aeronautics and Space Administration Science Mission Directorate September 29, 2011

Plank L, Hellerschmied A, McCallum J, Böhm J, Lovell J (2017) VLBI observations of GNSS-satellites: from scheduling to analysis. Journal of Geodesy 91(7):867–880, DOI 10.1007/s00190-016-0992-8

Sun J, Tang G, Shu F, Li X, Liu S, Cao J, Hellerschmied A, Böhm J, McCallum L, McCallum J, Lovell J, Haas R, Neidhardt A, Lu W, Han S, Ren T, Chen L, Wang M, Ping J (2018) VLBI observations to the APOD satellite. Advances in Space Research 61(3):823–829, DOI {10.1016/j.asr.2017.10.046}

Tornatore V, Haas R, Casey S, Pogrebenko S, Molera Calvés G (2014) Direct VLBI Observations of Global Navigation Satellite System Signals. In: Rizos C, Willis P (eds) Earth on the Edge: Science for a Sustainable Planet, Proc. IAG General Assembly, 2011, Springer Berlin Heidelberg, International Association of Geodesy Symposia, vol 6, 247–252

Toward Reliable Estimates of the Free Core and Inner Core Parameters from a Bayesian Inversion of VLBI and Gravimetric Data

Yann Ziegler [1], Sébastien B. Lambert [1], Séverine Rosat [2], Christian Bizouard [1]

Abstract During the last decades, many authors have provided their own estimates of the FCN parameters. Some of them have also tried to detect and characterize the FICN. The agreement between all of these studies is far from satisfying, however, whatever data set is used, either VLBI or gravimetric data. Before providing another set of estimates from a joint Bayesian inversion of data from both aforementioned techniques, we endeavor in the present work to quantify the accuracy with which the FCN and FICN could be determined, considering the available data and the likely errors that distort them. Our synthetic tests suggest that if the FCN period and quality factor could be estimated with uncertainties smaller than one day and 10% respectively, the FICN is still much more difficult to characterize, assuming it can be routinely detected at all.

Keywords FCN, FICN, Chandler Wobble, nutations, VLBI, gravimetry, Bayesian inversion

1 Introduction

The resonance due to the Earth's outer core and its nutation (Free Core Nutation, FCN) has long been characterized consistently from two independent data sets, namely the nutations amplitudes [3, 6, 4, 11, 15] estimated from Very Long Baseline Interferometry (VLBI) and the tidal gravimetric factors estimated from surface gravity variations recorded by superconducting gravimeters (SG) worldwide [7, 2, 10, 11]. The parameters of the Free Inner Core Nutation (FICN) have also been estimated but, so far, these values have been notably less reliable due to the weakness of the associated resonance amplitude, compared to the data uncertainty. This fact, along with the improvement of data analysis beforehand and still longer time series in both above mentioned techniques, has motivated our new attempt at estimating the Earth's interior parameters. Our main concern in this work is the assessment of the reliability of the estimated geophysical parameters. In particular, we focus on the FICN period and quality factor, which are especially difficult to reliably determine and for which previous studies have yielded results which are not in good agreement. In this regard, it is worth noticing that even the theoretical framework describing the FICN is still the topic of important ongoing works [9, 1].

1. SYRTE, Observatoire de Paris, Université PSL, CNRS, Sorbonne Université, LNE
2. IPGS/EOST, Université de Strasbourg/CNRS

2 Synthetic Data

To assess our capability to accurately determine the FCN and FICN parameters, we generate and invert synthetic data in which we can introduce perturbations as needed; the inversion of actual VLBI and gravimetric data will be discussed elsewhere. The synthetic data are generated using the formalism of [6], which we will name MHB in this work. In brief, we use the MHB resonance formula, whose parameters are also given in [6], to compute the synthetic nutation data set to be inverted. An example of such a data set with some noise added is depicted in Figure 1. The uncertainties associated with each data point is borrowed from the Paris Observatory VLBI analysis to be as realistic as possible. Then, we can add diverse perturbations to

these synthetic data: different levels of noise, outliers, or oceanic and atmospheric perturbations for example, and we check that we are able to properly recover the parameters used to generate the data.

In the following inversions, the annual prograde nutation is not included because of the abnormally small formal uncertainty associated with it, which puts an excessive weight on this specific data point. Indeed, because the amplitudes of the nutations have almost the same formal errors, the largest ones, such as the annual nutation, have especially small uncertainties, i.e. large weight, after normalization by the corresponding rigid Earth nutations, as required by the transfer function formalism of MHB. Apart from the annual prograde component, a few other nutations were also removed from the initial data set for similar reasons.

3 Synthetic Tests

We apply the Bayesian method to invert the synthetic nutations described in Section 2. Such an inversion technique is described in [4]; the key points of the Bayesian inversion are listed in [12], along with an interesting discussion of the philosophy behind it. We will not discuss here all the subtleties of the Bayesian inversion but it is worth reminding some of its important components. The estimated parameters are all given by a probability distribution instead of a single number with an associated uncertainty; these distributions reflect our limited knowledge. Thus, both the prior parameters and their posterior estimates take the form of distributions, the latter being summarized by *credible intervals* which have to be interpreted in the following way: knowing the data, there is a probability p that the real model (or parameter) is in the credible region (or interval) computed for value p. The credible intervals (CI) given here are computed for $p = 0.68$, which is similar to a 1-sigma interval in the case of a Gaussian posterior distribution. In the synthetic tests, to validate our method, we always check that the credible intervals provided by the Bayesian inversion are fully compatible with the expected results. The PyMC Python library [8] was used throughout this work to define the prior distributions and run the Monte Carlo Markov Chains on which our Bayesian inversion relies.

The first synthetic tests aim at estimating the influence of a broad but restrained random perturbation on all of the nutations. The origin of such perturbations can be diverse but in the synthetic tests, we simply generate them as a Gaussian noise whose standard deviation agrees with the claimed uncertainty of each data point. Of course, this agreement is not guaranteed to be valid in reality because the formal errors can be under- or overestimated for several nutations. For that reason, we will hereafter also discuss the influence of an outlier, a single strongly biased data point.

The inversion of noiseless synthetic data yields a period of -430.2 solar days for the FCN, as seen in the CRF, with a CI spanning 0.1 day. This value has to be compared with the target value of -430.21 days given by MHB and used to generate the synthetic data. The FCN quality factor is also properly determined, with the CI ranging from 19,800 to 20,200 for a target value of 20,046. The FICN is not so well characterized, even without any perturbation in the data: both its period and quality factor are determined with an uncertainty of about 10% to 20% and, for the period, the median estimate of $+995$ days is notably smaller than the target value of $+1,028$ days, keeping in mind that the data are noiseless. This fact suggests that the information contained in the data is not sufficient to strongly constrain the FICN parameters.

Adding noise in the data as described above, the results are similar for the FCN, despite, of course, somewhat larger CI. The resonance associated with the FCN is thus relatively insensitive to a realistic level of noise. On the contrary, several tests with the same level of noise but different noise values suggest that the estimation of the FICN parameters can be much more influenced by the noise. The difference between the median estimate and the target value can be as large as 20% for both the period and quality factor. Considering the weakness of the resonance associated with the FICN, it is surprising, however, that its parameters can still be generally well retrieved in spite of the substantial perturbations. Figure 2 depicts 1,000 models sampled by the Bayesian inversion for a synthetic data set with noise. The FCN is obviously well characterized whereas the spreading of the samples is much more visible for the FICN, even if, as stated before, the associated resonance is still reasonably well adjusted. When the noise level is increased by a factor of 2, the FICN cannot be retrieved anymore. The reason is twofold: firstly, the resonance becomes indistinguishable from the noise, and secondly, the uncertainty associated with the data does not reflect the actual er-

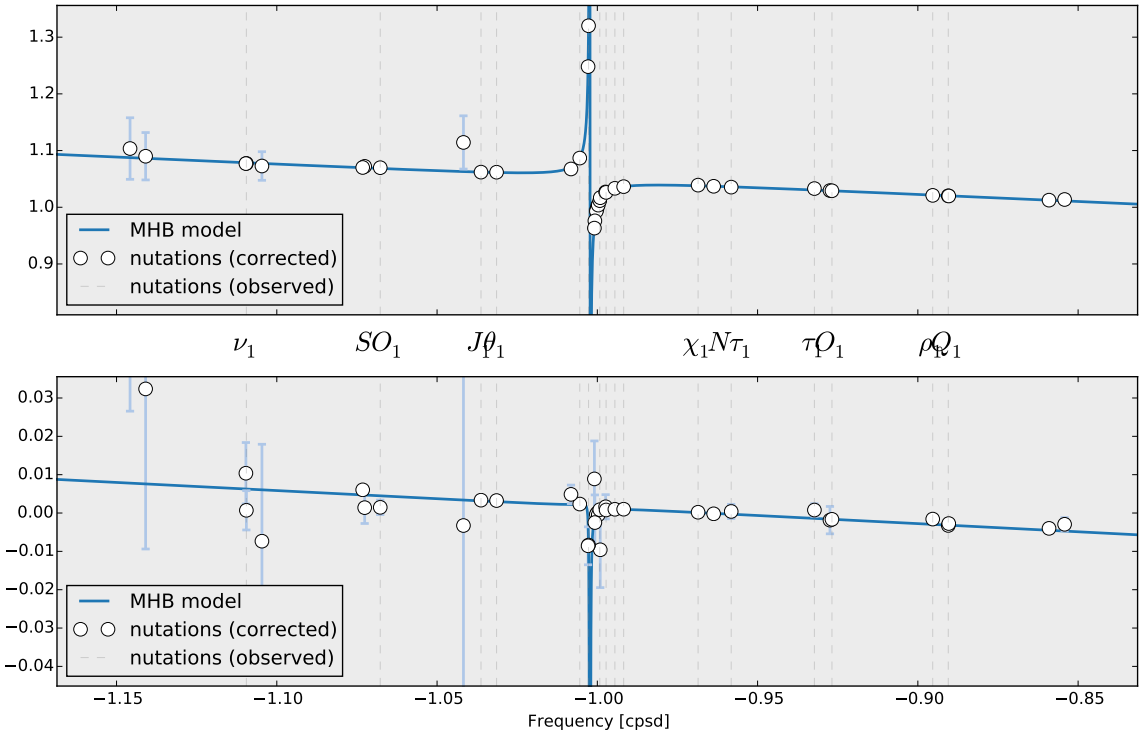

Fig. 1 Real (top) and imaginary (bottom) part of the MHB transfer function (blue line) and the generated synthetic data points with some noise added (white dot). The error bars are borrowed from the actual data of the Paris Observatory VLBI analysis. The frequency is in solar days in the terrestrial reference frame. Some nutations have been annotated with the corresponding tidal wave.

ror anymore, which is larger than expected, and the inversion fails to circumvent that problem. It is thus primordial not to underestimate the error on the nutations amplitudes before doing such an inversion.

Focusing on the FICN, we have also made synthetic tests with an outlier just next to the FICN resonance and synthetic tests with the FICN shifted toward higher or lower frequencies. These tests assess our ability to properly detect the FICN even if its period is somewhat larger or smaller than the actual standard estimate of about 1,000 days. This point is not critical for the FCN whose associated resonance is much bigger and surrounded by many nutations, contrary to the FICN. The results show that, even for the weak FICN resonance, neither an isolated outlier nor a departure of the resonance frequency from the expected value are enough to prevent a proper estimation of the eigenmode parameters. In the worst case, the CI become quite large (several tens of percent of uncertainty), especially regarding the quality factor, but the resonance can still be characterized with the target value of its parameters lying within the CI.

The last synthetic test we will discuss here is a complement to the noise tests, addressing the sensitive question of the atmospheric perturbation. Such a perturbation can reach up to 100 μas, with the largest perturbations being in the annual and semi-annual nutations. The oceans are a bigger perturbation for the nutations than the atmosphere, but they can be better corrected or even included in the model parameters, which is why we focus on the atmospheric effect here. The perturbations of the nutations amplitudes used in these tests were computed using the ECMWF atmospheric model. The results of adding the oceanic effect slightly differ from the results obtained when adding a realistic noise in the data. The target values are not within the CI anymore, except for the FICN period, which is probably just a lucky coincidence. The FCN period and quality factor do not dramatically depart from the target value, however, with an error on the period smaller than half a day and a quality factor close to 16,000 instead of 20,000. On the contrary, the quality factor of the FICN is notably overestimated, with a median value exhibiting both a large bias (1,500 instead of 640) and a large

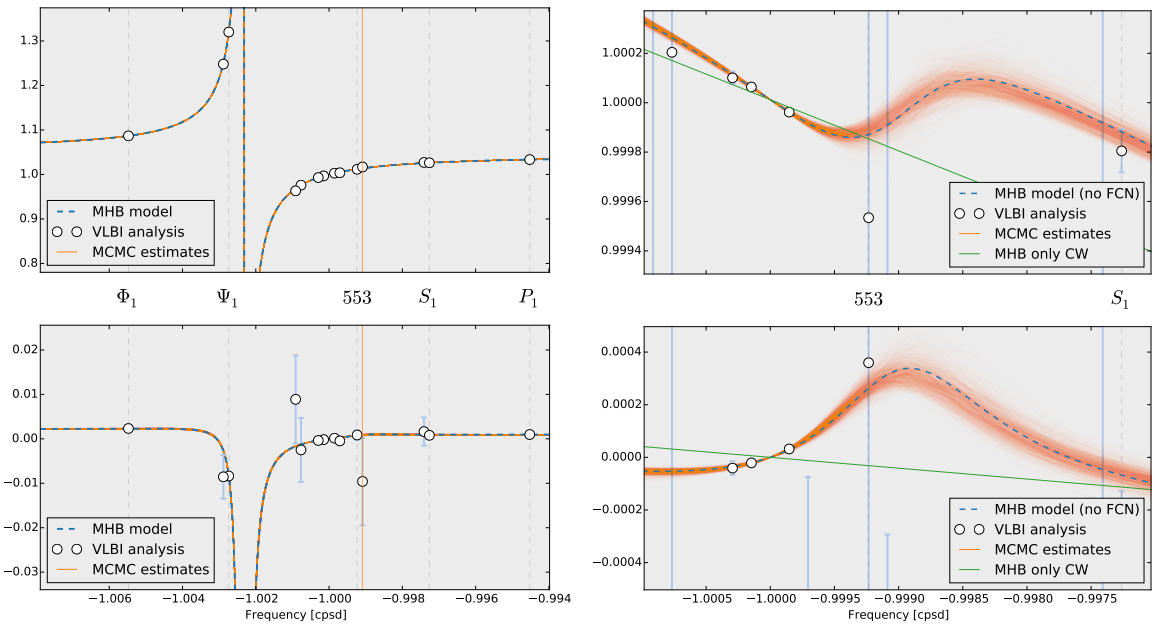

Fig. 2 One thousand models sampled by the Monte Carlo Markov Chain algorithm (orange) plotted against the MHB transfer function (dashed blue line). The white dots with blue error bars are the synthetic data points visible in Figure 1. The large resonance in the left plots is the FCN; at this scale the FICN is not visible but is indicated by the vertical orange line. On the right plots, the FCN was removed, and we have zoomed on the FICN frequency band. The green line indicate the transfer function with only the CW to highlight the effect of the FICN resonance.

uncertainty ($\pm 50\%$) which does not even compensate for the bias. The amplitude of the FICN resonance is significantly overestimated as well. These results prove that an uncorrected perturbation as small as the atmospheric one can have an especially strong influence on the estimation of the parameters of the FCN and FICN. Combining the atmosphere with other sources of errors, it is thus difficult to estimate the net effect of these perturbations when inverting real data.

The results of these synthetic tests confirm the high necessity to be particularly cautious when interpreting the parameters of the FCN and, especially, FICN.

4 Joint Inversion

After this systematic work on synthetic data, we can then return to the inversion of actual nutations amplitudes derived from VLBI nutation time series and tidal gravimetric factors estimated from SGs' time series. We will discuss elsewhere the preprocessing of such data and the actual numerical results obtained from their joint inversion. As yet, we rather discuss the potential advantages and pitfalls of such a joint inversion.

The combined inversion of VLBI and gravimetric data is much more complex than a mere numerical combination of each individual resonance parameter. Even if the FCN and, especially, the FICN are usually harder to characterize using gravimetric data, it does not prove a priori that the end result of the inversion will not be improved using both data set simultaneously. The gravimetric factors computed from gravity time series have larger uncertainties than the nutations obtained from VLBI and normalized by the rigid Earth nutations, but they also provide additional data points at some frequencies where the nutations are poorly determined. In addition, the larger uncertainties associated with the gravimetric factors better reflect the actual error made on their estimated value and are thus better suited to the Bayesian inversion, which is very sensitive to the data uncertainty, as stated earlier. Last but not least, because the gravimetric factors are derived from a completely different and independent technique, their joint use with VLBI data may also mitigate systematic errors in the latter.

5 Conclusion

Our synthetic tests suggest that we should be able to determine the FCN period with an uncertainty of at most one day, assuming the actual errors in the data are not much larger than expected. It might be interesting now to investigate whether the small variations of the FCN period from one study to the other, with an order of magnitude of one day or more, are of artificial or physical origin, as some authors have suggested a variability of the FCN frequency [13, 14]. Similarly, we have also found that the FCN quality factor could be probably determined now with an accuracy not larger than 10% (and not better than one percent), although not all recent studies have this level of agreement yet, for some unknown reason.

The FICN is still much harder to properly characterize. As illustrated and quantified by our tests, the resonance associated with this eigenmode is sensitive to most uncorrected perturbations in the inverted data set, and we are far from being able to determine its parameters accurately. Even in the idealistic case where there are no errors in the data, it is difficult to determine the FICN period with an error smaller than 30 days and an uncertainty smaller than 100 days. As soon as there are some uncorrected perturbations in the inverted data, the error can rise up to several hundreds of days. Thus, we might be able to detect and roughly characterize the FICN, but the interpretation of the estimated values for its period and, especially, quality factor must be made with great care. Such a conclusion also holds for the amplitude of the associated resonance and, importantly, for quantities related to the FICN parameters such as the electromagnetic coupling constant introduced by MHB and discussed more recently in [5].

Acknowledgements

This work was partly funded by CNES.

References

1. Crossley, D. J. and Rochester, M. G, 2014, “A new description of Earth’s wobble modes using Clairaut coordinates 2: results and inferences on the core mode spectrum”, Geophys. J. Int., 198, pp. 1890–1905, doi: 10.1093/gji/ggu232.
2. Defraigne, P., Dehant, V., Hinderer, J., 1994, “Stacking gravity tide measurements and nutation observations in order to determine the complex eigenfrequency of the nearly diurnal free wobble”, J. Geophys. Res., 99, pp. 9203–9213, and Correction 100, pp. 2041–2042, doi: 10.1029/94JB00133.
3. Herring, T. A., Gwinn, C. R., Shapiro, I. I., 1986, “Geodesy by Radio Interferometry: Studies of the Forced Nutations of the Earth - 1. Data Analysis”, J. Geophys. Res., 91, pp. 4745–4754, doi:10.1029/jb091ib05p04745.
4. Koot, L., Rivoldini, A., de Viron, O. and Dehant, V., 2008, “Estimation of Earth interior parameters from a Bayesian inversion of very long baseline interferometry nutation time series”, J. Geophys. Res. (Solid Earth), 113, B08414, doi: 10.1029/2007JB005409.
5. Koot, L., Dumberry, M., Rivoldini, A., de Viron, O., Dehant, V., 2010, “Constraints on the coupling at the core-mantle and inner core boundaries inferred from nutation observations”, Geophys. J. Int., 182, pp. 1279–1294, doi:10.1111/j.1365-246x.2010.04711.x.
6. Mathews, P. M., Herring, T. A. and Buffett, B. A., 2002, “Modeling of nutation and precession: New nutation series for nonrigid Earth and insights into the Earth’s interior”, J. Geophys. Res. (Solid Earth), 107, pp. 3–26, doi: 10.1029/2001jb000390.
7. Neuberg, J., Hinderer, J. and Zürn, W., 1987, “Stacking gravity tide observations in central Europe for the retrieval of the complex eigenfrequency of the nearly diurnal free-wobble”, Geophys. J. Int., 91, pp. 853–868, doi: 10.1111/j.1365-246x.1987.tb01671.x.
8. Patil, A., Huard, D. and Fonnesbeck, C., 2010, “PyMC: Bayesian Stochastic Modelling in Python”, J. Stat. Software, 35(4), pp. 1–81, doi: 10.18637/jss.v035.i04.
9. Rogister, Y. and Valette, B. 2009, “Influence of liquid core dynamics on rotational modes”, Geophys. J. Int., 176, pp. 368–388, doi: 10.1111/j.1365-246X.2008.03996.x.
10. Rosat, S., Florsch, N., Hinderer, J. and Llubes, M., 2009, “Estimation of the Free Core Nutation parameters from SG data: Sensitivity study and comparative analysis using linearized least-squares and Bayesian methods”. J. Geodyn., 48, pp. 331–339, doi: 10.1051/0004-6361/200811489.
11. Rosat, S., Lambert, S. B., Gattano, C. and Calvo, M., 2017, “Earth’s core and inner core resonances from analysis of VLBI nutation and superconducting gravimeter data”, Geophys. J. Int., 208, pp. 211–220, doi: 10.1093/gji/ggw378.
12. VanderPlas, J., 2014, “Frequentism and Bayesianism: A Python-driven Primer”, ArXiv e-prints, arXiv: 1411.5018 [astro-ph.IM].
13. Vondrák, J., Ron, C., 2009, “Stability of Period and Quality Factor of Free Core Nutation”, Acta Geodynamica et Geomaterialia.
14. Xu, J., Sun, H., 2009, “Temporal variations in free core nutation period”, Earthquake Science, 22, 4, pp. 331–336, doi:10.1007/s11589-009-0331-8.
15. Zhu, P., Rivoldini, A., Koot, L. and Dehant, V., 2017, “Basic Earth’s Parameters as estimated from VLBI observations”. Geodesy Geodyn., 8, pp. 427–432, doi: 10.1016/j.geog.2017.04.007.

Analysis of the Short VLBI Baseline at the Wettzell Observatory

Iván Herrera Pinzón [1], Markus Rothacher [1], Jan Kodet [2], Ulrich Schreiber [2]

Abstract Within this work, we present results on the assessment of the short baseline between the co-located VLBI telescopes at the Geodetic Observatory in Wettzell (Germany). VLBI sessions between July 2015 and June 2016 are processed using the VLBI capabilities of the Bernese GNSS Software to estimate geodetic parameters. Through the use of several parametrization approaches, this analysis shows a sub-millimeter agreement of the VLBI-derived baselines with the terrestrial measurements (local ties).

Keywords VLBI, co-location, short baselines, local ties, Terrestrial Reference Frame

1 Introduction

Short VLBI baselines, with baseline lengths of less than a few hundred meters, are much less suffering from errors in quasar coordinates, Earth rotation parameters, and tropospheric delays than long global baselines, and they are thus particularly well-suited to identify local effects and instrument-specific biases. These intra-technique experiments are expected to provide insights into systematic technique-related errors, eventually leading to a better agreement with the local ties at the fundamental sites. This constitutes a pre-requisite to improve the realization of the International Terrestrial Reference Frame (ITRF), to fulfill the GGOS goals in terms of accuracy and stability [6].

1. Institute for Geodesy and Photogrammetry. Swiss Federal Institute of Technology in Zurich (ETHZ)
2. Geodetic Observatory Wettzell. Institute for Astronomical and Physical Geodesy. Technical University Munich

For this purpose, the estimation of geodetic parameters (station coordinates, zenith tropospheric delays, clock offsets, and Earth orientation parameters) was performed for the short VLBI baseline at the Fundamental station Wettzell in Germany, realized by the legacy 20-m dish Radio Telescope Wettzell (RTW) and the new 13.2-m diameter TWIN Telescope Wettzell (TTW1). A tailored parametrization was developed, to work out the advantages and disadvantages of short baselines. Then, the main task was to compare these derived parameters with the terrestrial survey (for the coordinates) to study the performance of the VLBI solutions.

2 Methods

The data set used corresponds to 57 VLBI sessions of the IVS observing program, which contain the baseline RTW–TWIN1 [1]. These geodetic sessions were carried out between July 2015 and June 2016. Each session contains a subset of the stations of the global network. However, due to interference in cross-correlation caused by the presence of the pCal system in both radio telescopes, it was recommended to deselect the local Wettzell baseline after January 26, 2016. Therefore, the cross correlations of the short baseline are available only for 21 out of the 57 sessions. The VLBI data were taken from the NGS cards. Cable delays were applied to the data, when available. It is worth to notice that the cable delays for station TTW1 are not present, since the cable delay system was not available, so only those for the RTW could be applied. The NGS files were converted into baseline single difference files and processed in a tailored version of the Bernese GNSS

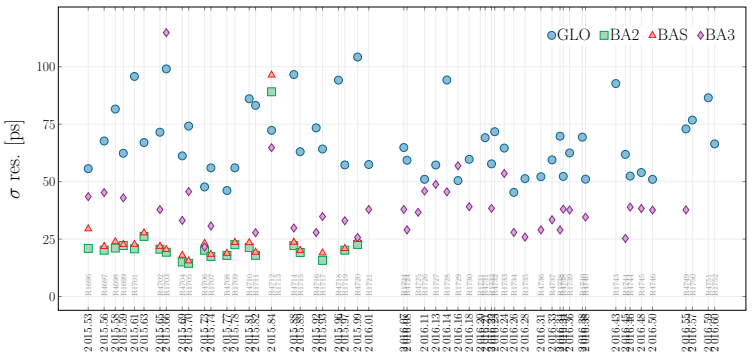

Fig. 1 Standard deviation of residuals per session [ps].

Table 1 Summary of the modeling and parametrization used.

	Global Sol. (GLO)	Baseline A (BAS)	Baseline B (BA2)	Baseline C (BA3)
Observations	All VLBI observations	WETTZ-WTZ13 observations	WETTZ-WTZ13 observations	NYALS-WTZ13 and NYALS-WETTZ
Coordinates	NNT/NNR w.r.t. ITRF2008	WETTZ constrained 1 mm	WETTZ constrained 1 mm	NYALS constrained 1 mm
Earth rotation	Rotation pole coordinates and UT1, 24 h intervals	not estimated	not estimated	not estimated
Troposphere	13 zenith wet delays VMF for every station and session	not estimated	13 zenith wet delays (VMF) for WETTZ in every session	13 zenith wet delays (VMF) for every station and session
Receiver clock	Two clock offsets for every station and session	Two clock offsets for WTZ13 per session	Two clock offsets for WTZ13 per session	Two clock offsets for WTZ13 per session

Software v5.2 [3,7]. For the parametrization, four different approaches were designed, where the modeling of the dry atmosphere, the solid Earth tides, and ocean loading are common for all these solutions. The first approach (**GLO**) is a global solution, where all VLBI observations are used. The datum for the station coordinates is defined by a minimum constraint condition, i.e., with NNR and NNT conditions w.r.t. ITRF2008. Earth rotation parameters, for 24-h intervals, are determined as a continuous piece-wise linear function. Zenith wet delays are estimated as a piecewise linear function with 2-h intervals, using the wet VMF model for mapping [2]. Receiver clock offsets are parameterized as a linear polynomial during the session, for each station except for WETTZELL. The second processing approach (**BAS**) is a short baseline solution, where only the RTW–TTW1 (WETTZELL–WETTZ13N) baseline observations are used. The datum for the station coordinates is given by constraining the coordinates of WETTZELL. Earth rotation parameters are not estimated, and receiver clock offsets are calculated every 24 hours for WETTZ13N, for each session. The main feature of this approach is that the troposphere wet delays between the two stations are not estimated, on the assumption that for such a small distance and small height difference, differences in tropospheric delays can be modeled. The third approach is a baseline solution (**BA2**), where only the WETTZELL-WETTZ13N baseline observations are used. Earth rotation parameters are not estimated and the datum and receiver clock offsets are defined in the same way as for the **BAS** solution. In contrast to the **BAS** solution, zenith wet tropospheric delays are estimated piece-wise linearly with a time resolution of 2 h and mapped with the wet VMF model for WETTZELL. Finally, to bridge the outage of data in 2016, a fourth processing chain (**BA3**) uses the station NYALES20, in Ny-Ålesund (Svalbard, Norway) with two baselines to Wettzell of ca. 3,300 km, to connect the two Wettzell telescopes. The datum for this solution is given by constraining the coordinates of the station NYALES20, while Earth rotation parameters are not estimated and receiver clock offsets are defined as in the **BA2** solution. Zenith wet tropospheric delays are set up as for the **GLO** solution. A summary of these strategies is shown in Table 1.

3 Results

3.1 Least Squares Residuals

To evaluate the quality of the estimation, the standard deviation of the residuals per session is provided. This step of the analysis is used to identify significant outliers. Session R1703 for the BA3 solution, and sessions R4712, R4716, and R4718 for the BAS and BA2 solution display an anomalous behavior (Figure 1). For the remaining sections of this work, these sessions are not considered for the statistical analysis of the results. The appropriate handling and down-weighting of the problematic observations is left for future work. After removing these sessions, the standard deviations of the residuals are 66.17 ps for GLO, 37.27 ps for BA3, 21.85 ps for BAS, and 19.90 ps for the BAS solution.

As expected, larger levels of noise are present in both global solutions (GLO and BA3), while the obtained standard deviations for the local solutions (BAS and BA2) is up to three times smaller. The improvement in the standard deviations obtained for the local baseline solutions supports the idea that these type of solutions are suitable for the precise analysis of the behavior of the local baseline, since the identification of error sources will be possible with more details than in the global solutions, where small effects are masked by the large residual values.

3.2 Clock Offsets WETTZ13N–WETTZELL

The parametrization used to calculate the clock corrections consists of two offsets per session with a linear behavior between these estimates. These two parameters may not accurately describe the session clock behavior during one session. To increase the time resolution and the statistical significance of the analysis of the clock behavior, a local baseline solution without the estimation of any parameter was done, where coordinates are given by the local tie and troposphere delays by models. In this way, the residuals of this estimation are equivalent to the clock corrections, plus the observation noise (and possibly other effects). Figure 2 shows the behavior for these residuals (straight lines, left axis) for sessions R4708 (left) and R4712 (right). Moreover, the deviations of these residuals/clock corrections w.r.t. a linear fit are calculated (right axis of Figure 2), and are used to characterize the clock behavior. Notice, for instance, how these residuals follow a quadratic pattern for session R4712, which suggests that modeling the clock with two clock parameters per session is not sufficient for this session. Table 2 summarizes the estimated drifts and the RMS of the residuals w.r.t. the linear fit for the sessions containing the short baseline. With clock drifts in the order of -16 to -18 ns/day and RMS values of the same order of magnitude as the residuals in Section 3.1, these data provide clock information comparable to the clock estimates of the BAS solution.

Table 2 Drift and RMS of the deviations from a linear fit for the VLBI clock estimates.

Session	VLBI Drift [ns/day]	VLBI RMS [ps]	Session	VLBI Drift [ns/day]	VLBI RMS [ps]
R4708	-18.032	16.6	R1715	-16.610	18.8
R1709	-18.188	25.3	R4716	-17.055	35.5
R4710	-18.160	21.5	R1717	-17.163	18.4
R1711	-18.423	28.7	R4718	-17.518	49.3
R4712	-17.832	85.9	R1719	-17.544	19.5
R1713	-16.922	118.0	R4720	-17.824	22.7
R4714	-16.422	23.1			

3.3 Coordinate Residuals and Repeatabilities (WETTZ13N)

The coordinate residuals w.r.t. the ITRF2008, in an ENU system, are calculated and displayed in Figure 3. A smaller scatter is obtained, as expected, for the local

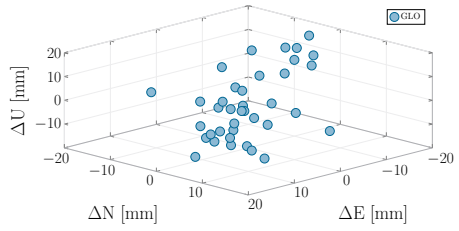

Fig. 3 Residuals per component [in mm] for the four approaches.

baseline solutions, where north and east components display a favorable behavior within a range of a few mm, while the height component shows a scatter about

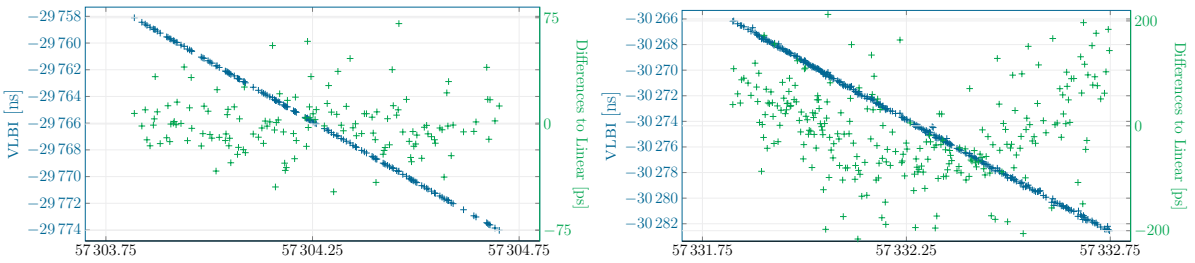

Fig. 2 Residuals from solutions without estimating any parameters (blue straight line) and differences to a linear fit (green scatter).

twice as large. Both global solutions (BA3 and GLO) show a significantly worse performance, due to the fact that most error sources grow with the baseline length. Nevertheless, these residuals do not exceed 10 mm. It is also apparent from Figure 3 that the estimation of the wet tropospheric delays is highly correlated with the performance of the height component, resulting in the larger scatter difference seen in the up component of the BAS and BA2 solutions. To compliment this analysis, the repeatabilities of the coordinates in an ENU system were calculated. The obtained values, $[1.21, 0.81, 2.84]$ mm for BAS, $[1.25, 0.85, 2.88]$ mm for BA2, $[4.53, 4.16, 9.14]$ mm for BA3, and $[7.11, 6.11, 9.51]$ mm for GLO, show in general higher values for the up component. The local baseline solutions BAS and BA2 display very good performance with values close to 1 mm and 3 mm, for the horizontal and vertical components, respectively.

3.4 Comparison with the Local Ties

The local ties from a terrestrial survey, described in [5], report a baseline length of 123.3070 m $\pm$ 0.7 mm. Baseline length differences w.r.t. this value are computed and represented in Figure 4. Moreover, the mean value and the repeatability (std. dev.) of the baseline length over the time series is calculated. This results in mean biases of -0.8 mm, -0.2 mm, -0.3 mm, and -0.1 mm for the GLO solution, BA3 solution, BAS solution, and BA2 solution, respectively. The corresponding repeatabilities are -4.9 mm for the GLO solution, 4.6 mm for the BA3 solution, 0.8 mm for the BAS solution, and 1.3 mm for the BA2 solution. The comparison of the baseline length shows an excellent agreement with differences clearly below 1 mm, albeit with much larger standard deviations for the global solutions. In addition to the baseline length, the differences per component w.r.t. the local ties are analyzed in an ENU system. Figure 5 displays these differences. Following the behavior of the repeatabilities, the up component shows a larger scatter, while the north component displays the best performance. This behavior is attributed to the orientation of the baseline, since RTW is located to the north of TTW1. From the four solutions, the BAS approach shows the best performance regarding the aforementioned indicators, on account of its parametrization, which is based on only data of the short baseline and estimates the smallest number

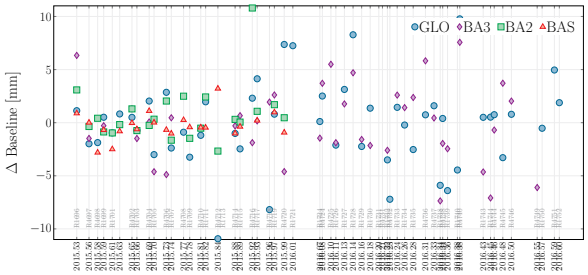

Fig. 4 Baseline length differences [mm] w.r.t. the local tie.

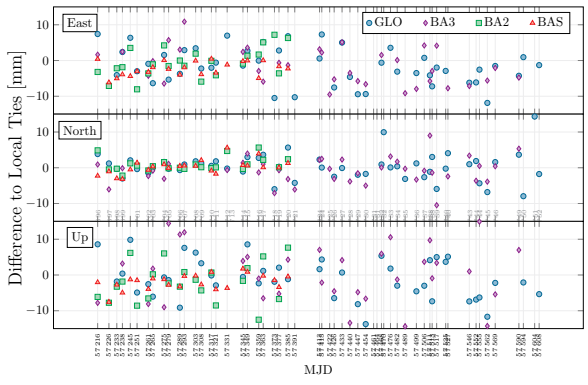

Fig. 5 ENU differences [mm] w.r.t the local tie.

of parameters (coordinates and clock offsets), which strengthens the estimated parameters. The vector of differences over the time series for this solution results in mean deviations of $[-2.04, -0.05, -1.60]$ and standard deviations of $[1.2, 0.8, 2.8]$ mm.

4 Summary and Future Activities

This work presents investigations on a short VLBI baseline, using several processing approaches in terms of local troposphere and clock parametrization. These solutions are subsequently compared with the local ties (baseline length and components), where a sub-mm agreement of the estimated baseline length with terrestrial measurements is found. The standard deviations found are about 1 mm and 3 mm for the horizontal and vertical component, respectively, and confirm the suitability of the BAS approach for the monitoring of VLBI short baselines. The strategy to avoid the estimation of the wet troposphere, as for such a small distance and small height difference, differences in tropospheric delays can be modeled, results in better coordinate repeatabilities, and thus is preferred for the study of the short baseline. Moreover, an analysis of the daily stability of the clocks was performed, where the deviations from a daily linear fit were considered. With daily drifts between -18 and -16 ns/day and average residuals of up to 50 ps, this analysis shows the limitations of the clock modeling and the need for further analysis, to reach the goals of accuracy and stability of GGOS. Future work will focus on the use of the local time transfer system, to improve the estimation of parameters.

Acknowledgements

The authors would like to thank the IVS [1] for providing the VLBI observations.

References

1. Behrend, D. Data Handling within the International VLBI Service. Data Science Journal (2013). doi:10.2481/dsj.WDS-011
2. Boehm, J., B. Werl, and H. Schuh (2006), Troposphere mapping functions for GPS and very long baseline interferometry from European Centre for MediumRange Weather Forecasts operational analysis data, J. Geophys. Res., 111, B02406, doi: 10.1029/2005JB003629.
3. Dach, R., Lutz, S., Walser, P., Fridez, P. Bernese GNSS Software Version 5.2. Astronomical Institute. Bern University (2015). doi:10.7892/boris.72297
4. Herrera Pinzón, I., Rothacher, M. Assessment of local GNSS baselines at co-location sites. J Geod (2018). doi:10.1007/s00190-017-1108-9
5. Kodet, J., Schreiber, K.U., Eckl, J. et al. Co-location of space geodetic techniques carried out at the Geodetic Observatory Wettzell using a closure in time and a multi-technique reference target. J Geod (2018). doi:10.1007/s00190-017-1105-z
6. Plag, H.P, Pearlman, M. Global Geodetic Observing System: Meeting the Requirements of a Global Society on a Changing Planet in 2020. Springer Berlin Heidelberg (2009). doi:10.1007/978-3-642-02687-4_9
7. Schmid, R. Zur Kombination von GPS und VLBI. PhD Thesis. Technische Universität München (2009)

Comparing Remote Atomic Clocks via VLBI Networks and Fiber Optic Links: the LIFT/MetGeSp Perspective

Monia Negusini [1], Roberto Ricci [1], Federico Perini [1], Mauro Roma [1], Claudio Bortolotti [1], Giuseppe Maccaferri [1], Matteo Stagni [1], Roberto Ambrosini [1], Cecilia Clivati [2], Davide Calonico [2], Anna Tampellini [2], Filippo Levi [2]

Abstract Very Long Baseline Interferometry experiments require an extremely precise synchronization between the atomic clocks keeping the time and frequency standards at radiotelescope observatories. Recently the availability of fiber optic links from a few radio observatories and their national metrological institutes has made the streaming of extremely stable frequency standards via optical atomic clocks possible (even two orders of magnitudes better than Rubidium or Hydrogen maser standards). Firstly, we present the infrastructure of the Italian Link for Frequency and Time (LIFT) and results of the MetGeSp project aimed at finally creating a common clock between two of the antennas of the VLBI Italian Network. Secondly, the results are shown from VLBI experiments in which the rms phase noise was used to accurately compare the synchronicity of atomic clocks located at a few European stations (Medicina, Noto, Yebes, Torun, and Matera). VLBI clock timing proves a valid alternative to satellite-based techniques such as the Global Navigation Satellite System or the Two-Way Satellite Time and Frequency Transfer.

Keywords Instrumentation: atomic clocks, Instrumentation: optical fibers, Instrumentation: VLBI

1 Introduction

The comparison of atomic clocks is important both *per se* and for Very Long Baseline Interferometry (VLBI) applications. Atomic clock comparisons, in particular between optical atomic clocks, are utilized for relativistic geodesy ([1], [2]) and in the future they will be instrumental for the redefinition of the SI second [3]. At the moment the primary standard is provided by Cesium fountains having a stability of the order 10^{-16} after a few hundred seconds of integration. In the future optical atomic clocks based on the Strontium or Ytterbium lattice technology will achieve a stability a factor of two better on a comparable integration time. At continental distances, frequency standard dissemination via optical fiber links is the most reliable and stable way of comparing high performance optical atomic clocks. For intercontinental distances, satellite techniques such as Global Navigation Satellite Systems (GNSS) and Two-Way Satellite Time and Frequency Transfer (TWSTFT) are still the most utilized ones. VLBI observations, in particular geodetic VLBI sessions, are currently being explored as a viable alternative to the less reliable GNSS and more expensive TWSTFT techniques.

A more stable frequency standard is also useful for VLBI observations:

- a narrower fringe search window can be achieved;
- the loss of phase coherence between stations can be mitigated ($\delta\nu/\nu < 1/\tau\nu \leq 10^{-13}$ where ν and τ are the observing frequency and integration time);
- the synchronization of Square Kilometer Array stations will benefit [4].

Moreover a better spectral purity of the atomic clock frequency standard obtained by an optical fiber link means that less Local Oscillator (LO) phase noise will be measured in single-dish/VLBI observations. Phase noise problems get more detrimental in the millimeter band as the LO phase noise scales as the square

1. INAF-Istituto di Radioastronomia
2. Istituto Nazionale di Ricerca Metrologica (INRIM)

of the number of multiplication steps from the 10 MHz RF signal to the sky frequency [5].

2 LIFT/MetGeSp Experiments

The LIFT (Italian Link for Frequency and Time) project and its successor (the Metrology for Geodesy and Space, in short MetGeSp, project) aim at providing Italy with an optical fiber link for frequency standard dissemination. The frequency standard generating clock is located at the Italian National Institute of Metrology (INRiM) in Turin. The link serves a metrological lab for relativistic geodesy in Modane (Frejus tunnel), the Milan Tech University, the INAF-Istituto di Radioastronomia radio station where radio and geodetic observations are performed, the Italian Lab for Non-linear Spectroscopy (LENS) in Florence where the accuracy of the optical clock frequency is tested, the Telespazio Facility in the Fucino Plain where one of the main stations of the European Galileo satellite network for global navigation is located, and finally the Matera geophysical station for space geodesy. The major radio astronomical goal of the MetGeSp project is the creation of a common clock between the Medicina 32-m radio telescope and the Matera 20-m radio telescope. A secondary goal of the project is providing the Medicina radio station with an accurate and stable frequency standard from Turin's INRiM for VLBI clock timing experiments with other (optical) atomic clocks abroad (see Section 4).

A detailed description of the optical fiber link is provided in [6] and [7]. For the purpose of this paper it will suffice to say that the RF signal generated by the INRiM clock is up-converted to the frequency of a 1.5 μm laser via an opto-electronic device (optical frequency comb), and the phase is kept in sync through a phase-locked loop. The laser signal is streamed through a 550-km dark fiber along which nine sub-stations equipped with Erbium-doped Field Amplifiers (EDFAs) counteract the signal attenuation. The EDFAs are remotely controlled from Turin to maximize their gain stability over time. A round-trip servo mechanism is also employed to provide a phase noise cancellation of the level of 10^{-19} in terms of frequency stability. Once at the Medicina radio station, the optical laser signal is regenerated and down-converted via an optical frequency comb to the RF domain. The resulting RF signal is compared to the local H-maser clock or used directly for VLBI.

The first geodetic experiment testing the LIFT infrastructure was the EUR137 in September 2015. The frequency standard provided by the LIFT link was alternated with the one of the local H-maser clocks and the data was analyzed as two separate stations in the same experiment. The results of this test are published in [8].

A few unlocks in the link suggested to us to start an unlock monitoring campaign lasting from May until early July 2017. During that campaign, a link uptime of about 97% was reported with very few and fixable unlocks caused by human activity at the commercial optical fiber sub-stations. H-masers in Turin and Medicina were compared and reported an Allan standard deviation of $\sigma_\tau \simeq 2 \times 10^{-14}$ on the phase difference after 10^3 seconds in agreement with expectations.

On July 6–7, 2017 and again on April 3–4, 2018 two geodetic 24-hour S/X-band sessions utilizing the VLBI stations in Medicina, Noto, and Matera were carried out to test the performance of the optical fiber link from Turin. The data were correlated using the Bologna DiFX ([9]) correlator and fringe fitted in HOPS *fourfit* [10]. The analysis was performed with CALC/SOLVE and nuSolve [11].

A few unlocks were still present in the former of the two test sessions, but these problems were fixed at the data analysis stage. In the latter test session no unlocks were detected. In the April 2018 test session only observation pairs from the Medicina-Matera baseline were used in the geodetic analysis solution. A plot with the group delay wrms residuals vs. observing time from the July 2017 session is shown in Figure 1 together with related statistics.

3 Analysis of CONT14 Campaign

To study how the VLBI and GPS techniques compare in determining clock models, we analyzed the clock solutions of the nine pairs of co-located stations taking part in the CONT14 geodetic campaign. The co-located stations were (VLBI/GPS): HOBART/hob2, HARTRAO/hrao, KOKEE/kokv, MATERA/mate, NYALES20/nya1, ONSALA60/onsa, WETTZELL/wtzr, YEBES40M/yebe, and ZELENCHK/zeck. The clock solutions were derived

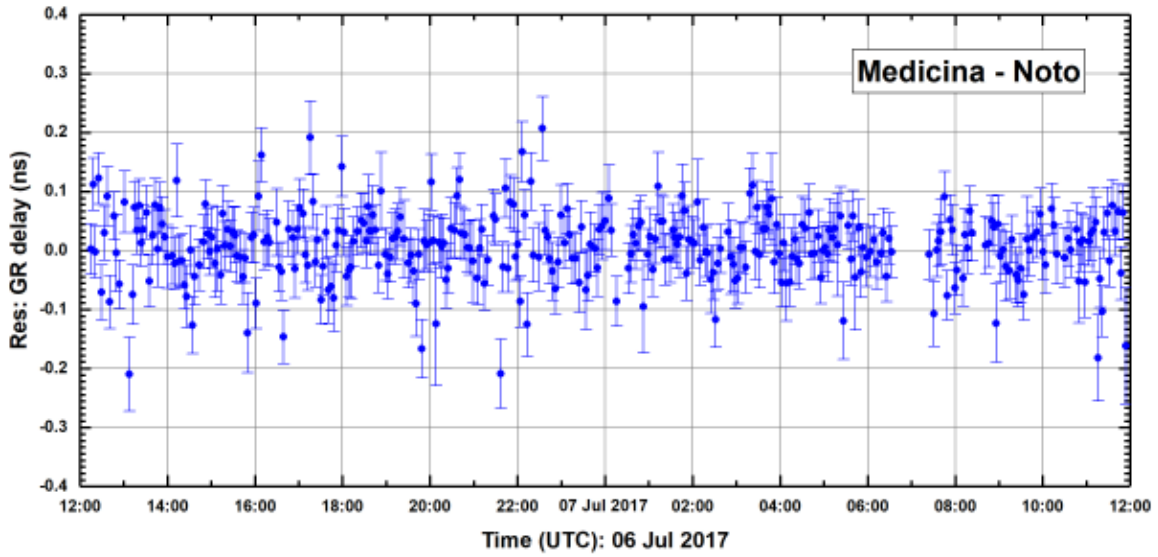

Fig. 1 Group delay residuals vs. observing time for the July 2017 experiment: Mc-Nt baseline wrms=56 ps; Full experiment wrms=46 ps.

through CALC/SOLVE with a quadratic model plus a one-hour Piece-Wise Linear continuous function with respect to the reference clock (Wettzell). These solutions were compared day-by-day with the ones obtained with GPS Precise Point Positioning, which were computed every 300 seconds and stored in the IGS repository. Before the comparison the GPS solutions were reduced to the same reference clock with the *Bernese* 5.2 software [12].

The Time Stabilty Analysis via Allan standard deviation showed σ_τ's at 1 second of comparable values between GPS and VLBI and in the range $10^{-12} - -10^{-11}$. Both VLBI and GPS present a power-law behavior in the σ vs. τ plots, with the former systematically exhibiting shallower slopes than the latter. Both VLBI and GPS slopes were also found to be shallower than the τ^{-1} expected behavior.

4 VLBI Clock Timing Tests

We performed a series of VLBI experiments to test clock timing during the months of January and February 2018. These observations involved the stations in Medicina, Noto, Matera, Yebes, Torun, and Metsahövi. Based on the work of [13] we used the interferometric phase rms noise statistics to estimate the synchronization of the station clocks. Atmospheric instabilities, gain-elevation effects, and thermal deformations of the antennas can all have degrading contributions to the inteferometric phase; therefore they should be minimized as much as possible. For these reasons the observations were carried out in the winter season on a point-like source (a bright geodetic standard calibrator: 1156+295) in 15-minute scans in three-hour runs at night time. While scheduling we also made sure that the observing target was at medium/high telescope elevations for all the antennas involved in each of the experiments in order to minimize the air mass absorption.

A summary of the observations reporting the project codes, the observing dates, the stations involved, the bands used, and whether the Medicina station was receiving or not the remote frequency standard from INRiM is provided in Table 1.

The S/X-band observations (VT001) were performed with the standard geodetic frequency set-up and bit rate. The reduction of these data is still on-going; therefore no results will be presented in this paper. The C-band observations were performed with a radio astronomical VLBI frequency set-up: the

Table 1 Summary of the VLBI clock timing observations.

Project code	Date	Stations	Band	Mc rem clock?
VT001	20180118	Mc,Nt,Ma,Ys,Mh	S/X	No
VT003	20180124	Mc,Nt,Tr	C	No
VT005	20180219	Mc,Nt,Tr	C	No
VT006	20180220	Mc,Nt,Tr,Ys	C	Yes

observing band was split into four contiguous 8-MHz wide sub-bands (IFs) of 32 frequency channels, each just below the sky frequency of 5 GHz. The data were correlated using the Bologna DiFX correlator and read into FITS files to be fringe fitted and analyzed with the radio astronomical software AIPS [14]. The data were read out from AIPS into ASCII tables, and the interferometric phase statistics were worked out scan by scan following the same scheme as in [13]: the scan samples were separated into couples (*even statistics*) and triplets (*odd statistics*), and then first differences and interpolated-value differences were computed together with their root mean square. This scheme was followed on the Right polarization RR of each sub-band and each baseline for the VT003, VT005, and VT006 experiments. For all the experiments we had a one-second sampling rate, and an 80% central band vector averaging was applied before reading out the phase ASCII tables from AIPS. The time synchronization was computed using the formula:

$$\Delta t_{\rm rms} = \frac{\Delta \phi_{\rm rms}}{2\pi \nu_0}$$

where $\Delta t_{\rm rms}$ is the rms time synchronization between clocks, $\Delta \phi_{\rm rms}$ is the interferometric phase rms noise, and ν_0 is the sky frequency at each sub-band center. The $\Delta t_{\rm rms}$ numerical values are in the range $1.1 - 1.9$ picoseconds for 15-minute scans — a result that is in good agreement with the values found by [13] on the same timescale. We also found similar statistical values for $\Delta t_{\rm rms}$ for remote and local clock set-ups for the Medicina station. Finally, the *even* statistics were found to be systematically larger than the *odd* ones within the relative error bars of 5% (*even*) and 6% (*odd*).

5 Conclusions

LIFT is an infrastructure able to deliver frequency standard signals from the Italian Institute of Metrology (INRiM) in Turin to remote locations via a fiber-optic link with unprecedented stability (Allan standard deviation of the order of 10^{-19}).

Geodetic VLBI experiments are performed with remote frequency standards provided by INRiM in Turin at the Medicina radio station with tens of picoseconds wrms residuals in group delay. This result is in good agreement with experiments utilizing local clocks.

Interferometric phase rms noise statistics were successfully used in remote and local clock timing with the radio astronomical and geodetic VLBI techniques. The results of our tests are quantitatively comparable with the ones performed by [13] that triggered our observations.

Acknowledgements

The authors thank the telescope operators in Medicina, Matera, Noto, Yebes, Torun, and Metsahövi for observing during the VLBI experiments.

References

1. C. Lisdat, G. Grosche, N. Quintin, C. Shi, S.M.F. Raupach *et al.* A clock network for geodesy and fundamental science, *Nature Communications*, 7, 1-7, doi: 10.1038/ncomms12443, 2016
2. J. Grotti, S. Koller, S. Vogt, S. Haefner, U. Sterr, *et al*. Geodesy and metrology with a transportable optical clock, *Nature Physics*, 14, 437-441, doi: 10.1038/s41567-017-0042-3, 2018
3. F. Riehle, Optical clock networks, *Nature Photonics*, 11, 25-31, doi: 10.1038/nphoton.2016.235, 2017
4. Y. He, K.G.H. Baldwin, B.J. Orr, R.B. Warrington, M.J. Wouters *et al*. Long-distance telecom-fibre transfer of a radio-frequency reference for radio astronomy, *Optica*, 5, 138, doi: 10.1364/OPTICA.5.000138, 2018
5. M. Rioja, R. Dodson, Y. Asaki, J. Harnett, S. Tingay. The impact of Frequency Standards on Coherence in VLBI at the Highest Frequencies, *Astronomical Journal*, 144, 121, doi:10.1088/0004-6256/144/121, 2012
6. D. Calonico, E.K. Bertacco, C.E. Calosso, C. Clivati, G.A. Costanzo *et al*. High-accuracy coherent optical frequency transfer over a doubled 642-km fibre link, *Appl. Phys. B*, 117, 979-986, 2014
7. C. Clivati, G.A. Costanzo, M. Frittelli, F. Levi, A. Mura, *et al.* A coherent fibre-optic link for Very Long Baseline Interferometry, *IEEE Trans on Ultrason. Ferroel. Freq. Contr.*, 62, 1907-1912, 2015

8. C. Clivati, R. Ambrosini, T. Artz, A. Bertarini, C. Bortolotti, *et al*. A VLBI experiment using a remote atomic clock via a coherent fibre link, *Nature Scientific Reports*, 7:40992, doi:10.1038/srep40992, 2017
9. A.T. Deller, S.J. Tingay, M. Bailes, C. West, DiFX: A Software Correlator for VLBI Using Multiprocessor Computing Environments, *Publications of the Astronomical Society of the Pacific*, 119, 318-336, doi: 10.1086/513572, 2007
10. R. Cappallo, HOPS fourfit users manual Version 1.0, HOPS web page: https://www.haystack.mit.edu/tech/vlbi/hops.html
11. S. Bolotin, K. Baver, J. Gipson, D. Gordon, D. MacMillan. "The VLBI Data Analysis Software *v*Solve: Development Progress and Plans for the Future", In D. Behrend, K. D. Baver and K.L. Armstrong editors, International VLBI Service for Geodesy and Astrometry 2014 General Meeting Proceedings, Science Press (Beijing), pages 253-257, ISBN 978-7-03-042974-2, 2014
12. R. Dach, S. Lutz, P. Walser, P. Fridez editors. "Bernese GNSS Software Version 5.2. User manual", Astronomical Institute, University of Bern, Bern Open Publishing. DOI: 10.7892/boris.72297; ISBN: 978-3-906813-05-9, 2015
13. P. Krehlik, L. Buczek, J. Kolodziej, M. Lipiński, L. Śliwczyński *et al*. Fibre-optic delivery of time and frequency to VLBI station, *Astronomy & Astrophysics*, 603, 48, doi:10.1051/0004-6361/201730615, 2017
14. E. Greisen and A. Heck, editors, "AIPS, the VLA, and the VLBA", Information Handling in Astronomy - Historical Vistas: p. 114, 2003 AIPS web page: http://http://www.aips.nrao.edu/index.shtml

A GPS-Based Study to Improve the Accuracy of Local Geodetic Ties at Co-located Sites that Exploits Small-Scale Atmospheric Structure

Dhiman Mondal [1], Pedro Elosegui [1], James Davis [2], Zuheir Altamimi [3], Virgílio B. Mendes [4]

Abstract The development of the next-generation of very long baseline interferometry (VLBI) systems, known as VLBI Global Observing System (VGOS), is well underway. Co-location of VGOS stations with instruments from the other space geodetic techniques (i.e., GPS, SLR, and DORIS) is essential for synergistic, robust global reference frame realization. The local ties between reference points of geodetic instruments at co-location sites effectively connect the various techniques together. Precise ties are required for a multi-technique reference frame that is suitable for high-accuracy geophysical applications such as global sea-level change. Unfortunately, the uncertainties of local tie vectors remain above 3 mm. We are investigating approaches that could improve the accuracy of relative positions estimates of the co-location sites. These approaches use external constraints based on local atmospheric structure at core geodetic sites where multi-techniques are co-located. The challenge is to add information to the geodetic solution based on our knowledge of atmospheric structure without biasing the estimates of the intersite vectors. Here, we present preliminary results from tests wherein atmospheric structure is used to enhance the strength of geodetic solutions and combinations. In this study, we use data from existing small-scale GPS networks as a proxy for co-location sites instrumented with next-generation geodetic systems.

1. MIT Haystack Observatory, Westford, MA 01851
2. Lamont-Doherty Earth Observatory, Palisades, NY 01964
3. Institut National de l'Information Géographique et Forestière (IGN), Paris, France
4. IDL, Faculdade de Ciências da Universidade de Lisboa, Lisbon, Portugal

Keywords GPS, VGOS, ITRF, atmospheric constraints

1 Introduction

Improving the accuracy and stability of the Terrestrial Reference Frame (TRF) is critical to determine precise locations on the dynamic earth that meets the scientific standard [1]. The benefit of the scientific observations would be significantly reduced without an accurate and stable TRF [2]. An ITRF is estimated using four major geodetic techniques: Very Long Baseline Interferometry (VLBI), Global Navigation Satellite System (GNSS), Satellite Laser Ranging (SLR), and Doppler Orbitography and Radiopositioning Integrated by Satellite (DORIS). To establish an accurate and stable TRF, the local geodetic ties can be one of the limiting sources of error, since determining the ties between two different techniques can be challenging due to limited accessibility of station reference points [3]. Thus, during the combination of the recent ITRF (e.g., ITRF 2014), the discrepant local ties were downweighted and space geodetic techniques were given more weight [3]. Space geodetic techniques deal with the timing of electromagnetic signals. The atmosphere slows down, bends the signal path, and causes atmospheric refraction, which was studied for single sites in many locations. Yet, ITRF-like solutions do not take into account the known atmospheric structure. Adding atmospheric constraints have the potential to improve the solution significantly. Improved agreement between space geodetic techniques at core geodetic sites (Figure 1) and local ties could help estimating a more robust and accurate future ITRF.

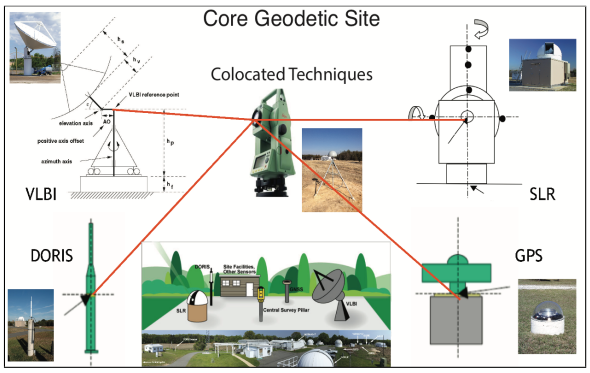

Fig. 1 An example of a core geodetic site with multiple geodetic techniques.

2 Objectives

This paper investigates approaches to improve the accuracy of site position estimates using external constraints (Figure 2). The constraints are generally based on the stochastic and systematic disturbance of the atmosphere at core geodetic sites. Here, we only focused on a GPS-based study because of the data availability and simplicity. We assumed the co-located GPS stations as a proxy for multiple co-located techniques. We will develop a software to read GAMIT [4] normal equations and impose atmospheric constraints incorporating other techniques in the future.

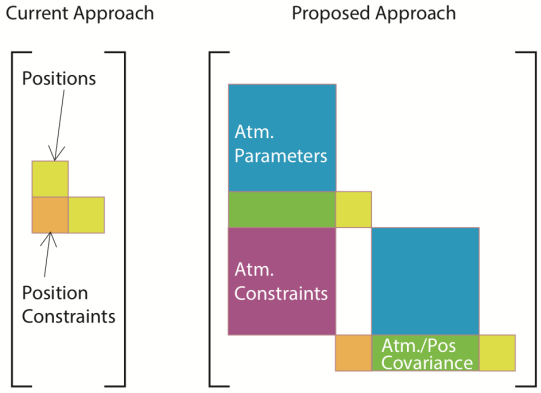

Fig. 2 Covariance Matrix of Geodetic Analysis. Left: Current approach – position parameters (yellow) at core sites are uncorrelated before local-tie constraints (orange) are applied. Right: Proposed approach – position parameters (yellow) are further constrained by atmosphere constraints (purple) applied to local atmosphere parameters (blue) via covariance with position parameters (green).

3 Data and Methods

To test our hypothesis, we selected two core geodetic sites, GGAO and Wettzell, with co-located GPS stations (Figure 3). The inter-station baselines at the core sites are 0 m to 140 m and the baseline between GGAO and WETT is 6500 km. We have used eight stations from both networks; GODE, GODN, GODS, and GODZ from the GGAO network, and WTZA, WTZR, WTZS, and WTZS from the WETT network. Among these stations, GODE and GODZ share the same GPS antenna and form a zero baseline, which provides an opportunity to test and validate our results.

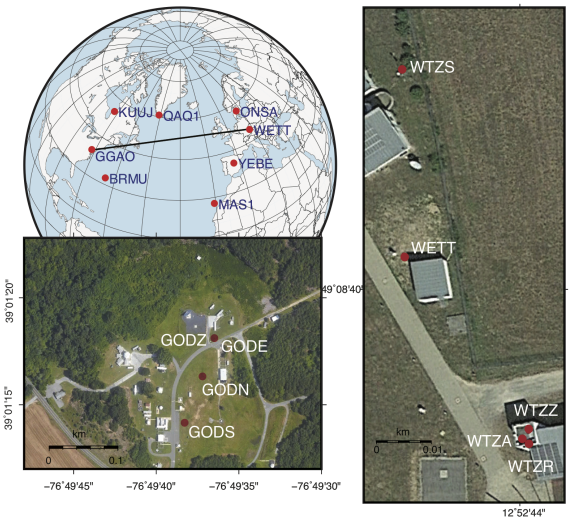

Fig. 3 GPS stations from GGAO (left) and WETT (right) used in this analysis.

We have processed these eight stations in the GAMIT GPS processing software [4]. Six other IGS stations (BRMU, MAS1, YEBE, ONSA, KUUJ, and QAQ1) were used as reference stations to stabilize the solution. The daily normal equations resulting from GAMIT were saved with both position and atmospheric parameters such as zenith delay and gradient as well as their fully populated covariance matrices. We have developed a software to read the normal equations and imposed simple atmospheric constraints on the local baseline using the constrained least squares method. The constraints are based on the local atmospheric structures (e.g., Kolgomorov-type turbulence and frontal systems). The result between

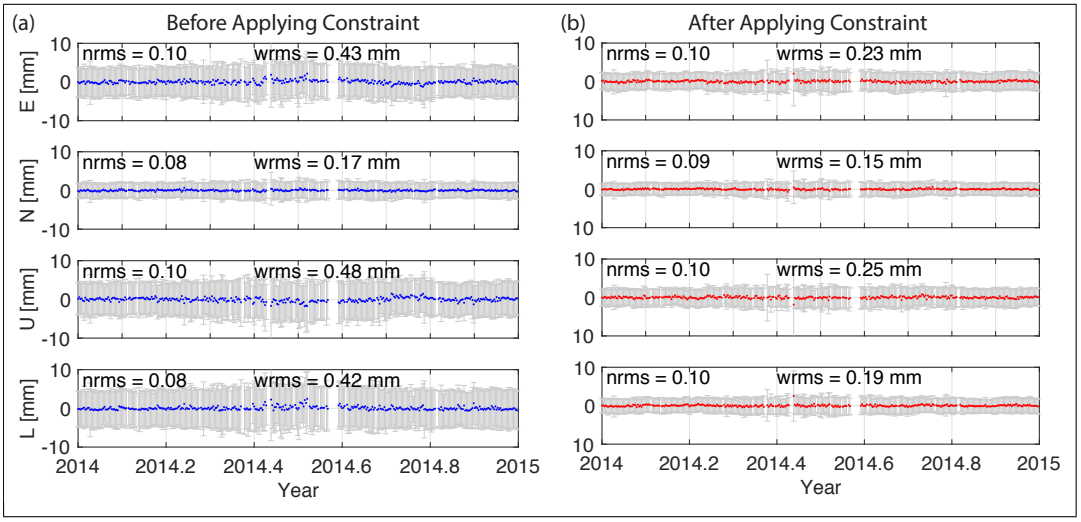

Fig. 4 GODE–GODZ (zero baseline) baseline scatter plot. a) Baseline scatter before applying atmospheric constraints, and b) Baseline scatter after applying atmospheric constraints.

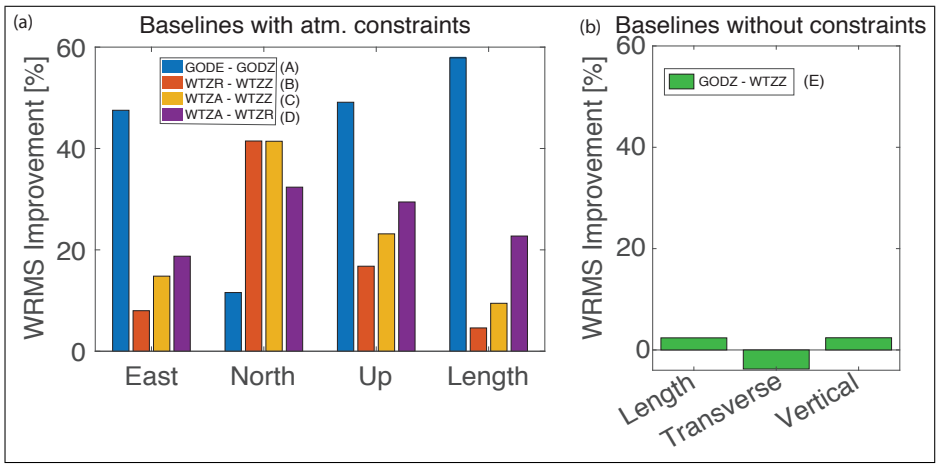

Fig. 5 a) Baselines with atmospheric constraints. b) Baseline without atmospheric constraints.

the constrained and non-constrained solutions were assessed whether it has any impact on baselines and their components.

4 Effect of Atmospheric Constraints on Geodetic Solutions

Here, we constrained the zenith total delay and multiple zenith delay differences between GODE and GODZ to be zero (Figure 4). This represents a ground-truth test because the two stations share the same GPS antenna; hence, it is a zero-baseline length. Similar constraints were applied to WTZA, WTZR, and WTZZ, because being only 1–3 m apart in practice they share the same atmosphere (Figure not shown here; summary is in Figure 5). We have compared the scatter of baseline component estimates before and after applying atmospheric constraints, and calculated in topocentric (i.e., east, north, and up) and baseline-centric (length, transverse, and vertical) coordinates for short and long baselines, respectively. Figure 4 shows that the baseline scatter of east, north, and up, and the length component between GODE and GODZ reduced by 50% after applying constraining the zenith total delay difference to be zero.

5 Conclusion and Future Steps

Our initial test suggests that adding atmospheric constraints into the combination reduced the scatter of topocentric baseline component and length estimates. In the future, we plan to analyze the multi-year solutions, incorporating data from the other geodetic techniques, and adding atmosphere constraints from meteorology and atmospheric dynamics.

Acknowledgements

This work is supported under NASA Space Geodesy Research Program award 16-SGR16-0002.

References

1. Committee on the Decadal Survey for Earth Science and Applications from Space, Space Studies Board, Division on Engineering and Physical Sciences, and National Academies of Sciences, Engineering, and Medicine, Thriving on Our Changing Planet: A Decadal Strategy for Earth Observation from Space. Washington, D.C.: National Academies Press, 2018.
2. G. Blewitt et al., Geodetic Observations and Global Reference Frame Contributions to Understanding Sea-Level Rise and Variability, in Understanding Sea-Level Rise and Variability, J. A. Church, P. L. Woodworth, T. Aarup, and W. S. Wilson, Eds. Oxford, UK: Wiley-Blackwell, 2010, pp. 256–284.
3. Z. Altamimi, P. Rebischung, L. Métivier, and X. Collilieux, ITRF2014: A new release of the International Terrestrial Reference Frame modeling nonlinear station motions: ITRF2014, Journal of Geophysical Research: Solid Earth, vol. 121, no. 8, pp. 6109–6131, Aug. 2016.
4. T. A. Herring, R. W. King, M. A. Floyd, and S. C. McClusky, Introduction to GAMIT/GLOBK, p. 50, 2015.

Comparison of Processing Strategy for Time and Frequency Transfer Using GNSS

Ryuichi Ichikawa [1], Hideki Narita [1], Yuka Miyauchi [2], Tadahiro Goto [1], Kuniyasu Imamura [1], Jun Amagai [3]

Abstract We have tested GNSS data processing for time and frequency (T&F) transfer prior to performing international VLBI T&F transfer experiments between two lattice clocks operated by INRIM (Italy) and NICT (Japan). Modified Allan deviation values show that precise point positioning (PPP) with ambiguity resolution (PPP-AR) and PPP by a Japan Aerospace Exploration Agency (JAXA) GNSS processing tool, MALIB, perform similarly with best-case one-day instabilities on the order of 10^{-15} for the Koganei–Medicina baseline. Although further investigation is required to evaluate the PPP-AR technique, preliminary results imply that this technique is sufficient for validating the international VLBI experiments between INAF and NICT for the comparison of two lattice clocks.

Keywords Time and frequency transfer, GNSS, PPP, IPPP, PPP-AR

1 Introduction

The National Institute of Information and Communications Technology (NICT) is planning to perform international frequency-transfer experiments using compact VLBI systems equipped with a broadband receiver during FY2018. The 34-m Kashima and 2.4-m Koganei antennas of NICT and another 2.4-m antenna system will be used in the experiments. We have already installed the latter antenna system at the Medicina Radio Astronomy Station of Italy in August 2018, near the 32-m antenna. The primary aim of the experiments is to perform a direct remote comparison of two optical lattice clocks, an *Yb* clock operated at the Istituto Nazionale di Ricerca Metrologica (INRIM), Turin, and a *Sr* clock of NICT, Koganei, as shown in Figure 1.

We will perform precise frequency transfer measurements using GNSS on the NICT-INAF baseline in order to validate and evaluate the VLBI experiments. We describe preliminary results in this short paper.

2 GNSS Time and Frequency Transfer

The time-transfer accuracy of VLBI experiments will be verified by comparison with that of an independent technique using the GNSS. Time and frequency (T&F) transfer using the GNSS code and carrier phase observations are popular techniques for precise clock comparisons. In particular, GNSS data processing based on precise point positioning (PPP), which is the standard technique for geodetic applications, allows highly precise T&F comparisons between remote clocks. PPP least-squares solutions showed improved stability relative to traditional GPS time synchronization methods such as the common-view GPS, reaching a stability of a few parts in 10^{-15} for an averaging time of one day [2].

3 Analysis

The conventional PPP processing strategy has treated the phase ambiguities of GNSS signals as float val-

1. National Institute of Information and Communications Technology (NICT)
2. Kashima Space Technology Center, NICT
3. Okinawa Electromagnetic Technology Center, NICT

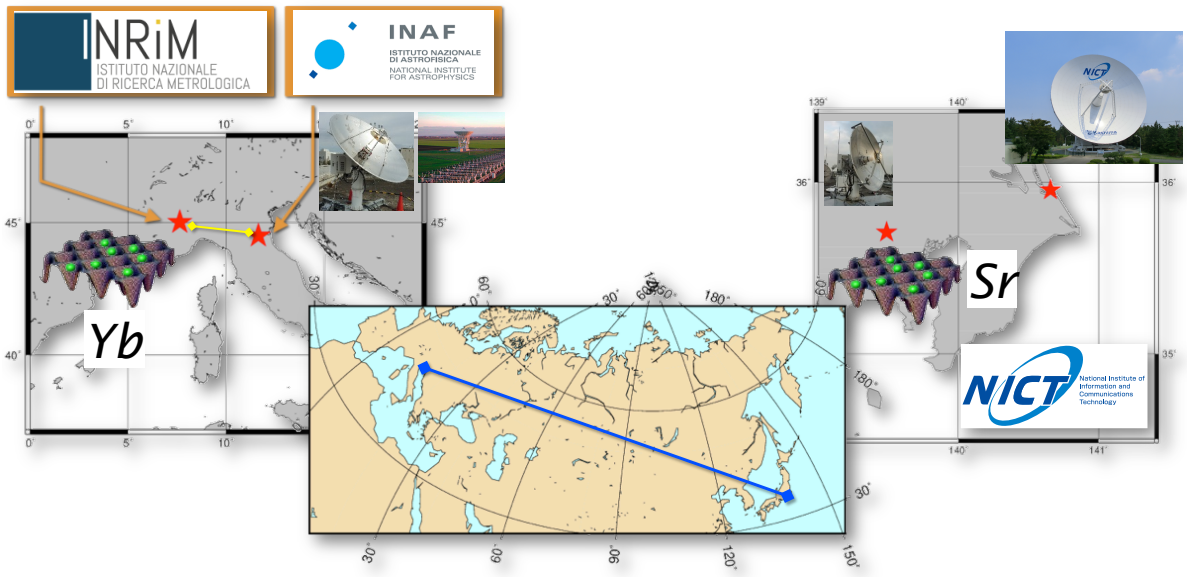

Fig. 1 Planned international VLBI experiments to link two optical lattice clocks on the INAF–NICT baseline. The *Yb* lattice clock at INRIM is linked to the clock at INAF via an optical fiber link.

ues. However, we have to take into account the integer-cycle nature of the phase ambiguities in order to overcome the current limitations of GPS for clock comparisons [3]. In recent years, new GNSS PPP processing tools that implement an integer carrier phase ambiguity resolution (AR) have been developed and used in practical applications. This technique is called PPP-AR or IPPP (PPP with integer ambiguity resolution). We have carried out time-transfer comparisons using GNSS in order to evaluate the performance of PPP-AR before the international VLBI T&F experiments involving Medicina and Koganei.

Table 1 Processing setting.

(legend in Figures 2–4)	Software	Orbit	Ambiguity Resolution
PPP-Wizard/AR	PPP-Wizard	GRG	Yes
PPP-Wizard/PPP (GRG)	PPP-Wizard	GRG	No
PPP-Wizard/PPP (IGS)	PPP-Wizard	IGS	No
MALIB/PPP-AR	MALIB	JXF	Yes
MALIB/PPP	MALIB	JXF	No

The GNSS data sets obtained from April 8 to May 10, 2017 were processed using two PPP-AR processing tools, namely, MALIB (MADOCA PPP Library) developed by the Japan Aerospace Exploration Agency (JAXA) and PPP-Wizard (PPP with integer and zero-difference ambiguity resolution demonstrator) developed by the Centre National d'Études Spatiales (CNES). We have used IGS and GRG products (precise orbit, satellite clock, and earth rotation parameters) for PPP-Wizard processing. In MALIB processing, we have used MADOCA products (precise orbit, satellite clock, and fractional cycle bias (FCB) data).

4 Results

Figure 2 depicts clock differences from each GPS analysis of the Koganei (NICT)–Medicina (INAF) baseline. Similar variations for both MALIB results (PPP-AR and PPP) are observed. The amplitude and phase of two variations are almost identical. On the other hand, all PPP-Wizard results show unknown diurnal signatures and offsets. The cause of these signatures is under investigation at present.

Modified Allan deviation (MDEV) values were derived for each GPS data processing in order to estimate the frequency link stability. Figure 3 depicts the results for the Koganei (NICT)–Medicina (INAF) baseline, while Figure 4 depicts the results for Koganei (NICT)–KRIS (KRISS: Korea Research Institute of Standards and Science). Fujieda et al. already demon-

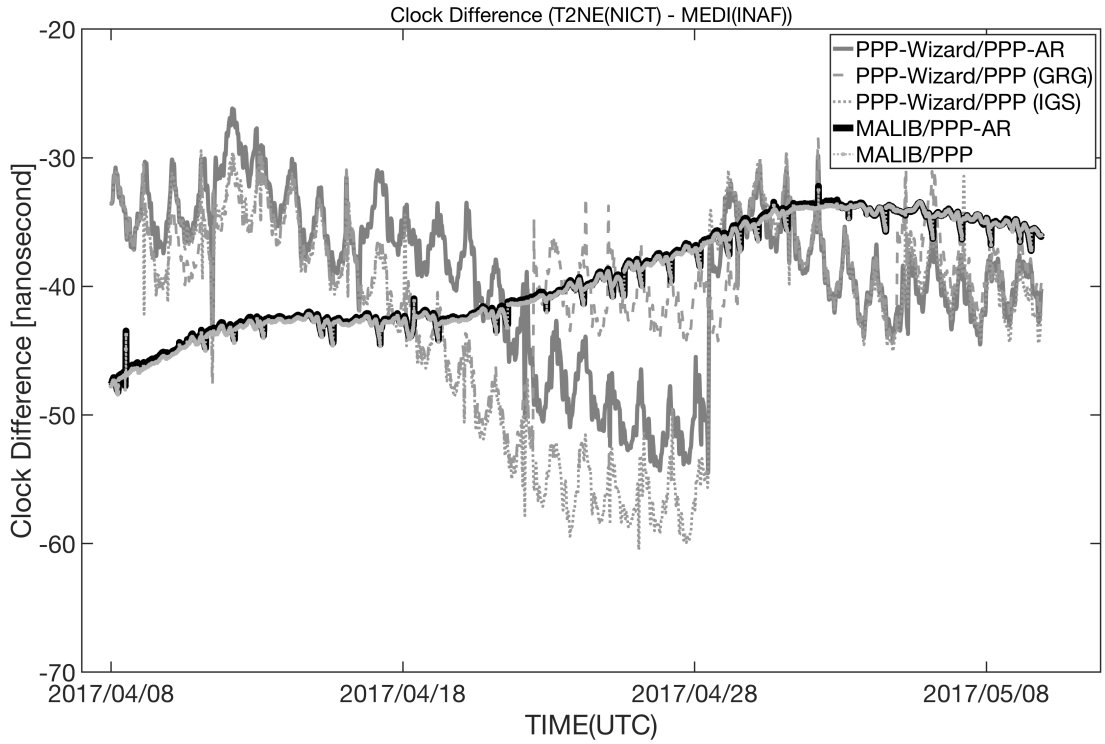

Fig. 2 Difference between UTC(NICT) and INAF clocks (MEDI).

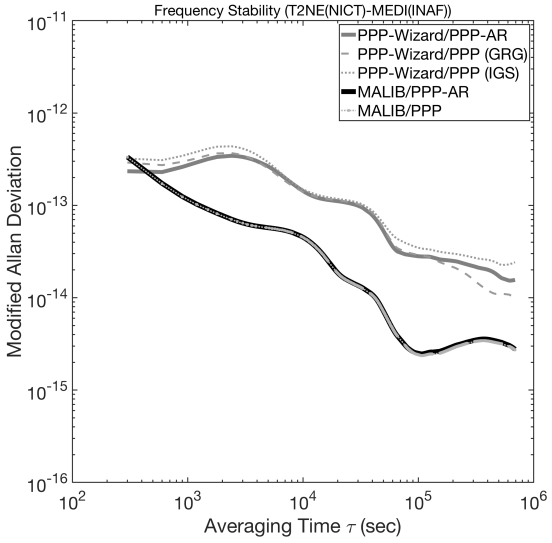

Fig. 3 Modified Allan deviation (MDEV) plot for frequency link over NICT–INAF (MEDI) using GNSS.

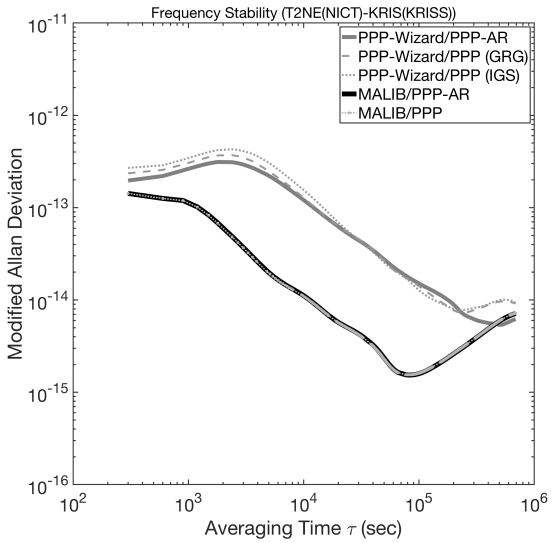

Fig. 4 A MDEV plot for frequency link over NICT–KRISS using GNSS.

strated that two-way carrier-phase satellite frequency transfer (TWCP) and IPPP have superior long-term stability between NICT and KRISS [4].

Both results show that PPP-AR and PPP by MALIB perform similarly with best case one day instabilities on the order of 10^{-15}. On the other hand, MDEV val-

ues obtained by PPP-Wizard processing were much worse and one day instabilities were on the order of less than 10^{-14}.

5 Conclusions

We have tested GNSS data processing for time and frequency (T&F) transfer prior to performing international VLBI T&F transfer experiments between two lattice clocks operated by INRIM (Italy) and NICT (Japan). Modified Allan deviation values obtained by the MALIB GNSS processing tool of JAXA show that both PPP-AR and PPP processing perform similarly with best case one day instabilities on the order of 10^{-15} for the Koganei–Medicina baseline. Preliminary results imply that this technique is sufficient for validating the international VLBI experiments between INAF and NICT for the comparison of two lattice clocks at NICT and INRIM. Although a superior stability by IPPP is not shown in our results, further investigation is required to evaluate PPP-AR.

6 Outlook

We will process the data sets using both the CSRS-PPP tool developed by Natural Resources Canada and the C5++ tool developed by NICT, Hitotsubashi University, and JAXA [1]. In addition, the international VLBI experiments between INAF and NICT have already started in early October 2018. The comparison results between two lattice clocks on the intercontinental baseline using GNSS and VLBI will be reported in the next fiscal year.

Acknowledgements

We thank JAXA for providing MALIB and related data sets and CNES for providing PPP-Wizard.

References

1. Hobiger et al., “Fully automated VLBI analysis with c5++ for ultra-rapid determination of UT1”, Earth Planets Space, vol. 45, no. 2, pp. 75–79, 2010.
2. Lahaye et al., “GNSS geodetic techniques for time and frequency transfer applications”, Advances in Space Research, 47, 253–264, doi:10.1016/j.asr.2010.05.032, 2011.
3. Petit et al., “1×10^{-16} frequency transfer by GPS PPP with integer ambiguity resolution”, Metrologia, 52. 301–309, doi:10.1088/0026-1394/52/2/301, 2015.
4. Fujieda et al., “Advanced Satellite-Based Frequency Transfer at the 10^{-16} Level”, IEEE Transactions on Ultrasonics, Ferroelectrics, and Frequency Control, Vol.65, Issue 6, DOI: 10.1109/TUFFC.2018.2821159, 2018.

Author Index

Author Index